

Sterile Neutrinos in Cold Climates

by

Benjamin J.P. Jones

Submitted to the Laboratory for Nuclear Science
in partial fulfillment of the requirements for the degree of

Doctor of Philosophy in Physics

at the

MASSACHUSETTS INSTITUTE OF TECHNOLOGY

September 2015

© Massachusetts Institute of Technology 2015. All rights reserved.

Author
Laboratory for Nuclear Science
August 26, 2015

Certified by
Janet M. Conrad
Professor of Physics
Thesis Supervisor

Accepted by
Nergis Mavalvala
Associate Department Head

Sterile Neutrinos in Cold Climates

by

Benjamin J.P. Jones

Submitted to the Laboratory for Nuclear Science
on August 26, 2015, in partial fulfillment of the
requirements for the degree of
Doctor of Philosophy in Physics

Abstract

Measurements of neutrino oscillations at short baselines contain an intriguing set of experimental anomalies that may be suggestive of new physics such as the existence of sterile neutrinos. This three-part thesis presents research directed towards understanding these anomalies and searching for sterile neutrino oscillations.

Part I contains a theoretical discussion of neutrino coherence properties. The open-quantum-system picture of neutrino beams, which allows a rigorous prediction of coherence distances for accelerator neutrinos, is presented. Validity of the standard treatment of active and sterile neutrino oscillations at short baselines is verified and non-standard coherence loss effects at longer baselines are predicted.

Part II concerns liquid argon detector development for the MicroBooNE experiment, which will search for short-baseline oscillations in the Booster Neutrino Beam at Fermilab. Topics include characterization and installation of the MicroBooNE optical system; test-stand measurements of liquid argon optical properties with dissolved impurities; optimization of wavelength-shifting coatings for liquid argon scintillation light detection; testing and deployment of high-voltage surge arrestors to protect TPC field cages; and software development for optical and TPC simulation and reconstruction.

Part III presents a search for sterile neutrinos using the IceCube neutrino telescope, which has collected a large sample of atmospheric-neutrino-induced events in the 1-10 TeV energy range. Sterile neutrinos would modify the detected neutrino flux shape via MSW-resonant oscillations. Following a careful treatment of systematic uncertainties in the sample, no evidence for MSW-resonant oscillations is observed, and exclusion limits on 3+1 model parameter space are derived. Under the mixing assumptions made, the 90% confidence level exclusion limit extends to $\sin^2 2\theta_{24} \leq 0.02$ at $\Delta m^2 \sim 0.3 \text{ eV}^2$, and the LSND and MiniBooNE allowed regions are excluded at >99% confidence level.

Thesis Supervisor: Janet M. Conrad
Title: Professor of Physics

Sterile Neutrinos in Cold Climates

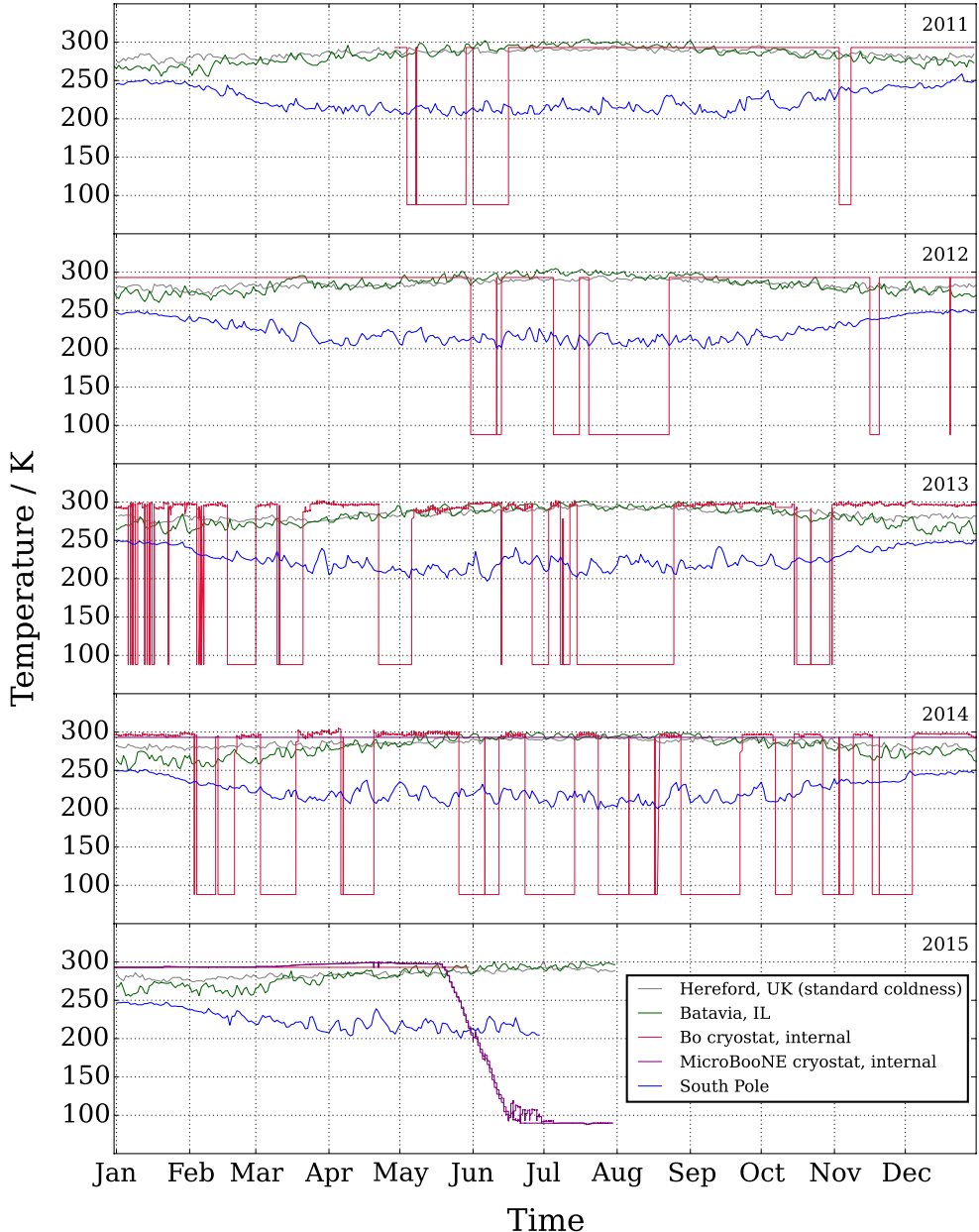


Figure 0-1: Temperature vs. time in several locations that feature prominently in this thesis. Hereford, UK provides the reference coldness against which other climates are compared. Mean daily temperature data for Hereford, Batavia and the South Pole are from the Hereford Credenhill weather station, the Dupage Airport weather station and the Amundsen Scott base respectively. Temperature data for the Bo test stand from 2011, 2012 and 2015 are inferred from liquid level monitor logs, and for 2013-2014 from a thermocouple inside the cryostat. MicroBooNE internal temperatures are from RTDs at the top and bottom of the cryostat.

Acknowledgments

It is no overstatement to say that one of the best decisions I have ever made was to join Janet Conrad’s research group at MIT. Whatever my scientific future holds, I will always be indebted to Janet for the formative experience of learning to be a scientist under her supervision. I firmly believe there to be no better physics PhD experience in the world than in the Conrad group, and I am very grateful for the all opportunities, encouragement and resources that being Janet’s student has afforded me.

It is also no overstatement to say that *the* best decision I have ever made was to marry my wife, Clementine. Nothing in this thesis would have been possible without your love, your patience and your support. And, of course, your proofreading. Thank you for accompanying me on this adventure, and the many more to come.

It is impossible to thank here everybody who has had a positive impact on my life and work over the last six years. But to give it my best shot, I’ll start by thanking all members of the MicroBooNE collaboration, all members of the IceCube collaboration, and all members of the Conrad group, past and present.

Thanks to Boris Kayser, André De Gouvêa and Joachim Kopp for guidance during my forays into neutrino theory. I am grateful for all you have taught me.

I thank all the experts I have worked with and learned from during my hardware work at Fermilab. I particularly thank Stephen Pordes, whose scientific approach and deep understanding have been an inspiration to me, and whose backing has been vital to my research. Others I am privileged to have learned from include Anna Pla-Dalmau, Walter Jaskierny, Sten Hansen, Flavio Cavanna, and Henning Back. I am also fortunate to have been supported by excellent technicians, including Ron Davis, Kelly Hardin, Jennifer VanGemert, and especially Bill Miner, upon whom the successes of all of my PAB campaigns hinged, and who always got-it-done, however unreasonable “it” was.

Thank you to my IceCube co-analyzers, Jordi Serra Salvadó and Carlos Argüelles Delgado – you are excellent physicists and great friends. I also particularly thank

Francis Halzen, Christopher Weaver and Jason Koskinen for the time and effort each dedicated, in different ways, to helping me to be effective within IceCube.

In addition to those listed above, I thank Jonathan Asaadi, Tom Alexander, Ben Carls, Eric Church, Gabriel Collin, Roxanne Guenette, Christina Ignarra, Teppei Katori, Wes Ketchum, Sarah Lockwitz, Andrzej Szelc, Thomas Strauss, Jason St. John, Josh Spitz, Kazu Terao, Matt Toups and Joseph Zennamo for being great collaborators and friends throughout my time at MIT and Fermilab. It's been a blast.

To the many friends, colleagues and collaborators who are unlisted but deserve my thanks, I apologize and thank you too.

Finally I thank my parents, Phil and Jill Jones, for all you did to help me get to here, which is precisely where I always wanted to be.

Contents

Prologue	13
I Active and Sterile Neutrinos	17
1 Introduction to Part I : The Physics of Neutrinos	19
1.1 Dear radioactive ladies and gentlemen...	19
1.2 Neutrinos in and beyond the Standard Model	21
1.3 Neutrino oscillations in vacuum and matter	25
1.4 Anomalies and sterile neutrinos	30
2 The Coherence Properties of Neutrino Beams	35
2.1 Internal and external wave packets	35
2.2 Environmentally induced decoherence	40
2.3 Neutrino beams as open quantum systems	48
<i>Publication : Dynamical Pion Collapse and the Coherence of Conventional Neutrino Beams (12 p)</i>	49
II The MicroBooNE Experiment	63
1 Introduction to Part II : A Liquid Argon Time Projection Chamber in the Booster Neutrino Beam	65
1.1 Liquid argon time projection chambers	65
1.2 The MicroBooNE TPC	68
1.3 Physics goals of the MicroBooNE experiment	70

2 Development and Installation of the MicroBooNE Optical System	73
2.1 Photomultiplier tube assemblies	73
2.2 Light guide detectors	76
2.3 Flasher calibration system	77
2.4 Readout and triggering	80
2.5 Vertical slice test of the optical system	81
2.6 Installation of the MicroBooNE optical system	83
3 Studies of Scintillation Light in Liquid Argon	87
3.1 The microphysics of liquid argon scintillation light	87
3.2 The Bo liquid argon scintillation test stand	91
3.3 The effects of impurities on liquid argon scintillation light	97
<i>Publication : A Measurement of the Absorption of Liquid Argon Scintillation Light by Dissolved Nitrogen at the Part-Per-Million Level (21 p)</i>	99
<i>Publication : The Effects of Dissolved Methane Upon Liquid Argon Scintillation Light (16 p)</i>	123
4 Development of Wavelength-Shifting Coatings for LArTPCs	141
4.1 Tetraphenyl-butadiene as a wavelength shifter	141
4.2 Wavelength-shifting coatings in the MicroBooNE experiment	142
4.3 Attenuation behaviour of TPB coated light guides	146
<i>Publication : A Simulation of the Optical Attenuation of TPB Coated Light Guide Detectors (7 p)</i>	146
4.4 Photodegradation of TPB coatings	155
<i>Publication : Photodegradation Mechanisms of Tetraphenyl-Butadiene Coatings for Liquid Argon Detectors (13 p)</i>	157
5 Surge Protection Systems for LArTPCs	171
5.1 Drift field and HV supply in MicroBooNE	171
5.2 Detector robustness under dielectric breakdown	172

5.3	Surge protection for LArTPC detectors	174
	<i>Publication : Testing of High Voltage Surge Protection Devices for Use in Liquid Argon TPC Detectors (24 p)</i>	175
5.4	Demonstration of surge protection on the MicroBooNE TPC	199
6	Simulation and Reconstruction Tools for Liquid Argon Detectors	203
6.1	The LArSoft framework	203
6.2	Optical simulations	204
6.3	Optical event reconstruction	210
6.4	TPC event reconstruction	216
7	Conclusion to Part II	225
III	The IceCube Experiment	227
1	Introduction to Part III: Studying Atmospheric Neutrinos with an Ice Cherenkov Detector	229
1.1	Atmospheric neutrino detection	229
1.2	The IceCube detector	231
1.3	Properties of the deep South Pole ice	233
1.4	The IceCube atmospheric muon neutrino sample	242
1.5	The sterile neutrino signature in IceCube	246
2	Monte Carlo Simulations for the IC86 Sterile Neutrino Analysis	249
2.1	Event generation and weighting	250
2.2	Modelling light propagation	254
2.3	Detector simulation, triggering, and filtering	256
2.4	Event selection and reconstruction	257
2.5	Production of NuFSGen Monte Carlo sets	259
3	Systematic Uncertainties in the IC86 Sterile Neutrino Analysis	261
3.1	DOM efficiency uncertainty	261

3.2	Ice property uncertainties	264
3.3	Cross section uncertainties	266
3.4	Earth density uncertainties	269
3.5	Flux uncertainties	273
4	Results of the IC86 Sterile Neutrino Analysis	283
4.1	Fit procedure and sensitivity	283
4.2	Pre-unblinding tests of data sample	287
4.3	Blind results of shape-only analysis	288
4.4	Inclusion of rate information	290
4.5	Tests of systematic uncertainties	295
4.6	Frequentist cross-checks using the Feldman Cousins method	300
5	Conclusion to Part III	307

Prologue

This thesis describes work towards addressing short baseline neutrino oscillation anomalies through experimental searches for, and improved theoretical understanding of, sterile neutrinos. Here I summarize its contents, and highlight my main contributions. A starred citation [N]* indicates a publication where I am a collaborating author, and a double star [N]** indicates first/corresponding author.

Part I - Active and Sterile Neutrinos

Chapter 1 introduces to the physics of neutrinos, oscillations and short baseline anomalies, and motivates searching for sterile neutrinos. **Chapter 2** describes inconsistencies in the standard theoretical treatment of neutrino oscillations, in particular the description of neutrino beam coherence. My contribution [1]** was a theoretical reformulation of the neutrino beam using the language of open quantum systems, leading to a novel treatment of oscillations which makes quantitative predictions of neutrino coherence properties without arbitrary initial-state assumptions.

Part II - The MicroBooNE Experiment

MicroBooNE is a short baseline neutrino oscillation experiment at Fermilab, which aims to confirm or refute the MiniBooNE short-baseline anomalies. **Chapter 1** describes the detector and the principles by which it operates. **Chapter 2** gives a detailed overview of the MicroBooNE optical system [2]*, which I collaborated with fellow group members at MIT to design, characterize and install. With a colleague at the University of Bern I proposed and implemented a fiber-optic flasher system for

PMT calibration [3]*. I also assembled and operated the Bo optical test stand [4]**, and used it to make a vertical slice test of the optical system.

Chapter 3 concerns the properties of liquid argon scintillation light. The Bo test stand is described, and two measurements where I was the leading investigator are reported: 1) The first measurement of the absorption of liquid argon scintillation light by nitrogen [5]**. This result has set the purity requirements for MicroBooNE and other large liquid argon detectors. 2) The first measurement of the effects of dissolved methane on liquid argon scintillation light [6]**. This result has set the purity requirements for dark matter detectors using underground argon.

Chapter 4 discusses the development of wavelength shifting coatings. I worked on characterization and optimization of TPB coated plates and light guides [7]*[8]* for MicroBooNE; I made calculations to predict how light is attenuated in light guides that accurately reproduce its nonexponential behaviour and environmental dependencies [9]** [10]*; And I studied the photodegradation of TPB coatings [11]*, using analytic chemistry techniques to identify the decay mechanism [12]**, and creating chemical stabilization techniques which inhibit degradation and improve performance.

Chapter 5 relates to the delivery and distribution of TPC high voltage. I collaborated on tests of the electrical strength of detector elements [13]* and devised a novel field cage protection system for MicroBooNE using high voltage surge arrestors. I led a small team to test and implement the system [14]**. Similar devices are now being included in the design of future LArTPCs as a best-practice [15]*.

Chapter 6 describes my contributions to LArTPC software. I was the sole author of the LArSoft full and fast optical simulations which are used to model light production and propagation in MicroBooNE, LArIAT, SBND and DUNE; I wrote the LArSoft FlashFinder and collaborated on cosmic ray rejection tools; And I developed TPC reconstruction algorithms including seed finding and bezier tracking, which provide curved 3D track finding within LArSoft.

Chapter 7 concludes Part II with a brief discussion of the status of the MicroBooNE experiment at the time of submitting this thesis.

Part III - The IceCube Experiment

The IceCube experiment is a one gigaton neutrino telescope at the South Pole, designed to search for astrophysical neutrinos. It has also collected a large sample of atmospheric neutrinos. Part III of this thesis presents the first search for sterile neutrinos through MSW-resonant oscillations at IceCube. I was one of the leading analyzers, along with Carlos Argüelles Delgado and Jordi Serra Salvadó at UW Madison. **Chapter 1** introduces the detector, the analysis sample, and the sterile neutrino signal.

Chapter 2 presents simulation tools which were developed for the analysis. I collaborated to develop the NuFSGen system, which allows consistent treatment of oscillations and neutrino evolution systematics via reweighting. I also produced and validated all of the simulation samples used in the analysis.

Chapter 3 discusses systematic uncertainties, which must be carefully controlled due to the subtle nature of the shape effect being probed. I contributed to the treatments of DOM efficiency, ice property, earth density, neutrino cross section and atmospheric neutrino flux systematic uncertainties used in the analysis.

Chapter 4 presents the results of the search, which my collaborators and I unblinded in May 2015. The fit procedure is described and the sensitivity is presented. The unblinded data are shown and an exclusion limit on MSW-resonant sterile neutrino oscillations is derived. An extension of the analysis from shape-only to rate+shape, and detailed post-unblinding checks of the systematic uncertainties are discussed. Finally, a validation of the result using the Feldman Cousins method is described.

Chapter 5 concludes Part III. A discussion of the significance of the analysis results in the context of world data is given, and prospects for future work are summarized.

Part I

Active and Sterile Neutrinos

Chapter 1

The Physics of Neutrinos

1.1 Dear radioactive ladies and gentlemen...

Wolfgang Pauli is credited with coining the phrase “not even wrong” to disparage untestable theories. In 1930 he proposed to solve two problems in particle physics with what he believed to be an untestable hypothesis. Pauli suggested that an unobserved particle, that he named the neutron, could both explain the anomalous spin-statistics of nitrogen and lithium nuclei and fix the apparent momentum non-conservation of nuclear beta decays [16]. Pauli’s original hypothesis was not “not even wrong”; in fact, it was demonstrably wrong. In 1932 James Chadwick discovered the agent which solved the spin-statistics problem [17], which had a mass similar to that of the proton, disqualifying it from solving the problem of beta decay kinematics. However, it would transpire that Pauli’s prescient suggestion of an invisible momentum-carrying particle emitted in beta decay was correct. In 1956, the unobservable particle, renamed the neutrino, was observed.

Using Enrico Fermi’s theory of the weak interaction [18], Hans Bethe and Rudolf Pierls calculated the interaction cross section of the neutrino on a nucleon, concluding that “there is no practically possible way of detecting the neutrino”[19]. Bruno Pontecorvo disagreed, proposing an experiment where neutrinos produced by a nuclear reactor could be detected by the neutrino-induced transformation $^{37}\text{Cl} \rightarrow ^{37}\text{Ar}$ in a large liquid volume [20]. Ray Davis performed this experiment at the Brookhaven

National Laboratory test reactor, and detected nothing [21]. His detector was insensitive to the reactor flux because of the then unknown non-equivalence of neutrinos and antineutrinos.¹ Fred Reines and Clyde Cowan performed a similar experiment with a different detection technology, this time sensitive to antineutrinos. The Project Poltergeist experiment at Savannah River detected the characteristic double-flash signature of inverse beta decays in liquid scintillator, providing the first direct observation of the electron antineutrino in 1956 [22], [23].

The radiochemical detector proposed by Pontecorvo and pioneered by Davis, which had failed to discover the neutrino, would still successfully revolutionize neutrino physics. In the late 1960s/early 1970s, Davis measured the solar neutrino flux by operating a 400,000-liter C_2Cl_4 detector at the 4850 ft level of the Homestake mine in Lead, South Dakota [24]. His result was discrepant with John Bahcall's precise predictions of solar neutrino production [25] by a factor of greater than two. The story of the solar neutrino problem is a long and fascinating one [26]. Its conclusion, finally confirmed by the Kamiokande experiment (1987 to 1995)[27], and the SAGE [28] and GALLEX [29] experiments in the 1990s, was that neutrinos change flavor as they cross the sun. The phenomenon of neutrino oscillation, to which this flavor change could be attributed, had been first postulated by Pontecorvo in 1957 [30], [31]. The extension of the formalism of oscillations in the presence of a matter potential such as the sun was devised by Lincoln Wolfenstein in 1977 and independently by Stanislav Mikhayev and Alexei Smirnov in 1986 [32]–[35].

The fact that neutrinos oscillate demonstrates that 1) they are massive and 2) they mix nontrivially. Such neutrinos can be incorporated into the Standard Model of particle physics, described in the next section, with a minimal extension. The recent history of neutrino physics has been primarily concerned with testing this extension and measuring its free parameters.

¹Technically, if the neutrino is a Majorana particle, the correct interpretation is helicity conservation in the parity-violating weak interaction rather than $\nu \neq \bar{\nu}$ (Section 1.2)

1.2 Neutrinos in and beyond the Standard Model

The particle content of the Standard Model

The Standard Model of particle physics is a Lorentz invariant quantum field theory with a gauge symmetry $SU(3) \times SU(2)_L \times U(1)$ which is spontaneously broken via the Higgs mechanism, through $SU(2) \times U(1) \rightarrow U(1)$.

From this information, the bosonic content of the minimal theory is specified. After symmetry breaking, uncharged massless photons mediate electromagnetic interactions; massless self-interacting gluons mediate strong interactions; massive W^\pm and Z bosons, with electric charge ± 1 and 0, respectively, mediate weak interactions; and a massive scalar Higgs boson interacts with all particles which acquired mass through the Higgs mechanism, with a coupling proportional to that mass.

Specifying the fermionic content of the model requires additional information. It is necessary to state how many fermions there are, in which representations of the gauge groups they fall, and with what charges. The $SU(3)$ assignment is straightforward. There are six quarks belonging to the fundamental representation of $SU(3)$ and six leptons which are singlets. The representations and charges in the electroweak sector $SU(2) \times U(1)$ are more complicated. The left-handed fermions are arranged into dou-

The figure consists of two parts. On the left is a grid of boxes listing the properties of various particles. The columns are labeled QUARKS, LEPTONS, and GAUGE BOSONS. The rows are labeled by particle type: u, c, t (up quarks); d, s, b (down quarks); e, mu, tau (leptons); nu_e, nu_mu, nu_tau (neutrinos); and g, gamma, Z, W (gauge bosons). Each box contains the particle name, its charge, mass, and spin. On the right is a table showing the weak isospin (T_3) and hypercharge (Y_W) assignments for each fermion. The fermions are listed in three rows: up quarks (u_L, d_L), down quarks (u_R, d_R), and leptons (e_L, ν_L , e_R). The gauge bosons are listed separately.

Fermion	$SU(3)$ Rep	$SU(2)$ Rep	T_3	Y_W
$(\begin{array}{c} u_L \\ d_L \end{array})$	3	2	$\pm 1/2$	$1/3$
u_R	3	1	0	$4/3$
d_R	3	1	0	$-2/3$
$(\begin{array}{c} e_L \\ \nu_L \end{array})$	1	2	$\pm 1/2$	-1
e_R	1	1	0	-2

Figure 1.1.1: Particle content of the Standard Model. Left: table of all Standard Model particles, listing mass, spin and charge, from [36]. Right: weak isospin and hypercharge assignments for fermions in the unbroken theory.

plets of $SU(2)$, whereas the right-handed fermions are $SU(2)$ singlets. Each particle can be labelled in terms of its weak isospin as (T_W, T_3) , and a $U(1)$ weak hypercharge Y_W . The electromagnetic charge after symmetry breaking is related to the charges of the unbroken theory by the Gell Mann-Nishijima relation, $Q = T_3 + \frac{1}{2}Y_W$. The right-handed neutrino is decoupled. This particle content is shown in Figure 1.

There are three generations of fermions with equivalent charge assignments. Each of the six quarks and three charged leptons has a different mass, determined by its Yukawa coupling to the Higgs field. Neutrinos are defined to be massless. The weak charged-current interaction in the quark sector is non-diagonal in the mass basis, so induces flavor mixing. In the lepton sector, the massless neutrino fields can be redefined to diagonalize the interaction, making leptonic mixing unphysical.

The masses, charges, representations and number of generations of fermions are determined experimentally, and it is not presently known whether there is an underlying principle which explains their values. The assignments within the Standard Model are notable in that they lead to a cancellation of the one-loop perturbative triangle anomaly (a condition for renormalizability of the theory). The addition of sterile neutrinos, uncharged under any gauge group, has the convenient property that this cancellation is not affected.

The Standard Model exhibits accidental conservation laws, including perturbative baryon (B) and lepton (L) number, anomalously broken to $B+L$, which may be further broken at high scales by new physics. The Standard Model also displays accidental conservation of electron, muon and tau number. These conservation laws are already known to be broken by beyond-standard-model (BSM) physics: specifically, by the existence of massive neutrinos.

Incorporating massive neutrinos into the Standard Model (SM)

Each SM fermion which is not a neutrino is represented by a Dirac spinor field. The four-component Dirac spinor ψ_D can be decomposed into left- and right-handed two-component spinors, via $\chi_{R/L} = (1 \pm \gamma_5)\psi_D$. These are eigenstates of chirality (Lorentz invariant). For massless fermions, chirality is equivalent to helicity (conserved). Mass

can be introduced via the Dirac term, which couples the left and right chiral fields:

$$L_D = m_D \bar{\psi}_D \psi_D = m_D (\bar{\chi}_L \chi_R + \bar{\chi}_R \chi_L). \quad (1.1)$$

This explicitly breaks chirality symmetry and renders helicity non-Lorentz-invariant. The Dirac term can be generated through the Higgs mechanism, where the mass, m_D , is set by the Higgs coupling strength. Massive neutrinos can be incorporated into the SM as four-component massive Dirac spinors with two components noninteracting.

Because they have no gauge charges, neutrinos could alternatively be described by Majorana spinors with only two degrees of freedom, η_L and $\bar{\eta}_L$. Mass can then be introduced via the Majorana term:

$$L_M = m_M (\bar{\eta}_L \mathcal{C} \bar{\eta}_L^T + \eta_L \mathcal{C} \eta_L^T), \quad (1.2)$$

where \mathcal{C} is the charge conjugation operator. As well as violating chirality conservation, this mass term also violates lepton number. The mass term for the Majorana spinor field resembles the Dirac mass term under the identification $\mathcal{C} \bar{\eta}_L^T = \eta_R$ and $\mathcal{C} \bar{\eta}_R^T = \eta_L$. Thus, a Majorana spinor behaves like Dirac spinor where the left-handed particle is physically equivalent to the right-handed anti-particle.

The distinction between Majorana and Dirac neutrinos is only observable at low energies, where helicity conservation does not suppress the differences in their phenomenology. While the nature of neutrino mass has potentially profound consequences for particle physics and cosmology, the oscillation physics of relativistic neutrinos, which is the subject of this thesis, depends only upon the relative values of the neutrino masses, and not upon how they are generated.

Parameters of the massive neutrino Standard Model ($m_\nu SM$)

There are three massless spinor neutrino fields in the Standard Model Lagrangian. A minimal extension involves introducing three Dirac or Majorana neutrino mass terms. This produces the massive neutrino Standard Model ($m_\nu SM$). The Hilbert space of

single-neutrino states in the m_ν , SM can be spanned by many different choices of basis. Of these, two are of particular interest.

$|\nu_i\rangle$ basis states are those which diagonalize the mass and kinetic terms in the Lagrangian. These represent neutrinos of definite mass. In the Standard Model i runs from 1 to 3. The $|\nu_\alpha\rangle$ basis, on the other hand, is that in which the weak interaction is diagonal. In the SM $\alpha = e, \mu, \tau$. The flavor states $|\nu_\alpha\rangle$ can undergo charged-current interactions only with the corresponding charged lepton.

In the mass basis it is possible to construct a well-defined Fock space and a simple field theoretical vacuum. In the flavor basis neither of these is possible. As a consequence, neutrino flavor states are not particle excitations in the sense usually understood in quantum field theory, but they are a convenient construction for defining interaction probabilities of neutrinos in certain approximate limits.

The mass and flavor bases are related by a unitary transformation:

$$\sum_i \psi_i |\nu_i\rangle = \sum_\alpha \psi_\alpha |\nu_\alpha\rangle \quad \rightarrow \quad \psi_\alpha = U_{PMNS} \psi_i, \quad (1.3)$$

where the various ψ 's are the spinor wave function of each component. Equivalently, in vector notation,

$$\begin{pmatrix} \psi_e \\ \psi_\mu \\ \psi_\tau \end{pmatrix} = U_{PMNS} \begin{pmatrix} \psi_1 \\ \psi_2 \\ \psi_3 \end{pmatrix}. \quad (1.4)$$

The matrix U_{PMNS} is the Pontecorvo–Maki–Nakagawa–Sakata matrix. The form of the PMNS matrix is limited by constraints imposed by unitarity and the allowed field redefinitions. The most general form of the matrix for a three-flavor scenario is

$$U_{PMNS} = \begin{bmatrix} 1 & 0 & 0 \\ 0 & c_{23} & s_{23} \\ 0 & -s_{23} & c_{23} \end{bmatrix} \begin{bmatrix} c_{13} & 0 & s_{13}e^{-\delta_{CP}} \\ 0 & 1 & 0 \\ -s_{13}e^{\delta_{CP}} & 0 & c_{13} \end{bmatrix} \begin{bmatrix} c_{12} & s_{12} & 0 \\ -s_{12} & s_{12} & 0 \\ 0 & 0 & 1 \end{bmatrix} \begin{bmatrix} e^{i\alpha} & 0 & 0 \\ 0 & e^{i\beta} & 0 \\ 0 & 0 & 1 \end{bmatrix} \quad (1.5)$$

with $c_{ij} = \cos\theta_{ij}$ and $s_{ij} = \sin\theta_{ij}$. The complex phase δ_{CP} parameterizes the extent of leptonic CP violation, absent if $\delta_{CP} = 0$. The Majorana phases α and β are only

Parameter	Value	Experiments
$\sin^2 2\theta_{12}$	0.846 ± 0.021	solar, reactor
$\sin^2 2\theta_{23}$	$\theta_{23} = 0.999^{+0.001}_{-0.017}$ norm / $1.000^{+0.000}_{-0.018}$ inv	accelerator, atmospheric
$\sin^2 2\theta_{13}$	0.093 ± 0.008	reactor, accelerator
δ_{CP}	unknown	accelerator
α, β	unknown	$0\nu\beta\beta$
$\Delta m_{12}^2/\text{eV}^2$	$(7.53 \pm 0.18) \times 10^{-5}$	solar, reactor
$\Delta m_{23}^2/\text{eV}^2$	$(2.52 \pm 0.07) \times 10^{-3}$ norm / $(2.44 \pm 0.06) \times 10^{-3}$ inv	accelerator, atmospheric
m_ν/eV	< 2	${}^3\text{H}$ β decay, cosmology
$m_{13} < m_{23}$	unknown	accelerator
Majorana / Dirac?	unknown	$0\nu\beta\beta$

Figure 1.1.2: Summary of the parameters in the $m_\nu SM$. Data from [37].

physical in the case of a Majorana neutrino. In the case of a Dirac neutrino, the ν and $\bar{\nu}$ fields are independent and can be redefined to absorb them.

The masses of the states $|m_i\rangle$ are free parameters. The majority of our empirical knowledge of neutrino masses is derived from oscillation experiments, which measure mass-squared differences $\Delta m_{ij}^2 = m_j^2 - m_i^2$ (Section 1.3). Thus, the three neutrino masses are usually specified in terms of an absolute mass scale m_ν , two mass-squared differences $|\Delta m_{12}^2|$ and $|\Delta m_{23}^2|$, and the boolean choice of heirarchy $m_{13} < m_{23}$.

Table 1.1.2 shows our present understanding of the parameters of the $m_\nu SM$. This table represents the achievements of many experiments and a generation of neutrino physicists. The still-unknown parameters δ_{CP} , m_ν , $m_{13} < m_{23}$ and the Dirac vs. Majorana nature of the neutrino are all being experimentally pursued.

1.3 Neutrino oscillations in vacuum and matter

Many of the parameters of the $m_\nu SM$ have been measured through experimental studies of neutrino oscillations. Oscillations refer to flavor transformations between weak interaction eigenstates which occur because neutrinos are both massive and nontrivially mixed. Experimentally it has been established that at least three types of

neutrino exist and participate in oscillations [37]. Some anomalies have also suggested the presence of additional, heavier neutrinos which participate in oscillations but do not add a weakly interacting flavor eigenstate, so are described as sterile. This section discusses the basic principles of neutrino oscillations in vacuum and in matter, and Section 1.4 reviews the experimental evidence for sterile neutrinos.

Neutrino oscillations in vacuum

This section gives the standard derivation of neutrino oscillations, following the presentation in [38]. We will revisit some of its central assumptions in Chapter 2.

We assert that there are N flavors of neutrino, which can be expressed in terms of N mass basis ν_i states or N flavor basis states ν_α . A neutrino is produced alongside a charged lepton of flavor α and detected via a charged-current interaction which produces a charged lepton of flavor β in a detector at some baseline L . The energy and momentum resolutions of the detector are not sufficiently precise that the mass eigenstates, ν_i , can be resolved.

The neutrino is born at t_0 with a perfectly defined momentum p :

$$|\psi(t_0)\rangle = \sum_i U_{\alpha i} |\nu_i\rangle e^{ipx} \quad (1.6)$$

and the state evolves in time according to the Schrodinger equation,

$$|\psi(t_1)\rangle = \sum_i U_{\alpha i} |\nu_i\rangle e^{ipx - iE_i(t_1 - t_0)} \quad (1.7)$$

$$E_i = \sqrt{p^2 + m_i^2}. \quad (1.8)$$

Assuming $m_i^2 \ll p^2$, the energy can be Taylor-expanded:

$$E_i = p_i + \frac{m_i^2}{2p} \quad (1.9)$$

We ask for the probability that the neutrino will be detected with flavor β at $x = L$. Since the neutrino is highly relativistic, all mass components travel at approximately

the speed of light and will arrive at $t = L$. The wave function at detection is:

$$|\psi(t_1)\rangle = \sum_i U_{\alpha i} |\nu_i\rangle e^{-i \frac{m_i^2}{2p} L} = \sum_i \sum_\gamma U_{\alpha i} U_{\gamma i}^* |\nu_\gamma\rangle e^{-i \frac{m_i^2}{2p} L}. \quad (1.10)$$

In the second equality we have decomposed the mass states in the flavor basis. To obtain the flavor-change probability, we take the product:

$$P_{\alpha \rightarrow \beta} = |\langle \beta | \psi(t) \rangle|^2 = \sum_{i,j} U_{\alpha i} U_{\alpha j}^* U_{\beta j} U_{\beta i}^* \exp \left\{ i \frac{\Delta m_{ij}^2 L}{2p} \right\}. \quad (1.11)$$

This formula describes an oscillating probability in L , with frequency modes proportional to $\Delta m_{ij}/4E$ for each $\Delta^2 m_{ij}$. As a simplified example, consider a two-state system. The most general allowed mixing matrix is:

$$U = \begin{pmatrix} \cos\theta & \sin\theta \\ -\sin\theta & \cos\theta \end{pmatrix}, \quad (1.12)$$

and the oscillation probability simplifies to:

$$P_{\alpha \rightarrow \beta} = \left| \delta_{\alpha\beta} - \sin^2 2\theta \sin^2 \left(\frac{\Delta m^2 L}{4E} \right) \right|. \quad (1.13)$$

In an N -flavor system with one mass, m_n , much larger than the others ($m_i, m_j \dots$), for sufficiently short baselines where $\Delta m_{ij}^2 L / 2p \ll 1$, the following approximation can be made:

$$P_{\alpha \rightarrow \beta} = \left| \delta_{\alpha\beta} - \sin^2 2\theta_{eff}^{\alpha\beta} \sin^2 \left(\frac{\Delta m_{ni}^2 L}{4E} \right) + \mathcal{O} \left(\frac{\Delta m_{ij}^2 L}{E} \right) \right|. \quad (1.14)$$

In the above formulas, $i, j \neq n$, and $\theta_{eff}^{\alpha\beta}$ is an effective mixing angle. This “two flavor” approximation is particularly useful in short-baseline oscillation experiments searching for sterile neutrinos with masses $m_s \gg m_\nu$.

Neutrino oscillations in matter

When neutrinos travel through matter, their oscillation behavior is modified by charged- and neutral-current interactions with the medium. In very low energy or short baseline regimes, the cross section for interactions is negligible and the neutrinos oscillate as in vacuum. At higher energies and longer baselines, when the scattering strength is small but non-negligible, coherent forward scattering is the dominant matter effect. In this process, the scattered part of the neutrino wave function interferes coherently with the unscattered component. The cross section for this scattering process is proportional to one power of the Fermi coupling G_F , rather than two in the case of incoherent scattering. Because the process is coherent, the state of the matter through which the neutrino is propagating is necessarily unchanged by the interactions and neutrino evolution can be modeled using a neutrino-optics treatment. In this treatment, matter effects are fully accounted for by introducing a *matter potential* which refractively modifies the neutrino propagation phases.

We will first discuss the effects of matter in the commonly studied ν_μ/ν_e system, following the treatment in [39]. In the presence of a matter potential the Schrodinger equation for neutrino evolution becomes:

$$i\frac{d}{dt} \begin{pmatrix} \nu_e(t) \\ \nu_\mu(t) \end{pmatrix} = \frac{1}{2E_\nu} M \begin{pmatrix} \nu_e(t) \\ \nu_\mu(t) \end{pmatrix}, \quad (1.15)$$

where M is the modified mass matrix:

$$M = \frac{1}{2} \begin{pmatrix} m_1^2 \cos^2 \theta + m_2^2 \sin^2 \theta + E_\nu (V_C + V_N) & \frac{1}{2} \Delta m^2 \sin 2\theta \\ \frac{1}{2} \Delta m^2 \sin 2\theta & m_2^2 \cos^2 \theta + m_1^2 \sin^2 \theta + E_\nu V_N \end{pmatrix}. \quad (1.16)$$

M is expressed in terms of the charged- and neutral-current matter potentials, which are functions of the electron and neutron density, respectively:

$$V_C = \sqrt{2} G_F N_e \quad V_N = -\frac{1}{\sqrt{2}} G_F N_n \quad (1.17)$$

Solving Eq.1.15 leads to neutrino oscillations with modified effective oscillation lengths and mixing amplitudes:

$$L_{matter}^{osc} = \frac{L_0^{osc}}{\sqrt{\cos^2 2\theta (1 - \frac{E_\nu V_C}{\Delta m^2 \cos 2\theta})^2 + \sin^2 2\theta}} \quad (1.18)$$

$$\sin^2 2\theta_{matter} = \frac{\sin^2 2\theta}{\cos^2(2\theta) \left(1 - \frac{E_\nu V_C}{\Delta m^2 \cos 2\theta}\right)^2 + \sin^2 2\theta}. \quad (1.19)$$

It is notable that only the electron potential features in these expressions. This is because the phase gained by interactions with the nucleons in the material is equivalent for both neutrino flavors, so does not modify the oscillation. Also notable is the behavior of the oscillation when $E_\nu V_C / \Delta m^2 \cos 2\theta \rightarrow 1$. In this situation, the effective mixing angle becomes $\sin^2 2\theta \rightarrow 1$ regardless of its initial value. This has the consequence that, assuming certain adiabaticity conditions are met², maximal flavor change occurs for neutrinos at the critical energy E_{crit} :

$$E_{crit} = \frac{\Delta m^2 \cos 2\theta}{\sqrt{2} G_F N_e}. \quad (1.20)$$

This is known as the MSW resonance. In the case of antineutrinos, the sign of V_C would be flipped to $V_C = -\sqrt{2} G_F N_e$ implying that only neutrinos, and not antineutrinos, can experience the resonance condition in the two-flavor ν_μ/ν_e system.

The subject of this thesis is oscillations with sterile neutrinos, which involves the four flavor $\nu_e/\nu_\mu/\nu_\tau/\nu_s$ system. In this case, the three active neutrinos interact with nucleons via the neutral-current interaction; the electron flavor neutrino interacts with electrons via the charged-current interaction; and the sterile neutrino does not experience any matter potential. By a similar mechanism to that described above, a resonance is expected between the active and sterile states, this time only in the antineutrino channel. The full formalism of MSW-resonant sterile neutrino oscillations requires a four-flavor treatment, the details of which can be found in [40]–[42].

For sterile neutrinos of mass around $\Delta m^2 \sim 1 \text{ eV}^2$, the resonance condition is achieved for antineutrinos crossing the Earth at energies around 1 TeV. This is near

²A complete discussion of the adiabaticity conditions can be found in [39].

the peak of the spectrum of the atmospheric neutrino flux detectable with IceCube, and Part III of this thesis will concern an experimental search for this signature. In the multi-TeV energy regime, however, further corrections to the simple MSW-resonant picture presented above must be made.

When E_ν becomes sufficiently large, incoherent neutrino-nucleon scattering becomes non-negligible, and the linear neutrino-optics approximation breaks down. In such cases, the Schrodinger equation for neutrino evolution in a matter potential, Eq. 1.15, is not valid, and a master equation which treats both coherent and incoherent interactions must be used. This master equation is described in [43]. Its solution, evaluated numerically for a given matter profile, describes the evolution of fluxes of each neutrino flavor. A software package called nuSQuIDs [44], [45] has been developed for this purpose. NuSQuIDs models flavor evolution in the standard 3-neutrino system, or in systems with up to six flavor basis states for studies of sterile neutrinos, in arbitrary matter potentials. A discussion of the oscillation probabilities derived from this calculation will be given in Section 1.5 of Part III.

1.4 Anomalies and sterile neutrinos

This section reviews the experimental anomalies which have suggested the existence of sterile neutrinos. A longer and more detailed overview can be found in [46].

The LSND anomaly

The LSND experiment [47] used a liquid scintillator detector to measure neutrinos and antineutrinos produced in a pion decay-at-rest beam at a baseline of 30 m. To make such a beam, 800 MeV protons are fired into a target, producing both π^+ and π^- which are stopped in a beam dump. The π^- component is rapidly captured electromagnetically in atomic orbitals with tight Bohr radii. The large overlap of the orbital with the nucleus then enhances the nuclear capture of the π^- , destroying it but producing no neutrinos. The π^+ in the beam also come to rest but do not capture. They instead decay through the chain $\pi^+ \rightarrow \mu^+ \nu_\mu$ followed by $\mu_+ \rightarrow e^+ \nu_e \bar{\nu}_\mu$. This

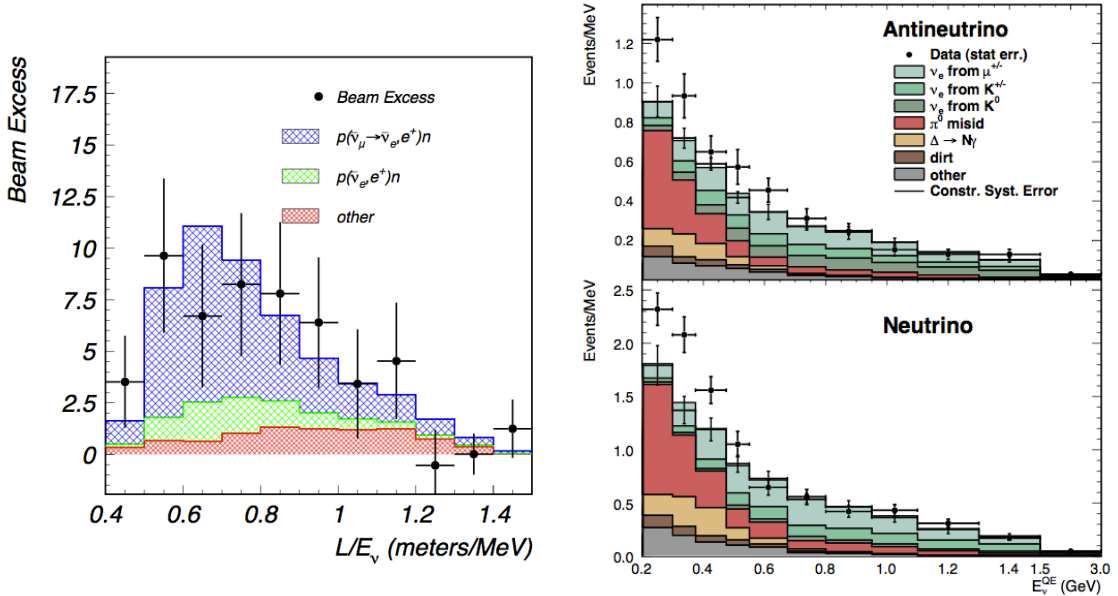


Figure 1.1.3: Left: The LSND electron antineutrino excess [48]. Right: The MiniBooNE electron neutrino and antineutrino excesses [49].

produces a pure beam of $\bar{\nu}_\mu$, ν_e and ν_μ , with a small $\bar{\nu}_e$ background at a level of 8×10^{-4} times the $\bar{\nu}_\mu$ flux.

LSND measured the flux of $\bar{\nu}_e$ using a sample of 28,896 C protons on target. A larger than expected rate of $\bar{\nu}_e$ was observed, with a shape consistent with the oscillations between $\bar{\nu}_\mu$ and $\bar{\nu}_e$ with $\Delta m^2 > 0.2 \text{ eV}^2$ [48]. This excess has significance of $>3\sigma$ and is shown in Figure 1.1.3, left.

The MiniBooNE anomaly

The MiniBooNE experiment was proposed to test the interpretation of the LSND excess as an oscillation [50] by searching for oscillations at different L and E , but similar L/E to LSND. MiniBooNE used a proton beam aimed at a beryllium target to produce charged pions and kaons which decay in flight, producing a tertiary beam of muon neutrinos and antineutrinos. A magnetic horn was used to focus one charge and defocus the other, allowing the experiment to run in modes where the flux is primarily ν_μ (neutrino mode) or $\bar{\nu}_\mu$ (antineutrino mode). MiniBooNE searched for appearance of ν_e in neutrino mode [51] and $\bar{\nu}_e$ in antineutrino mode [49]. In both cases an

excess over the expected background was observed (Figure 1.1.3, right). However, the excesses in both channels have a large low-energy component, whereas an LSND-like oscillation in a model with a single heavy sterile neutrino (also known as a 3+1 model) would peak at higher energies. A smaller excess at intermediate energy is present in antineutrino mode, but not in neutrino mode. The overall statistical significance of the MiniBooNE excess is 3.4σ in neutrino mode and 2.8σ in antineutrino mode.

Understanding the origin of the MiniBooNE low-energy excesses, and whether and how they are connected to neutrino oscillations, is the main goal of the MicroBooNE experiment, which will be the subject of Part II of this thesis.

The radiochemical anomalies

The SAGE [52] and GALLEX [29] experiments were solar neutrino detectors which observed neutrinos through the process:



After each month of exposure, the Ge was chemically extracted and counted by observing the radioactive decay of Ge back to Ga. The extraction and tagging efficiency of the radiochemical process is around 95% [53]. Calibration runs of the two experiments were made by deploying intense ${}^{51}\text{Cr}$ and ${}^{37}\text{Ar}$ electron capture sources inside the detectors [54], [55]. The rate of Ge production was measured and compared with the known source activity.

The ratio of expected to observed counts of ${}^{71}\text{Ge}$, averaged between the two experiments, was found to be 2.7σ low, with a value $R=0.86\pm0.05$. One interpretation of this result is that electron neutrinos could be oscillating into sterile states within the detector and hence evading detection [56].

The reactor anomaly

A similar event-rate deficit has been observed in reactor antineutrino experiments. In this case, at the time of running the experiments observed the expected event rates.

Later updates to the reactor flux calculations to include extra sub-dominant decay branches [57] led to an increase in the neutrino flux prediction by 9.8%.

The weighted average ratio of experimental to predicted neutrino interaction rates in 19 reactor neutrino experiments, including the ROVNO, SRP, BUGEY, Kranoyarsk, ILL, Goesgen groups of experiments is 0.927 ± 0.023 , which is 3σ in deficit. This can be interpreted as evidence for electron antineutrino disappearance to sterile states [58], although recent work has questioned the significance of the anomaly given the remaining uncertainties in the flux calculations [59].

Null results and the global picture

Several experiments have published null results or exclusions on sterile neutrinos in the 1 eV^2 range. The earliest null result was from KARMEN [60], a decay-at-rest experiment similar to LSND but at a baseline of 17.7 m at the ISIS rapid-cycling synchrotron. KARMEN ruled out a subset of the LSND allowed parameter space [61]. The Super Kamiokande atmospheric neutrino experiment has searched for fast oscillations of sterile neutrinos in the atmospheric neutrino spectrum, producing a limit on the mixing angle [62]. And, the MINOS experiment has searched for sterile neutrino oscillations through neutral-current disappearance and excluded significant parameter space [63] in the 3+1 model.

The experimental status of sterile neutrinos given all the world data must be quantified by global fits [64]–[66]. Figure 1.1.4, reproduced from [66] shows the allowed regions in 3+1 model parameter space from all experiments. Also shown are the allowed regions considering only neutrino experiments, or only antineutrino experiments, or only appearance channels, or only disappearance channels. Because all the experiments considered measure vacuum oscillations, the mixing is quantified in terms of the effective two-flavor mixing amplitude $\sin^2 2\theta_{\mu e}$ rather than the unitary mixing angles $\theta_{14}, \theta_{24}, \theta_{34}$ (to be discussed in Section III.1.5). A small island of allowed parameter space is present, centered around $\Delta m^2 \sim 1 \text{ eV}^2$ and $\sin^2 2\theta_{\mu e} \sim 0.2$.

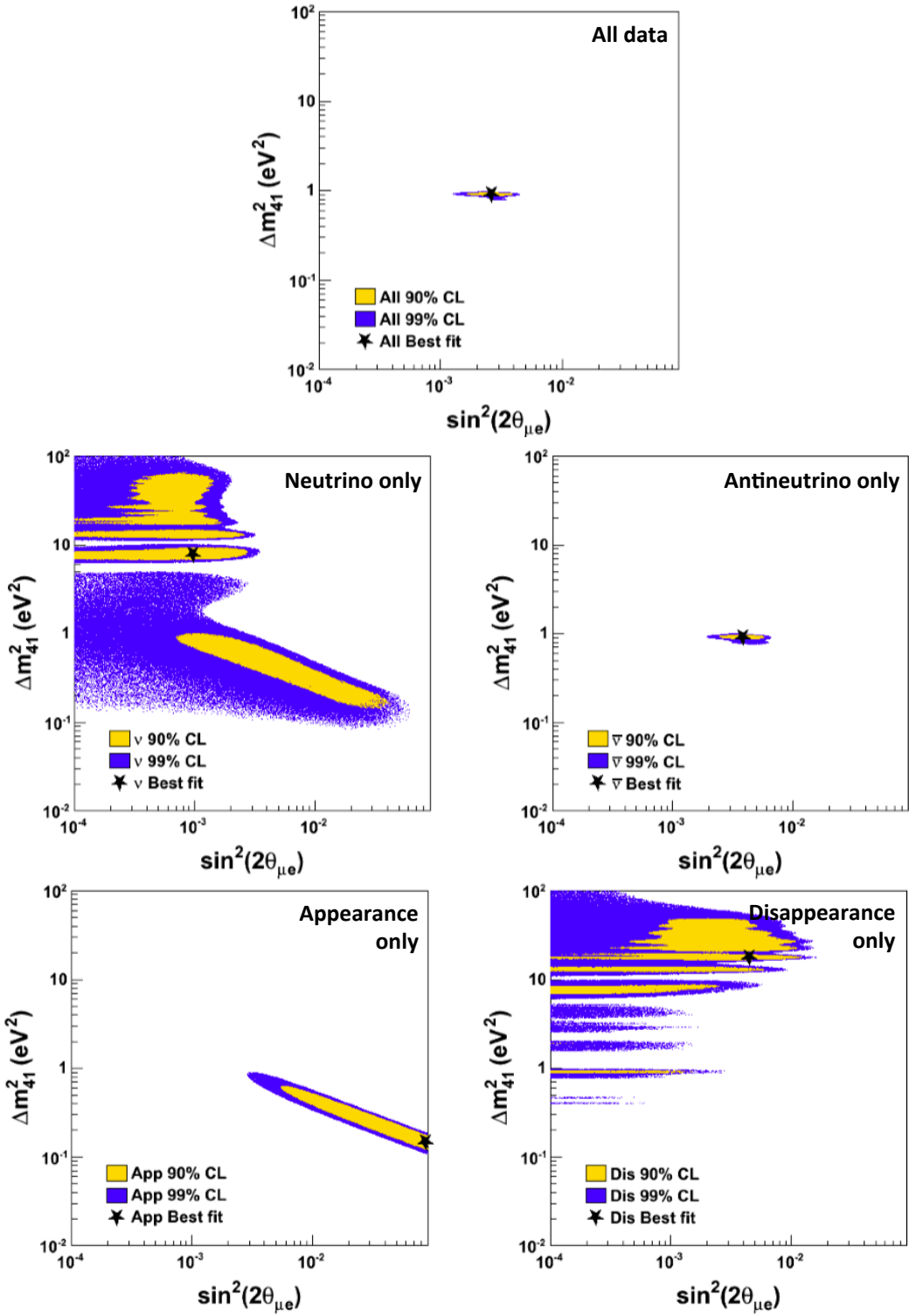


Figure 1.1.4: Allowed regions in 3+1 parameter space from world data, from [66].

Chapter 2

The Coherence Properties of Neutrino Beams

This chapter discusses the phenomenology of neutrino beam coherence. Section 2.1 discusses the validity of the plane-wave approximation, and the consequences of relaxing it to treat realistic neutrino sources. Section 2.2 discusses the physical origin of the coherent particle localization which occurs in accelerator neutrino beams. Finally, Section 2.3 presents a rigorous calculation of the coherence properties of neutrino beams, which requires no assumption of the initial state width to make quantitative predictions about neutrino coherence.

2.1 Internal and external wave packets

The theory of neutrino oscillations, described in Section 1.3, is built upon several assumptions which are violated in real experiments. One such assumption is that the neutrino is emitted in a plane wave state, which has definite energy or momentum. Were this true, the mass of the propagating neutrino could be determined from precise energy and momentum measurements. Regardless of whether a suitable detector exists, four-momentum conservation implies that the different mass components would produce distinct final states, and their coherent interference would be impossible.

Another failing of the plane-wave assumption regards the definition of the baseline

L . As a consequence of the uncertainty principle, a state of definite momentum has a totally delocalized position and therefore must have been emitted from an infinitely large source. For neutrinos emitted from such a source there is no way to define the oscillation baseline L , so oscillations cannot be consistently described.

These problems can be overcome by the introduction of a wave packet (see, e.g. [39]) for the neutrino. Instead of being emitted as a plane wave of definite flavor,

$$|\psi\rangle_{plane} = |\nu_\alpha\rangle|p\rangle = e^{ipx}|\nu_\alpha\rangle|x\rangle, \quad (2.1)$$

the neutrino has wave function $\phi(x)$, and momentum wave function $\tilde{\phi}(p)$ related to $\phi(x)$ via Fourier transform¹. If $\tilde{\phi}(p)$ is peaked at central momentum p_0 , flavor oscillations occur with a wavelength $L_{osc} = 2p_0/\Delta m^2$ within a spatial region defined by a moving envelope. For observable oscillations, $\tilde{\phi}(p)$ must be sufficiently wide that unambiguous mass determination is impossible. For a given momentum uncertainty σ_p , the uncertainty on the squared neutrino mass $m^2 = p^2 + E^2$ is:

$$\delta m^2 = 2p\sigma_p + 2E\sigma_E \sim 4p\sigma_p. \quad (2.2)$$

In natural units, the uncertainty principle states that $\sigma_x\sigma_p \geq \frac{1}{2}$. The condition that the mass states cannot be unambiguously identified ($\delta m^2 > \Delta m^2$) thus implies that:

$$\frac{L_{osc}}{2} \equiv \frac{2E}{\Delta m^2} \geq \sigma_x. \quad (2.3)$$

For minimal uncertainty states, wave packet localization to within a half oscillation length (one complete flavor change) and the non-definiteness of neutrino mass are equivalent conditions [38].

While resolving some paradoxes, the wave packet picture also adds complications. Consider the time evolution of $\phi(x)$ according to the Schrodinger equation:

$$H\phi = -\frac{\hbar^2}{2m}\nabla^2\phi(x) = i\hbar\frac{d\phi(x)}{dt} \quad (2.4)$$

¹In this chapter, \tilde{A} will represent the Fourier transform of A , for any A .

Because m features in the Hamiltonian, a neutrino produced in a state $|\psi(0)\rangle = \phi(x) \sum_i U_{\alpha i} |\nu_i\rangle$ will evolve into $|\psi(t)\rangle = \sum_i U_{\alpha i} \phi_i(x) |\nu_i\rangle$, where the wave functions for each mass eigenstate ϕ_i are inequivalent. Consider a Gaussian wave function with central momentum p_0 and position x_0 , and width σ_x in the position basis. For this state, the momentum wave function is also Gaussian with width $\sigma_p = 1/2\sigma_x$:

$$|\psi(t=0)\rangle = \int dp \psi(x, 0)|x\rangle = \int dx \exp\left[-\frac{(x-x_0)^2}{2\sigma_x^2}\right] e^{ip_0 x}|x\rangle \quad (2.5)$$

$$= \int dp \tilde{\psi}(p, 0)|p\rangle = \int dp \exp\left[-\frac{(p-p_0)^2}{2\sigma_p^2}\right] e^{ipx_0}|p\rangle. \quad (2.6)$$

Evolving the wave function according to the Schrodinger equation:

$$\tilde{\psi}(p, t)|p\rangle = \exp\left[-\frac{(p-p_0)^2}{2\sigma_p^2}\right] e^{i\sqrt{p^2+m^2}t}|p\rangle. \quad (2.7)$$

In the limit $\sigma_p^2 \ll E_0$, the exponent can be expanded to second order in p , and the position space wave function can be obtained via Fourier transform:

$$\psi(x, t) = N(t) e^{\frac{(x-\beta(p)t)^2}{2\sigma_x(t)^2}[1-iAt]} : \quad \sigma_x(t) = \frac{1}{\sigma_p} (1 + A^2 t^2); \quad A = \frac{m^2 \sigma^2}{E_0^3}. \quad (2.8)$$

The wave packet moves with velocity $\beta = p/E$ and disperses. States with the same central momentum but different masses travel at different group velocities. For a superposition of mass states, after sufficiently large distance the components will separate, and each can be identified by its arrival time. Interference is then impossible, and the neutrino beam appears as an incoherent mixture of flavors with no nontrivial distance or energy dependence [67].

Figure 1.2.1 illustrates the plane-wave, coherent and incoherent wave packet configurations. In the top panel, showing the plane-wave assumption, the neutrino is fully delocalized at time $t=0$. The oscillation probability is maximal when the plane waves are out of phase, and minimal when in phase, but the probability that there is a neutrino at any point in space is always 1. The middle panel shows the wave packet picture before coherence loss. Here the detection probability is finite only in a localized region which propagates with a finite group velocity. To first order in Δm^2 ,

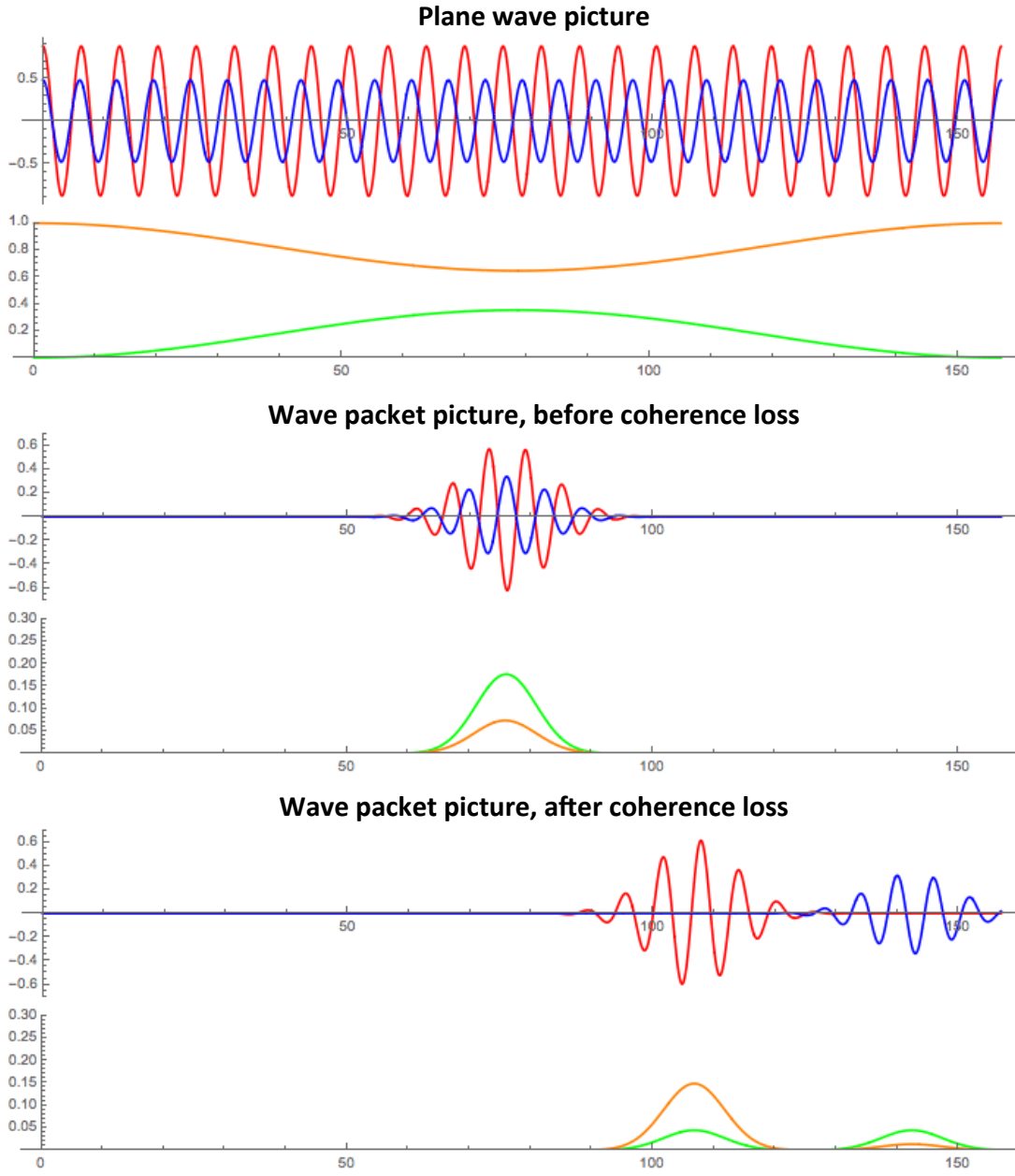


Figure 1.2.1: Red and blue lines show $\text{Re}[\phi(x)]$ for two mass states. Orange and green lines show the probability for detection of flavor components. Description in text.

oscillation maximum occurs in the same location as in the plane-wave picture. In the lower picture, the separation of mass wave-packets after long times is shown. After sufficient distance when the mass states have separated, there is no longer interference, and neutrino oscillations are suppressed.

We call the distance over which separation occurs the “coherence distance.’’ In

this model it is dictated by the wave packet width σ_x and the relative velocity $\Delta\beta$ of the mass states:

$$c\Delta\beta t_{sep} \sim \Delta\beta L_{sep} \ll \sigma_x. \quad (2.9)$$

The production process dictates the momenta of the emitted neutrinos, so $\Delta\beta$ can be straightforwardly calculated. In pion decay, for example, the central neutrino velocities are derived from two-body kinematics.

The wave packet width σ_x is more difficult to estimate. Intuitive arguments can be given suggesting the size of a nucleus, the extent of the neutrino source, the parent lifetime, the mean-free-path between collisions, or a detector resolution. These span a wide range of scales and vary between experiments. Prior to this work, a rigorous calculation of this width had not been made, which is an important omission from the theoretical treatment of neutrino oscillations. It is especially important for heavy sterile neutrinos, where coherence loss would be enhanced relative to the lighter active neutrinos.

Consider the specific case of neutrinos produced in pion decay $\pi \rightarrow \mu\nu$, which is the leading production process in accelerator neutrino beams. For a pion decaying in a vacuum, calculations have been made to express the neutrino state in terms of the parent pion wave function [68]–[71]. Neutrino oscillation phenomenology, including the effects of coherence loss, can then be derived in terms of the parent’s initial state. This is called an external wave packet approach, in contrast to internal wave packet approaches, where the neutrino wave function is postulated a priori.

With neutrino oscillation probability specified in terms of the pion wave function, an assumed initial state can be used to predict the neutrino coherence properties [72]–[74]. This approach remains unsatisfactory, because although the assumption may be more easily hidden, an arbitrary width assumption is still made. On the surface this problem appears indefinitely recursive, since determination of the neutrino behavior in terms of its parent, grandparent, or (great) n -grandparent state always requires an assumption about the ultimate ancestor.

As will be shown in the subsequent sections, the problem becomes tractable when

environmental interactions of the pion are taken into account. The air molecules in the beam pipe which undergo scattering interactions with the decaying pion play a key role in determining the coherence properties of the resulting neutrino. The *open quantum system* approach to neutrino coherence, distinct from the internal and external wave packet approaches, is one of the major results presented in this thesis. With this approach, coherence properties can be quantitatively understood without requiring arbitrary assumptions about the initial state.

2.2 Environmentally induced decoherence

The missing ingredients in the above discussion are the scattering interactions between the pion and the surrounding gas, which act to localize it through the generation of entanglement. This initiates an effective wave function collapse in the position basis. The localization scale is not determined by the mean-free-path between scatters, or by classical ignorance of the pion position, but by the resolution with which the environment can “measure” position. This phenomenon is called decoherence, and it has been studied both for applications in quantum computing and interferometry, and also because the resulting quantum-to-classical transition is of fundamental interest [75]. In this section I give a simple illustration of decoherence in interferometers, then discuss the analogous process of particle localization through scattering. Finally, Section 2.3 presents the open quantum system picture of neutrino beams.

Decoherence in Young and Talbot Lau interferometers

As a simple illustration, consider a two-slit experiment performed with single particles (Figure 1.2.2). In this classic experiment, a particle is emitted from a source some distance behind an absorbing sheet which has two slits, labeled A and B. The position of the particle arriving at a screen beyond the sheet is measured. For any position at the screen x , there are two classical trajectories which the particle could have taken, each having some classical probability $P_A(x)$ and $P_B(x)$. In classical mechanics, the

total probability for a particle to be detected at x is:

$$P_{clas}(x) = P_A(x) + P_B(x). \quad (2.10)$$

In quantum mechanics, on the other hand, trajectories are weighted by their complex amplitude $\psi(x)$ rather than their classical probability $P(x)$, where $P(x) = \langle \psi(x) | \psi(x) \rangle$. The probability of observing a particle at position x is:

$$P_{qm}(x) = \langle \psi_{tot} | \psi_{tot} \rangle, \quad (2.11a)$$

$$= \langle \psi_A + \psi_B | \psi_A + \psi_B \rangle, \quad (2.11b)$$

$$= \langle \psi_A | \psi_A \rangle + \langle \psi_B | \psi_B \rangle + 2\text{Re}\langle \psi_A | \psi_B \rangle. \quad (2.11c)$$

The final term on the right is responsible for the interference fringes observed in the quantum mechanical version of the experiment. Now we imagine that there is an environment of gas molecules which interact with the particle as it traverses the system. The environment starts in state $|E_0\rangle$ and evolves differently for each trajectory due to its coupling to the particle. The evolution can be described by:

$$|\psi_A\rangle|E_0\rangle \rightarrow |\psi_A\rangle|E_A\rangle, \quad |\psi_B\rangle|E_0\rangle \rightarrow |\psi_B\rangle|E_B\rangle. \quad (2.12)$$

The environment is part of the final state, so the detected pattern is now:

$$P_{env}(x) = \langle \psi_A | \psi_A \rangle + \langle \psi_B | \psi_B \rangle + 2\text{Re}\langle \psi_A | \psi_B \rangle \langle E_A | E_B \rangle. \quad (2.13)$$

We consider two extreme limits. In the case where $|E_A\rangle$ and $|E_B\rangle$ are very similar, either because the environmental coupling to the particle is weak or because its evolution is insensitive to the difference between A and B, we find $\langle E_A | E_B \rangle \sim 1$ and $P_{env}(x) = P_{qm}(x)$. The system is quantum mechanically coherent.

In the opposite limit, states $|E_A\rangle$ and $|E_B\rangle$ are very different, and so $\langle E_A | E_B \rangle \sim 0$ and $P_{env}(x) = P_{clas}(x)$. The presence of entanglements with the unobserved environment has converted a quantum mechanically coherent system into a classical-looking,

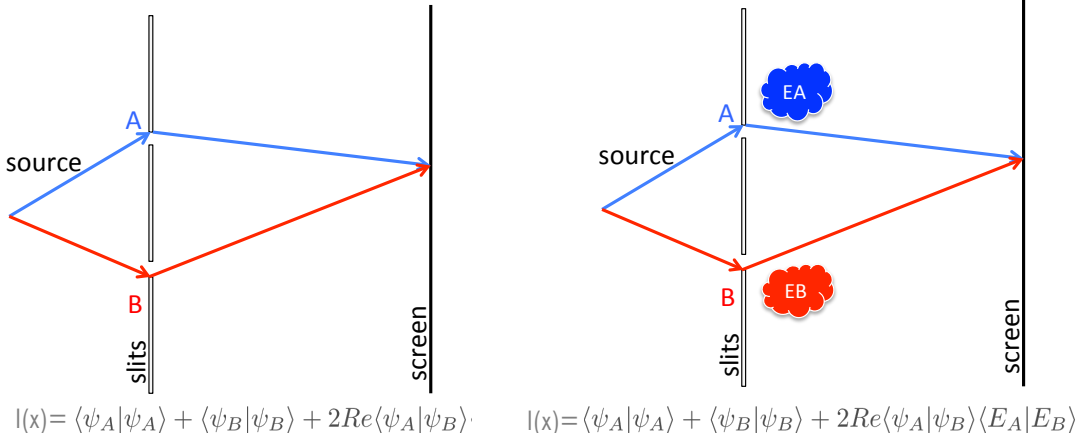


Figure 1.2.2: Young interferometer, with (left) and without (right) an environment.

incoherent one. This phenomenon is called environmental decoherence, and an analog of this process is responsible for all classical-looking states which we typically experience.

It is notable that experiments similar to the one described have been performed in the laboratory. In particular, Talbot Lau interferometry using fullerenes in a tunably imperfect vacuum exhibits exactly the decoherence behavior expected from environmental scattering with residual gas molecules [76]–[78]. Figure 1.2.3 is reproduced from [76] and shows the visibility of interference fringes becoming suppressed by interactions with residual gasses, in excellent agreement with the theoretical prediction.

Localization of particles by scattering

The localization of particles by scattering is conceptually a generalization of the above discussion. Consider a particle which is in a superposition of position states x_a and x_b , with some separation Δx_{ab} . It interacts with an environment which “measures” position with resolution ω_x through scattering interactions. If $\Delta x_{ab} \ll \omega_x$, then the environmental states which are evolve alongside each position are indistinguishable, $\langle E_a | E_b \rangle \sim 1$ and the superposition remains coherent. If the environmental resolution is much finer than the separation, $\Delta x_{ab} \gg \omega_x$, then the environment evolves differently alongside each of the two positions, leading to $\langle E_a | E_b \rangle \sim 0$. The maximal separation of position states for which $\langle E_a | E_b \rangle$ is large can be thought of as an upper

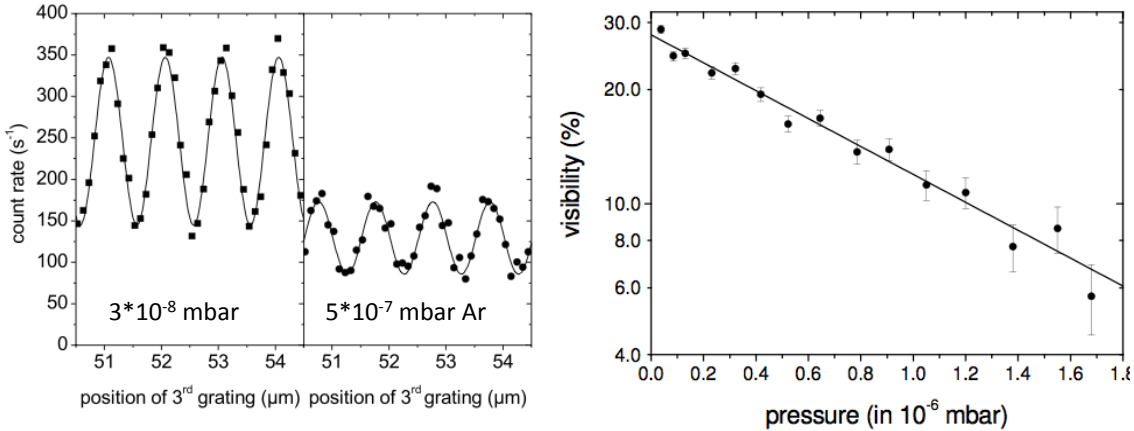


Figure 1.2.3: Measurement of decoherence by environmental scattering in a Talbot Lau interferometer [76]. The visibility of interference fringes as a function of grating separation was measured for incident C_{70} fullerene molecules. The fringe visibility is reduced when argon gas is bled into the chamber, as the fullerene trajectories are decohered by environmental interactions (left). The loss of visibility is in quantitatively good agreement with the prediction of decoherence theory (right).

limit to the length scale over which the particle can exhibit quantum mechanically coherent interference phenomena.

Thus, particles which develop environmental entanglements have two fundamental widths. The classical uncertainty on the particle position, or incoherent width, represents our ignorance as to the particle location. The coherent width, on the other hand, represents the length scale over which coherent interference can be observed. This width is dictated by the entanglement of spatially separated parts of the wave function with the environment.

Now imagine that the particle in the above example emits a neutrino, which is detected some distance away. Whether the neutrino trajectory emerging from position x_a and that emerging from position x_b can interfere coherently depends on the overlap of the experimental final states, which include the environment. If $\langle E_a | E_b \rangle$ is large, coherent interference is possible. If $\langle E_a | E_b \rangle$ is small, it is suppressed. Obtaining the exact oscillation pattern for neutrinos emerging from such environmentally entangled states, present in all experimental neutrino sources, requires a proper summation over all coherent, incoherent, and partially coherent neutrino trajectories.

This type of problem is most conveniently formulated in the language of density matrices [75], [79]. A density matrix represents a system which has a unique wave function (pure state) or a classical statistical mixture of them (mixed state):

$$\rho_{pure} = |\psi\rangle\langle\psi| \quad (2.14)$$

$$\rho_{mixed} = \sum_i p_i |\psi_i\rangle\langle\psi_i|. \quad (2.15)$$

p_i is the classical probabilities for the system to be prepared in a pure state ψ_i , although this statistical decomposition is not unique. Expressed in some complete basis $|q_i\rangle$, a general density matrix has the form $\rho = \sum_{ij} c_{ij} |q_i\rangle\langle q_j|$, for example, in the position basis $\rho = \int \rho(x_1, x_2) dx_1 dx_2 |x_1\rangle\langle x_2|$. It can be shown that coherent width of the density matrix corresponds to the off-diagonal width of the function $\rho(x_1, x_2)$, and incoherent width corresponds to its diagonal width. Measurements are made on density matrices by applying a positive-operator-valued-measure (POVM):

$$P(m_j) = Tr[M_j \rho], \quad (2.16)$$

where the trace operation implies taking a sum over a complete set of states, as $Tr[A] = \int dq \langle q | A | q \rangle$, and M_j are a complete set of operators $\sum_j M_j = 1$ which project onto the measurement states j . In this way, the probability $P(m_j)$ of measurement outcome m_j can be calculated for systems in arbitrary classical and quantum superposition.

Density matrices are particularly powerful for treating multi-partite systems. Consider a system with two parts, X and Y , which have basis states $|x_i\rangle$ and $|y_i\rangle$. The general form of the two-subsystem density matrix is:

$$\rho = \sum_{ijab} c_{ia;jb} |x_i\rangle\langle y_a| |x_j\rangle\langle y_b|. \quad (2.17)$$

A measurement $M_{x,j}$ made only on system $|x\rangle$ is made as follows:

$$P(m_j) = \sum_{nm} \langle x_m | \langle y_n | M_{x,j} \rho | x_m \rangle | y_n \rangle. \quad (2.18)$$

Because $M_{x,j}$ acts only on the X subspace, the trace over Y can be taken first, and is not affected by the M operator. Thus:

$$P(m_j) = \sum_{nm} \langle x_m | M_{x,j} | \langle y_n | \rho | y_n \rangle | x_m \rangle = Tr_x[M_x \rho_x]. \quad (2.19)$$

The object $\rho_x = Tr_y[\rho]$ is the reduced density matrix for the X system. Any measurement which can be made on X alone can be made using ρ_x . The trace already taken over Y accounts for all effects of entanglement with the unobserved subsystem. Notably, a pure state bipartite density matrix for XY will yield mixed state reduced density matrices in the X or Y spaces if there exists nontrivial entanglement between X and Y. This demonstrates, in a simple form, the emergence of classicality through entanglement with an external, unobserved system.

For a bipartite particle-environment system, the evolution of the particles reduced density matrix under the action of discrete scatters can be calculated under some loose assumptions [80]. First, we assume that the scattering processes by which information is transferred to the environment occur on much shorter timescales than the dynamical evolution of the system. This means each scatter corresponds to a transformation of the density matrix of the particle-scatterer system in a discrete step in terms of a scattering matrix T, as

$$\rho \rightarrow T \rho T^\dagger. \quad (2.20)$$

It is assumed that T conserves energy and momentum, so in a single encounter between the system with momentum q and the incoming scatterer with momentum k ,

$$\langle qk | T | q'k' \rangle = \delta(p' + k' - p' - k) a_{pk}(p' - p), \quad (2.21)$$

where $a(p' - p)$ is the probability amplitude for this momentum transfer. The next

assumption is that $a_{pk}(q)$ is a function of q only, and not of p or k . In our system, the thermal momentum of the air molecules is much smaller than the pion momentum, so can be neglected, making this a very good approximation. In this case $a_{pk}(q) = a(q)$. The problem is treated in a finite volume such that discrete momentum transfers are allowed. The effect of the T matrix on a plane-wave basis state of the particle (positions x) and environment (positions α) is:

$$T|pk\rangle = T e^{ipx} e^{ik\alpha} = \sum_q a(q) e^{i(p+q)x} e^{i(k-q)\alpha} = e^{ipx} e^{ik\alpha} \tilde{a}(x - \alpha), \quad (2.22)$$

where $\tilde{a}(x)$ is the discrete Fourier transform of $a(q)$, that is, $\tilde{a}(x) = \sum_q e^{iqx} a(q)$. Thus for a position space two-particle wave function $\psi(x, \alpha)$, the effect of a single scatter is:

$$\psi_f(x, \alpha) = T\psi_i(x, \alpha) = \psi_i(x, \alpha) \tilde{a}(x - \alpha). \quad (2.23)$$

We consider the effects of such scatters on the particle subsystem. To do this, we start with a general bipartite density matrix for the particle and scatterer, with the particle degrees of freedom x on the left and y on the right, and environment degrees of freedom α left and β right, as $\rho(x, y; \alpha, \beta)$. Tracing out the environment:

$$\rho_{part} = Tr_\epsilon[\rho] \quad (2.24)$$

$$= \int d\gamma \langle \gamma | \rho(x, y, \alpha, \beta) | \gamma \rangle \quad (2.25)$$

$$= \int d\gamma \psi_f^*(x, \gamma) \psi_f(y, \gamma) \quad (2.26)$$

$$= \rho_f(x, y) \frac{1}{V} \int d\gamma a(\gamma - x) a(\gamma - y). \quad (2.27)$$

At this point, the finite volume V can be taken to infinity and the convolution in Fourier space can be replaced with a multiplication in real space, leading to:

$$\rho_f(x, y) = \rho_i(x, y) \tilde{a}^*(y - x) = \rho_i(x, y) \widetilde{P}_q(y - x), \quad (2.28)$$

where $\widetilde{P}_q(y - x)$ is the Fourier transform of the momentum transfer probability distri-

bution $P(q)$. Any dependence on the phase of the scatterer drops out, and we merely have to supply a momentum transfer distribution in order to understand the effect of a single scatter on the particle reduced density matrix. This is a centrally important result regarding the decoherence of particles by environmental scattering.

Between scatters, the particle is effectively decoupled from the environment and evolves according to the unitary Von-Neumann equation:

$$i\hbar \frac{d\rho}{dt} = [H, \rho]. \quad (2.29)$$

This produces the same wave packet dispersion effects as described by Eq 2.8. The coherent broadening caused by dispersion competes with the coherent collapse caused by scattering, leading to a stable equilibrium coherent width. The effects of a scattering and unitary evolution on a particle reduced density matrix are illustrated in Figure 1.2.5 in the position basis, the momentum basis, and as a Wigner function.

There are at least two approaches which can be taken to model the time evolution of the decohering particle reduced density matrix. The first is to consider the continuum limit and introduce a master equation [81], which describes the evolution of the system under a continuous bombardment of scatterers. This approach was taken in [80] for non-relativistic particles, and the coherent widths and collapse times of various objects in various environments were calculated. Some of these are shown in Figure 1.2.4.

Cause of apparent wave function collapse	Free electron	$10\mu m$ dust	Bowling ball
300K air at 1 atm pressure	10^{-6} m	10^{-17} m	10^{-21} m
300K air in lab vacuum	10^7 m	10^{-13} m	10^{-18} m
Sunlight on earth	10^9 m	10^{-12} m	10^{-17} m
300K photons	10^4 m	10^{-12} m	10^{-16} m
Background radioactivity	n/a	10^{-11} m	10^{-15} m
Quantum gravity	10^4 m	10^{-9} m	10^{-15} m
GRW effect	10^{19} m	10^{-9} m	10^{-15} m
Cosmic microwave background	10^{10} m	10^{-8} m	10^{-14} m
Solar neutrinos	n/a	n/a	10^{-13} m

Figure 1.2.4: Coherent widths for various objects in different environments of scatterers calculated using a master equation approach [80].

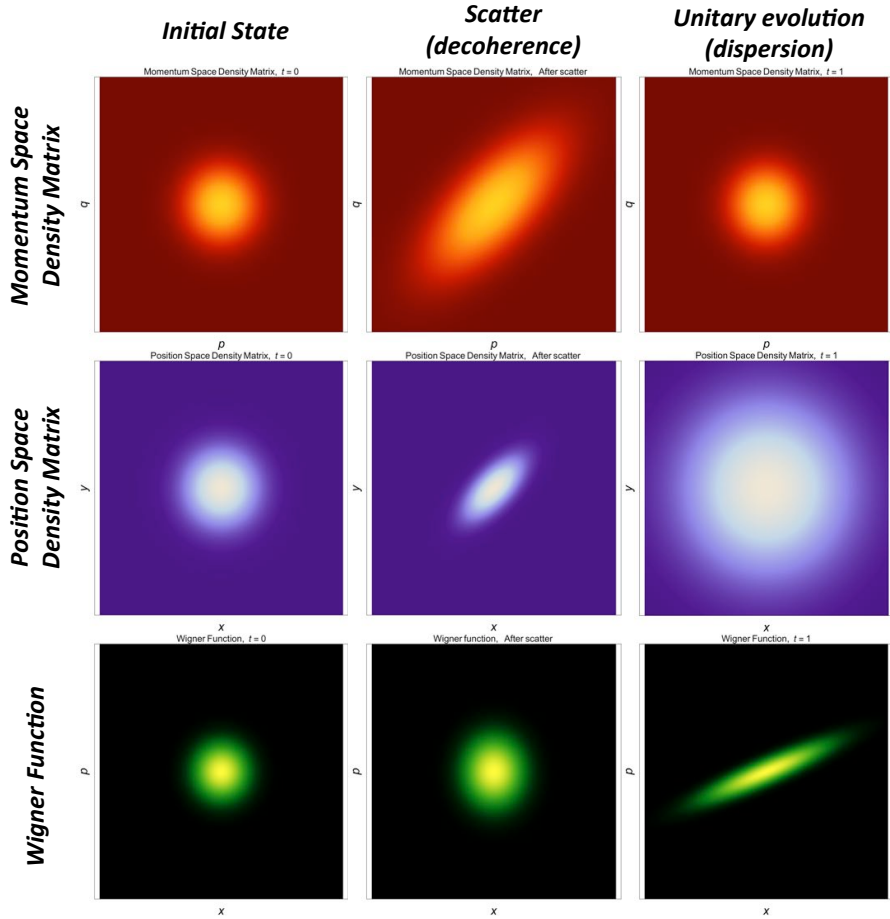


Figure 1.2.5: Changes in the shape of the density matrix and wigner function for a Gaussian wave packet under the influence of scattering (assuming a Gaussian momentum transfer distribution).

Another approach, developed in the following section, is to use a Monte Carlo technique. In this case the system is subjected to scatters at random times and allowed to evolve unitarily between each interaction. Its coherent and incoherent widths can be monitored as a function of time and its approach to an equilibrium width is observed.

2.3 Neutrino beams as open quantum systems

The coherence properties of neutrinos are determined by the details of the neutrino production process. In the case of accelerator neutrino beams, this is the decay of a pion into a neutrino and entangled muon in a gaseous environment (Figure 1.2.6).

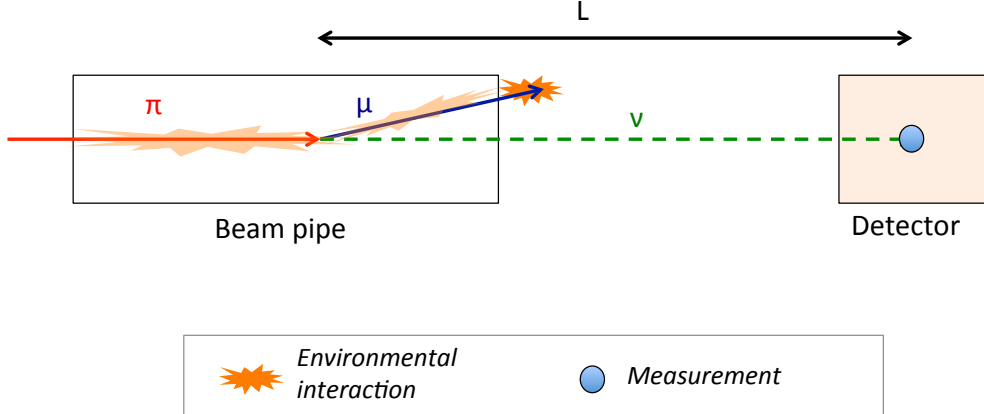


Figure 1.2.6: The neutrino production system for accelerator neutrino beams.

The formalism of multi-particle density matrices can be used to understand the coherence properties of such neutrino beams. The effects of environmental entanglement on the pion coherent width at the time of neutrino production can be calculated using a Monte Carlo simulation of environmental wave packet decoherence. The effects of entanglement with the unobserved muon are also important and have been discussed at length in the plane wave picture [82], and internal and external wave packet pictures [83]–[86]. In our formalism these effects are accounted for by tracing out the muon degrees of freedom from the bipartite neutrino-muon density matrix. These two ingredients yield the first prediction of neutrino coherence properties for the accelerator neutrino beam system which does not require an arbitrary assumption for the initial state.

In the following paper, published in Physical Review D as [1], this calculation is described, and the coherence distances for neutrino beams are predicted. This is the first calculation to account for the full pion-muon-neutrino-environment system and make a quantitative prediction for the neutrino coherence distance in accelerator neutrino beams without requiring an arbitrary initial state assumption.

Dynamical pion collapse and the coherence of conventional neutrino beams

B. J. P. Jones^{*}

Massachusetts Institute of Technology, Cambridge, Massachusetts 02139, USA

(Received 2 January 2015; published 4 March 2015)

In this paper we consider the coherence properties of neutrinos produced by the decays of pions in conventional neutrino beams. Using a multiparticle density matrix formalism we derive the oscillation probability for neutrinos emitted by a decaying pion in an arbitrary quantum state. Then, using methods from decoherence theory, we calculate the pion state which evolves through interaction with decay-pipe gases in a typical accelerator neutrino experiment. These two ingredients are used to obtain the distance scales for neutrino beam coherence loss. We find that for the known neutrino mass splittings, no nonstandard oscillation effects are expected on terrestrial baselines. Heavy sterile neutrinos may experience terrestrial loss of coherence, and we calculate both the distance over which this occurs and the energy resolution required to observe the effect. By treating the pion-muon-neutrino-environment system quantum mechanically, neutrino beam coherence properties are obtained without assuming arbitrary spatial or temporal scales at the neutrino production vertex.

DOI: 10.1103/PhysRevD.91.053002

PACS numbers: 14.60.Pq

I. INTRODUCTION

The standard formula describing neutrino flavor oscillation [1] has been widely experimentally verified [2]. However, it is known that its usual derivation, which proceeds via Taylor expansion of the phases of neutrino mass eigenstates in the plane-wave basis, contains several theoretical inconsistencies and assumptions that are not realized in any experiment. Attempts to fix these inconsistencies have involved the introduction of internal wave packets [3–5], the replacement of internal wave packets with external ones [6,7], field theoretical reformulations [7–9], and discussions of the role of the entangled muon in maintaining or suppressing coherence [8,10–14]. Many of these approaches turn a poorly formulated quantum mechanical problem into a theoretically robust calculation, but often at the cost of introducing arbitrary spatial or temporal scales. These scales have yet to be rigorously connected to experiments. Since several of these approaches predict observable coherence loss effects, especially in experiments searching for hypothetical sterile neutrinos, a robust quantum mechanical understanding of this system without arbitrary scales is needed.

In this paper we present a derivation of the oscillation probability for neutrinos produced in conventional neutrino beams. In such beams, relativistic pions are injected into a gas-filled decay pipe which is at atmospheric pressure, where they undergo electromagnetic interactions with gas molecules, eventually decaying to muons and neutrinos. The muons continue to interact with the environment but are undetected experimentally, and the neutrinos propagate over some baseline L before being detected via a weak interaction. The coherence properties of the resulting

neutrino beam are influenced by the initial pion state, the interactions of the pion with the decay-pipe environment, the presence of the entangled muon, and the source/detector configuration.

Our approach is to first derive the oscillation probability for neutrinos emitted from pions in an arbitrary initial state, consistently incorporating the constraints imposed by entanglement with an unobserved lepton (Sec. II). Then, using a representative pion density matrix, the classical (diagonal) and quantum (off-diagonal) uncertainties on the pion position are shown to lead naturally to two distinct neutrino coherence conditions (Sec. III). The first mechanism for coherence loss corresponds to a classical smearing of oscillation over the neutrino production point, the second to a distance-dependent suppression of oscillations via wave-packet separation. If either condition is not satisfied, neutrino oscillations will be suppressed, being replaced by an incoherent mixture of flavors with no nontrivial L or energy dependence.

With tools from decoherence theory we calculate the pion density matrix which evolves through interactions with the decay-pipe gas, and show how dynamical collapse leads to pion states with a stable and predictable quantum width in position space (Sec. IV). This width, in turn, allows the determination of the distance over which oscillations remain observable for a conventional neutrino beam, without requiring the introduction of arbitrary production or detection states (Sec. V).

We then discuss the implications of this result for the oscillations of standard and sterile neutrinos in accelerator neutrino experiments. We demonstrate that for standard neutrinos, no coherence loss is expected on terrestrial scales. Effects on terrestrial scales may be present for heavy sterile neutrinos, and we calculate the detector energy resolution required to observe such an effect.

*bjpjones@mit.edu

Finally, we discuss the similarities and differences in the coherence properties of other neutrino emission systems (Sec. VI), and present our conclusions (Sec. VII).

II. NEUTRINO OSCILLATIONS FROM DECAYS OF ARBITRARILY PREPARED PIONS

In this paper we use the density matrix formalism of quantum mechanics [15–17]. This is equivalent to the more prevalent wave-function formalism, although it accommodates more naturally both quantum and classical superpositions. This is particularly important in the presence of environmental entanglement, which acts to suppress coherence, effectively converting quantum uncertainties into classical ones within the neutrino subsystem. Aspects of neutrino oscillations have been analyzed using both wave-function [11,18] and density matrix [13,14] approaches, although no study to date has treated the full pion-lepton-neutrino-environment system. We find the multiparticle density matrix approach to be a powerful tool for this purpose, allowing treatment of the neutrino beam as an open quantum system and giving new insights into its coherence properties.

We work in a one-dimensional model, beginning with a general pion density matrix in the momentum basis ρ_π . This pion, with energy E_π , may either interact hadronically in the beam stop or decay with a 99.99% branching fraction via $\pi \rightarrow \mu\nu_\mu$ in the decay pipe. In the case where the pion decays, after a sufficiently long time t , the two-particle density matrix for the resulting entangled muon/neutrino state can be expressed in the basis of neutrino mass eigenstates $|m_i\rangle$ as

$$\rho(t) = N^2 U_{\mu i} U_{\mu j}^\dagger \Theta_{ij}(t) |m_i\rangle \langle m_j|. \quad (1)$$

In this equation, U is the unitary neutrino mixing matrix and N is a normalization factor. The momentum degrees of freedom are collected into matrix Θ_{ij} , shown in (2). The functions $p_\mu^i(p)$ and $p_\nu^j(p)$ represent the fixed momentum of a muon or neutrino as determined by two-body kinematics in the plane-wave basis. In each case, p is the momentum of the pion and the decay products have masses m_μ and m_i respectively.

$$\Theta_{ij}(t) = \int dp_1 dp_2 \rho_\pi(p_1, p_2) e^{i(E_\pi(p_1) - E_\pi(p_2))t} \times (|p_\nu^i(p_1)\rangle \langle p_\nu^j(p_2)|)_\nu (|p_\mu^i(p_1)\rangle \langle p_\mu^j(p_2)|)_\mu. \quad (2)$$

To trace out the leptonic degrees of freedom from (2) we express all of the leptonic states in terms of the basis states $p_\mu^a(p)$ corresponding to some neutrino mass m_a . These are related by $p_\mu^a(p_\pi) = p_\mu^i(p_\pi + 2\delta_\mu^{ia})$, where

$$\delta_\mu^{ia} = \frac{1}{2} \frac{dp_\mu^i}{dm_i^2} \left| \frac{dp_\mu^i}{dp_\pi} m_{ia}^2 \right| = -\frac{E_\pi}{2M^2} m_{ia}^2, \quad (3a)$$

$$M^2 = m_\pi^2 - m_\mu^2, \quad (3b)$$

with $m_{ia}^2 = m_i^2 - m_a^2$. The second equality in (3a) follows from momentum conservation, and (3b) assumes m_i to be much smaller than m_π and m_μ . Expressed in this basis, the muon degrees of freedom can now be traced out of (2), leading to the reduced density matrix for the neutrino subsystem:

$$\Theta_{ij}^\nu = \int dp \rho_\pi(p - \delta_\mu^{ij}, p + \delta_\mu^{ij}) e^{i\frac{p}{M^2} m_{ij}^2 t} \times |p_\nu^i(p - \delta_\mu^{ij})\rangle \langle p_\nu^j(p + \delta_\mu^{ij})|. \quad (4)$$

This object can be used to obtain the results of any measurement which can be performed on the neutrino alone, and incorporates the effects of both the initial pion state and the unmeasured entangled muon. An example of such a measurement is a neutrino oscillation experiment. A positive operator valued measure (POVM) is applied which selects a particular neutrino flavor state at baseline L , giving (5), the probability for neutrino detection in flavor α :

$$P(\nu_\alpha) = U_{\alpha j} U_{\alpha i}^\dagger U_{\mu i} U_{\mu j}^\dagger \int dq_1 dq_2 \langle q_1 | \Theta_{ij}^\nu | q_2 \rangle e^{i(q_1 - q_2)L}, \quad (5)$$

where summation over i and j is implicit. Substituting (4) into (5) leads to the final expression for the generalized oscillation probability,

$$P(\nu_\alpha, L) = U_{\alpha j} U_{\alpha i}^\dagger U_{\mu i} U_{\mu j}^\dagger \int dp \rho_\pi(p - \delta_\mu^{ij}, p + \delta_\mu^{ij}) e^{-i\phi_{ij}} \phi_{ij} = \frac{m_{ij}^2 p}{M^2} \left(\frac{E}{p} L - t \right). \quad (6)$$

We note that this expression does not depend on the muon final state, or its subsequent interactions. A general proof that this must be the case is presented in Appendix A.

III. PION STATE COHERENCE CONDITIONS

Equation (6) allows us to calculate the neutrino oscillation probability from any pion, prepared in a general state of coherent or incoherent superposition. In order to explore the coherence properties of such a system, we consider as an example a pion density matrix in the position basis, with Gaussian diagonal width σ_{diag} , off-diagonal width σ_{od} , and central momentum p_0 :

$$\rho = \int dx_1 dx_2 \exp \left[-\frac{(x_1 - x_2)^2}{2\sigma_{\text{od}}^2} - \frac{(x_1 + x_2)^2}{2\sigma_{\text{diag}}^2} \right] \times e^{-ip_0(x_1 - x_2)} |x_1\rangle \langle x_2|. \quad (7)$$

The diagonal width corresponds to the classical uncertainty on the pion position, whereas the off-diagonal width

corresponds to a quantum mechanical, coherent uncertainty. Substituting (7) into (6), after a few lines of algebra we can acquire the oscillation probability in the relativistic ($p_0 \gg m_\pi$) and nonrelativistic ($p_0 \ll m_\pi$) pion limits, as (8a)–(8b):

$$P_R(\nu_\alpha, L) = NU_{\alpha j} U_{\alpha i}^\dagger U_{\mu i} U_{\mu j}^\dagger \left[e^{i \frac{m_{ij}^2}{2p_0^2(m_\pi^2 - m_\mu^2)} L} \right] \left[e^{-\frac{(m_{ij}^2)^2(p_0^2 + m_\pi^2)}{8(m_\pi^2 - m_\mu^2)^2} \sigma_{\text{diag}}^2} \right] \left[e^{-\left(\frac{m_{ij}^2}{m_\pi^2 - m_\mu^2 p_0^2} \right)^2 \left(\frac{L^2}{2\sigma_{\text{od}}^2} \right)} \right] \quad (8a)$$

$$P_{NR}(\nu_\alpha, L) = NU_{\alpha j} U_{\alpha i}^\dagger U_{\mu i} U_{\mu j}^\dagger \left[e^{i \frac{m_{ij}^2 m_\pi}{m_\pi^2 - m_\mu^2} (1 + \frac{p_0}{m_\pi})^{-1} L} \right] \left[e^{-\frac{(m_{ij}^2)^2(p_0^2 + m_\pi^2)}{8(m_\pi^2 - m_\mu^2)^2} \sigma_{\text{diag}}^2} \right] \left[e^{-\left(\frac{m_{ij}^2}{m_\pi^2 - m_\mu^2} \right)^2 (1 + \frac{p_0}{m_\pi})^{-2} \left(\frac{L^2}{2\sigma_{\text{od}}^2} \right)} \right]. \quad (8b)$$

Describing the bracketed factors of (8a)–(8b) from left to right, the left factor contains the standard oscillation phase, reported here as a function of the central pion momentum p_0 . The central factor describes incoherent smearing caused by the production of neutrinos over a non-negligible spatial region. This is significant if the neutrino production region σ_{diag} is larger than the neutrino oscillation length. As well as a position-space interpretation, this effect also has an interpretation in the momentum basis, as the requirement that momentum wave packets for different mass states should overlap in order for oscillations to occur. The rightmost factor accounts for position-dependent wave-packet separation, which is a function of the off-diagonal width σ_{od} and becomes more severe with increasing L . Equation (8a), with which we will be primarily concerned, reduces to the standard formula for neutrino oscillations in the limits

$$\sigma_{\text{diag}} \ll \left(\frac{E_\pi^0}{2\sqrt{2}(m_\pi^2 - m_\mu^2)} m_{ij}^2 \right)^{-1} \quad (9a)$$

$$\frac{\sigma_{\text{od}}}{L} \gg \frac{1}{2\sqrt{2}p_0^2} \frac{m_\pi^2}{(m_\pi^2 - m_\mu^2)} m_{ij}^2 \quad (9b)$$

which can be considered as coherence conditions for neutrino oscillations to be observable.

Condition (9a), representing classical smearing of the oscillation, has been discussed at length as a source of incoherence, for example [18,19]. However, since the majority of experiments necessarily account for this classical averaging in their Monte Carlo simulations, it will not introduce unexpected effects for properly simulated neutrino experiments, so we will not discuss it further.

Condition (9b), on the other hand, is a constraint on the quantum mechanical width of the wave packet that dictates the distances over which wave packets for different mass eigenstates become separated spatially. This term can modify the standard neutrino transformation probability at large distances, and does not have a classical interpretation. Constraints similar to (9b) have been derived for the special case of a pure coherent state with $\sigma_{\text{od}}^2 = \sigma_{\text{diag}}^2 = 2\sigma_x^2$ [18,20]. However, the pion state which evolves in a typical neutrino beam is neither a pure state nor a minimal-uncertainty one, and the width σ_{od} has not been rigorously determined.

IV. EVOLUTION OF THE PION STATE IN A CONVENTIONAL BEAM LINE

We now turn to the determination of the pion state at neutrino production. In several prior studies of this system, a Gaussian state was assumed with width related to a physical scale in the problem, and the position and momentum space widths related by the minimal-uncertainty relation $\sigma_x \sigma_p = \hbar/2$. Interactions with decay-pipe gas are typically neglected. Following the method developed in [21], we show that the decay-pipe gas interactions are crucial to the coherence properties of the neutrino beam system. This is because the bombardment of a particle by environmental scatters leads to a highly squeezed state with a predictable quantum width. This “dynamical collapse” is experienced by the pion sufficiently early in its lifetime that all neutrinos can be assumed to be emitted from a pion with a stable equilibrium width.

Since we cannot track every air molecule in the decay pipe, the evolving pion is treated as an open quantum system. Air molecules undergoing local interactions with the pion encode information about its position into the environment, causing an effective collapse of its wave function in the position basis. As demonstrated in Ref. [21], the collapsing resolution of the environment is determined by the scale of momentum transfers. The effect of a single scatter with momentum transfer probability distribution $P(q)$ on the pion density matrix is

$$\rho_\pi(x_1, x_2) \rightarrow \rho_\pi(x_1, x_2) \tilde{P}_q(x_2 - x_1), \quad (10)$$

with $\tilde{P}_q(x_2 - x_1)$ being the Fourier transform of $P(q)$. This relationship was derived for nonrelativistic scatterers, but remains valid for the relativistic pion. Competing with the effective collapse caused by scattering is wave-packet dispersion, which acts to broaden the wave packet in position space between scatters. The competition between these two processes leads to a stable coherent width, which depends on the pion energy in two key ways. (1) the rate of dispersion for more energetic pions is suppressed by a Lorentz factor γ , and (2) the rate and momentum distribution of environmental scatters depends upon the pion energy.

To obtain the probability distribution of momentum transfers $P(q)$ we use the PAI model [22]. This model uses classical electromagnetism to determine the energy losses in a continuous medium parametrized by a complex index of refraction. The energy loss incorporates both ionization and Cherenkov losses, which are the dominant sources of momentum transfer for relativistic particles traversing matter at these energies. The imaginary part of the refractive index is related to the photoabsorption cross section of the material in the vacuum ultraviolet (VUV) range, and the real part is obtained via the Kramers-Konig relations. The continuous energy loss is then reinterpreted semiclassically in terms of discrete photon exchanges with electrons to give a distribution of momentum transfers. This distribution has been used to predict the fluctuations in dE/dx of ionizing particles in drift chambers and good agreement with experimental data is observed [22].

Since photoionization data for nitrogen are not available at the level of detail required, we use the photoionization spectrum for argon gas as input, making the assumption that the details of atomic shell structure will not cause large differences in the shape of the momentum transfer distribution. Predictions of our PAI model implementation were checked against those given in the original paper [22], and total dE/dx as reported in the [2], with good agreement observed in both cases. More information on our implementation of the PAI model and cross-checks is given in Appendix B.

The required outputs of the PAI model are (a) the complex decoherence function $\tilde{P}_q(x_2 - x_1)$ and (b) the scattering rate, both functions of pion energy and shown in Fig. 1. These are then used in a quantum Monte Carlo simulation of the dynamical collapse of the pion state.

We perform this Monte Carlo on a gridded space of dimension 2048×2048 . The resolution of this space in the momentum basis r_p is related to its resolution in the position basis by $r_p = 2\pi/r_x D$, specified for each initial state such that it is equally sized in the position and momentum grids at $t = 0$. The center of the grid corresponds initially to $x_G = 0$ and $p_G = p_0$, with these values updating as the grid moves to track the center of the wave packet.

We construct an initial Gaussian pure state of width σ_{initial} and central momentum p_0 in this space. The following procedure is then applied:

- (1) Sample the time-to-next-interaction, t_{evol} from a distribution $P(t_{\text{evol}}) = (\Delta t_{\text{scat}})^{-1} e^{-t_{\text{evol}}/\Delta t_{\text{scat}}(p_0)}$, where $\Delta t_{\text{scat}}(p_0)$ is the mean scattering time (Fig. 1, bottom);
- (2) In the momentum basis, unitarily evolve the state for a time t_{evol} ;
- (3) Fourier transform the density matrix into the position basis;
- (4) Apply the decoherence function $\tilde{P}(x_2 - x_1)$, an example of which is shown in Fig. 1, top.

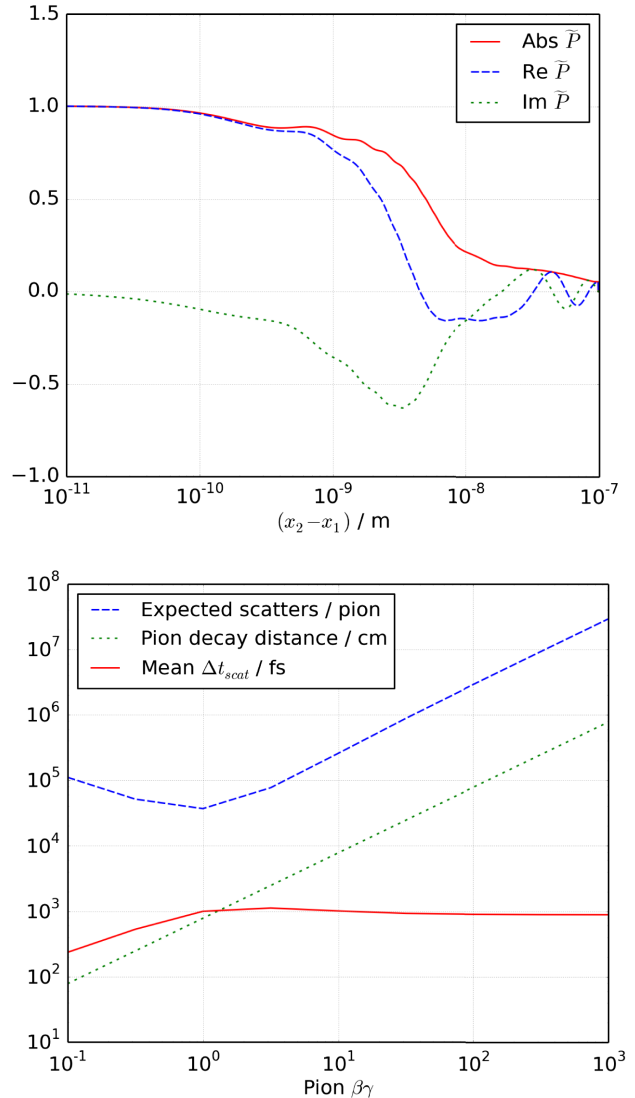


FIG. 1 (color online). Predictions of the photoabsorptive ionization (PAI) model. Top: the decoherence function for the pion in interaction with decay-pipe gas for $\beta\gamma = 10$. Bottom: pion scattering rate and other related quantities for pions of different momenta.

- (5) Fourier transform back to the momentum basis;
- (6) Continue until the density matrix overflows the grid boundaries in one of the two spaces.

After each interaction we record the diagonal and off-diagonal position- and momentum-space widths by calculating the standard deviation of the density matrix at its peak in the diagonal and off-diagonal directions. The calculation is halted when any width reaches one grid spacing, or when the amplitude of the wave packet at any edge of the grid is more than 1% of its peak. Further cross-checks of the simulation can be found in Appendix C. An example of the evolution of the

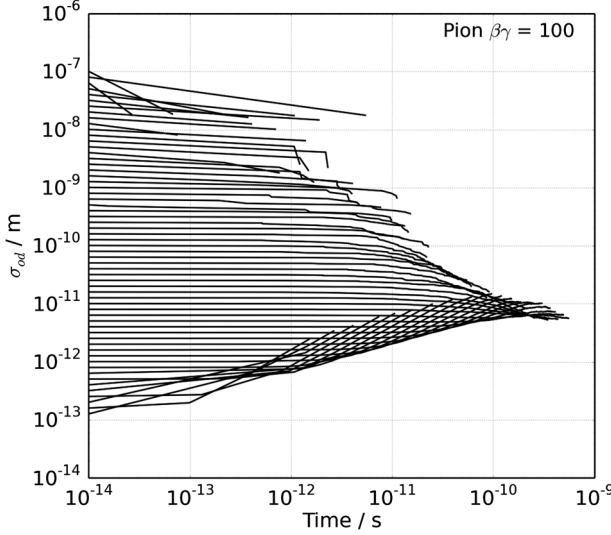


FIG. 2. The time-dependent coherent position-space width of pions with $\beta\gamma = 100$. Gaussian pure states of various widths are used as initial states in a quantum Monte Carlo. Each simulation is stopped when the wave packet no longer fits on the simulation grid in the position or momentum basis. Evolution towards a stable equilibrium width is observed.

coherent pion width for various initial states at $\beta\gamma = 100$ is shown in Fig. 2, where the convergence to an equilibrium width is clearly observed. A similar calculation can be performed for kaons, whose two-body decays give a subdominant flux contribution to conventional neutrino beams, by substitution $m_\pi \rightarrow m_K$. The asymptotic widths for pions and kaons of different energies are shown in Fig. 3.

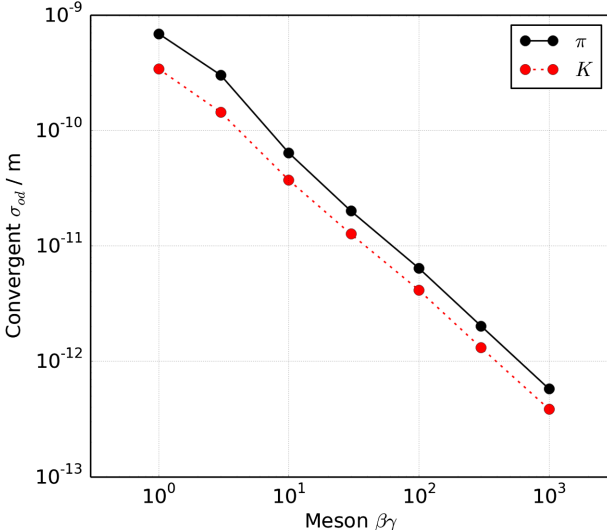


FIG. 3 (color online). Convergent widths for pions and kaons of different initial energies.

V. COHERENCE OF PION BEAMS AND OBSERVABILITY OF COHERENCE LOSS EFFECTS

The asymptotic coherent pion and kaon widths shown in Fig. 3 can be used with coherence condition (9b) to determine the distance over which the pion- and kaon-induced fluxes in conventional neutrino beams will become incoherent due to wave-packet separation. This distance is shown as a function of neutrino mass splitting in an effective two neutrino system with $m_{ij}^2 = \Delta m^2$, for several energy points in Fig. 4.

Existing and near-future accelerator neutrino experiments have baselines of up to 1300 km and beam energies from 10^2 to 10^5 MeV. Figure 5 shows the energy range and baseline for several such experiments, as well as the predicted coherence distance for several mass splittings, calculated using the relativistic formula (8a). The lowest energy point on this plot corresponds to a pion energy of 210 MeV, where nonrelativistic corrections may be expected. To illustrate the scale of such corrections we show the prediction of nonrelativistic expression (8b) at this point. We observe that the discrepancy with the relativistic prediction is small at these energies.

Over most of the energy range the coherence distance scales with E . This can be understood as emerging from the factor of p_0^2 in Eq. (9b) combined with the characteristic p_0^{-1} scaling of the convergent width, caused by Lorentz suppression of the pion dispersion rate. At low energies there are corrections both from the finite pion mass and from the energy dependence of the mean scattering time shown in Fig. 1.

It is clear from Fig. 5 that no loss of coherence is expected for the standard neutrinos produced in

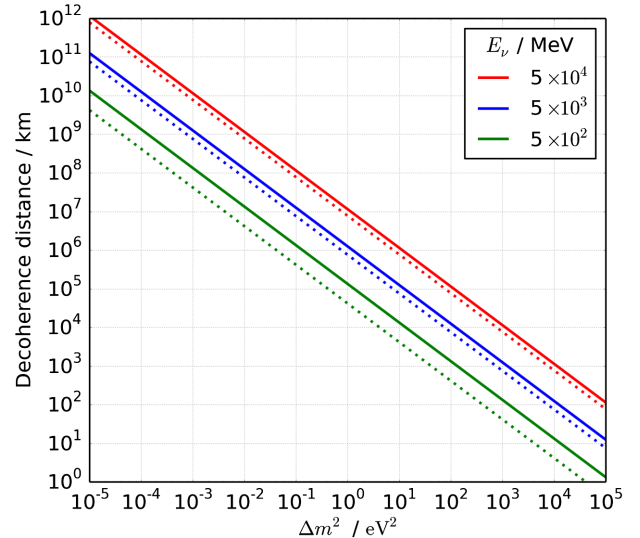


FIG. 4 (color online). Coherence distance for neutrinos of different energies produced in conventional neutrino beams. Solid: Two-body π^\pm decay. Dotted: Two-body K^\pm decay. Larger neutrino energies correspond to longer distances.

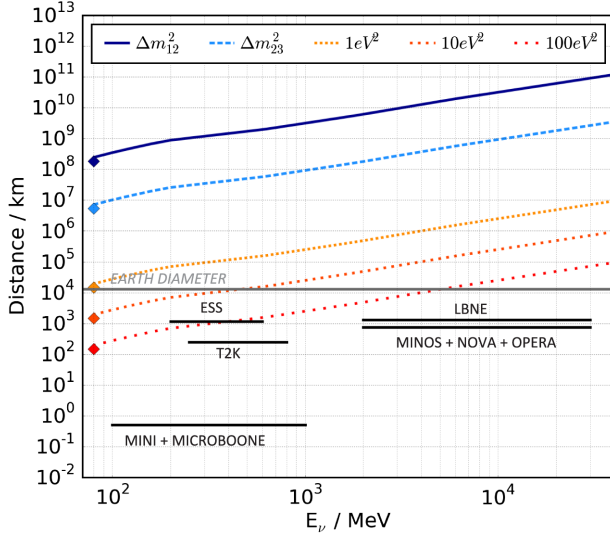


FIG. 5 (color online). The coherence distances for pion-induced neutrinos at several values of Δm^2 compared with the configurations of existing and proposed accelerator neutrino experiments. The lines use the relativistic expression (8a), whereas the diamonds show the prediction of the nonrelativistic expression (8b) at the lowest energies.

conventional beams on terrestrial distance scales. However, effects may be present for heavy sterile neutrinos. The experimental observability of these effects is directly related to the energy resolution of the far detector. At large L and Δm^2 , the oscillation phase $\Delta m^2 L / E$ varies rapidly as a function of energy. If this variation is more rapid than the energy resolution of the detector, an incoherent signal and a fast-oscillating one are indistinguishable.

Taylor expanding the oscillation phase $\Delta m^2 L / (E + \Delta E)$ in the limit of small $\Delta E/E$ gives the required energy resolution ΔE for observability of oscillations:

$$\Delta E < \frac{2\pi E^2}{\Delta m^2 L}. \quad (11)$$

Comparison of (11) with (9b) gives the range of $\Delta m^2 L$ over which loss of coherence both occurs and is experimentally observable. For such a space to exist at all, the energy resolution must satisfy

$$\Delta E < \frac{\pi}{\sqrt{2}\sigma_{od}(E)} \frac{m_\pi^2}{m_\pi^2 - m_\mu^2}. \quad (12)$$

This condition is shown in Fig. 6. In the range of terrestrial loss of coherence, a resolution < 0.1 MeV is required.

It may be possible to loosen this requirement with exotic experimental configurations. For example, if the pion traverses a decay volume with a higher density, the time between scatters will be reduced and the convergent wave-packet width will be narrowed, leading to enhanced position-space loss of coherence at shorter baselines.

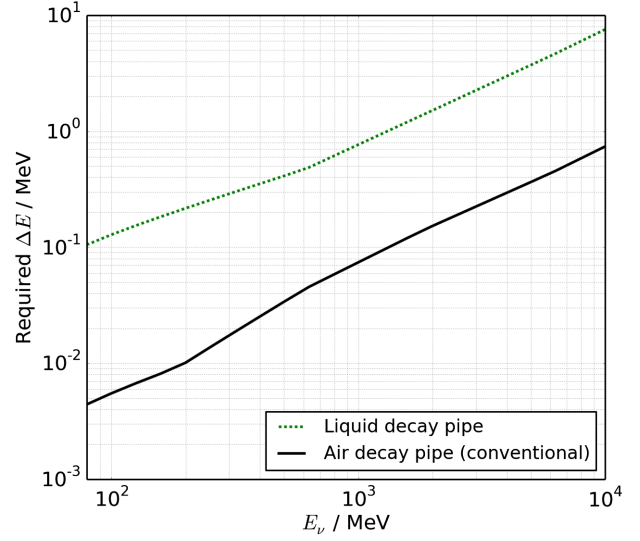


FIG. 6 (color online). The energy resolution required to observe coherence loss without fast oscillation in some part of the $\Delta m^2 L$ parameter space as a function of neutrino energy.

Consider a Gedankenexperiment where instead of air, a relativistic pion decays while traversing a high-density liquid. Producing such a beam in practice would introduce myriad experimental problems due to rapid energy loss of pions in the medium, but it provides an illustration of the scale of effects which can in principle be probed by changing the decay-pipe density. Using the PAI model for liquid argon, which is 1200 times more dense than air, we recalculate convergent wave-packet widths and the required energy resolutions for the observability of coherence loss, which are shown in Fig. 6. We see that although the energy resolution condition is relaxed, it remains very precise by existing neutrino detection standards.

VI. COHERENCE OF OTHER NEUTRINO OSCILLATION SYSTEMS

This paper has focused on the coherence properties of conventional meson-decay-in-flight neutrino beams. However, this is only one subclass of neutrino oscillation experiment, with others using different neutrino sources with different coherence properties. In this section we give a qualitative discussion of the similarities and differences between some of these systems.

Three-body decay in flight of muons in conventional neutrino beams requires a small modification of the calculation we have presented. The coherent width of the muon at the time of decay can be calculated using our method, and since its mass is similar to that of the pion, we expect to find similar coherent widths. The decay then proceeds $\mu \rightarrow e\nu\bar{\nu}$. To calculate the oscillation probability for the neutrino, for example, both the electron and the antineutrino must be traced out of the multiparticle density matrix. The momenta of the unobserved subsystem can be

reparametrized in terms of a total momentum and an invariant mass $m_{\mu\bar{\nu}}$, which implies that this system can be treated in our formalism as a neutrino recoiling against a variable-mass muon. Since each configuration of the antineutrino-muon subsystem is distinct, the neutrinos recoiling from different invariant masses will not interfere coherently. Thus the final expression for the oscillation probability will take the form of an integral of Eq. (6) over a probability distribution of $m_\mu = m_{\mu\bar{\nu}}$ values, with this distribution calculated from three-body kinematics. The coherence properties are likely to be quite similar to those of the pion-decay system.

Muon storage rings, on the other hand, produce neutrinos through the decays of muons which are circulated in an evacuated beam pipe to maintain a long storage time. In this case, ionizing interactions with residual gases may no longer be the dominant localizing influence, and our method of calculating the convergent wave-packet width using the PAI model is unlikely to be directly applicable.

Atmospheric neutrinos are primarily produced in the decays of charged pions and kaons in the upper atmosphere, with pions dominant at lower and kaons dominant at higher energies. The quantum mechanical system is essentially identical to that presented in this article, although the atmospheric density at the altitude where air showers develop is much less than that in accelerator neutrino beam decay pipes. Our calculation could be applied by simply adjusting the density of the decay-pipe gas to the atmospheric density, giving wider wave packets and longer coherence lengths. Because the expected effect is coherent broadening, wave-packet separation effects are unlikely to be experimentally observable for atmospheric neutrinos in Earth-based experiments.

Pion decay-at-rest beams present a similar quantum mechanical system to pion decay in flight, with the steps leading to Eq. (6) remaining valid. A different calculation is required for the initial pion width, since the momentum transfers involved in localizing a stopped particle are characteristically different to those produced by ionizing interactions in the relativistic case. Stopped π^- become trapped in atomic orbitals and capture on nuclei, so do not produce effective decay-at-rest beams. Stopped π^+ do not become trapped in atomic orbitals and become stopped somewhere in the material lattice until they decay. Electromagnetic and phonon interactions with the surrounding material are the primary localizing influence. A derivation of the coherence properties of decay-at-rest beams would require a microscopic model of the momentum transfers involved in these interactions with the pion to determine its coherent width at decay.

Reactor and solar neutrinos are produced by nuclear β decays of atoms in a hot, dense environment. The final state contains a daughter nucleus and an electron. In the density matrix formalism, the degrees of freedom of final state

which are not carried by the neutrino should be traced out to obtain the neutrino reduced density matrix. Accounting for all of the internal and external degrees of freedom of the daughter nucleus may require fairly involved nuclear physics. The localization of the initial state is also non-trivial, having contributions from the atomic interactions in the hot medium, photon exchange between the nucleus and its electron cloud, and Fermi motion within the nucleus itself. Although the latter certainly involves the largest momentum transfers, it is not conceptually clear what role is played by localization of the nucleon within the nuclear medium versus localization of the decaying nucleus within the bulk in determining the coherence properties of the emitted neutrino. This is a system whose coherence properties warrant further study, and where our calculation, though giving some insight, cannot be trivially applied.

VII. CONCLUSION

Using a multiparticle density matrix formalism we derived an expression for the oscillation probability of neutrinos produced by the two-body decays of pions in an arbitrary initial state. Assuming an example initial state with specified diagonal and off-diagonal widths in the position basis, we derived two coherence conditions for the observability of neutrino oscillations which set an upper limit on the classical width and a lower limit on the quantum mechanical width respectively. Modeling the dynamical collapse of a pion in a beam pipe using tools from decoherence theory and the PAI model to obtain realistic momentum transfer distributions, we calculated the coherence distances for neutrinos produced in conventional neutrino beams. To our knowledge, this is the first calculation to consistently treat the full pion-muon-neutrino-environment system. We find that no coherence loss should be expected for standard neutrinos on terrestrial scales in existing or proposed facilities. Sterile neutrinos with large masses ($> 10 \text{ eV}^2$) at low energies and long baselines may lose coherence through wave-packet separation on terrestrial scales, although a far detector with better energy resolution than is presently available is likely to be required in order to observe this effect.

ACKNOWLEDGMENTS

The author thanks Janet Conrad, André de Gouvêa, Boris Kayser and Joachim Kopp for discussions and guidance at all stages of this work, and particularly Janet Conrad and André de Gouvêa for the time they dedicated to helping prepare this manuscript. Thanks also to Jonathan Asaadi, Eric Church, Gabriel Collin, Yoni Kahn, Ben Safdi, Josh Spitz, and Jesse Thaler for a thorough reading of this paper and for valuable comments. The author is supported by National Science Foundation Grant No. PHY-1205175.

APPENDIX A: THE EFFECTS OF MUON-ENVIRONMENT INTERACTIONS

Here we give a proof that the environmental interactions or detection state of the entangled lepton cannot affect the oscillation phenomenology of a neutrino beam. While this conclusion is not difficult to reach intuitively via causality arguments, it is one which is either unclear or explicitly violated by several treatments of the neutrino beam system which can be found in the literature, so a formal derivation is useful.

Consider the muon-neutrino-environment system after the pion decay has taken place. This muon-neutrino subsystem is in an entangled state represented by reduced density matrix $\rho_{\mu\nu}$. We assume arbitrary entanglement at t_0 , but make a Schmidt decomposition into the ϵ (environment) and entangled $\mu\nu$ (muon and neutrino) subspaces (choosing a basis for each subsystem such that the entanglement is diagonal):

$$\rho(t_0) = \rho_{\mu\nu\epsilon}(t_0) = \sum_i \lambda_i \rho_{\mu\nu}^i \otimes \rho_\epsilon^i. \quad (\text{A1})$$

This density matrix will evolve into another fully entangled state as $\rho(t_0) \rightarrow \rho(t) = \rho_{\mu\nu\epsilon}(t)$. At any time we can obtain the reduced neutrino density matrix from the full density matrix by tracing out the other degrees of freedom:

$$\rho_\nu(t) = \text{Tr}_{\epsilon\mu}[\rho_{\mu\nu\epsilon}(t)]. \quad (\text{A2})$$

Any measurement we make on the neutrino alone can be represented by a POVM on the neutrino Hilbert space $\{O_\nu^{i=1\dots N}\}$, giving probability $P(o_j) = \text{Tr}_\nu[\rho_\nu O_\nu^j]$ of measuring outcome o_j , where $\sum_{i=1}^N O_\nu^i = 1_\nu$.

To time-evolve the system we apply the relevant muon-neutrino-environment Hamiltonian. We assume no interactions between the neutrino and the environment, although our conclusions remain valid even in the presence of neutrino-environment interactions, so long as the degrees of freedom coupling to the neutrino are different from those coupling to the entangled lepton. The muon and neutrino move apart from the origin and are assumed not to interact with one another after production. The muon will in general have an interaction with the environment. Finally all three parts have free evolution Hamiltonians. Therefore, the total Hamiltonian can be written:

$$\begin{aligned} H &= H_\nu + H_\mu + H_\epsilon + H_{\mu\epsilon}^{\text{Int}}, \\ &= H_\nu + H_{\mu\epsilon}. \end{aligned} \quad (\text{A3})$$

In the second line we have separated the Hamiltonian into a neutrino-only part and a muon-environment part. These act on different Hilbert spaces so will always commute, $[H_\nu, H_{\mu\epsilon}] = 0$. The time evolution operator for the entire system is

$$\begin{aligned} \mathcal{U}(t-t_0) &= T \left[\exp \left\{ i \int dt (H_\nu + H_{\mu\epsilon}) \right\} \right], \\ &= T \left[\exp \left\{ i \int dt H_\nu \right\} \right] T \left[\exp \left\{ i \int dt H_{\mu\epsilon} \right\} \right], \\ &= \mathcal{U}_\nu(t-t_0) \mathcal{U}_{\mu\epsilon}(t-t_0), \end{aligned} \quad (\text{A4})$$

where the second equality is valid because of the commutation properties already mentioned. Using this operator we evolve the initial density matrix:

$$\rho(t) = \mathcal{U}^\dagger \rho(t_0) \mathcal{U}, \quad (\text{A5})$$

dropping the arguments of the time evolution operators for simplicity of notation. We substitute the initial state (A1), and use the separability of the time evolution operator to find

$$= \sum_i \lambda_i \mathcal{U}_{\mu\epsilon}^\dagger [\mathcal{U}_\nu^\dagger \rho_{\mu\nu}^i(t_0) \mathcal{U}_\nu] \otimes \rho_\epsilon^i(t_0) \mathcal{U}_{\mu\epsilon} \quad (\text{A6})$$

which leads to (A7), the general expression for measurement probabilities for any neutrino observable at any time.

$$\begin{aligned} P(o_j, t) &= \text{Tr}_{\epsilon\mu} [\text{Tr}_\nu [\rho O_\nu^j]] \\ &= \sum_i \lambda_i \text{Tr}_{\epsilon\mu} [\mathcal{U}_{\mu\epsilon}^\dagger \text{Tr}_\nu [\mathcal{U}_\nu^\dagger \rho_{\mu\nu}^i(t_0) \mathcal{U}_\nu O_\nu^j] \otimes \rho_\epsilon^i(t_0) \mathcal{U}_{\mu\epsilon}]. \end{aligned} \quad (\text{A7})$$

We know that time evolution in quantum mechanics is unitary. This does not necessarily imply unitary evolution within a subsystem, however. The overall unitarity requirement gives

$$\mathcal{U}^\dagger \mathcal{U} = 1_{\nu\mu\epsilon} \quad (\text{A8a})$$

$$= 1_\nu \otimes 1_{\mu\epsilon} \quad (\text{A8b})$$

$$= \mathcal{U}_\nu \mathcal{U}_{\mu\epsilon} \mathcal{U}_{\mu\epsilon}^\dagger \mathcal{U}_\nu^\dagger. \quad (\text{A8c})$$

We know that time evolution for the neutrino subsystem is unitary, since it is identical to the free neutrino case. Therefore the states $U_\nu |\nu_i\rangle$ make just as good orthonormal basis states for taking a trace as $|\nu_i\rangle$, and $\text{Tr}_\nu [\mathcal{U}_\nu^\dagger A_{\mu\nu\epsilon} \mathcal{U}_\nu] = \text{Tr}_\nu [A_{\mu\nu\epsilon}]$, where $A_{\mu\nu\epsilon}$ is any general operator on the three system Hilbert space. This tells us that the muon-environment time evolution must also be unitary in its own Hilbert space $\mathcal{U}_{\mu\epsilon} \mathcal{U}_{\mu\epsilon}^\dagger = 1_{\mu\epsilon}$, leading to the conclusion

$$\text{Tr}_{\mu\epsilon} [\mathcal{U}_{\mu\epsilon}^\dagger A_{\mu\nu\epsilon} \mathcal{U}_{\mu\epsilon}] = \text{Tr}_{\mu\epsilon} [A_{\mu\nu\epsilon}]. \quad (\text{A9})$$

We can use this to simplify the above expression (A7) for neutrino measurement probabilities:

$$P(o_j) = \sum_i \lambda_i \text{Tr}_{\epsilon\mu} [\text{Tr}_\nu [\mathcal{U}_\nu^\dagger \rho_{\mu\nu}^i(t_0) \mathcal{U}_\nu O_\nu] \otimes \rho_e^i(t_0)]. \quad (\text{A10})$$

The operator $\mathcal{U}_{\mu e}$ no longer features in this expression. We conclude that any measurement made on the neutrino alone cannot be influenced by the subsequent evolution or environmental interactions of the entangled muon.

Correlated measurements on both subsystems would involve a measurement operator $O_{\mu\nu}$. In this case, the muon-environment interactions could, of course, affect the oscillation probabilities of neutrinos detected in coincidence with a particular subset of muons. This would correspond to a selection effect, with measurements which are made over all neutrinos, without reference to their associated muons, still returning values which are independent of the muon-environment interactions. Thus, by virtue of quantum mechanical unitarity, there is no spooky-action-at-a-distance or faster-than-light communication, and the interactions of muons with their environment cannot affect the neutrino oscillation probability in any experiment.

APPENDIX B: CONSTRUCTION OF THE PAI MODEL

There are two main sources of environmental interaction for pions in a neutrino beam line. The first is interaction with the magnetic fields of the focusing horn which steers the pions into a forward beam. In the lab frame, this field is purely magnetic, and so only transfers transverse momentum, having no decohering effect in the longitudinal direction important for neutrino beam coherence. Furthermore, the pion is only in the region of strong horn fields for a short time, spending most of its decay time traveling forward in the low field region.

The second source of environmental interaction is ionization losses and Cherenkov emission due to photon exchange with the beam-pipe gas. The energy loss of a relativistic particle passing through a gaseous environment is understood as being the result of many low energy scatters with nuclei and electrons. It is well known that the majority of the energy loss occurs through scattering with electrons rather than nuclei, the latter giving a contribution on the order of $O(10^{-4})$ to dE/dx . In what follows we will neglect the effects of scatters off nuclei completely, although a more complete treatment might include this small correction.

The distribution of momentum transfers for relativistic particles in matter has been studied in several contexts, including for the purpose of understanding ionization fluctuations in drift chambers. Therefore much of the existing data and modeling has focused on common drift chamber gases such as argon and methane.

One example of such a model is the PAI model [22]. In this model, classical electromagnetism is used to determine the energy losses in a continuous medium parametrized by a complex index of refraction n . This energy loss

incorporates contributions from both ionization and Cherenkov emission, which although both included, are not easily separable. The refractive index is determined from the photoabsorption spectrum of the material in the VUV range, which has been measured for argon and is shown in Fig. 7, reproduced from [22]. The continuous energy loss is reexpressed semiclassically in terms of discrete photon exchanges with electrons to give a distribution of momentum transfers.

The main result we need from the PAI model is Eq. (B1), giving the energy transfer cross section in terms of the photoabsorption cross section of the medium. In this formula, β is the ionizing particle velocity, E is the energy transfer by a single photon exchange, and $\sigma_\gamma(E)$ is the photoionization cross section of the material in the VUV range. ϵ_1 and ϵ_2 are the real and imaginary parts of the material index of refraction, which can be expressed in terms of the photoabsorption cross section via the definition of the absorption length, and then the Kramers Konig relation, as in Eqs. (B2a)–(B2b). The function Θ is defined in terms of the particle velocity and the index of refraction as in Eq. (B2c).

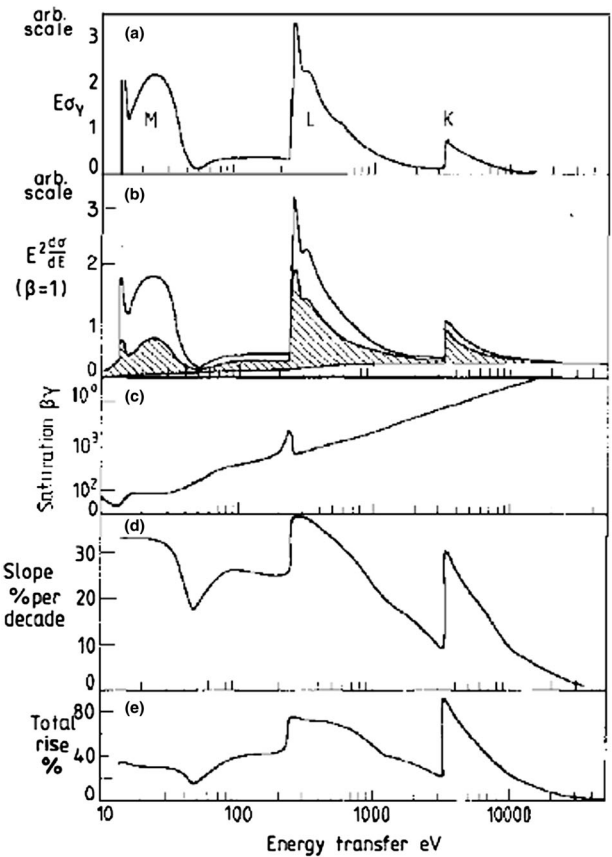


FIG. 7. Elements of the PAI model. The two panels of interest to us are the top panel, showing the photoabsorption cross section of argon gas, and the second panel, showing the calculated dE/dx from this model for $\beta = 1$. This figure is reproduced from [22].

$$\begin{aligned} \frac{d\sigma}{dE} = & \frac{\alpha}{\beta^2 \pi} \frac{\sigma_\gamma(E)}{EZ} \ln [(1 - \beta^2 \epsilon_1)^2 + \beta^4 \epsilon_2^2]^{-1/2} \\ & + \frac{\alpha}{\beta^2 \pi N \hbar c} \left(\beta^2 - \frac{\epsilon_1}{|\epsilon|^2} \right) \Theta + \frac{\alpha}{\beta^2 \pi} \frac{\sigma_\gamma(E)}{EZ} \ln \left[\frac{2mc^2 \beta^2}{E} \right] \\ & + \frac{\alpha}{\beta^2 \pi E^2} \int_0^E \frac{\sigma_\gamma(E')}{Z} dE' \end{aligned} \quad (\text{B1})$$

$$\epsilon_2 = \frac{Nc}{\omega Z} \sigma_\gamma(E) \quad (\text{B2a})$$

$$\epsilon_1 = \frac{2Nc}{\pi Z} P \int_0^\infty \frac{\sigma_\gamma(x) dx}{x^2 - \omega^2} \quad (\text{B2b})$$

$$\Theta = \arg(1 - \epsilon_1 \beta^2 + i \epsilon_2 \beta^2). \quad (\text{B2c})$$

The momentum transfer probability distribution and the number of scatters per centimeter are given by

$$P(q) = \frac{1}{\sigma} \frac{d\sigma}{dp} \frac{dN_{\text{scat}}}{dx} = \frac{1}{\langle E \rangle} \frac{dE}{dx} \quad (\text{B3})$$

and the normalized probability distribution for each discrete momentum transfer at several $\beta\gamma$ values is shown in Fig. 9, top.

We cross-check our implementation of this model in two ways. First, Fig. 9, bottom, shows our calculated momentum transfer distribution for $\beta = 1$ as compared to that given in [22]. There is good agreement everywhere except at the lowest momentum transfers, where it appears the Allison and Cobb calculation displays a small tail which is not present in our model. We suspect this could be the result of the choice of regularization in the Fourier transform. Since these are scatters with very small momentum transfer and so little decohering resolution, we do not expect this feature to be important for this calculation. Second, we calculate the total dE/dx predicted by this model as a

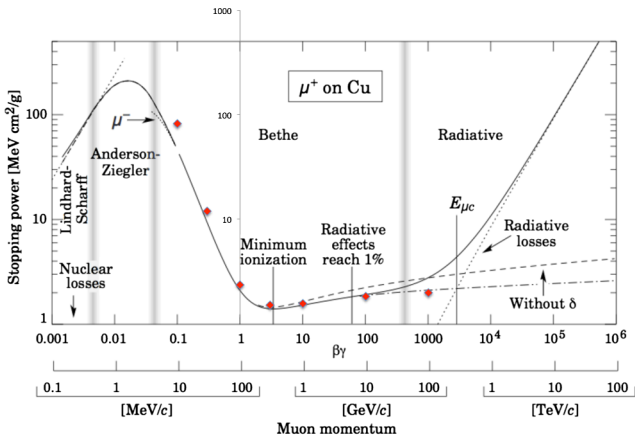


FIG. 8 (color online). dE/dx calculated using PAI model (diamonds) overlaid on the prediction from [2].

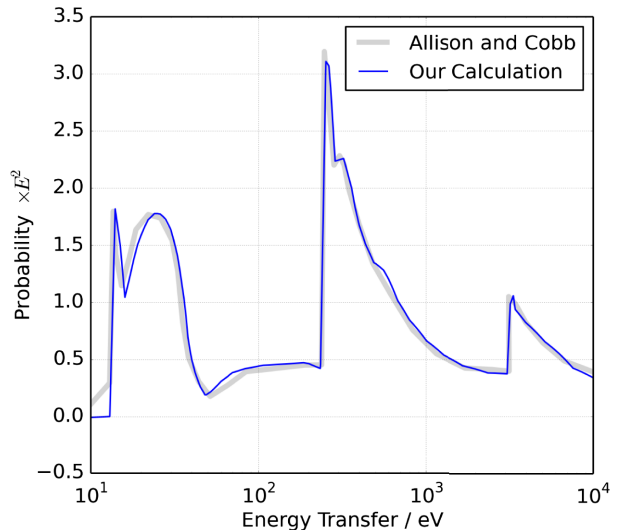
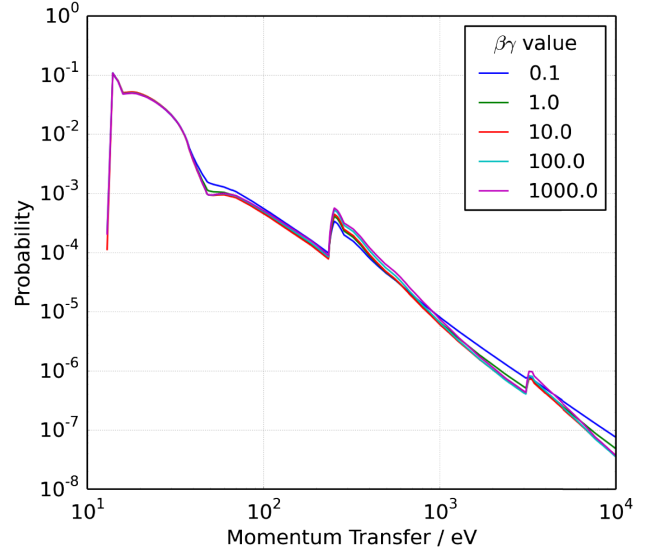


FIG. 9 (color online). Top: The momentum transfer distribution predicted by the PAI model for various values of $\beta\gamma$. Above $\beta\gamma = 1$ the distributions are very similar. Bottom: The energy transfer distribution calculated in our PAI model implementation, compared with that given in [22].

function of pion energy, and compare to the PDG. This is shown in Fig. 8, and again, good agreement is observed.

APPENDIX C: TESTS OF NUMERICAL DENSITY MATRIX EVOLUTION

Here we present some cross-checks of the density matrix evolution calculation which test that the convergent width depends only on the physics of the problem, and not the details of our simulation.

Rather than using the Monte Carlo technique with random scattering times, for these tests we model a “smoothed” evolution, using a constant time per scatter equal to the mean expected at the given pion energy, shown in Fig. 1. This generates deterministic rather than random

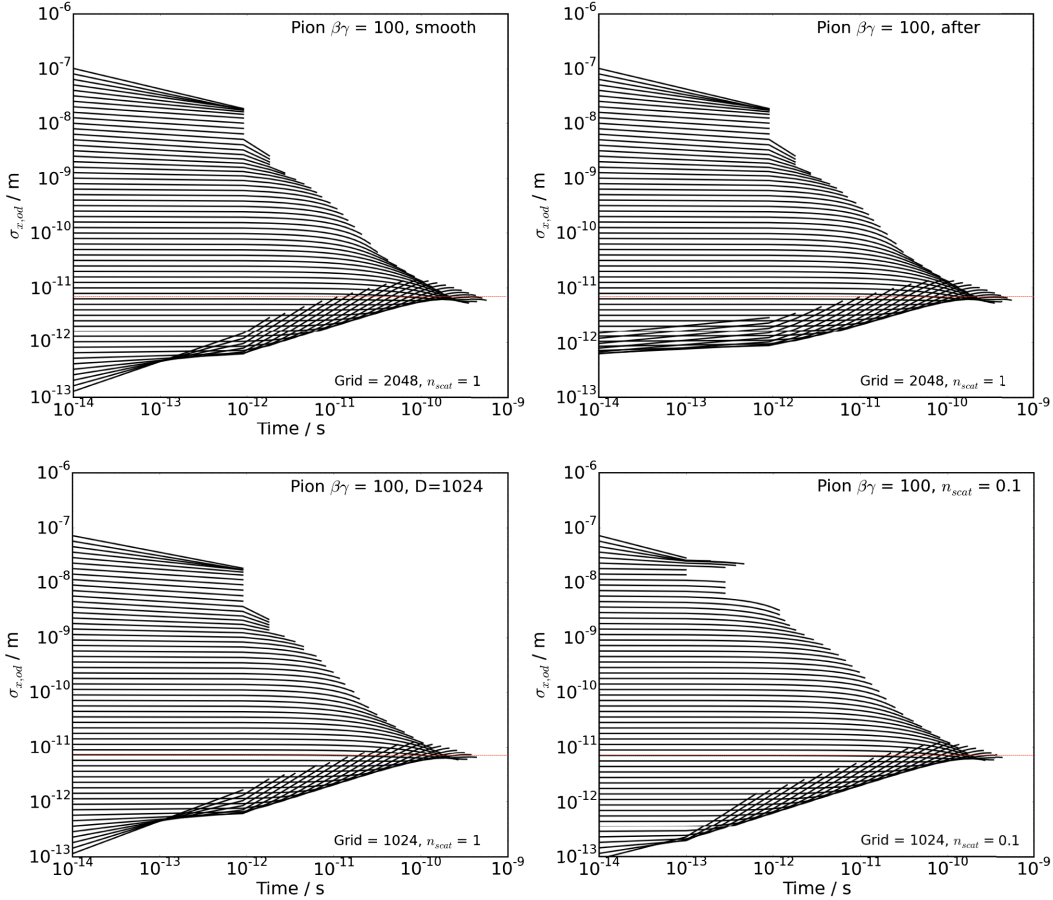


FIG. 10 (color online). Cross-checks of the model. Top left: baseline. Top right: measure width after unitary evolution, rather than after scatter. Bottom left: adjusted grid size 1024. Bottom right: $n_{\text{scat}} = 0.1$ approximation. The red line represents an identical width in each plot.

curves, which demonstrate more clearly the average behavior. The baseline model with smoothed evolution for $\beta\gamma = 100$ is shown in Fig. 10, top left. Comparison with Fig. 2 demonstrates that the smoothed evolution gives a similar approach to convergence and convergent width to the Monte Carlo evolution, but with the advantage that it can be used to test for systematics of the method independently of random fluctuations.

Using the smoothed model for $\beta\gamma = 100$ we checked that our results are not affected by the following purely calculational adjustments. We change the point in each cycle where the width is measured from directly after each scattering interaction to directly after each unitary evolution. The

resulting evolution is shown in Fig. 10, top right. We check that our result is not affected by the grid size, changing from a grid dimension of 2048 to 1024, shown in Fig. 10, bottom left. In the lowest energy cases for $\beta\gamma \leq 3$, to stabilize the calculation the Monte Carlo evolution was run using 0.1 scatters per evolution. That is, unitary evolution for $0.1 \times t_{\text{evol}}$ and application of a decoherence function $\widetilde{P}_q(x_2 - x_1)^{0.1}$. We check that this approximation, a weaker version of the continuum approximation used to describe systems by master equations, gives the same convergent width as the default evolution. This is shown in Fig. 10, bottom right. In all cases, a consistent convergent width and a similar approach to convergence is observed.

-
- [1] B. Pontecorvo, Zh. Eksp. Teor. Fiz. **33**, 549 (1957) [Sov. Phys. JETP **26**, 984 (1968)].
 - [2] K. A. Olive *et al.* (Particle Data Group), Chin. Phys. **C38**, 090001 (2014).
 - [3] B. Kayser and J. Kopp, arXiv:1005.4081.
 - [4] A. Asahara, K. Ishikawa, T. Shimomura, and T. Yabuki, Prog. Theor. Phys. **113**, 385 (2005).
 - [5] O. V. Lychkovskiy, Phys. At. Nucl. **72**, 1557 (2009).

- [6] E. K. Akhmedov and A. Y. Smirnov, *Phys. At. Nucl.* **72**, 1363 (2009).
- [7] E. Akhmedov and J. Kopp, *J. High Energy Phys.* 04 (2010) 377.
- [8] J. Wu, J. A. Hutasoit, D. Boyanovsky, and R. Holman, *Int. J. Mod. Phys. A* **26**, 5261 (2011).
- [9] M. Beuthe, *Phys. Rep.* **375**, 105 (2003).
- [10] D. Boyanovsky, *Phys. Rev. D* **84**, 065001 (2011).
- [11] B. Kayser, J. Kopp, R. H. Roberston, and P. Vogel, *Phys. Rev. D* **82**, 093003 (2010).
- [12] B. Kayser, arXiv:1110.3047.
- [13] J. Wu, J. A. Hutasoit, D. Boyanovsky, and R. Holman, *Phys. Rev. D* **82**, 013006 (2010).
- [14] A. G. Cohen, S. L. Glashow, and Z. Ligeti, *Phys. Lett. B* **678**, 191 (2009).
- [15] H. Breuer and F. Petruccione, *The Theory of Open Quantum Systems* (Oxford University Press, Oxford, 2007).
- [16] M. A. Schlosshauer, *Decoherence and the Quantum-to-Classical Transition* (Springer, New York, 2008).
- [17] M. A. Nielsen and I. L. Chuang, *Quantum Computation and Quantum Information* (Cambridge University Press, Cambridge, 2011).
- [18] E. Akhmedov, D. Hernandez, and A. Smirnov, *J. High Energy Phys.* 04 (2012) 052.
- [19] D. Hernandez and A. Y. Smirnov, *Phys. Lett. B* **706**, 360 (2012).
- [20] M. Beuthe, *Phys. Rev. D* **66**, 013003 (2002).
- [21] M. Tegmark, *Found. Phys. Lett.* **6**, 571 (1993).
- [22] W. Allison and J. Cobb, *Annu. Rev. Nucl. Part. Sci.* **30**, 253 (1980).

Part II

The MicroBooNE Experiment

Chapter 1

A Liquid Argon Time Projection Chamber in the Booster Neutrino Beam

MicroBooNE is a 170-ton liquid argon time projection chamber detector in the Booster Neutrino Beamline (BNB) whose primary goal is to provide a confirmation or refutation of the low energy anomaly observed by the MiniBooNE detector, 240 feet downstream in the same beam. In the event of a confirmation, MicroBooNE will be able to distinguish between electrons or photons as the source of the anomaly, which would be suggestive of exotic neutrino oscillation physics or hitherto unknown nuclear physics processes, respectively.

1.1 Liquid argon time projection chambers

The first proposal to use liquid argon as the detection medium in a particle physics experiment was made by Alvarez in 1968 [87]. Such a detector was implemented in 1974 by Willis and Radeka [88] who constructed a total absorption calorimeter with 200×2 mm argon gaps interspersed with 1.5 mm steel dividers, which was operated in test beams of pions, protons and electrons. This was the predecessor to the liquid argon devices which have become a standard in hadron collider calorimetry [89], [90].

The time projection chamber (TPC) was invented by Nygren in 1974 [91]. The proposal to implement a liquid argon TPC (LArTPC) for neutrino physics was made by Rubbia in 1977 [92], and the concept was implemented by the ICARUS collaboration [93]. Unlike a total absorption calorimeter, a LArTPC is a three-dimensional imaging detector, read out using several planes of sense wires at an edge of the active volume. A strong (500 V/cm) electric field drifts ionization charge towards the wire planes, where sensitive electronics record either the inductive signal of the drifting charge (induction planes) or the current derived from it entering the conductor (collection planes) [94]. By tuning the potentials of each plane appropriately, ideal transparency of the induction planes can be achieved [95]. The resulting image is a set of two-dimensional wire vs. drift time projections, which can then be reconstructed into a 3D calorimetric image using offline software. The basic steps in TPC image formation are sketched in Figure 2.1.1.

The drift distances that can be obtained are in principal limited by the achievable argon purity [96]. Contamination by electron-scavenging elements, including oxygen and water, must be minimized. This is achieved by selecting materials which minimize outgassing in the TPC vapor phase [97] and by continuous liquid and/or vapor phase purification [98]. Using these techniques, 20 ms charge lifetimes corresponding to drift distances of \sim 30 m have been demonstrated [99].

LArTPCs are inherently anisotropic detectors. Position resolution perpendicular to the drift direction is limited by the wire pitch and the charge spread due to transverse diffusion [100]. Resolution in the drift direction is limited by either the time resolution of the electronics or longitudinal diffusion. Calorimetric resolution is limited by the ability to apply a drift-time correction for electron losses, by contamination from wire and electronics noise, by quantized fluctuations in the ionization density, or by the effects of saturation for highly ionizing tracks [101], [102].

Saturation results from a charge recombination process where following thermalization, ionization electrons are attracted to the positively charged track core where they may reattach to parent ions [103]. As well as being a mechanism for charge loss, this process is a source of scintillation light (Section 3). The ionization and scintilla-

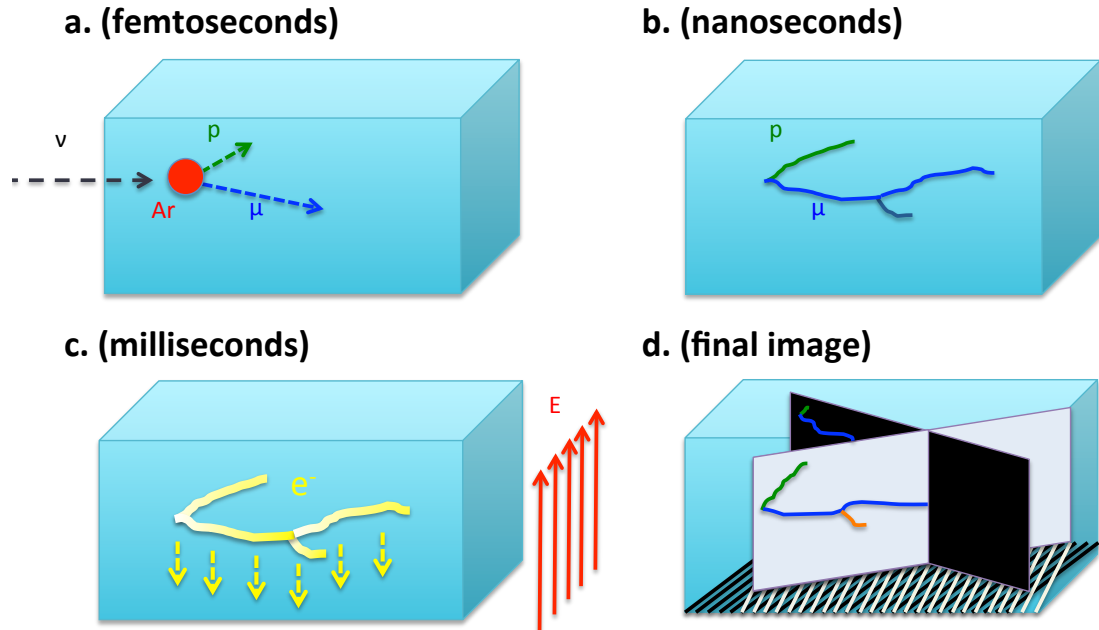


Figure 2.1.1: Cartoon showing the image formation process in a LArTPC detector. a) A neutrino undergoes a weak interaction with an argon nucleus, producing zero or more charged particles; b) The charged particles lose energy through ionization and scintillation, change direction through multiple scattering, and possibly undergo inelastic or delta-ray producing interactions; c) The liberated ionization electrons drift in the electric field to the sense wires; d) By measuring charge arrival times, each wire plane produces a two-dimensional image of the event.

tion yields in a TPC are thus anticorrelated [104], [105], with opposite and nontrivial dependences on the applied electric field [103] and local ionization density [106].

The development of the ICARUS detectors over the thirty years since Rubbia’s proposal has seen LArTPCs used as cosmic ray [107], solar neutrino[108] and accelerator neutrino [109] detectors. The ArgoNeuT experiment at Fermilab subsequently marked the beginning of a US-based program of liquid argon neutrino physics, producing several cross section measurements at a short baseline in the NuMI beam [110]– [113]. The MicroBooNE [114] experiment represents the second step in the US-based LArTPC neutrino program and will be described in some detail in this thesis.

There are two notable proposals for future US-based LArTPC experiments. First, the Fermilab Short Baseline (SBN) [15] proposal involves complementing the MicroBooNE detector with the 40-ton SBND (née LAr1ND) [115], [116] detector at 150 m



Figure 2.1.2: Left: Top view of the MicroBooNE cryostat in situ in the beamline, showing the locations of cable feedthroughs for each active system. Right: Side view of the MicroBooNE TPC during construction.

and the 600 ton ICARUS T600 [117] at 600 m to perform a multiple-baseline oscillation measurement in the BNB. Second, the DUNE (née LBNE) [118] collaboration proposes to deliver a 30 GeV neutrino beam 1300 km from Fermilab to a 34 kiloton LArTPC at Homestake, SD. DUNE will probe the leptonic CP phase δ_{cp} , and measure oscillations in multiple channels using both neutrinos and antineutrinos [119].

1.2 The MicroBooNE TPC

The MicroBooNE TPC has dimensions $2.5 \times 2.5 \times 10.4 \text{ m}^3$ and an active mass of 70 tons. It is operated inside a stainless steel cryostat containing 170 tons of purified liquid argon, which is situated in the Liquid Argon Test Facility (LArTF) at Fermilab. MicroBooNE will collect neutrinos from 6×10^{20} protons on target from the BNB [120], which is a conventional neutrino beam with mean neutrino energy 600 MeV.

The long TPC direction is aligned with the neutrino beam, defining the z axis of a right-handed coordinate system with y upwards. Three sensitive wire planes at

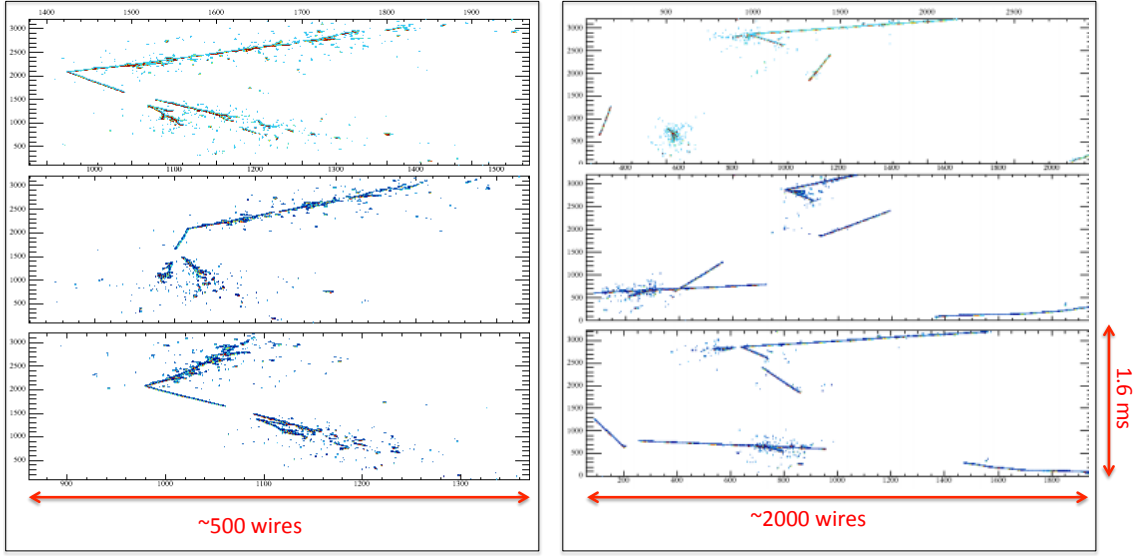


Figure 2.1.3: Left: A single neutrino event. Right: A neutrino event with background.

the $+x$ side have a 3 mm pitch and are oriented vertically and at ± 60 degrees. A total of 8256 stainless steel wires are connected to cold front-end application-specific integrated circuits (ASICs) which send amplified signals to 11 feedthroughs where further amplification takes place. Above cryostat these signals are processed by on-platform electronics. A photograph of the cryostat before insulation is shown in Figure 2.1.2, left, with various feedthroughs labelled.

The 500 V/cm drift field requires -128 kV DC to be supplied to the solid stainless steel cathode, which is stepped down using a voltage divider across 64 field-shaping rings. These elements are held in place by a machined G10 frame. The high voltage (HV) distribution system is discussed in Section 5, and a photograph is shown in Figure 2.1.2, right. The electron drift distance is 2.5 m in the x direction, with a drift time of approximately 1.6 ms. To maintain a high charge yield the argon is continuously recirculated and purified. The purity is monitored by three electron-drift ionization chamber detectors at points within the cryostat and cryogenics system.

The wire signals are digitized at 2 MHz. An example of simulated raw data for a neutrino-induced event with no background is shown in Figure 2.1.3, left. The vertical axis shows charge arrival time, with the wire number on the horizontal. Each panel

displays data from one wire plane. The interaction time, t_0 , and drift coordinate, x_0 , are not known from the TPC readout alone, due to the degeneracy introduced by finite drift velocity. For beam events, t_0 can be determined from the accelerator clock, and x_0 can be inferred. For non-beam events, neither can be known from the TPC information alone, but the arrival time of scintillation light can be used to break the degeneracy. For this reason, MicroBooNE incorporates an optical system to collect 128 nm scintillation light, which is described in Chapter 2.

The long drift times, during which cosmic backgrounds accumulate, make surface-based LArTPCs high-background detectors. Each recorded frame (one drift time of readout) contains 0 or 1 neutrino events and approximately 10 overlaid background events. A simulated example is shown in Figure 2.1.3, right. One way to isolate signal events is to geometrically match scintillation light arriving in time with the beam to TPC sub-events. This matching requires high-quality TPC and optical reconstruction. Progress on these problems will be presented in Chapter 6.

1.3 Physics goals of the MicroBooNE experiment

Low-energy excess and short-baseline oscillations

The primary goal of the MicroBooNE experiment is to investigate the MiniBooNE low-energy excess [51], [121]. By running in the same beam and at a similar baseline, MicroBooNE can confirm or refute the existence of the excess, and, if seen, provide a positive identification as electrons or photons. This is possible because liquid argon detectors can resolve the details of evolving electromagnetic events. Characterization of energy losses near the vertex allows differentiation between single e^- tracks and photon-induced pair production $\gamma \rightarrow e^+e^-$, which is not possible in Cherenkov detectors. The technique has been demonstrated by the ArgoNeuT collaboration [122], and the separation efficiency is shown in Figure 2.1.4, left. An electron excess would be evidence for exotic oscillation physics, whereas photons would point towards standard model processes [123], [124]. MicroBooNE expects to observe a 5σ or 4σ signal

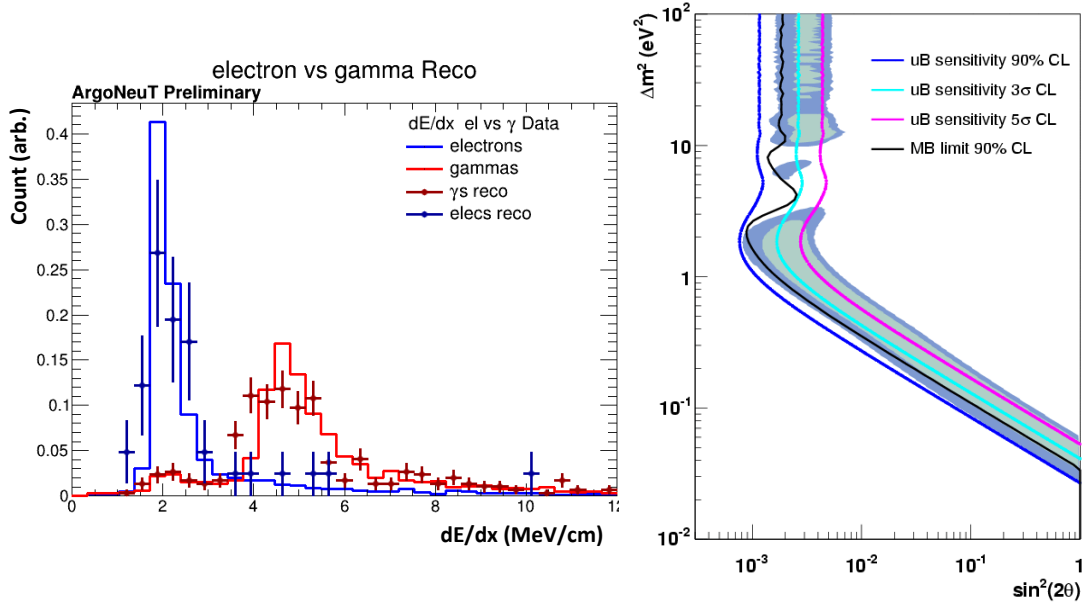


Figure 2.1.4: Left: LArTPC e/ γ separation efficiency, from [122]. Right: Projected sensitivity to sterile neutrinos in the 3+1 model [114].

if the excess is entirely due to electrons or photons, respectively [114].

As well as characterizing the low-energy excess, which is incompatible with the LSND appearance signal in a 3+1 model, MicroBooNE will also search for standard sterile neutrino oscillations through $\nu_\mu \rightarrow \nu_e$. MicroBooNE’s oscillation sensitivity is shown reproduced from [114] in Figure 2.1.4 right.

Cross sections

MicroBooNE will collect the highest statistics sample of neutrino interactions ever in a liquid argon detector. The ~ 1 GeV energy regime is particularly interesting for studying the nuclear physics of neutrino interactions. Investigations of final-state proton multiplicity and kinematics of charged-current quasi-elastic (CCQE)-like events can provide information about short range nuclear correlations [125]–[127], including two-particle–two-hole effects [128], [129]; meson exchange currents [130]–[132]; and other non-trivial nuclear processes [133], all of which can affect the interpretation of neutrino oscillation experiments [134]–[136].

MicroBooNE will make other important cross section measurements. These in-

clude the neutrino-induced kaon production cross section, a key background to future proton decay searches; the neutral current to charged current $\nu - p$ cross section ratio, which provides a probe of the spin-structure of the nucleon [137], [138] with implications for spin-dependent dark matter detection [139]–[141]; and the coherent pion production cross section, which is in tension between existing experiments [142]–[144].

Astroparticle physics and exotica

Supernova explosions release 99% of their energy in neutrinos, and these neutrinos are detectable by terrestrial experiments [145], [146]. MicroBooNE incorporates a dedicated supernova data stream and a connection to the SuperNova Early Warning System [147], such that in the event of a nearby supernova, continuous data will be written to disk for several hours. This data can be analyzed for events in the $\nu_e + {}^{40}\text{Ar} \rightarrow e + {}^{40}\text{K}^*$, $\bar{\nu}_e + {}^{40}\text{Ar} \rightarrow e^- + {}^{40}\text{Cl}^*$, or $\nu_x + e^- \rightarrow \nu_x + e^-$ channels. The information obtained, along with that from other experiments, can be used to better understand supernova explosions. If these can be well modelled, topics in neutrino physics [148]–[152], including sterile neutrinos [153]–[158], can be studied using supernova dynamics.

MicroBooNE can also search for exotic dark sector particles produced directly in the BNB target [159], [160]. In some scenarios the particle is heavy and arrives at the detector with a time-of-flight delay. In others, a unique interaction topology can be observed. Paraphotons, dark photons, weakly interacting massive particles (WIMPs), and other exotic particles can all be constrained with MicroBooNE data [161]–[164].

Liquid argon detector development

As the forerunner to future large LArTPC experiments in the US, MicroBooNE provides an important opportunity for technology development. Among other topics, improvements in HV distribution, light collection, LArTPC reconstruction methods and calibration techniques are required before a detector like DUNE can be realized. Progress in each of these areas will be reported in this thesis.

Chapter 2

Development and Installation of the MicroBooNE Optical System

The primary goal of the MicroBooNE optical system is to collect scintillation and Cherenkov light produced by charged particles, and from this, extract geometrical and timing information. This information is used to form a trigger and to reject cosmogenic backgrounds to neutrino events.

2.1 Photomultiplier tube assemblies

The sensitive elements of the MicroBooNE optical system are photomultiplier tubes (PMTs) [165]. The primary light collection system is comprised of 32 assemblies, each containing one R5912-02mod 8-inch PMT [166]. The PMT is held by a stainless steel mount that constrains the glass PMT bulb in a spring-loaded trap, which is formed using three Teflon-coated wires and three Teflon pads, shown in Figure 2.2.1. The mount sits inside a μ -metal shield, which prevents distortion of the PMT electron-optics by the Earths magnetic field [167]. This assembly is screwed onto a stainless steel back-plate, which is in turn mounted onto a support rack inside the detector. Above each PMT is affixed a wavelength-shifting plate.

PMTs must be used in regions of low electric field, so the racks are installed behind the TPC anode wireplanes, which are 85% transparent to normally incident

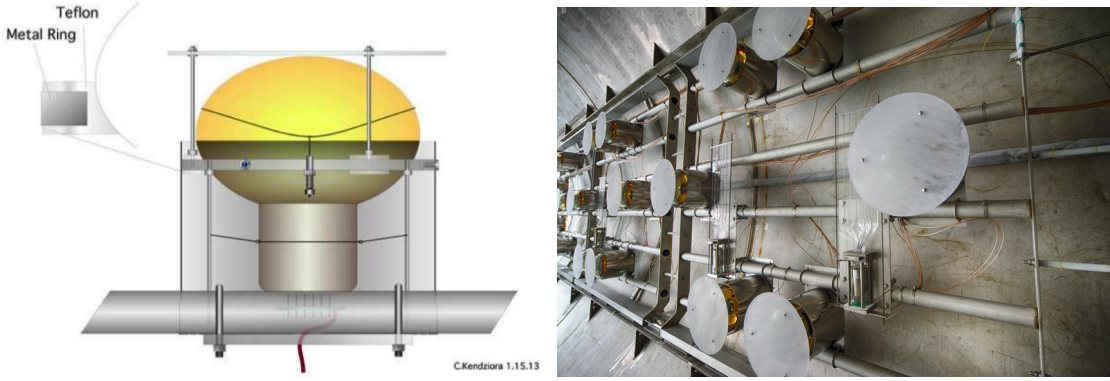


Figure 2.2.1: Left: Mechanical construction of one PMT assembly (credit Cary Kendziora). Right: the MicroBooNE PMT assemblies in situ (credit Fermilab VMS).

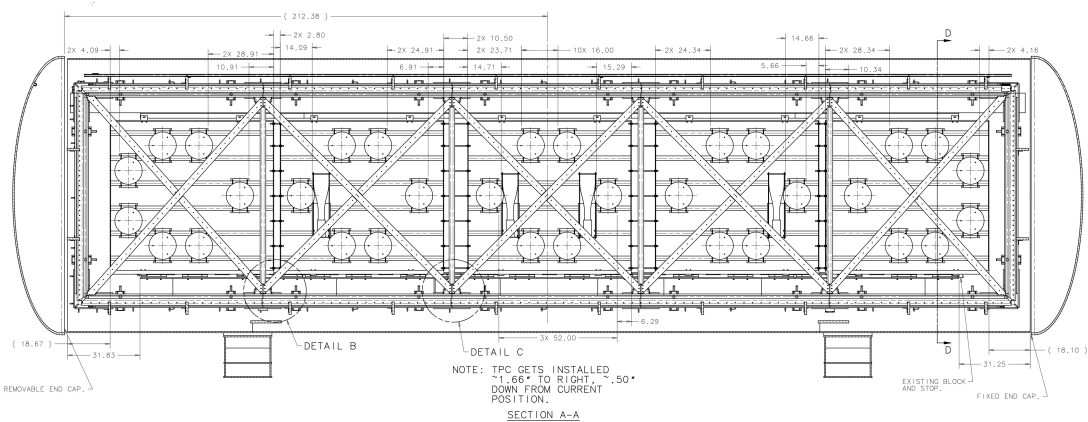


Figure 2.2.2: Arrangement of optical assemblies for the MicroBooNE optical system.

light. The geometrical arrangement of assemblies is chosen to avoid light blockage by the TPC frame, and is shown in Figure 2.2.2.

PMTs for low-light-yield applications typically use bialkali photocathodes due to their intrinsically low dark currents. These do not function well at cryogenic temperatures as the bialkali conductance falls prohibitively low below 150 K. This problem can be alleviated by adding a platinum undercoating between the photocathode and the PMT glass [168] to produce a cryogenically modified PMT, such as the R5912-02mod [169]. Absorption of photons in the platinum layer reduces the quantum efficiency of a modified device by around 20% relative to an unmodified PMT.

The photons produced by argon scintillation are effectively monochromatic with a wavelength of 128 nm [170]. The R5912-02mod has a borosilicate glass window,

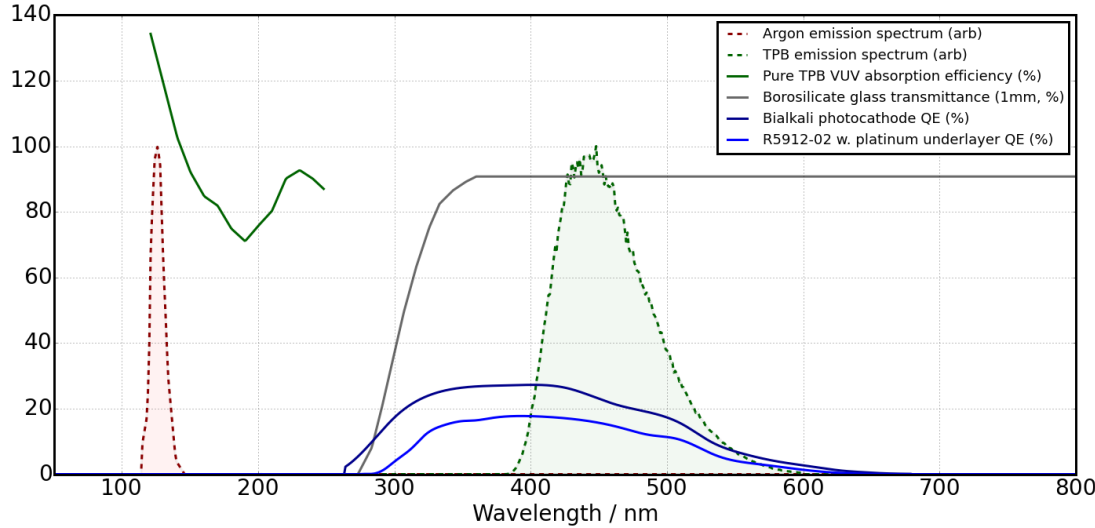


Figure 2.2.3: Scintillation spectrum of argon, from [170]; Emission spectrum of TPB from measurements described in Section 4; VUV absorption efficiency of TPB from [171]; borosilicate glass transmittance from [172]; Hamamatsu bialkali photocathode quantum efficiency from [173]; and platinum undercoated PMT quantum efficiency from data provided by Hamamatsu for MicroBooNE PMTs.

which has a rapidly falling optical transmittance at wavelengths below 300 nm [172]. The conversion efficiency of the photocathode is also low at these wavelengths [173]. To sensitize the PMT to 128 nm light, a wavelength-shifting coating with active ingredient tetraphenyl-butadiene (TPB) is employed. The coating efficiently converts 128 nm light to visible wavelengths, and it is applied to a 12-inch diameter acrylic plate in front of the PMT. The argon scintillation spectrum, glass transmission curve, photocathode spectral efficiency, TPB conversion efficiency and emission spectrum are shown in Figure 2.2.3. A quantitative discussion of the coating optical properties and PMT quantum efficiency in MicroBooNE will be given in Section 4.

Signal and HV for each PMT are carried by one RG316 cable running from the optical system detector feedthrough to each PMT. The cable terminates at an RO4000 [174] PCB base soldered directly to the PMT electrodes. The base resistively divides the applied potential and holds each dynode at its required operating voltage. Capacitive elements are present to maintain the linearity properties at high charge yields and decouple the signal and HV components. This base was designed specifically for

the MicroBooNE application and uses cryogenically robust components.

Each PMT in the MicroBooNE optical system was tested both warm and cold [2], and several were characterized in a longer term, high-purity liquid argon test stand. This will be discussed in Section 3.2. Installation and pre-commissioning of the optical system will be described in Section 2.6.

2.2 Light guide detectors

In addition to PMT-and-plate assemblies, the MicroBooNE optical system incorporates four light guide detectors [7], [8], [10], [175], two of which are visible in Figure 2.2.1, right. These use an acrylic bar with a wavelength-shifting coating, which guides light through total internal reflection to a 2-inch Hamamatsu R7725-mod PMT. The development and optimization of light guide detectors is an ongoing R&D project at MIT and Indiana University, and the four devices installed in MicroBooNE closely resemble those described in [7]. As well as enhancing the sensitive area of the optical system, running light guides in MicroBooNE provides a long-term test of the technology to assess its potential for future detectors.

The light guide concept has several advantages over a PMT-and-plate system for large detectors. The collection area per channel is enhanced, meaning that more optical coverage is provided using the same number of electronics channels, cables and feedthroughs; the detectors have a slim profile so can be slid between chambers in a multi-TPC detector, minimizing volume requirements; the light guide itself may be operated in high-field regions; and guiding light to a small collection area allows the use of photon detection technologies, such as silicon photomultipliers (SiPMs),[176] which are less expensive per channel than PMTs, have a more linear response, and do not require HV.

The R7725-mod PMTs were also characterized before installation. The performance of a light guide detector is primarily a function of the optical quality of its coating, which has been studied in detail. Work on this topic will be discussed in Section 4.

2.3 Flasher calibration system

The MicroBooNE optical system incorporates a flasher subsystem for monitoring the gain and timing of each PMT. This provides a tool for detector commissioning and for optical calibrations. A detailed technical description can be found in [3].

Each PMT is accompanied by one optical fiber [177] of length 12.84 ± 0.03 m, running from 2 cm in front of the photocathode to a custom-made flange in the center of the optical system feedthrough. A shorter fiber section couples to the long fiber and runs through the feedthrough to a patch panel outside the detector, where the LEDs and driving electronics are situated. A cartoon and photograph are shown in Figure 2.2.4. The fibers have a diameter of $600 \mu\text{m}$, with $30 \mu\text{m}$ cladding and an additional $25 \mu\text{m}$ buffer layer. This fiber was chosen due to its demonstrated cryogenic robustness, established in the Bo [4] and Luke [97] test stands at Fermilab.

To couple to the feedthrough, the internal fibers are bundled into a connector in a 6×6 grid with 1.5 mm spacing. The fiber ends were pulled through the connector

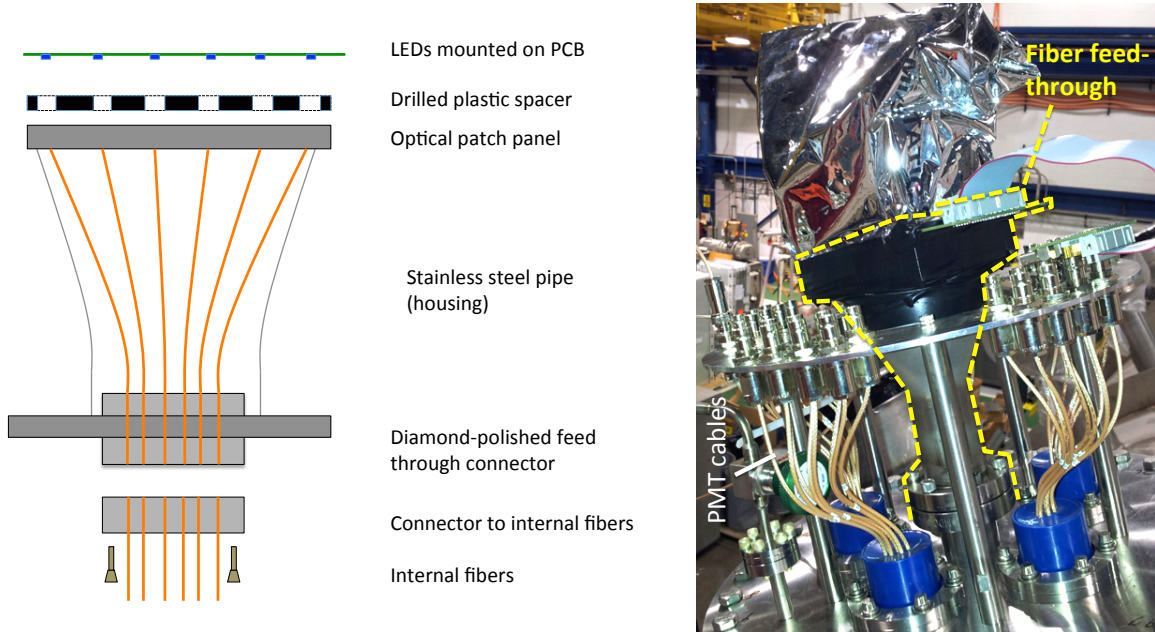


Figure 2.2.4: Left: Cartoon of the custom feedthrough design. The internal fiber connector couples to the feedthrough from below. Outside the flange, the fibers are spread onto a patch panel which couples to the LED array. Right: Photograph as installed on the cryostat, as used during the PMT installation tests. From [3].

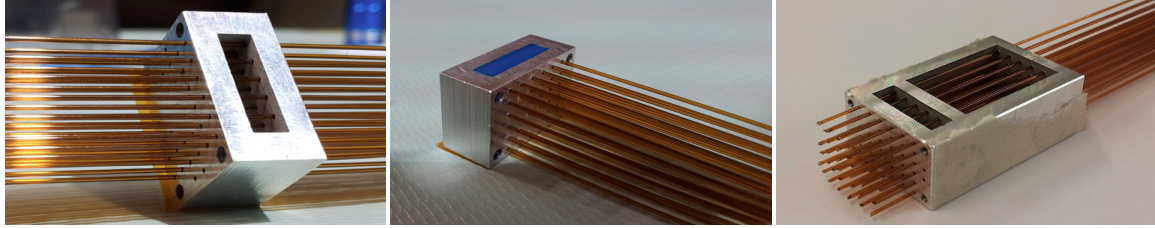


Figure 2.2.5: Preparation of the two connector parts. Left and center: internal connector. Fibers are drawn through, cut using a fiber cleaver, aligned and then set in sealant. Right: feedthrough connector. Fibers are drawn, set and then diamond polished. From [3].

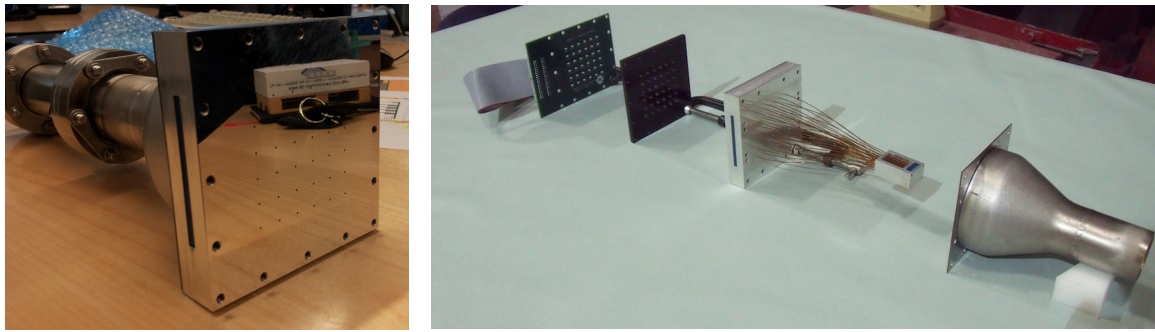


Figure 2.2.6: Left: the assembled feedthrough during the vacuum test, after diamond polish. Right: custom feedthrough components, exploded view. From [3].

(Figure 2.2.5, left), cleaved, aligned and then set with an epoxy sealant (Figure 2.2.5, center). This connector is coupled to a matching connector inside the feedthrough (Figure 2.2.5, right), by four screws and four alignment pins. The 1.5 mm grid spacing was chosen so the bundle can exit the detector through a 2-3/4" ConFlat (CF) flange.

To produce the feedthrough, designed specifically for this application and made using custom parts, short fiber sections were set into the internal and external coupling blocks with the fibers protruding from both sides. The set fibers and blocks were placed into a stainless steel housing, comprising a welded pipe, shoulder and blank CF flange (Figure 2.2.6, right). The feedthrough was sealed by setting the internal connector block into a machined CF flange using epoxy (Figure 2.2.5, right, and Figure 2.2.7, right). The protruding fiber ends were cut and both blocks were diamond polished to produce high-quality optical surfaces (Figure 2.2.6, left). The feedthrough was helium tested under vacuum and at 45 psig over-pressure and no leaks were found.

The internal end of each fiber is pointed at its PMT by an aluminum standoff



Figure 2.2.7: Left to right: the mounting stand-off which holds the fiber at each PMT; the stainless steel stand-off with its nylon-tipped set-screw; magnification of the prepared fiber end, which points towards the photocathode; connector block being set in the custom feedthrough. From [3].

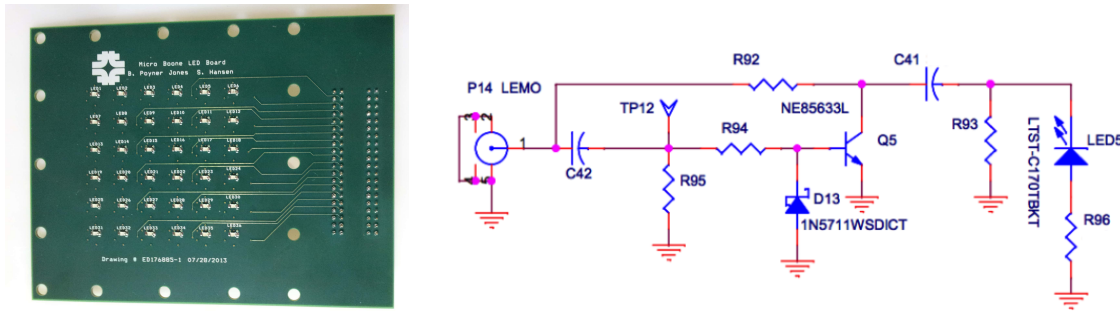


Figure 2.2.8: Left: An image of the LED board with the 400 nm LEDs mounted. Right: A single LED network schematic from LED flasher board. From [3].

(Figure 2.2.7, far- and mid-left). For each unit the fiber was drawn through the standoff, then cleaved, inspected for surface quality (shown in Figure 2.2.7, mid-right) and fixed in place using a nylon-tipped set-screw.

Outside the feedthrough, a PCB board with a matrix of 36×400 nm LEDs and driver circuits, shown in Figure 2.2.8, is mounted at the fiber patch panel. A black acrylic spacer provides a cavity for each LED and isolates them optically from one another. The driver circuits, shown in Figure 2.2.8, right, cause the LEDs to pulse with a luminosity proportional to the applied bias voltage in response to a transient trigger pulse. This circuit design provides a fast light pulses with rate-independent brightness [3]. The bias voltages and logic pulses are supplied to the LED board via two ribbon cables by a programmable driver board which interfaces

with a server on the MicroBooNE platform via USB. The board triggers in response to logic signals supplied on two input terminals. These pulses can be produced either by a signal generator for commissioning runs, or by the MicroBooNE DAQ system. The LEDs can be pulsed in two modes: 1) simultaneously, for timing calibrations, or 2) sequentially, for individual gain calibrations and crosstalk measurements. A channel-to-channel timing calibration of 0.68 ns precision can be achieved [3]. The system was used to test the MicroBooNE optical system during installation (Section 2.6) and for routine calibration during data taking.

2.4 Readout and triggering

Above the detector, signal and HV components for each PMT are separated by splitter modules. The splitter further divides the signal across two outputs, one of which has a $10\times$ attenuation. Recording both high- and low-gain channels using the 50Ω terminated electronics increases the dynamic range of the system at the high end.

The next step is pulse shaping. PMT pulses with widths of 10 ns cannot be well sampled by the 64 MHz readout ADC. By linearly applying a shaping kernel of approximately 100 ns FWHM and fitting the rising edge, PMT pulses can be well sampled and few ns timing resolution can be retained. Shaped pulses also have the advantage that the amplitude correlates strongly with the total charge.

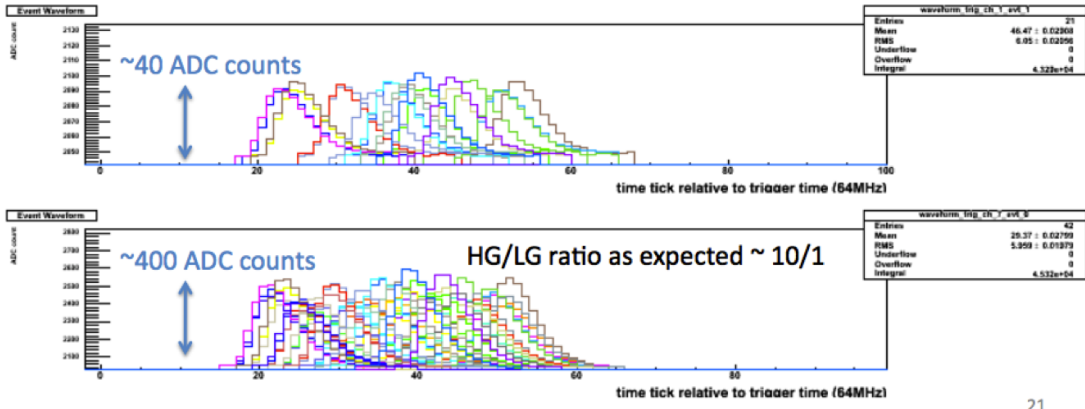
The shaped pulses are sent to front-end-modules (FEMs) with on-board ADCs. For a pulse to be recorded by the FEM it must meet certain threshold conditions and not fall into regions of dead-time, the details of which are beyond the scope of this discussion. A trigger card makes the decision whether to write the pulses supplied by the FEM to disk. In the case of neutrino beam running, a signal from the accelerator clock triggers a full readout of the system for 15 μs around the beam gate. The data volume can be reduced by rejecting background-only TPC events by further applying a PMT activity condition. The readout system interfaces with an on-platform server via a control card over Ethernet. Recorded data is transmitted by optical fiber to the counting room for further processing. More information can be found in [178]–[180].

2.5 Vertical slice test of the optical system

Using the Bo test stand described in Section 3.2, a vertical slice test (VST) of the MicroBooNE optical system was run for an extended period in high-purity liquid argon. The slice included a MicroBooNE-specification PMT, TPB-coated plate, base electronics, cable feed through, HV power supply, interlock system, splitter, shaper, FEM, trigger card, control card, server, impurity monitors, and in later runs the additions of μ -metal shield, redesigned PMT mounts, splitters and feedthroughs. At least one of every active component in the system was tested, and in many cases the design was modified based on the information acquired about its performance.

The configuration of the Bo test stand for vertical slice test runs is shown photographically in Figure 2.2.11, right. Two PMTs are deployed, and can be exposed to flashing LED light delivered by optical fibers. The system was used to record light from both visible (420 nm) LEDs directed at the PMT photocathode, and ultraviolet (275 nm) LEDs directed at the wavelength-shifting plate. Pulses recorded via the MicroBooNE readout system in response to the firing of a visible LED near the photocathode are shown in Figure 2.2.9. This test provided the first demonstration of cold PMT readout with MicroBooNE electronics.

Studies were also made of the response of the system to 128 nm scintillation light, from both cosmic rays and calibration sources. A plot of the self-trigger rate as a



21

Figure 2.2.9: A series of scintillation pulses recorded using the full MicroBooNE readout system and the Bo vertical slice test.

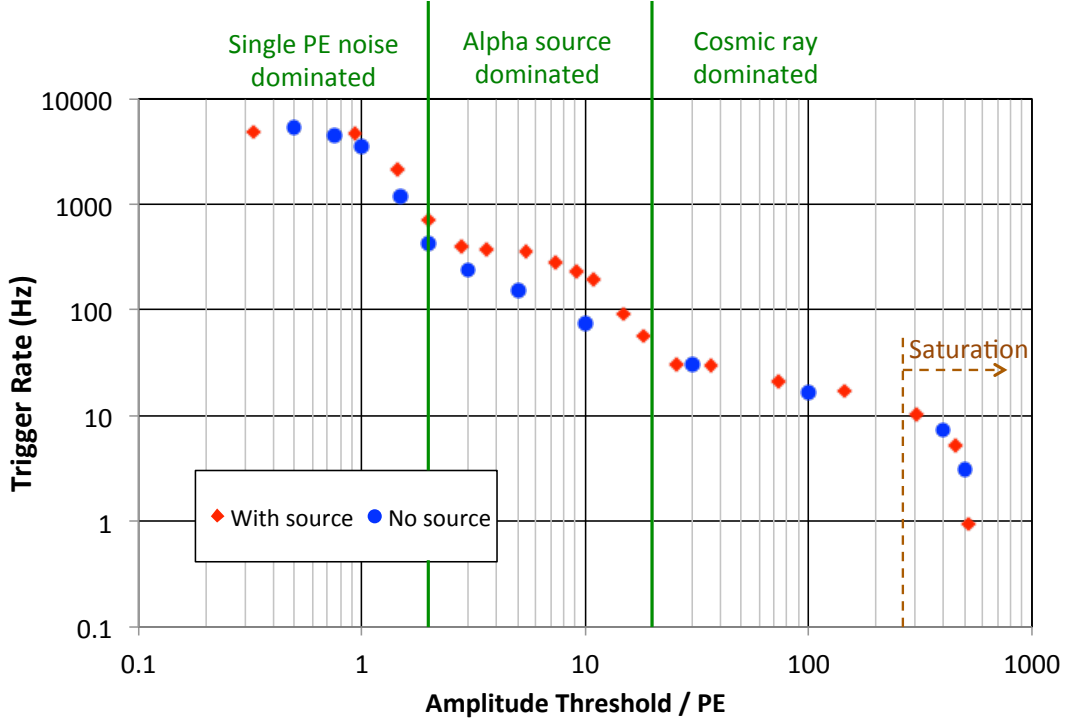


Figure 2.2.10: Left: Trigger rate in the BoVST with and without a ^{210}Po alpha source deployed. Regions of PMT activity from various sources are visible. Right: Pulse shape saturation curve for the MicroBooNE PMT measured in BoVST.

function of trigger threshold with and without ^{210}Po source deployed is shown in Figure 2.2.10. The contributions of the single photo-electron (PE) dark rate (~ 5 kHz), the polonium alpha source (~ 200 Hz) and cosmic rays (~ 100 Hz) are clearly visible.

Properties of the PMT assembly, including gain stability, linearity and global collection efficiency (GCE) were studied. Gain stability within 1% over week-long periods was observed. Using two different geometries, the GCE for 128 nm light was extracted by observing the PMT response to scintillation from the 5.3 MeV mono-energetic ^{210}Po source. At a source-to-plate distance of 8 inches, a GCE of $0.961 \pm 0.08\%$ (stat. error only) photoelectrons per 128 nm photon was measured. A similar efficiency of $0.958 \pm 0.09\%$ (stat. error only) photons per 128 nm photon was measured at 14.5 inches. These measurements provide the reference values for 128 nm collection efficiency used in MicroBooNE optical simulations.

Pulse shape nonlinearities of the PMT were also studied, and found to become

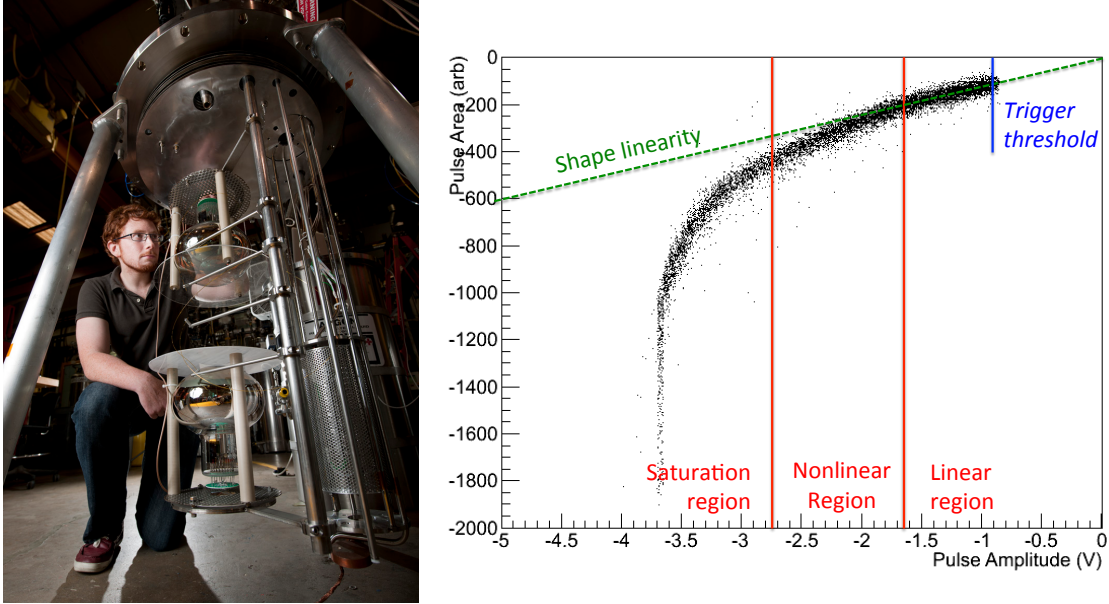


Figure 2.2.11: Left: photograph of the Bo test stand configuration used for the BoVST (credit Fermilab VMS). Right: plot showing the shape linearity of cosmic-ray induced PMT pulses. Shape linearity is maintained to amplitudes of around 1.7 V (300 PE), at which point nonlinearity sets in. Amplitude saturation occurs at 3.7 V (670 PE).

significant at around ~ 300 PE in pulse amplitude, with full amplitude saturation occurring at ~ 670 PE. Thus, for pulses of more than 300 PE, pulse shape cannot be described by linear superposition of single photoelectron pulses. This defines the range of validity for deconvolution-based pulse shape analyses, and for the linear PMT response simulations in LArSoft (Section 6). These data are shown in 2.2.11

More information on the MicroBooNE PMT and readout characterizations made with the BoVST can be found in [180]–[182]. The Bo test stand and its associated cryogenics are described in greater depth in Section 3.2, where non-MicroBooNE-specific liquid argon scintillation studies are presented.

2.6 Installation of the MicroBooNE optical system

The MicroBooNE optical system was installed and tested in November-December 2013. The first part to be installed was the optical system feedthrough, penetrated by 40 unbroken RG316 cables running for 16.5 m inside the detector and terminated

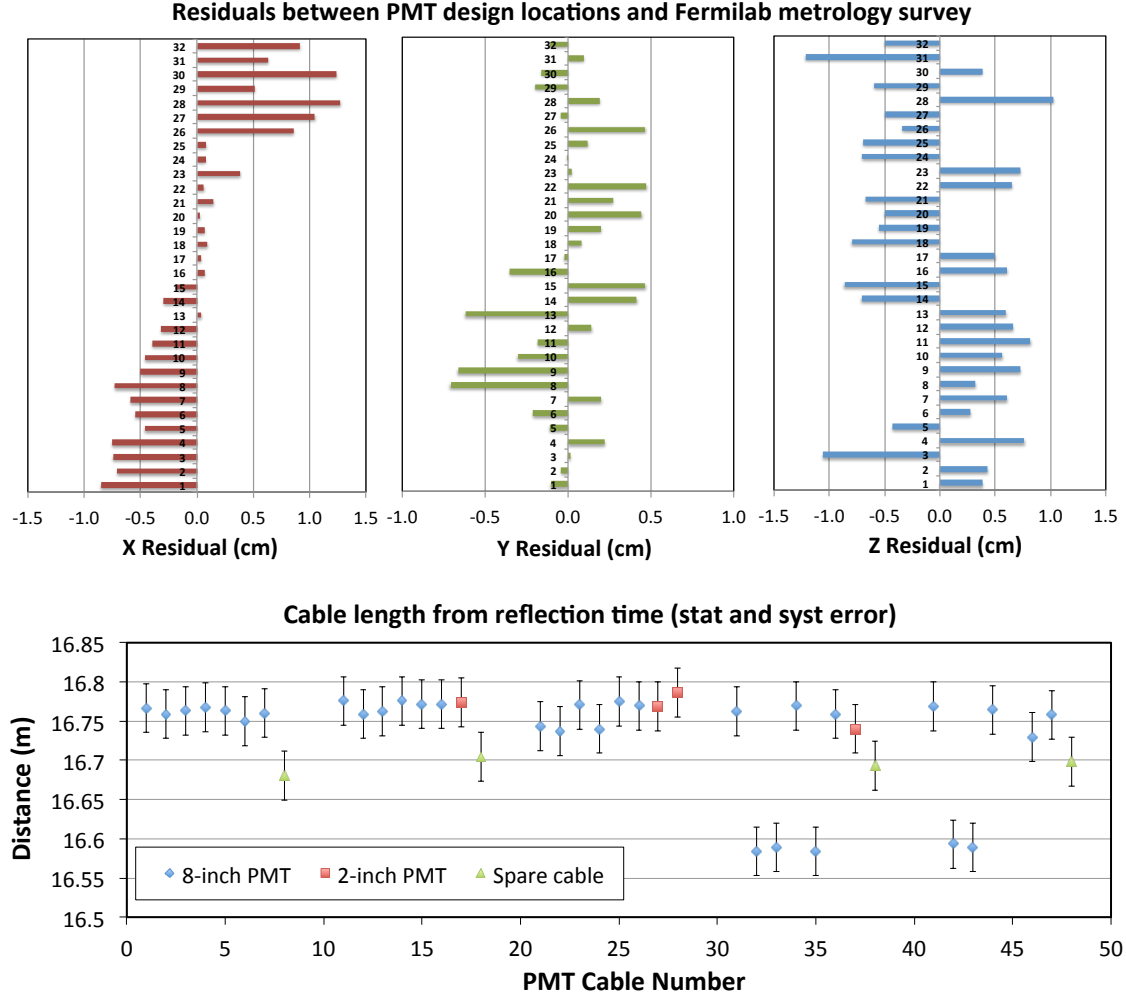


Figure 2.2.12: Top: residuals on PMT installation positions from Fermilab metrology survey. Bottom: cable lengths as measured by pulse reflection. The five outliers are cables which were shortened when repairing PMT base electronics during installation.

at SHV connectors in a patch panel mounted above the flange. Each of the 32×8 -inch PMT assemblies and four light guide assemblies was cleaned and constructed, soldered to the relevant cable, and installed onto one of five rack sections. Upon completion, each rack section was rolled into the detector on Thompson rails and the next one was lifted into position. Following PMT installation, the calibration fibers were routed and the fiber feedthrough was installed. The PMTs were installed with uncoated placeholder TPB plates to prevent photodegradation of the coating (see Section 4.4). The real plates were installed directly before the TPC installation, at which point the assemblies became inaccessible.

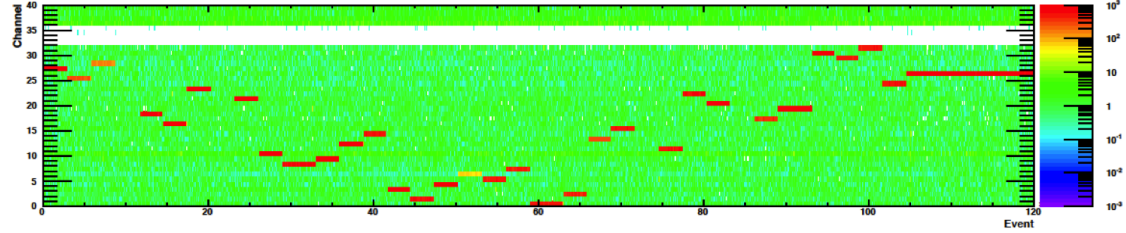


Figure 2.2.13: Charge detected as a function of channel, per event, in a MicroBooNE optical system pre-commissioning run.

After diagnosing and repairing some problematic channels, all PMTs functioned as expected. The impedance of every channel was tested at the feedthrough, in each case a stable and correct value for the base resistance of $4.02 \pm 0.01 \text{ G}\Omega$ for the 8-inch and $4.88 \pm 0.01 \text{ G}\Omega$ for the 2-inch PMTs was obtained. The cable lengths were measured using pulse reflection and found to be compatible with expectations, all within a few centimeters of the prepared length, apart from five shorter cables which were re-cut by $\sim 10 \text{ cm}$ during base repairs (Figure 2.2.12, bottom). The positions of the installed PMTs were surveyed by the Fermilab metrology group, and the installation was found to be accurate to within an average of 0.6 cm in x , 0.3 cm in y and 0.7 cm in z position (Figure 2.2.12, top). The as-found positions will be used in subsequent MicroBooNE simulation and reconstruction tasks.

Following installation, the 36 PMT channels were connected to a readout crate containing splitters, HV supplies and readout electronics. The cryostat was optically isolated and the system was exercised. Data was taken using the real PMT readout electronics, converted to LArSoft raw data format and processed using low-level calibration modules as each fiber was flashed in sequence. Figure 2.2.13 shows the charge recorded per channel as a function of event number. The colored blocks show every connected PMT detecting photons when it is illuminated, with crosstalk between channels constrained to levels below 0.1%, where the stray light background becomes dominant.

Calibration software was developed to measure the PMT gain based on Poissonian analysis of the LED-induced light-intensity distribution. Example fits are shown in Figure 2.2.14, top. A first-pass calibration was made, tuning the HV on each PMT to

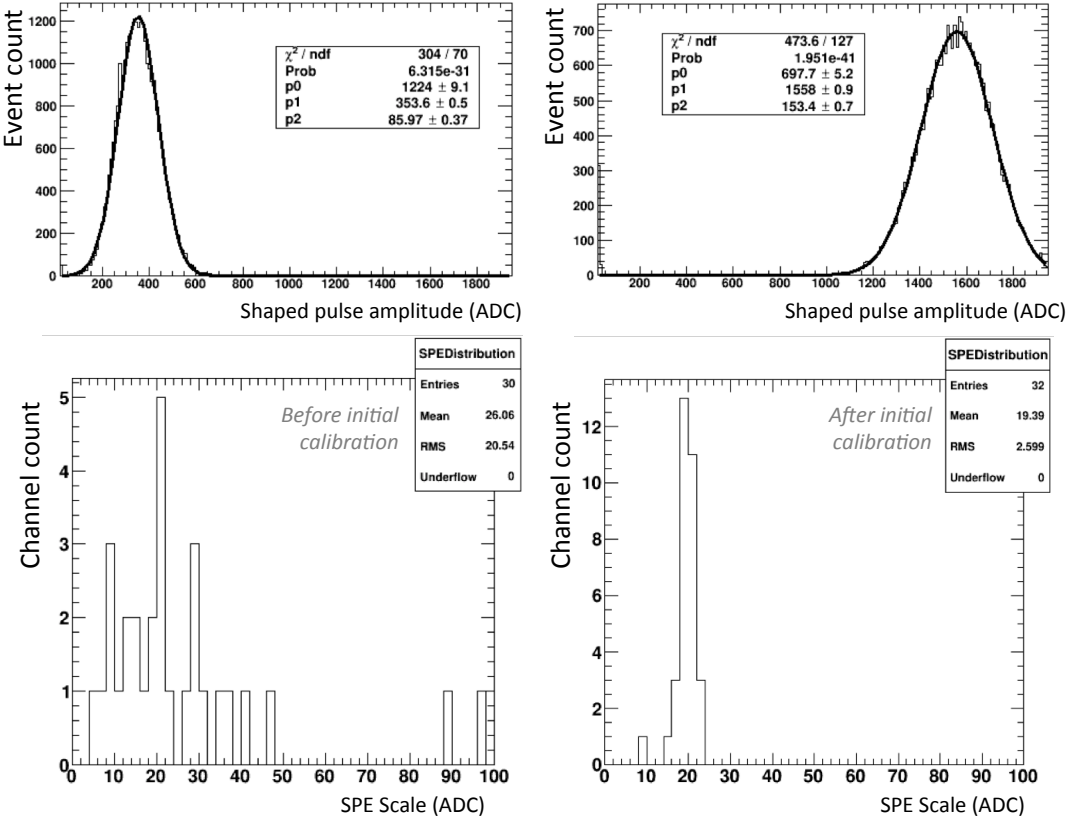


Figure 2.2.14: Results of calibration analyzers applied to digitized MicroBooNE optical system data. Fits of Gaussian distributions to the detected charge distribution per channel are used to measure the PMT gain, and the PMT HV is adjusted to bring the SPE scales to the target value of 20 ADC counts.

achieve the desired charge scale of 1/20 single photoelectrons (SPE) per ADC. The single PE scale distribution before and after this preliminary calibration run is shown in Figure 2.2.14, bottom left and right.

Following these tests, the readout crate was disconnected. The TPB plates were installed and the TPC was rolled into the cryostat. After welding on the end-cap, the MicroBooNE detector was transported across Fermilab and installed into the beamline at the LArTF facility. Further commissioning of the PMT system will take place when the detector is filled with liquid argon, and is commencing at the time of writing this thesis.

Chapter 3

Studies of Scintillation Light in Liquid Argon

3.1 The microphysics of liquid argon scintillation light

Liquid argon scintillates with a yield of tens of thousands of photons per MeV, with dependencies on particle type, dE/dx , electric field strength and argon purity. The emitted light has a narrow wavelength spectrum peaking at 128 nm, which is shown as a function of photon energy in Figure 2.3.2, left, reproduced from [183]. The time profile of the scintillation emission has at least two components, a fast component with a time constant of around 6 ns and a slow component with a time constant of around 1500 ns. These are understood to be produced by the radiative decays of diatomic excimer states which are created by energy transfer from scintillating particles, the fast component originating from a singlet $^1\Sigma_u$ excimer state to the ground state, and the slow component from the decay of a triplet $^3\Sigma_u$, delayed by intersystem crossing. The scintillation time profile was measured as a function of electric field in [103], and the profile at 0 and 6 kV/cm is reproduced in Figure 2.3.2, right. Both the prompt singlet scintillation peak and a tail of the slow triplet decays are visible, with the slow tail suppressed at high electric field.

There are two production mechanisms for the excimer states responsible for liquid argon scintillation light, illustrated in Figure 2.3.1. The first is self-trapped exciton

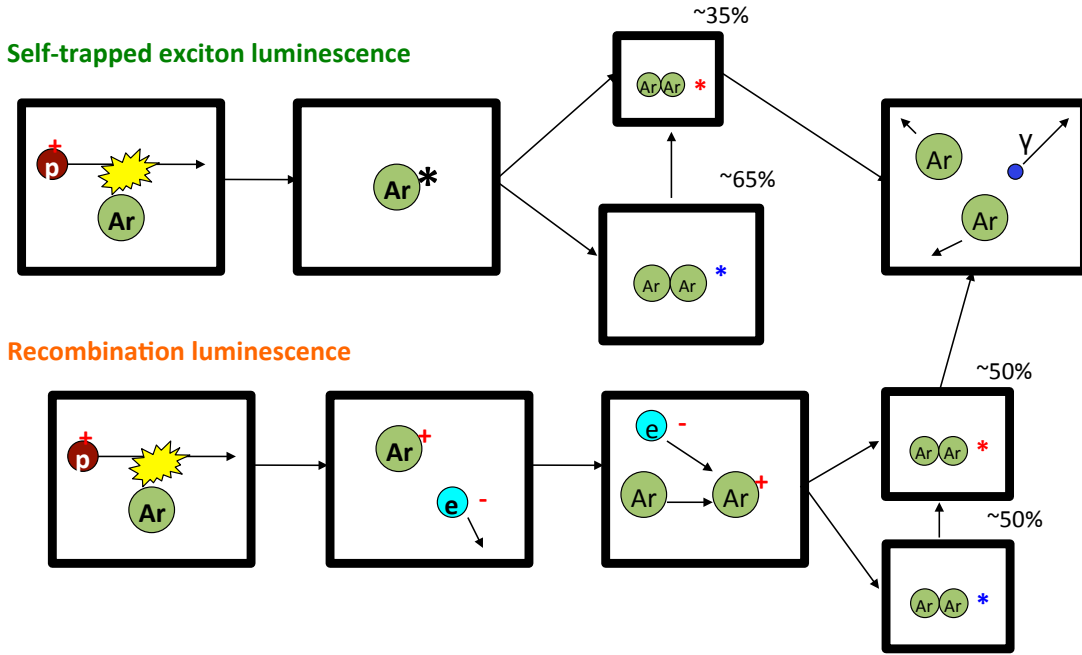


Figure 2.3.1: A cartoon showing the microphysical processes involved in liquid argon scintillation light production.

luminescence. In this process, an argon atom electromagnetically excited by an ionizing particle becomes self-trapped by the surrounding argon producing a singlet to triplet excimer ratio of around 65:35. The second process is recombination luminescence. In this case, sufficient energy is transferred to ionize the target argon atom, leading to a free electron cloud around the positively charged track core. The positively charged argon ions bind into charged argon dimer states. The free electrons thermalize, and columnar recombination with the positively charged argon dimers takes place over a timescale of 1 ns [184]. The recombination leads to excimer states, which are produced in a ratio of approximately 50:50 singlets to triplets.

The free charges involved in recombination luminescence explain many properties of liquid argon scintillation light, including its dependencies on electric field and ionization density. The application of an electric field draws the electron cloud away from the positively charged track core before recombination can occur, so strong electric fields inhibit recombination and suppress the scintillation yield, while increasing the detectable charge [103] (Figure 2.3.3). Statistical fluctuations in recombination

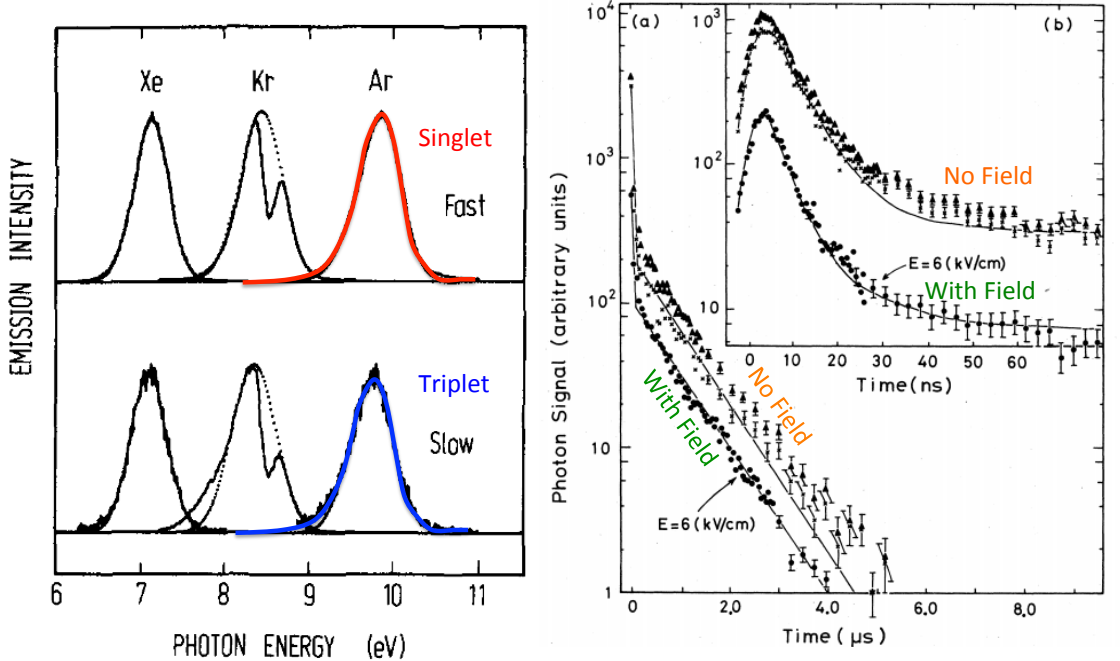


Figure 2.3.2: Left: Spectrum of fast and slow scintillation light from noble liquids, reproduced from [183]. The singlet and triplet emissions for argon are highlighted. Right: time profile of scintillation from liquid argon at zero field (mixture of self-trapped exciton and recombination luminescence) and 6 kV/cm (self-trapped exciton luminescence only), reproduced from [103].

also lead to anticorrelation of charge and light on an event-by-event basis [185]. The recombination rate is proportional to the local densities of both free electrons and positive ions, so the square of the local ionization density. Recombination is therefore enhanced for highly ionizing particles [102]. This results in a characteristic dE/dx dependence in the time profile of scintillation light [106], which can be used for pulse-shape-based particle identification [186], [187].

Although attempts to measure the absorption length of pure argon at 128 nm have been hindered by the presence of impurities [188], it is expected to be much longer than the length scale of existing or proposed LArTPCs. This is because a) scintillation photons are emitted from bound excimer states, so are not energetic enough to re-excite the argon bulk and b) a large Stokes shift of the excimer states

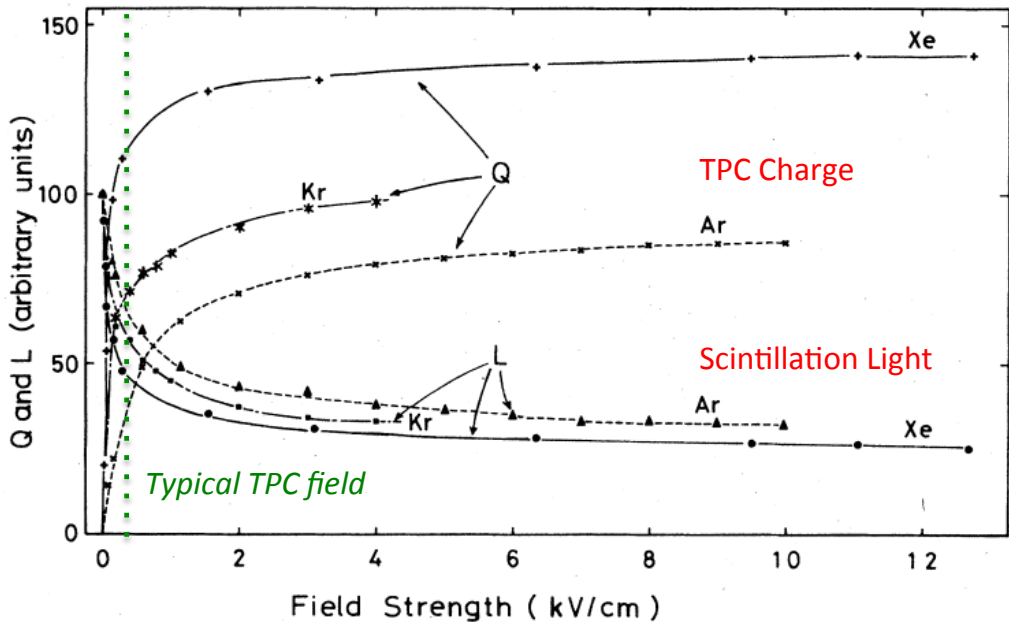


Figure 2.3.3: The effect of electric field on light and charge yields, from [103].

also prevents re-excitation of thermally occurring Ar_2 molecules in the liquid [189]. Scattering processes, on the other hand, do occur on length scales comparable to the size of existing detectors. In particular, Rayleigh scattering of 128 nm light from thermal density fluctuations in the liquid has a predicted scattering length of approximately 90 cm [190]. Scattering causes the light propagating between a source and optical detector to take a longer path than the direct line of sight, and affects the arrival times and directions of detected photons. This is particularly important for t_0 determination in a LArPC. A direct measurement of the Rayleigh scattering length has been made [191] and a value 66 cm was obtained, shorter than the theoretical prediction.

As well as scintillation light, liquid argon produces Cherenkov radiation. The Cherenkov threshold and yield is dictated by the liquid refractive index, which is 1.35 at 128 nm [192]–[194]. Cherenkov light production is very prompt and emission is non-isotropic, producing a directed cone. The time structure and geometry of Cherenkov light may be employed by future fast optical detectors. [195].

3.2 The Bo liquid argon scintillation test stand

The Bo test stand is a high-purity liquid argon apparatus for studies of liquid argon scintillation light at the Proton Assembly Building (PAB), Fermilab. The test stand was built to characterize MicroBooNE PMT assemblies (Section 2.5), and gradually extended with additional features to serve as a liquid argon optical detector R&D facility. A photograph showing Bo *in situ* with some large components labelled is shown in Figure 2.3.4.

Cryogenics and Monitoring

The Bo cryostat is a 250-liter vacuum-insulated vessel with inner diameter 22 inches and depth 40 inches. Bo shares common fill and vent lines with the Luke cryostat, which houses the Fermilab Materials Test Stand [97]. Argon is supplied to the Bo

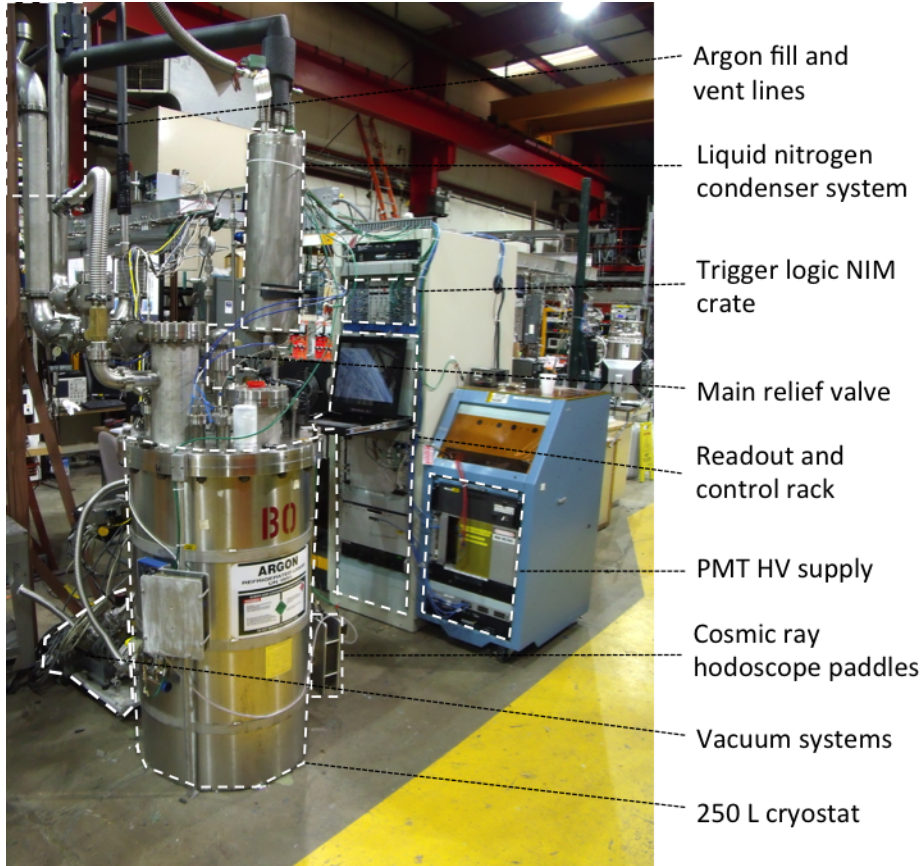


Figure 2.3.4: Labelled photograph of the Bo test stand.

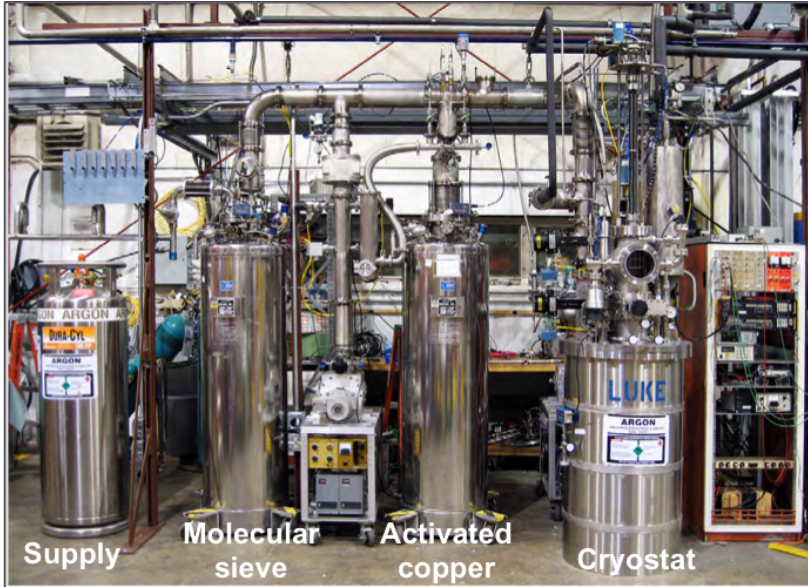


Figure 2.3.5: The Bo and Luke argon supply line and filters, reproduced from [196].

and Luke cryostats via regenerable filters from up to four dewars connected to an evacuable manifold. The filtration system consists of four-angstrom molecular sieves for the removal of water, and activated copper granules for the removal of oxygen. Both filters can be regenerated simultaneously by heating and flowing a dry gas of 5% hydrogen in argon through the system. The hydrogen reduces the oxidized copper, and the heat causes absorbed water to desorb from the surface of the molecular sieves into the gas. The argon carrier gas prevents the ignition of hydrogen passing over the hot filter elements. The supply system for the Bo and Luke cryostats is shown in Figure 2.3.5.

The argon delivered to Bo after filtration has part-per-billion (ppb) concentrations of oxygen and water impurity. Since the test stand does not employ continuous purification, water outgassing from the stainless steel in the vapor region of the test stand leads to a steadily increasing water concentration. Being non-polar, oxygen does not adsorb strongly to steel surfaces, so the oxygen content remains low. Nitrogen is neither removed nor filtered, so the nitrogen concentration in Bo is equivalent to the impurity level in the supply liquid. The specification from the vendor for the research grade argon used for Bo studies is 2 parts-per-million (ppm), although the

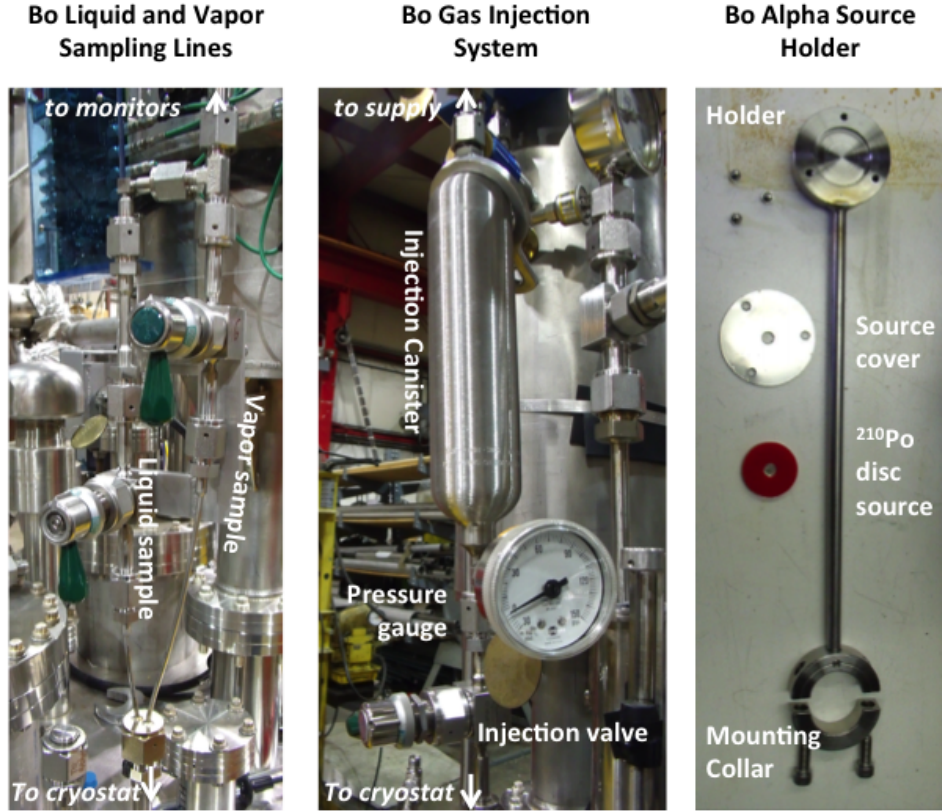


Figure 2.3.6: Some labelled components of the Bo test stand.

actual concentration varies between batches and on occasion has been as low as tens of ppb.

The concentrations of oxygen, nitrogen and water content in Bo can be monitored via capillaries in the liquid and vapor phases, through sample lines shown in 2.3.6, left. The argon drawn from the volume is analyzed by trace impurity monitors [197]–[199]. The oxygen and nitrogen measurements are expected to be faithful to the actual concentrations in the system. The water measurement gives only an upper limit due to outgassing of water in the sample line. Finally, a poly-tube sample pipe runs approximately 100 ft to a Universal Gas Analyzer (UGA) [200], which can be used to monitor levels of contaminants via mass spectrometry at the tens of ppm level and above, depending on the target ion mass-to-charge ratio.

To avoid contamination by outgassing water, the Bo cryostat and fill lines are evacuated for up to five days, or until the vacuum reaches $< 1 \times 10^{-6}$ Torr as measured

by an electronic vacuum gauge inside the cryostat. This is achieved using two stages of vacuum pumping, first using a high-volume rough pump for a few hours and then switching to a turbo pump for the remaining time. Once the desired vacuum has been achieved, liquid is brought through the filter system and into the cryostat through vacuum-jacketed fill lines.

When the fill is complete, the temperature and pressure of the argon is maintained by a liquid nitrogen refrigeration system. This system recondenses boiled-off argon vapor into the liquid through heat exchange from the argon vapor to the nearby nitrogen. The level of liquid in the condenser system is controlled automatically and is adjusted to maintain the pressure of the system at a specified value. The typical running point is 10-12 psi above atmospheric pressure. The condenser level control system involves a capacitive level probe and two electronic valves which control the liquid nitrogen supply, run by an industrial controls system.

Because of the condenser, the Bo cryostat can be run as a closed system. The level is monitored using a capacitive level probe, the temperature is measured using a thermocouple, and the pressure is measured using an electronic pressure gauge. If any of these deviate outside their allowed ranges, an alarm is raised. In the event of a condenser failure, a pressure relief at 35 psi prevents dangerous over-pressures.

Dopants and impurities can be injected into Bo via a pressurisable gas injection canister which is fitted to the cryostat lid via a 2 3/4" ConFlat flange, shown in Figure 2.3.6, center. The canister is charged to a known pressure from an external gas source, measured using an analog pressure gauge, and then injected into the liquid argon volume via a capillary by opening the injection valve.

Light sources

Radioactive sources can be deployed into Bo using a set of source holders. The most commonly used sources in Bo are ^{210}Po alpha sources of activity 0.01 - 0.1 μCi [201]. ^{210}Po is a pure alpha emitter which produces mono-energetic scintillation deposits of energy 5.3 MeV. The path length of a single 5.3 MeV alpha particle in liquid argon is 50 μm [202], which is effectively a point source for studies performed in the Bo test

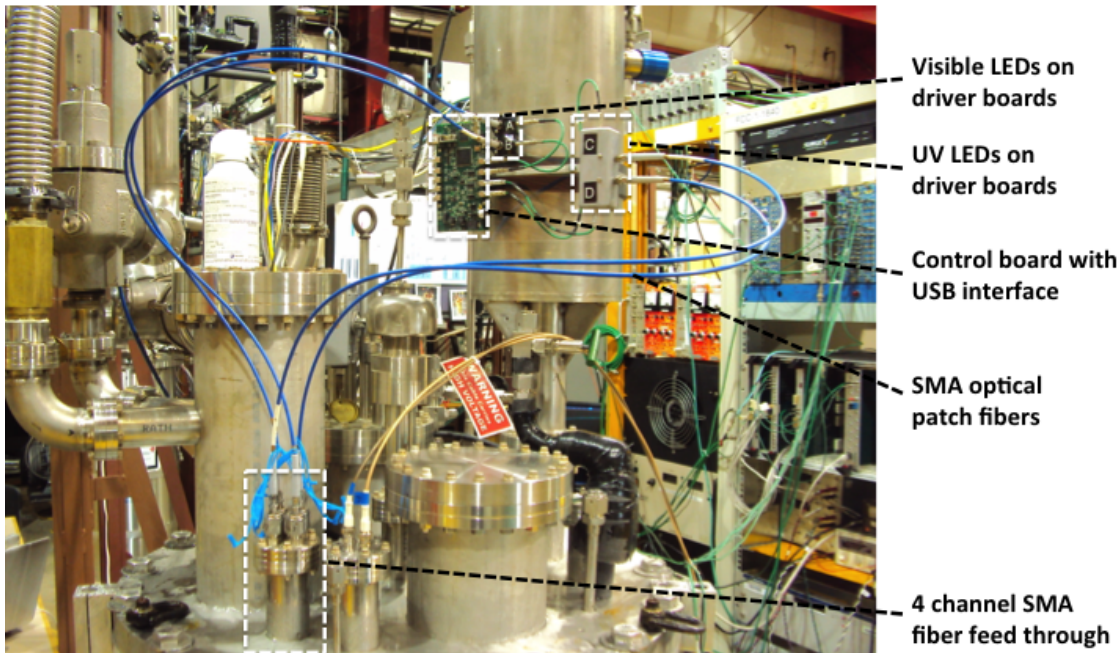


Figure 2.3.7: The optical fiber calibration system of the Bo test stand.

stand. An example source holder which was produced for use in Bo is shown in figure 2.3.6, right. A trigger rate plot in Bo with and without a source deployed was shown in Figure 2.2.10 as part of the MicroBooNE vertical slice test.

Bo can also be used to measure cosmic-ray induced scintillation light. Either by self-triggering an optical detector or by selecting particular through-going cosmic rays using pairs of hodoscope paddles, the scintillation light from minimally ionizing muons can be studied.

The final available light source is an LED calibration system, a photograph of which is shown in Figure 2.3.7. Four UV-transmitting polymide-coated fused-silica fibers are set into 1/2" flanges using stycast epoxy. Each fiber runs to an SMA connector, to which external jacketed fibers can be coupled. Externally, 1 m long polymer-jacketed patch fibers run to LEDs onto which further SMA connectors are mounted. Two visible (420 nm) and two ultraviolet (270 nm) LEDs are used to provide visible and UV photons respectively. The LEDs are pulsed using driver circuits and driver boards similar to those described in Section 2.3.

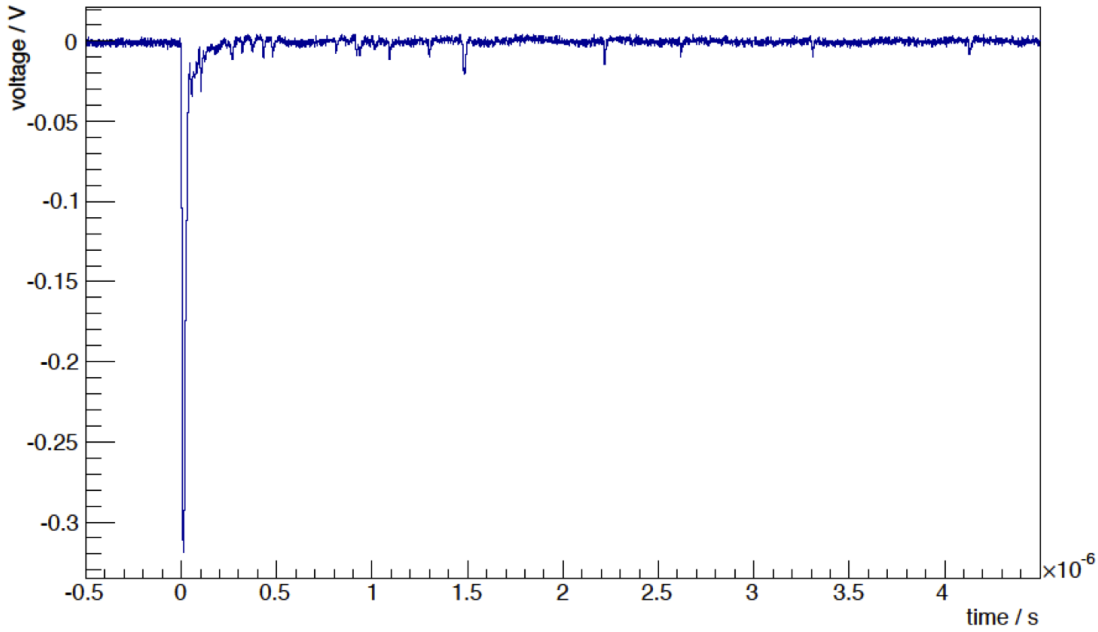


Figure 2.3.8: A liquid argon scintillation waveform recorded by the Bo test stand.

Light detection systems

Several light detection technologies have been operated in Bo. For PMT systems, including MicroBooNE-style optical assemblies, signal and high voltage are supplied through a single RG316 cable via an epoxy-potted feedthrough [203] which is soldered directly to the PMT base inside Bo and terminated at SHV at the flange.

Outside the cryostat, this cable is connected to a MicroBooNE-style splitter circuit. The splitter is placed directly on the lid of Bo, since it was found that maintaining short PMT-to-splitter cable lengths minimized signal reflections from the non-back-terminated base and improved pulse quality. Several splitter iterations were tested in order to achieve the cleanest possible PMT pulses. HV is supplied to the DC terminal by a Lambda power supply, located in a dedicated rack adjacent to the cryostat. The AC terminal of the splitter can be connected to a readout device, such as an oscilloscope or a MicroBooNE FEM module and associated readout hardware. An example PMT pulse induced by a cosmic ray is shown in figure 2.3.8.

Light guides instrumented with two-inch R7715 PMTs have also been operated in Bo [10]. Delivery of HV and signal extraction are performed analogously to the

MicroBooNE-style PMT assembly. SiPM-instrumented light guides have also been used [204]. In this case, no high voltage is required, the required bias voltage being only \sim 25 volts.

3.3 The effects of impurities on liquid argon scintillation light

In section 3.1, the properties of scintillation light in pure argon were described. Argon in real detectors contains traces of impurities that can have significant effects on the properties of scintillation light. Their concentrations depend on:

1. contamination entering the system through leakage or diffusion;
2. remnant gases in the volume before it is filled;
3. outgassing from internal surfaces;
4. impurity levels in the raw argon supply;
5. filtration performed in the detector's cryo-system;

Contamination through item (1) is prevented by using a hermetically sealed and leak-checked system. By evacuating or by running an argon gas purge [205], residual gases responsible for (2) can be reduced to very low levels. Evacuation or dry purging for a prolonged time also allows outgassing water from surfaces (3) to desorb into the volume and be largely removed. Since outgassing is a diffusive process, it continues at a steadily decreasing rate as the water surface concentration falls. Once the detector is filled, the low temperature of the liquid phase suppresses desorption of water from surfaces below the liquid level. However, desorption in the vapor phase can remain significant, and large volumes of absorptive material like plastics and sheathed cables are typically minimized in the ullage region.

Argon from commercial vendors can be purchased at various purity specifications, but typical purities of research-grade gases are 1 ppm in oxygen, nitrogen and water.

The required purity specification to maintain meter-scale free electron lifetimes in a TPC detector is of order 100 parts per trillion (ppt). To achieve this, continuous purification is required. The production and filtering mechanisms, items (4) and (5), vary from detector to detector, depending on size, drift requirements and other constraints such as radio-purity. The following subsections describe cases of interest for liquid argon neutrino and dark matter detectors. Measurements made in Bo which directly impact the purity specifications of present and future experiments are presented.

Impurities in neutrino experiments

The argon for neutrino experiments is produced by industrial distillation of air, which contains argon at a concentration of 0.93% by volume. The impurities which are present at the largest concentrations are therefore nitrogen, oxygen and water, which can be controlled by the vendor to the ppm level. Oxygen and water are removed by filters in the cryo-systems of LArTPC experiments to achieve long free-electron lifetimes.

Oxygen, water and nitrogen all cause reductions in the scintillation yield of liquid argon through two mechanisms, absorption and quenching, shown in cartoon form in figure 2.3.9. Quenching refers to an excitation-transfer process where the argon excimer is dissociated non-radiatively via interaction with an impurity molecule. Quenching becomes significant at concentrations where the mean time between the excitation transfer interactions is similar to or shorter than the lifetime of the argon excimer state. The effect is therefore most prominent for the long-lived triplet state excimers, and causes both a reduction in scintillation yield and a shortening of the scintillation time constants.

As shown in [206], [207], quenching becomes significant at 10 ppb-level concentrations of water and oxygen. This is far above the allowed concentration for TPC operation, so no scintillation quenching due to these molecules is expected in such detectors. Since it is unharful to charge drift and expensive to filter, nitrogen is not usually removed during the fill or recirculation of LArTPC detectors. Nitrogen is

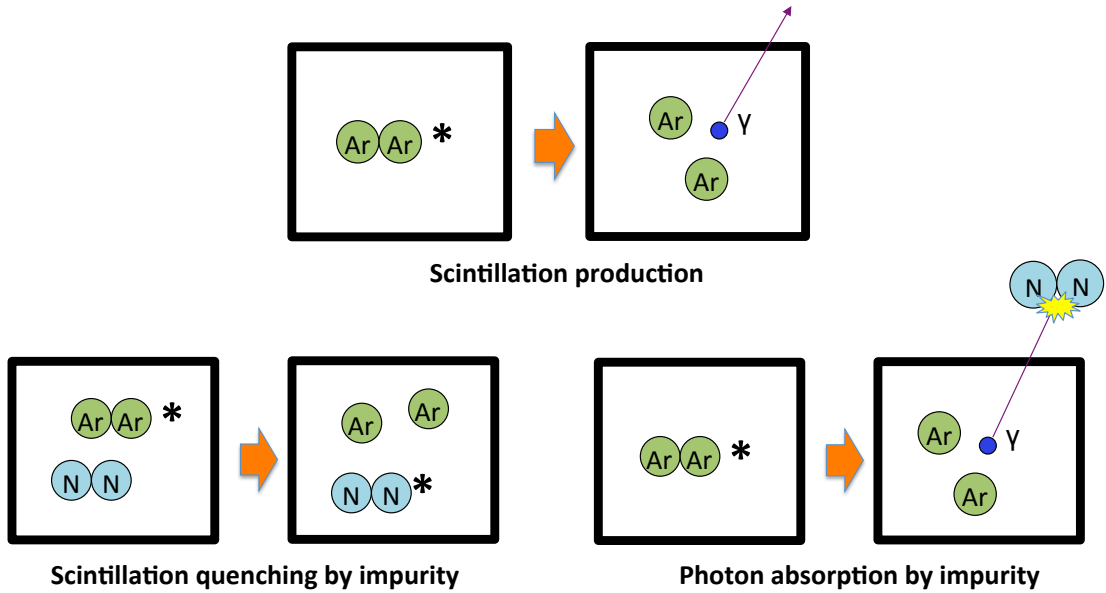


Figure 2.3.9: Cartoon showing the effects of absorption and quenching by an impurity in argon.

therefore present at the level supplied by the vendor. The effects of nitrogen quenching in liquid argon were first studied in small test cells [208], which showed the onset of quenching occurring at 2 ppm and characterized its effects. Some of these measurements were repeated with nitrogen injections into the BoVST, and compatible results were obtained [209].

The other process through which the light yield is reduced is absorption. This refers to the loss of 128 nm photons by interaction with dissolved impurity molecules during propagation between source and detector. Absorption becomes more significant for larger detectors due to longer photon path lengths. Because of TPC purity requirements, oxygen and water absorption is not expected to be significant [210]. Nitrogen absorption, however, can be significant for large detectors such as MicroBooNE and DUNE, and its photon absorption cross section at 128 nm is not well known. The following paper, published in the Journal of Instrumentation as [5], reports the first measurement of 128 nm light absorption by nitrogen in liquid argon. This was used to set the purity requirements during MicroBooNE argon procurement and will dictate those for future detectors such as DUNE.

RECEIVED: June 19, 2013

ACCEPTED: July 4, 2013

PUBLISHED: July 24, 2013

A measurement of the absorption of liquid argon scintillation light by dissolved nitrogen at the part-per-million level

B.J.P. Jones,¹ C.S. Chiu, J.M. Conrad, C.M. Ignarra, T. Katori and M. Toups

*Massachusetts Institute of Technology,
77 Massachusetts Avenue, Cambridge, MA 02139, United States of America*

E-mail: bjpjones@mit.edu

ABSTRACT: We report on a measurement of the absorption length of scintillation light in liquid argon due to dissolved nitrogen at the part-per-million (ppm) level. We inject controlled quantities of nitrogen into a high purity volume of liquid argon and monitor the light yield from an alpha source. The source is placed at different distances from a cryogenic photomultiplier tube assembly. By comparing the light yield from each position we extract the absorption cross section of nitrogen. We find that nitrogen absorbs argon scintillation light with strength of $(1.51 \pm 0.15) \times 10^{-4} \text{ cm}^{-1} \text{ ppm}^{-1}$, corresponding to an absorption cross section of $(4.99 \pm 0.51) \times 10^{-21} \text{ cm}^2 \text{ molecule}^{-1}$. We obtain the relationship between absorption length and nitrogen concentration over the 0 to 50 ppm range and discuss the implications for the design and data analysis of future large liquid argon time projection chamber (LArTPC) detectors. Our results indicate that for a current-generation LArTPC, where a concentration of 2 parts per million of nitrogen is expected, the attenuation length due to nitrogen will be 30 ± 3 meters.

KEYWORDS: Scintillators, scintillation and light emission processes (solid, gas and liquid scintillators); Noble liquid detectors (scintillation, ionization, double-phase); Photon detectors for UV, visible and IR photons (vacuum) (photomultipliers, HPDs, others)

ARXIV EPRINT: [1306.4605](https://arxiv.org/abs/1306.4605)

¹Corresponding author.

Contents

1	The effects of nitrogen upon argon scintillation light	1
2	Experimental configuration	2
3	Data acquisition and analysis	6
3.1	Measurement of the Single Photoelectron Scale and Stability	7
3.2	Construction of a Fit Function Describing Signal and Background Components	9
4	Cross-checks of nitrogen concentration in the liquid phase	12
5	Results	13
6	Comparison to world data and implications for LArTPCs	15

1 The effects of nitrogen upon argon scintillation light

Liquid argon scintillation light is used as a particle detection tool in many current and future neutrino and dark matter experiments [1–6]. The features of liquid argon which make it particularly apt as a detection medium in such experiments include its relatively low cost, its high scintillation yield of tens of thousands of photons per MeV, and the transparency of pure liquid argon to its own scintillation light, which is emitted at a wavelength of 128 nm [7]. Highly purified liquid argon can also achieve a very long free-electron lifetime [8], making it an ideal active medium for liquid argon time projection chamber (LArTPC) detectors. These detectors may utilize scintillation light as a trigger, a cosmic-ray rejection tool, and a method to obtain extra information for augmenting TPC-based reconstruction techniques.

It is widely known that whilst high-purity argon possesses these useful qualities, tiny concentrations of impurities, such as nitrogen at the part-per-million (ppm) level [9] or oxygen and water at the tens of parts-per-billion (ppb) level [10], can have a very damaging effect both upon the argon scintillation yield through the process of scintillation quenching and upon the argon transparency at 128 nm through ultraviolet absorption. Argon scintillation proceeds via the production of singlet and triplet eximer states, which subsequently decay to individual argon atoms and a 128 nm photon [11]. The singlet and triplet eximers have lifetimes of 6 ns and 1500 ns [12] respectively, which lead to argon scintillation light production with two characteristic time constants. The quenching process involves an interaction of eximers with impurity molecules, resulting in an excimer dissociation with no photon produced. Due to the longer lifetime, a triplet state is more likely to interact with an impurity molecule before producing a scintillation photon than a singlet state. Hence scintillation quenching typically affects the slow component of argon scintillation light much more than the fast component, though both scintillation mechanisms can be significantly suppressed at large

enough concentrations. Absorption, on the other hand, refers to the loss of emitted 128 nm photons by interaction with nitrogen molecules during propagation between production and detection points, thus it affects the slow and fast components in the same way. This is the quantity we aim to measure in this paper.

In LArTPC experiments, the concentrations of water and oxygen must already be controlled at the tens to hundreds of parts-per-trillion (ppt) level in order to maintain a long free-electron lifetime for charge drift [8]. Nitrogen, however, does not damage the free-electron lifetime, and is significantly more difficult to remove from the argon during the purification process than oxygen or water. Hence LArTPC experiments like MicroBooNE and LBNE expect to operate in a regime with ppm levels of nitrogen dissolved in the active volume. Tight requirements upon the allowed nitrogen concentration to prevent significant losses of scintillation light may be a cost driver for the cryogenics system and active medium in such an experiment.

Previous studies of the quenching effects of nitrogen in small test cells show that below around \sim 2 ppm, scintillation quenching from nitrogen is not likely to cause significant problems for LArTPC experiments [10]. However, the effects of nitrogen absorption upon 128 nm argon scintillation light travelling over long distances have not previously been measured. Knowledge of this vital parameter is necessary to understand the argon purity requirements for future large detectors. Furthermore, it will be an important parameter for detector simulations and data analysis of both current- and future-generation LArTPC experiments with optical systems.

In this paper we describe measurements made using a high-purity liquid argon test stand at the Fermi National Accelerator Laboratory (Fermilab). We inject controlled amounts of nitrogen gas into high-purity argon and measure the light absorption effect by comparing the light yield from a polonium-210 alpha source held in two positions relative to a cryogenic photomultiplier tube (PMT) assembly. From these measurements we are able to extract the absorption cross section of dissolved nitrogen and explore its expected effects in LArTPC detectors in the concentration range 0–50 ppm.

2 Experimental configuration

The tests described in this paper were performed in the 220-liter vacuum-insulated “Bo” cryostat at the Proton Assembly Building at Fermilab. The cryostat is evacuated for several days to remove contaminants before filling. Then research-grade liquid argon is passed through a system of re-generable filters and molecular sieves, described in [13], to fill the vessel with high-purity liquid argon to a level between 76 and 89 cm. The remaining few centimeters of the 55.9 cm diameter cylindrical vessel are occupied by argon vapor.

A diagram and photograph of the apparatus inside the cryostat are shown in figure 1. Attached to the cryostat lid is a support structure which holds a single optical assembly consisting of a Hamamatsu R5912-02mod cryogenic PMT, cryogenic base electronics, and a wavelength-shifting plate, more details about which can be found in [14–16]. Argon scintillation light with a wavelength of 128 nm can be captured by tetraphenyl butadiene (TPB) in the plate coating and re-emitted as visible light. The TPB emission spectrum has a peak wavelength of around 450 nm [16], which is well matched to the peak quantum efficiency of the cryogenic photomultiplier tube [17]. Some of this light leads to the production of photoelectrons at the PMT photocathode, which are amplified by

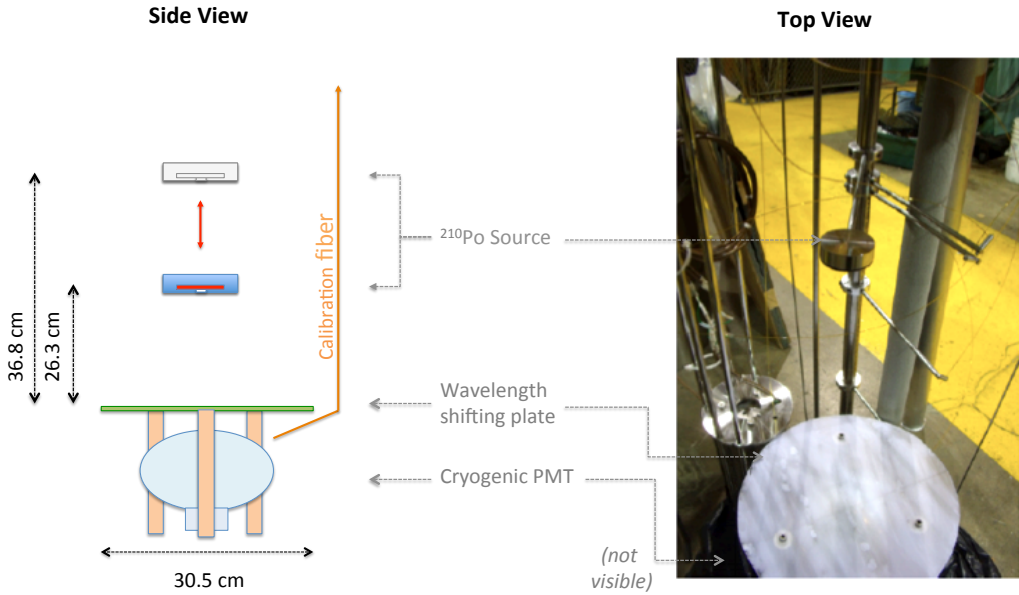


Figure 1. Diagram and photograph of the experimental configuration for this study.

the PMT dynode chain. For this study the PMT high voltage is set at 1100 V, which provides a stable gain of around 10^7 [14]. Signal and high voltage are both carried by one common 50Ω RG-58 cable which penetrates the cryostat through a potted epoxy feedthrough [18]. Outside the cryostat the AC signal is split from the DC high voltage using a splitter unit, and the signal is connected to a Tektronix DPO5000 oscilloscope terminated at 50Ω and running at one gigasample per second.

A polonium-210 disc source is held an adjustable distance above the wavelength-shifting plate in a stainless steel source holder. This source produces monoenergetic alpha particles of 5.3 MeV which scintillate in the liquid argon and produce 128 nm scintillation light, which can be detected by the PMT assembly.

The number of photons detected for each alpha particle is expected to be approximately Poisson distributed with a mean determined by the initial photon yield, the geometrical configuration of the experiment, and the assembly global collection efficiency, which is defined as the number of amplified photoelectrons produced for each incident 128 nm photon on the wavelength-shifting plate. In this study we measure the light yield at different nitrogen concentrations relative to a configuration with the same geometry and clean argon (defined below), thus making this analysis insensitive to the global collection efficiency of the assembly and the absolute scintillation yield, and only dependent upon the stability of the photomultiplier gain and the stability of the scintillation yield.

The argon delivered to the Proton Assembly Building has a typical nitrogen concentration of < 1 ppm. It is then passed through molecular sieves and filters to remove water and oxygen, a process which also removes some nitrogen. We monitor nitrogen concentrations using an LD8000 Trace Nitrogen Analyzer [19]. The measured N_2 concentration in the argon delivered in a fresh fill of our apparatus is 37 ppb. In this very low concentration range, our measurement accuracy suffers,

since it is near the sensitivity limit of our nitrogen monitor. However, the nitrogen concentration is far below the range where the effects of quenching are significant [10], and our results will show that it is also below the concentration range where we would expect any significant absorption. Hence this argon is "clean" for the purposes of our study.

The pressure inside the cryostat is maintained at 10 psi relative to atmospheric pressure with a liquid-nitrogen-cooled condenser tower, which re-condenses argon vapor into the liquid. When the condenser is running, the cryostat is a closed system with no vapor or liquid able to enter or leave the volume. The liquid level is measured using a capacitive level monitor and for these studies was stable at 79 cm, in contact with a 22 cm argon vapor region at the top of the cryostat.

We monitor trace impurity levels in both the liquid and gas phases from capillary pipes which penetrate the cryostat lid and run to oxygen, water, and nitrogen impurity monitors. Oxygen and water were both found to be present at the tens of ppb level. Since we perform measurements relative to an initial light yield, it is the stability of these impurity concentrations rather than their absolute values which is important for our measurement. The oxygen concentration was stable to within 2 ppb, and the water concentration stable to within 4 ppb for both runs documented in this paper.

We inject controlled amounts of gaseous nitrogen into the liquid through an injection capillary. This capillary is connected to a 300 cm³ canister which can be charged to a known pressure with nitrogen from a gas cylinder which can then be released into the liquid. After injection, the nitrogen inside Bo comes to a vapor-liquid equilibrium state, with stable but different concentrations in the liquid and gas phases. The equilibration process takes approximately 30 minutes. When not being charged for injection, the injection line from the nitrogen cylinder up to and including the gas canister is vented into the atmosphere and then evacuated to ensure no additional leakage of nitrogen into the volume occurs. The complete nitrogen injection and sampling apparatus is shown schematically in figure 2.

This measurement uses the results of two experimental runs that were taken approximately three weeks apart. This is the amount of time required to disassemble, reconfigure, pump down and refill the apparatus. Each run was started with 79 cm of high-purity argon, and nitrogen was injected a few ppm at a time until we had reached a concentration of approximately 50 ppm. After each set of injections we measured the light yield visible from the alpha source. The two runs had the source positioned at different distances from the PMT assembly. We compare the detected light yield from a source placed 36.8 cm ("far configuration") from the assembly to the detected light yield from the same source placed 20.3 cm ("near configuration") from the assembly as a function of nitrogen concentration. Using this data we extract the absorption strength of nitrogen dissolved in argon.

In order to interpret the experimental data which will be presented, first consider the effect of injecting a substance which leads to a particular percentage of light absorption per centimeter and a simultaneous scintillation quenching effect. If we were to inject a fixed quantity of this substance and measure the same fractional light loss for both source configurations, we would conclude that the scintillation yield has been reduced and we have observed a pure quenching process. If there is a greater fractional light loss for the further source, we may be seeing either pure absorption, or a combined quenching and absorption process. Taking the ratio of the remaining fractional light yield from the near configuration to the remaining fractional light yield from the far configuration, the quenching effect cancels, and we are left with a measurement only sensitive to the absorption

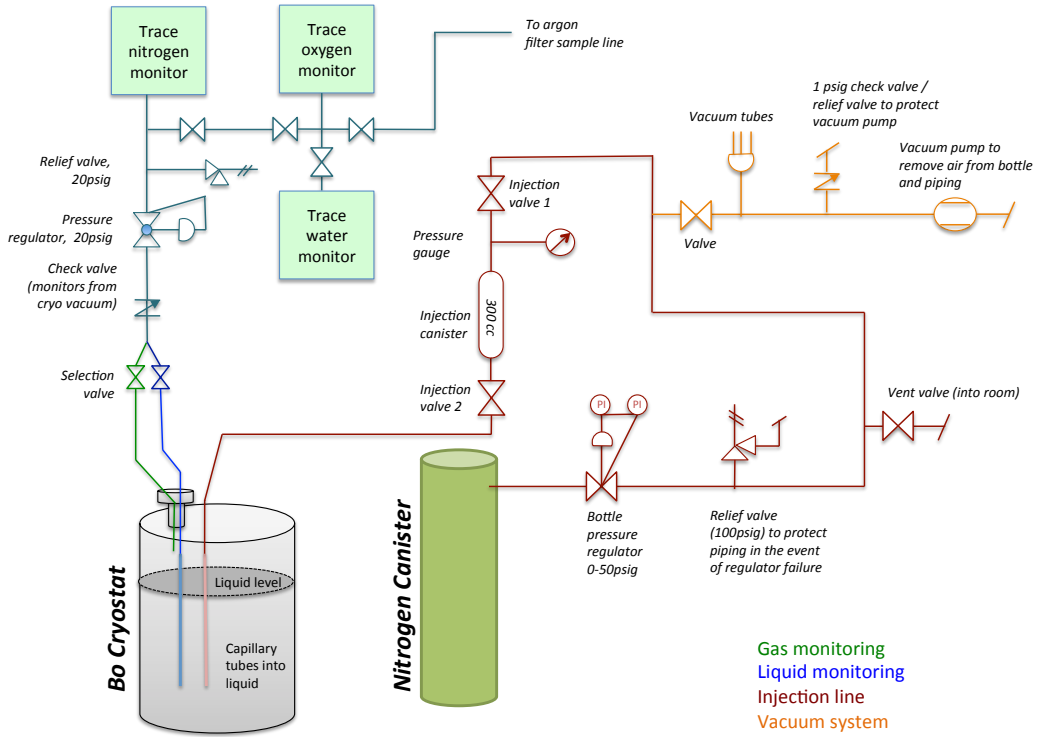


Figure 2. Schematic of the nitrogen injection and gas sampling apparatus used in this test.

strength. This is the quantity we aim to measure in this paper. The effects of nitrogen upon scintillation quenching of prompt and slow light have been studied elsewhere [10], and will be the subject of a future study with this apparatus [20].

The photons which propagate from source to plate have a distribution of path lengths, as illustrated in the cartoon in figure 3, left. In order to understand the relative fractional light yield expected between the two source positions for a given absorption strength, we perform a ray tracing simulation and attenuate each ray according to its distance of travel from source to plate. The fractional light yield at each source position due to absorption is shown in figure 3, left. We define the fractional light yield ratio as the fractional light yield from the near source position divided by the fractional light yield from the far source position. In the presence of absorption this number is larger than one, as the light from the far source position is more strongly attenuated due to the longer path lengths of the light rays. The fractional light yield ratio as a function of absorption strength extracted from the ray tracing model is shown in figure 3, right.

Our goal is to find the conversion factor between percentage absorption per centimeter and nitrogen concentration in argon by comparing the measured fractional light yield ratio as a function of nitrogen concentration to the curve of figure 3, right. We find that, in our region of interest of 0% to 1% per centimeter absorption, corresponding to the concentration range 0 to 50 ppm, the curve of figure 3, right can be well approximated by a straight line. Thus we can extract the absorption strength of nitrogen by measuring the gradient of the linear relationship between fractional light

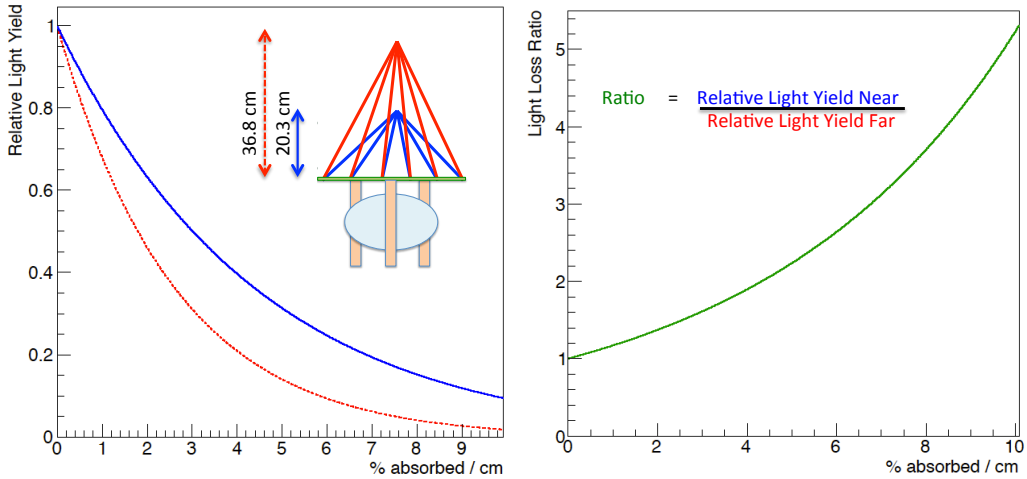


Figure 3. Left: fractional light yield expected as a function of absorption strength for each source position. Right: ratio of the two fractional light yields, in which any quenching effect cancels.

yield ratio and nitrogen concentration, and from this also the molecular absorption cross section of dissolved nitrogen in argon to 128 nm light.

3 Data acquisition and analysis

A typical PMT pulse initiated by alpha scintillation is shown in figure 4, and the characteristic singlet and triplet scintillation components of liquid argon with time constants 6 ns and 1500 μ s respectively are clearly visible as a large prompt peak followed by trailing single photoelectron pulses, respectively. As described in the introduction, the slow light component from the triplet state is much more susceptible to scintillation quenching than the prompt light component. Therefore, since the focus of this study is nitrogen absorption, we consider only the light in the prompt peak, measuring the total charge recorded between -10 and +40 ns relative to the time of a -30 mV falling edge trigger. We tested for the effects of pulse size bias due to this narrow prompt light window by comparing the pulse area spectrum recorded using this 50 ns window to the pulse area distribution recorded using an extended 70 ns window and observed no biasing effect.

To obtain the relative light yield detected at the PMT for each concentration point, PMT waveforms are recorded using a Tektronix DPO5000 oscilloscope, and the area within the prompt window is histogrammed in real time. For illustration, the distribution of pulse areas for a few concentration points is shown in figure 5. The falling cosmic-ray-induced background remains approximately unchanged whilst the Poisson-like alpha peak is diminished in intensity by the injection of nitrogen.

In order to quantify the charge recorded in a light pulse from an alpha particle in terms of amplified photoelectrons, the average single photoelectron charge was measured using a pulsed LED. The measurement of the absolute single photoelectron scale and gain stability will be discussed in section 3.1.

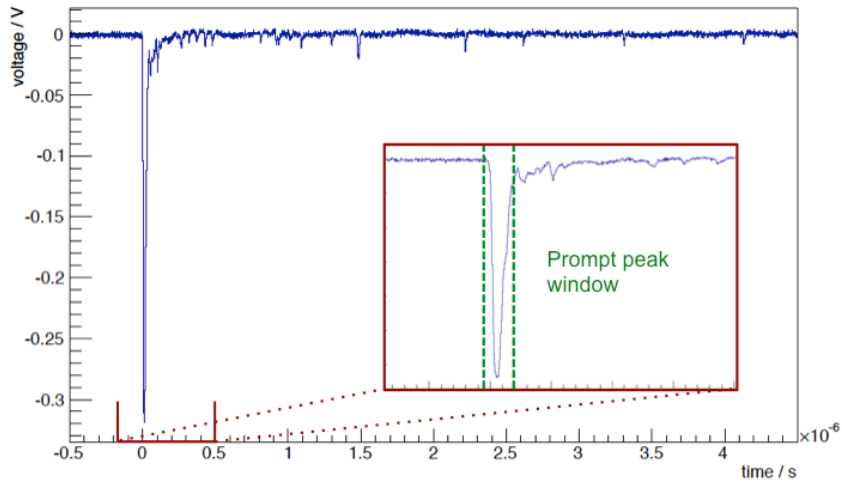


Figure 4. A typical PMT waveform produced by the light from a scintillating alpha particle in the near source configuration.

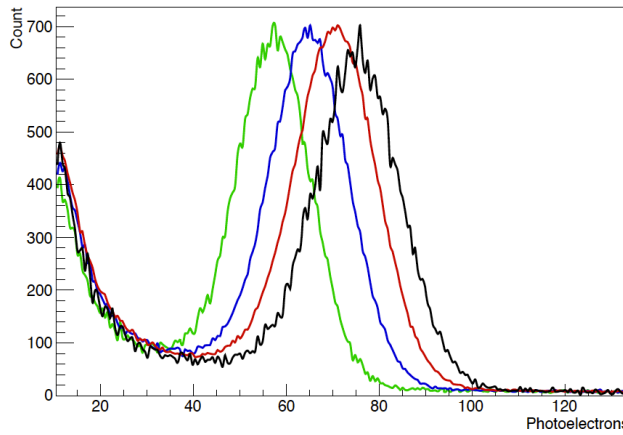


Figure 5. Pulse area distributions for the near configuration for, right to left (color online): 37 ppb (black), 3.7 ppm (red), 7.4 ppm (blue), 15.5 ppm (green) of nitrogen in argon.

To extract the relative light yield from the source at each concentration point, we fit to a function which has a term describing the falling cosmic background and a term describing alpha-induced Poisson-like peak. The construction of this function will be discussed in section 3.2.

3.1 Measurement of the Single Photoelectron Scale and Stability

We normalize all measured light yields to the single photoelectron scale, which we refer to hereafter as $\langle \text{SPE} \rangle$. For this study, $\langle \text{SPE} \rangle$ is measured using a pulsed LED between every set of nitrogen injections. It will be shown in section 3.2 that our attenuation length measurement is relatively insensitive to the absolute $\langle \text{SPE} \rangle$ scale so long as it is constant for the duration of each run. However, the stability of the gain between different points within the same run is crucial. The gain

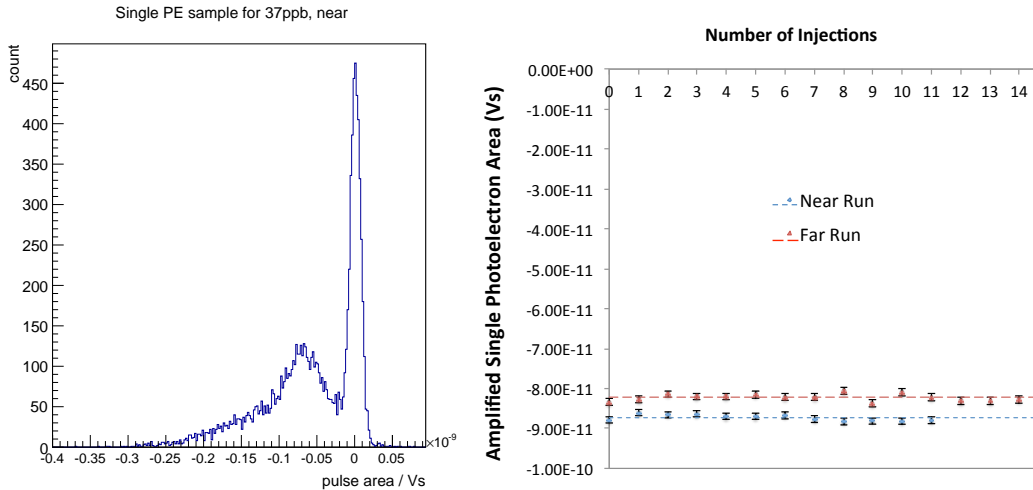


Figure 6. Left: single photoelectron sample area distribution for the pre-injection data point in the near source configuration run. Right: single photoelectron stability for each of the two runs reported in this paper. The dashed lines show the average single PE size for each run, used to normalize the alpha pulses. The error bars represent the spread of measurements about the mean, and are folded into the nitrogen absorption measurement as a systematic error.

stability is obtained by calculating the spread of $\langle \text{SPE} \rangle$ values within the run. Since the $\langle \text{SPE} \rangle$ spread gives the leading systematic error in this study, we make several independent cross-checks of gain stability, which all give similar results and will be described below.

To measure $\langle \text{SPE} \rangle$, A 400 nm LED is driven at a rate of 100 Hz and connected to an optical fiber which penetrates the Bo lid through a fiber-optic feedthrough. The other end of the fiber is pointed directly at the PMT photocathode from a distance of around 1 cm. The LED driving voltage is chosen such that a significant fraction of all pulses do not produce any measurable response in the PMT. In this way, we collect a sample of mostly single photoelectron pulses. Producing a histogram of the areas of PMT pulses initiated by this low intensity LED gives a superposition of the amplified single photoelectron distribution with a sharply falling baseline noise spectrum. This charge distribution is shown in figure 6, left. At much higher LED voltages, two and three photoelectron peaks were clearly observable at multiples of the single photoelectron size.

We measure the average single photoelectron charge by calculating the mean pulse area between limits of -0.03 nVs (to cut off the falling baseline noise tail) and -0.18 nVs (to cut off unavoidable two and higher photoelectron pulses). This data is shown in figure 6, right. Using this method we measure a gain stability of 0.91% for the near configuration run and 1.09% for the far configuration run. Since this is comparable to the precision of the $\langle \text{SPE} \rangle$ measurement, we conclude that the PMT gain is approximately stable and that $\langle \text{SPE} \rangle$ is a constant for the duration of each run. To account for any gain fluctuations we fold in the observed $\langle \text{SPE} \rangle$ variation throughout the run as a systematic error on all measured light yields. The small adjustment to $\langle \text{SPE} \rangle$ caused by the contamination of rare > 1 PE pulses in the sample is not corrected for, since our final result will be insensitive to this shift.

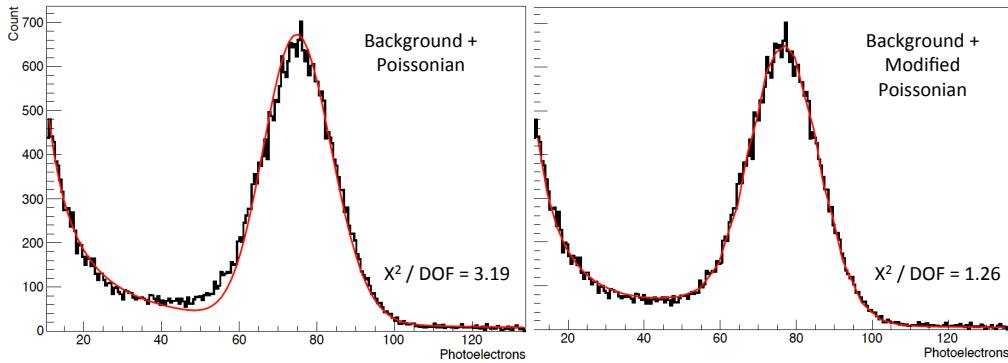


Figure 7. Left: best fit for naive Poisson distribution plus background. Right: best fit for modified Poisson distribution accounting for source shadowing plus background. The shadowing function is tuned on an independent dataset, so both functions have the same number of free parameters in this fit.

For the near configuration run, as well as using an LED to measure $\langle \text{SPE} \rangle$, we also performed measurements of the areas of single photoelectron pulses in the slow tail of the alpha scintillation light. The benefit of this method is that a very clean sample of known single photoelectron peaks can be obtained, with negligible two and higher photoelectron contamination. This method yielded a single photoelectron scale variation of 1.02% between all concentration points, in good agreement with $\langle \text{SPE} \rangle$ fluctuations measured using the LED. The absolute single photoelectron scale measured in this manner deviates from the LED $\langle \text{SPE} \rangle$ measurement by 7%. This deviation is much below the level where it would have an impact upon our final result, as is shown later in section 3.2 and figure 9.

A further constraint on the gain stability is provided by repeated measurements of the light yield at the same nitrogen contamination point performed many hours apart. These measurements will be described in section 5, and show deviations of less than 0.5% over around eight hours. This method constrains deviations due to both the single photoelectron scale and also the effects of any additional outgassing impurities, such as water or oxygen.

3.2 Construction of a Fit Function Describing Signal and Background Components

The distributions of prompt pulse areas shown in figure 5 have two components: a cosmic-ray-induced falling background and an alpha-induced Poisson-like signal peak. A simple fit to a Poisson distribution added to a power-law background model is shown in figure 7, left, and clearly does not reproduce the measured distribution well in the region below the peak. In this section we describe the construction of an improved function which provides a more accurate model of the detected light yield, ultimately producing the fit function shown in figure 7, right.

There are essentially two possible explanations for the discrepancy shown in figure 7, left: either the cosmic-induced background is not well modeled by a power law and has an enhanced contribution in this intermediate range; or the alpha-induced pulses do not produce a simple Poisson distribution, but rather a distribution with an enhanced low tail. Some amount of the latter effect is expected from partial occlusion of the edges of the alpha disc source by its stainless steel holder, which we refer to henceforth as “shadowing”.

Using a sample of individual waveforms recorded in clean argon, we can separate the signal and background samples using pulse shape discrimination (PSD). Since the majority of cosmic rays are minimum ionizing particles (MIPs) whereas alpha particles are highly ionizing, the slow component of argon scintillation light is more heavily quenched for the alpha-induced subsample. The distribution of pulse amplitudes vs total area within 3.2 microseconds of the trigger for a clean argon sample in the near configuration is shown in figure 8, top left. Taking the ratio of area to amplitude, two clear peaks emerge, shown in figure 8, top right. We separate the sample as shown in figure 8 into “cosmic-like” and “alpha-like” subsamples, with the pulse area distributions shown in the lower panels of figure 8. The power-law background model reproduces the cosmic-like distribution with $\chi^2/DOF = 1.05$. The low tail of the alpha-like sample is not modeled well by a Poisson distribution, suggesting some shadowing of the source by its holder is present. Some leakage of the cosmic sample into the alpha sample is seen to occur at very low light intensity, so the region below 20 photoelectrons is not included in the alpha sample fit. Incorporation of a shadowing function as described below improves the χ^2/DOF value for the alpha subsample from 4.55 to 1.14.

We cannot rely on PSD to separate the cosmic- and alpha-induced subsamples when nitrogen contamination is present, since quenching of the argon slow component would introduce an undesirable bias into the discrimination condition. However, since the shadowing of the source is not dependent upon the nitrogen concentration, a function describing the shadowing effect can be obtained using the clean argon sample where PSD is effective, and used to construct a modified Poisson distribution to be used for each subsequent fit.

The form of the shadowing function is constrained by its expected scaling as the total light yield is reduced. Due to the geometry of the source holder, most area elements on the source disk are unshadowed, all contributing with equal intensity to the main Poisson-like peak. A small region consisting of shadowed area elements around the edge of the disk are assumed to produce Poisson-distributed light yields whose means are a fixed fraction of the Poisson mean from the unshadowed elements. The distribution of area elements as a function of their Poisson means is referred to as the shadowing function. The precise functional form of the shadowing function is not known *a priori*, but a good fit to the alpha-like distribution is given by assuming a slowly rising exponential below the unshadowed peak. The best-fit shadowing function before convolution with Poisson distributions is shown in figure 9, left. After convolution with Poisson distributions this shadowing function produces the signal distribution shown in figure 8, bottom right.

The final fit function used in this analysis is applied to non-PSD-separated samples and is given by a sum of two terms: a power-law-distributed background term and the modified Poisson distribution described above. The relative light intensity is extracted from the modified Poisson distribution and normalized to the relative light intensity for clean argon, and these values are shown for the near sample in figure 9, right. Since our attenuation curves are generated by taking the ratio between the contaminated-argon light yield and an initial clean-argon light yield, they should be relatively insensitive to the absolute single photoelectron scale, so long as it is stable over the course of each run. By considering single photoelectron scales 20% higher and 20% lower than our measured value, we find the three measured attenuation curves are indeed indistinguishable within our systematic errors. The three overlaid curves are all shown in figure 9, right.

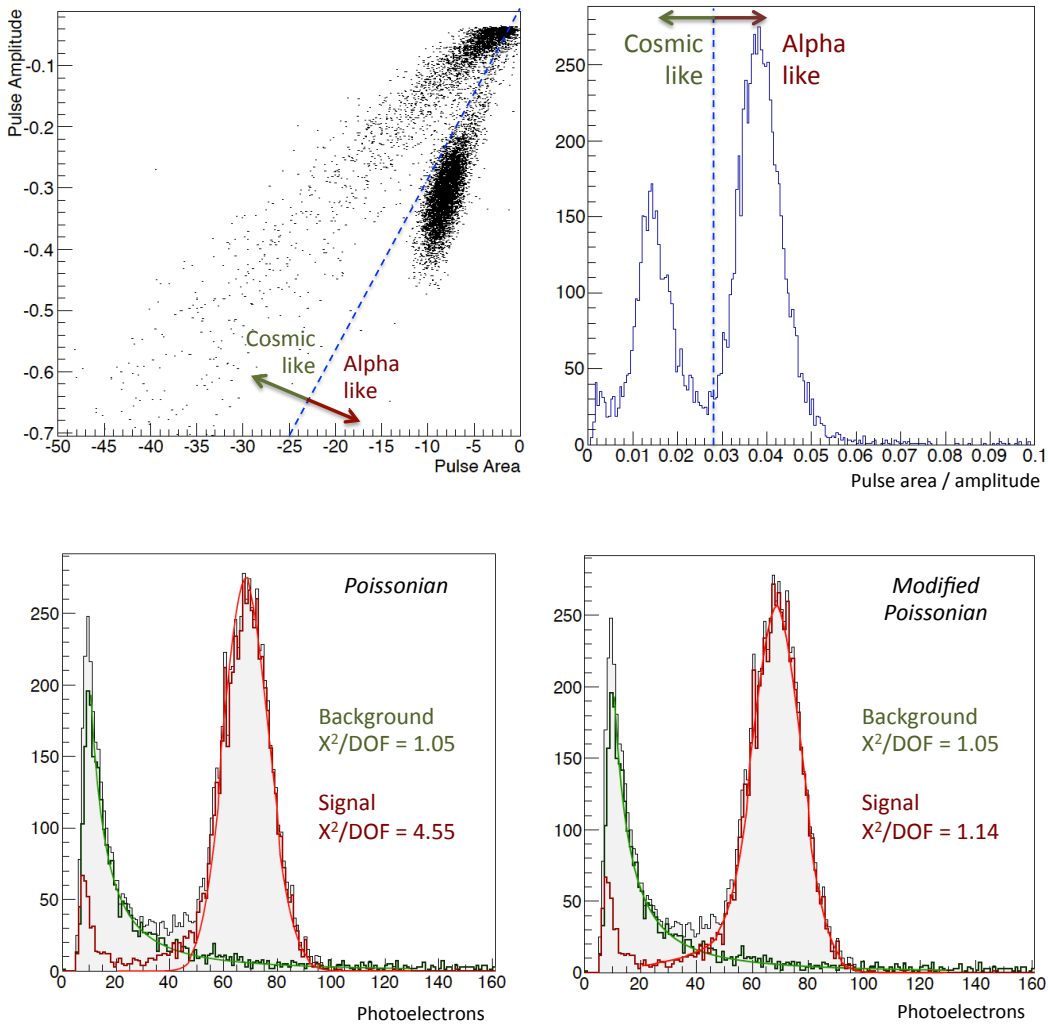


Figure 8. Top left: pulse amplitude vs area in 3.2 microseconds after the trigger for clean argon in the near configuration. Distinct populations of alpha- and MIP-induced pulses are visible. Top right: the ratio of total area / amplitude is used as the PSD variable. Bottom left: fits of each component to the power-law background and Poisson distributed alpha signal model. Bottom right: fits of each component to the power-law background and modified Poissonian model incorporating the effects of source shadowing.

We note that whereas the alpha particles are nonrelativistic and do not produce Cerenkov light, the light detected from cosmic rays is expected to have a small Cerenkov component. Using information from [21] we estimate that around 1–2% of the photons produced by cosmic muons traversing Bo originate from the Cerenkov process. Since the absorption measurement described in this paper requires a precise measurement of the alpha light yield only, this small Cerenkov component does not affect our final result.

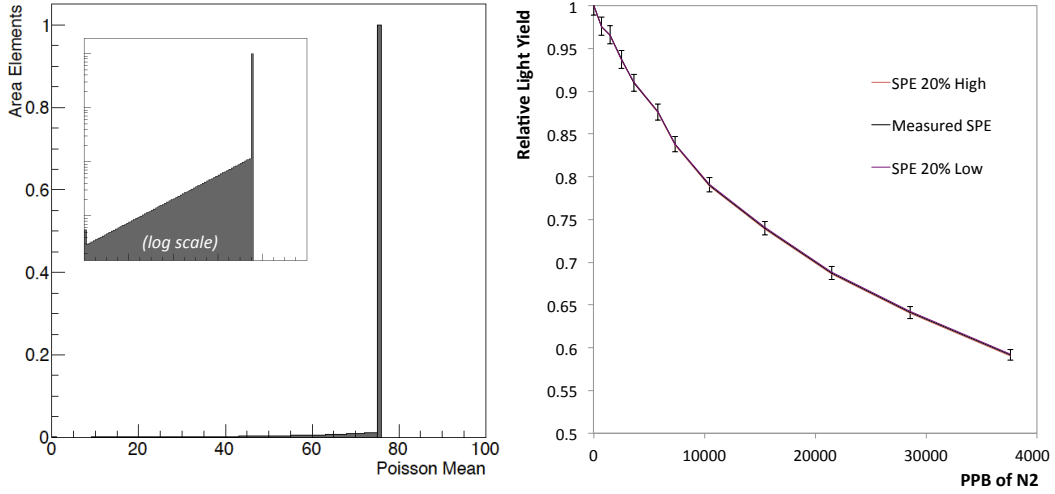


Figure 9. Left: the best-fit shadowing function for the clean argon, near-source calibration sample. Right: the relative light yield as a function of nitrogen concentration for the near source configuration for three values of the single photoelectron scale.

4 Cross-checks of nitrogen concentration in the liquid phase

Even with a trace nitrogen monitor, the measurement of tiny concentrations of nitrogen in liquid argon has many subtleties. To ensure that our measurements of the nitrogen concentration in the liquid are faithful to the real concentration, we perform several cross-checks.

After injection, nitrogen added to the cryostat becomes distributed between the liquid and gas phases in a vapor-liquid equilibrium, with an equilibration time of around 30 minutes. We calculate the relationship between the equilibrium concentrations in liquid and vapor phases in two ways: 1) by referencing saturation pressure tables of argon and nitrogen [22], and 2) using the commercially available REFPROP software package [23]. By sampling from both the liquid and gas phase capillaries, we can determine whether the relative measured concentrations are in agreement with these predictions. These measurements and both sets of predictions are shown in figure 10, left. The agreement between the measured data points and both models indicates that vapor-liquid equilibrium has been reached, and that the measurement of the nitrogen concentration from the liquid phase sample line is indeed a faithful measurement of the nitrogen concentration in the liquid.

We can also predict the expected nitrogen concentration in the liquid after each set of injections from our knowledge of the injection volume and pressure. Due to the relevant density difference, the total mass of argon in the vapor phase is much smaller than the total mass of argon in the liquid phase. Since the nitrogen concentration in both phases is in the few ppm range, the total fraction of injected nitrogen which resides in argon vapor volume is negligible after equilibration. Therefore, approximately all injected nitrogen gas dissolves into the liquid. The prediction of the injected mass of nitrogen has a large systematic error due to our uncertainty of the exact injection volume including space in valves, capillary piping, etc.; the limited precision of the injection pressure gauge; and the imprecisely known temperature of the injected gas. However, the measured nitrogen concentration in the liquid agrees with our prediction to within its systematic error bar of 15%,

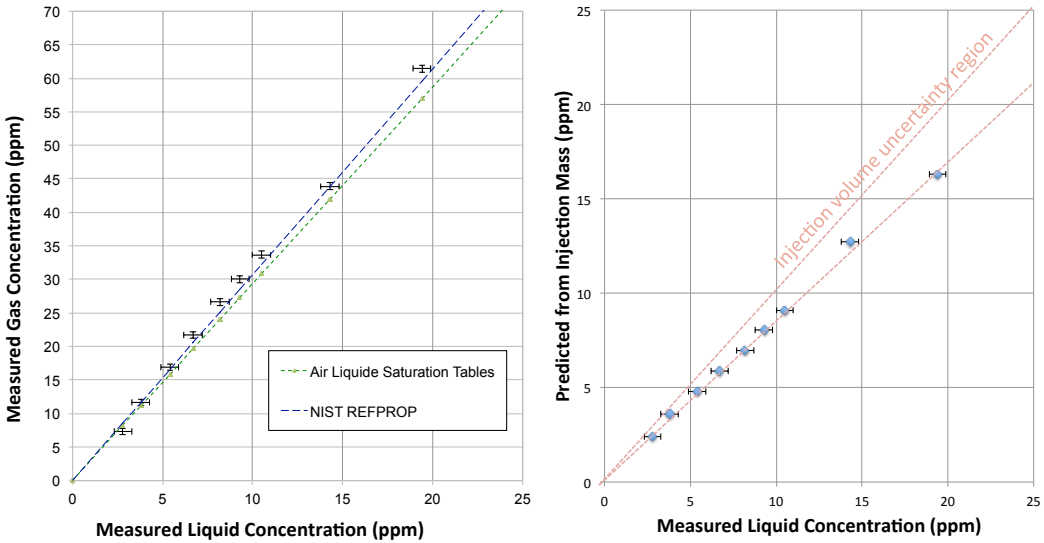


Figure 10. Cross-checks on the liquid concentration measurement. Left: measured liquid and vapor N_2 concentrations compared with two calculations of the vapor liquid equilibrium condition. Right: comparison of the liquid N_2 concentration to the injected mass. The uncertainty on the predicted injection mass comes primarily from the uncertainty of the precise injection volume.

providing further support that the trace nitrogen concentration measured from the liquid sampling capillary is faithful to the actual nitrogen concentration in the argon volume. A comparison between the predicted and measured concentrations is shown in figure 10, right.

5 Results

The relative light yields for each source configuration are shown in figure 11, left. A divergence of the two datasets is visible, showing clearly the effects of nitrogen absorption.

For each concentration point we make one or more nitrogen gas injections, allow time for equilibration, record a sample of single photoelectron pulses, and then measure the alpha light yield distribution. This process takes two to three hours, and one run of measurements takes around one week (not including time taken to purge, fill and configure the system). To test that the observed reduction in light yield is indeed a consequence of the introduced nitrogen contamination and not the outgassing of water or some other system instability, we twice repeated measurements at the same concentration point at the end of one day and beginning of the following day, mid-run. We found that the light yield was stable to within 0.5% over these periods, in contrast to its reduction during periods of nitrogen injection. This data is shown in figure 11, right.

Since the precise concentration points probed in the two datasets are different, we cannot take the ratio of light yields directly. To find the fractional light yield ratio, we interpolate one dataset with a polynomial and take the ratio to the measured data points of the other. A quartic polynomial provides a good fit to both datasets and is used in this analysis. We are free to choose to interpolate either the near or far dataset. We use both schemes and then take the average of the two results as

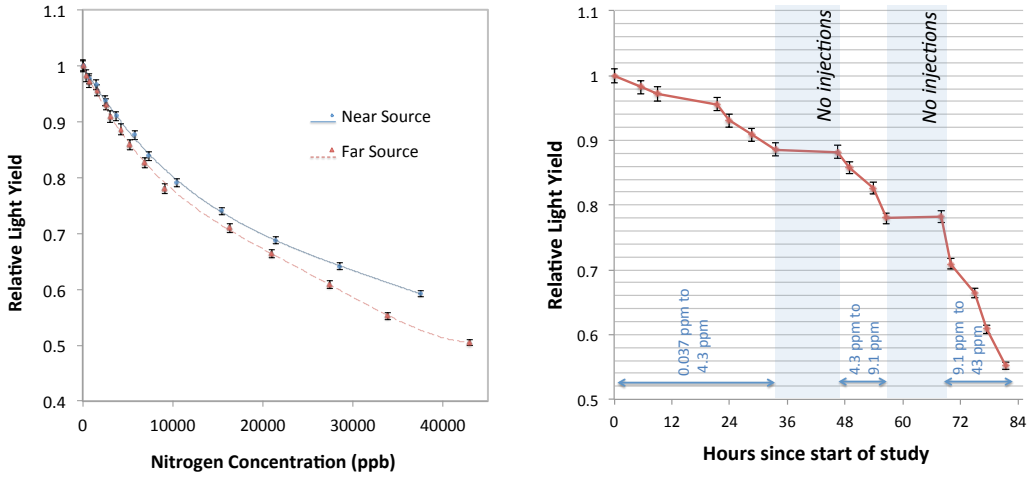


Figure 11. Left: near and far configuration datasets, along with quartic interpolated curves. The separation of the two curves is evidence of nitrogen absorption. Right: the relative light yield from the far run as a function of time. During the periods when no nitrogen was injected, the light yield remained stable to within 0.5%.

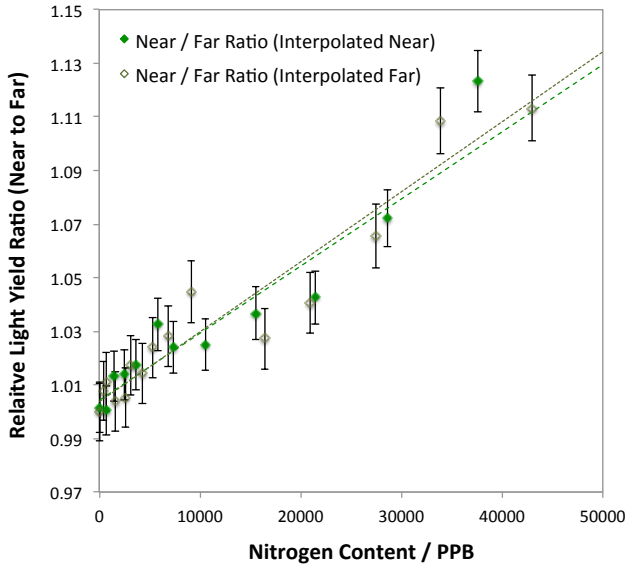


Figure 12. The fractional light yield ratio between the near and far configurations for both interpolation schemes. The dashed lines show the best linear fit for each scheme.

our final value for the absorption strength. The near-to-far ratios extracted by both interpolation schemes are shown in figure 12, along with best-fit lines for both schemes. The error bars in both cases have contributions from the fit error on the alpha light yield parameter and the single photoelectron scale added in quadrature.

The largest fractional light yield ratio observed is 1.11 at 43 ppm, which, according to our ray

Interpolation Scheme	Measured Absorption Strength $\text{cm}^{-1}\text{ppm}^{-1}$	Measured Cross section $\text{cm}^2 \text{molecule}^{-1}$
Interpolated Near	$(1.47 \pm 0.15) \times 10^{-4}$	$(4.88 \pm 0.51) \times 10^{-21}$
Interpolated Far	$(1.54 \pm 0.15) \times 10^{-4}$	$(5.11 \pm 0.5) \times 10^{-21}$
Average Value	$(1.51 \pm 0.15) \times 10^{-4}$	$(4.99 \pm 0.51) \times 10^{-21}$

Table 1. The absorption strength and molecular absorption cross sections of nitrogen to argon scintillation light, as measured in this study. Note that the near interpolation and far interpolation schemes do not give independent results, and the quoted errors are 100% correlated.

tracing model, corresponds to less than 1% absorption per centimeter. In this range, the relationship between the light yield ratio and the percentage absorption per centimeter is well approximated by a straight line with a gradient of 0.170 in units of ratio change per (%/cm). We can thus extract the correspondence between concentration of nitrogen and percentage absorption per centimeter by comparing this gradient to that of the best-fit lines of figure 12.

Having extracted the absorption strength in units of percentage loss per centimeter per ppm of nitrogen, we can further use the known density of liquid argon and molecular mass of nitrogen to extract the molecular absorption cross section in units of $\text{cm}^2 \text{molecule}^{-1}$. These quantities represent the central result of this work; they are presented in table 1. We take the average of the numbers from the two interpolation schemes as our final result. The spread of these two values from their mean gives a measure of the systematic error introduced by using this interpolation method, and this is added in quadrature with the characteristic uncertainty of each measurement to give our final uncertainty estimate.

6 Comparison to world data and implications for LArTPCs

We have measured the absorption cross section at the wavelength of liquid argon scintillation light of small quantities of nitrogen dissolved in liquid argon. This is an important parameter for the design and operation of large LArTPCs, and in the following section we briefly compare our result to world data on nitrogen absorption and discuss the consequences of our measurement for these experiments.

Figure 13, reproduced from [24], shows the world data on nitrogen absorption cross sections in the vacuum ultraviolet (VUV) with our measurement overlaid. It is immediately clear that measurements in the relevant wavelength range are sparse. Further, most existing measurements consider warm nitrogen in the gas phase. This is a very different regime from our study, which considers ppm concentrations of nitrogen in solution at liquid argon temperature and 10 psi above atmospheric pressure. However, despite these differences, our data are compatible with existing measurements and suggest that the nitrogen absorption cross section rises sharply over the range 120–130 nm.

Typically the effects of impurity absorption in LArTPCs are described in terms of an absorption length. To convert from percentage absorption per ppm centimeter (p) to an absorption length (A) in meters, we use the formula

$$A = -\frac{1m}{100\log(1 - p\chi * 1cm)}$$

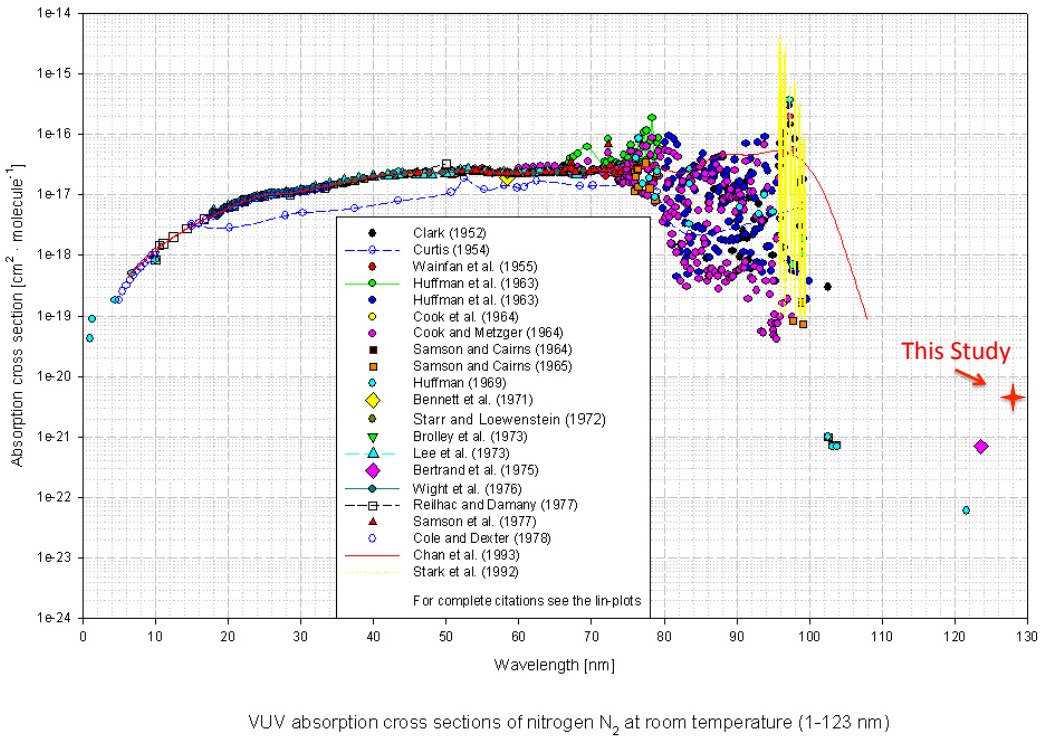


Figure 13. World data on VUV nitrogen absorption reproduced from [24], with this measurement overlaid.

Argon Specification	Concentration of N ₂	Absorption Length
Measured N ₂ concentration of clean argon for this study	37 ppb	1790 ± 160 m
AirGas research (grade 6) argon [25]	1 ppm	66 ± 6 m
MicroBooNE cryogenic specification	2 ppm	30 ± 3 m
Start of liquid recirculation phase of Liquid Argon Purity Demonstrator, Run 2 [26, 27]	8 ppm	8.2 ± 0.7 m
AirGas industrial (grade 4) argon [25]	100 ppm	0.65 ± 0.06 m

Table 2. The absorption length expected in argon samples of different nitrogen contamination levels. These values assume that absorption due to other impurities such as water and oxygen, and the self absorption of liquid argon, can be neglected in all cases. This is likely to be a good assumption for all but the first entry.

where χ is the concentration of nitrogen in ppm. Using the measurement of p obtained from this study, we can make a plot of A as a function of the nitrogen concentration χ . We show this relationship on a log-log plot in figure 14 top, and in the region of interest from 0 to 50 ppm on a linear plot in figure 14, bottom. Table 2 lists a few useful reference points of nitrogen concentration in different liquid argon samples.

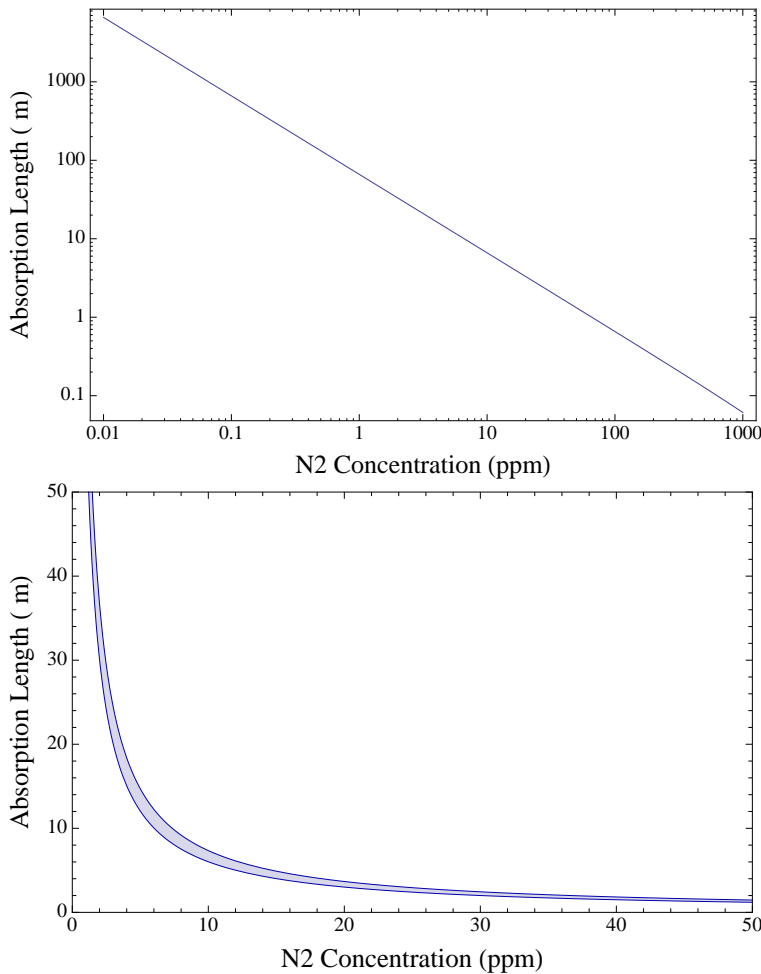


Figure 14. Absorption length of nitrogen impurities as a function of nitrogen concentration. Top: on a log-log scale over many orders of magnitude. Bottom: on a linear scale over the 0–50 ppm range relevant for current generation LArTPC detectors, with the one sigma region measured in this paper shaded.

As well as being a vital parameter for the design of cryogenic systems for large LArTPCs and possible future dark matter experiments, the absorbing effects of nitrogen must also be taken into account for simulation and data analysis of the current generation of experiments. As a representative example, in the MicroBooNE experiment the concentration of nitrogen in the liquid will be monitored using a trace nitrogen analyzer, similar to that used in this study, at regular intervals. Using the attenuation length vs. concentration relationship measured here, the effects of attenuation due to nitrogen can be incorporated into optical simulations, and corrections may be applied to optical data either before or after event reconstruction. This is likely to be particularly important for the optical detection of low-energy processes such as supernova neutrinos.

However, the main conclusion which can be derived from this study is that the absorbing effect of nitrogen to argon scintillation light is relatively weak. Even with a loose purity specification

of 10 ppm of nitrogen, the absorption length of argon with dissolved nitrogen is several meters. Hence the measurement presented in this paper suggests that nitrogen absorption is unlikely to be a significant problem for large LArTPCs, assuming certain relatively weak purity constraints are satisfied. This information may help to reduce the costs involved in designing and filling such future detectors.

Acknowledgments

We thank Stephen Pordes for giving us access to the Bo cryostat and its associated cryogenic system, and for a careful reading of this manuscript. We also thank Jong Hee Yoo and Adam Para for kindly loaning us pieces of equipment used in this study, Clementine Jones for proofreading this paper and Roberto Acciarri and Flavio Cavanna for offering helpful guidance and insightful comments. We are very grateful to Bill Miner, Ron Davis and the other technicians who have assisted us at the Proton Assembly Building, Fermilab for their tireless hard work to provide us with cryogenic facilities of the very highest standard. The authors thank the National Science Foundation (NSF-PHY-1205175) and Department Of Energy (DE-FG02-91ER40661). This work was supported by the Fermi National Accelerator Laboratory, which is operated by the Fermi Research Alliance, LLC under Contract No. De-AC02- 07CH11359 with the United States Department of Energy.

References

- [1] LBNE collaboration, T. Akiri et al., *The 2010 Interim Report of the Long-Baseline Neutrino Experiment Collaboration Physics Working Groups*, [arXiv:1110.6249](https://arxiv.org/abs/1110.6249) [[INSPIRE](#)].
- [2] A. Rubbia, *Towards GLACIER, an underground giant liquid argon neutrino detector*, *J. Phys. Conf. Ser.* **375** (2012) 042058 [[INSPIRE](#)].
- [3] B.J.P. Jones, *The Status of the MicroBooNE Experiment*, *PoS(EPS-HEP2011)* **436** [[arXiv:1110.1678](https://arxiv.org/abs/1110.1678)] [[INSPIRE](#)].
- [4] ICARUS collaboration, A. Menegolli, *ICARUS and status of liquid argon technology*, *J. Phys. Conf. Ser.* **375** (2012) 042057 [[INSPIRE](#)].
- [5] DEAP collaboration, M. Boulay, *DEAP-3600 Dark Matter Search at SNOLAB*, *J. Phys. Conf. Ser.* **375** (2012) 012027 [[arXiv:1203.0604](https://arxiv.org/abs/1203.0604)] [[INSPIRE](#)].
- [6] MINICLEAN collaboration, K. Rielage, *Status and prospects of the MiniCLEAN dark matter experiment*, *AIP Conf. Proc.* **1441** (2012) 518 [[INSPIRE](#)].
- [7] W. Lippincott et al., *Scintillation time dependence and pulse shape discrimination in liquid argon*, *Phys. Rev. C* **78** (2008) 035801 [*Erratum ibid. C* **81** (2010) 039901] [[arXiv:0801.1531](https://arxiv.org/abs/0801.1531)] [[INSPIRE](#)].
- [8] B. Baibussinov et al., *Free electron lifetime achievements in Liquid Argon Imaging TPC*, *2010 JINST* **5** P03005 [[arXiv:0910.5087](https://arxiv.org/abs/0910.5087)] [[INSPIRE](#)].
- [9] WARP collaboration, R. Acciarri et al., *Oxygen contamination in liquid Argon: Combined effects on ionization electron charge and scintillation light*, *2010 JINST* **5** P05003 [[arXiv:0804.1222](https://arxiv.org/abs/0804.1222)] [[INSPIRE](#)].
- [10] WARP collaboration, R. Acciarri et al., *Effects of Nitrogen contamination in liquid Argon*, *2010 JINST* **5** P06003 [[arXiv:0804.1217](https://arxiv.org/abs/0804.1217)] [[INSPIRE](#)].

- [11] M. Suzuki and S. Kubota, *Mechanism of proportional scintillation in argon, krypton and xenon*, *Nucl. Instrum. Meth.* **164** (1979) 197 [[INSPIRE](#)].
- [12] M. Antonello et al., *Analysis of liquid argon scintillation light signals with the icarus t600 detector*, Technical Report ICARUS-TM/06-03 (2006).
- [13] A. Curioni et al., *A Regenerable Filter for Liquid Argon Purification*, *Nucl. Instrum. Meth. A* **605** (2009) 306 [[arXiv:0903.2066](#)] [[INSPIRE](#)].
- [14] T. Briese et al., *Testing of Cryogenic Photomultiplier Tubes for the MicroBooNE Experiment*, [arXiv:1304.0821](#) [[INSPIRE](#)].
- [15] C. Chiu et al., *Environmental Effects on TPB Wavelength-Shifting Coatings*, *2012 JINST* **7** P07007 [[arXiv:1204.5762](#)] [[INSPIRE](#)].
- [16] B. Jones, J. VanGemert, J. Conrad and A. Pla-Dalmau, *Photodegradation Mechanisms of Tetraphenyl Butadiene Coatings for Liquid Argon Detectors*, *2013 JINST* **8** P01013 [[arXiv:1211.7150](#)] [[INSPIRE](#)].
- [17] Hamamatsu, *Hamamatsu r5912 specification sheet*, <http://www.datasheetcatalog.org/datasheet/hamamatsu/R5912.pdf>.
- [18] Douglas Electrical Components, *Ductorseal epoxy potted feedthrough*, <http://www.douglaselectrical.com/ductorseal>.
- [19] LDetek, *Ldetek trace nitrogen in argon or helium analyzer design report*.
- [20] B. Jones et al., *A study of the scintillation quenching effects of liquid nitrogen in argon*, in preparation (2013).
- [21] M. Antonello et al., *Detection of Cherenkov light emission in liquid argon*, *Nucl. Instrum. Meth. A* **516** (2004) 348 [[INSPIRE](#)].
- [22] Aire-Liquide, *The aire liquide gas encyclopedia*, <http://encyclopedia.airliquide.com/encyclopedia.asp>.
- [23] NIST, *Refprop users guide*, <http://www.nist.gov/srd/upload/REFPROP9.pdf>.
- [24] H. Keller-Rudek and G.K. Moortgat, *Mpi-mainz-uv-vis spectral atlas of gaseous molecules*, <http://www.atmosphere.mpg.de/spectral-atlas-mainz>.
- [25] AirGas, *Airgas liquid argon specifications*, <http://www.airgas.com>.
- [26] B. Rebel et al., *Results from the Fermilab materials test stand and status of the liquid argon purity demonstrator*, *J. Phys. Conf. Ser.* **308** (2011) 012023 [[INSPIRE](#)].
- [27] T. Tope, *Liquid argon purity demonstrator*, talk given at CPAD workshop on Liquid Argon TPC Detectors, <https://indico.fnal.gov/conferenceDisplay.py?confId=6395>.

RECEIVED: August 9, 2013

ACCEPTED: August 17, 2013

PUBLISHED: September 26, 2013

Erratum: A measurement of the absorption of liquid argon scintillation light by dissolved nitrogen at the part-per-million level

B.J.P. Jones,¹ C.S. Chiu, J.M. Conrad, C.M. Ignarra, T. Katori and M. Toups

*Massachusetts Institute of Technology,
77 Massachusetts Avenue, Cambridge, MA 02139, United States of America*

E-mail: bjpjones@mit.edu

ERRATUM TO: 2013 JINST 8 P07011

ABSTRACT: We correct a mistake in the calculation of the molecular absorption cross section of nitrogen, and a minor plot labelling mistake, which were found after publication of this paper.

1 Molecular absorption cross section calculation

It has come to our attention that the calculation of the molecular absorption cross section of nitrogen in [1] contains a mistake. The cross section should be $(7.14 \pm 0.74) \times 10^{-21}$, and not $(4.99 \pm 0.51) \times 10^{-21} \text{ cm}^2 \text{ molecule}^{-1}$ as stated in the paper.

Having corrected this mistake, table 1 should read:

Interpolation Scheme	Measured Absorption Strength $\text{cm}^{-1} \text{ppm}^{-1}$	Measured Cross Section $\text{cm}^2 \text{ molecule}^{-1}$
Interpolated Near	$(1.47 \pm 0.15) \times 10^{-4}$	$(6.98 \pm 0.71) \times 10^{-21}$
Interpolated Far	$(1.54 \pm 0.15) \times 10^{-4}$	$(7.30 \pm 0.73) \times 10^{-21}$
<i>Average Value</i>	$(1.51 \pm 0.15) \times 10^{-4}$	$(7.14 \pm 0.74) \times 10^{-21}$

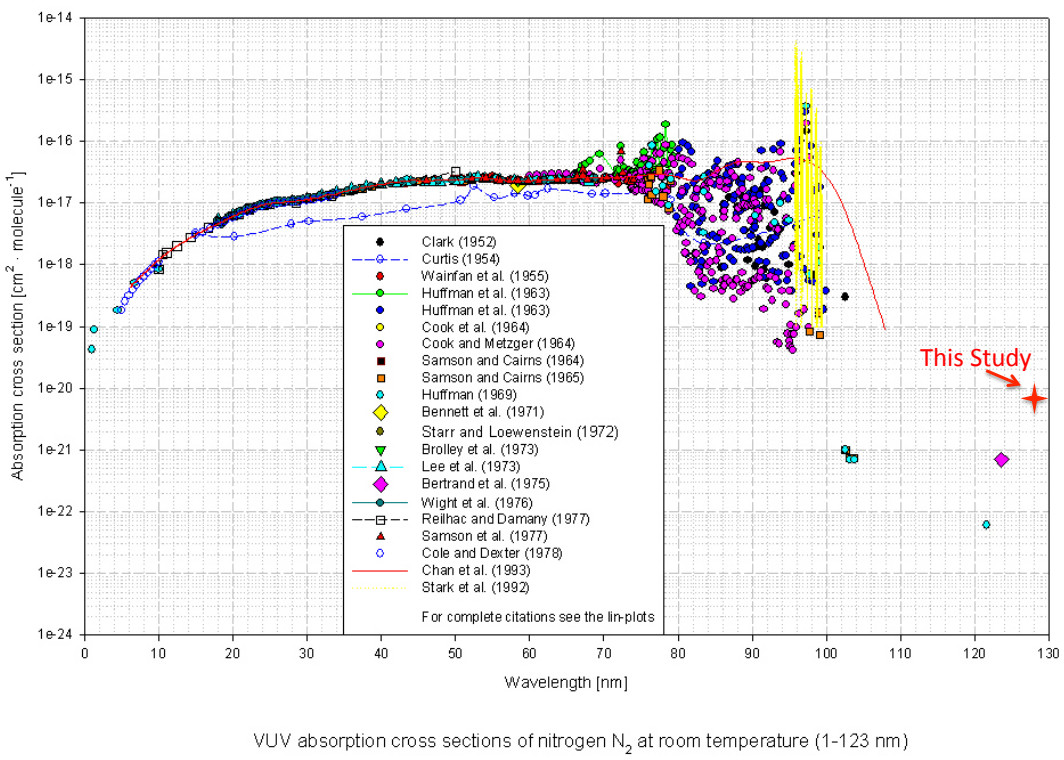
An updated figure 13, showing the updated value is given overleaf. This value is not used elsewhere in the paper. Therefore all conclusions regarding the implications of nitrogen absorption effects in liquid argon TPC detectors remain valid and numerically accurate.

2 Figure 8 axis label

The x axis label of figure 8, top right, should read “Pulse amplitude / area” and not “Pulse area / amplitude”

¹Corresponding author.

2013 JINST 8 E09001



References

- [1] B. Jones et al., *A Measurement of the Absorption of Liquid Argon Scintillation Light by Dissolved Nitrogen at the Part-Per-Million Level*, 2013 *JINST* **8** P07011 [[arXiv:1306.4605](https://arxiv.org/abs/1306.4605)].

Impurities in experiments employing radio-pure argon

Liquid argon dark matter experiments such as WArP [211], ArDM [212], DEAP [213], MiniCLEAN [214] and DarkSide [215], and experiments to measure coherent neutrino-nucleus scattering such as CLEAR [216] have strict radio-purity requirements in order to prevent radiogenic backgrounds. The signal of interest to such experiments is the nuclear recoil from a scattering interaction on an argon nucleus. This recoil has energy of order 10 keV and is highly ionizing. Highly ionizing backgrounds, such as alpha emitters typically have larger energy scales, so are easily distinguished from the recoil signal by an energy cut. Lightly ionizing radiogenic backgrounds include beta emissions, which have a continuous spectrum to zero energy. Since the argon scintillation pulse shape depends on the local ionization density, pulse-shape discrimination can be used to reduce this background by a factor of 100 [187]. However, even after this reduction, leakage of beta-decay electrons into the signal region form the main background for existing noble liquid dark matter detectors [217]–[219].

Fiducial cuts can be used to reject beta emissions from detector walls and structural elements, so the isotope responsible for the majority of beta-induced backgrounds in liquid argon dark matter detectors is ^{39}Ar , which is present at a level of 1 Bq/kg in naturally occurring argon [220]. ^{39}Ar has an endpoint of 565 keV, a half-life of 269 years, and is produced cosmogenically by spallation of ^{40}Ar in air.

Since the production mechanism is cosmogenic, argon which has been shielded from cosmic-ray interactions for more than 269 years can be expected to be depleted in concentration of ^{39}Ar . One such source of argon has been identified: carbon dioxide wells exploited for the oil industry contain argon gas at the few hundred ppm level [221]. Argon from several sites has been assayed for radio-purity, with concentration of 6.6 mBq/kg of ^{39}Ar being reported in argon from gas wells in Cortez, Colorado [222]. An ongoing effort is underway to distill and purify this argon for use in highly radio-pure dark matter detectors [223].

Because this argon is distilled from a gas mixture very different from air, it contains

a different set of trace impurities than industrial argon [224]. Among these is methane, which is removed by cryogenic distillation from a factor of four times the argon concentration to the ppm level. Further removal of methane requires non-regenerable filtration techniques, for example, hot getters, which is a relatively resource-intensive procedure. Methane has been shown to be unharful to free electron lifetime even at percent levels [225], although in large concentrations it can enhance recombination through effects on electron thermalization [226], reducing the charge yield. The following paper, published in the Journal of Instrumentation as [6], describes a study of the effects of dissolved methane on liquid argon scintillation light performed in the Bo test stand. A purity specification of tens of ppb is found, which is driven primarily by absorption of 128 nm light by methane. A quenching process is observed which had not been previously reported in the liquid phase. Visible re-emission at wavelengths detectable by PMTs, which has been reported in gas phase mixtures [227], [228], is ruled out at levels usable by existing argon scintillation detectors.

This study provides the purity specification for methane in scintillation detectors using underground argon. It also provides the upper limit for concentrations of methane-based sources that can, following the example of liquid xenon experiments [229], be deployed to calibrate liquid argon dark matter detectors. Finally it has the implication that mixed methane-argon TPCs [225], [230], which have potential applications in neutrino physics, will not be able to observe liquid argon scintillation light without further optical doping.

RECEIVED: August 16, 2013

REVISED: September 24, 2013

ACCEPTED: December 11, 2013

PUBLISHED: December 23, 2013

The effects of dissolved methane upon liquid argon scintillation light

B.J.P. Jones,^{a,1} T. Alexander,^b H.O. Back,^c G. Collin,^a J.M. Conrad,^a A. Greene,^a T. Katori,^a S. Pordes^d and M. Toups^a

^a*Massachusetts Institute of Technology,
77 Massachusetts Avenue, Cambridge, MA 02139, U.S.A.*

^b*University of Massachusetts at Amherst,
710 N Pleasant St. Amherst MA 01003, U.S.A.*

^c*Princeton University,
Princeton, NJ 08540, U.S.A.*

^d*Fermi National Accelerator Laboratory,
Batavia, IL 60510, U.S.A.*

E-mail: bjpjones@mit.edu

ABSTRACT: In this paper we report on measurements of the effects of dissolved methane upon argon scintillation light. We monitor the light yield from an alpha source held 20 cm from a cryogenic photomultiplier tube (PMT) assembly as methane is injected into a high-purity liquid argon volume. We observe significant suppression of the scintillation light yield by dissolved methane at the 10 part per billion (ppb) level. By examining the late scintillation light time constant, we determine that this loss is caused by an absorption process and also see some evidence of methane-induced scintillation quenching at higher concentrations (50-100 ppb). Using a second PMT assembly we look for visible re-emission features from the dissolved methane which have been reported in gas-phase argon methane mixtures, and we find no evidence of visible re-emission from liquid-phase argon methane mixtures at concentrations between 10 ppb and 0.1%.

KEYWORDS: Noble liquid detectors (scintillation, ionization, double-phase); Photon detectors for UV, visible and IR photons (vacuum) (photomultipliers, HPDs, others); Photon detectors for UV, visible and IR photons (gas) (gas-photocathodes, solid-photocathodes)

ARXIV EPRINT: [1308.3658](https://arxiv.org/abs/1308.3658)

¹Corresponding author.

Contents

1 Motivations for studying methane in liquid argon	1
2 Experimental configuration for this study	2
3 The effect of methane upon prompt scintillation light yield	6
4 Argon scintillation time constants, quenching and absorption	8
5 Searching for visible re-emission features	13
6 Implications for neutrino and dark matter experiments	14

1 Motivations for studying methane in liquid argon

Many current- and future-generation neutrino and dark matter experiments use liquid argon as an active medium [1–7]. The detection of weakly interacting particles-of-interest in such a detector involves collecting ionization charge and/or scintillation light produced in the argon bulk. In order to achieve a large target mass with a reasonable number of sensitive detector elements, the detection of both light and charge typically takes place some distance from the interaction point. For charge collection, this is achieved by drifting free electrons in an electric field, as in a time projection chamber (TPC). For light detection, sensitive elements such as PMTs [8] or light guides [9] are placed around the boundaries of an argon target volume. Because argon is transparent to its own scintillation light, some fraction of the isotropically produced scintillation light is captured by these sensitive elements.

Both charge and light production and propagation are known to be affected adversely by small concentrations of dissolved impurities. The commercially available argon which is used in most liquid argon detectors is manufactured by the distillation of air, and typically arrives from the vendor with part-per-million (ppm) levels of contaminants such as water, oxygen and nitrogen [10]. For a TPC detector, water and oxygen must be removed in a subsequent filtering process to the hundred parts per trillion level in order not to damage the free electron lifetime [11]. In a scintillation detector, not only water and oxygen, but also nitrogen must be controlled at the ppm level in order to prevent scintillation quenching [12–14] and absorption [15].

A new generation of dark matter experiments, which require highly radiopure argon [7], plan to use argon that is not distilled from air, but rather Underground Argon (UAr) extracted from underground sources. This argon has the advantage of having low levels of the radioactive isotope ^{39}Ar [16], a source of background in such detectors. The UAr is extracted from carbon dioxide wells that are comprised of 96% carbon dioxide and 2% nitrogen, alongside sub-percent levels of other gasses, including 5,700 ppm methane and 600 ppm argon. Locally at the CO₂ well, an Ar-He-N₂ mixture is extracted from the crude CO₂ gas, with methane levels below the sensitivity on

the *in situ* gas analyzer [17]. The gas mixture is sent to the Fermi National Accelerator Laboratory for further purification, where, after He removal, cryogenic distillation removes the N₂ and purified UAr is produced [18]. This cryogenic distillation process not only concentrates the UAr, but also has the effect of concentrating any residual trace amounts of methane. It is therefore critical to know what concentration of methane is permissible in the UAr scintillation experiments in order to understand what purification techniques are required to remove the methane, which can be technically difficult.

On the other hand, mixed methane and liquid argon TPCs have been proposed as detectors for low-energy neutrino physics [19]. The benefit provided by the methane admixture is that free protons are present in the detector as interaction targets. This reduces the threshold for the interactions of low-energy neutrinos, such as those from the sun, or from supernovae, or man-made neutrinos from decay-at-rest sources. Free protons may also make neutron captures detectable in a liquid argon scintillation detector, allowing for coincidence tagging of low-energy antineutrino inverse-beta-decay interactions ($\bar{\nu}_e + p \rightarrow e^+ + n$).

The effects of methane upon charge collection have been shown to be minimal, even at few-percent level concentrations [19]. However, the effects of methane upon liquid argon scintillation light have not been investigated previously. As such, no specification on the allowed methane concentration for a scintillation detector currently exists. World data on the VUV absorption cross section of pure methane, taken at room temperature and pressure, suggest that significant absorption may be expected at relatively low concentration levels [20]. Studies of scintillation light from gaseous argon-methane mixtures, however, have reported a visible emission feature at a wavelength of a 431 nm [21, 22]. This motivates a determination of the effects of methane impurities in liquid argon detectors, operating under realistic scintillation detection conditions.

In this paper we examine the effects of methane upon the light yield from alpha particles detected in a liquid argon scintillation detector, and quantify the concentration scale to which methane must be removed in order to prevent significant scintillation light losses relative to pure argon.

2 Experimental configuration for this study

These tests were performed using the Bo cryostat and gas injection system, which was previously used to study the effects of nitrogen contamination in argon in [15]. The cryostat is a vacuum insulated cylinder with a diameter of 55.9 cm which can be filled to a level of approximately 100 cm with high purity argon, supplied via a system of molecular sieves and regenerable filters [23]. For this study, the cryostat was filled with argon to a level of 76 ± 1 cm and maintained at a pressure of 12 ± 0.2 psig by a liquid nitrogen condenser system.

Inside the cryostat are situated two cryogenic PMT assemblies. The first assembly, which will be referred to hereafter as PMT-UV, is comprised of a wavelength shifting plate supported above an 8-inch cryogenic Hamamatsu R5912-02mod PMT [8], which is mounted inside a mu-metal shield. The wavelength shifting plate is a 12-inch disc of clear acrylic upon one side of which is a coating of tetraphenyl butadiene (TPB) suspended in a polystyrene matrix [24–26]. The purpose of the plate is to capture the 128 nm argon scintillation light and re-emit at visible wavelengths, with an emission spectrum peaked around 450 nm where PMT quantum efficiency is high [27]. A polonium disc alpha source is held 20 cm from the face of PMT-UV, providing a source of scintillation light

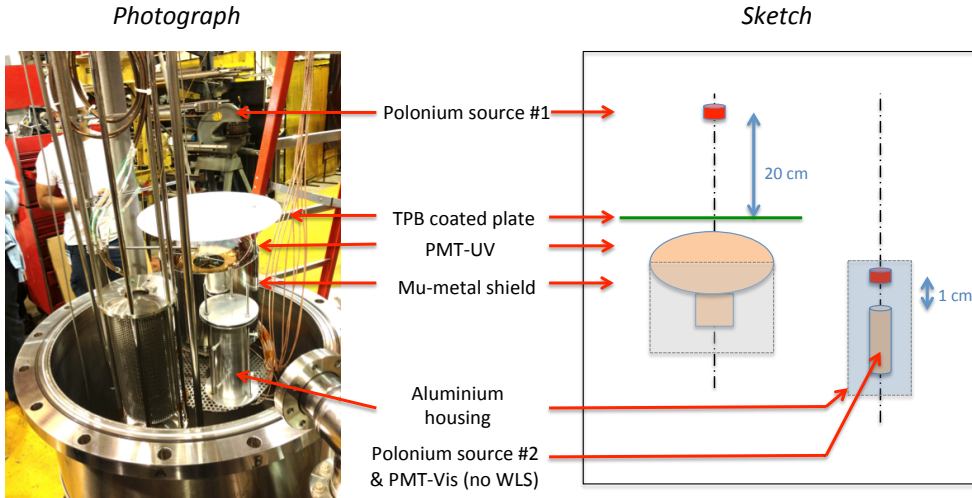


Figure 1. A labeled photograph and sketch showing the internal Bo configuration used in this study.

in the form of monoenergetic 5.3 MeV alpha particles. Monitoring the light yield at PMT-UV as methane is added indicates to what extent the 128 nm argon scintillation light has been absorbed or quenched by the injected methane. In addition to scintillation light from the polonium alpha source, PMT-UV also detects the scintillation light produced by cosmic rays traversing the Bo volume, and would also be sensitive to visible re-emission features if any were present.

The second assembly, which will be referred to hereafter as PMT-Vis, is comprised of a 2-inch Hamamatsu R7725-mod PMT, housed inside an aluminium cylinder. The 2-inch PMT has no accompanying wavelength shifter and is shielded by the aluminium cylinder from visible light generated by the PMT-UV wavelength shifting plate. A second polonium disc alpha source is held 1 cm from the face of the PMT-Vis. Openings in the base and around the top edge of the aluminium cylinder provide space for argon to flow through the two inch assembly to ensure that there is mixing throughout the system. Since there is no wavelength shifter, this PMT is insensitive to the 128 nm argon scintillation light, so can be used to test for the emergence of possible visible re-emission features. The 5.3MeV alpha particles produced by the polonium source have a range of only $50 \mu\text{m}$ in liquid argon, so can be treated as point light sources for our purposes. With a source to PMT distance of 1 cm, the 2-inch diameter PMT face subtends a solid angle of more than 30% to these point light sources. The PMT quantum efficiency is around 20% at visible wavelengths. Accounting for these two factors we expect to be able to collect at least 6% of emitted visible photons. Therefore an emission feature as small as 10 visible photons / MeV, which produces an average of 53 visible photons per alpha particle would lead to a detected distribution with a Poisson mean of three photoelectrons. This signal would be clearly visible above background in our apparatus.

Signal and high voltage for each PMT are carried by common RG-316 type coaxial cables, and split outside of the cryostat by a HV splitter unit. The signal is connected to a Tektronix DPO5000 oscilloscope terminated at 50Ω and sampling at 1 gigasample per second.

Our measurement involves making injections of small amounts of methane gas into the liquid argon volume, and studying the light yield at both PMT-UV and PMT-Vis. Methane injections are

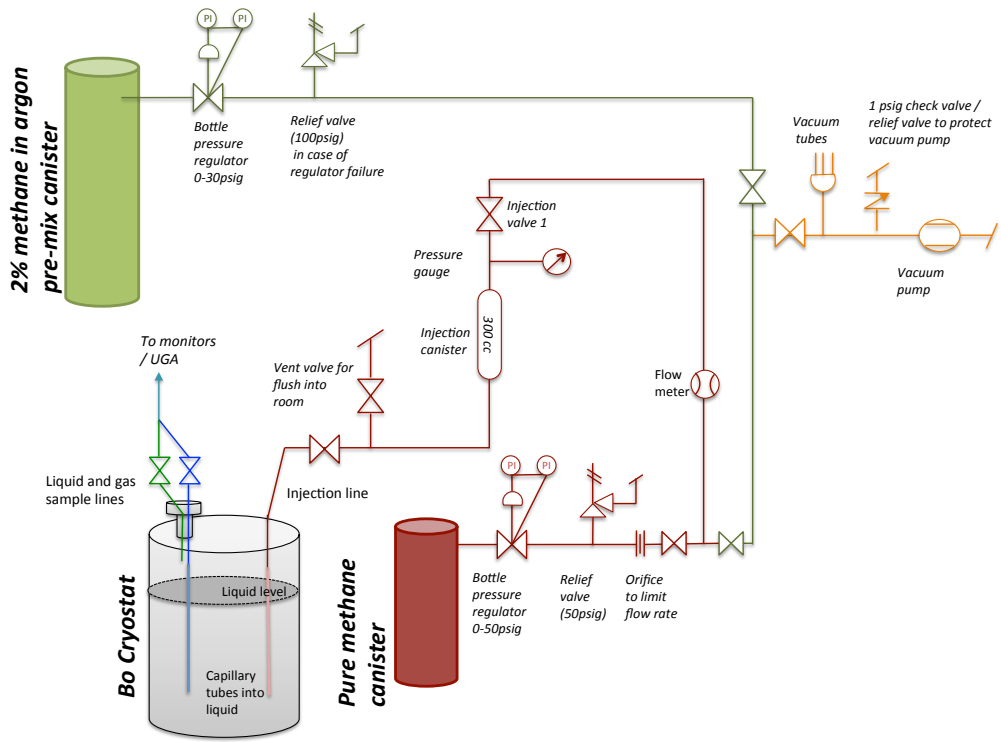


Figure 2. A diagram showing the layout of the sample and injection lines connected to the Bo cryostat for this study. The majority of the data reported in this paper were acquired by injecting from the 2% methane in argon canister.

made via a 300 cm³ injection canister which can be charged to a known pressure with an injection gas, and then released through a capillary pipe into the liquid volume. The injection pressure is measured using an analog pressure gauge which has a precision of 1 psig. The internal Bo pressure into which the gas is released is recorded by an electronic pressure gauge with a precision of 0.1 psig. After being released into the Bo volume, the injected gas circulates and eventually reaches an equilibrium distribution between the liquid and vapor phases. The apparatus also includes sample capillary lines for the liquid and vapor phases which can be used to feed monitors and gas analyzers when required. A diagram showing the layout of the injection and sample lines used in this study is shown in figure 2.

The equilibration time of methane in argon following an injection in this system determines the amount of time which must be left between methane injection and light measurement. We measured the equilibration time of the system after a methane injection in a preliminary study using a universal gas analyzer (UGA) [28]. First, the gas analyzer was connected to the Bo liquid sample line with the cryostat held at 12 psig. A stable methane concentration at the noise floor of the device, corresponding to around 0.01% methane per mole¹ was observed. At a known time, the UGA piping was disconnected from the Bo cryostat and connected to a bottle of 2% methane-in-

¹All concentrations reported hereafter will be implicitly given as molar ratios

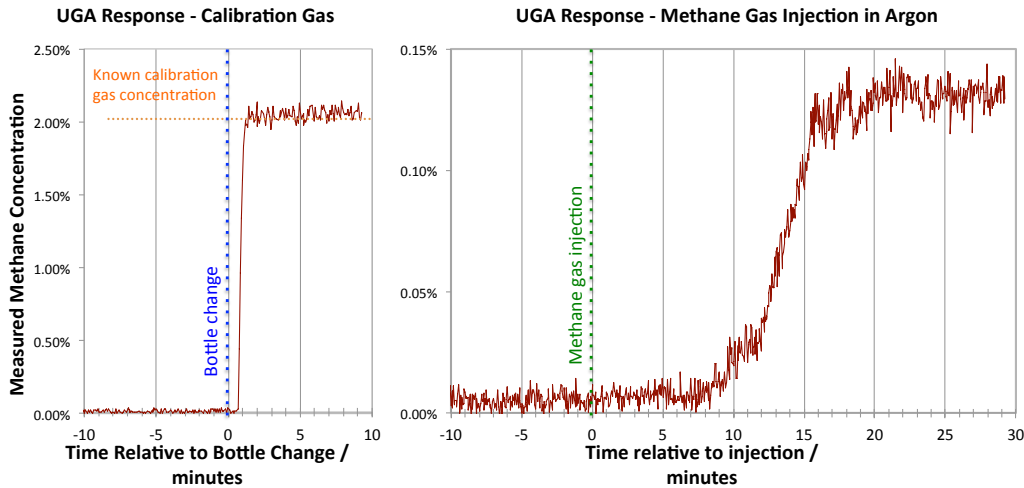


Figure 3. Left: time taken for reported methane concentration by UGA to stabilize after swapping source from Bo sample line to calibration gas at the Bo cryostat location. This quantifies the flow time in the sample piping and the lag time of the UGA. Right: Time taken for reported methane concentration by UGA to stabilize after an injection of methane into pure argon in the Bo cryostat. The equilibration time is approximately 20 minutes.

argon calibration gas regulated at 12 psig. The time taken for the methane concentration reported by the UGA to stabilize to 2% was approximately one minute, which sets the timescale for flow of gas through the 30 m supply pipe and the lag time of the measuring device. Then, with Bo reconnected and the methane reading stable at the noise floor once again, an injection of around 0.1% methane was made into Bo. The reported methane concentration by the UGA is seen to rise gradually, and then stabilize after approximately 20 minutes. Since we already know that the flow time in the piping and the UGA response time is much shorter than this, we conclude that 20 minutes is the equilibration time for methane injected into the cryostat to reach an equilibrium distribution between the gas and the liquid phases. These measurements can be seen in figure 3. We allow a conservative 40 minutes of equilibration time between any injection and light yield measurement. The concentrations of methane we investigate in this paper are far below the sensitivity of the UGA, and so we cannot use it to quantify the injected methane. Our only concentration measurements come from the known volume and pressure of the injected gas, which is accompanied by relatively large systematic uncertainties. We describe these below.

In order to achieve ppb level concentrations of methane in argon, we inject a pre-mixed gas of 2% methane in argon via a 300 cm³ injection canister, charged to a known pressure with gas at room temperature and then discharged into the liquid. To achieve injected methane concentrations at the 10 ppb level, the injection pressure must be set fairly low relative to the design pressure of the injection system. The lowest methane concentration point requires a 15 psig injection into the 12 psig Bo liquid volume. Using the ideal gas law, we can determine that the 3 psi of injected pre-mixed gas contains 5×10^{-5} moles of methane. The Bo liquid volume is a cylinder of diameter 55.9 cm and height 76 cm, which corresponds to approximately 6530 moles of argon. Thus a 15 psig injection into the 12 psig volume leads to an increase in methane concentration by 8 ppb.

Table 1. Contributions to the systematic uncertainty of the injected methane concentration for a 15 psig injection into the 12 psig liquid volume.

Quantity	Value	Unit	Contribution to Concentration Uncertainty
Injection pressure precision	15 ± 0.5	psig	16.5%
Injection volume	300 ± 45	cm ³	15%
Gas temperature	290 ± 10	K	3.4%
Internal pressure stability	12 ± 0.2	psig	1.7%
Liquid level	76 ± 1	cm	1.3%
Total injected	8.0 ± 1.9	ppb	23.7%

The dominant systematic uncertainties which affect the injected concentration are the injection pressure gauge precision of ± 0.5 psig, and the imprecisely known injection volume, which has an uncertainty of $\pm 15\%$ due to volume associated with valves and piping. There are other sub-dominant contributions to the total uncertainty, which are enumerated in table 1. Adding all the uncertainties in quadrature leads to an overall concentration uncertainty of 24% for this lowest pressure injection. The extent to which these uncertainties are correlated between injections is difficult to quantify in our apparatus, and as such we conservatively assign all concentrations the same worst-case fractional error of 24%. For future higher precision studies, the injection system may be improved by installing a smaller canister or higher precision pressure gauge to produce much more precisely known concentrations. For the purposes of this paper, however, a logarithmic scan of the relevant concentration range is already very instructive.

3 The effect of methane upon prompt scintillation light yield

In order to study the effects of injected methane upon the prompt scintillation light yield, we follow a very similar procedure to the one described in [15]. We collect the areas of 40,000 pulses using a falling-edge trigger applied to PMT-UV. The pulse area is evaluated and histogrammed online by the oscilloscope in a window which extends from -50ns to +100ns relative to the trigger time. The histogram is then saved from the oscilloscope for further analysis offline. We subtract the measured DC baseline and then fit the measured pulse area distribution with a function describing a poisson-like peak with corrections for source shadowing added to a falling power-law background. Since the geometry of the alpha source holder is unchanged from that used in [15], we use the same experimentally determined shadowing function from that study, more details of which can be found in [15], section 3. The pulse area spectrum and best fit function for two concentration points from this study are shown in figure 4. The light yield as a function of methane concentration is determined by the poisson mean of the alpha-induced peak at each concentration point.

The single photoelectron (SPE) scale which sets the pulse area normalization is measured at several points throughout the run using late scintillation light. To obtain the single photoelectron area distribution, 10,000 individual waveforms are analyzed using a peak-finding algorithm which isolates likely SPE pulses between 500 ns and 1400 ns following a falling-edge trigger, by identifying times where the waveform has a large and negative dV/dt over 5 samples. An example

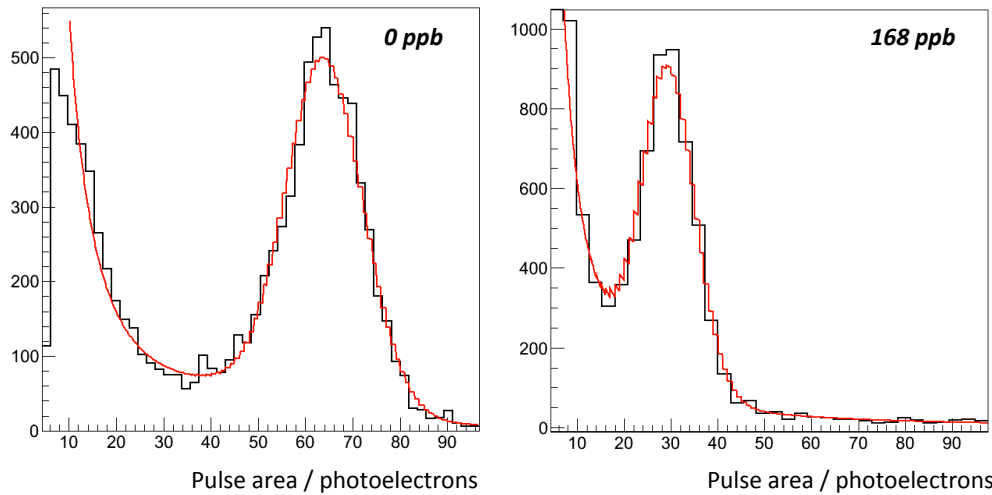


Figure 4. The PMT-UV pulse area spectrum and best fit function for the 0 ppb and 168 concentration points. The fit function is a modified poissonian distribution superposed with a falling power law background, as described in [15].

waveform with the SPE candidate positions highlighted is shown in figure 6, left. The baseline-subtracted areas of the SPE candidate pulses are evaluated by integrating from the beginning of the pulse until the amplitude falls back above threshold. The SPE areas are histogrammed, and a gaussian fit to the peak of this histogram gives the measured SPE scale. A sample pulse area histogram with fitted peak is shown in figure 6, right. Using this method, the measured SPE scale is found to be stable to within 2.5% over the course of the run.

An alternative method of evaluating the SPE scale is to calculate the average area of all SPE candidate pulses found. This method gives a SPE scale which is approximately 20% higher than that obtained by fitting the peak, and this discrepancy is likely caused by contamination of the sample with pulses of which have contributions from more than one photoelectron, which appear in the large area tail of the distribution. The SPE scale stability obtained with this method is 1.02%, over the duration of the run. In this analysis we use the peak-fitting method rather than the average area method to evaluate the SPE scale, as it is less sensitive to the effects of the multiple photoelectron pulse contamination. Ultimately, our conclusions will rely only upon the stability of the SPE scale rather than its absolute value, and we include the measured SPE stability of 2.5% as a systematic error on the normalization of each measured light yield.

In our previous publication [15] we also measured the SPE scale using a pulsed LED. This method was found to give a SPE scale consistent with the peak-finding method to within 7%. The effects of shifts in the SPE scale by up to 20% were investigated, and found to have no significant biasing effect on the relative prompt light yield measurement as a function of concentration.

The measured light yield as a function of methane concentration is shown in figure 5. The dominant systematic error on the light yield measurement is the SPE scale stability. We see no observable light loss below 10 ppb, and then steady losses of scintillation light between 10 ppb and 1 ppm. Beyond 1 ppm of methane, the alpha peak was no longer observable. Overlaid on the figure are the predictions of the expected light yield as a function of methane concentration for absorption strengths of 0.02%, 0.03% and 0.04% $\text{ppb}^{-1}\text{cm}^{-1}$ as determined by a ray tracing simulation of our

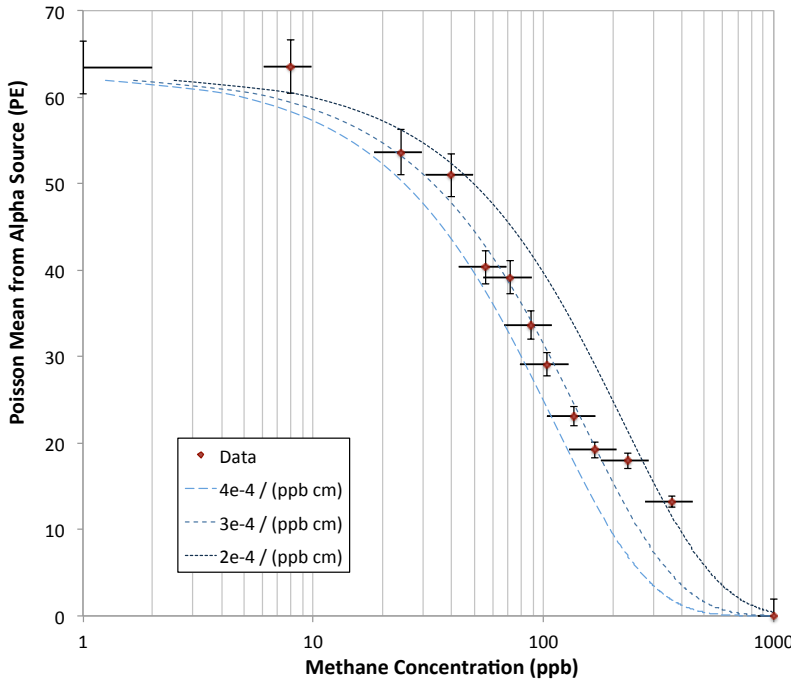


Figure 5. The measured prompt scintillation light yield from a monoenergetic polonium 210 alpha source as a function of methane concentration. Horizontal error bars are given by the precision of the injection pressure gauge. Vertical error bars are given by the single photoelectron scale added in quadrature with the peak fit error. The left-most point is for pure argon. The overlaid curves show the predicted attenuation behavior based on a ray tracing simulation for three characteristic attenuation strengths. At the right-most point, the alpha-induced peak was no longer visible.

apparatus, normalized to the emitted light intensity for clean argon. These correspond to molecular absorption cross sections of $9.5 \times 10^{-18} \text{ cm}^2$, $1.4 \times 10^{-17} \text{ cm}^2$ and $1.9 \times 10^{-17} \text{ cm}^2$ respectively. Our data are in approximate agreement with previous measurements of the methane absorption cross section at 128 nm, made at room temperature and pressure with pure methane gas [20]. We address in more detail whether the losses we see can be attributed to absorption effects alone in section 4.

As a cross-check that the light losses observed were a result of methane injection and not out-gassing of water or some other system instability, we collected similar datasets without injecting methane 12 hours apart during the middle of the run, and found stability of the light yield to within 1.2%. This is to be contrasted with the tens-of-percent light losses observed over 12 hour periods during methane injections. These data are shown in figure 7. In a separate run, a single methane injection of 1 ppm was made and the alpha-induced poisson-like peak was immediately extinguished.

4 Argon scintillation time constants, quenching and absorption

The light losses described in section 3 could be the result of quenching, absorption or both. In this context, quenching refers to a process where the excimers involved in the liquid argon scin-

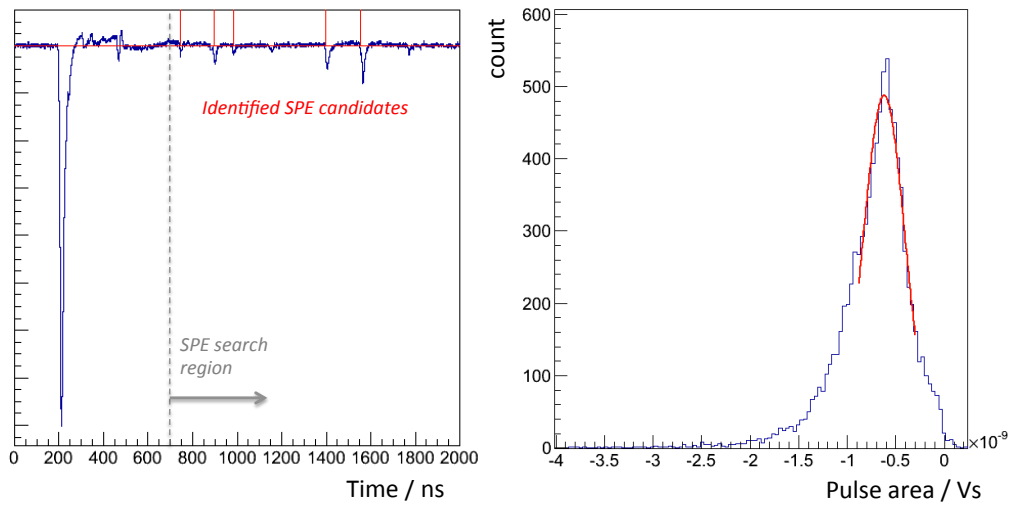


Figure 6. Left: a sample waveform showing where SPE candidates were found in the late scintillation light signal. Right: the distribution of SPE areas, with peak fit shown in red.

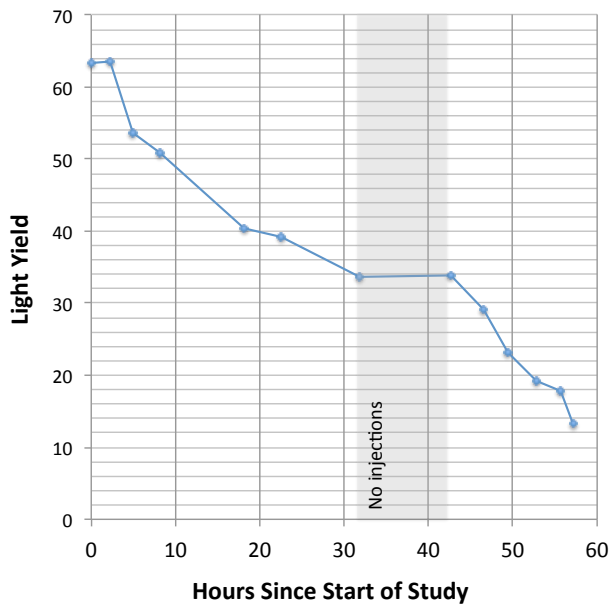


Figure 7. The prompt light yield as a function of time during this study. For the period where no methane was injected, the light yield was found to be stable to within 1.2%

tillation process are dissociated by interaction with an impurity molecule without emitting a scintillation photon. This mechanism affects late, triplet-state scintillation light much more strongly than prompt, singlet-state light, leading to a reduced time constant and late-to-total light ratio. Absorption, on the other hand, refers to the loss of photons due to interactions with impurities during propagation between source and detection points, and affects both prompt and slow scintillation light equivalently.

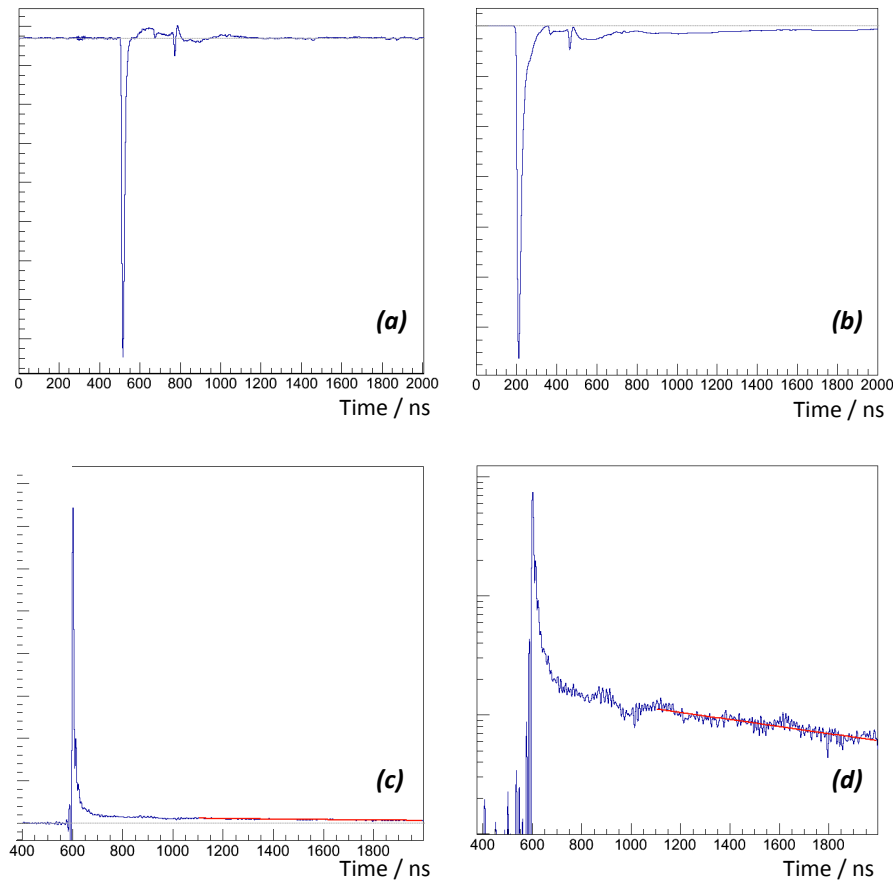


Figure 8. (a) The averaged single photoelectron pulse shape, obtained with a pulsed LED. (b) The average raw pulse shape for scintillation deposits in clean argon. (c) The average deconvolved pulse shape for scintillation deposits in clean argon on a linear scale, with exponential fit overlaid in red. (d) The average deconvolved pulse shape for scintillation deposits in clean argon on a logarithmic scale, with exponential fit overlaid in red.

To distinguish between these two types of processes we investigate the effects of methane concentration upon the time constant of the late liquid argon scintillation light. If the large methane-induced losses observed in the prompt scintillation light are a result of a quenching process, we would expect large changes in the slow scintillation time constant at concentrations at or below those where the prompt peak is affected. A pure absorption process would affect both components equally, leading to an overall reduction in light yield with no change of time constant.

The method used to extract the late scintillation time constant resembles the method reported in [12]. The single photoelectron response shape was first measured using a pulsed LED, optically coupled to a fiber which points at the PMT-UV photocathode. Then, 10,000 self-triggered and baseline-subtracted waveforms were summed to produce an average PMT-UV pulse shape for scintillation deposits at each concentration point. The summed waveform undergoes some pre-processing to prevent ringing artifacts from deconvolution, including the application of a smooth

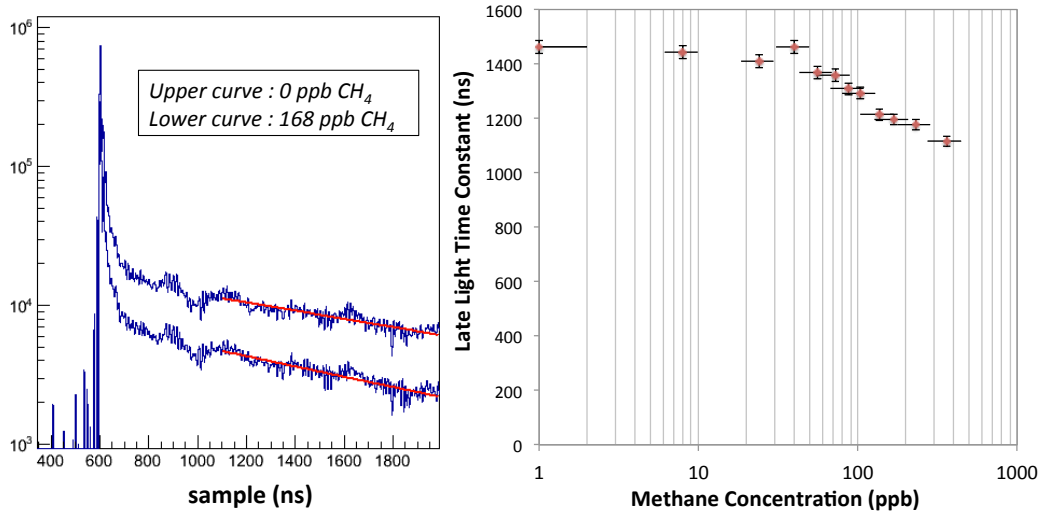


Figure 9. Left: average deconvolved pulse shapes and exponential fits for two concentration points. The red lines show the best-fit exponentials for each point. Right: the measured late light time constant vs methane concentration. Vertical error bars are given by the RMS discrepancy between fitting the first and second half of each dataset. The left-most point is for clean argon.

sigmoid window function at the sample edges, and pre- and post-padding with zeroes to prevent wraparound effects. The summed waveform is then deconvolved using the single photoelectron pulse shape as a deconvolution kernel, and an optimized Weiner filter combined with low-pass filter is applied to suppress noise and deconvolution artifacts.

This process removes all linear shape effects due to the PMT anode response, PMT undershoot, ringing in the PMT base electronics, and reflections in cables. The single photoelectron shape and average raw pulse shapes before and after deconvolution for clean argon are shown in figure 8. Nonlinear contributions to the pulse shape are not removed by this method. As such, the reported late-light time constant obtained from this method is valid only to the extent that the PMT and electronics response is linear. The level of system nonlinearity is very difficult to quantify. For the purposes of this study, we assume that the system response is linear and thus the measured time constants are faithful. Since our primary focus is upon changes in the late scintillation time constant rather than its absolute value, our main conclusions remain valid even in the presence of small nonlinear shape effects. To ensure that pulse shape effects have not biased our prompt light measurements in section 3 we can make a simple consistency check, comparing the average prompt areas obtained from raw and deconvolved pulses at each concentration point. These data are shown in fig 10, right, and show good linearity within experimental uncertainties.

To extract the late-light time constant we fit the deconvolved pulse shape from 500 ns to 1400 ns after the prompt pulse with a falling exponential. The 500 ns delay is chosen to avoid the effects of afterpulsing, deconvolution artifacts from the sharp edge of the prompt peak and the effects of any possible intermediate scintillation time constants. Two deconvolved average waveforms and their corresponding fitted exponential functions are shown in figure 9, left. The dependence of the measured time constant on methane concentration is shown in figure 9, right.

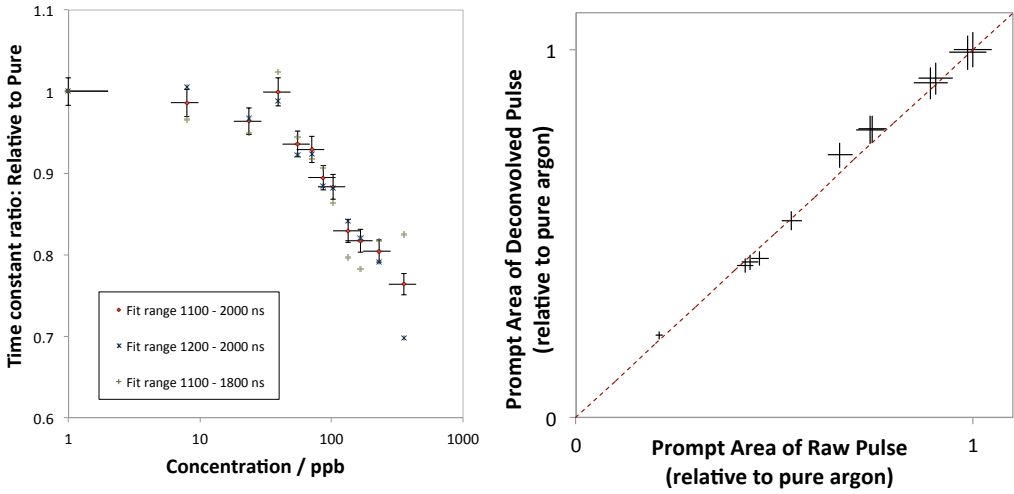


Figure 10. Left: ratios of the time constant for contaminated argon to the time constant for pure argon, obtained using the full fit window (1100–2000 ns) and two reduced fit windows (1200–2000 ns and 1100–1800 ns) which yield pure argon time constants of 1462 ± 25 ns, 1627 ± 28 ns and 1455 ± 25 ns respectively. Right: Ratio of the average prompt areas of raw and deconvolved pulses at each concentration.

As has been discussed in appendix C of [12], different definitions of the argon scintillation time constants and different fit methods used to extract them from deconvolved pulses can lead to different numerical values. By fitting exponentials to shorter sections of the deconvolved pulse we were able to obtain time constants between 1450 and 1630 ns for clean argon. However, the trend observed in the time constants as a function of methane concentration, quantified by comparing the time constant for pure argon to the time constant for contaminated argon, is found to be unchanged within experimental uncertainty regardless of which fit window is used. Some examples are shown in figure 10, left. In this study we are interested in this variation, rather than the absolute value of the time constant. For this reason, the error bars shown in figure 9 do not include this correlated systematic uncertainty, and are determined instead by the discrepancy between the time constants obtained from independently fitting the first and second half of the dataset for each concentration point, with the fit performed over the full fit region.

These data show very clearly that the majority of the light losses observed in the prompt scintillation light yield are not the result of a quenching process. The late scintillation time constant remains long even when significant prompt light losses are observed. Some evidence of a quenching process is observed at higher concentration values, but this effect is much too small to explain the observed light losses in the prompt peak. The two curves of figure 9 are for an unquenched and a heavily quenched point from this study. The change in time constant between the 0 and 168 ppb concentration points is relatively small, whereas a significant loss of light yield for both prompt and late light components is clearly visible.

We do not have the ability to test this apparent quenching behavior at much higher concentrations of methane in this detector, since the absorption effect is dominant and blocks a large fraction of the light required to observe the quenching. A detailed study of this quenching process would be ideally performed in a much smaller detector, where light losses due to absorption between

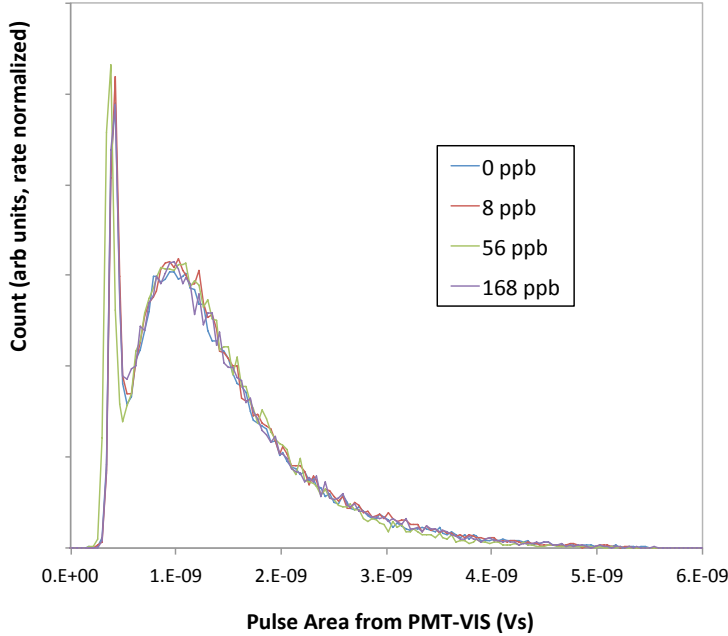


Figure 11. The rate-normalized charge per pulse measured on PMT-Vis, showing pedestal and SPE. No SPE rate increase or higher intensity visible emission feature is observed as methane is injected.

source and detector are smaller. However, for any realistic scale neutrino or dark matter detector, the absorption effect is likely to be the dominant mechanism of light loss.

5 Searching for visible re-emission features

It has been reported that a visible scintillation emission feature has been observed in gas-phase mixed argon and methane drift chambers [21]. The feature is suggested to be a 431 nm emission line resulting from interactions between argon excimers and various energy levels of methane molecules [22]. A competing non-radiative decay route at high methane densities is suggested to quench the emission, which is likely to suppress any such feature in a liquid phase mixture, where the molecular mean-free-path is much smaller than in the gas phase. However, if some visible emission feature is present despite the strong absorption of 128 nm scintillation light, it could help to circumvent the problems associated with the absorption by allowing visible light to propagate across the detector, unabsorbed by methane.

We search for visible emission features by measuring the areas of self-triggered PMT signals from PMT-Vis within a narrow window of a falling-edge trigger. This PMT is optically isolated from most of the argon volume, but has a polonium disc source held 1 cm from the PMT face. In pure argon, no features larger than the single photoelectron background peak are observed.

The single photoelectron dark rate in clean argon is comparable to the alpha source rate; they are around 200 Hz and 100 Hz respectively. This means that even triggering at the single photo-electron level, any alpha induced visible emission feature would be observable over background.

Rate-normalized histograms of pulse areas for several methane concentration points are shown in figure 11. No change in the single photoelectron rate is observed, and no higher intensity features are detected for any concentration point. These data were taken up to 168 ppb of methane, by which point 70% of the 128 nm scintillation light was being absorbed. We also performed a logarithmic scan of concentration points between 1 ppm and 0.1% methane by mole, none of which have any observable 128 nm scintillation light, and saw no evidence of strong visible re-emission features at any concentration.

6 Implications for neutrino and dark matter experiments

Our results show that significant light loss is to be expected when as little as tens of ppb of methane are mixed into liquid argon, due to ultraviolet absorption of 128 nm photons. The loss of light is accompanied by no detectable visible re-emission, and as such, this poses a problem for any scintillation detectors operating in this methane concentration range.

In the case of dark matter detectors using UAr, to eliminate the adverse affect of methane on argon scintillation, it is clear that the argon must contain less than 10 ppb of methane. To reach this goal, hot getters can be used [29]. Since the light losses are attributed to an absorption process, the exact purity specification will depend on the geometry of the detector in question, with larger detectors requiring higher purity.

For TPC detectors aiming to use argon/methane mixtures in order to provide free protons, the detection of scintillation light is likely to be impracticable. In order to provide a reasonable number of free protons for their physics goals, these detectors would need to contain methane at the few percent level or higher. Whilst this type of argon/methane mixture has been shown to have acceptable properties for electron drift and charge collection [19], our studies show that such a detector would be blind to scintillation light, because of the methane absorption effect.

At higher concentrations, we have also seen evidence of an apparent quenching effect, which is inferred from a reduction of the late scintillation light time constant. The configuration of our apparatus described in this paper is not well suited to studying the quenching effect in detail, since by the time the effect is large, most of the emitted light has been absorbed between source and detector. This is likely also to be true of any realistic neutrino or dark matter experiment, and so the practical implications of this quenching effect are limited. A detailed study of the effect could be made in a test with a much smaller source to PMT path length, and with a data acquisition system capable of recording longer waveforms in order to capture many lifetimes of late scintillation light.

Acknowledgments

We would like to thank Clementine Jones for proofreading this paper, and Bill Miner, Ron Davis and the other technicians who have assisted us at the Proton Assembly Building, Fermilab for their tireless hard work to provide us with cryogenic facilities of the very highest standard. The authors thank the National Science Foundation (NSF-PHY-1205175, NSF PHY-1211308 and NSF PHY-1242585) and Department Of Energy (DE-FG02-91ER40661). This work was supported by the Fermi National Accelerator Laboratory, which is operated by the Fermi Research Alliance, LLC under Contract No. De-AC02- 07CH11359 with the United States Department of Energy.

References

- [1] LBNE collaboration, T. Akiri et al., *The 2010 interim report of the long-baseline neutrino experiment collaboration physics working groups*, [arXiv:1110.6249](https://arxiv.org/abs/1110.6249).
- [2] A. Rubbia, *Towards GLACIER, an underground giant liquid argon neutrino detector*, *J. Phys. Conf. Ser.* **375** (2012) 042058.
- [3] B.J.P. Jones, *The status of the MicroBooNE experiment*, *PoS(EPS-HEP2011)* 436 [[arXiv:1110.1678](https://arxiv.org/abs/1110.1678)].
- [4] ICARUS collaboration, A. Menegolli, *ICARUS and status of liquid argon technology*, *J. Phys. Conf. Ser.* **375** (2012) 042057 .
- [5] DEAP collaboration, M. Boulay, *DEAP-3600 dark matter search at SNOLAB*, *J. Phys. Conf. Ser.* **375** (2012) 012027 [[arXiv:1203.0604](https://arxiv.org/abs/1203.0604)].
- [6] MiniCLEAN collaboration, K. Rielage, *Status and prospects of the MiniCLEAN dark matter experiment*, *AIP Conf. Proc.* **1441** (2012) 518.
- [7] DarkSide collaboration, T. Alexander et al., *Light yield in DarkSide-10: a prototype two-phase argon TPC for dark matter searches*, *Astropart. Phys.* **49** (2013) 44 [[arXiv:1204.6218](https://arxiv.org/abs/1204.6218)].
- [8] T. Briese et al., *Testing of cryogenic photomultiplier tubes for the MicroBooNE experiment*, *2013 JINST* **8** T07005 [[arXiv:1304.0821](https://arxiv.org/abs/1304.0821)].
- [9] B. Baptista et al., *Benchmarking TPB-coated light guides for liquid argon TPC light detection systems*, <http://www.airgas.com>.
- [10] AirGas, *Airgas liquid argon specifications*, <http://www.airgas.com>.
- [11] B. Baibussinov et al., *Free electron lifetime achievements in liquid argon imaging TPC*, *2010 JINST* **5** P03005 [[arXiv:0910.5087](https://arxiv.org/abs/0910.5087)].
- [12] WARP collaboration, R. Acciarri et al., *Effects of Nitrogen contamination in liquid Argon*, *2010 JINST* **5** P06003 [[arXiv:0804.1217](https://arxiv.org/abs/0804.1217)].
- [13] WARP collaboration, R. Acciarri et al., *Oxygen contamination in liquid argon: combined effects on ionization electron charge and scintillation light*, *2010 JINST* **5** P05003.
- [14] R. Acciarri et al., *Effects of nitrogen and oxygen contamination in liquid argon*, *Nucl. Phys. Proc. Suppl.* **197** (2009) 70.
- [15] B. Jones, C. Chiu, J. Conrad, C. Ignarra, T. Katori, et al., *A measurement of the absorption of liquid argon scintillation light by dissolved nitrogen at the part-per-million level*, *2013 JINST* **8** P07011 [*Erratum ibid.* **8** (2013) E09001] [[arXiv:1306.4605](https://arxiv.org/abs/1306.4605)].
- [16] J. Xu et al., *A study of the residual ^{39}Ar content in argon from underground sources*, [arXiv:1204.6011](https://arxiv.org/abs/1204.6011).
- [17] H.O. Back et al., *First large scale production of low radioactivity argon from underground sources*, [arXiv:1204.6024](https://arxiv.org/abs/1204.6024).
- [18] DarkSide collaboration, H. Back et al., *First commissioning of a cryogenic distillation column for low radioactivity underground argon*, [arXiv:1204.6061](https://arxiv.org/abs/1204.6061).
- [19] E. Aprile, K. Giboni and C. Rubbia, *Drifting electrons over large distances in liquid argon-methane mixtures*, *Nucl. Instrum. Meth. A* **253** (1987) 273.
- [20] H. Keller-Rudek and G.K. Moortgat, *Mpi-mainz-uv-vis spectral atlas of gaseous molecules*, www.atmosphere.mpg.de/spectral-atlas-mainz.

- [21] O. Siegmund et al., *A parallel plate imaging proportional counter with high background rejection capability*, *IEEE Trans. Nucl. Sci.* **28** (1981) 478.
- [22] T.J. Sumner et al., *Scintillating drift chambers-the nature of the emission process in Ar/CH₄*, *IEEE Trans. Nucl. Sci.* **29** (1982) 1410.
- [23] A. Curioni et al., *A regenerable filter for liquid argon purification*, *Nucl. Instrum. Meth. A* **605** (2009) 306 [[arXiv:0903.2066](https://arxiv.org/abs/0903.2066)].
- [24] B. Jones, J. VanGemert, J. Conrad and A. Pla-Dalmau, *Photodegradation mechanisms of tetraphenyl butadiene coatings for liquid argon detectors*, *2013 JINST* **8** P01013 [[arXiv:1211.7150](https://arxiv.org/abs/1211.7150)].
- [25] V. Gehman et al., *Fluorescence efficiency and visible re-emission spectrum of tetraphenyl butadiene films at extreme ultraviolet wavelengths*, *Nucl. Instrum. Meth. A* **654** (2011) 116 [[arXiv:1104.3259](https://arxiv.org/abs/1104.3259)].
- [26] V. Gehman, T. Ito, W. Griffith and S. Seibert, *Characterization of protonated and deuterated tetra-phenyl butadiene film in a polystyrene matrix*, *2013 JINST* **8** P04024 [[arXiv:1302.3210](https://arxiv.org/abs/1302.3210)].
- [27] Hamamatsu, *Hamamatsu r5912 specification sheet*, <http://www.datasheetcatalog.org/datasheet/hamamatsu/R5912.pdf>.
- [28] Stanford Research Systems, *SRS universal gas analyzer*, <http://www.thinksrs.com>.
- [29] SAES group S.p.A., private communication.

Chapter 4

Development of Wavelength-Shifting Coatings for LArTPCs

4.1 Tetraphenyl-butadiene as a wavelength shifter

Liquid argon scintillates in a wavelength range where optical detectors such as PMTs and SiPMs are insensitive. This lack of sensitivity stems from the very short absorption length of 128 nm photons in glasses, polymers and semiconductor materials. In order to make liquid argon scintillation light detectable by sensitive optical elements, a wavelength shifter can be employed. One common choice for neutrino and dark matter experiments is 1,1,4,4-tetraphenyl-butadiene (TPB), which absorbs efficiently in the vacuum ultraviolet (VUV) and emits at visible wavelengths with an emission spectrum peaked around 425 nm [231].

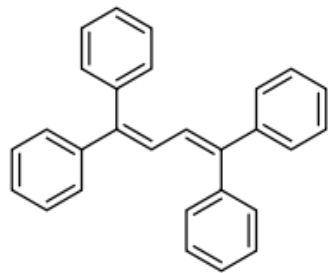


Figure 2.4.1: The chemical structure of 1,1,4,4-tetraphenyl-butadiene

The chemical structure of TPB is shown in figure 2.4.1, and in its solid form TPB is a white powder of needle-like crystals [232]. TPB coatings can be made in several ways. One common method for depositing a layer of pure TPB onto a glass or metallic substrate is evaporative coating [233]–[236]. The resulting coating has a high wavelength-shifting efficiency but is mechanically fragile. TPB also dissolves in several solvents, including toluene, chloroform and methylene chloride [237] and can be painted in solution onto surfaces by spraying [237], dip coating [238] or brushing. The addition of a polymer such as acrylic or polystyrene to the solution produces a coating which has TPB embedded in a solid matrix, leading to a more mechanically robust coating but with a lower wavelength-shifting efficiency than pure TPB.

4.2 Wavelength-shifting coatings in the MicroBooNE experiment

As described in Section 2, the MicroBooNE optical system comprises 32 8-inch PMTs behind wavelength-shifting plates and four coated light guide detectors. The TPB coatings for both types of assembly are made by dissolving TPB in toluene with either acrylic or polystyrene and brush coating the solution onto acrylic. The mixture is dried in air at room temperature leading to a coating of TPB in a polymer matrix. The plate and light guide coatings have different requirements and so are made according to different recipes to achieve the optimal characteristics.

MicroBooNE TPB plate coatings

The MicroBooNE plate coating is optimized to have the highest possible light yield in transmission mode, shown in figure 2.4.2, left. The coating is made using a 1:1 mixture of TPB in polystyrene, applied in three layers. As the coating dries, the solution becomes over-saturated with TPB, which precipitates into crystals at the surface. This gives the coating a white, rough surface. A photograph of the plate coating is shown in Figure 2.4.2, right.

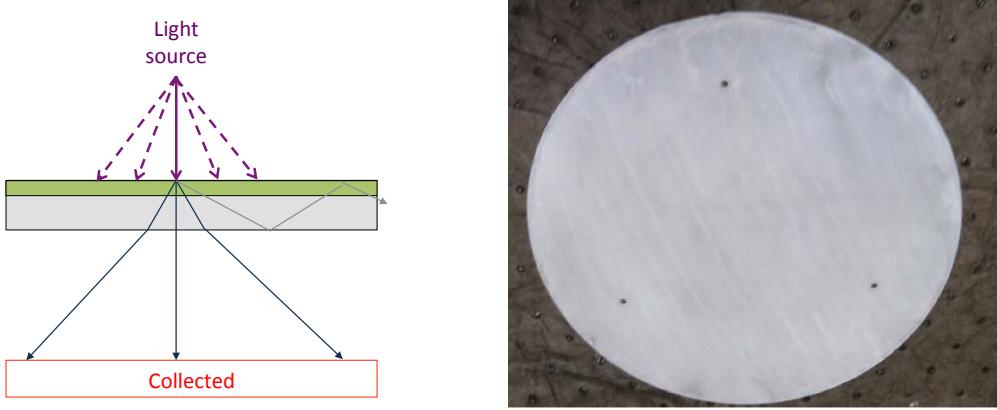


Figure 2.4.2: Left: Cartoon showing the TPB plate emission in transmission mode. Purple lines represent incident VUV photons, blue lines are emitted visible photons, and grey lines represent lost light. Right: photograph of a coated MicroBooNE plate.

Because 128 nm light does not penetrate deeply into the coating, most of the wavelength shifting occurs at the precipitated TPB surface. The emission spectrum, shown in Figure 2.4.3, is therefore very similar to that of pure TPB. This spectrum was measured using a Hitachi F-4500 fluorescence spectrophotometer with a 270 nm incident beam, selected using a grating from a xenon lamp. The spectrophotometer and lamp were calibrated using a standard rhodamine dye sample before the measurement. The region between 525 and 600 nm is omitted due to a large harmonic spectrometer artifact at twice the incident wavelength, which obscures the spectrum.

Figure 2.4.3 also shows the wavelength-dependent quantum efficiency of the 8-inch R5912 PMT. The specification which is publicly available[166] is for the non-platinum undercoated model. Hamamatsu also provided four sample quantum efficiency curves for the MicroBooNE PMTs, which are lower than that of the non-cryogenic model, but have a similar spectral shape. The mean and standard deviation of these curves is shown. The spectrum-averaged quantum efficiency for the MicroBooNE PMTs with the plate emission spectrum is calculated to be $15.3 \pm 0.8\%$ per visible photon incident on the photocathode.

In reference [171], the absolute wavelength-shifting efficiency of evaporative coatings was measured in the wavelength range 120 to 250 nm at room temperature. An efficiency of 1.2 ± 0.1 visible photons per incident UV photon was reported at 128

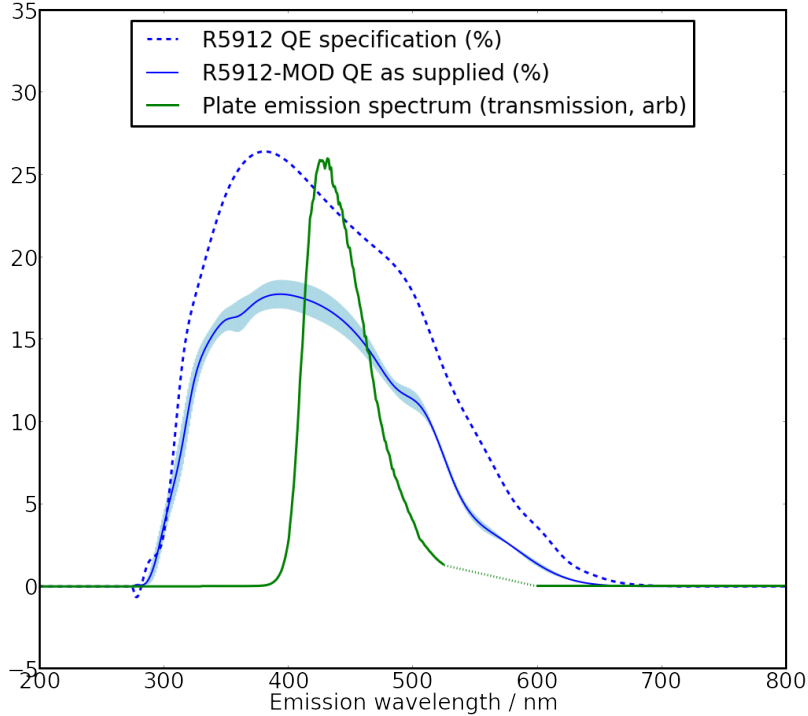


Figure 2.4.3: Measured emission spectrum of MicroBooNE plate coating overlaid on PMT quantum efficiency curves. The specification for the non-platinum undercoated PMT is from [166], and the blue band shows the mean and standard deviation of the four quantum efficiency curves available for the installed MicroBooNE PMTs.

nm. In [239], the efficiency of evaporative TPB coatings was shown to be temperature dependent, with an increase of 1.22 ± 0.14 between room temperature and 87 K. In [240], the relative efficiency of MicroBooNE coatings to evaporative coatings was measured both at room temperature using a vacuum monochromator and at 87 K in a liquid argon test stand. The plate coating was found to have an efficiency of 0.67 ± 0.07 relative to an evaporative coating of the type used in [171]. Putting these pieces of information together, we find that we expect an efficiency of 0.98 ± 0.17 emitted visible photons per incident 128 nm photon at 87 K for the plate coating.

MicroBooNE light guide coatings

In the case of light guides, the coating is optimized for maximum light output in guided mode, shown in Figure 2.4.4, left. The total light yield depends not only on the absolute wavelength-shifting efficiency of the coating, but also on the attenua-

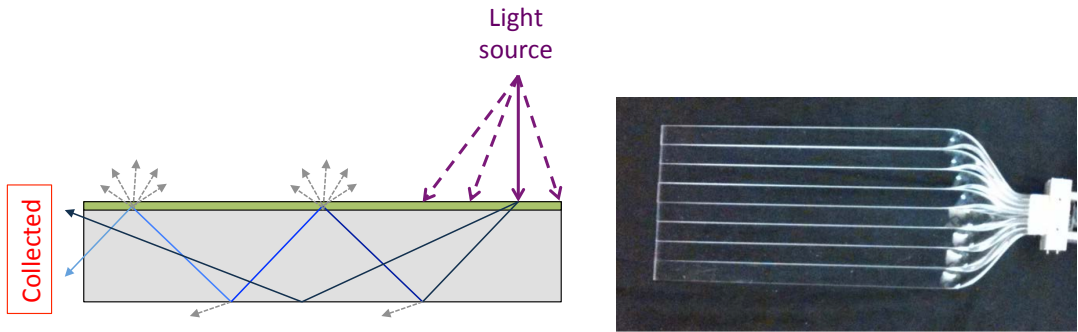


Figure 2.4.4: Left: Cartoon showing the light guide emission in guided mode. Purple lines represent incident VUV photons, blue lines are emitted visible photons, and grey lines represent lost light. Right: photograph of a coated MicroBooNE light guide.

tion of visible light as it is transmitted to the instrumented end. As such, minimal absorption and scattering at the acrylic-argon boundary is required. This optically smooth coating is composed of 33% TPB in 67% ultraviolet-transmitting acrylic by mass, with ethanol added as a surfactant, brush coated onto acrylic as a single layer. A photograph of the resulting visibly transparent coating is shown in Figure 2.4.4, right. The emission spectrum of the light guide coating was measured and is shown in Figure 2.4.5, overlaid on the quantum efficiency specification of the R7725 PMT [241]. Using the same methods already discussed, the light guide coating is found to have an efficiency of 0.25 ± 0.05 at 128 nm and 87 K. Its emission spectrum is broadened relative to pure TPB spectrum due to interactions with the polymer matrix. Sensitivity of TPB fluorescence to its microenvironment has been described in [242]–[245], and [239] reports similar spectral broadening in polystyrene substrates.

The emission spectrum of the light guide coating was studied as a function of incident wavelength and reported in [7]. Figure 2.4.6, top shows the two-dimensional excitation-emission spectrum of a short light guide section in guided mode, over the incident wavelength range 250–600 nm. The emission spectrum is approximately independent of excitation wavelength in the range 250 to 380 nm. At longer wavelengths the incident photon has insufficient energy to excite the molecule and the efficiency drops. The dip at 280 nm is present only when ethanol is added to the coating. There

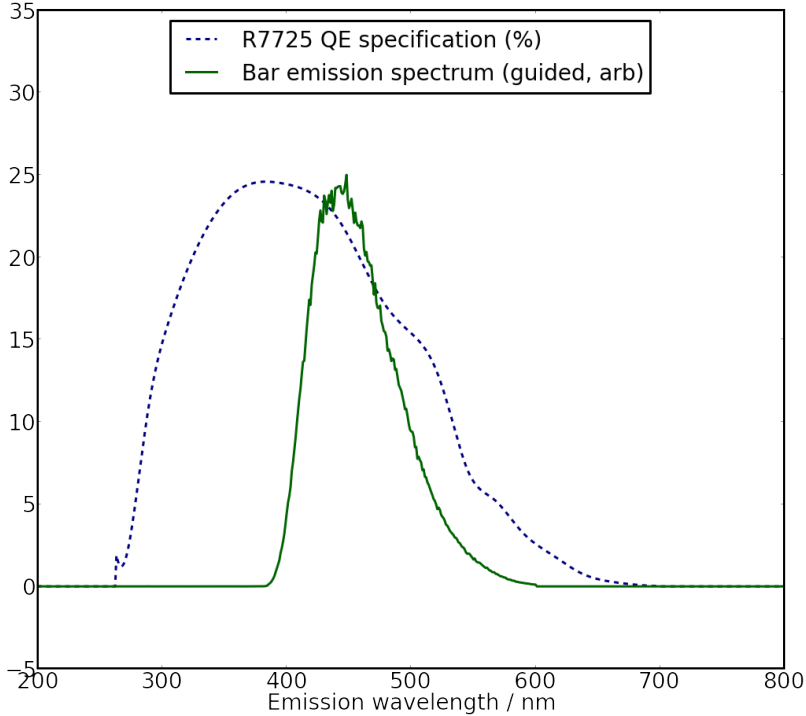


Figure 2.4.5: Measured emission spectrum of MicroBooNE light guide coating overlaid on PMT quantum efficiency curve. The specification for the non-platinum undercoated PMT is from [241].

is a significant Stokes shift between the absorption and emission spectra, although the presence of an overlap region implies that some reabsorption is to be expected during visible light transmission, even for perfectly prepared bar surfaces.

4.3 Attenuation behaviour of TPB coated light guides

Once visible light has been emitted from a TPB coating into an acrylic light guide, it must propagate to the instrumented end to be detected. The attenuation behavior was studied experimentally [7], and two unexpected results were obtained. First, the measured attenuation length was different in air and liquid argon. Second, the attenuation was not exponential in shape. These effects can be understood by considering photons propagating in the bar and experiencing surface losses. The calculation in the following note demonstrates these effects using a simplified model and was published in the peer-reviewed proceedings of the LIDINE 2013 conference as [9].

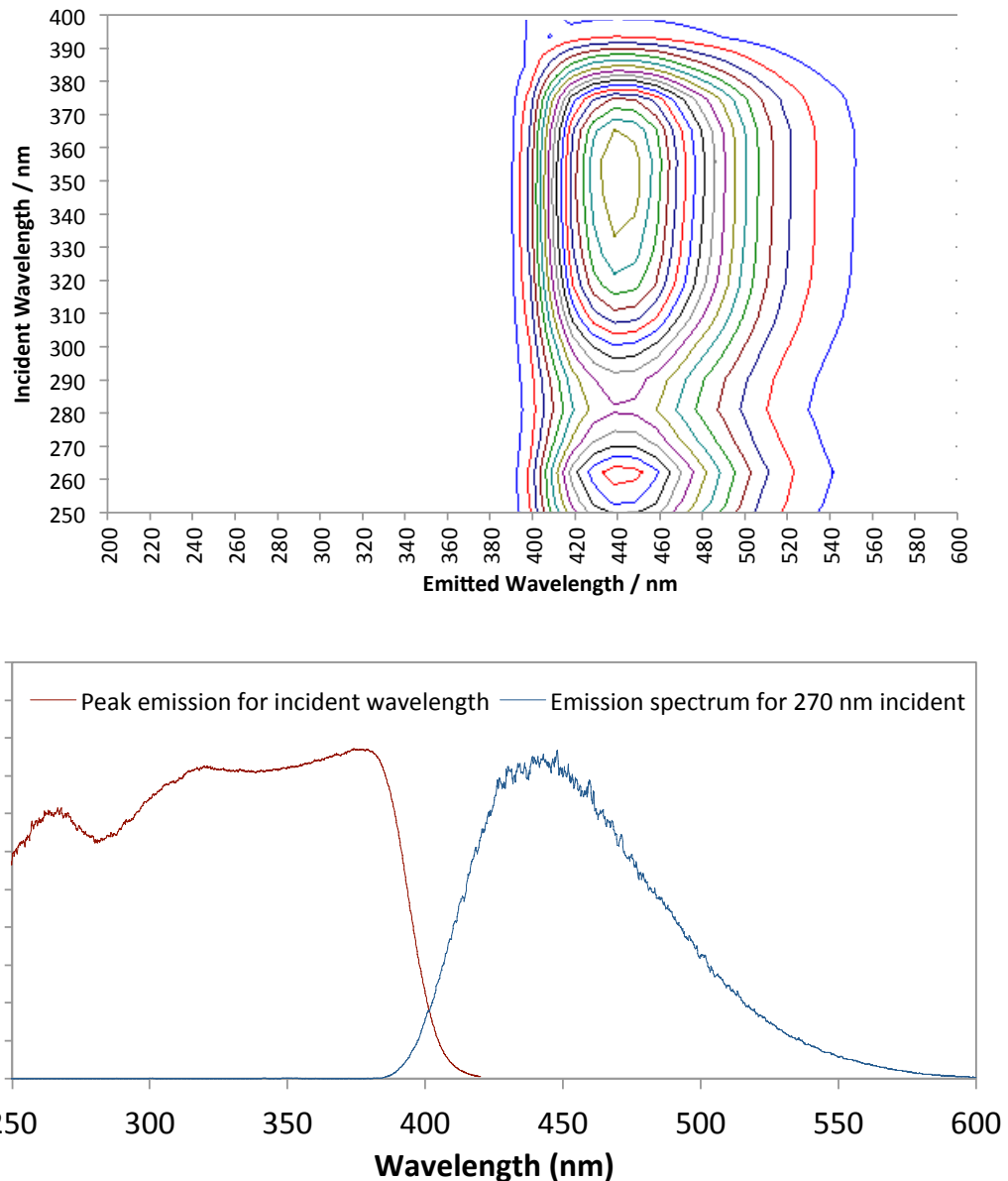


Figure 2.4.6: Top: two dimensional excitation-emission spectrum for light guide coating. Bottom: absorption (measured via emission at peak wavelength) and emission spectra for the light guide coating. These are a vertical and a horizontal slice through the top contour plot, respectively.

RECEIVED: July 22, 2013

ACCEPTED: August 31, 2013

PUBLISHED: October 28, 2013

LIGHT DETECTION IN NOBLE ELEMENTS (LIDINE 2013)
29th – 31st MAY 2013, FERMI NATIONAL ACCELERATOR LABORATORY
ILLINOIS, U.S.A.

A simulation of the optical attenuation of TPB coated light-guide detectors

B.J.P. Jones¹

*Massachusetts Institute of Technology,
77 Massachusetts Avenue, Cambridge, MA 02139, U.S.A.*

E-mail: bjpjones@mit.edu

ABSTRACT: This note is provided as a supplementary section to accompany the paper [1] which has been included in these proceedings. It describes some simple simulations which were performed in order to understand the attenuation behaviors of acrylic light-guides operated in air and argon, which were characterized in [2]. Whilst these simulations are only at the level of sophistication of a toy model, they illustrate interesting non-exponential light attenuation effects and the differences between operating light-guide based detectors in argon and air environments. We investigate the effects of surface absorption, surface roughness and wavelength dependence, and use a model tuned on the light-guide attenuation curve measured in air to make a prediction of the light-guide attenuation curve in argon. This curve is compared with data from a liquid argon test stand, and an improvement over a simple exponential model is observed.

KEYWORDS: Scintillators, scintillation and light emission processes (solid, gas and liquid scintillators); Noble liquid detectors (scintillation, ionization, double-phase); Photon detectors for UV, visible and IR photons (gas) (gas-photocathodes, solid-photocathodes)

ARXIV EPRINT: [1307.6906](https://arxiv.org/abs/1307.6906)

¹Corresponding author.

Contents

1	Introduction and motivation	1
2	Description of the ray tracing model	1
2.1	Effective absorption length from surface losses	3
2.2	Non-exponential form of attenuation curves	4
2.3	Incorporating wavelength dependent effects	4

1 Introduction and motivation

A series of tests of coated acrylic light guide detectors for future liquid argon TPC detectors have been made in both air and argon [2]. Both cast and extruded acrylic bars were tested in air, and these have different surface finishes and transverse dimensions, and hence different attenuation behaviors. In the first round of tests, only cast acrylic bars were tested in argon. During analysis of the attenuation data taken in argon and air, two unexpected features emerged. First, the attenuation length measurement obtained from the two sets of tests were not in good agreement. Second, the attenuation behavior in argon was not observed to obey a simple exponential decay.

Whilst initially these features were thought to be caused by instrumental effects in the test stands, subsequent analysis shows that these effects should be expected, to some extent. This note describes a toy simulation which illustrates the origin of both the argon vs air attenuation length discrepancy and of nonexponential attenuation. The model has a single free parameter, corresponding to the coefficient of surface absorption, which we tune using data taken in air and use to make a prediction of the attenuation curve in argon. Despite being a significant oversimplification of the real test geometry, which involves several different surfaces with different absorption coefficients, the prediction made for argon is a significant improvement over a simple exponential attenuation curve when compared with data. Future studies of coated and uncoated light-guide surface properties could be used to tune a more advanced model with stronger predictive power.

2 Description of the ray tracing model

To model the expected light attenuation behavior in acrylic light guides operated in argon and air we have performed a series of simple ray tracing simulations. In these simulations, isotropic light rays are generated, and each ray is assigned a weight determined by the attenuation processes under consideration. This weight represents the probability that a photon following this trajectory will arrive at the detection end of the light guide, where there is a coupling to a photomultiplier tube or silicon photomultiplier. The relative detected light yield is given by the sum of the weights of all the isotropic rays emitted from a wavelength shifting surface. The bar is represented by a region of

solid acrylic with refractive index 1.49, in an environment of either air with refractive index 1.0, or argon with refractive index 1.23. The critical angle for total internal reflection is given by

$$\sin\theta_c = \frac{n_{\text{environment}}}{n_{\text{acrylic}}} \quad (2.1)$$

In principle, light which impinges upon a surface at an angle larger than this will have a reflection coefficient of 1, and light at lower angles will experience a partial reflection with a calculable coefficient $R(\theta)$. In our model, light rays are emitted by the TPB coating isotropically, and for those rays emitted into the bar we calculate the angle of reflection against each set of surfaces. The number of reflections is then given by

$$N_i = \frac{1}{\tan\theta_i} \frac{L}{w_i} \quad (2.2)$$

Where L is the length of the bar, θ_i is the angle of the ray to the surface normal and w_i is the width of the bar in this direction. The index i labels the two sets of surfaces.

We can imagine three main sources of light attenuation:

1. Loss of light rays from partial reflection below θ_c
2. Absorption of light in the acrylic bulk
3. Absorption of light rays at each bounce due to an imperfect optical surface

We account for (1) by applying an attenuation factor α_1 to each ray which is below the critical total internal reflection angle, where

$$\alpha_1 = \prod_i R(\theta_i)^{N_i} \quad (2.3)$$

The factor $R(\theta)$ is the reflection coefficient expected for a light ray impinging upon an ideal surface separating two materials of different refractive indices, averaged over polarizations.

Additional corrections to this factor may be expected to occur from surface roughness, which causes small changes to the angle of incidence and reflection with each bounce, and therefore allows light rays to deviate outside the region of total internal reflection and escape. We modeled the effect of random surface deviations of between 0.01 and 0.1 radian per bounce, and found a very minimal effect upon the attenuation curves. This is because such small deviations only cause significant losses for light which is very near the critical angle, which in practice is a negligible fraction of all detectable light rays. Surface roughness on the scale of the wavelength of light requires a more in depth treatment, and has not been investigated.

Previous measurements of bulk attenuation in many commercially available acrylics at 440 nm give attenuation lengths of several meters [3]. This suggests that the 40 cm attenuation observed in our light guides is likely to be primarily due to the surface losses of factor (3). Therefore, we assume that the effects of bulk absorption are negligible compared to surface effects. This assumption could be easily relaxed if more information on the bulk or surface properties of our acrylic become available. For the purposes of this model, we set

$$\alpha_2 = 1 \quad (2.4)$$

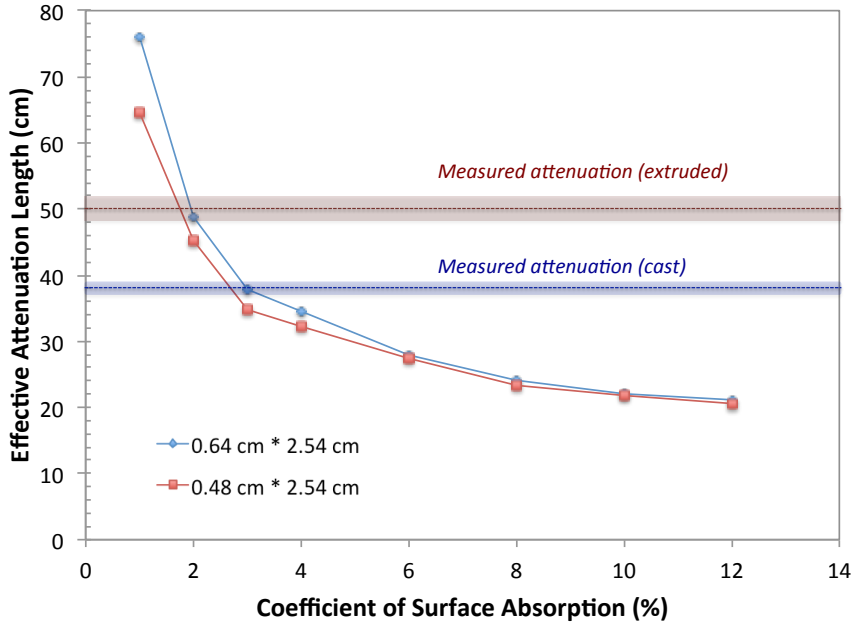


Figure 1. Calculated attenuation due to surface absorption for different light guides. Measurements from [2] are overlaid. A full description is given in the text.

Factor (3) is incorporated into our model by reducing the weight of each light ray by a constant coefficient of surface absorption, R_S for each reflection. Previous studies of acrylic light guides [4] suggest that R_S is in the few percent range. However, we expect the numerical value of R_S to depend heavily on the manufacturing process and surface finish of the particular acrylic bars used, and so we treat it as a free parameter in the model.

$$\alpha_3 = (1 - R_S)^{\sum_i N_i} \quad (2.5)$$

The total attenuated weight of each ray is then given by $\Pi_j \alpha_j$, and the total light output of the bar is given by the sum of the weights of many randomly generated isotropic light rays.

2.1 Effective absorption length from surface losses

Assuming an infinite bulk absorption length, we can calculate the effective attenuation length in the 20–50 cm region for different surface absorption coefficients. The actual attenuation length generated by surface absorptions has a dependence on the transverse bar dimensions, since a narrower bar leads to more bounces per unit length than a wider bar.

We have simulated the effective 20–50 cm attenuation length for both 0.48×2.54 cm bars and 0.64×2.54 cm bars in air for several values of the coefficient of surface absorption. The calculated attenuation lengths are shown in figure 1. If all attenuation in our light guides were from surface absorption, we expect a per-bounce absorption coefficient of around 2% for the extruded acrylic bars (which have the smaller cross section), and around 3% for cast acrylic bars (which have the larger cross section).

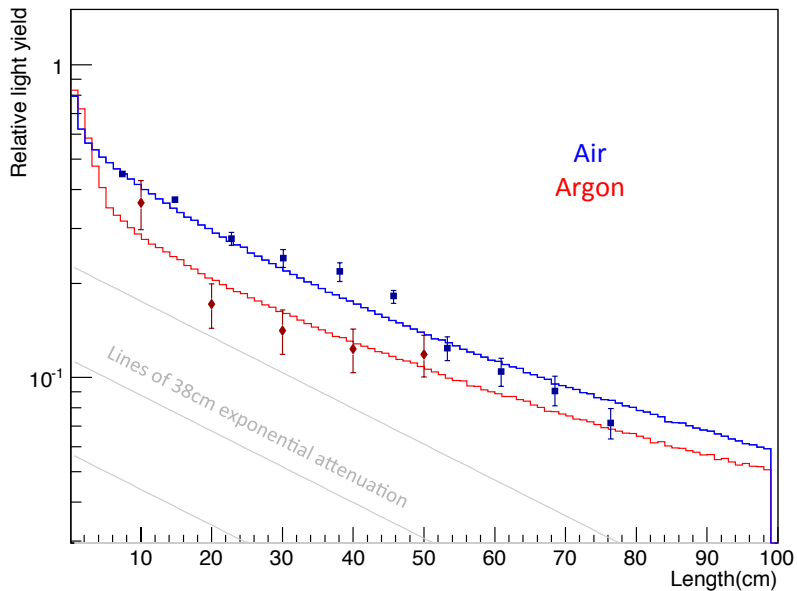


Figure 2. Calculated attenuation curves assuming identical bars operated in argon and air, with 3% surface absorption per reflection and a long bulk attenuation length. Data from [2] are overlaid.

2.2 Non-exponential form of attenuation curves

The form of the attenuation curve produced by our model is not expected to be exponential. Since both the number of surface reflections per unit length and the subcritical ray reflection coefficient depend on the angle of the ray being traced, rays at different angles are lost at different rates. Therefore the angular composition of the light beam is changed at larger distances, and the attenuation behavior has a nontrivial distance dependence. The attenuation behavior also depends on the refractive index of the operating environment, since the critical angle and subcritical ray reflection coefficients both have a refractive index dependence. Hence we expect to see different attenuation behavior in argon and air.

Assuming that the cast acrylic rods used in both the argon and air studies have identical indices of refraction and surface absorption coefficients, we can calculate the shapes of the attenuation curves given an infinite bulk attenuation length. These curves are shown, with measurements from [2] overlaid, on figure 2. On the same plot are marked lines of 38 cm exponential attenuation to highlight the nontrivial attenuation behavior. The only tunable parameter in this simulation is the per-reflection absorption coefficient, which is set to 3%, as extracted from the effective attenuation length of the cast acrylic light guides in air as described in section 2.1.

2.3 Incorporating wavelength dependent effects

Measurements of attenuation of monochromatic light at the University of Indiana indicate that TPB coated light-guide attenuation has a wavelength dependence over the TPB emission spectral range.

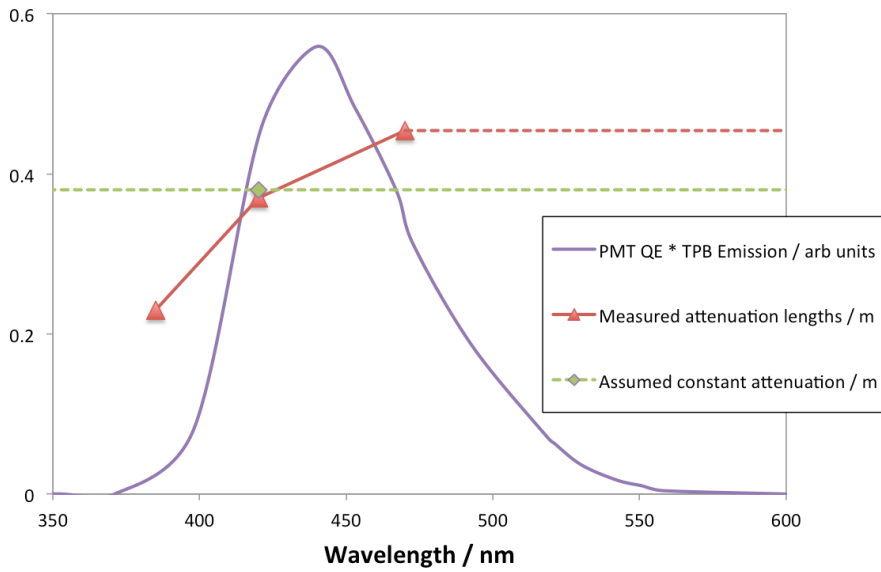


Figure 3. Measured wavelength dependence over relevant spectral range (red), compared to previously assumed constant attenuation (green). Extrapolated ranges with no data are shown as dashed lines.

The measured wavelength dependent attenuation is overlaid on a curve showing TPB emission spectrum multiplied by PMT quantum efficiency, which gives the relevant spectrum of detectable rays, in figure 3. There is a 10–20% variation over the range of interest, leading to contributions both above and below the previously assumed constant attenuation length of 38 cm. We expect this variation to produce an additional nonexponential contribution to the attenuation behavior.

Incorporating these effects into the ray tracing simulation described above, we can produce an attenuation curve with a wavelength dependent surface absorption. This curve is shown overlaid on the previously generated curve, which assumed a constant absorption coefficient, in figure 4. We see that the overall effect averaged over all detectable rays is minimal, mainly because there are both positive and negative contributions at different points in the spectral range. We have also investigated the effect of this wavelength dependence on the simple bulk attenuation model, and found its impact to be similarly minimal.

Acknowledgments

This work was supported by the National Science Foundation (PHY-1205175).

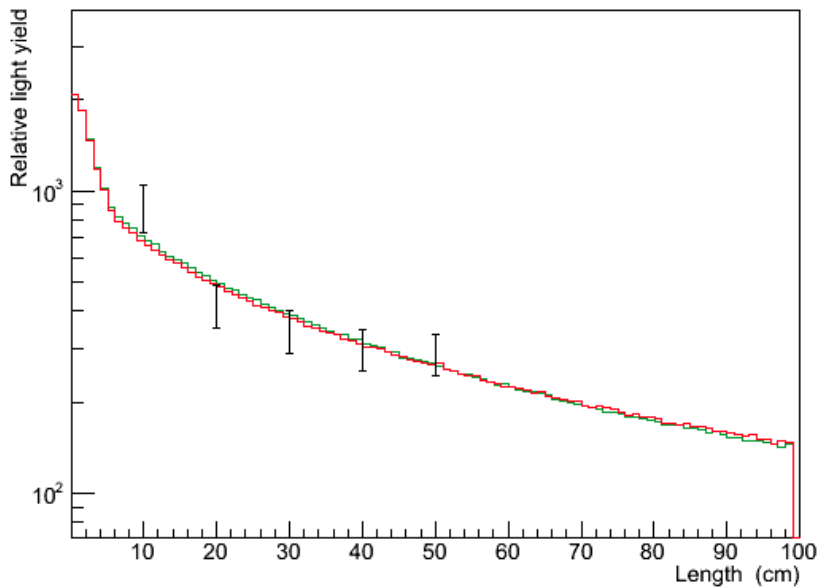


Figure 4. Nonexponential attenuation generated by wavelength dependent (red) and wavelength independent (green) ray tracing models.

References

- [1] C.M. Ignarra, *TPB-coated light guides for liquid argon TPC light detection systems*, included in the proceedings of *LIDINE Conference*, Illinois U.S.A. (2013).
- [2] B. Baptista et al., *Benchmarking TPB-coated light guides for liquid argon TPC light detection systems*, [arXiv:1210.3793](https://arxiv.org/abs/1210.3793).
- [3] N. Phan, *Acrylic Attenuation Measurements for the MiniCLEAN Dark Matter Detector*, <http://panda.unm.edu/pandaweb/undergraduate/programs/honorsThesis/NguyenPhanThesis2009.pdf>.
- [4] P. Huffman, *TPB Coated Detectors for the nEDM Experiment*, <http://tpb.lns.mit.edu/mediawiki>.

4.4 Photodegradation of TPB coatings

TPB coatings have been shown to degrade under exposure to UV light [11]. For large liquid argon detectors such as MicroBooNE and LBNE, internal components including wavelength-shifting coatings cannot be accessed for maintenance after installation. Coating degradation during installation or over long periods during normal operation could have disastrous consequences for the sensitivity of a light collection system. Understanding the mechanisms of TPB degradation and finding measures that can be taken to prevent it is therefore of great interest.

Two grades of TPB are available from Sigma Aldrich [232]. In preliminary tests, the standard-grade TPB (with a purity specification of 99%) was found to degrade in performance more rapidly than the scintillation-grade sample (with a purity specification of 99.99%) under UV exposure, suggesting that impurities in the TPB are involved in the degradation process.

In an attempt to identify the relevant impurities, samples of new and degraded TPB were studied using NMR spectroscopy [246]. Samples were prepared in a deuterated chloroform solution and underwent 1000 scans in a Bruker DMX-500 11.7 Tesla NMR spectrometer. Comparison of the ^1H -NMR spectra of standard- and scintillation- grade TPB shows an impurity which is present only in the standard-grade sample, with characteristic resonance peaks at 6.16, 7.06 and 7.12 ppm. These spectra are shown in 2.4.7. After exposure to UV light for one day, both standard- and scintillation-grade samples displayed traces of this impurity. Further study with selective excitations of the isolated impurity peaks, some of which are shown in Figure 2.4.8, demonstrated that the impurity was itself an aromatic compound, with the aromatic peaks buried under the TPB spectrum and therefore not visible in the ^1H scans. The evolution of this compound in the scintillation grade sample after UV exposure demonstrates that the photo-initiating impurity is produced when TPB is exposed to UV light, even if it is not initially present in the sample.

Since the photo-initiating product was not identifiable by its NMR signature alone, further studies were performed using gas chromatography coupled to mass spectrom-

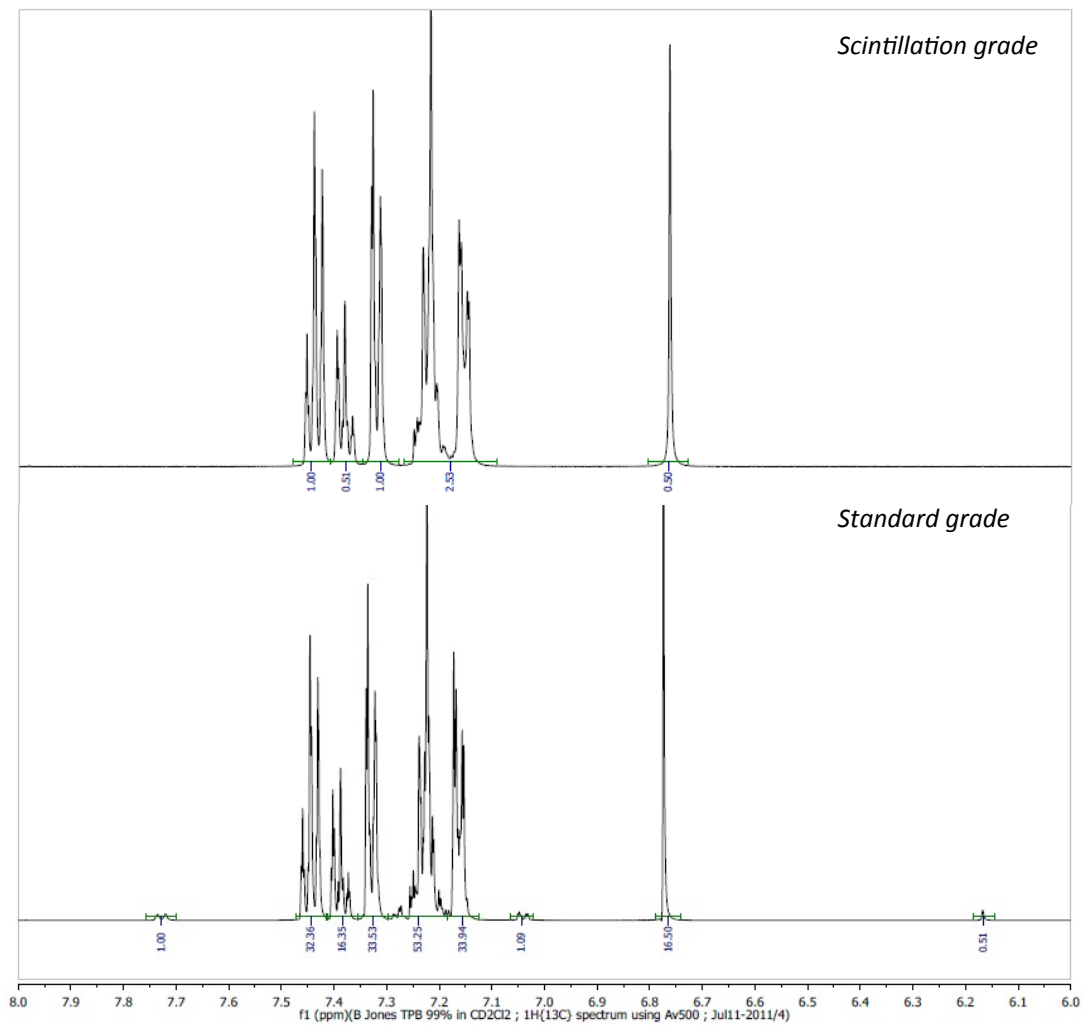


Figure 2.4.7: ^1H NMR spectra. Top: Scintillation grade TPB. Bottom: Standard-grade TPB. Impurity peaks appear at peaks at 6.16, 7.06 and 7.12 ppm.

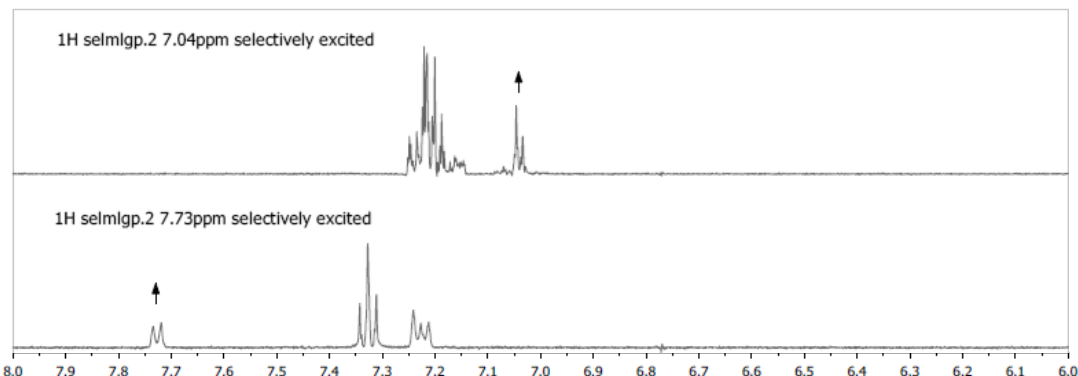


Figure 2.4.8: Selective excitation of ^1H NMR impurity peaks demonstrating the presence of hidden aromatic activity.

etry (GCMS). These measurements identified the compound as benzophenone and characterized its accumulation in TPB samples under UV exposure. Studying the benzophenone production rate led to the probable identification of the degradation process as a radical mediated photo-oxidation reaction. The addition of radical mediating dopants to TPB was shown to slow its degradation, confirming this interpretation. An improvement to the TPB light yield and a delayed degradation behavior were demonstrated using a 20% admixture of the radical mediator 4-tert-butylcatechol. These studies are described in the attached paper, which was published in the Journal of Instrumentation as [9].

This result demonstrates that the degradation mechanism is an oxidation process, so is not expected to occur inside running noble liquid detectors. Delayed degradation and enhanced initial performance were demonstrated using a radical inhibitor, showing that coatings can be made both brighter and more robust by chemical stabilization. Only two additives were tested in this work as a proof of principle. The successful demonstration of stabilization opens significant opportunities for further improvement of TPB coatings using radical inhibiting compounds.

RECEIVED: December 4, 2012

ACCEPTED: December 22, 2012

PUBLISHED: January 23, 2013

Photodegradation mechanisms of tetraphenyl butadiene coatings for liquid argon detectors

B.J.P. Jones,^{a,1} J.K. VanGemert,^b J.M. Conrad^a and A. Pla-Dalmau^b

^a*Massachusetts Institute of Technology,*

77 Massachusetts Avenue, Cambridge, MA 02139, United States of America

^b*Fermi National Accelerator Laboratory,*

PO Box 500, Batavia, IL 60510, United States of America

E-mail: bjpjones@mit.edu

ABSTRACT: We report on studies of degradation mechanisms of tetraphenyl butadiene (TPB) coatings of the type used in neutrino and dark matter liquid argon experiments. Using gas chromatography coupled to mass spectrometry we have detected the ultraviolet-blocking impurity benzophenone. We monitored the drop in performance and increase of benzophenone concentration in TPB plates with exposure to ultraviolet (UV) light, and demonstrate the correlation between these two variables. Based on the presence and initially exponential increase in the concentration of benzophenone observed, we propose that TPB degradation is a free radical-mediated photooxidation reaction, which is subsequently confirmed by displaying delayed degradation using a free radical inhibitor. Finally we show that the performance of wavelength-shifting coatings of the type envisioned for the LBNE experiment can be improved by 10-20%, with significantly delayed UV degradation, by using a 20% admixture of 4-tert-Butylcatechol.

KEYWORDS: Noble-liquid detectors (scintillation, ionization two-phase); Scintillators, scintillation and light emission processes (solid, gas and liquid scintillators); Photon detectors for UV, visible and IR photons (gas) (gas-photocathodes, solid-photocathodes)

ARXIV EPRINT: [1211.7150](https://arxiv.org/abs/1211.7150)

¹Corresponding author.

Contents

1	The use of TPB in neutrino and dark matter experiments	1
2	Degradation behavior of TPB	3
3	Identification of impurities in TPB powders with GCMS	4
3.1	Use of GCMS to identify and quantify impurities	4
3.2	Impurity GC peaks in TPB powders	5
4	Monitoring benzophenone buildup in TPB coatings	6
5	Benzophenone spiking studies, active coating thickness and discoloration	6
6	Chain termination with free radical inhibitors	8
7	Conclusions	10

1 The use of TPB in neutrino and dark matter experiments

Liquid argon is the active medium in many existing and forthcoming particle physics detectors. Examples include liquid argon time projection chambers (LArTPCs) for neutrino studies, such as the ICARUS [1], ArgoNeuT [2], MicroBooNE [3], and LBNE [4] experiments, and low-background scintillation detectors for dark matter searches such as the DEAP [5] and MiniCLEAN [6] experiments.

Being inexpensive and inert, argon makes an ideal active medium for a LArTPC, where a long free-electron lifetime must be achieved. Argon is also an excellent scintillator, producing several tens of thousands of photons per MeV deposited. Further, high-purity argon is transparent to its own scintillation light. These characteristics make argon one of the favorite active media for low-background scintillation detectors.

Many LArTPCs also take advantage of argon scintillation light, which brings several benefits above simply recording charge deposits. Light collection systems which detect the flash of light accompanying a neutrino event can be used to acquire timing information about the event with a much higher precision than is possible with charge measurements alone. This timing information is an important background rejection tool for experiments deployed in pulsed neutrino beams, and is of particular importance for surface-based detectors such as MicroBooNE and LBNE, which both plan to implement extensive light collection systems. A light collection system in a LArTPC can cover a large detector volume with a relatively small number of channels, making the formation of trigger logic more straightforward than it would be using TPC wires, which typically number in the tens of thousands. There are also opportunities to use scintillation light for event reconstruction,

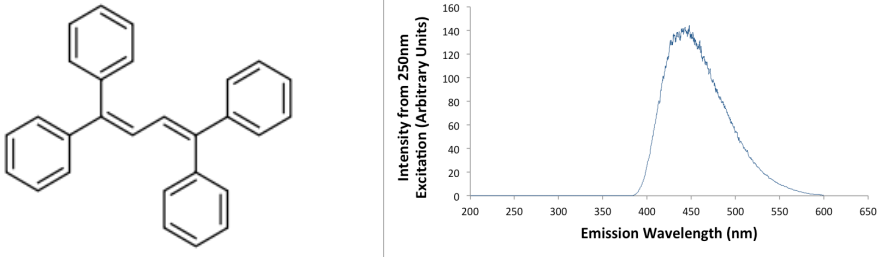


Figure 1. The chemical structure of TPB (left) and emission spectrum (right) [8].

especially given its widely reported nontrivial time structure, which is used to determine the local ionization density of keV scattering events in dark matter detectors [7].

Scintillation light in liquid argon is produced at a wavelength of 128 nm. Argon is highly transparent at this wavelength, so the light can be collected by detectors outside of the active region. However, most optical detectors, including cryogenic photomultiplier tubes (PMTs), are insensitive to 128 nm light. Tetraphenyl butadiene (TPB) is a fluorescent compound with the chemical structure shown in figure 1, which has a high absorption coefficient at 128 nm and a visible emission spectrum with a maximum around 450 nm. Since this is a good match to the peak quantum efficiency of standard cryogenic PMTs, TPB is commonly used as a wavelength shifter in liquid argon scintillation detectors. Thus, in order to make PMTs sensitive to argon scintillation light, a coating of TPB is applied either to the PMT face, as in ICARUS, or to a separate plate which sits in front of the PMT, which is the strategy favored by MicroBooNE, as well as MiniCLEAN. A lightguide-based detector which transmits TPB-shifted light to PMTs several meters from the interaction point is also being developed, for the future LBNE detector [8].

There are several ways of applying TPB coatings, including evaporative coating, dip coating and painting. Evaporative coatings of pure TPB have the highest reported efficiency at 128 nm, with 1.3 visible photons being produced for each one incident 128 nm photon [9]. These coatings are fragile, however. In order to produce a more sturdy coating, TPB is often mixed into a toluene / polystyrene solution and painted onto the surface. In this paper we consider two types of films, which are similar to the coating planned for the MicroBooNE optical system and one coating being considered for the LBNE optical system, respectively. The MicroBooNE-type coating is designed to give the highest light yield possible for a polystyrene-based coating, and uses a 1:1 TPB-to-polystyrene ratio, with 1 g of each dissolved in 50 ml of toluene which is brush coated onto acrylic plates. At this concentration, the TPB crystallizes out of solution onto the plate surface as the toluene evaporates, leading to an opaque, rough finish. This coating will be referred to as the “rough” coating. The LBNE-type coating is designed to give a smooth optical surface for application on lightguides. For this coating, a 1:2 TPB-to-polystyrene ratio is used, with 0.5 g of TPB per 50 ml of toluene. With this composition, the TPB stays in solution as the coating dries, leading to a transparent polystyrene film with TPB suspended in the polystyrene matrix. This coating will be referred to as the “smooth” coating.

A third, polystyrene-free coating was prepared for gas chromatography coupled to mass spectrometry (GCMS) studies, as polystyrene solutions were found to be damaging to the chromatogra-

phy column. This coating consists of 1g TPB per 50 ml toluene brush coated onto the plate surface. All coated plates used in this study were cut from acrylic sheets of thickness 1/8" and were of size 4 cm x 4 cm. Half a milliliter of one of the aforementioned solutions was dripped onto the plate surface and then spread and smoothed with an acid brush. All plates were dried for at least 30 minutes in a fume hood before use.

2 Degradation behavior of TPB

It has been previously reported that TPB coatings degrade when exposed to UV light, both losing efficiency [10] and turning yellow in color [11] as a function of exposure. This UV sensitivity is an undesirable feature in light collection systems for large experiments, since it leads to more difficult installation procedures and comes with the risk of in situ degradation during the lifetime of the detector. Gaining understanding of and seeking strategies to prevent such degradation is therefore of significant interest in the field of argon scintillation detection, and may be of value to a wider community of TPB users.

In this paper, we measure the wavelength-shifting performance of TPB coatings with a Hitachi F-4500 fluorescence spectrophotometer, using an incident wavelength of 270 nm and measuring the emitted intensity at the TPB emission peak. This strategy prevents backgrounds from direct reflections or ambient light from contributing significantly to the measured efficiency. Using a reference plate kept in the dark we can correct for spectrophotometer drift, which leads to changes of a few percent in the reported efficiency over the duration of any study. In the following sections, the term "performance" will denote the corrected peak emission intensity; "relative performance" will refer to the ratio of the corrected intensity after degradation to an initial corrected intensity.

Two grades of TPB are commercially available: scintillation grade, which has a purity specification of >99.9%, and standard grade, which has a purity specification of >99%. It has been noted before that the standard grade product is much more susceptible to discoloration, turning bright yellow after a few hours of exposure to sunlight. The scintillation grade product does not turn bright yellow, rather an off-white color, and has a longer characteristic degradation time.

The relative efficiency of plates produced using the "rough" coating with standard and scintillation grade TPB as a function of exposure to sunlight is shown in figure 2. Both curves are normalized to have their initial efficiency be equal to 1, and each data point is corrected for spectrophotometer drift using the measured efficiency of the reference plate.

The intensity of the sunlight naturally varied over the course of the study, so the scale on the horizontal axis should not be taken to be linear. However by using sunlight we can ensure that both plates received the same exposure, which has proved difficult to implement with lamp-based studies, where slight changes to the geometry of the setup or stability of the lamp are difficult to control. In this study, the standard grade plate is seen to degrade significantly faster than the scintillation grade plate. The observation that the standard grade sample both loses performance and experiences discoloration at a higher rate than the scintillation grade sample is suggestive that both of these features are a consequence of initial impurities present in the sample.

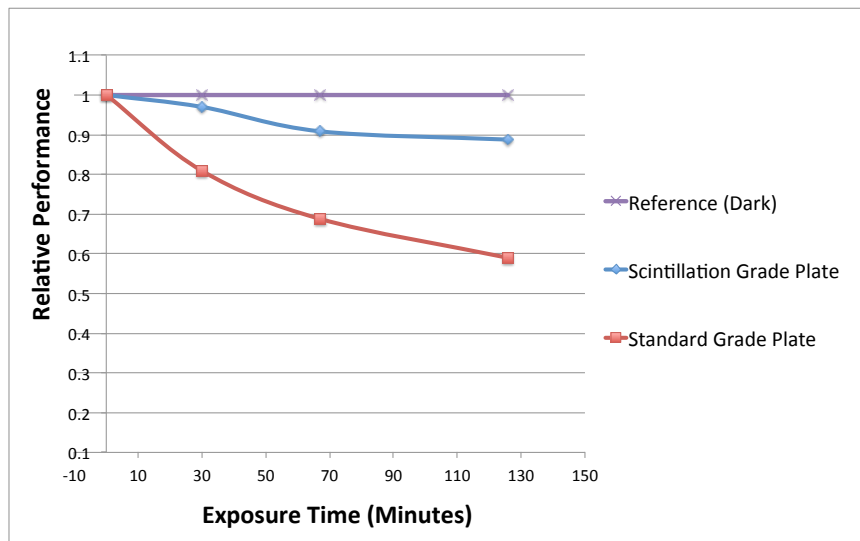


Figure 2. Degradation of standard and scintillation grade TPB plates with “rough” coating, as a function of exposure to direct sunlight.

3 Identification of impurities in TPB powders with GCMS

3.1 Use of GCMS to identify and quantify impurities

We used an Agilent 7820A Gas Chromatograph with a 5975 Mass Selective Detector to identify and quantify impurities in TPB powders and coatings. This process involves two stages. First, different components of the sample are separated by their diffusion time in a gas chromatography (GC) column. Then, each chromatographically separated component is fed into a mass spectrometer (MS). The mass spectrum can be compared to a database of known spectra to elucidate a likely identity for the component.

After making preliminary mass-scan runs which identified impurities present in the sample, a custom GC method was created to accurately quantify their concentrations. This method incorporated a temperature gradient of 120°C to 250°C, increasing at a rate of 5°C per minute. This profile was chosen due to the different retention times exhibited by benzophenone and TPB. Benzophenone would elute with the solvent at higher initial temperatures, whereas TPB would remain in the chromatography column at lower oven temperatures. The method was also set to maintain a constant flow rather than a constant pressure. All injections were manual with a 5 μ l syringe which was rinsed with solvent between each injection.

The MS was set to acquire data in selective ion mode because of the sensitivity needed to detect the low benzophenone levels. Each ion group was set to monitor the four most common ions for each compound. Due the small size of the benzophenone peak compared to the TPB signal, in most cases a manual integration was required.

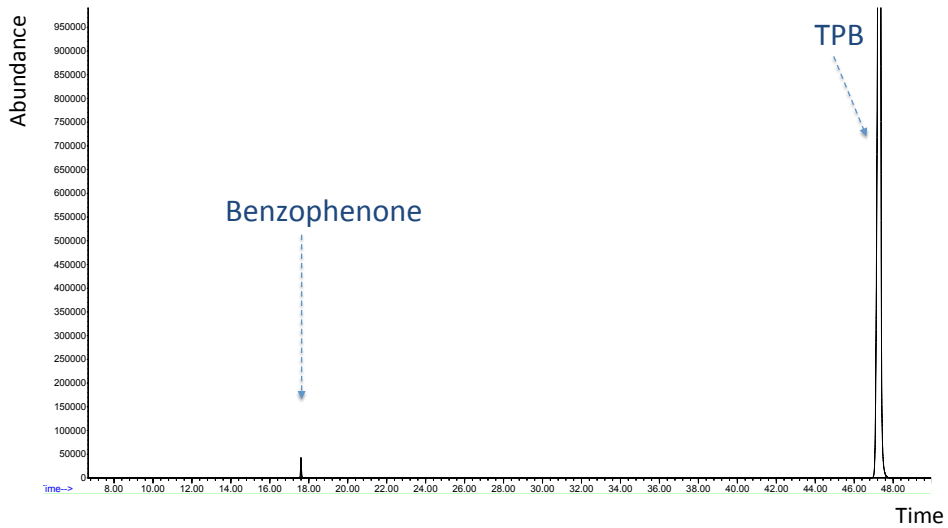


Figure 3. Chromatograph of unexposed standard grade TPB in toluene.

Sample	Benzophenone / TPB Peak Ratio
Scintillation Grade (Unexposed, White)	4.13×10^{-6}
Standard Grade (Unexposed, White)	8.43×10^{-6}
Standard Grade (Exposed, Yellow)	1.82×10^{-5}

Table 1. Benzophenone-to-TPB peak area ratios in powder TPB samples.

3.2 Impurity GC peaks in TPB powders

An example chromatograph for standard grade TPB dissolved in toluene is shown in figure 3. The large peak at 47 minutes is identified as TPB. The peak at around 17.5 minutes is identified with a high confidence level as benzophenone, which is a commercially available UV blocker and photoinitiator [12] and a likely photooxidation product of TPB. The benzophenone concentration was measured by comparing the benzophenone to TPB peak areas in three powder samples: unexposed standard grade, unexposed scintillation grade, and standard grade TPB exposed to UV light to the point of yellowing. The benzophenone-to-TPB peak ratio from each are reported in table 1

When TPB is dissolved in toluene and applied as a plate coating, the benzophenone concentration is seen to increase significantly, with the benzophenone-to-TPB peak ratio increasing from order $10^{-4}\%$ in power samples, to around 0.01% in samples taken from freshly coated plates. This may be a result of the necessary light exposure involved in painting and drying the plate, or of a reaction which occurs in solution. The initial benzophenone concentration varies between batches of plates, but sets made from a common solution and subjected to a common storage procedure appear to have consistent benzophenone concentrations to within 20%.

4 Monitoring benzophenone buildup in TPB coatings

The results of section 3 are suggestive that the buildup of the benzophenone occurs when TPB is exposed to UV light. To test this hypothesis we prepared many identical plates with scintillation grade TPB coatings. TPB was dissolved in toluene to make a solution of concentration 0.02 g/ml, and each plate received one coating made from 0.5 ml of this solution. As mentioned in section 1, polystyrene was omitted for this test because it was found that polystyrene solutions would not give consistent results and eventually lead to clogging of the GC column.

Each plate was stored in the dark, wrapped in a mylar sheet, until we were ready to begin exposing it to UV light. Immediately after removing each plate from the dark we measured the initial wavelength shifting efficiency using the spectrophotometer procedure described in section 2. It was then exposed to a 365 nm UV lamp for a number of hours, and then the efficiency was measured again. The ratio of these two measurements tells us the extent of the plate degradation. Next, the plate was placed into a small bath of 20 ml toluene and sonicated for five minutes in order to dissolve off the TPB coating. Two μl the solution was injected into the spectrometer and the benzophenone / TPB peak ratio was recorded. Using many plates we monitor the benzophenone content and plate performance as a function of exposure time, which is shown in figure 4. Since several plates were under the lamp simultaneously, the geometry of the setup means that not all got exactly equal exposure. This leads to some uncertainty in the total integrated UV exposure, which is evident in the horizontal scatter observed in the data points of figure 4. Plotting benzophenone content against plate performance loss bypasses this issue and yields a very clear correlation, as is shown in figure 5. We assign a constant error of 7% in absolute performance to the spectrophotometer measurements, which is determined by the spread of efficiencies measured for the unexposed reference plate, and 10% to the benzophenone / TPB peak ratio, which is the approximate spread observed in repeated measurements of the same solution.

5 Benzophenone spiking studies, active coating thickness and discoloration

We have observed the accumulation of sub-percent levels of benzophenone in TPB coatings under exposure to UV light. Benzophenone is a commercially available UV blocker and photoinitiator, so it is tempting to attribute the loss of performance of TPB coatings to the partial absorption of incident light by the accumulated benzophenone, preventing it from being absorbed and re-emitted by TPB.

In order to test the UV-blocking properties of benzophenone built up within the TPB layer, we prepared “smooth” plates spiked with different benzophenone concentrations and looked for a change in performance relative to unspiked plates. In order to ensure that we were not misled by natural plate-to-plate variations, we acquired high statistics by preparing four plates at each concentration and measured the performance of each plate at four different locations on its surface. The results of this study are shown in figure 6.

We note first that up to a benzophenone concentration of around 10% by weight, no significant loss of performance is observed, except for a few outlying points which seem to indicate a tendency for a less uniform TPB distribution within the coating when benzophenone is added. Only when there is twice as much benzophenone as TPB do we see the levels of degradation observed in UV exposure studies.

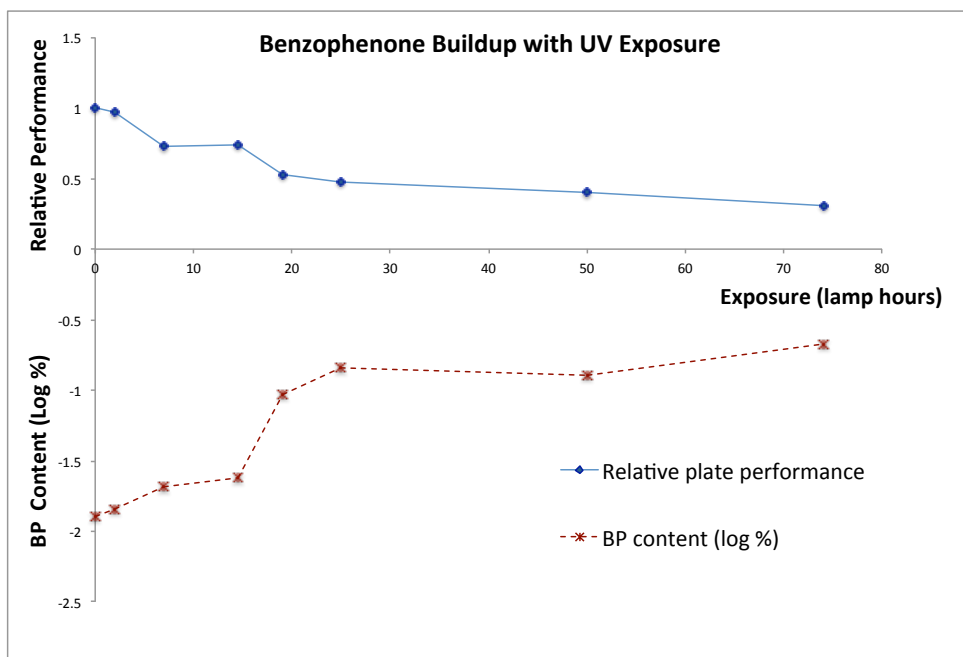


Figure 4. Degradation of plate performance and accumulation of benzophenone with exposure time.

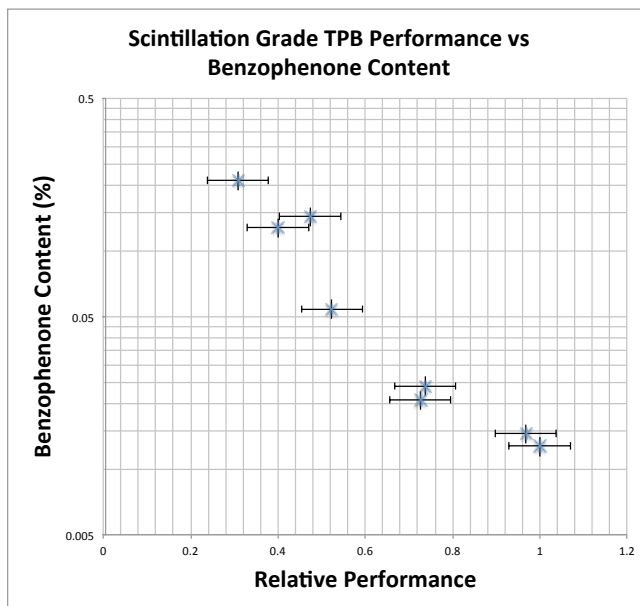


Figure 5. Performance vs benzophenone content (note log scale).

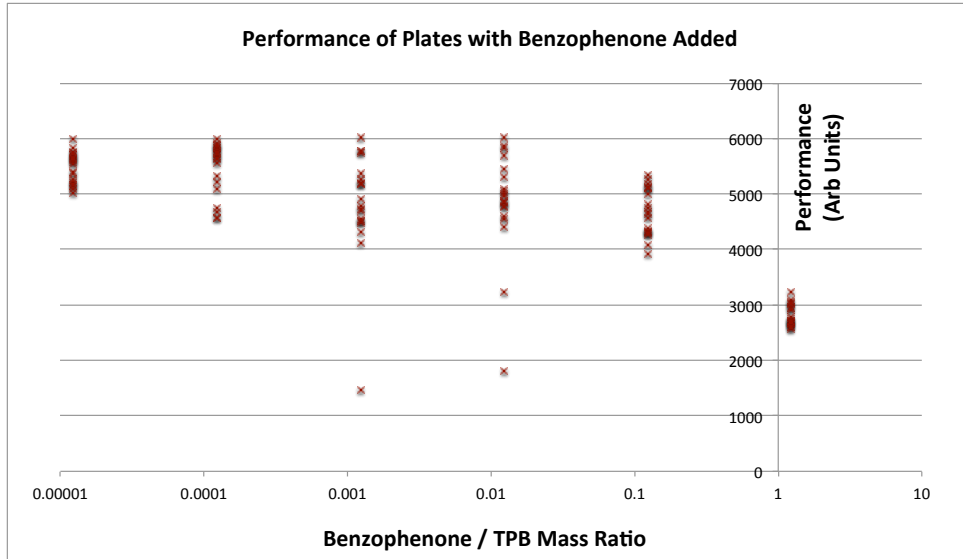


Figure 6. Performance of Benzophenone Spiked Plates.

In TPB-coated plates, only the very top layer of the coating under study is optically active, with all UV light being absorbed in a thin surface layer. In this case, the local benzophenone density at the plate surface would be expected to be much higher than the global benzophenone concentration across the entire coating, since it has received a higher UV light exposure. This produces an effective UV-blocking film of benzophenone which prevents the underlying TPB from receiving the incident light.

This type of skin effect is common in polymer photodegradation [13], and is to be expected in TPB, especially in light of recent studies which demonstrate that the efficiency of evaporative coatings is independent of their thickness [14].

Our spiking results suggest that the skin layer of degraded plates must have a composition of almost 100% benzophenone, and from this fact and the known density of polystyrene we can estimate the thickness of the optically active TPB layer to be of the order 100 nm, from a total coating thickness of order 100 μm .

We also note an increased tendency for plates made with added benzophenone to turn yellow in color under light exposure. A photograph showing two similarly degraded plates, prepared with and without added benzophenone, is shown in figure 7. We speculate that this effect may be due to the buildup of benzophenone derivatives, many of which are known to be both yellow in color and strongly UV-blocking [15].

6 Chain termination with free radical inhibitors

The amount of benzophenone accumulation displayed in figure 4 is initially approximately exponential as a function of light exposure. This is suggestive of a free radical-mediated chain reaction, which is a common mechanism of light-induced degradation, often encountered in polymer chemistry. [16]. Several compounds exist which can be used to terminate such chain reactions

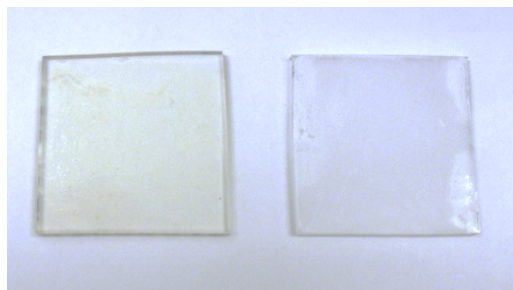


Figure 7. Similarly degraded plates with (left) and without (right) added benzophenone.

prematurely, and thus prevent the light-generated free radicals from causing further degradation. To test whether this degradation is indeed a free radical-mediated photooxidation, and to see if it is possible to stabilize the coating, we investigated two such chain termination compounds: 3,5-di-tert-butyl-4-hydroxytoluene (BHT) and 4-tert-Butylcatechol (BC).

For both “rough” and “smooth” coatings, BHT was found to produce a less uniform coating with regions of high and low TPB density. For this reason, it was difficult to extract consistent results from coatings with BHT admixtures. We are continuing to investigate methods of improving the coating quality of BHT / TPB mixtures.

BC admixtures did produce a homogeneous coating. We even observed a slight tendency towards more TPB remaining suspended in the polystyrene matrix rather than crystalizing on the surface for the “rough” plates.

We investigated plates with BC / TPB ratios between 0.1 ppm and 200% by weight, and a stabilizing effect was observed for mass ratios above 1% BC / TPB. After establishing the relevant concentration range, we prepared many plates with mass ratios between 1 and 200% and monitored their degradation over a few-hour period of simultaneous exposure to direct sunlight using the previously discussed spectrophotometer procedure. Figure 8 shows the absolute efficiencies of plates prepared at various concentrations, as a function of exposure time. At each concentration point we used two identical, separately prepared plates, to illustrate the spread in coating performance. The plates used were made with the “smooth” coating. The results show that the addition of around 20% of BC appears not only to improve the initial performance of the coating, but also to slow its degradation. This is a confirmation that we are indeed seeing a free radical-mediated reaction.

We tested that this effect is repeatable by preparing many plates with 0% and 20% BC, in both the “rough” and “smooth” styles, and monitoring their performance as a function of sunlight exposure. The data for this study are shown in figure 9. We note that the “smooth” plates reliably see a 10-20% improvement in initial light yield and an extended degradation time, such that after 200 minutes of exposure, the stabilized coatings are ~200% as efficient at the nonstabilized coatings.

The “rough” plates are not improved. This appears to be due to the fact that less TPB crystallizes onto the surface when BC is added, with more remaining suspended in the polystyrene layer. It may be possible to turn this effect into an overall improvement for the “rough” plates also, by increasing the quantity of TPB in the mixture to restore the surface density to its value when no BC is added. We plan to investigate this possibility in the near future. Since the surface layer is responsible for most of the wavelength-shifting capability of the “rough” plates, and most of the BC remains in the polystyrene matrix, we see little effect upon the coating lifetime for this sample.

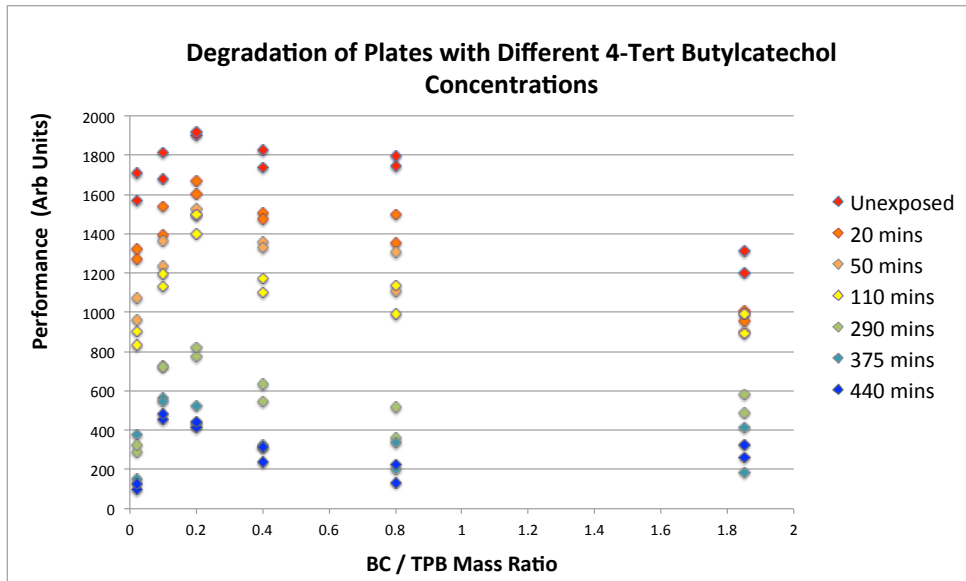


Figure 8. Degradation of plates with different BC / TPB mass ratios.

7 Conclusions

We have identified benzophenone as a compound produced in TPB films which are exposed to ultraviolet light. Since benzophenone is a known ultraviolet blocker and photoinitiator [12], it seems likely that its presence is intimately related to the performance degradation observed in TPB coatings. Using GCMS and fluorescence measurements we have found a strong correlation between benzophenone concentration and performance loss in TPB coatings with various UV exposures.

By preparing plates with benzophenone / TPB mixtures we have shown that if benzophenone is the primary cause of performance loss, it must be accumulated within a thin, optically active surface layer of the coating. This type of skin effect is common in photochemistry [13] and is supported by the results of other groups who have studied TPB films of varying thicknesses [14].

The previously reported coating discoloration [11] also appears to be related to the presence of benzophenone, as plates spiked with additional benzophenone are observed to turn significantly more yellow than TPB-only plates under exposure to similar light levels.

The initially exponential buildup of benzophenone under light exposure is suggestive of a free radical-mediated TPB photooxidation reaction, which was tested by exposing plates with an admixture of the free radical inhibitor 4-tert-Butylcatechol. The delay in degradation provided by BC confirms that TPB degradation is a free radical-mediated reaction.

An admixture of 20% BC by weight leads to an initial improvement of the coating efficiency by 10-20% and a delayed fluorescence degradation such that after 200 minutes of sunlight exposure, the BC-protected coating is more than 200% as efficient as the unprotected coating. A program to

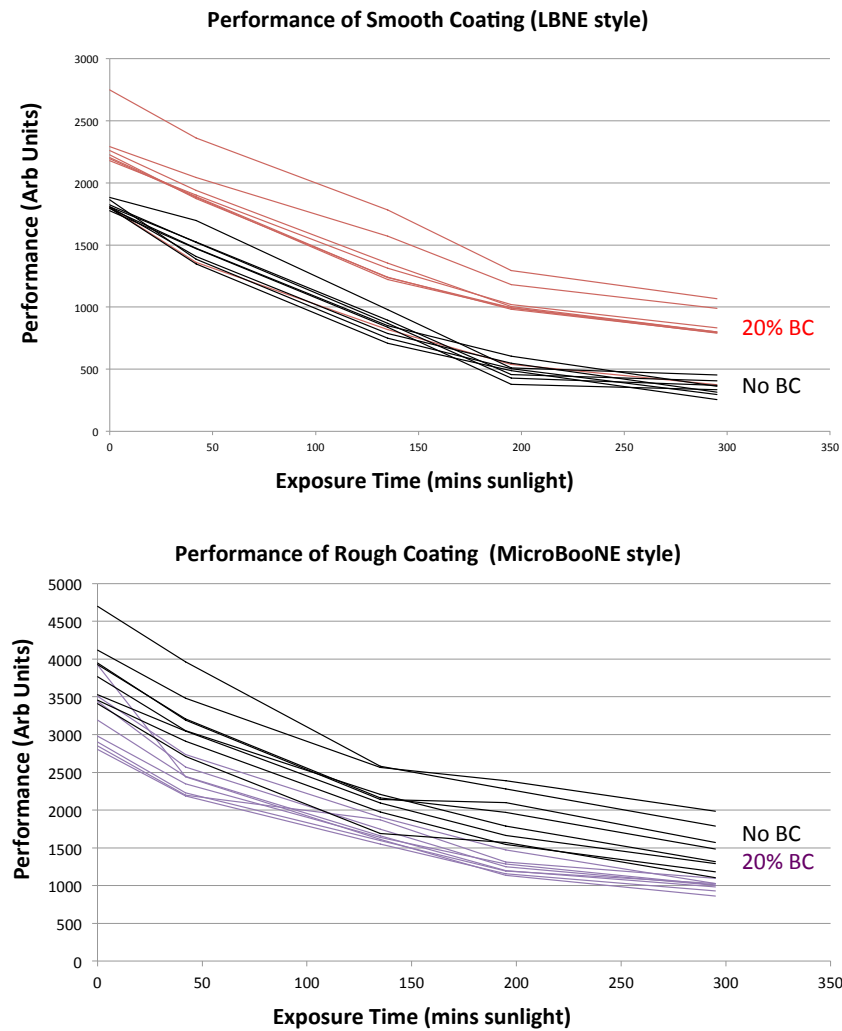


Figure 9. Study of 20% vs 0% BC plates, with both the "rough" and "smooth" style coating.

study other stabilizing compounds is underway. It is possible that other free radical inhibitors may be found which can improve the lifetime of TPB coatings even more significantly.

Acknowledgments

We would like to thank Christie Chiu for her help in performing preliminary studies related to this paper. The authors thank the National Science Foundation (NSF-PHY-084784) and Department Of Energy (DE-FG02-91ER40661). This work was supported by the Fermi National Accelerator Laboratory, which is operated by the Fermi Research Alliance, LLC under Contract No. De-AC02-07CH11359 with the United States Department of Energy.

References

- [1] ICARUS collaboration, A. Menegolli, *ICARUS and status of liquid argon technology*, *J. Phys. Conf. Ser.* **375** (2012) 042057.
- [2] ARGO-NEUT collaboration, O. Palamara, *Neutrino Detection in the ArgoNeuT LAr TPC*, [arXiv:1110.3070](https://arxiv.org/abs/1110.3070).
- [3] B.J.P. Jones, *The Status of the MicroBooNE Experiment*, *PoS(EPS-HEP2011)* **436** (2011) [[arXiv:1110.1678](https://arxiv.org/abs/1110.1678)].
- [4] LBNE collaboration, T. Akiri et al., *The 2010 Interim Report of the Long-Baseline Neutrino Experiment Collaboration Physics Working Groups*, [arXiv:1110.6249](https://arxiv.org/abs/1110.6249).
- [5] DEAP collaboration, M. Boulay, *DEAP-3600 Dark Matter Search at SNOLAB*, *J. Phys. Conf. Ser.* **375** (2012) 012027 [[arXiv:1203.0604](https://arxiv.org/abs/1203.0604)].
- [6] MINICLEAN collaboration, K. Rielage, *Status and prospects of the MiniCLEAN dark matter experiment*, *AIP Conf. Proc.* **1441** (2012) 518.
- [7] P. Kryczynski, *Pulse Shape Discrimination in liquid argon and its implications for Dark Matter searches using depleted argon*, *Acta Phys. Polon. B* **43** (2012) 1509 [[arXiv:1210.1019](https://arxiv.org/abs/1210.1019)].
- [8] B. Baptista, L. Bugel, C. Chiu, J. Conrad, C. Ignarra, et al., *Benchmarking TPB-coated Light Guides for Liquid Argon TPC Light Detection Systems*, [arXiv:1210.3793](https://arxiv.org/abs/1210.3793).
- [9] V. Gehman, S. Seibert, K. Rielage, A. Hime, Y. Sun, et al., *Fluorescence Efficiency and Visible Re-emission Spectrum of Tetraphenyl Butadiene Films at Extreme Ultraviolet Wavelengths*, *Nucl. Instrum. Meth. A* **654** (2011) 116 [[arXiv:1104.3259](https://arxiv.org/abs/1104.3259)].
- [10] C. Chiu, C. Ignarra, L. Bugel, H. Chen, J. Conrad, et al., *Environmental Effects on TPB Wavelength-Shifting Coatings*, *2012 JINST* **7** P07007 [[arXiv:1204.5762](https://arxiv.org/abs/1204.5762)].
- [11] R. Jerry, L. Winslow, L. Bugel and J. Conrad, *A Study of the Fluorescence Response of Tetraphenyl-Butadiene*, [arXiv:1001.4214](https://arxiv.org/abs/1001.4214).
- [12] M. Baril et al., *Iarc monographs on the evaluation of carcinogenic risks to humans - benzophenone*, World Health Organization (1977).
- [13] N. Grassie and G. Scott, *Polymer Degradation Stabilisation*. Press Syndicate of University of Cambridge (1985).
- [14] R. Francini et al., *Studies of thin film tpb coatings*, October, 2012, private communication.
- [15] Sigma-Aldrich, *Materials safety data sheets: products 92841, 59647, 413151, h36206*.
- [16] H.R. Alcock, F.W. Lampe and J.E. Mark, *Contemporary Polymer Chemistry*, Prentice Hall (2003).

Chapter 5

Surge Protection Systems for LArTPCs

5.1 Drift field and HV supply in MicroBooNE

A strong electric field must be applied across the active volume of a LArTPC to drift ionization charge to the sensitive readout plane. The design field strength of the MicroBooNE detector is 500 V/cm. Since the full drift length from cathode to anode wires in MicroBooNE is 2.56 m, a total potential difference of 128 kV must be applied.

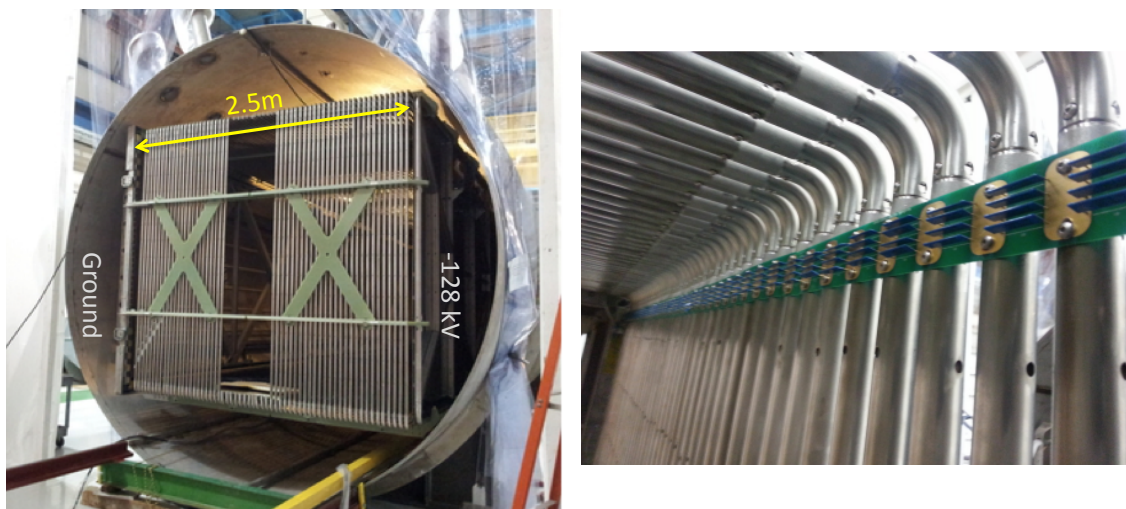


Figure 2.5.1: Left: The MicroBooNE TPC as installed in the cryostat. Right: the resistor boards of the MicroBooNE field cage potential divider.

To protect the sensitive electronics at anode wires, a negative voltage is supplied to the cathode rather than a positive one to the anode to create this potential difference. A photograph of the MicroBooNE TPC highlighting the anode and cathode is shown in Figure 2.5.1, left.

High voltage for MicroBooNE is supplied by a Glassman LX150N12 HV supply, via a current-limiting resistor and ripple filter immersed in transformer oil and 25 feet of Dielectric Sciences 2134 cable. A feedthrough based on the design used by ICARUS [93] penetrates the cryostat at a flange in the downstream end of the detector. The feedthrough is jacketed by 1 inch of ultra-high molecular weight polyethylene and then a grounded outer shield of stainless steel. Inside the cryostat, a spring-loaded tip on the feedthrough couples into a receptacle on the cathode. The exposed polyethylene insulation between the feedthrough tip and the outer shield has rectangular grooves cut into it to impede the evolution of streamer breakdowns.

Field-shaping rings create a uniform electric field in the x direction between the cathode and anode. MicroBooNE has 64 field-shaping rings, and a 2 kV potential difference is maintained between each ring using a resistive potential divider. The resistors of the potential divider in the original MicroBooNE design are 1 G Ω Ohmite SlimMox 104E resistors, which are applied in sets of four in parallel to provide a ring-to-ring resistance of 250 M Ω . The potential divider is shown installed on the field cage in Figure 2.5.1, right.

5.2 Detector robustness under dielectric breakdown

The breakdown strength of liquid argon was first measured in 1942 [247], and at higher precision in 1960 [248], using spherical electrodes with separation of up to 100 μm . Spark breakdowns were reported at field strengths of around 1 MV/cm, with demonstrated dependencies on electrode geometry and surface preparation. This reference value was used in the design of the MicroBooNE TPC, with cathode and field cage geometries optimized to avoid regions of high field strength.

The measurements of [248] were made using argon of 99.95% purity, with 0.05%

contamination by residual gases from industrial distillation. More recent investigations using ultra-pure TPC-quality argon, with part-per-billion contamination levels, have demonstrated dielectric breakdowns at field strengths as low as 40 kV/cm [249]–[251]. These studies were made after the construction of the MicroBooNE TPC was largely complete, and led to concerns about the robustness of the detector in the event of a spark discharge.

A specific failure mode in the event of a discharge was identified. If a spark were to form between the cathode or a field cage ring and the cryostat, the conducting spark path would allow charge to drain from that element, bringing it to a voltage near ground. The adjacent field cage elements would remain charged for an amount of time dictated by the resistive and capacitive network of the TPC, demonstrated by electrical simulations to be of order 0.1-1 s [252]. These simulations also showed that voltages as high as 90 kV could be held across one set of field cage resistors in the worst cases. The resistors, rated to 10 kV in air, may then fail. This failure mode is discussed in more detail in [14], which is reproduced in Section 5.3.

In order to establish the true failure voltage of the SlimMox resistors, an open-air liquid argon test stand with a prototype MicroBooNE HV feedthrough was used to supply a voltage across a populated MicroBooNE resistor board. The board was mounted using copper contacts to the inside of a sample cage submerged in liquid argon, shown in Figure 2.5.2, right. The top electrode was in contact with the HV feedthrough tip, and the lower electrode grounded to the stainless steel cryostat. A DC voltage was supplied by a Glassman LX150N12 power supply, increasing in 2 kV steps from 0 to breakdown. The current drawn was measured using the current monitoring probes on the supply. The resistors functioned linearly up to the breakdown voltage, as shown Figure 2.5.2, left. When they could no longer withstand the applied voltage the resistors failed violently with a loud, bright spark. The failure caused two of the resistors to shatter, as shown in Figure 2.5.2, right.

Using this setup, the failure voltages of a high statistics sample of SlimMox resistors were measured, and published in [13]. Figure 2.5.3 shows the resulting distribution of failure voltages. The lowest failure observed was at 30 kV, and the mean

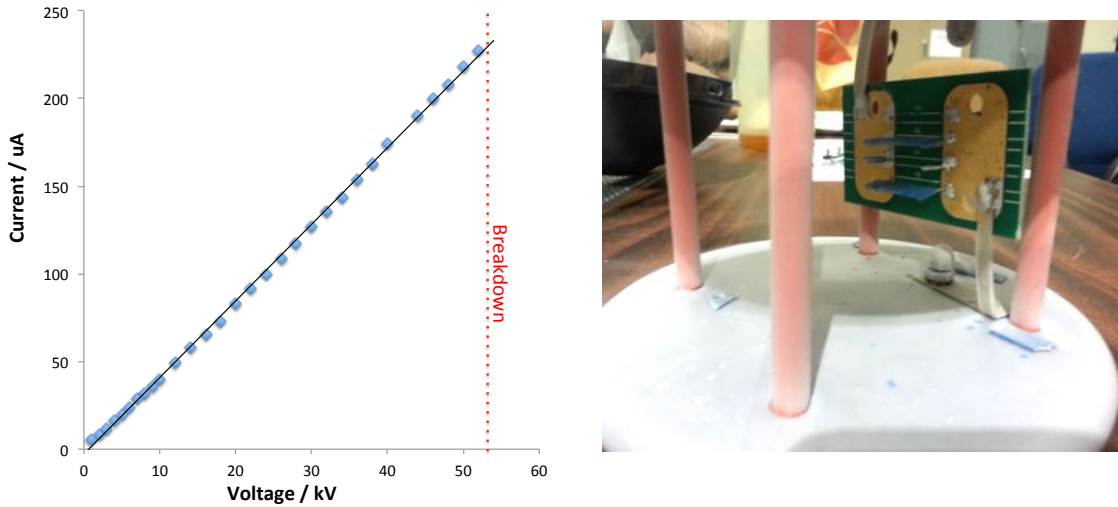


Figure 2.5.2: Left: The current drawn by the SlimMox resistors as HV was applied. Right: Sample cage with resistor test board after resistor failure at 52 kV. Blue debris are shattered parts of the resistor.

was 67.58 kV, both below the expected transient voltages in a MicroBooNE spark discharge.

Several proposals were made to solve this problem and for redundancy, two solutions were implemented. First, the resistors in the most vulnerable locations nearest the cathode were replaced with sets of two parallel Metallux 969.23 ($500\text{ M}\Omega$) resistors, which are rated to a higher voltage of 48 kV. Eight of these resistors were tested in the liquid argon breakdown test stand and found to be robust up to the full detector design voltage of 128 kV. The second proposal was the implementation of a surge protection network on the MicroBooNE TPC, which is described in the following section.

5.3 Surge protection for LArTPC detectors

The MicroBooNE surge protection system was proposed in order to circumvent the resistor failure problem described in section 5.2. The design principle is to apply devices with a suitably nonlinear resistance connected in parallel with the field cage resistors to clamp over-voltages in the event of a spark discharge. This does not

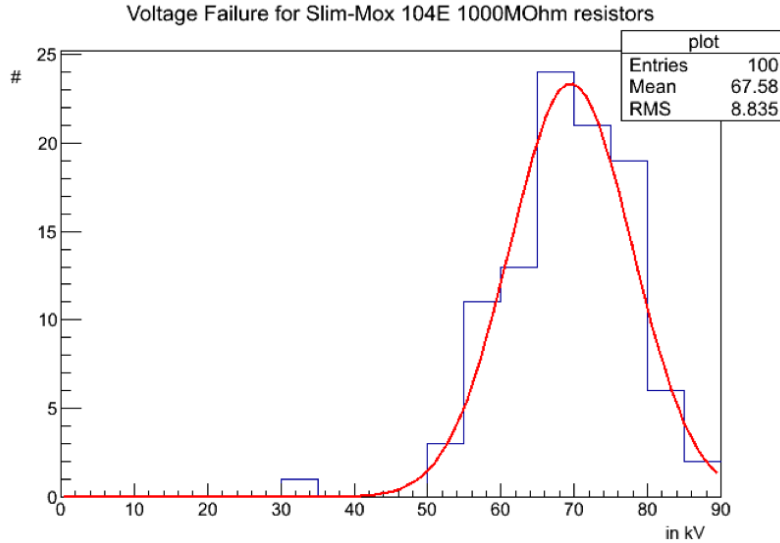


Figure 2.5.3: Distribution of failure voltages of SlimMox resistors, reproduced from [13]

interfere with TPC operation during normal running, but it prevents large voltages from evolving across vulnerable components during a discharge.

In the following paper, published in the Journal of Instrumentation as [14], a wide range of tests of high voltage gas discharge tubes and varistors were made, demonstrating their suitability for use in liquid argon TPC detectors. Then in section 5.4, tests of a surge protection network on the MicroBooNE TPC are described, which demonstrate the clamping action of varistor-based surge protection in every tested discharge scenario.

Following this work, surge protection systems have been deployed in the MicroBooNE [114] and LArIAT [253] experiments and are being included as standard in the designs of future LArTPC detectors including SBND [15].

RECEIVED: June 19, 2014

ACCEPTED: July 22, 2014

PUBLISHED: September 2, 2014

Testing of high voltage surge protection devices for use in liquid argon TPC detectors

J. Asaadi,^a J.M. Conrad,^b S. Gollapinni,^c B.J.P. Jones,^{b,1} H. Jostlein,^d J.M. St. John,^e T. Strauss,^f S. Wolbers^d and J. Zennamo^g

^a*Syracuse University,
900 South Crouse Ave, Syracuse, NY 13244, U.S.A.*

^b*Massachusetts Institute of Technology,
77 Massachusetts Avenue, Cambridge, MA 02139, U.S.A.*

^c*Kansas State University,
Manhattan, KS 66506, U.S.A.*

^d*Fermi National Accelerator Laboratory,
Batavia, IL 60510, U.S.A.*

^e*University of Cincinnati,
2600 Clifton Ave, Cincinnati, OH 45220, U.S.A.*

^f*University of Bern,
Albert Einstein Center, LHEP, Sidlerstrasse 5, CH-3012 Bern, Switzerland*

^g*University of Chicago, Enrico Fermi Institute,
5801 S Ellis Ave, Chicago, IL 60637, U.S.A.*

E-mail: bjpjones@mit.edu

ABSTRACT: In this paper we demonstrate the capability of high voltage varistors and gas discharge tube arrestors for use as surge protection devices in liquid argon time projection chamber detectors. The insulating and clamping behavior of each type of device is characterized in air (room temperature), and liquid argon (90 K), and their robustness under high voltage and high energy surges in cryogenic conditions is verified. The protection of vulnerable components in liquid argon during a 150 kV high voltage discharge is also demonstrated. Each device is tested for argon contamination and light emission effects, and both are constrained to levels where no significant impact upon liquid argon time projection chamber functionality is expected. Both devices investigated are shown to be suitable for HV surge protection applications in cryogenic detectors.

KEYWORDS: Voltage distributions; Noble liquid detectors (scintillation, ionization, double-phase); Cryogenic detectors

¹Corresponding Author.

Contents

1	Introduction	1
2	Devices under test	4
3	Behaviour under cryogenic conditions	6
4	Robustness under repeated surges in liquid argon	10
5	Practical considerations for use in LArTPCs	14
5.1	Purity considerations	14
5.2	Light emission	17
6	Conclusions	18

1 Introduction

Large liquid argon time projection chambers (LArTPCs) are of great importance to the field of experimental neutrino physics [1–5]. The increasing scale of such detectors is motivated by the need to collect a large sample of neutrino interactions, often at a distance from a pulsed neutrino beam. Liquid argon TPCs for direct dark matter detection [6–10] are also increasing in scale, a large fiducial volume being required to explore the parameter space of small dark matter interaction cross sections which the next generation of such experiments intends to probe.

To provide a strong enough electric field for electron drift over a large distance to readout wires near ground, a high voltage must be supplied to the cathode of the TPC. To increase the drift length of a liquid argon TPC whilst maintaining a fixed electric field strength, the high voltage supplied must increase proportionally. For the present generation of large LArTPCs, voltages of order 100 kV are required in order to provide a constant 500 V/cm electric field for approximately two meters. To ensure uniformity, this field is usually shaped by a series of field cage rings which are connected by resistors, thus creating a voltage divider. This network is shown schematically in figure 1, top left.

The need for larger LArTPC detectors with higher applied voltages has led to new studies of the dielectric strength of liquid argon [11–13]. In contrast to the commonly used reference value of 1.4 MV/cm from ref. [14], which was measured using only moderately pure argon, recent investigations have shown that the dielectric strength of argon at LArTPC purity with sub-ppb concentrations of oxygen and water may be much lower than anticipated, with ref. [12] reporting breakdowns at 40 kV/cm. In addition to argon purity, the breakdown voltage of liquid argon also depends upon electrode geometry, surface finish and accumulated space charge in ways which are not well understood at the present time. In addition to implementing a LArTPC detector design

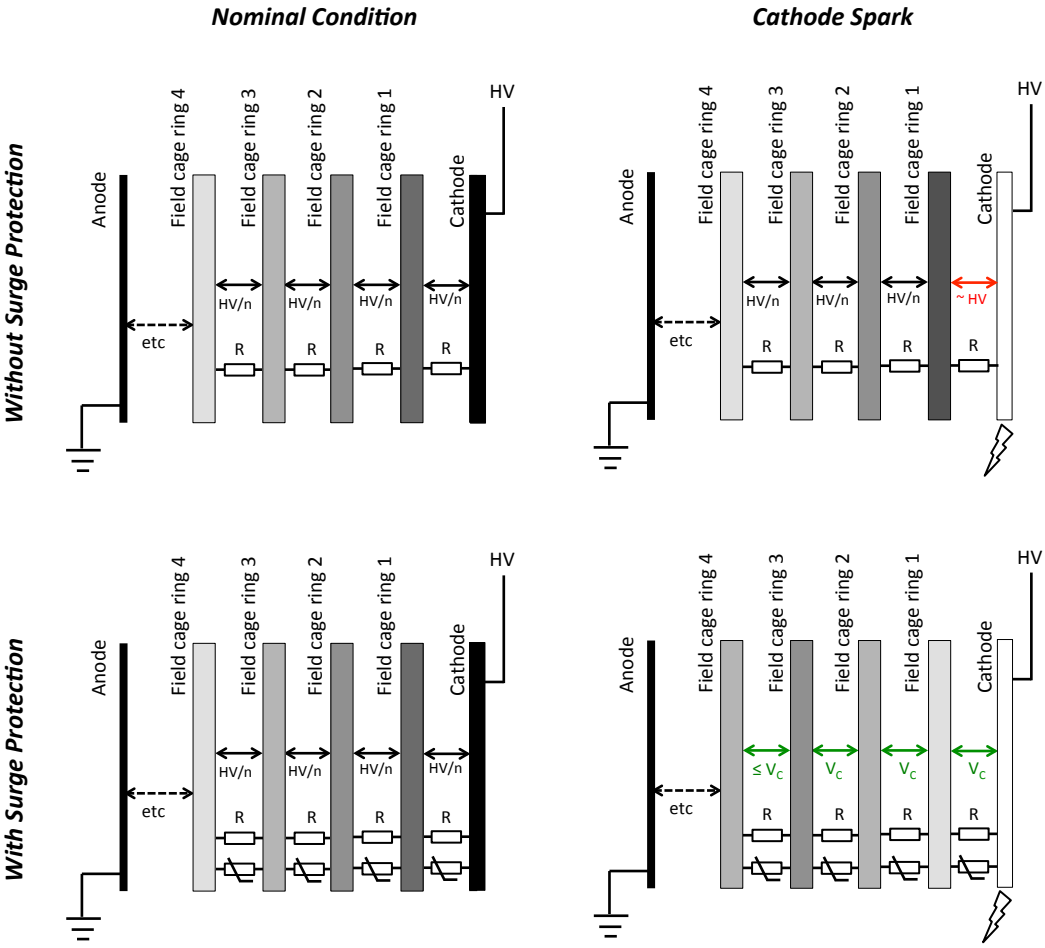


Figure 1. A cartoon showing the behavior of the field cage potential divider in nominal (left) and fault (right) conditions, without (top) and with (bottom) surge protection. Both with and without surge protection, in nominal running the applied high voltage is divided uniformly between the n field cage rings. In the case of a spark from the cathode, a large transient over-voltage may exist for elements near the spark location, which can take a long time to disperse. The scale of the over-voltage is determined by the field cage capacitances, with the full experiment HV being the worst case (shown). With surge protection applied, the largest transient which can evolve is limited by the clamping voltage of the device. The exact voltages evolved in each case depend on the details of the capacitances and geometry of the field cage.

which minimizes the likelihood of internal HV discharges occurring, it is also prudent to take steps to protect components which are vulnerable to damage in the event of an unexpected high voltage discharge.

High voltage breakdowns across the liquid argon volume can cause serious damage to electrical components in a TPC detector. Components which may be at risk include not only those which are directly in the spark path, but also those which experience large potential differences some time after the spark has dissipated, due to transient over-voltages in the field cage. For a large liquid argon TPC like MicroBooNE or LBNE, typical capacitances between elements of the field

cage will be of order $0.1 - 1 \text{ nF}$, whereas the resistances between some elements in the field cage network are of order $0.1 - 1 \text{ G}\Omega$. This suggests that the relaxation time of the system after a high-voltage discharge may be of order $0.1 - 1 \text{ s}$. During this time, a significant fraction of the full high voltage of the experiment can be held between elements which would ordinarily only experience a moderate potential difference. An over-voltage in case of a discharge arises due to the distribution of interelectrode capacitances given by the geometry of the electrode (cathode-field cage-cryostat) system. The field cage voltage divider without and with surge protection is illustrated schematically in figure 1.

One method of protecting electrically sensitive components from large transient over-voltages is the application of a surge arrestor. A surge arrestor is a device which is insulating at low voltages, but allows a current to flow if a critical voltage is exceeded. This prevents large potential differences from being developed across a vulnerable component by allowing charge to be redistributed within the system more quickly than is allowed by the intrinsic resistances. Commercially available surge protectors include varistors [15] and gas discharge tubes (GDTs) [16], both of which are used widely in various industrial applications. The commercially available surge arrestors at the time of writing have not been rated for use at liquid argon temperatures and none have been previously used in a running LArTPC detector.

In this paper we report on tests of high voltage GDTs and varistors for the protection of vulnerable components in the event of HV discharges in LArTPCs. The specific application which initiated this investigation is the protection of field cage resistors for the MicroBooNE detector. The requirements for this application are given below. The derivation of these requirements based on the MicroBooNE TPC geometry and electrical properties, as well as the experimental testing performed to verify these properties, are outside the scope of this paper and will be reported in a future publication [17]. Our goal is to demonstrate that both GDTs and varistors continue to function well in a cryogenic environment and do not have detrimental effects on key aspects of LArTPC operation, and as such are appropriate for both this specific application, and more general use cases in cryogenic TPC detectors. The requirements for a surge protection device suitable for the MicroBooNE detector are:

- The device must have a significantly higher resistance than the field cage resistances of $250 \text{ M}\Omega$ at the nominal operating voltage of 2 kV .
- The device must clamp the over-voltage that evolves during a fault condition to less than the voltage which can damage the field cage resistors in liquid argon, determined experimentally to be 30 kV [33].
- The device must be able to survive repeated discharges of the system, which are estimated to deposit at most 2 J of energy per device
- The device must function in cryogenic temperatures and in the dielectric environment of LArTPC purity liquid argon.
- The device must not damage the argon purity in the detector
- The device must not emit a sufficient light to interfere with the optical systems of the experiment in the nominal running condition

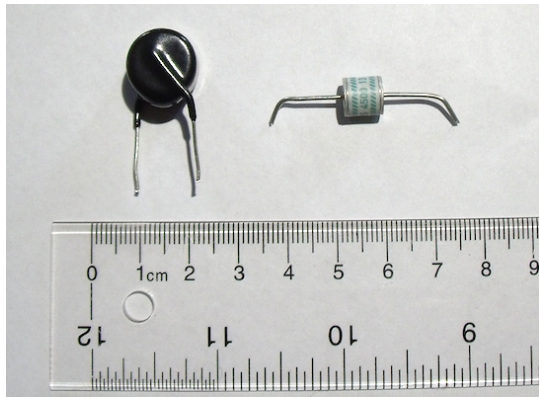


Figure 2. Photograph of the devices under test. Left: Panasonic ERZ-V14D182 varistor. Right: EPCOS A71-H45X GDT

Section 2 gives a brief discussion of the devices under test. In section 3, we demonstrate the functionality of GDTs and varistors in cryogenic environments and investigate how the insulating and clamping properties are altered in a liquid argon environment. In section 4 we show how devices degrade under repeated surges when immersed in liquid argon and demonstrate their robustness in the expected surge conditions in a large LArTPC. In section 5 we investigate the effects of the devices on argon purity and the ambient photon background. Finally in section 6 we present our conclusions and briefly describe the surge protection solution implemented in the MicroBooNE detector.

2 Devices under test

Varistors

Varistors, also known as “metal oxide varistors” (MOVs) and “zinc oxide nonlinear resistors” (ZNRs), are commercially available surge protection devices, which use a pressed zinc oxide ceramic held between two electrodes. Often the device is also encapsulated in a coating of epoxy, plastic or glass for electrical insulation. The matrix of zinc oxide grains behaves as a large network of p–n semiconductor junctions. This network produces a highly nonlinear I–V characteristic, with larger voltages giving lower effective resistances. An example I–V curve is shown in figure 3, left. The varistor offers protection to sensitive components when it is applied in parallel with them, by allowing a large current to flow when there is an over-voltage. This prevents large potential differences from developing over the vulnerable component, with the maximum voltage which can be developed being “clamped” at a lower value than in the unprotected circuit. The voltage at which clamping occurs depends upon the available current, but the highly nonlinear I–V characteristic means the clamping voltage varies little over many orders of magnitude of applied currents. In the literature and data sheets, the clamping or varistor voltage is reported as the applied voltage for which a specified current can flow, though the exact reference current varies from source to source. For the purposes of this paper, we will define the clamping voltage as the applied voltage when

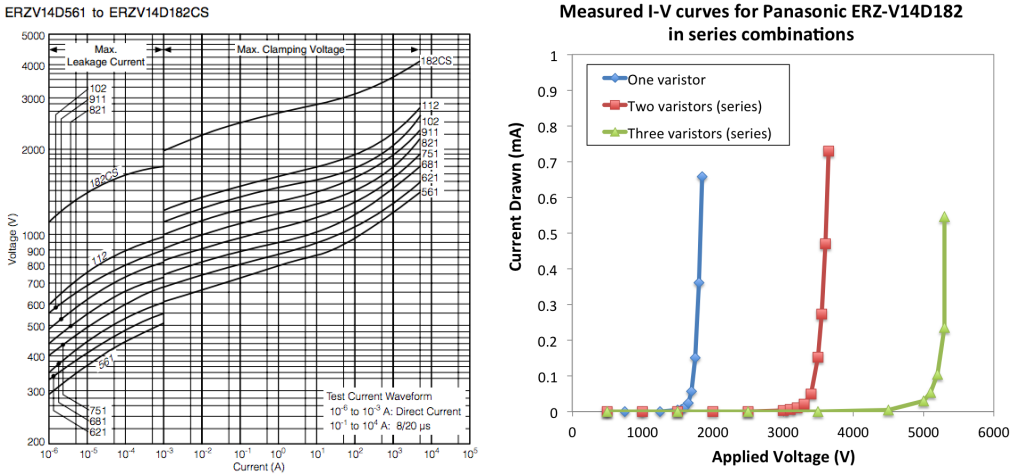


Figure 3. Left: I-V characteristic for the Panasonic ERZ range of varistors, from ref. [15]. Right: measured I–V characteristic of series combinations of Panasonic ERZ-V14D182 varistors in air, shown on a linear scale to demonstrate additivity of clamping voltages. The clamping voltage scales by a factor of N for N varistors in series.

0.5 mA of current can flow. For more information on the physics and functionality of varistors, see ref. [18].

Commercially available varistors of the appropriate size for mounting on a MicroBooNE-scale TPC field cage span clamping voltages from 6 to 1800 V. Since this voltage range is below the required 2 kV, no single device appears to be appropriate for field cage protection, where the nominal applied voltage 2 kV must be held with low current leakage. This is a commonly encountered situation in the field of surge protection, and can be solved by applying N devices in series [19]. The applied voltage is then shared approximately equally between devices, effectively increasing the clamping voltage by a factor of N . Even if there are small mismatches between the I–V characteristics of the individual units, the smoothly varying nature of the I–V curve ensures that a stable voltage sharing is achieved for any series combination. The measured I–V characteristic for a single varistor and sets of two and three in series are shown in figure 3, right.

By adjusting the varistor grain size, device dimensions and dopant composition, different clamping voltages and energy tolerances can be achieved. The device we investigate in this paper (figure 2, left) is the Panasonic ERZ-V14D182 [15], whose I–V curve is shown on the left hand side of figure 3. This device has a clamping voltage of 1800 V, a maximum surge energy rating of 510 J for an industry standard 8/20 μ s pulse, and is rated for the temperature range –40 to +85 C. Two or three devices in series can provide an appropriate clamping behavior for the MicroBooNE application.

Gas Discharge Tubes (GDTs)

Gas discharge tube arrestors, or GDTs, are commercially available surge protection devices which consist of a small volume of gas inside a ceramic housing, in contact with two electrodes. In the event of an over-voltage, a spark forms between the electrodes which allows a large current to flow.

Current continues to flow until the voltage across the device drops below the extinction voltage. The amount of charge which flows across the device before extinction occurs depends on the available current feeding the discharge. At the spark voltage, GDTs undergo a discontinuous transition from the resistive to conductive state, causing the device to act as a crowbar. This transition, and the eventual extinction, may not always occur at exactly the same voltage with repeated pulses. This means that unlike varistors, GDTs do not have a smooth and well defined I–V characteristic.

By changing the device geometry, and gas composition and pressure, different spark-over voltages can be achieved. For the application described above, we require a GDT with a DC breakdown voltage above 2 kV, but below 30 kV. The device we investigate in this paper (figure 2, right) is the EPCOS A71-H45X [20], which has a DC spark-over voltage of 4500 V, an insulation resistance specification of $> 10 \text{ G}\Omega$, a current rating of 2.5 kA for an industry standard 8/20 μs pulse, and a temperature rating of -40 to $+90^\circ\text{C}$. Extinction occurs at around 500 V warm and cold. Devices with both higher and lower DC spark-over voltages are available. For the model chosen, a single unit can provide the appropriate clamping behaviour for the MicroBooNE applicaiton.

3 Behaviour under cryogenic conditions

It is vital for the proper function of a surge arrestor that it remain sufficiently insulating under the nominal applied voltage, and become sufficiently conducting to provide clamping in a surge condition. We observe that both varistors and GDTs experience changes in their electrical characteristics when operated at cryogenic temperatures. The varistor voltage and GDT DC spark-over voltage were characterized for 168 varistors and 60 GDTs both in air (warm) and in liquid argon (cold). Batches of around 20 devices were mounted on a specially constructed wheel which can be steered to place electrical contacts across each component sequentially. This test wheel was operated both in the air and immersed in an open dewar of liquid argon to characterize a large sample of devices.

For each device, the voltage supplied using a calibrated DC high voltage supply is gradually increased from zero. For varistors, the voltage supplied when a total current of 0.5 mA is drawn is recorded. For GDTs, we record the largest voltage supplied before the GDT transitions into a conducting mode, exceeding the 0.8 mA trip current of the power supply. In what follows we will refer to the relevant recorded voltage as the clamping voltage, despite the different definition in each case. For the first batch of 20 devices the repeatability of the characterization was established by measuring the warm clamping voltage two times each. These data are shown in figure 4. The varistors have a clamping voltage which is repeatably measurable to within a few volts. The GDTs have more variability in the clamping voltage, taking a somewhat random value each time. All devices clamp well within their specification, which is 1800^{+180}_{-100} V for the varistors, and 4500 ± 900 V for GDTs.

The clamping voltage was compared warm and cold for the two samples. The cool-down procedure involved holding the devices in the argon vapor around 10 cm from the liquid surface for around 10 minutes, before immersing the wheel completely in the liquid. A further 10 minutes was allowed for the temperature of the wheel and attached devices to equilibrate with the liquid argon. The warm and cold clamping points of each device are shown in figure 5. For varistors the clamping voltage always drops when cold, and there is a strong correlation between the warm

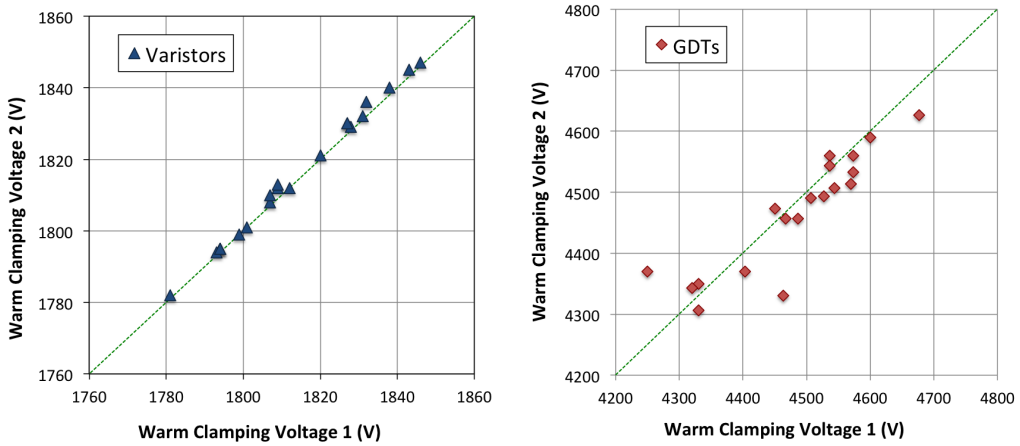


Figure 4. Repeatability of warm clamping measurement for varistors (left) and GDTs (right). Measurement 1 and measurement 2 were made for the same device, approximately 30 minutes apart. The varistors have a very stable clamping point, whereas the voltage at which GDTs clamp is somewhat random each time.

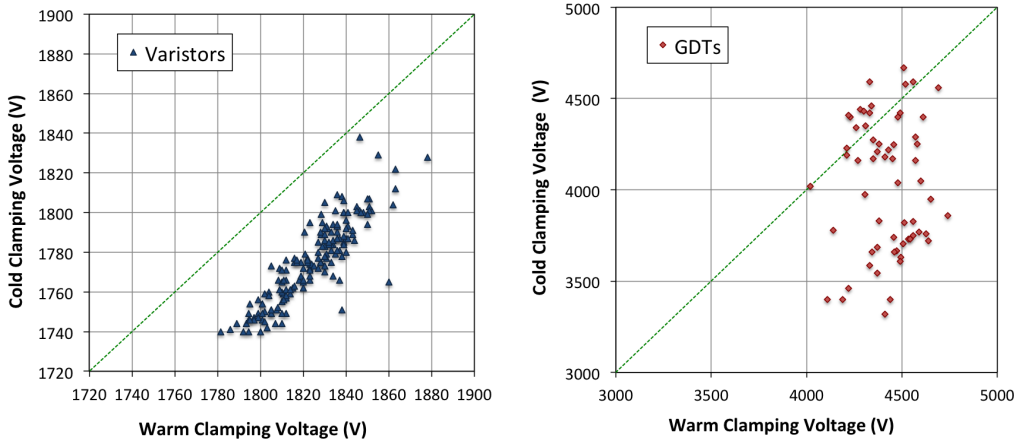


Figure 5. Cold versus warm clamping voltage for varistors (left) and GDTs (right).

and cold values. For GDTs there is no clear correlation, although the cold clamping voltages are typically lower and more scattered than warm.

As well as being suitably conducting in the surge regime, a surge protection device must be sufficiently insulating under the nominal applied voltage. For our application this is 2 kV for single devices, or 2 kV/ N per device for N devices in series, where for varistors N must be at least 2. The leakage current for both varistors and GDTs was investigated both warm and cold.

For varistors, a stable DC current is drawn at the nominal applied voltage. To measure the varistor curve warm and cold, the circuit shown in figure 6, left was used. The measured I–V characteristic warm and cold is shown in figure 6, right. The interpretation of the leakage current over long timescales is not trivial, since the varistor has a finite capacitance which charges through

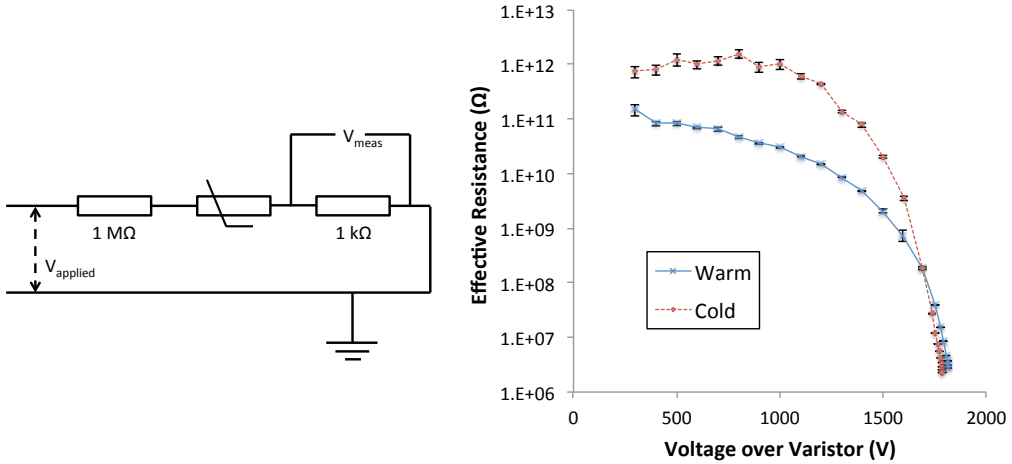


Figure 6. Left: circuit used to characterize varistor leakage behavior in warm and cold. Right: effective varistor resistance measured in warm and cold conditions.

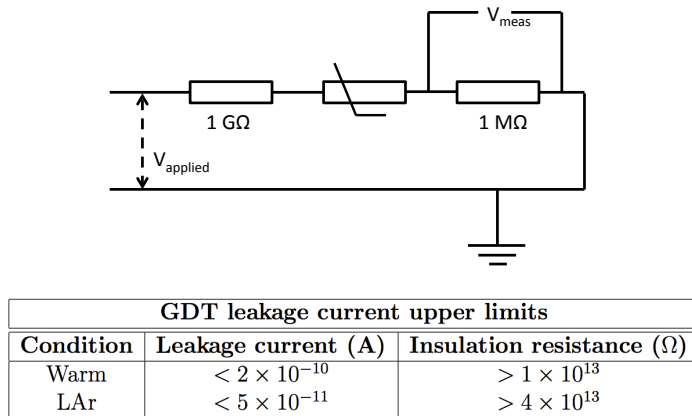


Figure 7. Top: circuit used to characterize GDT leakage behavior in warm and cold. Bottom: effective leakage current and resistance measured in warm and cold conditions at 2 kV applied voltage.

a large resistance. This results in a capacitive component to the leakage current which decays over a few minute timescale as well as a possible DC resistive component. The measurements shown in figure 6 represent the leakage current measured within a few seconds of voltage being applied, and give a lower limit to the effective insulating resistances which can be expected at long times.

For GDTs, the leakage current was measured using the circuit shown in figure 7, top. If the resistance of the device is much greater than $1\text{ G}\Omega$, the full applied voltage in this circuit is dropped across the surge arrestor. By measuring the voltage across the $1\text{ M}\Omega$ resistor, we measure the current flowing in the circuit and hence the insulating resistance of the surge arrestor. When the circuit was biased at 2 kV, a small, fluctuating voltage was observed. We record the largest value of the fluctuating voltage to give an upper limit on the leakage current, which is tabulated in figure 7.

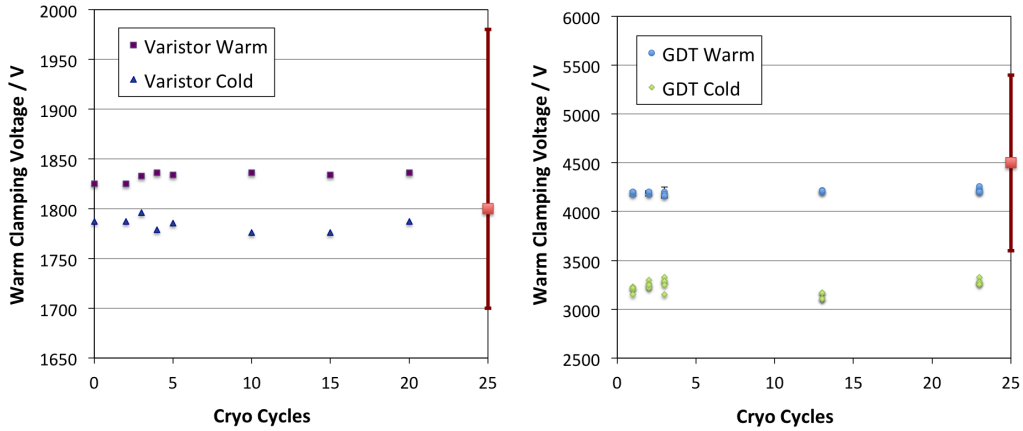


Figure 8. The effect of cryo-cycling upon varistor and GDT clamping voltage. Both devices are electrically unaffected by repeated cycles. The red bar on the right of each plot shows the specification provided by the manufacturer for the warm clamping voltage.

For the MicroBooNE application, an insulating resistance much larger than the $2.5 \times 10^8 \Omega$ field cage resistors is required. Both devices satisfy this criterion by a large margin.

Another requirement is that the devices must operate stably in a cryogenic environment over long timescales without experiencing random discharges, large leakage fluctuations or damage caused by argon seepage. To address the first two points, 14 of each device were biased at the nominal operating voltage in parallel, in an open liquid-argon filled dewar. The trip on the power supply was set to 100 nA. For both GDTs and varistors, the power supply remained un-tripped for over 72 hours, demonstrating 1000 device-hours of stable operation.

A longer term test was performed for two of each device over three weeks in a high purity argon environment. This tests not only that the devices do not degrade when submerged in argon, but also that they operate as expected in the dielectric environment of high purity argon. All four devices continued to exhibit the expected behavior in the insulating and clamping regimes for the full three weeks of the study.

In addition to being submerged in liquid argon, a batch of GDTs and varistors were also tested by submerging them in liquid nitrogen in an open dewar. The devices display similar insulating and clamping properties in this environment as they do in liquid argon. This is possible for the GDTs even though they contain nitrogen gas as the spark medium, because the gas is held at a sufficiently low pressure that it is not allowed to liquefy within the device. This point will be discussed further in section 5.1.

Although repeated or fast transition between liquid argon temperatures and ambient temperatures is never foreseen for devices used in LArTPC's, the effect of such cryogenic cycling was investigated for these devices. These tests were done to demonstrate both their mechanical and electrical robustness under extreme cryogenic conditions. GDTs were observed to be very robust - the device was mechanically and electrically unaffected by 23 violent cycles between air and liquid argon environments, being heated with a heat gun between each dunk. The warm and cold

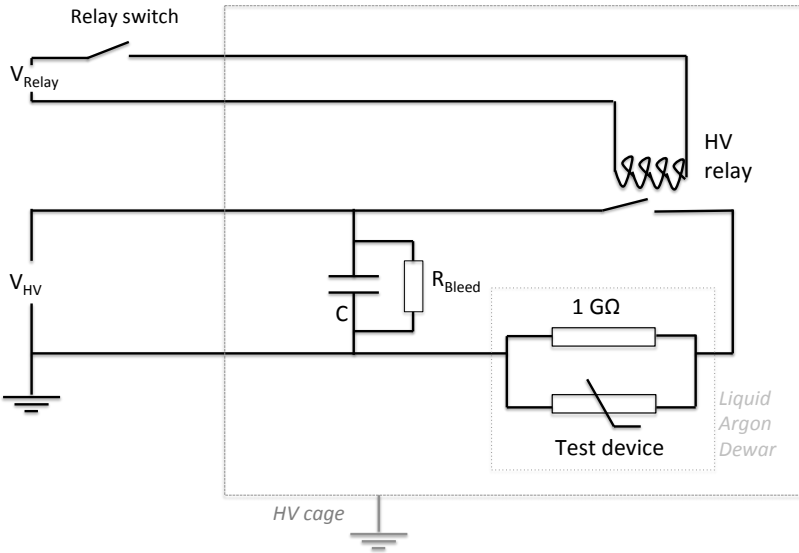


Figure 9. Circuit diagram of the HV pulse test. The rate of discharge into the test device is limited only by the resistance of the cables in the system.

clamping voltages at various times during this process are shown in figure 8, right. Varistors were not quite so robust, requiring a gentler cool-down procedure. Under the more violent procedure applied to GDTs, some varistors were observed to develop small hairline cracks in their epoxy coating. These cracks did not appear to affect the function of the device, having no impact upon its clamping or insulating properties. With a gentler cycle more closely resembling the conditions expected during a detector fill, with the varistor held briefly in the vapor between each immersion or removal, there was no damage to the component either visible by eye or electrically. The warm and cold clamping voltages at various stages during this process are shown in figure 8, left.

4 Robustness under repeated surges in liquid argon

An important characteristic of a surge protection device is its lifetime under the influence of repeated surges. All surge protection devices have a finite lifetime and ratings. Where given, these usually relate to an industry standard surge condition such as an 8/20 μs or 10/1000 μs (rise time / fall time) current pulse, delivered in air and at room temperature.

The expected use cases in LArTPCs do not reflect these idealized conditions. Furthermore, in many industrial applications, surge protection components can be considered as sacrificial, being replaced after the end of their lifetime. In cryogenic experiments, the experiment design may make them inaccessible for long intervals, during which time they must survive repeated surges. Understanding the longevity of these devices in these conditions is of central importance.

To address these questions for GDTs and varistors a test stand was designed to deliver voltage surges of the scale expected in a HV discharge event in a large LArTPC. In MicroBooNE, the largest expected discharges would deposit 2 J into a device in a worst case scenario. To test the

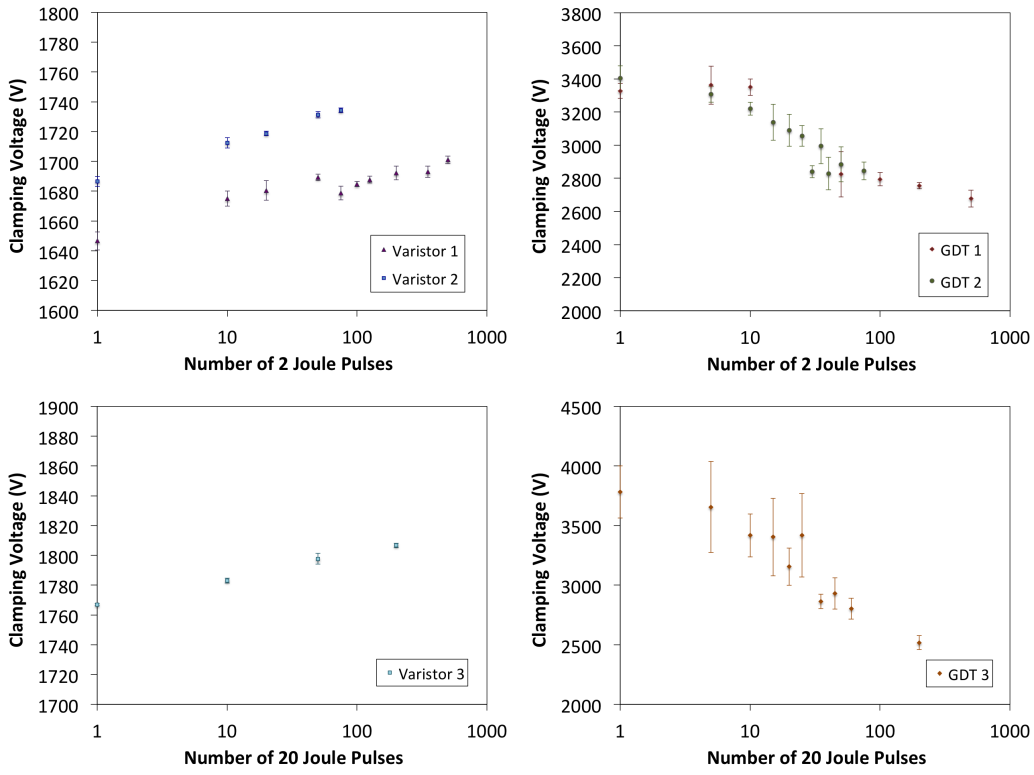


Figure 10. Change in clamping voltage of varistors (left) and GDT's (right) with repeated 2J and 20J surges in liquid argon.

robustness of the devices, controlled voltage surges of known energy were produced charging a large capacitor to a known voltage using a high voltage supply, and then rapidly discharging the capacitor through the device under test, in an open dewar of liquid argon. The discharge is triggered by closing a high voltage relay. A 2J pulse is generated by charging a 50 nF capacitor to 9 kV and discharging it through the capacitor. 20J pulses were also delivered to over-test the device, generated by charging a 1 μ F capacitor to 6.5 kV. A schematic of the test apparatus is shown in figure 9.

Using this apparatus, 500 pulses of 2J were delivered to one GDT and one varistor, each submerged in liquid argon. At various intervals during the application of the 500 test pulses the clamping voltage for the device under test was remeasured, as shown in the top two plots of figure 10. Both devices experienced some drift in the clamping voltage. The varistor clamping voltage rose within the first few pulses before stabilizing, but always remained within the specifications for the device. This is in contrast to the degradation behavior reported in the literature for varistors, which suggests that the clamping voltage experiences a steady decay towards zero [18]. However, modern varistors are known to have different degradation behavior to those available at the time of those sources due to the introduction of new dopants and manufacturing processes [19]. The GDT clamping voltage is observed to drop with repeated surges, which is consistent with the reported degradation behavior in the literature [21]. The approximately exponential decay suggests that the

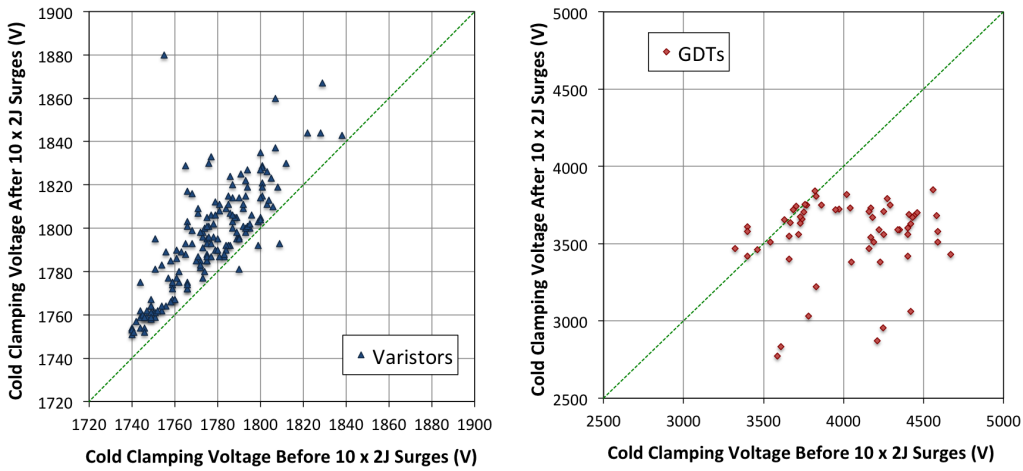


Figure 11. Shift in clamping voltage for 168 varistors and 60 GDTs with ten 2 J surges.

device will remain above the critical 2 kV threshold for many more than 500 surges. A second specimen of each device was subjected to 75 pulses to check the reproducibility of the degradation behavior, and a consistent behavior was observed. With pulses of 20 J, a similar trend is observed for both varistors and GDTs. For varistors the change in clamping voltage is not appreciably different from the 2 J case. For GDTs the degradation is more dramatic, but the device still appears robust for up to 200 pulses. These data are shown in figure 10, bottom.

Using the wheel apparatus described in section 3, the 168 varistors and 60 GDTs were subjected to ten pulses of 2 J each, administered using a 100 pF capacitor charged to 6.3 kV. The distribution of clamping voltages before and after these pulses are shown in figure 11.

The tests described above exercise the energy dissipation capability of each surge arrester. In these tests, a pulse of voltage significantly less than the design high voltage of a large LArTPC was used. This is reasonable, because the surge arrestors prevent the potential differences in the system from rising above the clamping voltage, so they should not have to stand off any voltage significantly above this clamping voltage during a discharge event. In spite of this, there remains a possibility that rapid transient over-voltages up to the full supply voltage may be encountered on short timescales due to inductive effects in the system. To test that the devices are robust against such over-voltages, and offer suitable protection to vulnerable components in this condition, a 150 kV transient test was performed.

The test setup is shown in figure 12. One MicroBooNE resistor board, an example of which is shown in figure 13, complete with four Ohmite Slim-Mox 104E 1 G Ω resistors was mounted inside a sample cage consisting of rounded metal plates separated by plastic rods. The resistor board with no surge arrestors attached is referred to as unprotected. The resistors can also be protected by adding surge arrestors in two configurations: 1) two varistors linked in series and applied in parallel across the resistors and 2) two GDTs applied in parallel across the resistors. An example of a protected resistor board mounted in the test cage is shown in figure 13(left), with two GDTs in parallel with the four SlimMox resistors. The cage was immersed in a 200 L open liquid argon cryostat, which was grounded within a high voltage cage. The bottom plate of the assembly

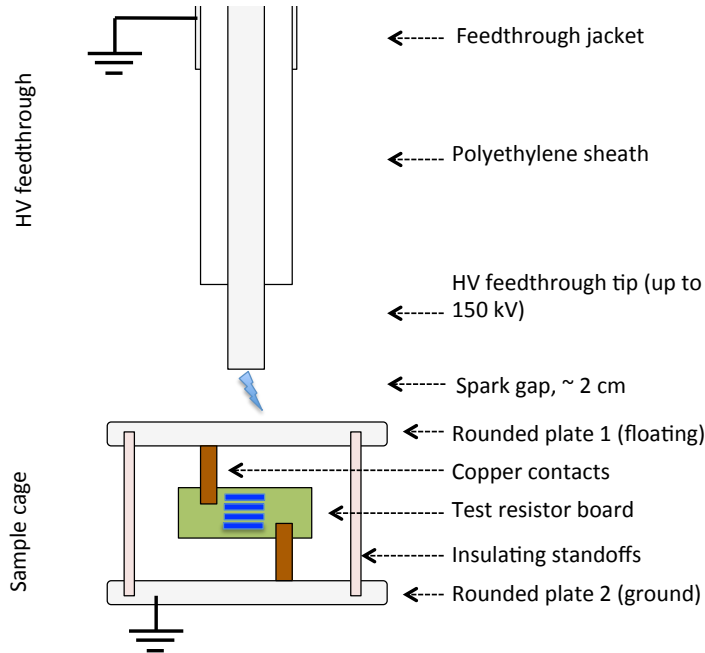


Figure 12. Diagram of the apparatus used to perform the 150 kV transient test.

was placed in contact with the lower surface of the cryostat, grounding it. The top plate remains electrically floating, isolated from ground by the field cage resistors.

A high voltage feedthrough was inserted into the dewar, with the tip held around 2 cm from the top plate to create a spark gap in the liquid argon. This feedthrough was charged up to a maximum of 150 kV using a Glassman (series LX) high voltage supply, and held at voltage until a spark developed across the argon gap between the feedthrough tip and the top plate. At the instant of the spark, a conducting path forms between the feedthrough and the top plate, bringing it up to the full applied voltage. In the case where a surge protector is applied, the charge stored in the feedthrough and cable, which has a capacitance of around 500 pF, is drained through the spark and the conducting surge arrestor to ground. This current draw causes the supply to trip. The total stored capacitive energy in the feedthrough and cable is around 5 J, and a large but not precisely known fraction of this will be dissipated into the surge arrestor. In the case where an unprotected resistor board is used, the resistors have to stand off the full supply voltage, and if this voltage is large enough, one or more of the resistors will fail. In both cases, the design of the test produces conditions which resemble the expected transient over-voltage condition in a LArTPC spark event.

Sparks began to be observed at 50 kV, and the applied voltage was stepped up in 5 kV steps with at least 20 sparks being delivered at each voltage point, up to the supply limit of 150 kV. The varistor-protected board was tested first, and after the end of the test the board was removed and the varistors were taken off. The varistors were characterized and found to display the expected clamping behavior, and the resistors on the board were undamaged. The test was repeated with GDTs, and again, all components visibly survived the application of sparks up to 150 kV, and the GDTs and resistors exhibited the correct properties after removal. Finally the GDTs were removed

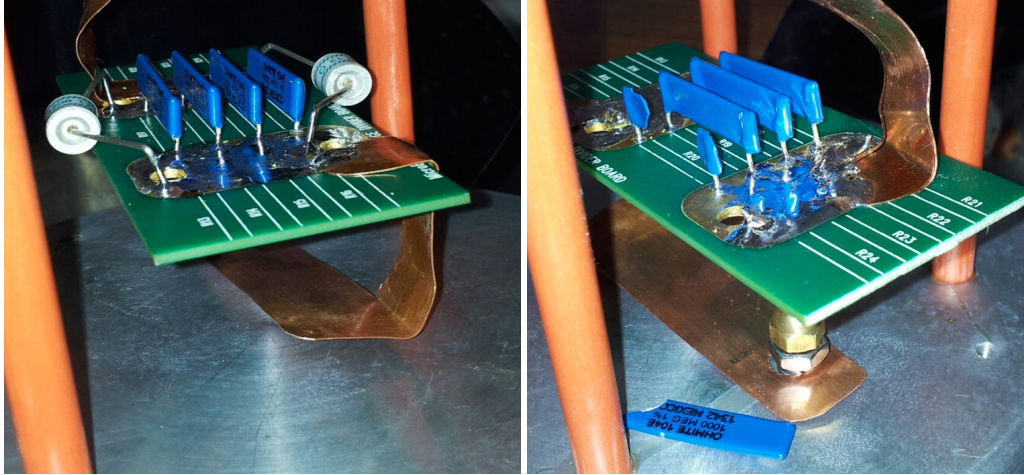


Figure 13. Left: photograph showing the protected resistor board following the delivery of $20 \times 150\text{ kV}$ transient surges. Right: photograph showing the same board after delivery of a single 70 kV transient surge when no surge protection is applied.

leaving only bare resistors. One of the unprotected resistors failed upon the first spark at a voltage of 70 kV , being destroyed as shown in figure 13, right.

This test not only shows that GDTs and varistors can survive brief transients of the full supply voltage, but also provides an explicit demonstration of the protection offered to vulnerable components in the event of a HV surge. At least one of the same resistors which were able to survive multiple 150 kV discharges when protected with surge arrestors was found to fail at much lower voltages when unprotected.

5 Practical considerations for use in LArTPCs

As well as demonstrating that varistors and GDTs exhibit the required surge protection behavior in a cryogenic environment, it is also important to ensure that they do not interfere with the normal operation of a liquid argon detector in other ways. In particular, liquid argon TPCs have strict purity requirements. Also, large scale LArTPCs usually have sensitive optical systems, so the emission of a large photon flux during normal operation would be unacceptable. In this section we describe tests performed to establish possible purity and light emission effects of varistors and GDTs.

5.1 Purity considerations

Two GDTs and two varistors were analyzed with the Fermilab Materials Test Stand (MTS) [22]. The MTS consists of a sample cage into which components and materials can be placed, which is lowered into a 250 L volume of high purity liquid argon. The free electron lifetime in this argon volume is continuously monitored using an electron-drift purity monitor. After 55 hours in the liquid with the argon filters disabled, the electron lifetime remained at or above 9 ms at all times, in the presence of both GDTs and varistors. This demonstrates that these devices do not introduce electron-scavenging impurities into LArTPC detectors.

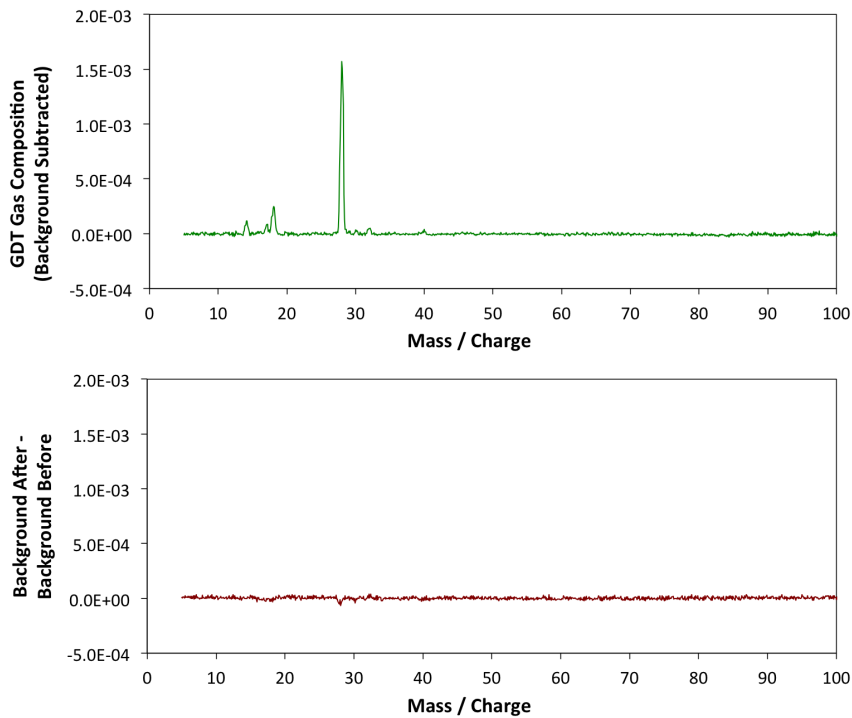


Figure 14. Background subtracted UGA spectra. Top: GDT gas composition. The peaks at 28, 17-18, and 14 correspond to singly ionized nitrogen, water, and doubly ionized nitrogen, respectively. Bottom: repeated carrier gas background measurement with new gas sample in chamber.

Varistors' all-solid construction means that even in the event of a catastrophic mechanical failure, the surge protector will bring no new materials into contact with the surrounding medium. For gas discharge tubes, a rupturing of the device within the detector could lead to the contents becoming dissolved into the argon volume in the event of a catastrophic failure. The effect of this type of failure upon detector purity was also established. To determine the composition and concentration of gasses inside the EPCOS A71-H45X, a single unit was broken in the presence of a pre-characterized helium carrier gas. This mixture was fed to a universal gas analyzer (UGA) [23], and the mass spectrum of the carrier gas before and after rupture of the GDT were compared. The difference is shown in figure 14, top. After this characterization, the system was flushed with fresh carrier gas, which was again characterized with the UGA. The stability of the carrier gas composition measurement is shown in figure 14, bottom, on the same scale. Using this method, it was established that the GDT contains nitrogen gas at a pressure of 250 Torr. No other compounds in the mass range $4 < A < 300$ were observed above the noise floor of the UGA, which corresponds to a limit of 3 Torr in the GDT. No oxygen peak was observed, demonstrating that the measured nitrogen peak is not a result of environmental contamination. A small peak from water contamination was observed, which is likely caused by outgassing from the steel piping of the analyzer rather than the GDT itself. Comparison with the Paschen curve for nitrogen confirms that pure nitrogen at the measured pressure, within the geometry of the device, would produce the expected

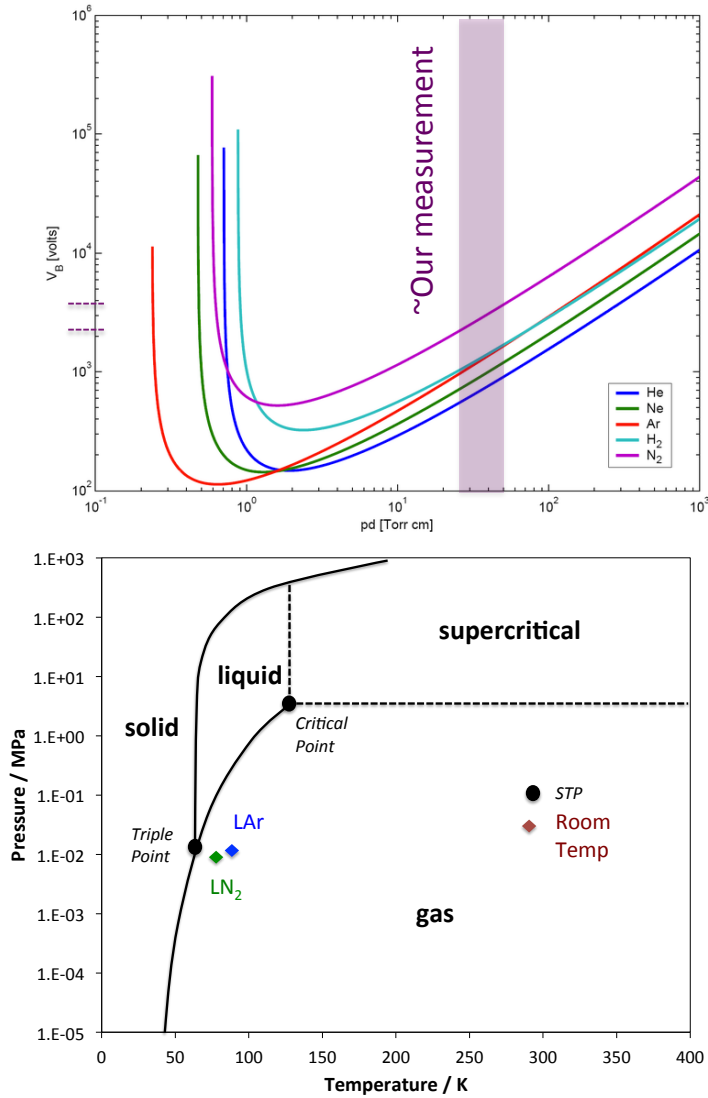


Figure 15. Top: Paschen curves for common gases, reproduced from [26]. Our measurement of the nitrogen pressure in the EPCOS GDT suggests a breakdown voltage of 3 – 4 kV, in line with observed behavior. Bottom: phase diagram for nitrogen, reproduced from [27]. At the measured concentration and constant volume, nitrogen would be in the pure vapor phase in LAr, LN₂, and warm environments, explaining the observed functionality of the GDT.

spark breakdown strength, as shown in figure 15, top. Comparison with the phase diagram of nitrogen demonstrates that nitrogen at this pressure at room temperature is expected to remain in the vapor phase at both liquid argon and liquid nitrogen temperatures when held at constant volume, which is consistent with our observations of the cryogenic functionality of the device, shown in figure 15, bottom.

Small contaminations of nitrogen are known to be acceptable for TPC operation. However, nitrogen at the part-per-million level can have detrimental effects upon liquid argon scintillation

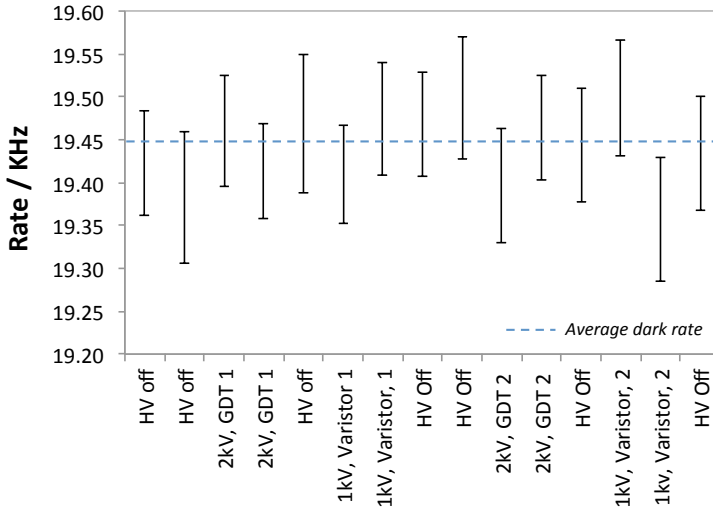


Figure 16. The rate of a single photoelectron trigger with different devices held at nominal high voltage around 15 cm from an LBNE lightguide detector.

light collection [24, 25]. Our measurements show that a single GDT, which has a volume of approximately 0.4 cm^3 , contains $6 \times 10^{-6} \text{ mol}$ of nitrogen gas. As an example, if one GDT were to leak into the MicroBooNE detector, which contains 170 tons of liquid argon, this would introduce a nitrogen contamination of around 1.4×10^{-12} . This is far below nitrogen concentrations which are problematic for scintillation light collection.

5.2 Light emission

The devices under consideration are to be operated at a nominal voltage of 2 kV (this voltage would be applied across a single GDT, or two or more varistors in series). In past detectors, some electronic components have been reported to glow when HV is applied [28]. In order to establish whether there is light emission associated with the operation of GDTs and varistors at nominal voltages, two of each were installed alongside tests of prototype optical detectors for the LBNE experiment [29], in the TallBo optical test cryostat at Fermilab [30].

The prototype optical detectors consist of an acrylic light guide coated in a wavelength shifting TPB coating [29]. This is coupled to three silicon photomultiplier (SiPM) detectors which have their signals fed to a shaper. For this test, the shaped signal from one SiPM was viewed using an oscilloscope. Binning the pulse amplitudes shows a clear separation of each N photoelectron peaks up to at least 20. The detectors have an estimated average collection efficiency of $O(0.03\%)$ [31] for 128 nm liquid argon scintillation light. A trigger was set at 10 mV, which is below the single photoelectron level of 12 mV, and the single photoelectron trigger rate was determined by counting the number of triggers in five minutes. The rate when no voltage was supplied to any surge protector was $19.44 \pm 0.02 \text{ kHz}$, which includes both thermionic SiPM noise and the prompt and late scintillation signals from cosmic ray muons passing through the detector. The rate was compared to that measured when each device was biased at 2 kV for GDTs, or 1 kV for varistors. No significant additional single photoelectron rate was observed, which sets an upper limit on the detected rate of

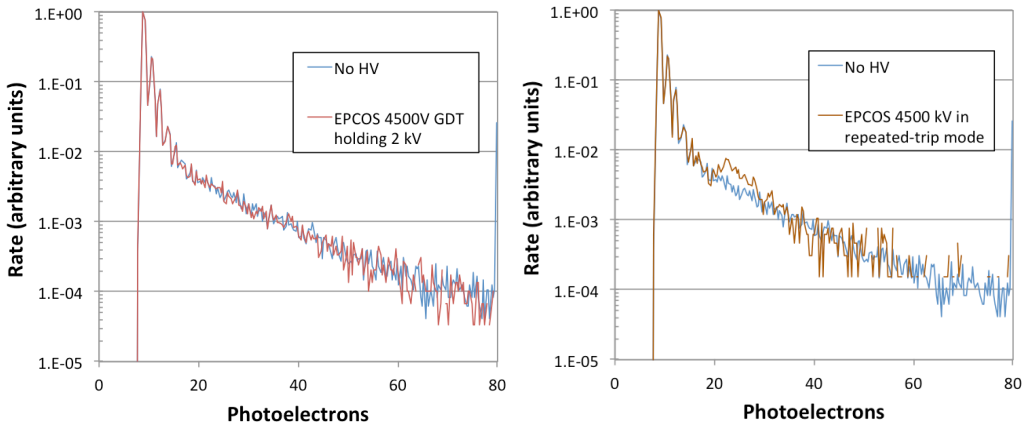


Figure 17. The pulse amplitude spectra in both the nominal (left) and discharge (right) conditions, compared to the cosmic ray background in TallBo.

100 Hz at a distance of 15 cm, which is below the level where there would be interference with a LArTPC optical system. These data are shown in figure 16.

With the power supply set above the clamping point, light emission was observed for the GDTs, originating from the spark formed inside the device. No light emission was observed for varistors. In this mode, the power supply repeatedly biased the device and then tripped, leading to short bursts of light. The spectrum of pulses recorded from the SiPM for the GDT operated in nominal and over-voltage mode is shown in figure 17, left and right. In the over-voltage mode, a distinct feature is seen at around 20 photoelectrons. In a real transient over-voltage situation, this pulse is likely to be very small in comparison to the light emitted by the initial spark which caused the discharge.

6 Conclusions

We have demonstrated in this paper that high voltage GDTs and varistors continue to function as surge protection devices in a liquid argon environment. In both cases, the devices become more insulating in the non-conducting regime, and continue to exhibit clamping behavior, albeit at a somewhat reduced clamping voltage. For GDTs, the clamping voltage is seen to drop significantly to a value not strongly correlated with the warm clamping voltage, whereas for varistors the change is smaller, and there is a strong correlation between warm and cold clamping voltages.

The devices have also been demonstrated to be robust under application of the surge energies and voltages to be expected in the HV discharge of a current-generation LArTPC experiment. Furthermore, they have been demonstrated to offer protection to a specific class of vulnerable components, the resistors originally selected to be used in the MicroBooNE field cage. The possible effects of each device upon argon purity have been investigated and both are found to be benign. Finally, both devices have been tested for light emission under nominal operating conditions and no large photon flux was observed. Both classes of device have been shown to be appropriate for use in LArTPC experiments as surge protection devices.

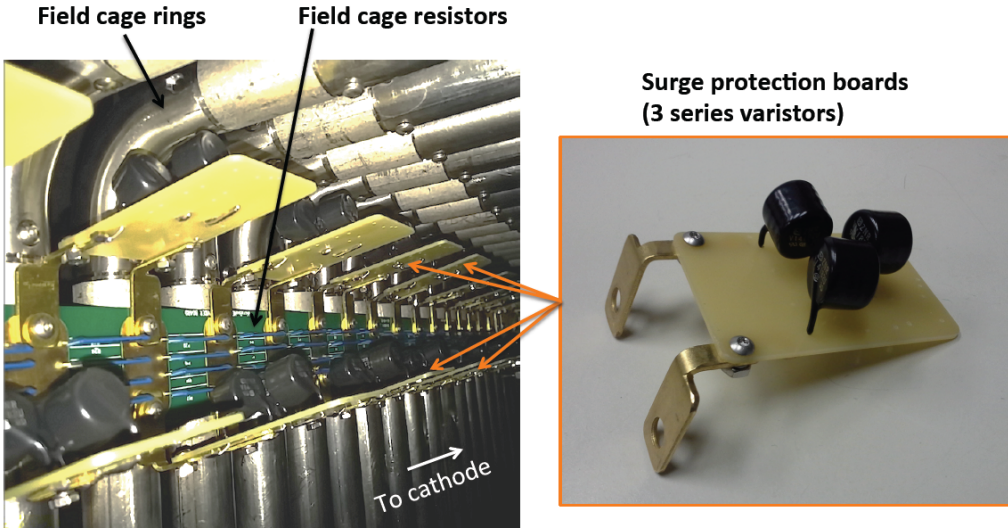


Figure 18. The MicroBooNE surge protection system, as installed in the TPC. Each set of field cage resistors between the cathode and field cage ring number 32 is placed in parallel with three series varistors.

When applied in parallel with a vulnerable component, both classes of surge protector prevent the voltage from rising above a critical clamping voltage for long timescales, ensuring that the sensitive component is not held in a large over-voltage condition. Although both act as surge protectors, there are key differences in functionality between GDTs and varistors. Varistors have a smooth I–V curve, free from hysteresis, producing a gradual clamping behavior. An increasing current supply is met with a decreasing resistance, thus preventing a large potential difference from evolving. GDTs, on the other hand, transition discretely from the open to conductive state when a critical voltage is reached, acting as a crowbar. Current is allowed to flow through the GDT until the potential difference between the electrodes falls below the GDTs extinction voltage, which is significantly lower than the initial spark-over voltage. This will occur when the current source driving the discharge is exhausted, which is expected to take on the order of microseconds in a TPC discharge event, assuming a suitable current limiting resistor is used in line with the HV power supply.

Even with surge protectors applied, very short transients, with timescales on the order of the light travel time across the detector may be present. Understanding these transients requires a detailed analysis of the inductive, capacitive and resistive couplings within the field cage. The dynamics of these transients within the MicroBooNE TPC have been studied, but these studies are beyond the scope of this paper, and will be presented in a future publication [17]. The role of a surge protector is to prevent such over-voltages from being maintained over timescales long enough to cause component damage, and in cases where the current supply driving the discharge is finite, as it is in a LArTPC spark condition, they perform this role in a relatively application-independent way.

There are advantages and disadvantages to both GDTs and varistors for high voltage surge protection. In particular, easily mountable varistors are not commercially available in the appropriate voltage range for typical LArTPC applications, so several devices must be used in series. This

requires more solder connections and mounting hardware than in the case of a GDT, where a single unit may be mounted directly in parallel with the vulnerable component to be protected. On the other hand, the gradual clamping behavior and well defined I–V curve of varistors makes it easier to model the dynamics of the field cage in surge conditions using software such as SPICE [32].

As a result of this work, a varistor based surge protection system was installed in parallel with the MicroBooNE TPC resistor chain between the the cathode and the thirty-two nearest field cage rings. Sets of three series varistors, having a combined clamping voltage of 5.26 ± 0.04 kV, were mounted on G10 boards and affixed using brass contacts to the mount points of the field cage resistor boards on the TPC frame. A picture is shown in figure 18.

As well as being suitable for this specific application, this work demonstrates generally that GDTs and varistors continue to act as surge protection devices in liquid argon environments. As such, both classes of device may find wider applications in electrical protection of sensitive components in LArTPC detectors.

Acknowledgments

We thank Walter Jaskierny for assistance in the design and implementation of safe and conclusive high voltage tests, and Jonathan Woodworth of ArrestorWorks for helpful consultations on industrial use of varistors. We thank Henning Back helping us to perform gas analysis using a UGA which is part of the low-radioactivity argon purification project, Stuart Mufson and Denver Whittington for the equipment and expertise used to measure light emission from devices in the Bo test stand, Stephen Pordes for allowing us access to the MTS and other facilities at the Proton Assembly Building, Ewa Skup for operating the MTS, and Sarah Lockwitz for setting up the MicroBooNE HV feedthrough test stand. We also thank our MicroBooNE collaborators for giving helpful feedback at all stages of this work, in particular Linda Bagby, Jennifer Raaf, Regina Rameika, Anne Schukraft, and Michele Weber.

This work was supported by the Fermi National Accelerator Laboratory, which is operated by the Fermi Research Alliance, LLC under Contract No. De-AC02- 07CH11359 with the United States Department of Energy. The surge protection components under test, and the work by BJP and JMC, were funded by the National Science Foundation grant PHY-1205175. JA is supported by National Science Foundation grant PHY-1068553. SG is supported by the Department of Energy through grant DE-FG03-99ER41093 and JMSJ through grant DE-SC0011784. TS acknowledges the support of the Swiss National Science Foundation. JZ is supported by the University of Chicago.

References

- [1] G. Raselli, *ICARUS T600: Status and perspectives of liquid-argon technology for neutrino physics*, *Nuovo Cim.* **C036** (2013) 243.
- [2] C. Adams et al., *The Long-Baseline Neutrino Experiment: Exploring Fundamental Symmetries of the Universe*, [arXiv:1307.7335](https://arxiv.org/abs/1307.7335), (2013).
- [3] H. Chen et al., *Proposal for a New Experiment Using the Booster and NuMI Neutrino Beamlines: MicroBooNE*, [fermilab-proposal-0974](https://arxiv.org/abs/fermilab-proposal-0974) (2007).

- [4] INTENSITY FRONTIER NEUTRINO working group, A. de Gouv  a et al., *Working Group Report: Neutrinos*, [arXiv:1310.4340](https://arxiv.org/abs/1310.4340).
- [5] S.K. Agarwalla et al., *The mass-hierarchy and CP-violation discovery reach of the LBNO long-baseline neutrino experiment*, *JHEP* **05** (2014) 094 [[arXiv:1312.6520](https://arxiv.org/abs/1312.6520)].
- [6] A. Zani, *The WArP Experiment: A Double-Phase Argon Detector for Dark Matter Searches*, *Adv. High Energy Phys.* **2014** (2014) 205107.
- [7] K. Rielage, *Status and prospects of the MiniCLEAN dark matter experiment*, *AIP Conf. Proc.* **1441** (2012) 518.
- [8] DEAP collaboration, M.G. Boulay, *DEAP-3600 Dark Matter Search at SNOLAB*, *J. Phys. Conf. Ser.* **375** (2012) 012027 [[arXiv:1203.0604](https://arxiv.org/abs/1203.0604)].
- [9] DARKSIDE collaboration, M. Bossa, *DarkSide-50, a background free experiment for dark matter searches*, *2014 JINST* **9** C01034.
- [10] A. Badertscher et al., *ArDM: first results from underground commissioning*, *2013 JINST* **8** C09005 [[arXiv:1309.3992](https://arxiv.org/abs/1309.3992)].
- [11] R. Acciarri et al., *Liquid Argon Dielectric Breakdown Studies with the MicroBooNE Purification System*, [arXiv:1408.0264](https://arxiv.org/abs/1408.0264).
- [12] A. Blatter et al., *Experimental study of electric breakdowns in liquid argon at centimeter scale*, *2014 JINST* **9** P04006 [[arXiv:1401.6693](https://arxiv.org/abs/1401.6693)].
- [13] F. Bay et al., *Evidence of electric breakdown induced by bubbles in liquid argon*, [arXiv:1401.2777](https://arxiv.org/abs/1401.2777).
- [14] D. Swan and T. Lewis, *Influence of Electrode Surface Conditions on the Electrical Strength of Liquified Gases*, *J. Electrochem. Soc.* **107** (1960).
- [15] Panasonic Corporaiton, *ZNT Transient Surge Absorbers*, <http://industrial.panasonic.com/www-data/pdf/AWA0000/AWA0000CE2.pdf>.
- [16] EPCOS, *EPCOS Product Profile 2013: Surge Arresters and Switching Spark Gaps*, <http://www.epcos.com/blob/174146/download/5/ueberspannungsableiter-und-schaltfunkentstrecken.pdf>.
- [17] MICROBOONE collaboration, *The MicroBooNE Detector*, in preparation.
- [18] T.K. Gupta, *Application of zinc oxide varistors*, *Journal of the American Ceramic Society* **73** (1990) 1817.
- [19] J. Woodworth of ArrestorWorks, personal communication.
- [20] EPCOS, *EPCOS A71-H45X Data sheet*, <http://www.epcos.com/inf/100/ds/a71h45xx2590.pdf>.
- [21] Bourns Corporation, *First Principles of a Gas Discharge Tube (GDT) Primary Protector*, http://www.bourns.com/pdfs/bourns_gdt_white_paper.pdf.
- [22] B. Rebel et al., *Results from the Fermilab materials test stand and status of the liquid argon purity demonstrator*, *J. Phys. Conf. Ser.* **308** (2011) 012023.
- [23] Stanford Research Systems, *Universal gas analyzer manual*, <http://www.thinksrs.com/downloads/PDFs/Manuals/UGAm.pdf>.
- [24] WARP collaboration, R. Acciarri et al., *Effects of Nitrogen contamination in liquid Argon*, *2010 JINST* **5** P06003 [[arXiv:0804.1217](https://arxiv.org/abs/0804.1217)].

- [25] B.J.P. Jones, C.S. Chiu, J.M. Conrad, C.M. Ignarra, T. Katori and M. Toups, *A Measurement of the Absorption of Liquid Argon Scintillation Light by Dissolved Nitrogen at the Part-Per-Million Level*, 2013 *JINST* **8** P07011 [Erratum *ibid.* **8** (2013) E09001] [[arXiv:1306.4605](https://arxiv.org/abs/1306.4605)].
- [26] M.A. Lieberman and A.J. Lichtenberg, *Principles of plasma discharges*, Wiley (2005).
- [27] Wolfram Alpha, *Phase diagram for nitrogen*, <http://www.wolframalpha.com>.
- [28] M. Hofmann, *Liquid scintillators and liquefied rare gases for particle detectors background-determination in double chooz and scintillation properties of liquid argon*, Master's thesis, Technische Universitat, Munchen, Germany (2012).
- [29] B. Baptista et al., *Benchmarking TPB-coated Light Guides for Liquid Argon TPC Light Detection Systems*, [arXiv:1210.3793](https://arxiv.org/abs/1210.3793), (2012).
- [30] B.J.P. Jones, *Results from the Bo Liquid Argon Scintillation Test Stand at Fermilab*, 2013 *JINST* **8** C09003.
- [31] D. Whittington, private communication.
- [32] L.W. Nagel and D. Pederson, *Spice (simulation program with integrated circuit emphasis)*, Tech. Rep. UCB/ERL M382, EECS Department, University of California, Berkeley, April 1973.
- [33] L.F. Bagby, S. Gollapinni, C.C. James, B.J.P. Jones, H. Jostlein et al., *Breakdown voltage of metal-oxide resistors in liquid argon*, [arXiv:1408.4013](https://arxiv.org/abs/1408.4013).

5.4 Demonstration of surge protection on the MicroBooNE TPC

Although the MicroBooNE resistive divider is a simple DC circuit, capacitances between the field cage, cathode and cryostat make it nontrivial to predict the behavior of transient currents in the system. Tests were therefore made to demonstrate the clamping action of varistors *in situ* using the MicroBooNE TPC and cryostat.

Discharges were generated by delivering voltage to the cathode to charge the system and then removing the HV supply whilst simultaneously bringing a field cage tube to ground with a double-pole-double-throw switch. This simulates the effect of a spark discharge with immediate power supply trip. Since a 2 kV ring-to-ring voltage cannot be applied without breakdowns in air, a lower supply voltage and correspondingly smaller varistors (12 V clamping) and resistors ($10 \text{ M}\Omega$) were used, creating a scaled model of the MicroBooNE system. Voltages up to 800 V were applied across the first ten field cage rings (numbered T1-T10, T1 being nearest the cathode). A $1.25 \text{ G}\Omega$ resistor between T10 and ground simulates the resistance of the rest of the field cage. An oscilloscope terminated at $10 \text{ M}\Omega$ was connected across a pair of field cage tubes via a $10\times$ amplifier and a $1 \text{ G}\Omega$ decoupling resistor. The circuit diagram is shown in Figure 2.5.4, left, and a photograph in Figure 2.5.4, right.

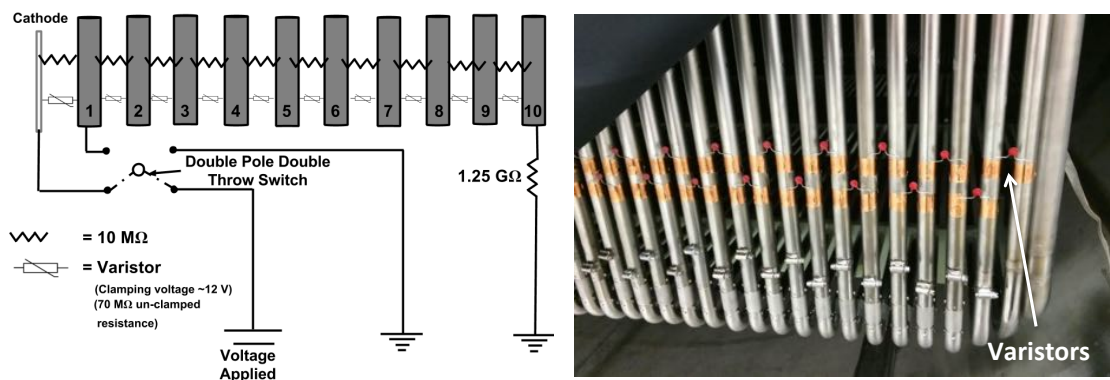


Figure 2.5.4: Left: circuit diagram of scaled-model test on the TPC. Right: photograph showing low voltage varistors applied in parallel with the field cage resistors.

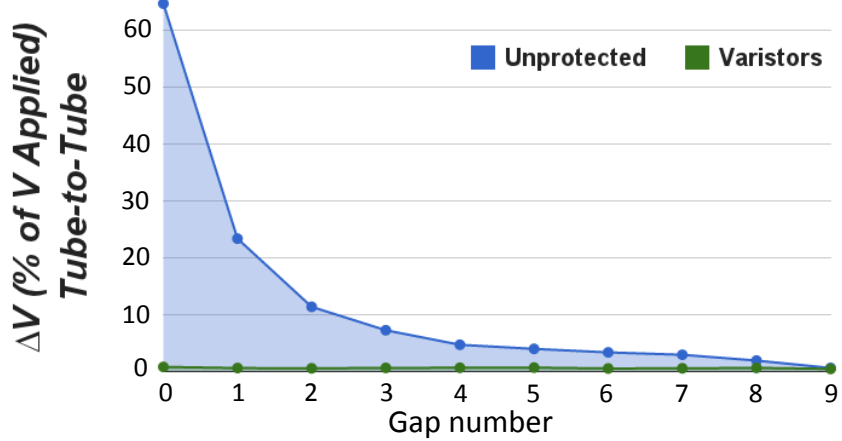


Figure 2.5.5: Maximum voltage evolved across each resistor when T1 is discharged to ground in the protected and unprotected networks.

The top four panels of Figure 2.5.6 show the voltages in the protected and unprotected systems when T1 is discharged. In the unprotected case, the potential on T1 drops immediately to zero and the potentials on adjacent elements decay gradually. This leads to a large transient voltage across the resistors. When varistors are added both T1-cathode and T1-T2 potential differences are clamped, with all elements discharging rapidly. Similar tests were made with discharges of T1, cathode and T6, and monitoring the voltage across each gap. Clamping was effective in all cases. Figure 2.5.5 shows the voltage across each resistor in the T1 discharge condition.

A real spark event may incompletely drain the charge from the affected element. This situation was studied by brushing the charged field cage with a braid, generating several microsparks. Clamping was observed to be effective. Furthermore, in a real spark discharge the HV trip will not be instant, but may take up to 1 s. In MicroBooNE, an $80 \text{ M}\Omega$ current limiting resistor in line with the HV supply prevents large currents from the supply, and is an important component in this scenario. We included it in the scaled system by adding a $470 \text{ k}\Omega$ resistor between the power supply and cathode, and discharged the field cage without removing the HV (Figure 2.5.6, bottom). Clamping was again effective in this situation.

These tests demonstrate that varistor-based surge protection can robustly clamp over-voltages in TPC detectors under a wide variety of discharge conditions.

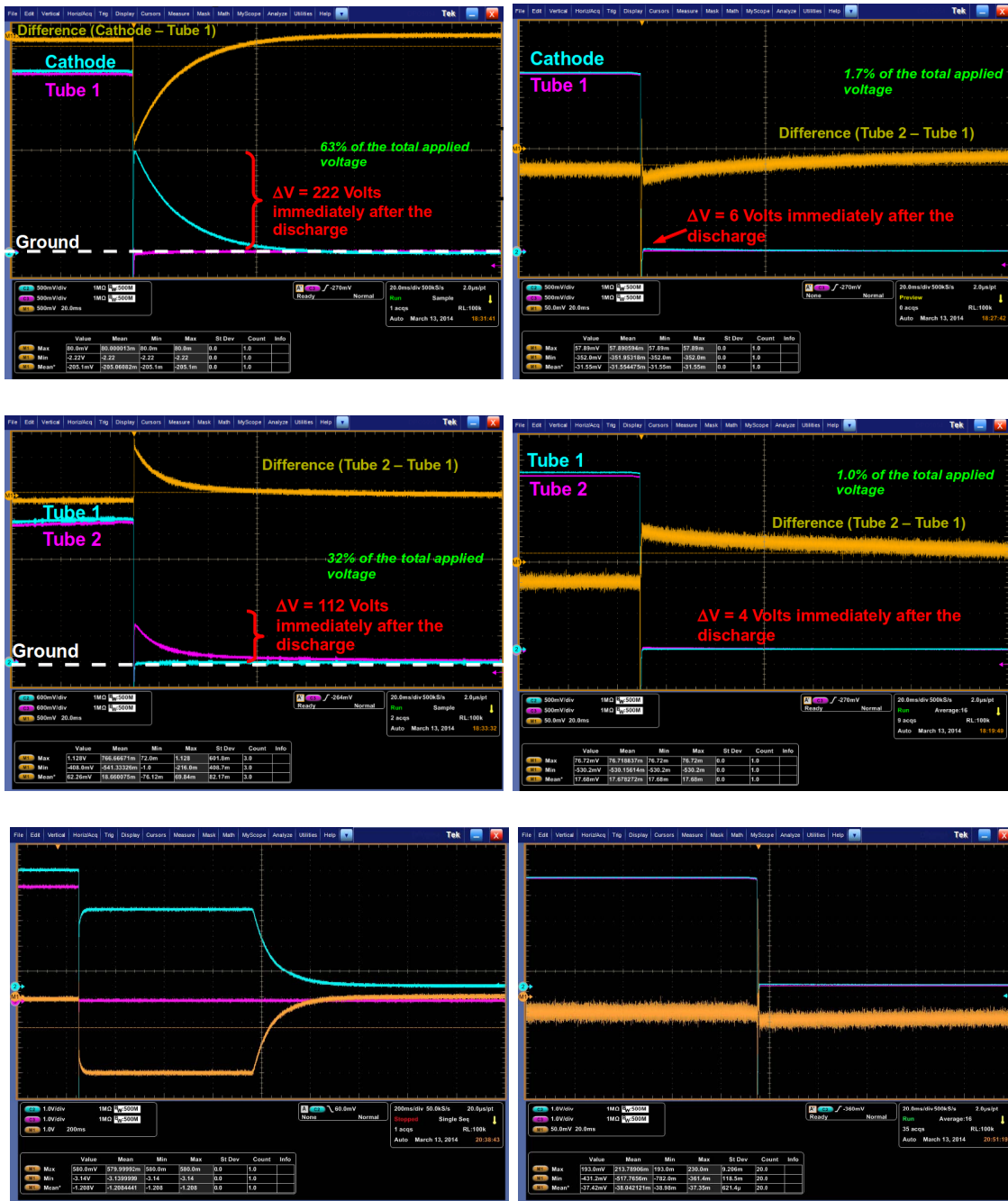


Figure 2.5.6:

Voltages evolved in unprotected (**left**) and protected (**right**) TPC circuit.

Top : Transient voltages evolved between T1 and the cathode with T1 discharge

Middle : Transient voltages evolved between T1 and the T2 with T1 discharge

Bottom : Transient voltages evolved between T1 and cathode with T1 discharge and long HV trip time.

Chapter 6

Simulation and Reconstruction Tools for Liquid Argon Detectors

6.1 The LArSoft framework

LArSoft [254] is a software framework for performing simulation, reconstruction and analysis tasks for LArTPC experiments. MicroBooNE is one in a series of LArSoft users, including ArgoNeuT, LArIAT, SBND and DUNE. Simulation and reconstruction for liquid argon detectors is a complicated problem with many facets. This chapter focusses on my own contributions, rather than providing a wide survey.

Simulations in LArSoft

The LArSoft simulation chain starts with an event generator, such as a particle gun or a neutrino generator like GENIE [255]. This simulates particles emerging from a primary interaction, which are then propagated through the detector geometry, supplied in GDML format [256], by a GEANT4 [257] simulation. The interface between GEANT4 and LArSoft is implemented in the LArG4 module, which is the backbone of simulations for MicroBooNE and other LArSoft experiments. LArG4 not only tracks particles and their energy losses but also stores photons arriving at sensitive optical detectors after light propagation and electrons arriving at sense wires after

charge drift. The microphysics of attenuation and diffusion of the ionization signal is simulated, as are the scattering, reflection and absorption of scintillation photons. The resulting detected charge and light per channel are stored in the event.

TPC and PMT signal simulation and digitization are then performed by experiment-dependent modules. The outputs of these modules are waveforms, which should be comparable to those produced by the detector electronics. These can then be fed to reconstruction algorithms for further processing. The goal of the LArSoft simulation is to predict particle production, propagation and detector response as accurately as possible for both neutrino interactions and background events, such as cosmic rays.

6.2 Optical simulations

Optical simulations in LArSoft are fully described in the MicroBooNE technical note [258] and summarized here. Optical physics simulations in LArSoft can take one of two forms: full or fast simulation. Both are implemented within LArG4 and make use of its configurable physics list functionality, which was developed for this application. This allows LArSoft simulations to define a custom GEANT4 physics list from a set of physics constructors at runtime, and to select between full optical, fast optical or no optical simulation.

Full Optical Simulation

The full simulation involves stepping individual photons through the detector volume. Each photon is treated as an individual particle object. The number of photons stepped is usually reduced by a constant factor representing the optical detector collection efficiency at 128 nm, thereby scaling the photon count at production rather than detection in order to reduce time and memory requirements. For MicroBooNE this factor is around 1%, based on measurements in the Bo test stand described in Section 2.5.

The physics constructor for the full optical simulation in LArSoft has been adapted from the standard GEANT4 optical physics constructor. Default implementations

for scintillation and Cherenkov production, Rayleigh scattering and absorption in the bulk are used. A custom fast reflectivity model is implemented, whereby material boundaries have specified diffuse and specular reflectances for each material boundary type. The default implementation of wavelength-shifting processes is also included, although at present most LArSoft experiments incorporate the wavelength-shifting physics into an estimate of the optical detector collection efficiency rather than simulating it at the photon level. An exception is the LArIAT experiment, which incorporates wavelength-shifting foils with near 4π solid angle coverage [259]. In this case, the photon-level wavelength shifting functionality is required.

Properties of the liquid argon, including its optical characteristics, are loaded into LArSoft by a dedicated materials service. This was first developed to facilitate optical simulations and allows the important physical parameters to be globally accessible by reconstruction and simulation algorithms in a consistent way.

The optical physics processes within LArSoft are configured by default as follows. Scintillation production is configured with a photon momentum spectrum centered at 9.7 eV and a shape which is taken from [183]. Singlet and triplet scintillation components are included, with time constants of 6 and 1500 ns, respectively, although tensions within the literature suggest these will require finer tuning using data from LArSoft experiments [204], [208], [234], [260]. The scintillation yield is defined per particle type using an extension of the relationship shown in [261], and the absolute yield for a minimum ionizing particle is set to 24,000 photons per MeV, assuming a constant electric field strength of 500 V/cm.

Cherenkov photons are produced with yields and energies corresponding to the Frank-Tamm spectrum of Cherenkov radiation, given a continuous parameterization of the liquid argon refractive index derived from the references in [192]–[194]. Rayleigh scattering is enabled, with the scattering length specified over the range of photon energies from 1.8 eV to 10.8 eV, and is 90 cm at the peak of the argon scintillation spectrum [190]. Tension with the experimental value from [191] suggest this may require further tuning using MicroBooNE data. The bulk absorption length is set to 2000 m as a placeholder. Depending on the purity achieved, shorter absorption

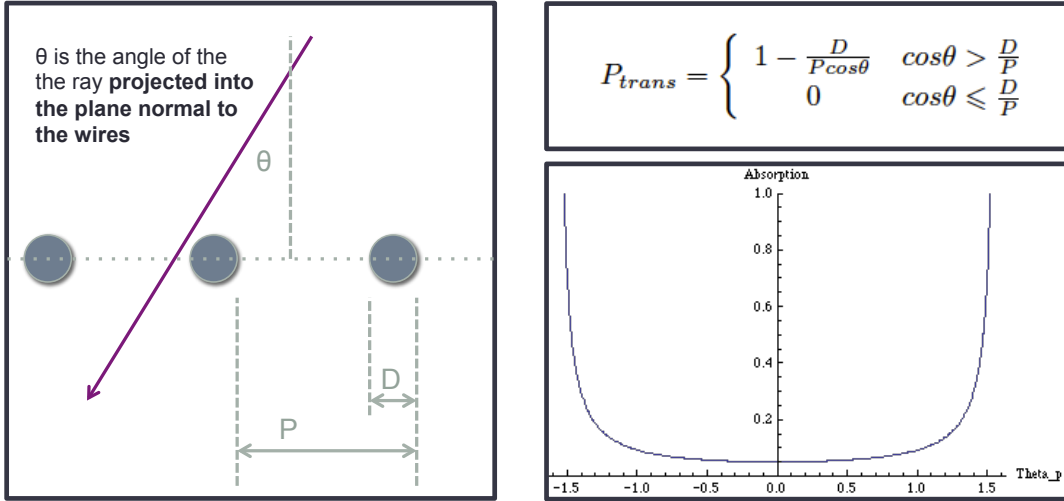


Figure 2.6.1: Illustration of the simple treatment of wire plane absorption in LArSoft.

lengths may need to be used to tune the optical simulation by future experiments.

A simplified reflectivity model is used, whereby each type of boundary in the detector is supplied with a wavelength-dependent total reflectivity and specular/diffuse reflection fraction. For preliminary studies only the steel/argon boundaries at the edge of the cryostat are reflective, with all other surfaces, including wires, field cage, etc., being opaque. The steel/argon boundaries have a total reflectance of 25%, of which 50% is specular, with these numbers being taken from [262].

A custom treatment of semitransparent surfaces is incorporated. For a given surface, any angularly dependent transmission spectrum can be applied. This allows a modeling of the non-uniform angular dependence of photon transmission through the detector wire planes. LArG4 includes derived classes which implement optical attenuation by one or many planes of cylindrical wires which are assumed black to 128 nm light. A cartoon of the wire plane opacity model is shown in Figure 2.6.1.

Photons are counted at detector volumes whose names match a strings supplied to the LArSoft geometry service. These volumes may represent PMTs or another element defined as optically sensitive, for example, a wavelength-shifting surface. At geometry construction time, the volumes matching the appropriate name string in the GDML file are assigned optical detector IDs and become sensitive within the LArSoft

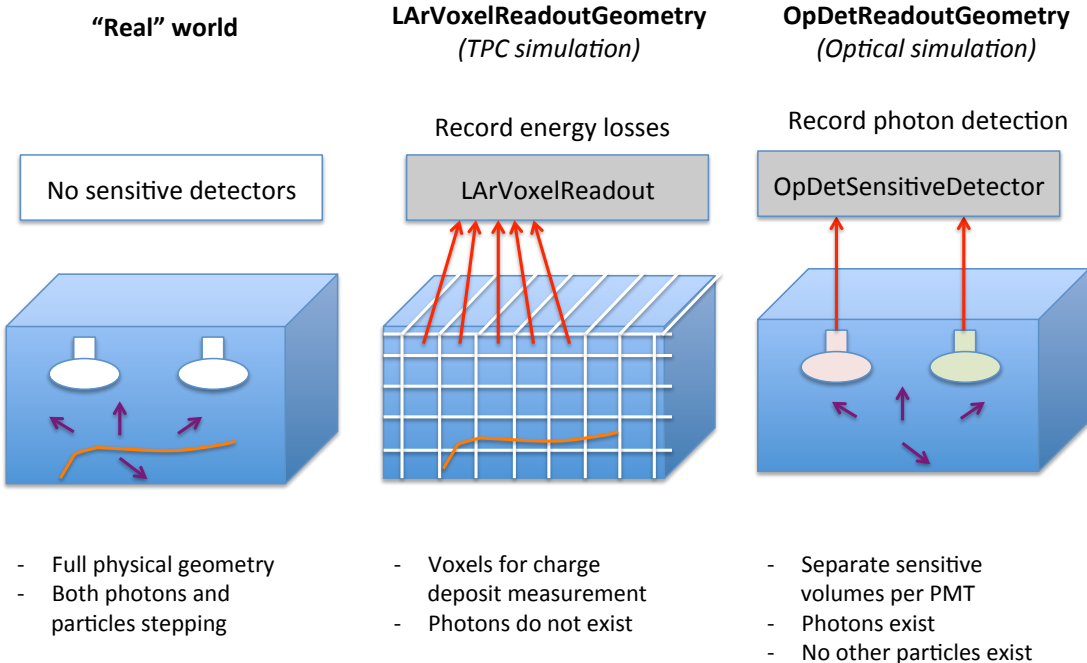


Figure 2.6.2: A cartoon which illustrates the three parallel simulation geometries used in the LArSoft GEANT4 implementation.

simulation.

The sensitive elements are placed in a separate GEANT4 parallel world geometry (one of three used in LArSoft - see Figure 2.6.2). Only photons are tracked in this geometry, which ensures that only they can trigger the optical detection process. This scheme also means that photon step size is not limited by the TPC voxel size, which provides a significant performance improvement. Upon photon detection, tracking of the photon is stopped and the arrival time and detection location are stored in a detected photon table. At the end of the run, this table is queried to generate simulated photon data products to store in the event. The same table is filled by the fast simulation method, and hybrid fast and full simulations can also be run.

Fast Optical Simulation

Since the number of optical photons generated per event is of order tens of millions per GeV, full optical simulation is a very computationally expensive process. However, since scintillation in argon is isotropic, the visibility (defined as the fraction of

generated photons which will reach a given optical detector) can be pre-calculated at each point in the detector. The fast optical simulation takes this approach.

The liquid argon volume of the detector is coarse-grained into optical voxels, the size of which must be chosen to be smaller than the resolution of the optical system but can be significantly larger than the TPC voxelization scale. The optical fiducial volume incorporates all regions which are visible to the optical system, which in general extends further than the TPC fiducial volume. By default, the complete cryostat volume is optically voxelized, although if there are invisible regions for a specific detector then a smaller optically active volume can be specified.

A dedicated run of the full optical simulation can be made to create a lookup table which contains the visibility of each voxel to each optical detector. This run creates a specified number of isotropic 128 nm photons, uniformly distributed across each voxel volume at time $t=0$. These photons propagate and are detected using the full photon simulation. After photon propagation, the number of detected photons at each optical detector is used to build the optical visibility lookup table. This process is automated by a dedicated photon visibility service, which communicates with the event generation, simulation and analysis parts of the chain to ensure they are correctly configured when a table-building job is run.

Once the visibility table has been generated, the probability that a given 128 nm photon will reach a specified optical detector can be quickly accessed using the photon visibility service, which is available to both simulation and reconstruction modules. The LArG4 physics list can be configured to include the fast optical physics constructor, which implements the lookup-based fast scintillation process. The generation parameters for scintillation light in the fast scintillation process are equivalent to those used in the full simulation. However, instead of placing optical photons onto the GEANT4 particle stack, detected optical photons are inserted directly into the detected photon table probabilistically, based on the visibility of the detector location where the scintillation occurred. The arrival times of the photons are also smeared based on the distribution of production times. The sum of detected photons from each voxel where scintillation emission occurred gives the total optical detector response.

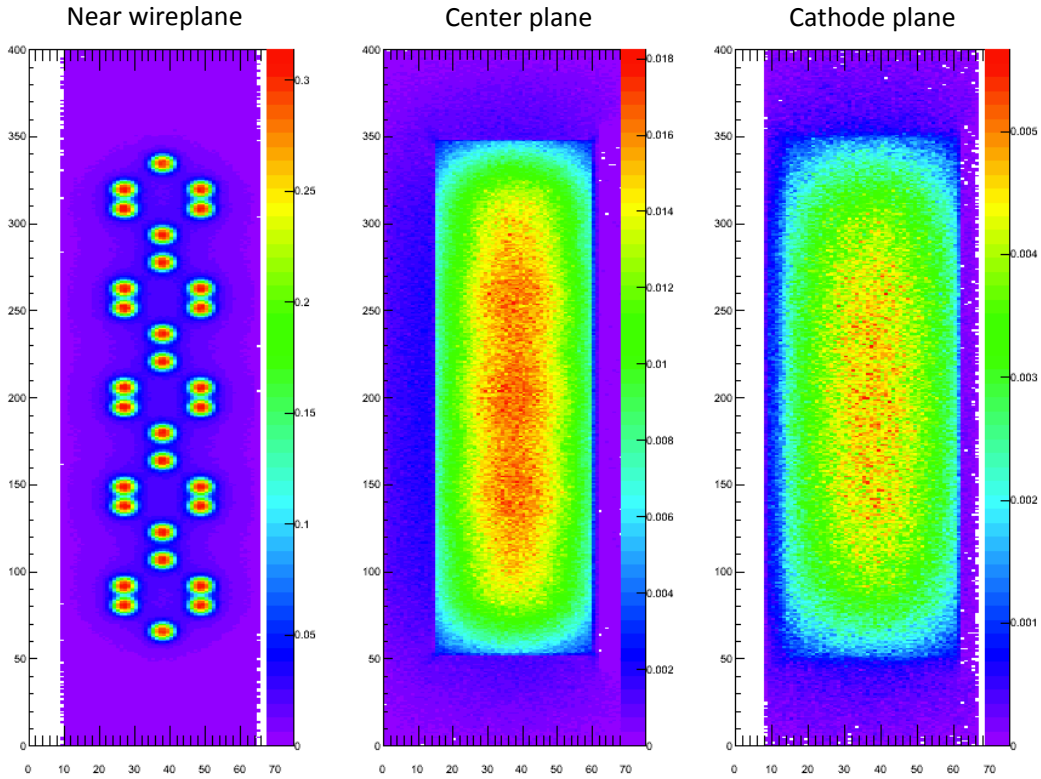


Figure 2.6.3: An example of slices through an optical visibility table. This shows the visibility at various points in the MicroBooNE detector. This plot was made from the optical visibility table using the optical library analyzer module.

The photon library is both geometry- and voxelization-scheme-specific, and changes to either require a full regeneration, which is a computationally intensive task. The effects of Rayleigh scattering, reflection and absorption are also built into the visibility table. Changes to the argon scintillation production properties and optical detector efficiencies, on the other hand, can be made without regenerating the table.

Tools for Optical Simulations

There are several tools in LArSoft for optical simulation validation and basic analysis. The photon counter module is an analyzer which produces analysis trees and histograms representing the properties of the detected photons in each optical detector. The module extracts per-optical-detector and per-event information and can be used for both full and fast simulation outputs. This same module is also used to

generate the optical visibility library used by the LArSoft fast simulation.

There is a light source event generator which can be configured to generate photons at a specified wavelength and with a specified geometry and emission time. Optionally, the light source can be configured to step through each optical voxel event by event or through a custom set of arbitrary geometrical configurations specified in a text file. This event generator is particularly useful for investigating the optical response to different event geometries and is used in the generation of the photon visibility library.

A library analyzer module exists to produce detector visibility maps and other histograms based on the loaded visibility library. This module is used to validate the optical library and obtain information about the detector response to light deposits at different points. Some histograms produced by this module for the MicroBooNE optical library are shown in figure 2.6.3.

6.3 Optical event reconstruction

Optical reconstruction of liquid argon events is also performed within LArSoft. In order to fully exploit the data produced by the detector, reconstruction algorithms must be performed on TPC data, on optical data, and then on the combination.

As discussed in Section 1.2, a primary goal of the MicroBooNE optical system is to tag cosmic background events which pile up on TPC frames containing beam events. Measurements of the cosmic ray rate made in LArTF [263] show that MicroBooNE will observe cosmic muons at a rate of approximately 5 kHz. This corresponds to $6 < N_\mu < 11$ cosmic muons per frame, at 68% confidence level.

There are several ways to tag on-beam and off-beam events. First, one can reject clear volume-crossing tracks and those which have charge arrival times which would be unphysical for a beam event. The remaining background, which includes most neutron- and gamma-induced activity as well as several difficult muon topologies, must be removed by either high-level TPC analysis or by tagging the sub-event times using the optical system and rejecting off-beam-time activity.

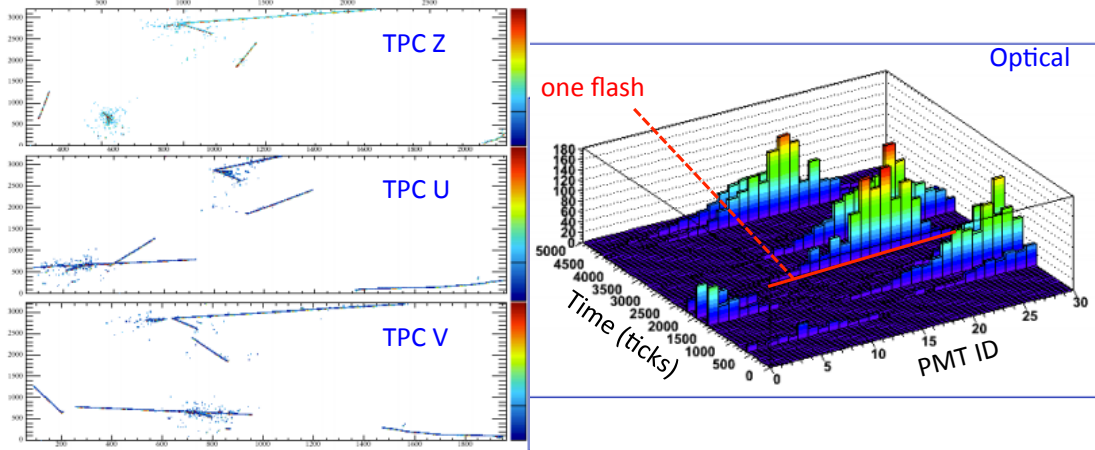


Figure 2.6.4: A sample signal+background event simulated in MicroBooNE, showing both TPC and PMT information.

Figure 2.6.4 shows the expected optical and charge information recorded for a typical neutrino event in MicroBooNE. The TPC view shows several sub-events at different positions in the detector, one of which is a neutrino-induced signal event. It is difficult to distinguish which sub-event this is using the TPC alone. The optical information shows photons arriving at different PMTs correlated in time. The light arrives in several "flashes" which illuminate many PMTs.

To optically tag a TPC sub-event, the pattern of light observed by the optical system at a given time must be matched to a charge distribution for a sub-event in the TPC. The first step of this process is to associate activity in different PMTs which is believed to be produced by the same sub-event, and from this extract low-level geometrical information on where the optical event occurred in 3D space. This task is accomplished by the LArSoft **FlashFinder**. This module accepts digitized PMT waveforms as input and performs pulse finding and matching, producing **OpFlash** objects as output. An **OpFlash** has a center and size in 3D space as well as an association to all constituent pulses. The 3D object can then be compared either with 3D reconstructed TPC objects or projected back into the TPC coordinate system. The relationship between the various coordinate systems involved in TPC-to-PMT correspondence is shown in Figure 2.6.5.

Flash finding takes place in several stages. First, pulses are identified in the

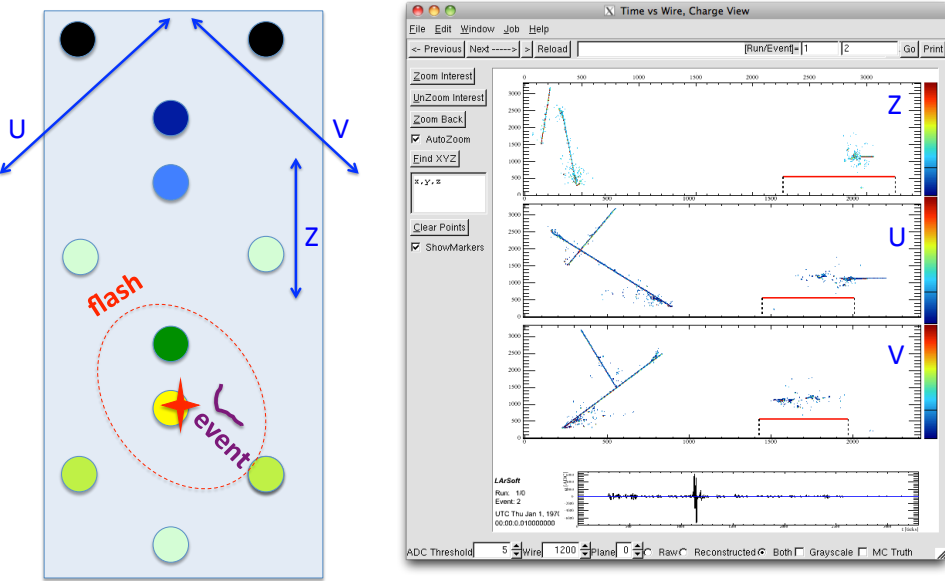


Figure 2.6.5: Left: cartoon showing the relationship between the flash and TPC coordinate systems. Flashes exist in 3D space, their position being determined by light distributed on PMTs. TPC information exists in projections of this space. Right: event display showing a beam + background event, with the reconstructed on-beam flash projected onto the TPC coordinates. For this event, it is clear which sub-event is neutrino induced. In more general cases, matching flashes to TPC activity requires more advanced algorithms.

digitized PMT readout frames, and their areas, times and widths are extracted. These processed pulses are stored in the event as optical hits (`OpHits`) and the information contained within them is used for the remaining steps of flash finding.

Next, broadly time-binned accumulator histograms are filled for the whole event to isolate regions in time where significant optical activity occurred. Two accumulators are used with half-bin offsets to prevent loss of pulses through bin straddling. If a bin in the accumulator crosses a specified charge threshold, all of the contributing `OpHits` are collected into a proto-flash. Because there are two accumulator histograms, one `OpHit` may be in up to two proto-flashes. To relieve this degeneracy, the proto-flashes are sorted from largest to smallest, and each in turn is allowed to lay a unique claim to the `OpHits` it contains, which are prevented from appearing in each subsequent proto-flash. This removes duplicate proto-flashes, which fall below threshold when

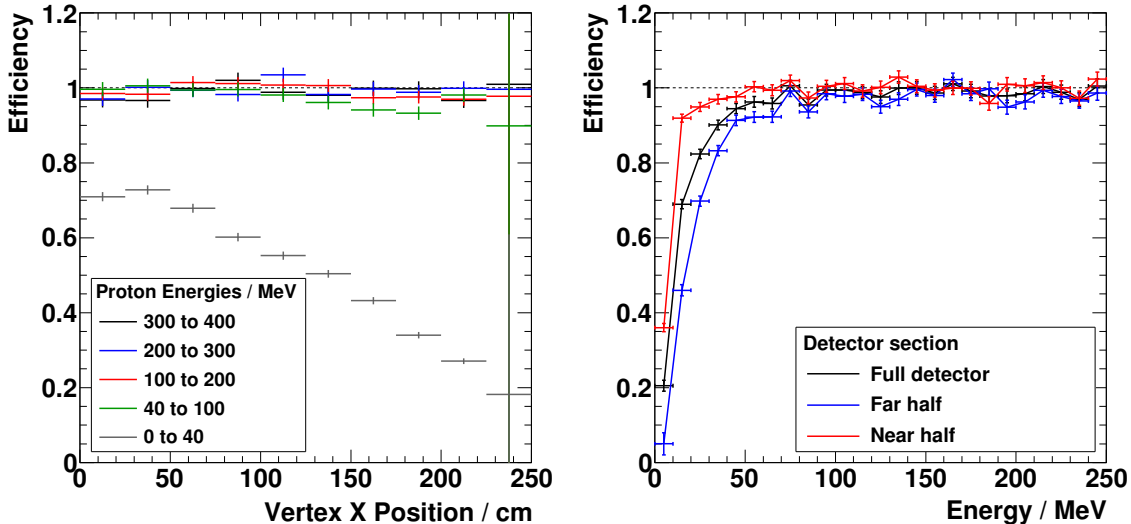


Figure 2.6.6: The flash-finding efficiency in MicroBooNE for low-energy (0-400 MeV) single protons distributed uniformly over the detector. Left: efficiency versus drift coordinate (PMTs are at $X = 0$ side). Right : efficiency versus energy.

their overlapping `OpHits` are subtracted.

Next, since each bin in the broadly binned accumulator, which maps to a single proto-flash, may contain several actual flashes, the `OpHits` are clustered within the proto-flash based on their time-widths. Starting with the largest `OpHit`, nearby smaller ones are associated to it. This collection is labelled as a flash, and clustering is repeated for the remaining unclustered `OpHits`. Collections which do not cross a specified charge threshold (set by default to 2PE) are discarded.

The `FlashFinder` has been tested on several classes of events. Of particular interest are the efficiency of the system for observing flashes as a function of event energy; the position resolution of geometrical information carried by the flashes; and the calorimetric information which can be obtained from scintillation light.

These properties were assessed with a sample of 0-400 MeV single-proton events. This event class was chosen because the tracks are highly ionizing and thus the light emission is well localized in space. This means that the performance of the optical system could be assessed without assumptions about the reconstruction performance of the TPC. For more lightly ionizing tracks, such as muons, which are extended light sources, the information acquired about the event using the PMT system will

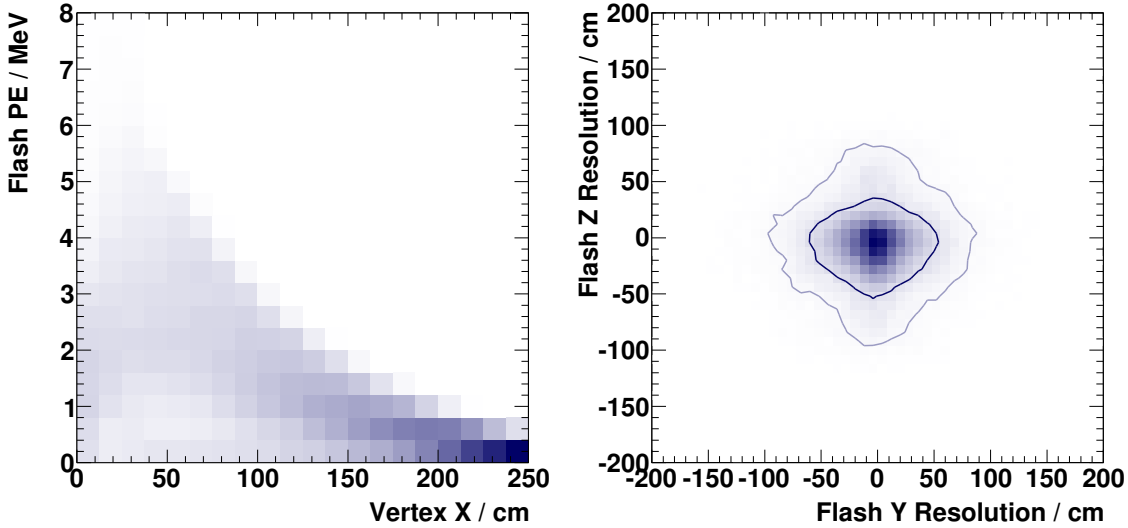


Figure 2.6.7: Flash properties for low-energy proton events. Left: light yield versus drift position. Right: Flash transverse position resolution. The two contours contain 68% and 90% of the events, respectively.

be dependent on how well the track is reconstructed using the TPC.

Figure 2.6.6 shows the efficiency for finding at least one flash in the single-proton events. This efficiency is a function of both the event energy and the vertex position, the latter representing the track-to-PMT distance in MicroBooNE. The system design specification of high efficiency for 40 MeV tracks is met over the full detector. Nearer to the wire plane, good efficiency is observed for lower energies. The calorimetric performance of the system also depends on the vertex position. Figure 2.6.7, left, shows the number of photoelectrons detected per MeV of light produced for events with $100 \text{ MeV} < E_{\text{true}} < 400 \text{ MeV}$.

Transverse position resolution of the optical system is a key parameter for matching tracks to flashes for cosmic-ray rejection. A very simple way to estimate the flash position is to evaluate the geometric center-of-gravity (COG) of the collected photons in the y and z directions. This can be used to seed more advanced, likelihood-based reconstructions which exploit more fully the information contained in the detected photons. The transverse resolution obtained using the COG approach for events with $100 \text{ MeV} < E_{\text{true}} < 400 \text{ MeV}$ is shown in Figure 2.6.7, right, and is around 50 cm, which is of the same order as the PMT-to-PMT spacing.

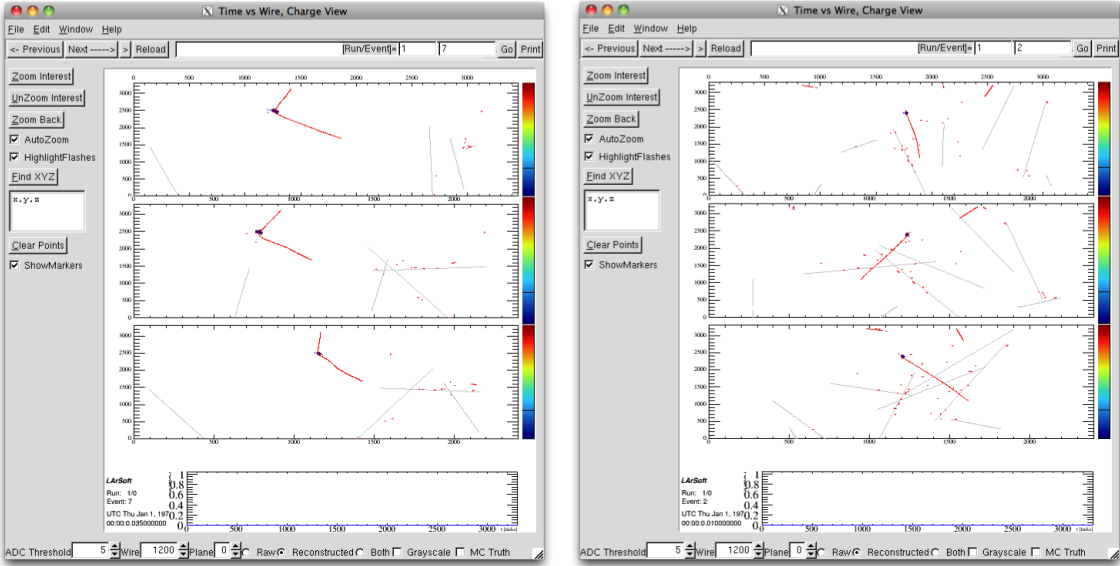


Figure 2.6.8: Two examples of cosmic-ray rejection using likelihood-based flash-to-track association. The neutrino vertex is shown in blue, flash-compatible tracks are shown in red, and flash-incompatible tracks are shown in gray.

Once flashes have been identified, the next stage in optical event reconstruction is to match them to reconstructed TPC sub-events. One effective method of rejecting non-beam activity is to discard any reconstructed tracks which, were they related to a beam-induced event, would have produced too much light on one or several PMTs to be compatible with a flash which was observed in time with the beam. Using this technique, preliminary studies have shown that 90% of long reconstructed cosmic tracks can be rejected. Shorter tracks corresponding to delta rays or other electromagnetic activity are not effectively tagged, but can likely be rejected by proximity to long muon tracks in later analysis.

Figure 2.6.8 shows two typical neutrino with cosmic background events. The lines shown are reconstructed Bezier Tracks (Section 6.4). The neutrino vertex is shown in blue, flash-compatible tracks are shown in red, and flash-incompatible tracks are shown in gray. This technique is still in development, but shows significant promise for cosmic-ray rejection in MicroBooNE.

6.4 TPC event reconstruction

Due to the fine spatial resolution of LArTPC detectors, the complex nature of the detected events, and the nontrivial coordinate systems in which 3D information is recorded, LArTPC event reconstruction is a complicated and unsolved problem. This section describes the `BezierTracking` method, which was the first LArSoft algorithm capable of curved track reconstruction and remains one of a small number of available 3D tracking algorithms as MicroBooNE begins to take first data. The method is summarized here, and details can be found in the MicroBooNE technical note [264].

LArSoft TPC event reconstruction begins with `Hit` finding. A `Hit` is a reconstructed pulse on a wire, induced by moving charge. The raw pulses have a shape dictated by the field and electronics response, which is removed by deconvolution. The resulting signals are fit to Gaussians and the total integrated charge, amplitude,

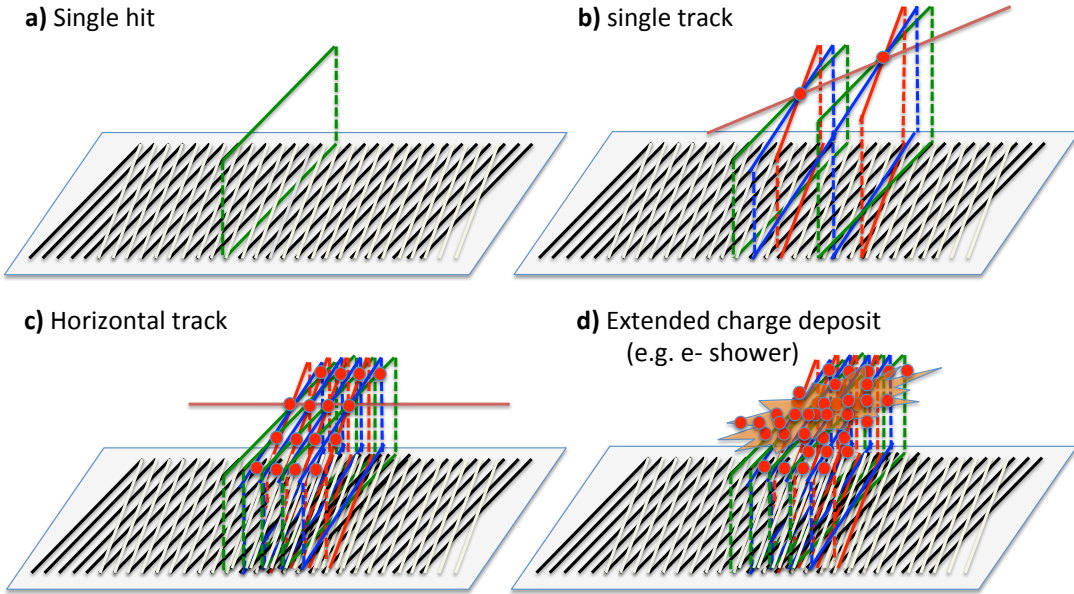


Figure 2.6.9: (a) A hit on a wire plane represents charge along a line in 3D space. (b) For easily reconstructable topologies, `Hits` across three views can be matched in time to form `SpacePoints` marking 3D charge deposition points. (c) For tracks in unreconstructable directions, such as along the wire planes, reliable `SpacePoints` cannot be formed due to incompleteness of the wire³-time coordinate system. (d) for extended objects such as showers, the problem of `SpacePoint` aliasing becomes even more severe. In all cases, black and grey lines represent wires, red/green/blue lines represent `Hits`, and red dots represent `SpacePoints`.

channel and time can be extracted. When the time of interaction, t_0 , is known, a `Hit` represents charge produced at some point along a line in 3D space, as shown in Figure 2.6.9a.. A minimally ionizing particle traversing the detector induces `Hits` on all TPC wires it crosses with high efficiency.

The fundamental problem of LArTPC event reconstruction is translating the information from 2D `Hits` into a 3D image. Several approaches to this problem have been taken, primarily distinguished by when in the process the jump is made from the 2D TPC coordinate space into real 3D space.

The earliest the 2D to 3D transition can be made is at the `Hit` level. `Hits` occurring at similar times can be matched together to form a set of 3D `SpacePoints`, which represent spatial positions where the charge may have originated (Figure 2.6.9b). Due to the incomplete information stored in the wire plane projections, aliased space points are also produced where no charge was deposited. These aliased points can be problematic for pattern-finding algorithms, especially for tracks in difficult directions, such as coplanar with the wires (Figure 2.6.9c). Since the relationship of `Hits` to `SpacePoints` is many-to-many, associating charge density to positions in 3D space using `SpacePoints` is not trivially possible. These problems are further compounded for objects covering a large 3D region, such as electromagnetic showers (Figure 2.6.9d). Despite these caveats, one approach to 3D reconstruction is to seek `SpacePoint` patterns using algorithms designed to mitigate the effects of aliasing and charge sharing, such as the LArSoft 3D Kalman filter `KalmanSPS`.

A second approach is to produce 3D hypotheses directly using projective 2D information. This avoids aliasing by making assumptions about the continuity of the object being fitted, which forbids unphysical `Hit` combinations. This is the approach favored by the 2D projective Kalman filter `KalmanHit`. A third approach is to use only the `SpacePoints` which are in reliably un-aliased regions and use projective 2D information to connect them. This is the basis of `BezierTracking`.

The first step in the `BezierTracking` process is `SeedFinding`. The seeding software developed for this purpose is highly efficient, and as such has also become the common starting point for most other LArSoft tracking algorithms. A `Seed` repre-

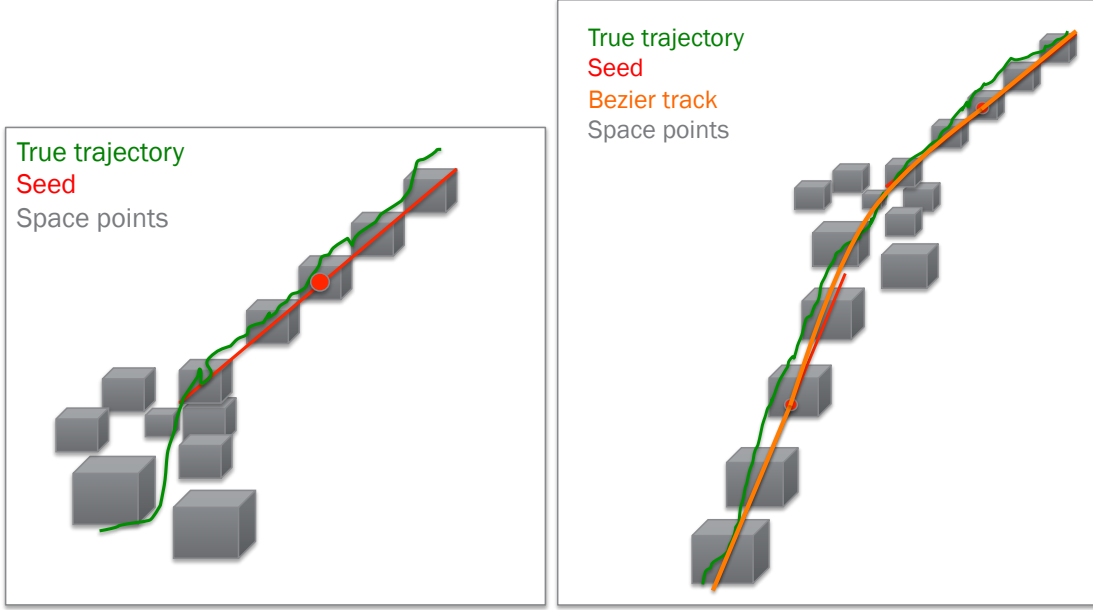


Figure 2.6.10: Cartoon showing a seed (left) and bezier track (right), overlaid on the true particle trajectory, and the relevant set of possible `SpacePoints` obtained from the TPC.

sents an unambiguous, quasi-straight, 3D region of event activity, defined by a 3D point and a vector with a length extending in both directions. This is shown as a cartoon in Figure 2.6.10, left. `Seeds` are reconstructed by the LArSoft `SeedFinder` algorithm, which identifies regions where the TPC activity across all planes in the TPC indicates an unambiguous straight direction and provides information about these sections as instances of the `Seed` data product.

An event which has been successfully seeded is shown in 2D and 3D event displays in Figure 2.6.11. In the 2D view of Figure 2.6.11, left, `Seeds` are shown projected into each plane as straight lines with the central position marked by an empty circle. In the 3D view of Figure 2.6.11, right, `Seeds` are shown as white lines with white spheres at the center. The efficiency of the `SeedFinder` has been quantified using a sample of single muons with energies between 100 MeV and 2 GeV, produced as part of the MicroBooNE *Monte Carlo Challenge* MCC5. As shown in Figure 2.6.12, the efficiency is very high for all but the shortest tracks. The efficiency was also quantified for simulated through-going cosmic muon tracks [265], and was 100%, within the statistical uncertainties of the study.

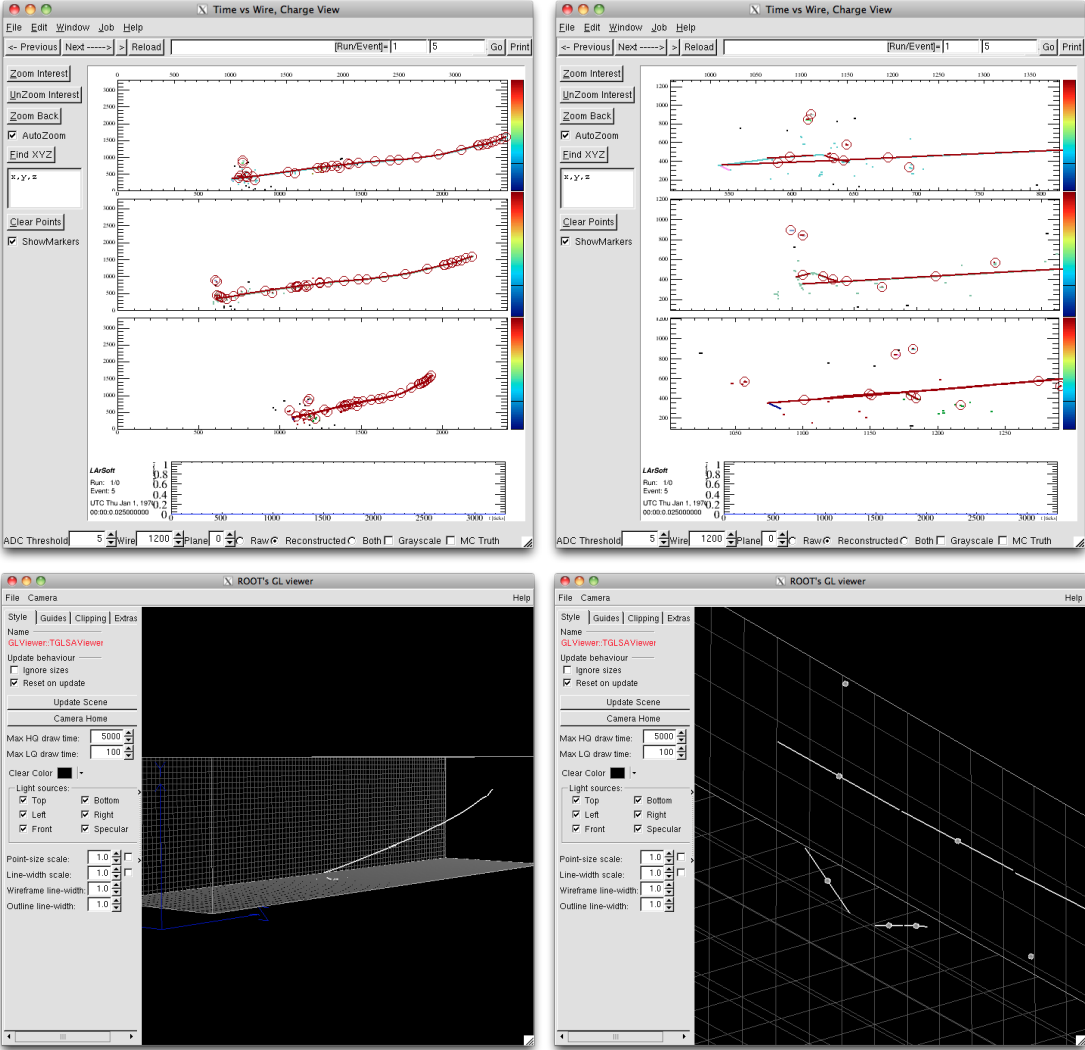


Figure 2.6.11: A seeded LArSoft event, shown in 2D (left) and 2Ds (right). The full event is shown in the upper views, and a zoomed-in section is shown in the lower ones.

A **BezierTrack** is a continuous trajectory in 3D space which is made by connecting **Seeds**. The unambiguously determined segments are used to guide the track object through areas where there is aliasing or pileup. A cartoon is shown in Figure 2.6.10, right. The method of connecting the **Seeds** is to use cubic or quartic 3D bezier curves, as shown in Figure 2.6.13. A particular connection between **Seeds** is valid if and only if it can be made without any point on the trajectory being more than a specified distance, the *TrackResolution*, from at least one hit in every view. After connecting all allowable pairs of **Seeds**, the smooth segments are assembled into a continuously

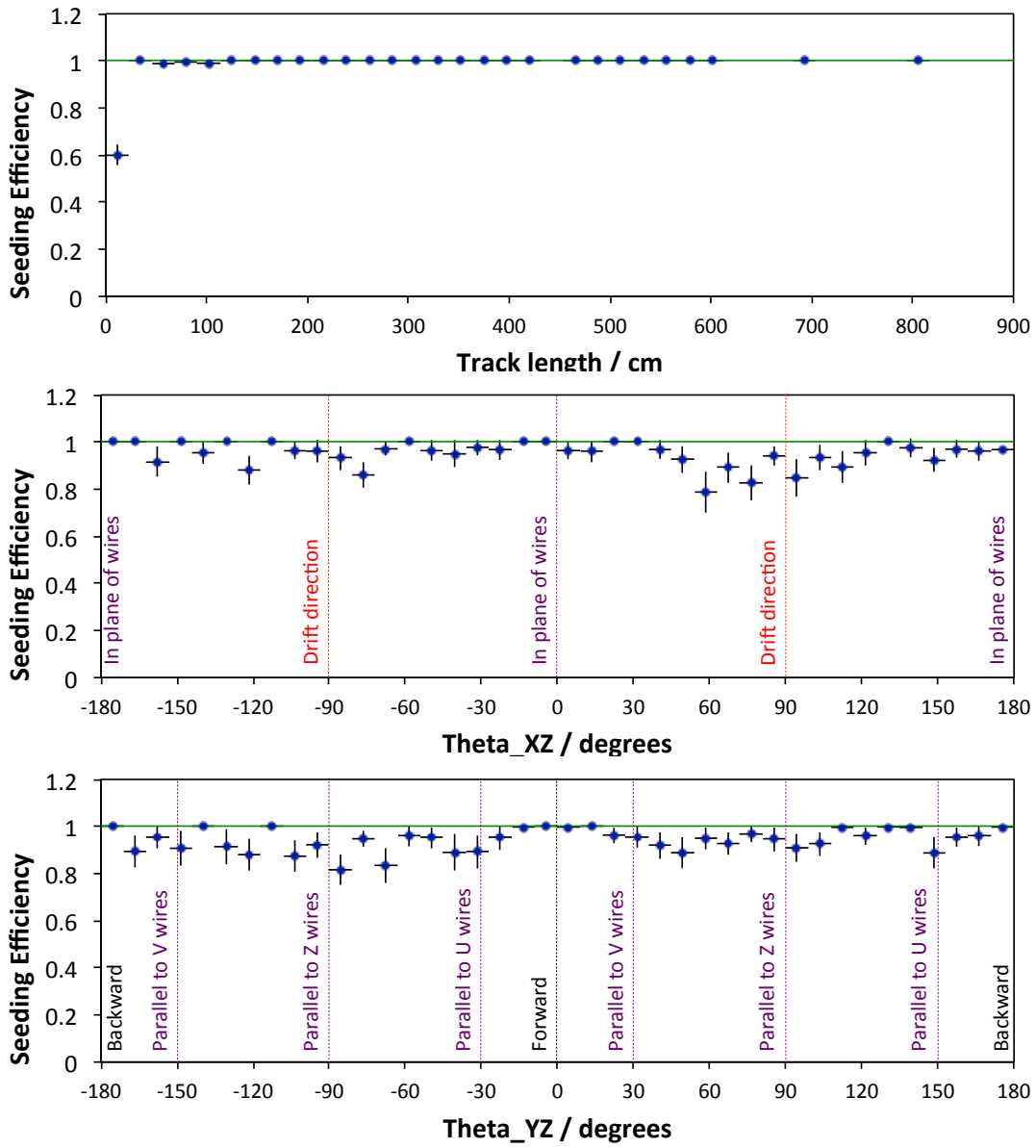
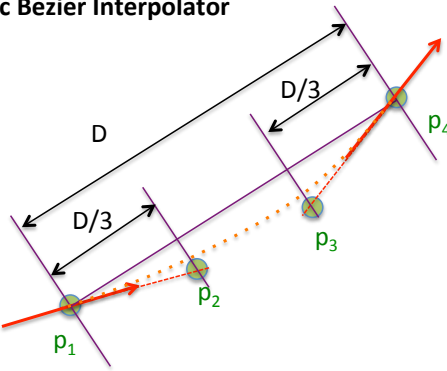
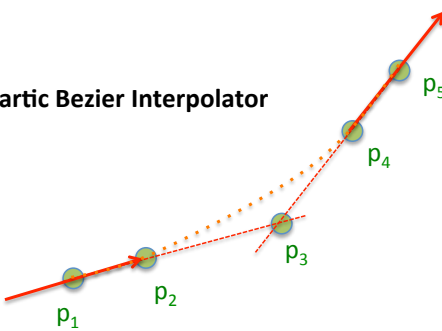


Figure 2.6.12: Plots showing the efficiency of seed-finding on low-energy single muons. The seed finding efficiency is close to 1 for all tracks longer than 20 cm.

Cubic Bezier Interpolator

$$0 < s < 1$$

$$V(s) = p_1 (1-s)^3 + 3 p_2 s(1-s)^2 + 3 p_3 s^2(1-s) + p_4 s^3$$

Quartic Bezier Interpolator

$$0 < s < 1$$

$$V(s) = p_1 (1-s)^4 + 4 p_2 s (1-s)^3 + 6 p_3 s^2 (1-s)^2 + 4 p_4 s^3 (1-s) + p_5 s^4$$

Figure 2.6.13: Cubic and quartic bezier interpolators which can be used in bezier tracking.

interpolated trajectory. The resulting `BezierTrack` object is a geometrical entity which can be queried for its position and direction in 3D space, or projected into the 2D wire plane views, at any point along its length.

After assembling sets of `Seeds` into `BezierTracks`, pairs in the `BezierTrack` collection are tested for overlap, and in some cases are merged. `BezierTracks` which have been reconstructed as overlapping, or as almost touching, can be combined with tolerances specified by user-configurable parameters. Following track joining, bezier vertexing is performed, extrapolating distinct tracks to common vertices. Finally, bezier calorimetry can be used to obtain the pitch-corrected dQ/dx value as a function of the coordinate along the track.

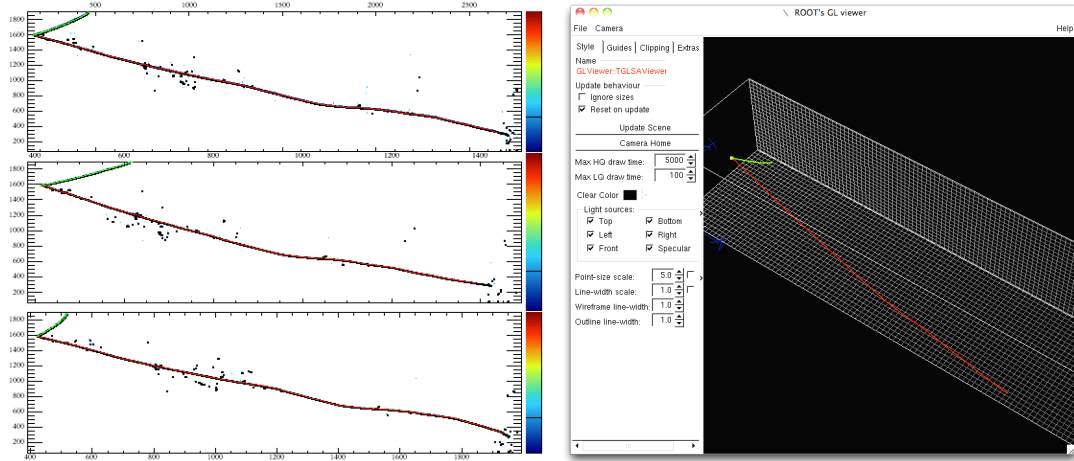
Two examples of simulated MicroBooNE events reconstructed with `BezierTracking` are shown in Figure 2.6.14. The first example shows a CCQE-like event. Both the muon and proton tracks are well reconstructed and the vertex is found. The second example shows a cosmic background spill with many through-going muon tracks.

In all but one of the cases, the full track length is reconstructed in 3D, despite the crossing topologies and pileup in the 2D projections.

The performance of the `BezierTracker` was quantified systematically using 7991 simulated, fully contained muons as part of MCC5. The standard reconstruction chain was applied, including wire signal processing, `HitFinding`, `FuzzyClustering`, `SeedFinding` and `BezierTracking`. To count a track as well reconstructed, the start point must fall within 5cm of the true vertex, and the reconstructed track must run for more than 50% of the true track length. The total efficiency of the Bezier tracker under these conditions was 80%. A tighter requirement of 90% track length reduces the efficiency from 80% to 66%. These losses can be mitigated in the future by more effective partial-track stitching. Further requiring a track angle match within 10 degrees at the vertex leads to an efficiency of 53%. Figure 2.6.15 shows the performance of the algorithm with and without the initial angle requirement. These plots were made as part of a tracking algorithm cross-comparison study by Sowjanya Gollapinni (KSU).

LArTPC event reconstruction is a complex problem to which many approaches can be taken. `SeedFinding` is the first step in most LArSoft tracking algorithms, and the LArSoft `SeedFinder` appears to perform well for a large class of important events. The `BezierTracking` algorithm shows promise for long track reconstruction, although to perfect its performance further development of both the tracker and upstream clustering algorithms are likely required.

CCQE-Like



Cosmic ray background

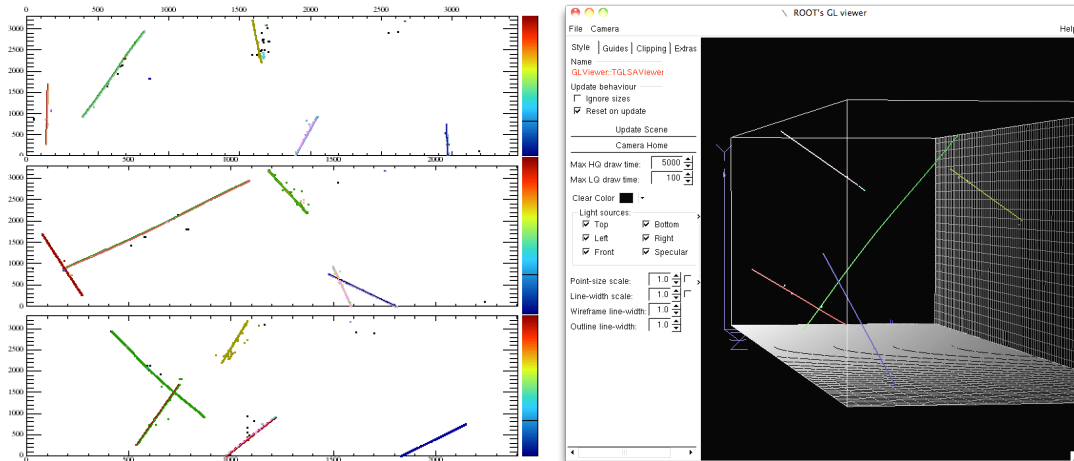


Figure 2.6.14: Two examples of simulated MicroBooNE events, reconstructed using the **BezierTracker** algorithm. 2D projections showing the **Hits** in the event are shown on the left with the reconstructed bezier track overlaid in color. On the right, a 3D event display shows the reconstructed **BezierTracks** in 3D space. The top event shows a CCQE-like muon+proton event. The lower event is a simulated MicroBooNE cosmic background spill.

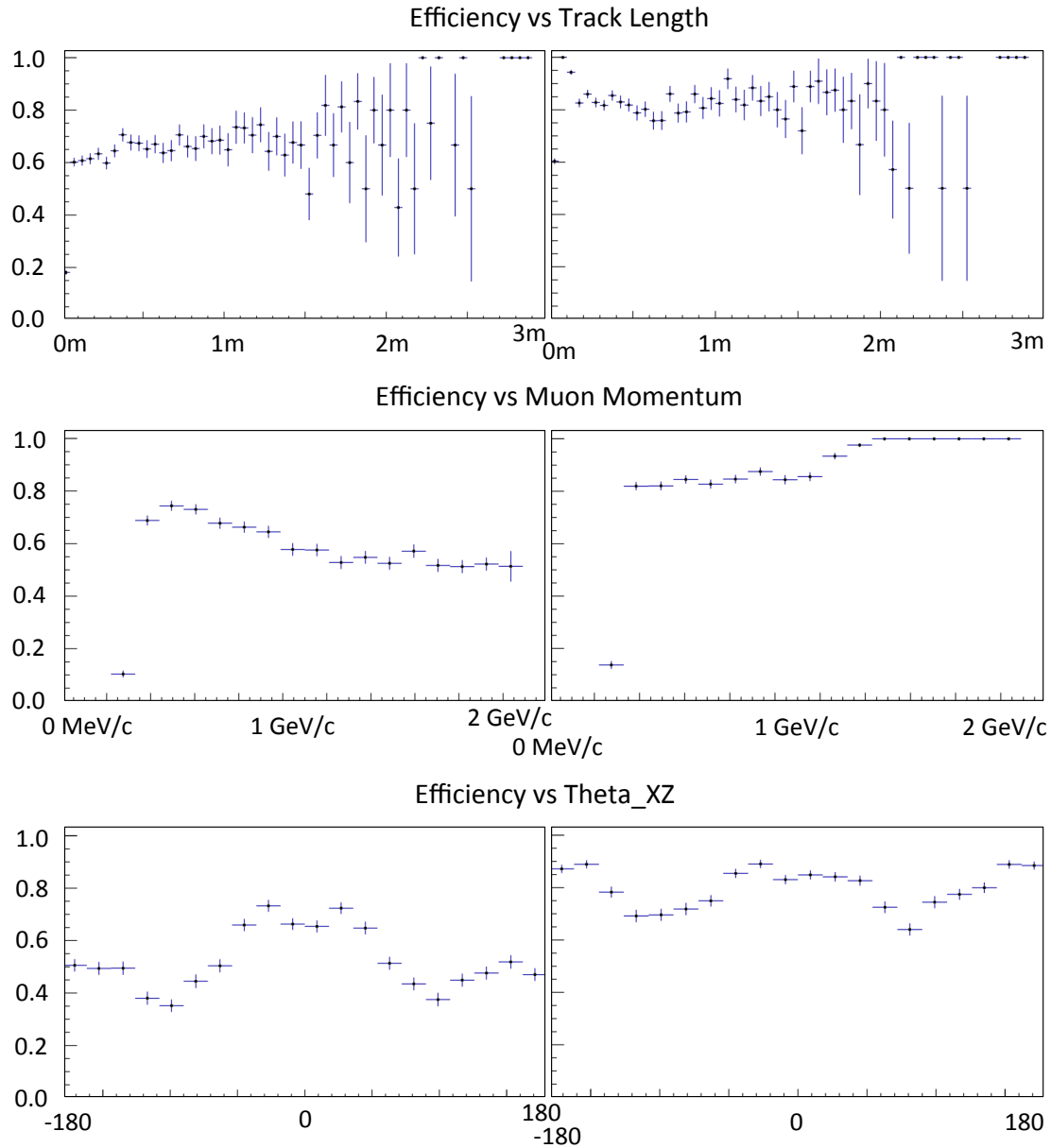


Figure 2.6.15: Plots showing the efficiency of `BezierTracker` reconstruction on a simulated single-muon sample of 7991 contained events. A residual between the track start point and the true vertex of less than 5 cm is required, and at least 50% of the track length must be reconstructed. The left column shows the efficiency with an angle cut of 10 degrees; the right with no initial angle cut. These plots were made as part of a tracking algorithm cross-comparison study by Sowjanya Gollapinni (KSU).

Chapter 7

Conclusion to Part II

At the time of writing this thesis, the MicroBooNE experiment has been filled and purified, and its sensitive systems are being commissioned using cosmic ray data. Every optical unit is operational, has been calibrated using the flasher system, and is taking data (Figure 2.7.3). The TPC has detected its first tracks at low drift fields (Figure 2.7.2), and the ramp to nominal drift field is due to commence imminently. MicroBooNE is set to begin taking neutrino data in October 2015.



Figure 2.7.1: The author and a collaborator diligently following the progress of the MicroBooNE experiment. Photo credit: Fermilab VMS

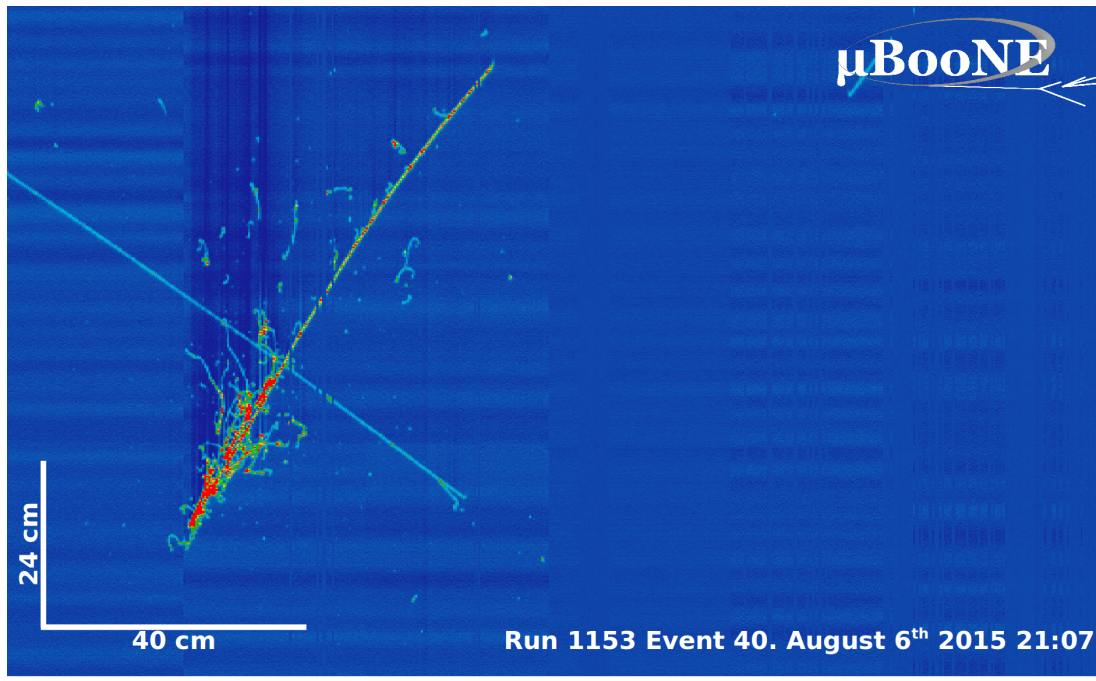


Figure 2.7.2: Two cosmic-ray induced subevents recorded during the first day of operating the MicroBooNE detector at 58 kV drift field.

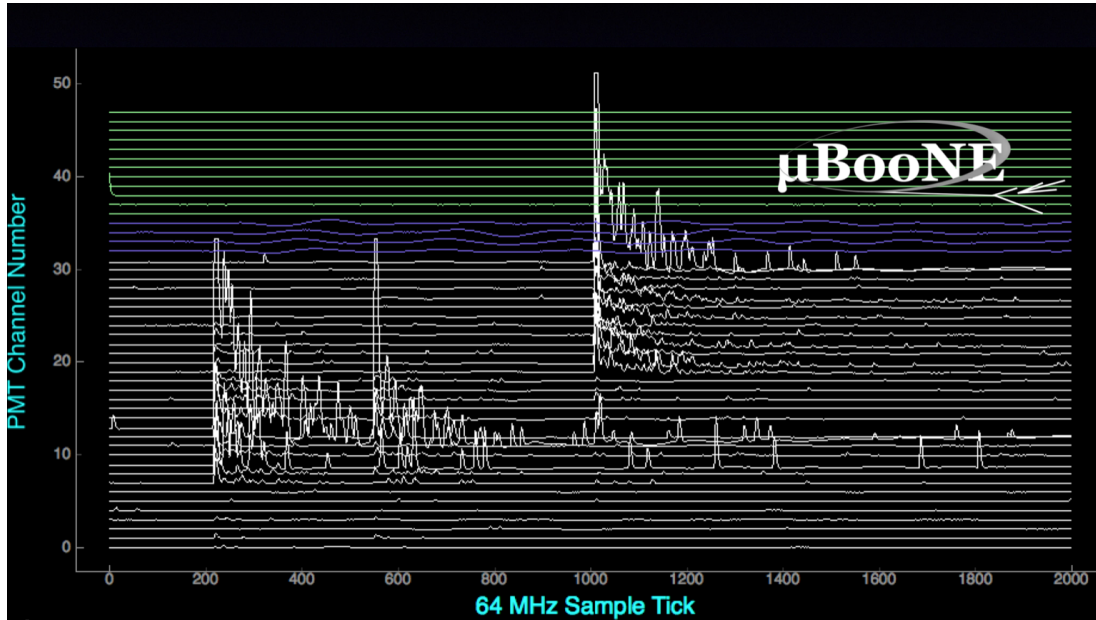


Figure 2.7.3: Waveforms induced by two cosmic ray sub-events at different spatial locations in the MicroBooNE detector, recorded using the calibrated and fully operational optical system.

Part III

The IceCube Experiment

Chapter 1

Studying Atmospheric Neutrinos with an Ice Cherenkov Detector

This part of the thesis presents a search for MSW-resonant sterile neutrino oscillations in the atmospheric neutrino flux at IceCube. This chapter introduces atmospheric neutrinos (Section 1.1), the IceCube detector and its active medium (Sections 1.2 and 1.3), then describes the event sample (Section 1.4) and some properties of the hypothetical sterile neutrino signal (Section 1.5).

1.1 Atmospheric neutrino detection

Atmospheric neutrinos are produced in cosmic-ray air showers, primarily through the decays of charged pions and kaons. They were first detected in 1965 by scintillation detectors in the Kolar Gold Fields, India [266], and the East Rand gold mine in South Africa [267]. Precision measurements of their properties were not made until the 1980s, when large underground experiments searching for proton decay [268], [269] became operational. Atmospheric neutrinos represented the main backgrounds for these experiments, so a robust understanding of their fluxes was required.

One such experiment was Kamiokande in the Kamioka mine in Japan, which measured the rates of charged-current $\nu_\mu/\bar{\nu}_\mu$ and $\nu_e/\bar{\nu}_e$ interactions [270]. The number of electron-like events was consistent with the theoretical prediction, but the number

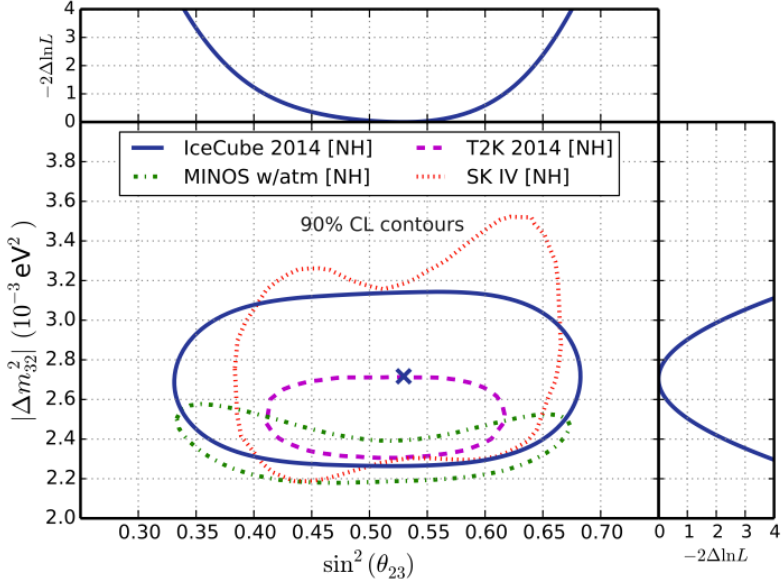


Figure 3.1.1: IceCube, T2K, MINOS and SuperKamiokande oscillation measurements, from [275].

of muon-like events was significantly low. A conclusive explanation of the atmospheric $\nu_\mu/\bar{\nu}_\mu$ deficit was provided by the SuperKamiokande (SK) experiment [271], which was massive enough to collect a large sample of multi-GeV neutrino-induced muons. In this higher energy range, the muon produced in a charged-current interaction is very collinear with its parent neutrino, so the path length between the detector and the production point around the Earth can be extracted from the muon zenith angle. By measuring the muon flux as a function of zenith, SK established with more than 6σ significance that muon neutrinos were oscillating with a large mixing angle and a mass-squared difference in the range $10^{-3} < \Delta m^2/eV^2 < 10^{-2}$ [27], [272]. Because the electron neutrino flux was consistent with the no-oscillation prediction, a two-flavor $\nu_\mu \rightarrow \nu_\tau$ oscillation was suggested. Confirmation of the result was provided by the MACRO [273] and Soudan-2 [274] experiments.

SK has continued to refine measurements of the properties of atmospheric neutrinos [276]. Good consistency with the same parameters measured to similar precision in accelerator neutrino experiments is observed [277], [278], providing a strong cross-check of the oscillation hypothesis. Evidence for ν_τ appearance has been observed statistically with a significance of 3.8σ [279]. And, in light of a non-zero value of θ_{13} ,

full three-flavor oscillation analyses have been performed [280].

The IceCube experiment at the South Pole was first proposed in order to search for ultra-high-energy astrophysical neutrinos [281], which were successfully discovered in 2013 [282]–[284]. The main background to the astrophysical signal is a large flux of atmospheric neutrinos. The detector has a target mass of around 10^9 tons making it the largest neutrino detector ever constructed – 5×10^4 times more massive than SK. Using the lowest-energy neutrinos in the IceCube sample, $\nu_\mu/\bar{\nu}_\mu$ disappearance from oscillations has been measured and found to be consistent with SK and other experiments. Figure 3.1.1, from [275], shows the present IceCube [275], SK [276], T2K [278] and MINOS [277] measurements of θ_{23} and Δm_{23}^2 .

Because IceCube has a very large mass and effective area, it can probe a higher energy portion of the steeply falling flux than previous atmospheric neutrino experiments. In the $1 \text{ TeV} < E_\nu < 100 \text{ TeV}$ energy range, where the effects of standard neutrino oscillations are negligible, the presence of sterile neutrinos could induce MSW-resonant oscillations. These oscillations would strongly modify the energy and zenith spectrum of atmospheric neutrinos at the location of the IceCube detector. A search for this signature is the focus of this part of this thesis.

1.2 The IceCube detector

The IceCube detector [285] has an active medium of $1 \times 1 \times 1 \text{ km}^3$ of glacial ice beneath the South Pole. Strings of 60 digital optical modules (DOMs) [286], which each contain a Hamamatsu R7081-02 PMT [287], readout electronics [288], flasher calibration systems [289] and HV modules inside a pressure-resistant housing are deployed into hot-water-drilled holes which penetrate $\sim 2.5 \text{ km}$ into the ice. A picture of the DOM design is shown in Figure 3.1.2, right.

The strings are arranged on a triangular lattice with approximate spacing 125 m and vertical separation 18 m. Modules were deployed during the austral summers between 2007 and 2010, with the full 86-string detector of 5160 DOMs being completed in 2010, to commence data taking in 2011. The analysis presented here uses this first

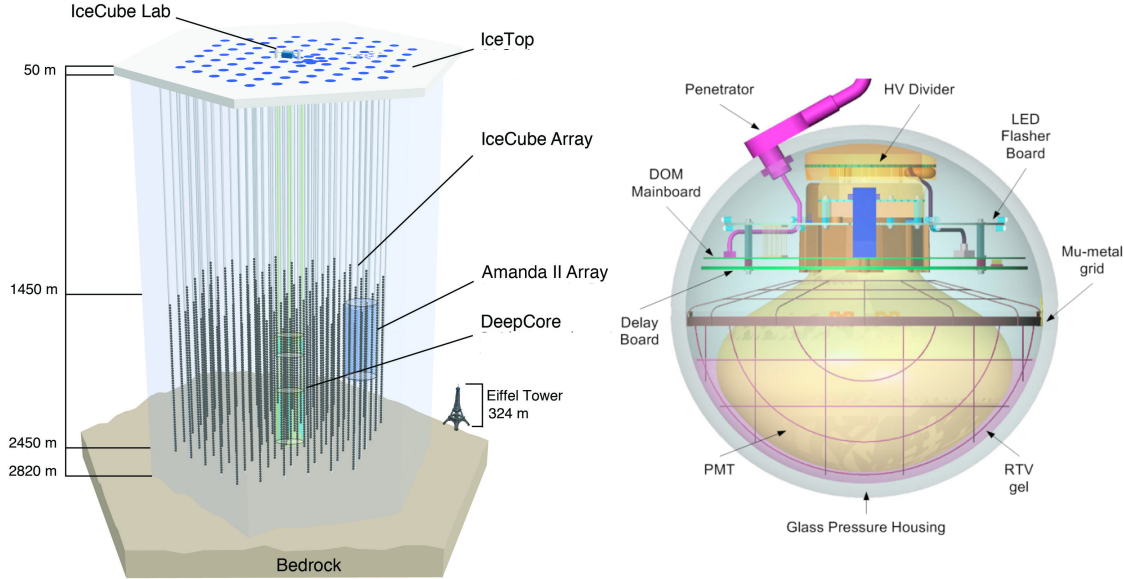


Figure 3.1.2: Left: The IceCube detector geometry. Right: Construction of the IceCube digital optical module (DOM)[292].

year of data from the detector in its 86-string configuration (IC86).

Within the IceCube lattice, a higher density infill array called DeepCore [290] is deployed, which reduces the energy threshold of the central detector region to $\mathcal{O}(10)$ GeV. Deep Core was used in the IceCube three-neutrino oscillation analysis [275]. The sterile neutrino analysis uses light detected on all the IceCube and DeepCore DOMs. Also within the IceCube volume is the AMANDA array [291], which was the predecessor of IceCube and has been decommissioned. The geometry of IceCube is shown in Figure 3.1.2, left.

IceCube measures Cherenkov light radiated by relativistic charged particles in ice. This light propagates over 100 - 1000 m distances between the production and detection points and is only visible due to the remarkably high transparency of the ice. Even with this transparency, the detector response is sensitive to ice properties which are not known *a priori*. Because the ice conditions depend on the climate history of the Earth they are not reproducible in a laboratory setting, and so characteristics of the ice must be inferred from *in situ* measurements. The following section describes various measurements that have been made of the South Pole ice and how its properties affect particle detection at IceCube.

1.3 Properties of the deep South Pole ice

This section briefly describes the optical properties of the South Pole ice that are critical to the functionality of the IceCube detector, and the optical modeling of ice properties which is implemented in IceCube simulations that are used for the sterile neutrino analysis.

Absorption and scattering

Before deployment of the AMANDA and IceCube experiments, properties of glacial ice were typically estimated by measuring the extinction of light across an extracted ice core. This method has several disadvantages, including: 1) an ice core must be removed for analysis without disturbing its transmission properties and 2) scattering and absorption both cause extinction and cannot be separated. The AMANDA collaboration developed a method to study absorption and scattering lengths using the time profiles of light detected at deployed DOMs from a distant light source [294].

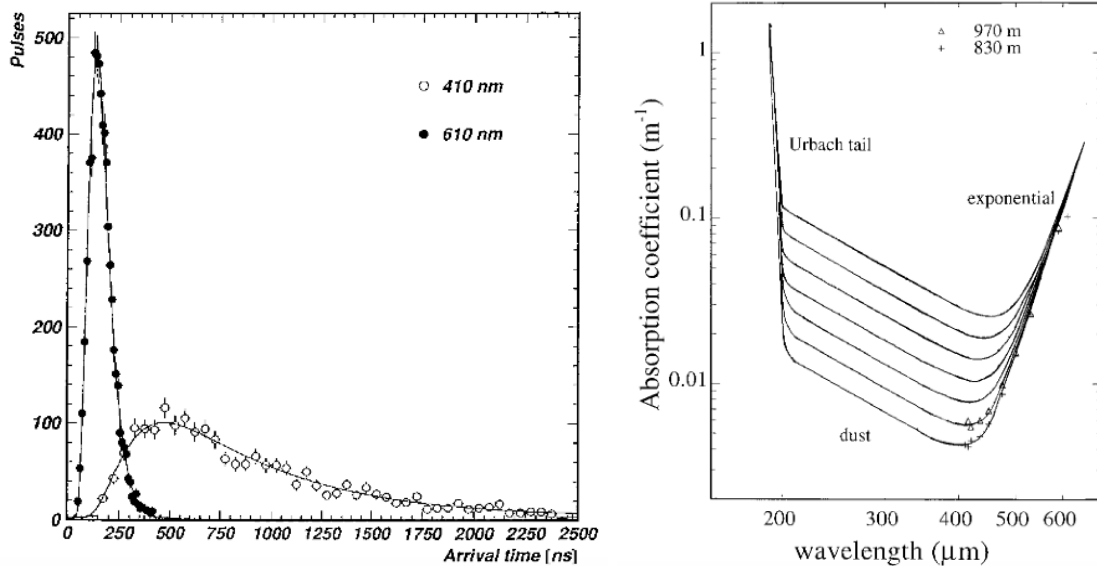


Figure 3.1.3: Left: Arrival time distributions for photons traveling between a source and emitter at different wavelengths. The different pulse shapes are a result of a different interplay between absorption and scattering. Right: absorption coefficient of photons in ice at depths of 830 m and 970 m. (from [293])

Scattering induces longer photon path lengths and so populates a late light tail. The different wavelength dependencies of these two processes means that the arrival time distribution varies with wavelength for differently colored light sources. An example at two wavelengths is shown in Figure 3.1.3, left, from [293].

Initial measurements of scattering and absorption coefficients were made using DOMs deployed between 800 and 1000 m which constitute the AMANDA-A prototype [293], [295]. Monochromatically selected pulses of laser light with 4 ns duration were injected through 1 km fibers to diffusers 30 cm below each DOM, and the light from each fiber was observed at 80 PMTs across four strings. Absorption and scattering were separated using the time dependencies of the detected photon distribution.

Absorption lengths as long as 200 m were observed, demonstrating that glacial ice is the most transparent known solid at visible wavelengths [293]. The wavelength dependence of the absorption showed deviations from the exponential spectrum of pure ice, implying the presence of absorbing impurities. The absorption spectrum between 200 and 600 nm can be modeled using a three-component model, with coefficients varying as a function of depth: at the lowest wavelengths, the exponential Urbach tail is present; at intermediate wavelengths, dust absorption with a λ^{-2} wavelength dependence; and in the infra-red, exponential absorption through multi-phonon emission. Curves from this model are shown in Figure 3.1.3, left, compared with AMANDA-A data. This functional form is used in IceCube ice models, with dust absorption strength proportional to dust concentration and the pure-ice absorption tails adjusted according to their theoretical temperature (and hence depth) dependencies.

Scattering was also studied [295]. A factor of two change in scattering length was observed over 200 m of depth, which was attributed to the pressure dependence of the bubble density in the ice. This ice was formed by compression of compacted snow, and the air bubbles trapped by this process are effective centers for Mie scattering. At high pressure, however, bubbles are unstable relative to an air-clathrate phase¹. The refractive index of the clathrate is only 0.4% different to ice [296], so it does not act as an effective scattering center. The AMANDA-A study was made in a region

¹A clathrate is a solid phase with air molecules situated in interstices of the ice crystal lattice

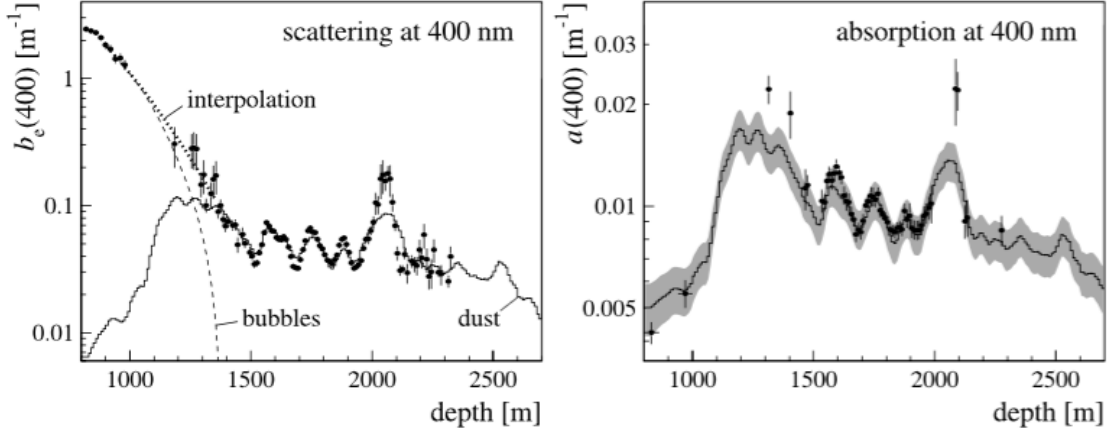


Figure 3.1.4: Correlation with dust concentration of the scattering and absorption strengths $b_e = \lambda_e^{-1}$ and $a = \lambda_a^{-1}$ (from [297])

where bubbles are rapidly disappearing with depth, explaining the observed depth dependence of the scattering coefficient.

In the deeper ice where IceCube is situated, the scattering due to bubbles becomes subdominant to dust. This was studied using the AMANDA-B detector, which contains 600 DOMs between depths of 1500 m and 2000 m, with three additional strings extending 350 m above and below the main array [297]. Light from multiple sources was observed throughout the detector to measure ice properties at different wavelengths and depths. The properties of the ice were studied using simulations of photon propagation and mathematical machinery of significantly more complexity than in the AMANDA-A studies. The result was the first iteration of the IceCube “ice model,” which implements layer-by-layer scattering and absorption coefficients, fit to data from flashing LEDs at different depths.

The fitted absorption and scattering profiles are shown in Figure 3.1.4. At depths below the clathrate transition, the scattering and absorption coefficients are observed to be strongly correlated, suggesting that dust grains are the dominant centers for both scattering and absorption (Figure 3.1.4). This motivated precise studies of the dust distribution in ice.

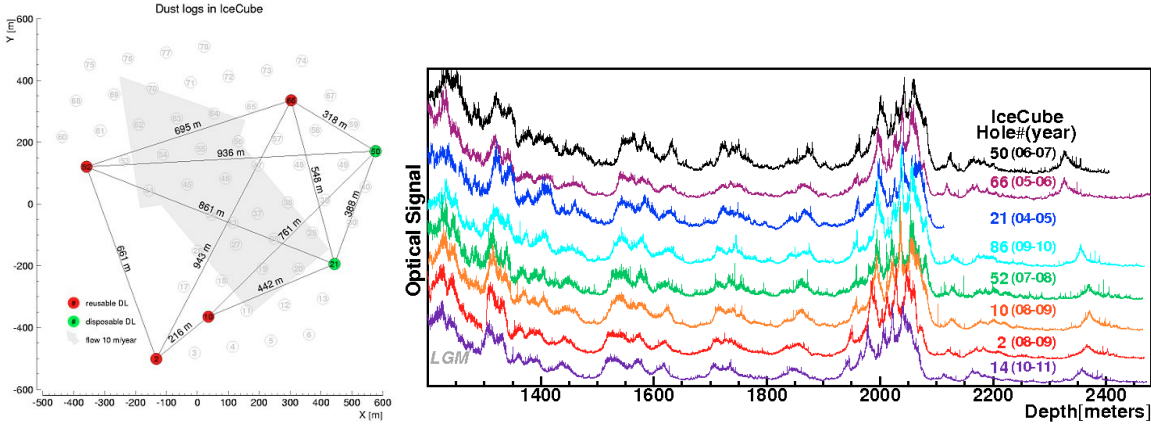


Figure 3.1.5: Dust logs in IceCube, made before deployment of the respective strings (from [298])

Dust logging and tilt mapping

To precisely measure the dust concentration as a function of depth, a dedicated dust-logging device was developed [299]. The dust logger used a beamed light source aimed into the ice and detected back-scattered photons on the opposite side of a set of light-blocking baffles. Dust loggers were initially deployed into three water-filled AMANDA-B holes before DOM insertion, measuring the dust profile with sub-cm depth precision.

The program of dust logging for AMANDA established several interesting facts. 1) Identification of features in the dust log with known features in the dust spectrum from other sites provided an age-vs.-depth relationship for South Pole ice [300]. Ice at 2 km is 65,000 years old. 2) There is a large dust concentration at 1300 m corresponding to the last glacial maximum. 3) There are discrete spikes in the dust concentration on few-cm scales throughout IceCube and AMANDA detectors that correspond to known volcanic eruptions. 4) A steadily varying dust concentration due to atmospheric dust, independent of volcanic peaks, runs through the full detector volume. 5) A thick “dust layer” is present at approximately 2000 m. This is approximately the center of the IceCube detector. 6) There is a strong correlation between the dust concentration and scattering and absorption lengths measured in AMANDA (Figure 3.1.4).

Dust loggers were also deployed in six IceCube holes [298], and the results are

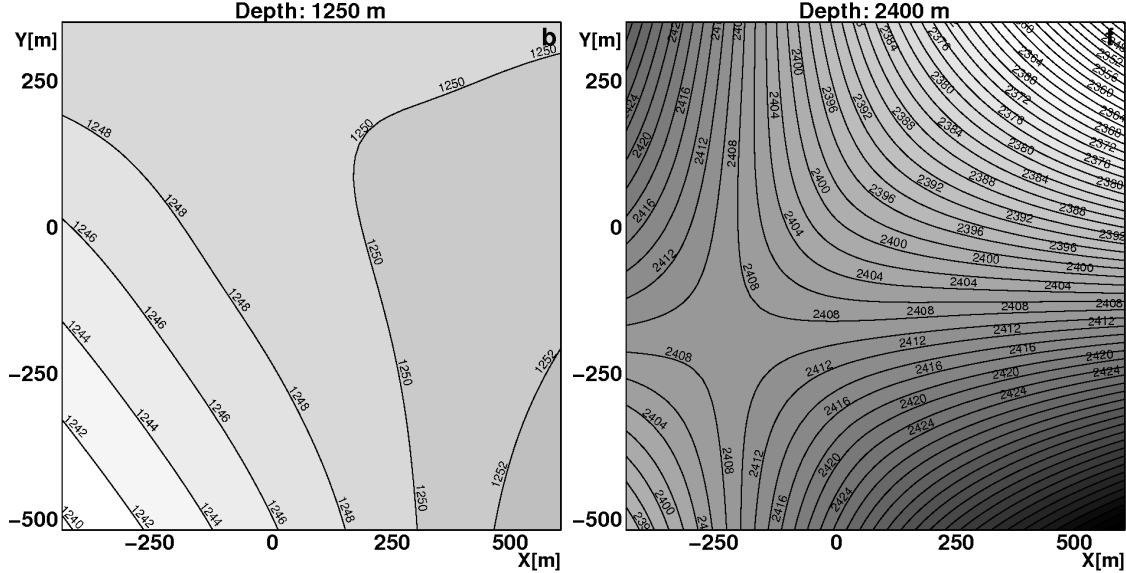


Figure 3.1.6: Two slices of the tilt map extracted from the IceCube dust logs, showing layers of assumed constant ice properties (isochrones). (from [298])

shown in Figure 3.1.5. Differences in the peak depths across the detector show that the layered deposits appear to have a distortion, or “tilt.” A tilt map was derived and extrapolated to cover the full detector, two sections of which are shown in Figure 3.1.6. This tilt map specifies the shape of the layers of constant ice properties corresponding to a unique deposition time (isochrones) as a function of depth and lateral position in the IceCube ice model. The isochrones are no longer coplanar as they were at deposition time due to flow and shearing of the ice.

Bulk ice models in IceCube

The full IceCube detector consists of 86 strings of 60 DOMs, each of which incorporates a calibration board with six flasher LEDs. A layered ice model is tuned using light from these flashers. The unfolding of ice properties from flasher data is computationally difficult and the ice model is continuously evolving in complexity.

The first IceCube ice models were direct extensions of the AMANDA-B methods [297], culminating in the AHA/WHAM! models (2007). These were replaced in 2009 by the independently developed South Pole Ice (SPICE) model. The SPICE family has undergone several major iterations and is presently the default ice model for

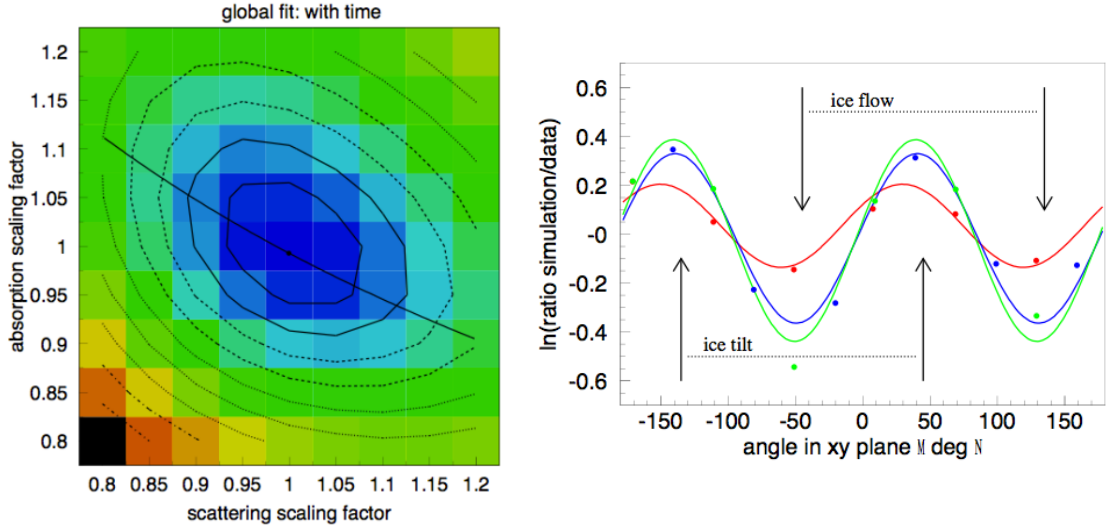


Figure 3.1.7: Left: Ice ellipse from SPICE, from [289]. Right: Ice anisotropy measured from string 63, from [303]

IceCube. Salient features of the the three most recent iterations will now be described.

SPICE Mie

The SPICE Mie [289] model is tuned using 40-string flasher data, fitting a six-parameter model to each 10 m ice layer. Of the six parameters, two are free in the fit (the absorption and scattering strengths), and the remaining four are tied to the values measured in AMANDA studies.

To improve the model of the angular distribution for scattering, two distinct scattering functions are superposed to give an “improved” scattering function. The first is the Henyey Greenstein (HG) [301] function, parameterized in terms of a mean scattering angle, $g \sim \langle \cos\theta \rangle$. The second is the Liu function [302] which is more forward peaked than HG. g is fixed to a value of 0.9 to match the Mie angular function, and the ratio of HG to Liu is fit to 0.55 : 0.45 using flasher data. To reduce the number of photons which must be simulated for the fit, DOM radii were oversized in the fitting procedure by a factor of 16. This approximation will be discussed in Section 2.2.

The fit is performed in two steps to improve convergence: First, the overall scattering and absorption scales across the whole detector are extracted; second, the

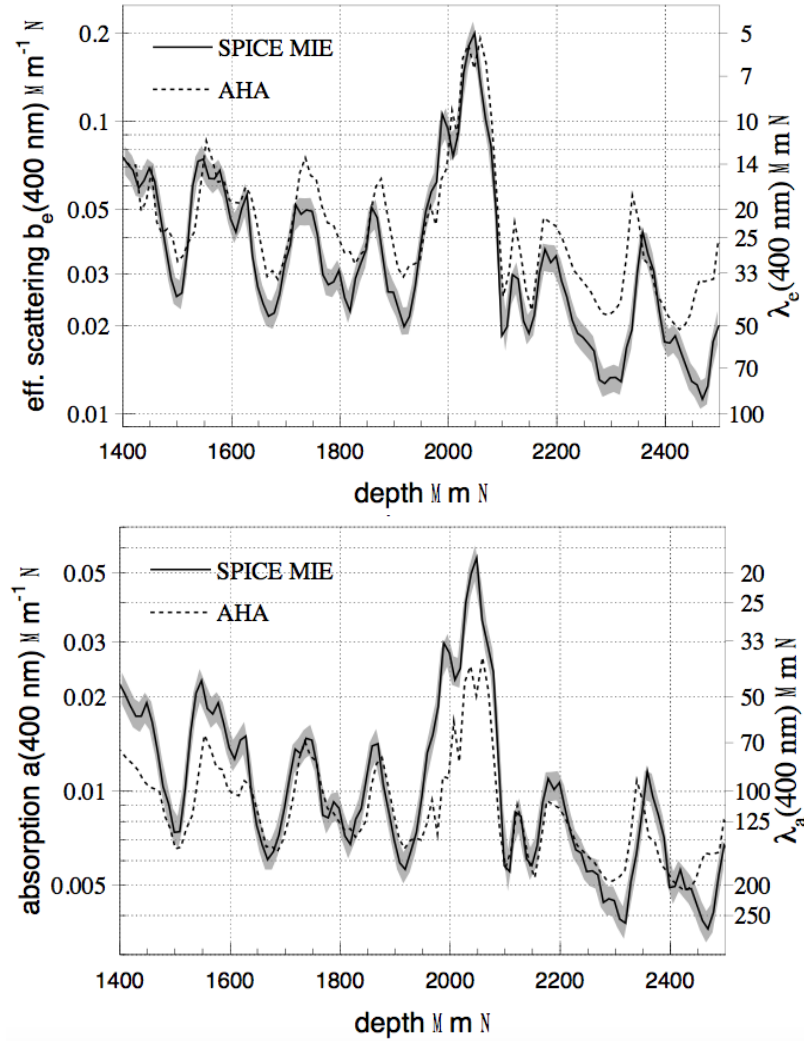


Figure 3.1.8: Scattering and Absorption Lengths from SPICEMie and AHA (the previous standard IceCube ice model) (from [289])

layer-by-layer coefficients are fit. This procedure is applied first without and then with fine-grained timing information. The fitted global scales of scattering and absorption are anti-correlated (Figure 3.1.7, left). The allowed region is sometimes referred to as the “Ice ellipse”. Due to optimizations in the minimizing procedure, it is not practicable to extract such ellipses layer-by-layer, so only uncertainties on the global scattering and absorption scale, averaged over the detector, are known. Tilt is included in the model by applying the tilt map from dust logging (Section 1.3) to deform the layers of the model. SPICE Mie is the central ice model for this analysis, and its absorption and scattering functions vs. depth are shown in Figure 3.1.8.

SPICE Lea

The primary improvement of the SPICE Lea model over SPICE Mie is the inclusion of propagation anisotropy [303]. This refers to the dependence of absorption strength on photon propagation direction, which has been observed in both flasher data and using Cherenkov light from muons. The axis of anisotropy is aligned with the ice flow, allowing preferential propagation of light in that direction. This suggests an interpretation in terms of elongated dust grains stretched by the glacial shear. The scale of the anisotropy is approximately 16% per 100 m of propagation distance.

Data from flashing a single string was used to measure the ice anisotropy in SPICE Lea. The intensity of the detected light as a function of direction and distance is shown in Figure 3.1.7, left. This anisotropy has been incorporated into the ice model via the replacement of the scattering function with a function dependent upon the incident direction [303]. Re-fitting the scattering and absorption model after accounting for the anisotropy leads to changes in the scattering and absorption parameters beyond their one sigma error bands from SPICE Mie, particularly in the dustiest layers. SPICE Lea is used as a discrete ice variant in this analysis, to constrain the effects of ice anisotropy. These effects have been small in most previous IceCube analyses.

SPICE³

SPICE³ (“SPICE-Cubed”) is the next-generation ice model and is still in development. In SPICE³ the LED brightness, angular emission distribution and DOM efficiency are fit for every DOM. This absorbs DOM-to-DOM and LED-to-LED variations in 37740 new model parameters. Light from seven flashing strings, rather than one, is used to characterize ice anisotropy across the detector. DOMs are not oversized, removing a possible source of systematic uncertainty. New dust log data has become available and is used to improve the tilt map. At the time of writing, SPICE³ was still in validation and not ready for use in the analysis.

Comparing ice models via model error

The quality of the fit between ice model versions is often compared using the *model error* variable. This encodes the similarity between light yield distributions above 10 photoelectrons in real vs. simulated flasher calibration events. Although a small value represents a better optical model, there is no simple way to apply the measured value in analysis. However, comparison of model error allows comparison of the quality or similarity of models. The *model errors* for various IceCube models are tabulated in Figure 3.1.9.

Ice Model	Model Error	Notes
AHA	55%	
WHAM! (2007)	42%	
SPICE (2009)	29%	
SPICE Mie (2010)	29%	central model for this analysis
SPICE Lea (2012)	20%	used to check anisotropy effect
SPICE ³ (2014)	11%	development only - not used

Figure 3.1.9: Model errors for various IceCube ice models

Hole Ice

To install IceCube strings, holes are made in the ice using a hot-water drill. The hole is filled with water, which refreezes after DOM deployment. The freezing process occurs from the outside of the column inwards. When liquid water is in contact with the hole wall, air which was previously held in the clathrate state diffuses into the liquid, forming bubbles. These bubbles introduce extra scattering in the vicinity of the string, effectively symmetrizing the DOM angular response: down-going photons that would have been detected with low efficiency can be scattered back upward into the DOM. Conversely, up-going photons that would have been detected with high efficiency can be scattered away.

A simple model of the hole ice is employed in IceCube simulations. The effective angularly dependent DOM efficiency is modified with a function derived from a standalone Mie-scattering Monte Carlo. The mean-free-path for bubble scattering,

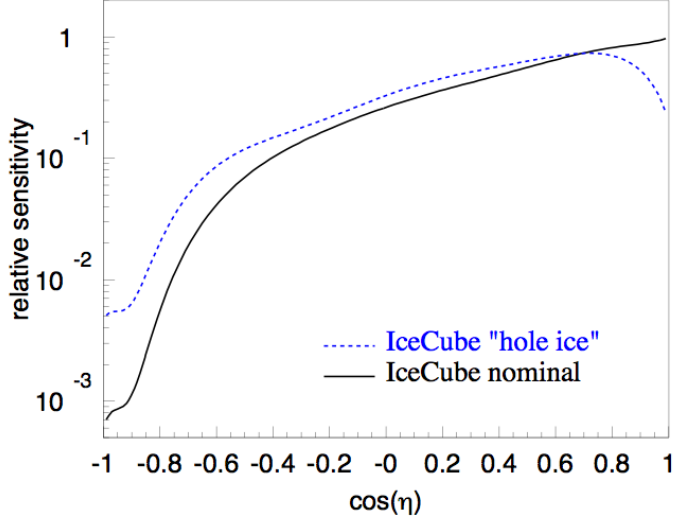


Figure 3.1.10: Hole ice correction function as used in IceCube MC (from [289])

λ , is a free parameter. A good fit to data is found for $\lambda \sim 50$ cm, across a column of diameter 30cm. The modified angular response function is shown in Figure 3.1.10.

The hole-ice column has also been observed *in situ* using cameras deployed in pressure housings [304]. These highlighted interesting features of the hole ice: The cloudy ice column does not fill the hole, but is estimated to cover only the central 16 cm; the DOMs are not aligned with the center of the hole so the effect is azimuthally asymmetric; and there are small opaque features against the DOM surface which appear to be artifacts of the refreezing process. Despite these features, the simple parameterization of the hole-ice function has performed well in dedicated studies of the hole-ice effect, and has not yet been superseded.

1.4 The IceCube atmospheric muon neutrino sample

Atmospheric neutrino interactions in IceCube are detected via their charged daughter particles emitting Cherenkov light in the instrumented ice which is collected by one or more DOMs and transmitted to the IceCube lab at the surface. If the event passes one of the enabled triggers, it is stored to disk. The data on disk is filtered using a set of software modules which constitute the Processing and Filtering (PnF) system,

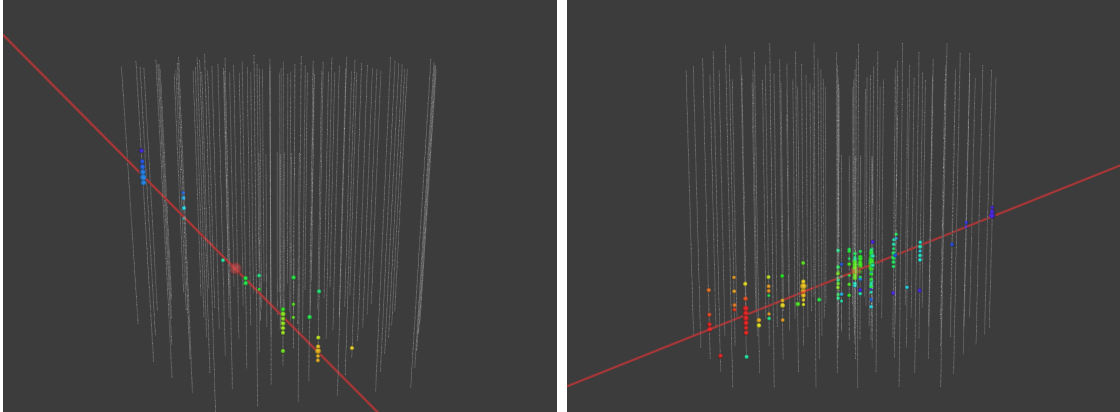


Figure 3.1.11: Two simulated events from the IC86 up-going muon sample. DOM pulses after noise cleaning are shown as colored points, with red representing earlier and blue representing later times. The true and reconstructed trajectories are both shown as red lines, but the angular reconstruction is sufficiently accurate that they cannot be distinguished by eye. The true energies are 1.5 TeV and 9 TeV respectively.

and a subset is transmitted by satellite link to The North² for further processing.

Two main signatures are observable for atmospheric neutrinos in the 100 GeV to 100 TeV energy range. Electron and tau neutrinos induce cascade events, which are spatially localized electromagnetic or hadronic showers. Because the event is compact there is a high probability of full containment, but directional information is limited. Cascade reconstruction is typified by fine energy but coarse directional resolution.

Muon neutrinos produce muons which range out over many kilometers [37], [305] leading to track-like topologies. Two sample events are shown in Figure 3.1.11. Because the track is long and straight, good directional reconstruction is achievable (see Section 2.4), but since majority of events are not contained, the energy resolution is poor. The long range of the muon leads to a greatly enhanced detector target mass.

Measuring non-contained down-going muon neutrinos is impracticable due to the high penetrating muon background from air showers. The total background rate is around 3 kHz, to be compared with the rate of detectable neutrino interactions of \sim 10 mHz. If the sample is restricted to up-going neutrinos, however, the cosmic muon background contamination becomes small due to the stopping power of the Earth.

²Any point on Earth which is not the South Pole is in “The North” in IceCube nomenclature.

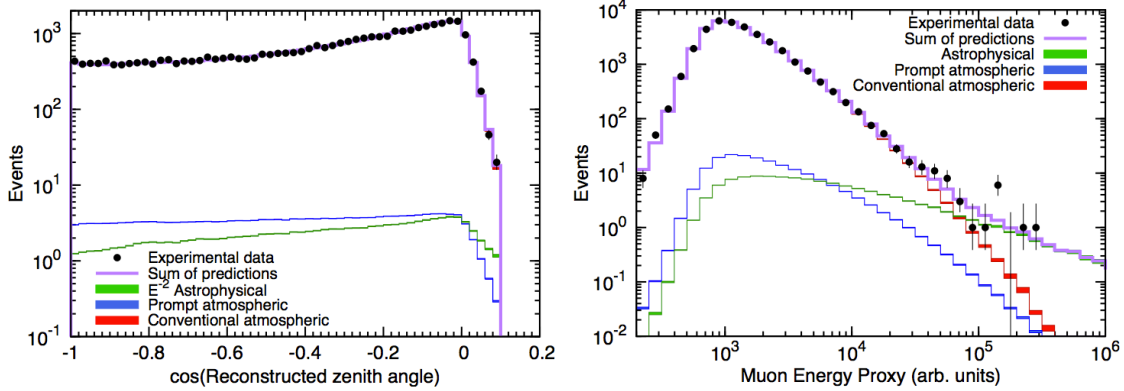


Figure 3.1.12: Results of the IC79+86 diffuse analysis, from [307])

The analysis presented in this thesis uses an event selection developed to search for diffuse astrophysical neutrinos [306], [307]. This sample consists of muons with reconstructed zenith angles between up-going and 5° above the horizon, corresponding to an overburden of at least 12 km of water due to IceCube's underground location. The diffuse astrophysical component populates the highest energy tail of this sample.

There are two levels of triggering applied at the detector. A Hard Local Coincidence (HLC) condition is applied at the per-DOM level, such that the modules only transmit their full waveforms to the surface if at least one nearby DOM also registered activity within a $1\ \mu s$ window. All transmitted DOM responses are then processed at the surface by a suite of detector-wide triggers. This analysis uses the Simple Multiplicity Trigger (SMT) with a threshold of 8, which requires at least 8 HLC launches to accumulate within a $5\ \mu s$ window. If the SMT8 trigger fires, data is recorded for a readout window of $10\ \mu s$ around the trigger.

We use data selected by the `MuonFilter11` module, which is designed to accept up-going or high-energy down-going muon tracks with high efficiency. The expected rate of atmospheric-neutrino-induced events passing this filter is 1.17×10^{-2} Hz. This is superposed on a down-going cosmic muon background with a rate of 32.6 Hz, which must be removed by offline event selection [306].

The sample event selection is described in the supplementary material of [307]. A second level of filtering (L2) is performed on the output of the `MuonFilter11` stream, where higher level reconstructions and event-splitting algorithms are run to better re-

construct the event direction and energy. Events which fail to meet the `MuonFilter11` criteria after re-reconstruction are discarded. A cut on the mean detected-photon distance from the track is applied to reject poorly reconstructed events. Track quality cuts, based on the likelihood returned by the tracking algorithms, are applied. A Bayesian reconstruction check is made, comparing the track reconstructed with a prior on its probable direction to the actual reconstructed hypothesis. Well reconstructed events overwhelm this prior, which is heavily biased towards down-going muon bundle events, and still return an up-going hypothesis. A two-dimensional cut on zenith angle and brightness is applied to reduce leakage of cosmic muon backgrounds into the sample. Finally, the event is reconstructed with the detector split into parts, and the consistency of the reconstructed parts is checked against the full-detector reconstruction. This removes backgrounds due to coincident air shower events. The efficiency of this event selection is 24% for neutrino-induced events from an E^{-2} sample, and the sample purity is better than 99.9%.

In this energy regime, muon energy losses are radiative and therefore stochastic. Energy reconstruction is performed using the MuEx method, which makes a likelihood analysis of fluctuating light emission along the track [308]³. The output of the MuEx algorithm is a proxy for muon energy. The performance of the reconstruction and interpretation of its output will be discussed in Section 2.4. The sample distribution in energy and zenith from [307] is shown in Figure 3.1.12.

To search for sterile neutrinos, we are primarily interested in intermediate energies where the statistics are high and shape effects can be measured. Thus, we restrict the sample to the energy range $400 \text{ GeV} < E_{\text{reco}} < 20 \text{ TeV}$, which helps to avoid systematic uncertainties associated with detector noise, geomagnetic effects and standard oscillations at low energy, as well as backgrounds from prompt and astrophysical neutrinos at high energy. We consider a single year of data from the full 86-string detector configuration (IC86). The approach will be to perform a Poissonian likelihood analysis of the shape of the detected flux, using discrete and continuous nuisance parameters to account for the effects of systematic uncertainties.

³In this reference, the MuEx method is called “Single template (widened PDF).”

1.5 The sterile neutrino signature in IceCube

The signature we search for in this analysis is an MSW-resonant $\bar{\nu}_\mu$ disappearance, which occurs in the antineutrino channel in 3+1 models (see Section I.1.3). Figure 3.1.13 shows the oscillation effect calculated using the NuSQuIDs package for ν_μ and $\bar{\nu}_\mu$ at the global best-fit point of the 3+1 model. Several features are evident:

- For both ν_μ and $\bar{\nu}_\mu$, vacuum-like oscillations are visible at low energies, with variation in both energy and zenith.
- For $\bar{\nu}_\mu$ only, an MSW-resonant depletion is visible for core-crossing trajectories.
- For both ν_μ and $\bar{\nu}_\mu$, the fluxes are depleted by absorption at high energy. This depletion effect is smaller than what would be expected with only active neutrinos, since the Earth is transparent to sterile neutrinos.

The MSW resonance condition depends on the sterile neutrino properties, matter density profile (both in magnitude and smoothness) and neutrino energy. The resonance energy E_{crit} (Part I, Eq.1.20) is proportional to Δm^2 , and IceCube is most sensitive to the resonance when E_{crit} is in a range where the statistics of the energy distribution (Figure 3.1.12), are high. For very low masses, the resonance condition is satisfied below the sample energy range, and vacuum-like oscillations occur on baselines longer than the Earth diameter so cannot be observed. For very high masses, the resonance occurs above the sample energy range, and vacuum oscillations occur but are too fast in energy to be resolved, instead appearing as a depletion in the total neutrino rate. For masses in the range $0.05 \lesssim \Delta m^2 \lesssim 5 eV^2$, the resonance can occur within the sample energy range and its shape effect may be resolvable.

The dependence of the oscillation phenomenology upon the mixing parameters is complicated, and is discussed in [40]–[42]. Unlike in a vacuum oscillation experiment where the two-flavor approximation of Part I, Eq.1.14 can be made, reducing the effects of the three unitary mixing angles $\theta_{14}, \theta_{24}, \theta_{34}$ to a single effective parameter $\theta_{\mu e}$, the phenomenology of matter-enhanced sterile neutrino oscillation generally depends on all three angles and two CP-violating phases. In this analysis we follow the

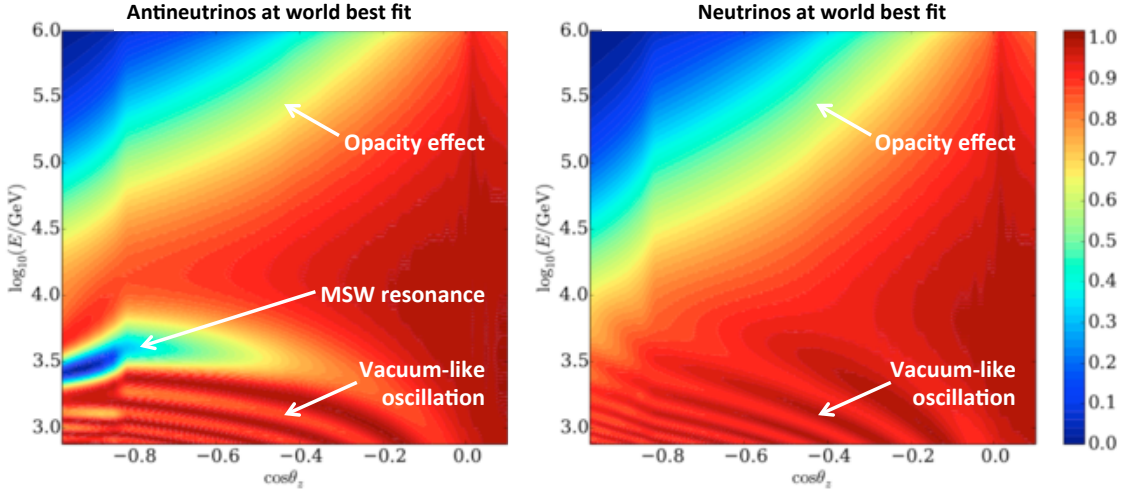


Figure 3.1.13: Disappearance probability in neutrinos and antineutrinos as a function of true neutrino energy and zenith for a 3+1 model with $\theta_{24} = 0.2$ and $\Delta m^2 = 1\text{eV}^2$

treatment in [40] and use a model where $\theta_{14} = \theta_{34} = 0$, which produces the smallest overall oscillation effect for a given $\theta_{\mu e}$ value. Models with $\theta_{14} \neq 0, \theta_{34} \neq 0$ can also be constrained with our data sample. For these models, the MSW peak is smaller in amplitude, but the overall disappearance effect is larger over a wider parameter space. Because of the large energy smearing in our analysis, searching for the smallest disappearance signal for a given value of $\theta_{\mu e}$ is a conservative way to test the sterile neutrino hypotheses corresponding to vacuum-like oscillation anomalies.

Only $\bar{\nu}_\mu$ experience the MSW resonance, whereas both ν_μ and $\bar{\nu}_\mu$ are present in our sample via μ^+ and μ^- tracks, from which no charge information can be extracted. The oscillation features in the summed fluxes are less dramatic than those seen in the separated ν_μ and $\bar{\nu}_\mu$ channels. Furthermore, because containment of the events is not required, detected muons have lost an unknown amount of energy when entering the instrumented volume. This smears the energy downwards, which hides the fine details of the shape effect. Track energies and angles are then reconstructed by imperfect algorithms with finite resolutions (Section 2.4), adding further smearing. The oscillation effect in reconstructed quantities at several parameter points is shown in Figure 3.1.14. 10-15% deficits correlated over many bins are expected for hypotheses of interest. Also shown in Figure 3.1.14 is the MiniBooNE/LSND allowed region,

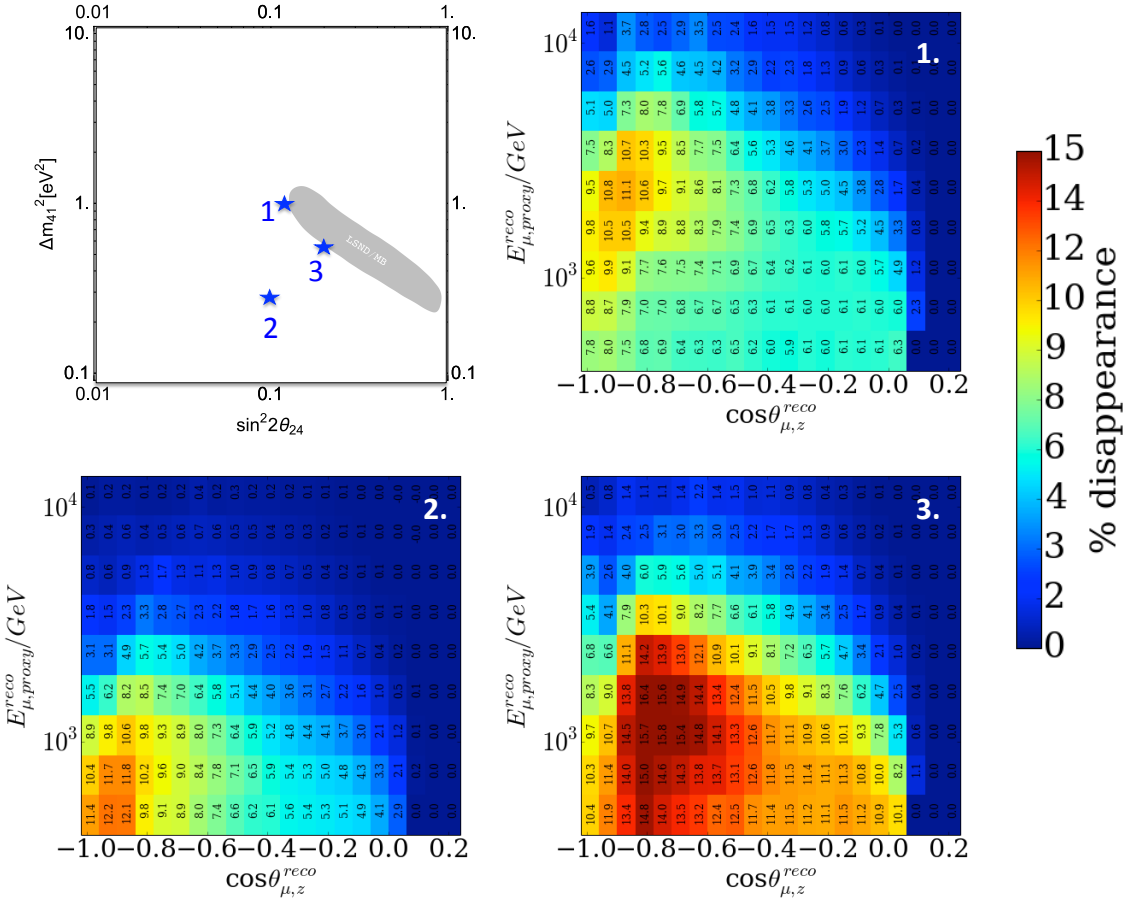


Figure 3.1.14: Survival probability for various sterile neutrino parameter points in reconstructed quantities.

drawn using a convention developed in [40], which is to project the allowed region derived from the appearance signals with U_{e4} fixed at the global best-fit point from [65]. Because this is a projection at a fixed U_{e4} rather than a marginalization, this should be considered as a guide to the interesting parameter space rather than a formally defined allowed region. The impact of our measurements of θ_{24} upon the allowed parameter space for vacuum appearance experiments will ultimately be derived from global fits to world data.

We are searching for small shape effects in the neutrino spectrum, so careful control of systematic uncertainties is required. These include uncertainties in detector response, ice properties, Earth density, neutrino cross sections and atmospheric neutrino flux. The following sections will concern work done to treat these effects.

Chapter 2

Monte Carlo Simulations for the IC86 Sterile Neutrino Analysis

For this analysis, a new Monte Carlo simulation scheme called `NuFSGen` was developed to give a finer control of systematic shape effects and a more accurate treatment of oscillation hypotheses than the standard IceCube `NuGen` simulation method. This chapter describes this scheme, as well as the production and validation of simulation samples for the sterile neutrino analysis. Table 2.1 outlines the steps used to produce our `NuFSGen`-based Monte Carlo samples, and the alternative simulation approaches that are discussed for context in this chapter.

Step	Our Samples	Alternatives
Event generation	<code>LeptonInjector</code> (<code>NuFSGen</code>)	<code>NuGen</code>
Event weighting	<code>LeptonWeighter</code> (<code>NuFSGen</code>)	<code>NuFlux</code>
Photon simulation	<code>Hybrid-photonics-CLSIM</code>	<code>CLSIM</code> , <code>PPC</code> , <code>Photonics</code>
DetSim/Trigger/Filter	Standard IC86 scripts	
Event selection	From [307]	
Reconstruction	<code>MuEx</code>	

Table 2.1: Steps used in producing, processing, selecting and reconstructing the samples used in this analysis, and the alternative methods mentioned in this chapter.

2.1 Event generation and weighting

Neutrino event generation in IceCube simulations is typically performed using a Monte Carlo program called **NuGen**. This section describes **NuGen** and then the alternative **NuFSGen** approach developed for this analysis.

NuGen neutrino generation

Given an injected energy spectrum, **NuGen** stochastically propagates neutrinos across the Earth and simulates the interactions of the survivors near the detector. Neutrinos can be lost due to absorption, or migrated in energy through neutral-current or tau-regeneration processes. Those which are absorbed via charged-current interactions are re-simulated from the absorption point with a modified weight and treated as neutral-current scatters as a method of performance optimization. This and other optimizations imply that each neutrino at the detector does not have a one-to-one correspondence with an injected particle.

The remaining neutrinos after Earth propagation are forced to interact in or before the IceCube volume. Charged-current muon neutrino events are generated in a column pointing towards the detector, whose length is chosen such that 99% of all muons which could reach the detector are simulated. Since muon energy losses in our range of interest are primarily radiative, which is a random process with large fluctuations, many generated muons do not reach the detector and are discarded. Conversely, a small tail of long-range muons which could have reached the detector are unsimulated. Because the energy spectrum is steeply falling, the rate of these events, which have small energies when they reach detector, is negligible compared to the much larger rate of closer and lower energy particles. Neutral-current interactions of all neutrino flavors, and charged-current electron and tau neutrino interactions induce cascades which are simulated in the detector volume and a small surrounding region. **NuGen** events are generated according to a reference energy spectrum and weighted to a primary flux prediction using the **NuFlux** program or one of its variants.

The final state charged-particle content is sampled from a pre-calculated table

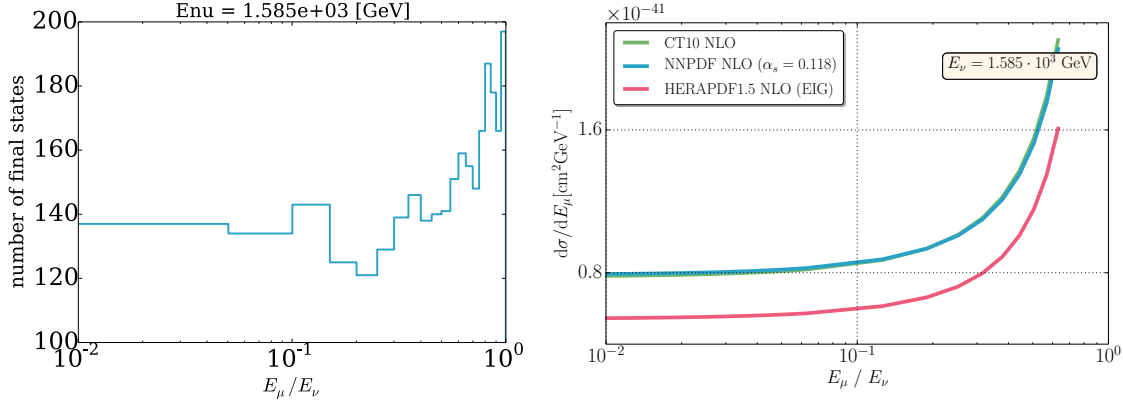


Figure 3.2.1: The final state inelasticity distributions for the **NuGen** (left) and **NuFSGen** (right) simulations.

of final states for the appropriate neutrino energy. Figure 3.2.1, left, shows the distribution of allowed final state inelasticities in the **NuGen** simulation for $E_\nu = 1.585$ TeV, which is near the peak of the sample energy distribution. This illustrates the granularity of the **NuGen** final state prediction.

NuFSGen event generation

Due to the stochastic nature of the **NuGen** method and its optimizations, oscillation and propagation effects cannot be trivially decoupled to re-weight events to an oscillation hypothesis. The limited library of **NuGen** interaction final states is also not well suited to a high-statistics flux-shape analysis. For these reasons, the **NuFSGen** method was developed. **NuFSGen** involves both event generation and weight calculation steps. A cartoon showing how the method compares to **NuGen** is shown in Figure 3.2.2.

The event generation step is called `LeptonInjector`. Final states such as muons or cascades are generated at the detector according to a reference energy spectrum and a continuous doubly differential cross section. Per-event information about the generation probability, event inelasticity and flavor are stored into the event. No oscillation or propagation physics is accounted for at generation time. To use **NuFSGen** Monte Carlo, a pre-simulated library of such events must be subsequently weighted to a desired cross section and post-propagation flux hypothesis.

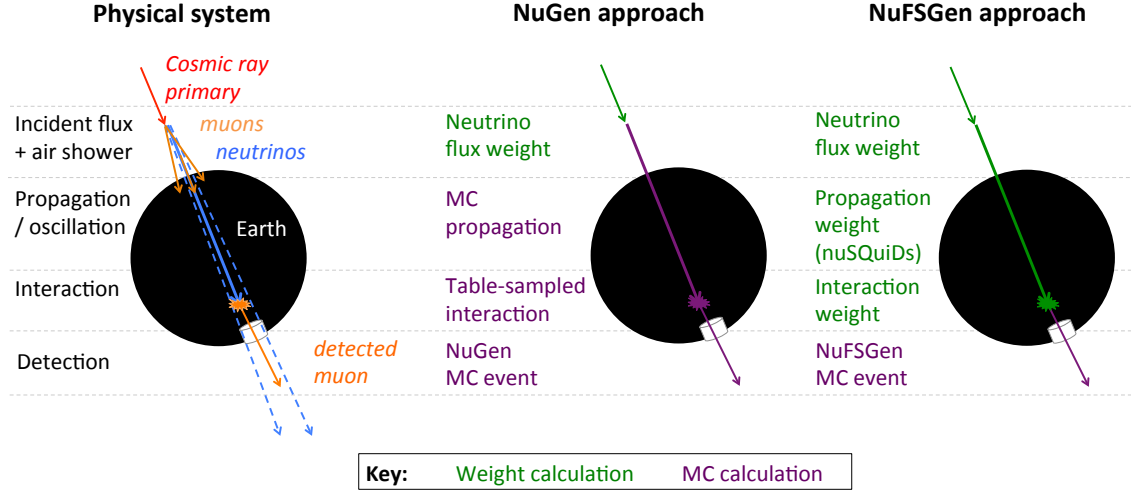


Figure 3.2.2: Illustration showing the NuGen and NuFSGen Monte Carlo schemes.

NuFSGen event weighting is performed by the `LeptonWeighter` package, which requires as inputs 1) a cross section model and 2) an at-detector flux hypothesis. Several deep inelastic scattering (DIS) doubly differential cross sections have been calculated from parton distribution functions and are supplied as splined functions over neutrino energy, and Bjorken x and y . A slice through three of the implemented cross section splines, showing $d\sigma/dE_\mu$ at $E_\nu = 1.585$ TeV, is shown in Figure 3.2.1, right. This is to be compared to the final state distribution sampled in NuGen, shown in Figure 3.2.1, left. These models will be described in Section 3.3.

The flux hypothesis depends on both the primary neutrino flux at production and on the propagation physics of the neutrinos between production and detection. The primary neutrino spectrum is supplied as a spline over $\log(\text{energy})$ and zenith. The central flux hypothesis used in this analysis is the HKKM model [309], [310], matched to a Gaisser parameterization [311] above 700 GeV. This is a standard atmospheric flux model, which has been used in previous IceCube analyses [307], [312]. Other flux predictions, based on the calculations in [313], are also used to account for the uncertainty on the atmospheric neutrino flux. These will be discussed in Section 3.5.

Propagation of the neutrino flux across the Earth as a function of energy, zenith and flavor depends on both oscillation and interaction effects. This calculation is performed by the NuSQuIDs package, which numerically solves the neutrino evolu-

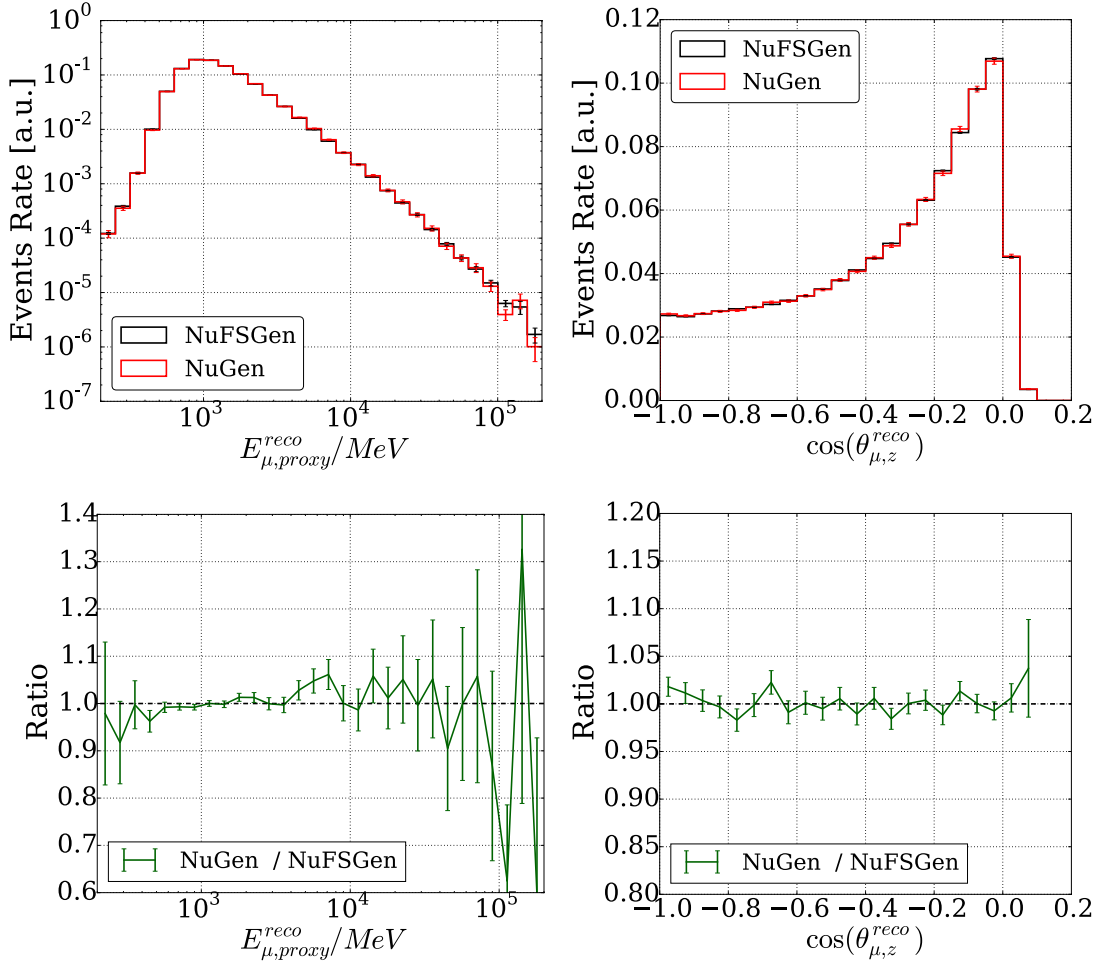


Figure 3.2.3: Comparison of NuGen and NuFSGen Monte Carlo methods for the no-oscillation hypothesis at event-selection level.

tion master equation accounting for absorption, regeneration and oscillations [45]. A propagated flux hypothesis is used to produce a weight for each neutrino energy, zenith and flavor at the detector, sampled from NuSQuIDs by `LeptonWeighter`.

Processed and weighted NuFSGen and NuGen samples were compared at analysis level for the no-oscillation hypothesis. As demonstrated in Figure 3.2.3, excellent agreement was observed. To achieve this agreement, bugs were isolated and fixed in both the official NuGen and development NuFSGen samples. This shows that NuFSGen has value not only as a new weighting-based treatment of oscillations and flux systematics, but also as an independent cross-check of standard simulation tools.

2.2 Modelling light propagation

Light propagation in IceCube is typically modeled by directly simulating the trajectories of photons as they scatter through an ice model as described in Section 1.3, using the **CLSIM** or **PPC** packages. The two are functionally equivalent, and the **CLSIM** propagator is used in this analysis, due to its integration into the IceCube simulation production infrastructure.

An alternative photon propagator is the semi-analytic **Photonics** [314], which is less accurate but substantially faster than **CLSIM** or **PPC**. To enhance simulation speeds, the approximately isotropic light from cascades can be modeled using **Photonics** with direct **CLSIM** simulation of photons produced in non-isotropic track-like topologies. The so-called **Hybrid-photonics-CLSIM** approach is used in this analysis for all samples where **Photonics** data tables were available. This accelerates simulations sufficiently that they can be performed in reasonable times on CPU clusters, whereas full **CLSIM** propagation is only practicable on GPUs.

Further speed enhancements can be achieved using the “DOM-oversizing” approximation, which is employed in the majority of IceCube simulations. This involves reducing the number of photons being stepped by artificially increasing the collection area of each DOM in the simulation geometry. If the effective radius presented to an arriving photon is increased by a constant factor O , the number of photons simulated can be reduced by a factor of O^2 , resulting in approximately the same detected photon count in the far-field limit. To minimize distortion of the photon arrival time distribution, the DOM size is increased only perpendicularly to the direction of photon travel. The oversizing geometry transformation is shown schematically in Figure 3.2.4. Although this approximation is good in the far-field limit, in the near-field regime, the effects of extending the DOM laterally and reducing the photon yield do not cancel exactly. Tracks passing very near to a particular DOM therefore deposit an incorrect photon count.

The effects of DOM oversizing were studied both at single-photon level and at analysis level. To study the effects at single-photon level, a simulation was run whereby

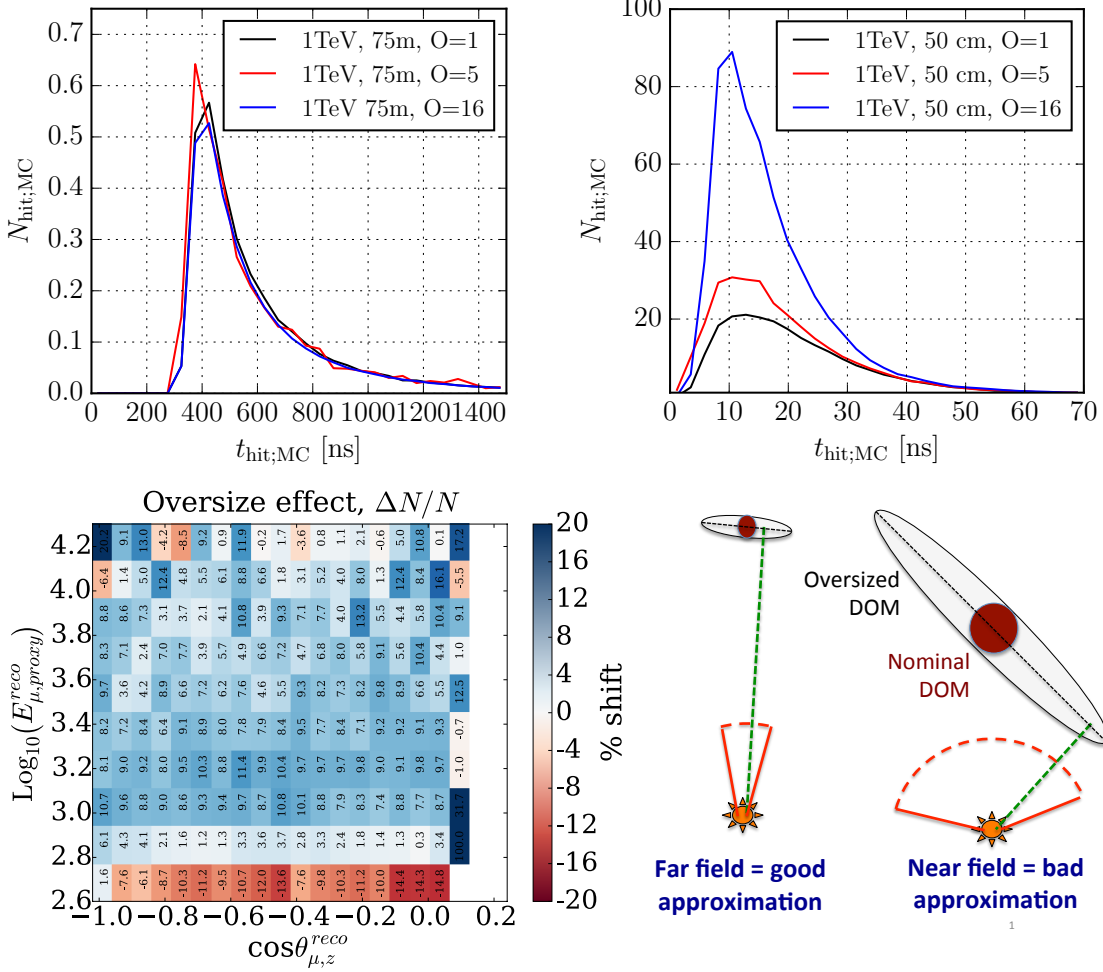


Figure 3.2.4: Top: oversizing effects on photon arrival time distribution from 1 TeV cascades in the far-field (left) and near-field (right) regimes. Bottom left: effect of oversizing on analysis sample. Bottom right: illustration of oversizing transformation.

1 TeV cascades were injected into a simplified detector geometry with DOMs at various lateral distances from the injection point, and the light was propagated in a test geometry with a single DOM at a fixed position. The oversize scales studied were:

- $O=1$: No oversizing enabled
- $O=5$: Default oversizing employed in official simulations
- $O=16$: Oversizing used in ice model tuning to flasher data

Figure 3.2.4, top, shows arrival time distributions from 1 TeV cascades generated with different oversizing scales in the far-field (75 m) and near-field (0.5 m) lim-

its. These and other studies showed that, at distances larger than ~ 1 m, $O=5$ is a good approximation to a physical DOM. The $O=16$ approximation is used for ice model tuning with flashers, which are necessarily at least 125 m horizontally from the detecting DOM. The $O=16$ approximation was thus determined to be valid at all source-to-DOM distances which would impact ice model tuning.

The effect of oversizing on higher level analysis observables is event selection and reconstruction dependent. The IC86 up-going muon event selection is cut-based and incorporates track quality cuts that can be sensitive to mis-modeling effects such as oversizing, even if only a small number of DOMs on the track are affected. A Monte Carlo sample with $O=1$ was generated and compared with the standard $O=5$ sets. As shown in Figure 3.2.4, bottom left, a 10-15% deficit of events is observed at the lowest energies, with extra events appearing at higher reconstructed energies.

For the central model used in this analysis a fully non-oversized sample was generated. This takes $\sim 25\times$ longer to generate than the standard $O = 5$ samples. A correction derived from comparison of the non-oversized to oversized samples was applied to discrete variant samples (Section 3.2), which were all generated with $O = 5$. The correction function is applied at the final reconstructed level and corresponds to adjusting each bin content by the values shown in Figure 3.2.4, bottom left. The accuracy of this correction was assessed by comparing oversize-corrected SPICE Lea simulation to non-oversized SPICE Lea samples, and was found to be accurate to within statistical precision of the test.

2.3 Detector simulation, triggering, and filtering

After simulating the propagation and collection of photons, the PMT and electronics responses are simulated. The IceCube DOM simulation implements pulse shaping, amplitude and timing jitter, pre- and after-pulsing and pulse saturation. Noise is added using the `vuvuzella` model [315], which is tuned to generate random pulses with realistic timing correlations. The trigger is then simulated, and level 1 and level 2 filtering stages are applied. Finally, scripts to select and reconstruct the up-going

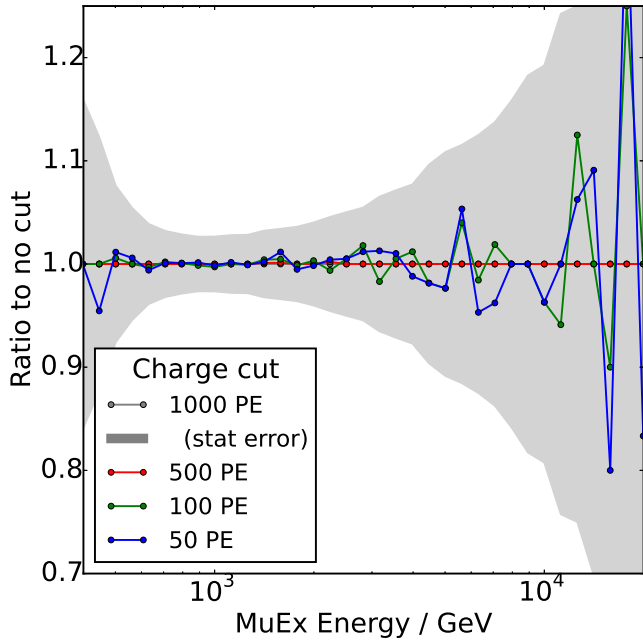


Figure 3.2.5: Test of effects of saturation on analysis sample. No bias is observed when high charge DOMs are removed from the reconstruction, showing that details of the saturation model are not a source of systematic uncertainty.

muon sample and extract analysis quantities into a lightweight data format are run.

The sensitivity of the analysis sample to the details of DOM saturation were assessed using data from IC79. This dataset, which is statistically independent of the IC86 sample but selected with the same cuts, was re-reconstructed with very bright DOMs removed above various thresholds. Sensitivity to mismodelled saturation behaviour would appear as a threshold-dependent bias. No bias was seen within the statistical precision of the sample, as shown in Figure 3.2.5 .

2.4 Event selection and reconstruction

Selection and reconstruction are performed analogously to the IC79+86 diffuse analysis (Section 1.4), but using improved simulations and using a more modern MuEx reconstruction. Changes in the final-level distributions were observed at the 10% level, due to removal of oversizing from the simulation procedure, and several minor simulation bugs which affected the spectrum at low energies.

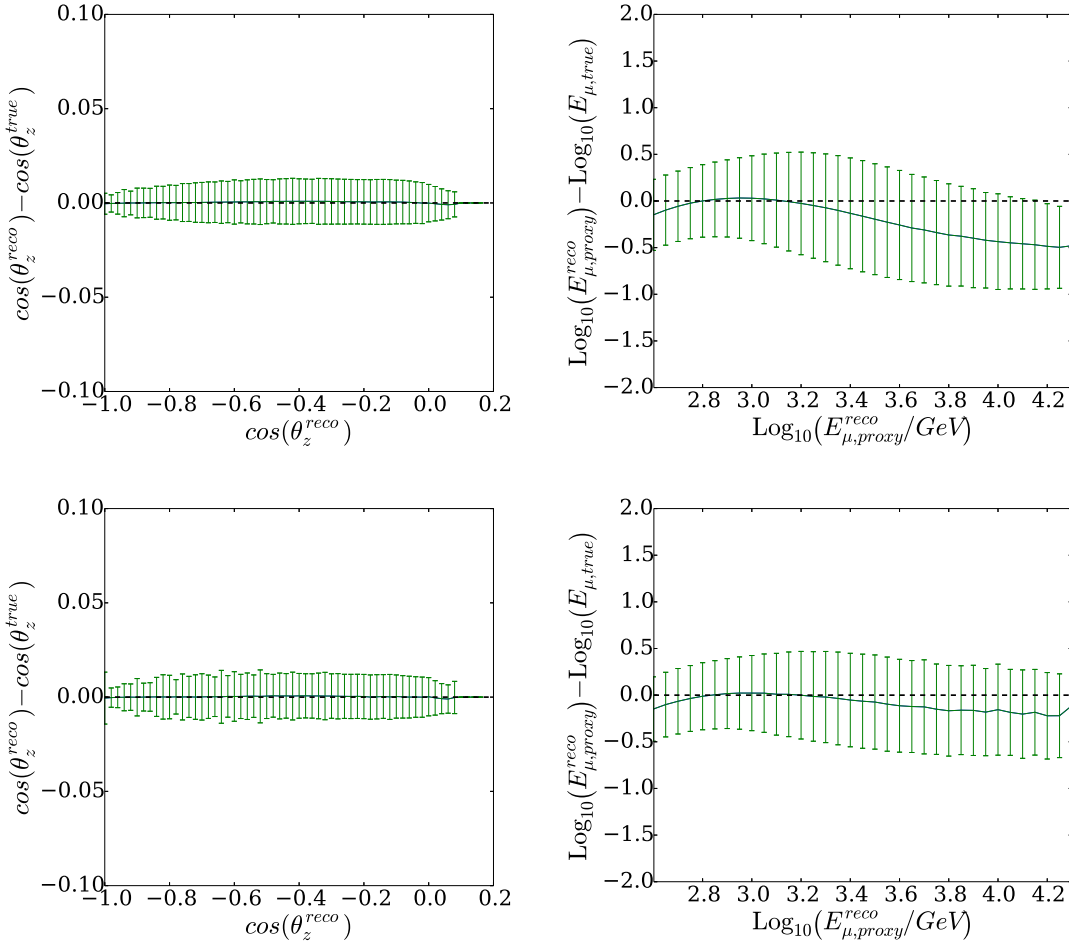


Figure 3.2.6: Performance of energy and zenith reconstructions in the selected sample. These plots show the 1σ range of residuals, given a particular reconstructed value. Top: sample with E^{-2} spectrum. Bottom: sample weighted to HKKM flux.

The performance of the energy and zenith reconstructions were evaluated using the central NuFSGen sample at analysis level. Figure 3.2.6 shows the 1σ bands of true quantities given a specified reconstructed value, in two cases of interest: for the unweighted Monte Carlo sample, generated with an E^{-2} spectrum, and for the sample weighted to the HKKM flux hypothesis. The zenith proxy is an unbiased estimator with resolution $\sigma_z \sim 0.013$, whereas the energy proxy exhibits a sample-dependent bias but is a relatively good estimator with approximate resolution $\sigma_{\log(E)} \sim 0.5$.

The dependence of the energy estimator on the underlying spectrum is a natural consequence of reconstructing a steeply falling distribution. This is further illustrated

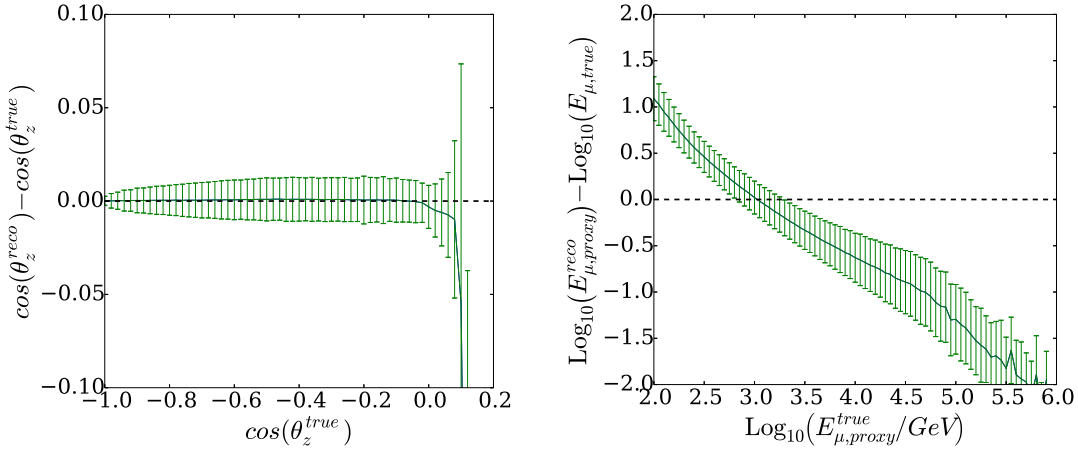


Figure 3.2.7: Performance of the energy and zenith proxies as a function of true quantities. A significant energy bias is observed, which is the expected behavior of an estimator which is unbiased when applied to a steeply falling spectrum.

by considering the resolution expressed as a function of true quantities shown in Figure 3.2.7. In contrast to Figure 3.2.6, which showed the energy proxy to be a good estimator of true energy when a particular reconstructed value is obtained, Figure 3.2.7 shows that for a given true energy, the reconstructed energy is biased by the assumed spectrum used in the MuEx likelihood problem. For this reason, care must be taken when interpreting the energy proxy as a reconstructed energy on an event-by-event basis without reference to the underlying spectrum.

2.5 Production of NuFSGen Monte Carlo sets

To use the NuFSGen technique, a large library of simulated events distributed over the observable final states is required. Systematic effects which cannot be accounted for by re-weighting, such as those related to the optical properties of the ice, must be handled at photon-simulation level and hence require specialized sets to be generated. For this analysis, in order for the statistical uncertainty on the Monte Carlo to be small compared with the shape effects under consideration, samples which are approximately $10\times$ larger than the official IceCube simulation production sets and a factor of $100\times$ larger than the IceCube official systematics sets, are required. The

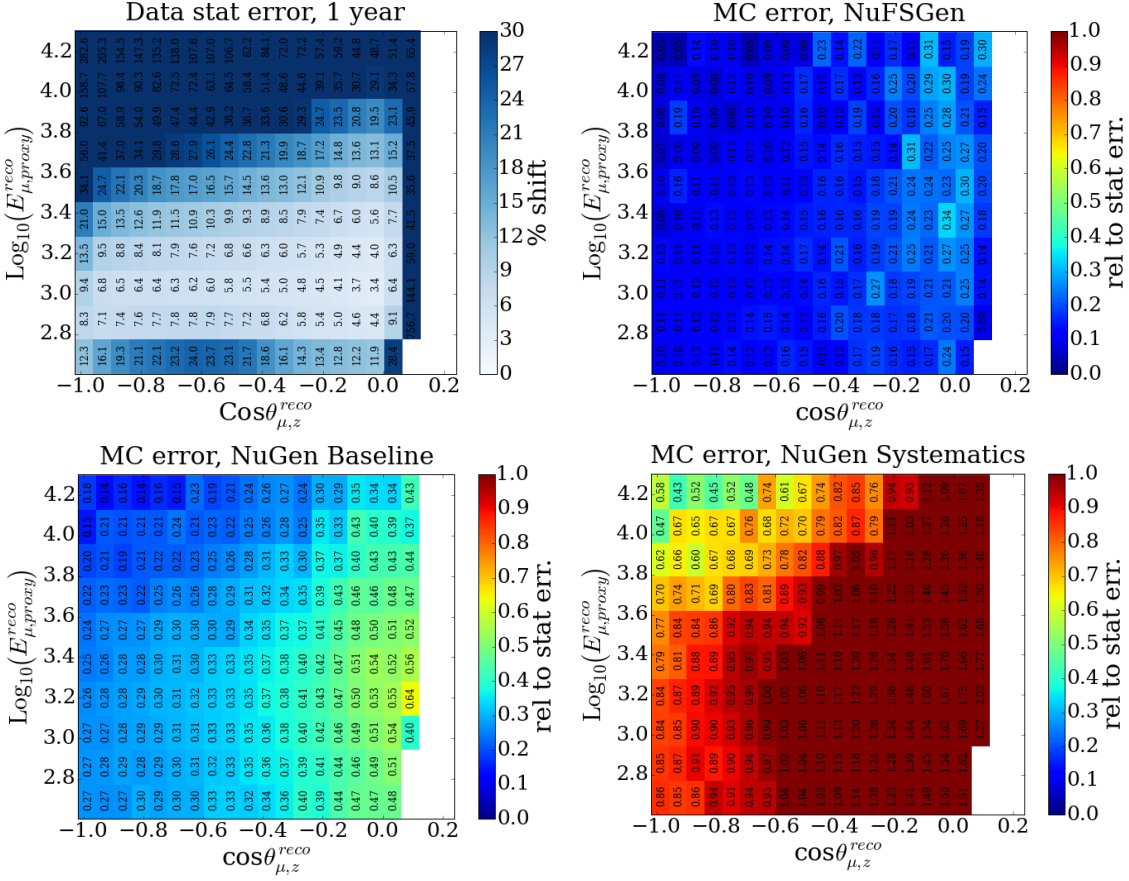


Figure 3.2.8: Approximate statistical error per bin in the sterile neutrino analysis for various samples. Top Left: IceCube official production, baseline Monte Carlo set. Top right: NuFSGen baseline set. Bottom left: IceCube official baseline Monte Carlo set. Bottom right: IceCube official systematic variant sets.

uncertainty per bin in each of these cases is shown in Figure 3.2.8.

A substantial production effort was undertaken to produce these samples using the computing resources of the UW-Madison-based NPX cluster, its associated GPU farm, and the Open Science Grid (OSG). Due to technical nuances of each sample, different resources were required in each case. Complete production and validation took around eight months. The samples produced include an $O = 5$ SPICE Mie set, produced exclusively on the OSG; a SPICE Lea set, produced locally on the UW-Madison GPU farm; A non-oversized SPICE Mie set, also produced using GPUs; and ice absorption and scattering variant sets, produced using a combination of CPU and GPU resources. These samples will be discussed further in Section 3.2.

Chapter 3

Systematic Uncertainties in the IC86 Sterile Neutrino Analysis

The IC86 sterile neutrino analysis is a search for small shape effects in the atmospheric neutrino flux. This requires careful control of systematic uncertainties in the detector response, ice properties, neutrino interactions, Earth density and initial flux shape. This chapter describes the methods we have developed to treat these systematics.

3.1 DOM efficiency uncertainty

The absolute photon collection efficiency of the IceCube DOMs has been measured for several PMTs in a laboratory setting [287]. Unfortunately, shadowing by the DOM cable and the unknown optical conditions in the hole after refreezing mean that this measurement does not necessarily translate directly to an in-ice efficiency. From an analysis viewpoint, the several factors which modify the DOM collection efficiency are combined into a single parameter called the *UnshadowedFraction*, by which the laboratory-measured efficiency should be multiplied. The *UnshadowedFraction* has been measured in ice using a sample of stopping muons [308], [316], and a value of 0.99 ± 0.03 was found¹. However, recent analyses which include the *UnshadowedFraction*

¹For historical reasons some references use a different notational convention, where the nominal DOM efficiency is $0.9 \times$ the *UnshadowedFraction*=1 value.

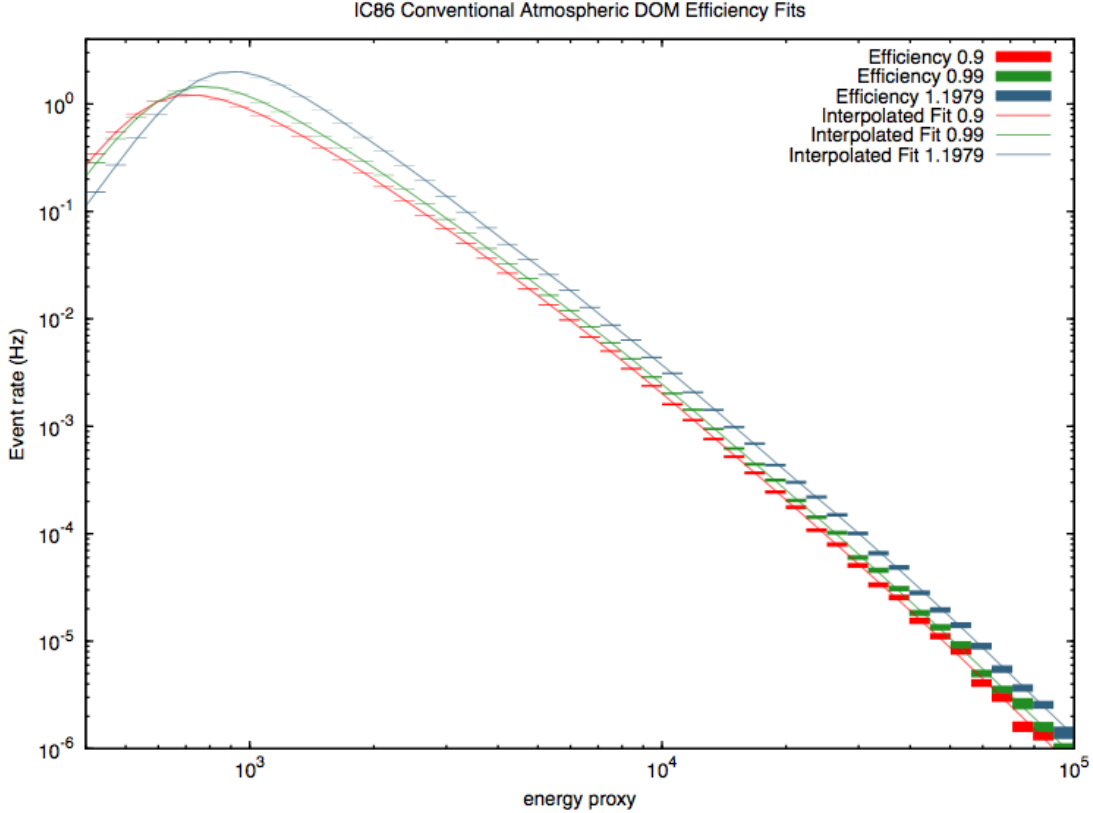


Figure 3.3.1: Reproduced from [306]. Slices through the continuous dom efficiency spline used in the IC79+86 diffuse analysis. The blocks show the uncertainty on directly produced Monte Carlo, and the lines show slices through the continuously parameterized DOM efficiency spline

as a free nuisance parameter have found significantly higher values [306], [307].

A higher absolute DOM efficiency results in a reduced true energy scale for detected events. This causes both a shift in the position of energy distribution peak, and also allows events to move across the trigger threshold altering the normalization of the sample. Further nontrivial effects are present in the high level quantities used in event selection and reconstruction. For this analysis, tools to parameterizing the effects of DOM efficiency in a continuous manner were adapted from the diffuse analysis developed using the same sample [306], [307]. There, several simulation samples were generated with different values of the *UnshadowedFraction*, and a penalized spline [317] was used to produce a continuous model of the effect of varying DOM efficiency on the bin contents of the final-level energy distribution. Figure 3.3.1, reproduced

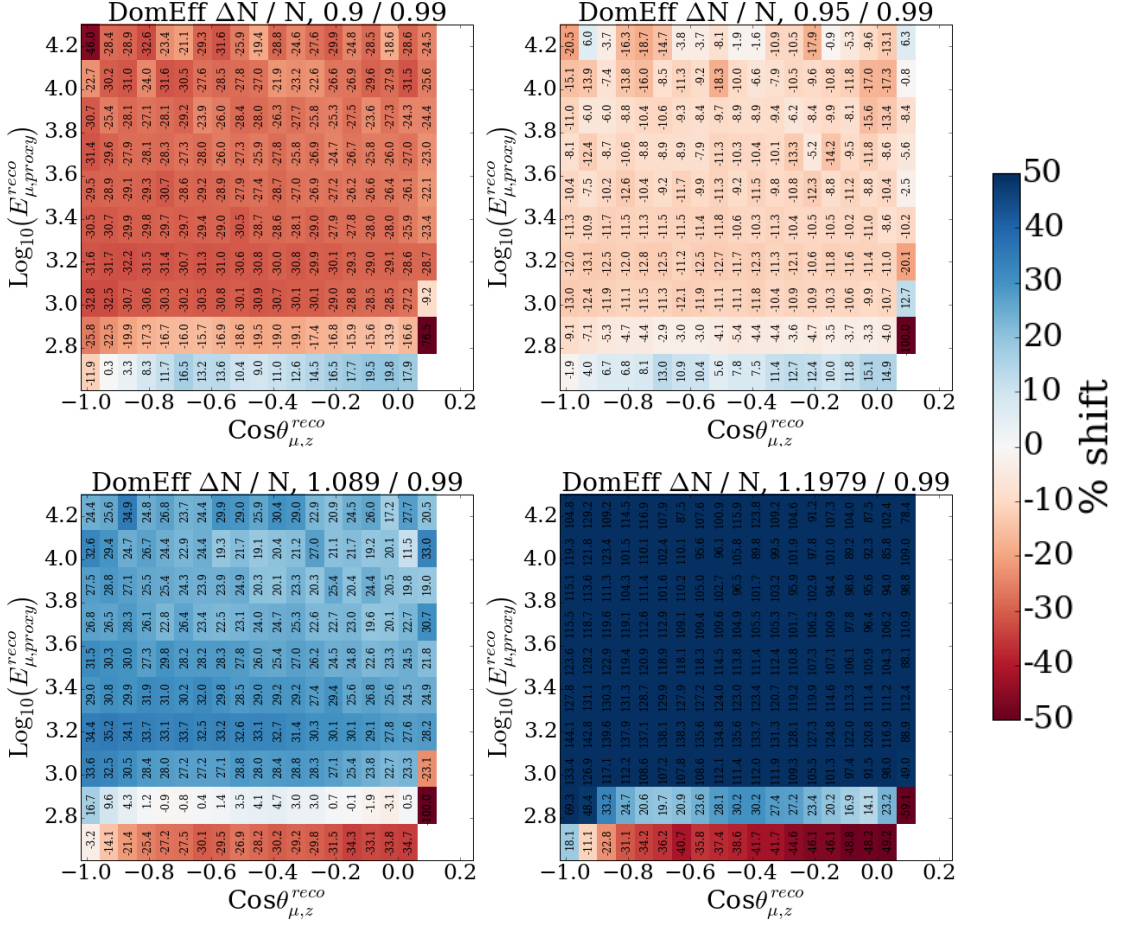


Figure 3.3.2: Shape effect of changing DOM efficiency, relative to the central value $\text{UnshadowedFraction}=0.99$. From top left to bottom right, $\text{UnshadowedFraction}=0.9$, 095, 1.089, 1.1979.

from [306], shows slices through the spline at several efficiencies compared to directly produced Monte Carlo sets, with excellent agreement in all cases.

Although using the same event selection, this analysis has important differences from the IC79+86 diffuse analysis. First, only IC86 data is used, so the detector configuration in Monte Carlo is not equivalent. Second, we are interested in shape effects in a two dimensional space rather than energy features alone, so zenith as well as energy shape is important. Third, improved Monte Carlo samples have been produced for use with the NuFSGen method. Fourth, improved versions of the reconstruction tools have become available.

For the above reasons, new Monte Carlo samples were made for splining, and the

spline method was extended to capture the shape of the analysis-level distribution in two dimensional energy-zenith space rather than energy alone. The several DOM efficiency sets were generated using a method of downsampling, first producing a set with the highest desired *UnshadowedFraction* (1.1979) and then randomly discarding detected photons between the light propagation and detector simulation steps to make the lower efficiency sets. The down-sampled sets are then independently processed through detector simulation, triggering, filtering, selection and reconstruction stages. This procedure significantly reduces the computational overhead of the photon simulation, which is a bottleneck in simulation production.

Two dimensional distributions in the analysis space showing the effects per bin of changing from the measured value of *UnshadowedFraction*=0.99 are shown in 3.3.2. In the analysis fit, a seed value of 0.99 is used and the *UnshadowedFraction* is allowed to vary with a flat prior. Because the energy peak position is a prominent feature of the distribution, good convergence is observed even when no prior is used. Using the derived spline, round-trip tests were made where particular DOM efficiencies were injected and recovered by a fit seeded at the nominal point. The fitted efficiency was always within 0.1% of the injected value, demonstrating the correct functionality of the spline-based DOM efficiency implementation.

3.2 Ice property uncertainties

The IceCube ice model has several thousand free parameters which are minimized in an iterative fit procedure using LED flasher data [289]. The fit does not produce uncertainty estimates on those parameters, and so evaluating the uncertainty of the ice model in a quantitative way in a given analysis is a nontrivial exercise. The strategy used in this analysis is to generate a small number of representative perturbations of the ice model and quantify the effect of detector-wide shifts in various parameters. These discrete systematic variants serve two purposes. First, our final likelihood will be minimized over discrete sets, meaning that if the data favors any variant over the central model at any hypothesis point, this set will provide the likelihood used in

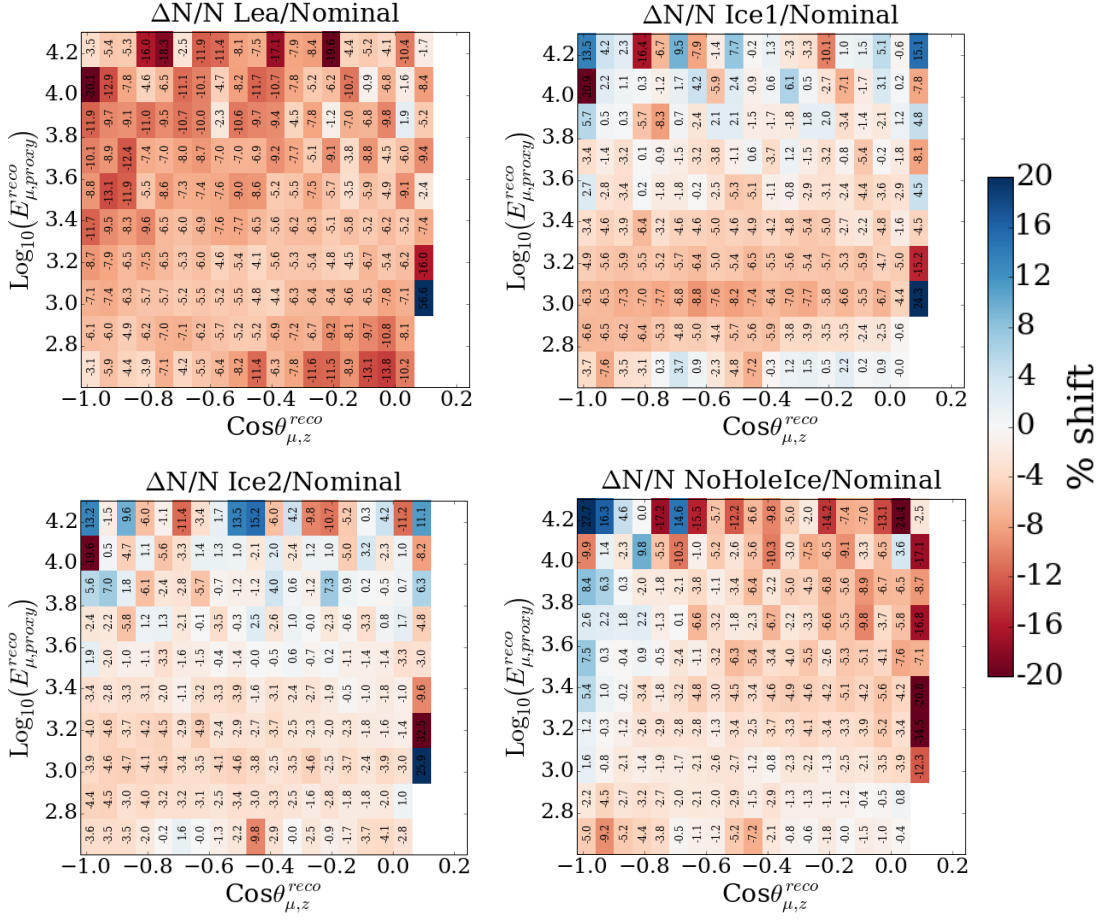


Figure 3.3.3: Shape effect of various ice model effects, evaluated by generating comparing discrete NuFSGen Monte Carlo sets.

hypothesis testing. Second, the analysis results from choosing each discrete variant will be compared, to ensure that the analysis is not highly sensitive to such variations.

The central ice model used in this analysis is SPICE Mie, which does not include anisotropy, but implements layer-by-layer absorption and scattering coefficients. SPICE Mie is favored because it was the default ice model used in IceCube Monte Carlo at the time of analysis development, and because the non-anisotropic response can be tabulated for Hybrid-Photonics-CLSIM calculations (see Section 2.2), whereas the newer SPICE Lea model requires fully analytic propagation of all photons, a much slower task only practicable on GPUs. To evaluate the scale of shape effects expected from neglecting anisotropy, a discrete systematic variant was generated using the

SPICE Lea model. The shape effect is shown in Figure 3.3.3, top left, as the ratio of the residual-per-bin to the SPICE Mie value. The SPICE Lea sample has a slightly lower overall normalization, which likely stems from a lower efficiency in track-quality cuts which were tuned on SPICE Mie. Little shape discrepancy is observed.

In the ice model fit, the absorption and scattering coefficients are first fit globally over the detector, and then layer-by-layer. The uncertainty on the global scattering and absorption scales was evaluated in this first fit stage yielding the uncertainty ellipse which was shown in Figure 3.1.7. From this ellipse, we observe that that 10% variations in absorption and scattering coefficients are compatible with the observed flasher data at 90% confidence level. Monte Carlo samples were generated with 10% globally shifted scattering and absorption coefficients across the detector to quantify the effect on the analysis observables. The discrepancies per bin are shown in Figure 3.3.3, top right and bottom left. Some shape effect is visible, but it is much smaller than the expected statistical uncertainty per bin, shown in Figure 3.2.8.

As described in Section 1.3, the ice column immediately surrounding the DOMs has different optical properties than the bulk ice because of bubbles which precipitate during the refreeze process. This “hole ice” changes the effective angular response of the DOM and may have a nontrivial effect on the analysis sample. To quantify the scale of effects which can be expected from hole ice mis-modeling, we compare an extreme case where the DOM is assumed to have its laboratory-derived angular response to the nominal hole ice model. These two DOM angular response functions are shown in Figure 3.1.10. The comparison at analysis level shown in Figure 3.3.3, bottom right. Once again, the observed shape effect is small compared with the statistical uncertainty per bin expected in data.

3.3 Cross section uncertainties

In our energy range of interest, neutrino-nucleon scattering processes can be well described by neutrinos exchanging vector bosons with individual partons in the nucleon. This is known as the deep inelastic scattering (DIS) regime. The charged current and

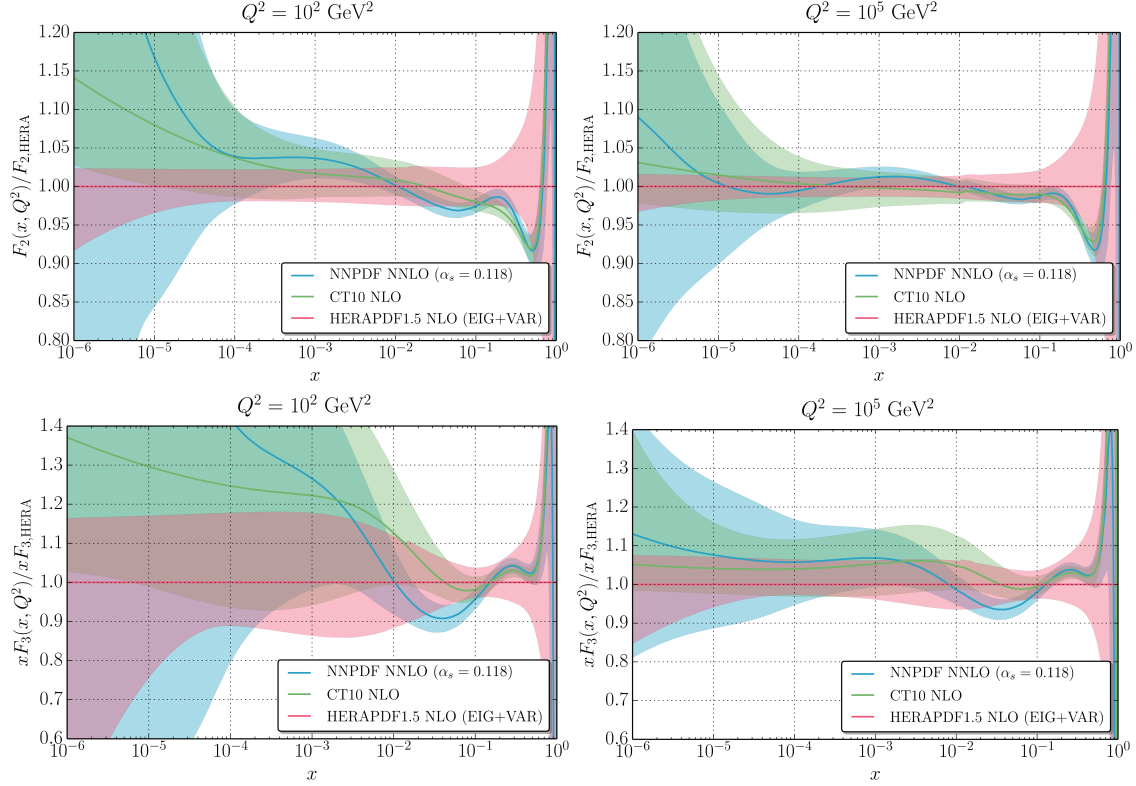


Figure 3.3.4: The F_2 and F_3 structure functions used in this analysis, shown as a ratio to HERAPDF central value. The lines show the central values and the colored bands show 1σ uncertainty regions.

neutral current cross sections have the form:

$$\frac{d^2\sigma_{\nu N}^{CC/NC}}{dxdy} = \frac{G_F^2 s}{2\pi} \left[(1-y)F_{2,\nu N}^{CC/NC} + y^2 F_{1,\nu N}^{CC/NC} \pm y(1-\frac{y}{2})xF_{3,\nu N}^{CC/NC} \right] \quad (3.1)$$

where $(+/-)$ correspond to $(\nu/\bar{\nu})$ scattering, and F_1 , F_2 and F_3 are structure functions that encode the effects of nucleon structure on the scattering cross section. The structure functions are specific to a particular nucleon (p/n) and scattering process (CC/NC), but in the parton model they can be written in terms of the distributions of momenta of valence and sea quarks in the nucleon. Also in the parton model, the Callan Gross relation imposes $F_L = 2xF_1 - F_2 = 0$, leaving only F_2 and F_3 as independent degrees of freedom, which are expressed in terms of parton distribution functions (PDFs) of quarks and gluons in the nucleon. The PDFs are extracted by global fits to data from many scattering channels by various theoretical collaborations.

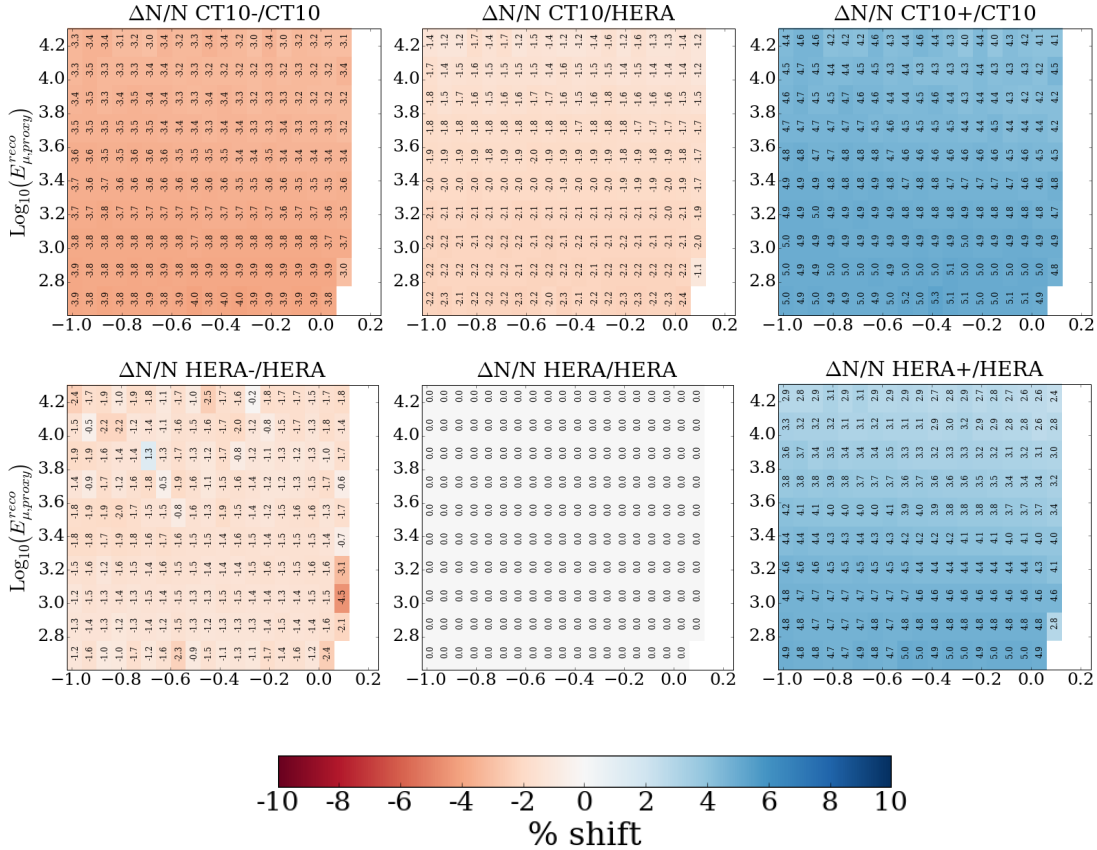


Figure 3.3.5: Effect of cross section model on analysis-level event distribution.

To estimate the scale of cross section uncertainty in the neutrino analysis sample we consider three separate sets of PDF functions at their central values and at $\pm 1\sigma$ of their stated uncertainty bands. The PDFs we consider are HERAPDF [318], CT10 at next-to-next-to-leading order [319], and NNPDF [320]. Slices through the structure functions F_2 and F_3 at two example Q^2 values are shown for νp charged current scattering in Figure 3.3.4. To illustrate the scale of uncertainty, the functions are shown relative to the HERAPDF central value, which is the cross section used in our central model. More information on the deep inelastic scattering cross section implementations used in this analysis can be found in [321].

The final state kinematics in the NuFSGen central sample after event selection are shown in Figure 3.3.6. This illustrates the ranges of x and y at which are most important for this analysis. The effects of changing the PDF on the final state event

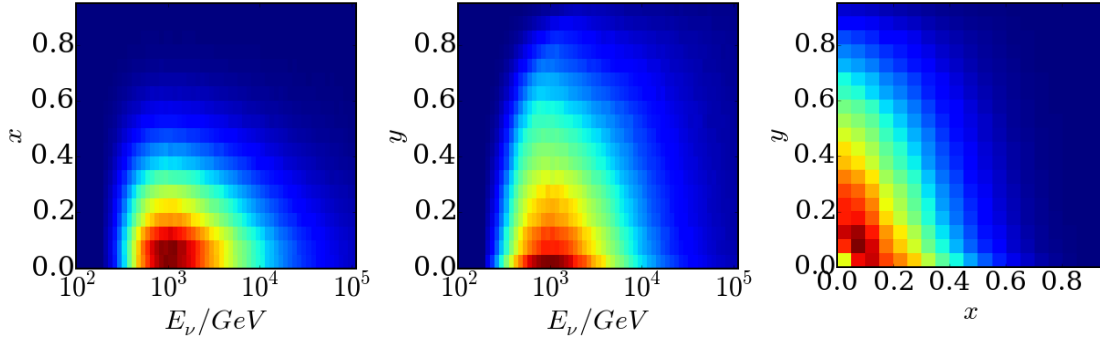


Figure 3.3.6: Final state kinematics in the selected NuFSGen central sample. Left: Bjorken x vs. true neutrino energy; Middle: Bjorken y vs. true neutrino energy; Right: Bjorken x vs. Bjorken y.

distribution, evaluated using fully weighted NuFSGen Monte Carlo, are shown in Figure 3.3.5. Technical problems with the NNPDF spline implementation mean it is not included in the results reported here, but it will feature in the final version of the analysis. Because the effects of cross-section uncertainty are very small relative to other systematics, only a very minor correction is expected from this omission. For the results presented here, the six cross section models shown in Figure 3.3.5 are used as discrete systematic variants.

3.4 Earth density uncertainties

The Preliminary Reference Earth Model (PREM) [322] is a parameterization describing the radial density profile of the Earth, and is the standard matter distribution assumed in IceCube analyses. The density profile is spherically symmetric with a radial dependence expressed by a piecewise function, formed from smooth polynomial segments connected at sharp discontinuities, as shown in Figure 3.3.7. The presence of the discontinuities and their locations are inferred from features in seismic reflection data, and the shapes of the segments between them are derived from a fit to s-wave, p-wave and normal mode data, constrained by the well known geodetic variables of Earth mass, moment of inertia and radius.

To assess the effects of Earth model uncertainty, the effects of making distortions

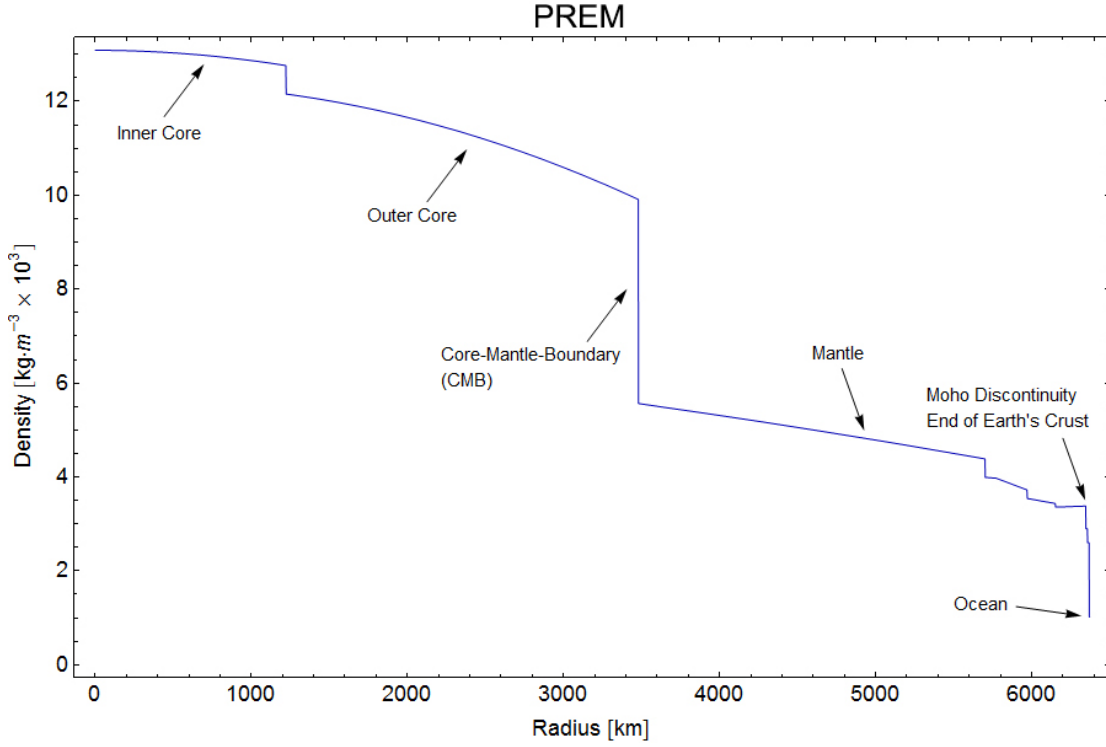


Figure 3.3.7: The PREM Earth density profile [322]. Plot is from [323].

of the PREM model were tested. The density of the earth at radius r is represented as a function of a dimensionless variable x , where $x = r/R_{Earth}$ with $x=0$ corresponding to the center of the earth and $x=1$ the surface. The PREM density is thus written as $\rho_{PREM}(x)$. To construct perturbed models, a small polynomial correction is added:

$$\rho(x) = \rho_{PREM}(x) + \rho_1(x), \quad (3.2)$$

$$\rho_1(x) = \sum_n^{N_{max}} a_n x^n. \quad (3.3)$$

We can choose the number of polynomial terms N_{max} , and randomly select values of the coefficients a_n . Not every choice of parameters $\{a_0 \dots a_{N_{max}}\}$ produces a physically reasonable perturbation. In particular, only those perturbations which preserve the mass and moment of inertia of the Earth are allowed. These two conservation

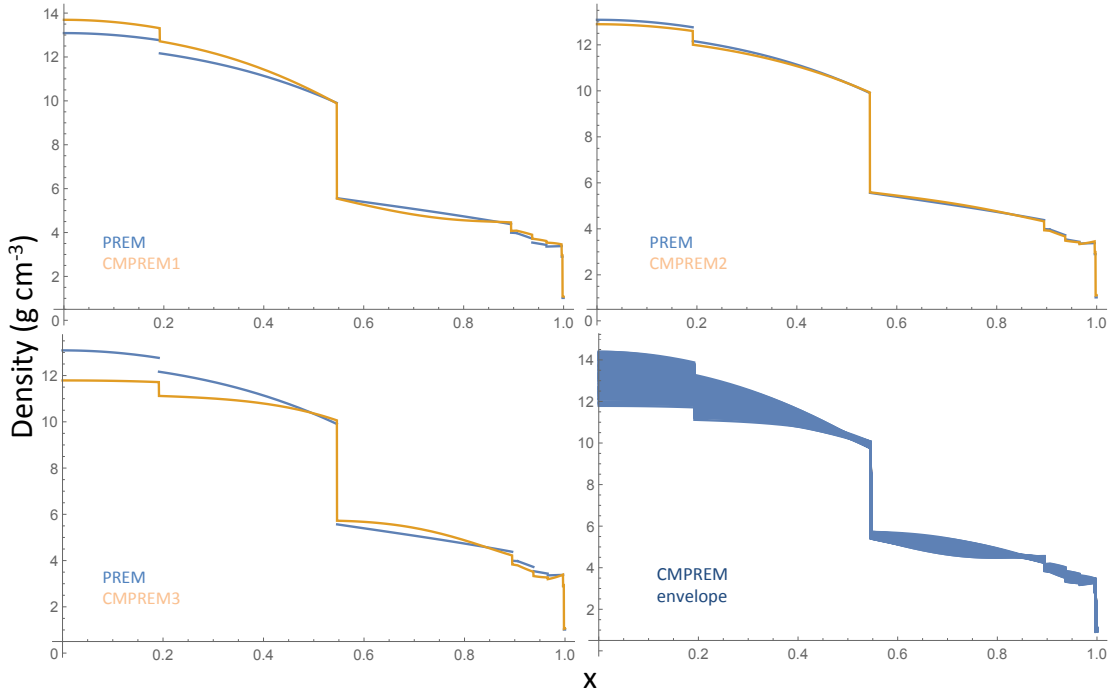


Figure 3.3.8: Examples of CMPREM models compared to the PREM. Bottom right shows the envelope of 100 models.

conditions can be written:

$$\Delta m = \int x^2 \rho_1(x) dx = \sum_n^{N_{max}} a_n \frac{x^{n+1}}{n+1} = 0, \quad (3.4)$$

$$\Delta I = \int x^4 \rho_1(x) dx = \sum_n^{N_{max}} a_n \frac{x^{n+3}}{n+3} = 0. \quad (3.5)$$

We also impose the condition that the derivative of the matter density should change continuously across the center of the Earth, rather than reaching a sharp point at $x=0$. This is already satisfied by the PREM, so the condition on our perturbation is:

$$\left[\frac{d\rho_1}{dx} \right]_{x=0} = a_1 = 0. \quad (3.6)$$

Equations Eq.3.4 and Eq.3.5 can then be solved for a_0 and a_2 expressed in terms of the remaining $N_{max}-3$ free parameters. Random choices of the remaining parameters $\{a_3 \dots a_N\}$ are made, and models meeting two further conditions are accepted:

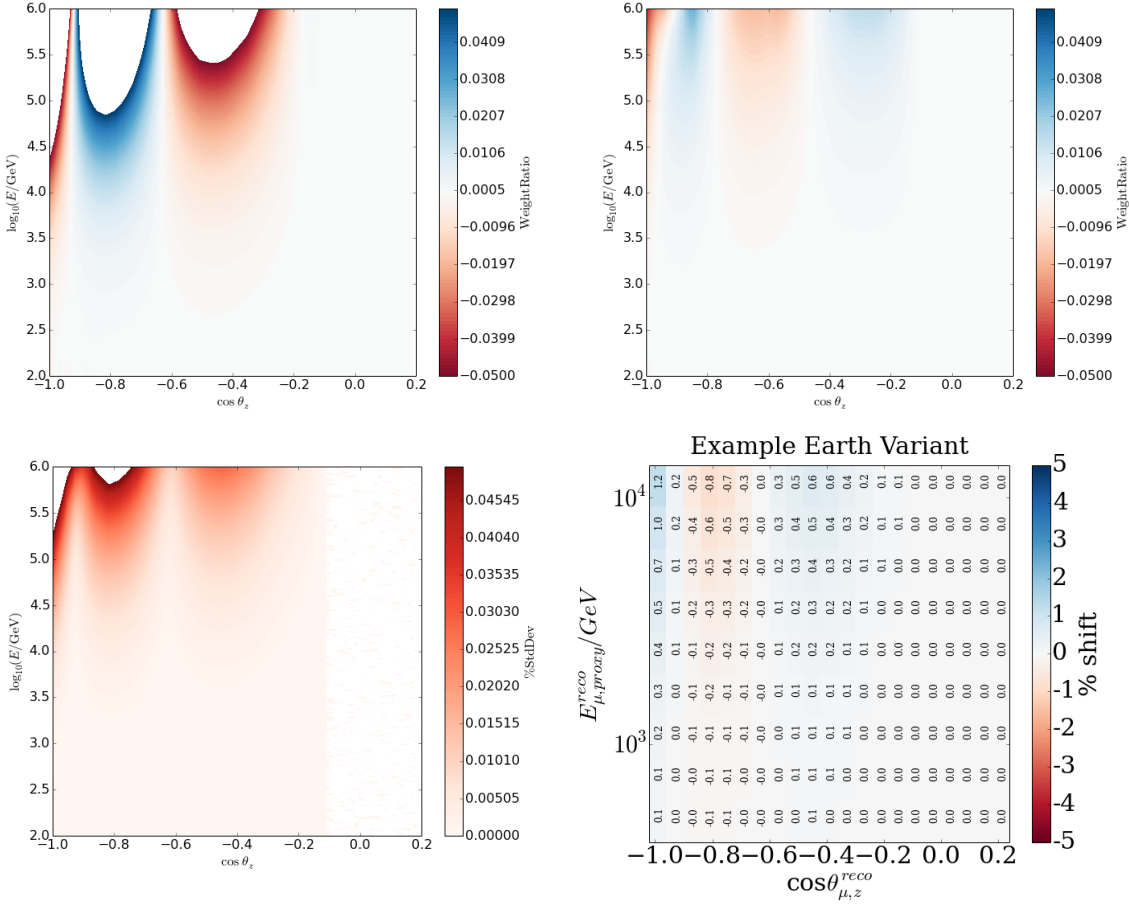


Figure 3.3.9: The effect on Earth density perturbations on the neutrino flux in the no-steriles model. Top left and right: neutrino flux effect in two example CMPREM models. Lower left: RMS over in 100 CMPREM models. Lower right: Analysis level effect for one of the largest perturbations.

1. The perturbation should not lead to a density profile which has a positive derivative at any point in the core or mantle, so near its center the earth should always move from more to less dense in the outward direction.
2. The perturbation should not change the local density by more than 10% relative to the PREM prediction at any point. This is conservative relative to statements of the PREM uncertainty which can be found in geology literature [324].

With these conditions, we generate a set of perturbed models which are physically reasonable and do not violate the tight constraints on the Earth mass or moment of inertia. These models necessarily have correlated densities at low and high radius.

For example, a model with a heavier core than the PREM must have a lighter mantle in order not to violate conservation of mass of the Earth.

Using $N_{max} = 10$, we generated 100 randomly modified PREM models. Three examples of constrained, modified PREM (CMPREM) models and the envelope of all allowed models are shown in Figure 3.3.8. The neutrino flux was propagated through these models using nuSQuIDS and at the no-steriles hypothesis point, to quantify whether Earth mis-modelling can fake a sterile neutrino signature. The resulting distortion in true neutrino variables is shown for two example models in Figure 3.3.9, top. The RMS distortion across all models is shown in Figure 3.3.9, bottom left. Effects are visible only at the highest energies, where neutrino absorption in the Earth is strong. Weighting to our central flux and cross section and propagating the simulation to analysis level, the effect of those perturbations on the reconstructed variables for one of the largest randomly generated perturbations is shown in Figure 3.3.9, bottom right. The effect is small compared to the expected statistical error, shown in Figure 3.2.8.

Although the effect of earth uncertainty can be neglected for the no-steriles hypothesis, models including a sterile neutrino will be affected differently by the Earth density uncertainty. In these cases, resonant matter effects are present which are sensitive to the density of the Earth along the neutrino trajectory. For this reason, ten discrete randomly perturbed PREM models are included as discrete variants in the analysis.

3.5 Flux uncertainties

Atmospheric neutrinos are produced by the decays of hadrons in cosmic-ray-induced air showers in the upper atmosphere. These decays compete with inelastic interactions with air molecules in the evolving shower [311]. At higher energies, the hadronic interaction cross section and decay length are both larger, so increasing energy suppresses neutrino production by favoring interaction over decay. Since the pion proper lifetime is longer than the kaon proper lifetime, neutrino fluxes from pions become suppressed

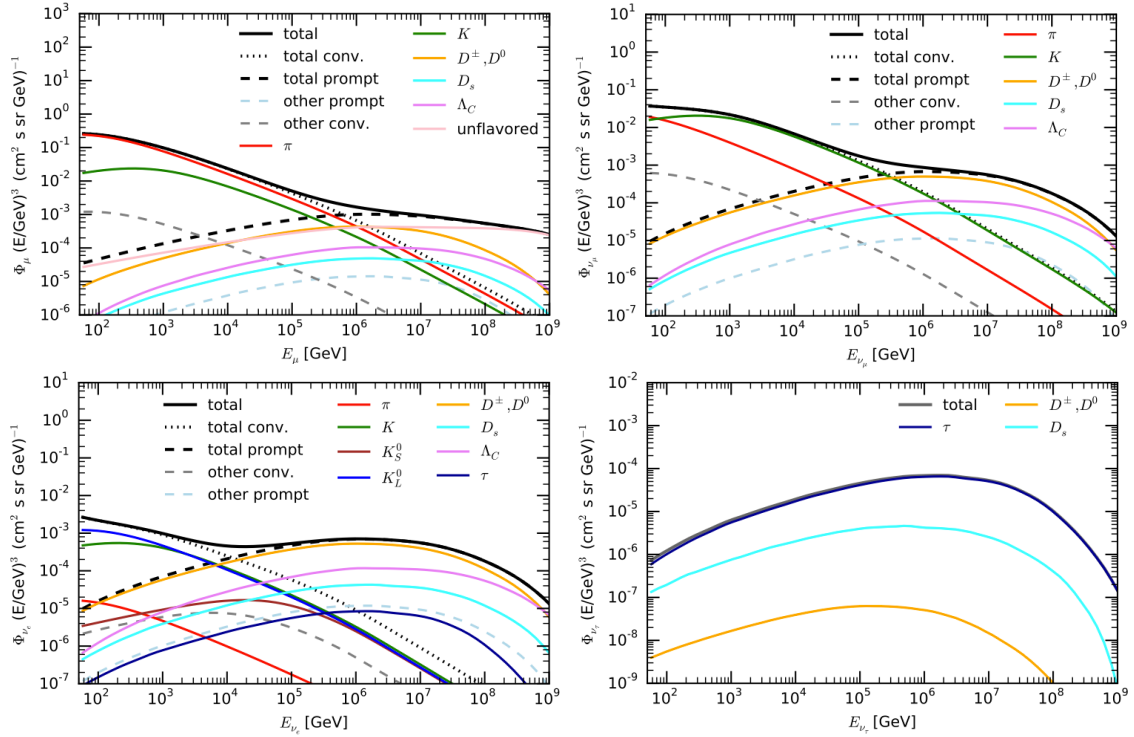


Figure 3.3.10: Calculated fluxes of muons and neutrinos originating from different parent particles in air showers, from [313].

by interactions at a lower critical energy. Thus pion decays are the dominant source of neutrinos at the lowest energies ($\lesssim 50$ GeV), with kaon decays becoming dominant at intermediate ones. At the very highest energies ($\gtrsim 10^5$ GeV), kaon decays also become suppressed by interactions, and “prompt” neutrinos from short-lived charmed hadrons D^\pm , D_s and Λ_C become dominant. Figure 3.3.10 shows the predicted origin and energy spectra of cosmic muons and neutrinos, from [313]. Various predictions of the atmospheric neutrino flux exist [313], [325]–[330], often tuned on primary composition data and measured muon rates. However, there are significant uncertainties associated with the atmospheric neutrino flux prediction.

These uncertainties stem from three main sources: 1) the incident primary composition and spectrum, 2) the hadronic physics of the evolving air shower, 3) the density profile of the atmosphere. Each will now be discussed.

Primary cosmic ray flux uncertainties

The energy spectrum of primary cosmic rays responsible for producing atmospheric neutrinos in our energy range of interest follows an approximately $E^{-\gamma}$ power law with $\gamma \sim 2.75$. The uncertainty in the spectral slope is treated using a nuisance parameter $\Delta\gamma$, which modifacitae the spectrum by a multiplicative factor:

$$\phi(E) \rightarrow \phi(E) \left(\frac{E}{E_0} \right)^{-\Delta\gamma} \quad (3.7)$$

The correction is implemented in an approximately normalization conserving way by choosing the pivot point E_0 near the median of the energy spectrum, at 2.02 TeV. A Gaussian prior with width 0.05 limits the spectral shift to values consistent with measured primary energy spectra [37].

The cosmic ray spectrum also has discrete features such as knee(s) [37], [333]. These are expected to be smeared out in the final neutrino energy spectrum since cosmic rays of any specific energy produce a wide range of neutrino energies. The shape uncertainty due to discrete spectral features is assessed by comparing three primary cosmic ray models as discrete systematic variants. These are the Honda-Gaisser model with Gaissser-Hillas H3a correction [331] and the Zatespkin Sokolskaya model [332], both of which fit models with five mass components and three source populations to experimental data; and the Polygonato [333] model, which posits that the cosmic ray knee is a result of multiple other knee-like features in each of the composition components. These models are used as inputs to the 1D analytic air shower simulation code ² of [313], and the effects on the neutrino energy spectrum are shown in Figure 3.3.11.

Air shower evolution uncertainties

Because hadron production in airshowers is very forward, high energy experimental data is sparse and QCD calculations have large uncertainties. This uncertainty

²These calculations were performed by Gabriel Collin, MIT [334], using code from [313].

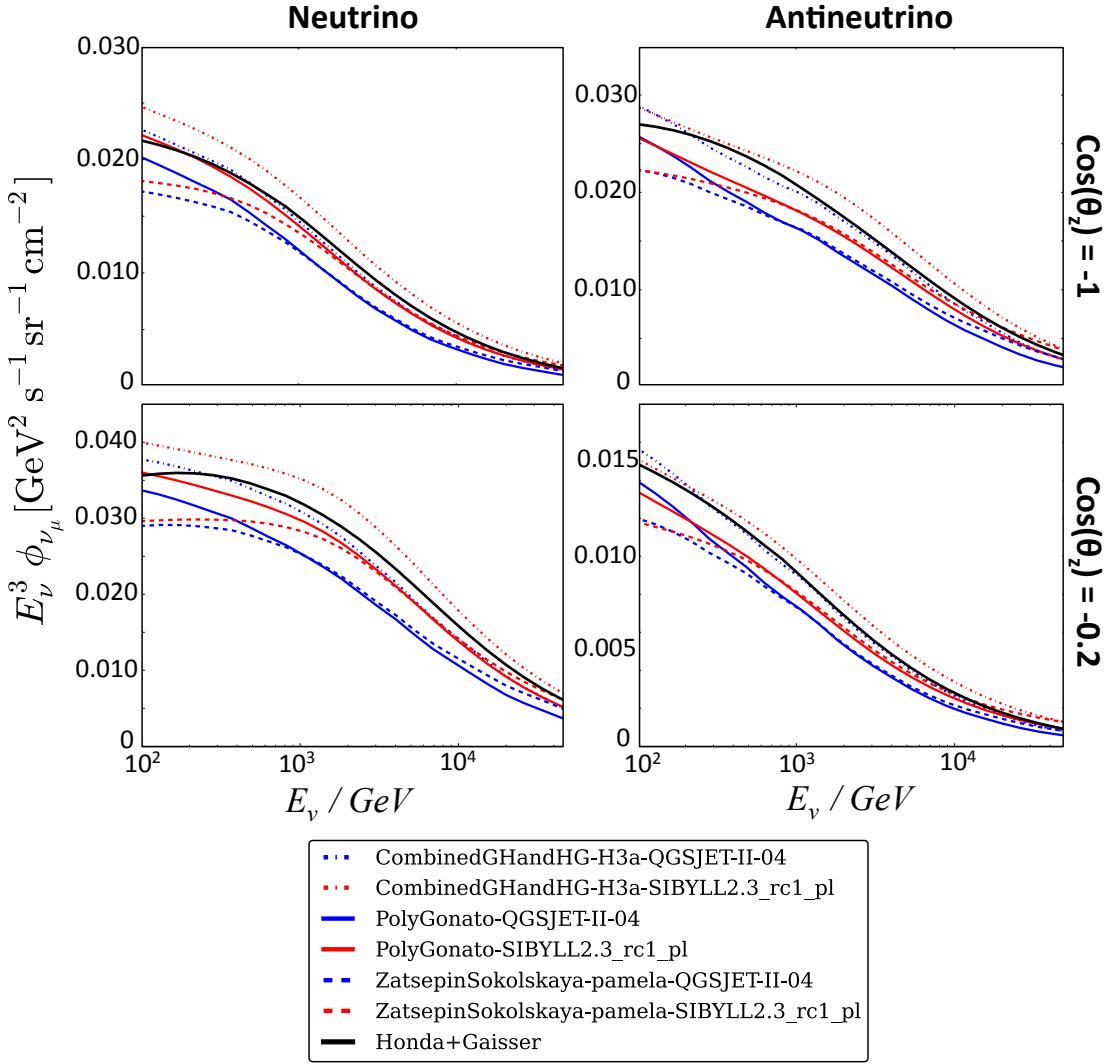


Figure 3.3.11: Neutrino energy spectra for different primary composition and hardonic model hypotheses.

translates to an uncertainty on the neutrino flux, which we treat using both discrete variants and continuous parameters.

As well as the HKKM central model, the effects of two different hadronic models are tested. The analytic air-shower evolution code of [313] was used to make flux predictions given for each incident cosmic ray spectrum and each hadronic model [334]. The two models studied are QGSJET II-04 [335] and SIBYLL-2.3 [336]. The predicted neutrino fluxes are shown compared to the central model in Figure 3.3.11. As well as these discrete variants, several continuous distortions of the hadronic model

are implemented to cover the space of physical fluxes.

Because of the lifetime difference between pions and kaons, the low energy neutrino flux is dominated by pion production, whereas the high energy flux is dominated by kaon production. The ratio between pion and kaon forward-production cross sections is therefore a source of spectral shape uncertainty. For each air shower model, including the central model, the pion- and kaon-induced neutrino fluxes are separated into two templates, which are allowed to float individually. The total flux normalization is absorbed into the flux normalization parameter discussed below, and the pion / kaon ratio is allowed to float as a nuisance parameter within a Gaussian prior of $\pm 10\%$.

The neutrino-to-antineutrino flux ratio is similarly allowed to float as a nuisance parameter. The prior on $\nu/\bar{\nu}$ is chosen to be 5%, which covers the values between discrete models, as shown in Figure 3.3.11. This has a small effect on the no-steriles hypothesis because the ν and $\bar{\nu}$ spectral shapes are similar. However, when an MSW-resonant oscillation is present, only antineutrinos are affected in a 3+1 model. Thus this parameter can float to suppress the resonance amplitude of a given oscillation hypothesis, which has implications for experimental sensitivity.

Atmospheric density uncertainties

The atmospheric density profile dictates how air showers evolve by influencing the competition between interaction and decay of high energy mesons. Uncertainty on the atmospheric density is therefore a source of uncertainty in the neutrino flux.

The atmospheric density used in the flux evolution calculations described above is provided from the Atmospheric InfraRed Sounder (AIRS) satellite [337]. AIRS travels in a heliosynchronous orbit and measures the Earths atmosphere using infrared and microwave sounding instruments at each latitude twice daily. This technique measures pressure-dependent absorption effects which encode the temperature profile as a function of atmospheric depth. This is deconvolved into a temperature profile as a function of altitude, latitude, longitude and time by NASA, and is provided with statistical and systematic uncertainties in daily-averaged, 8-day averaged and

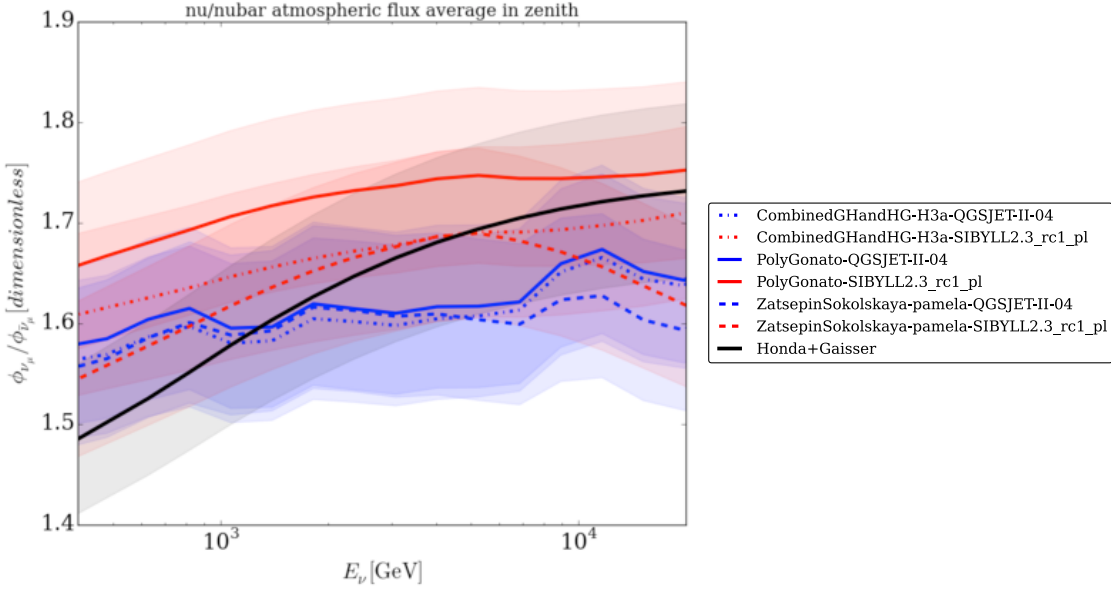


Figure 3.3.12: Plot showing the $\nu/\bar{\nu}$ ratios predicted by different air shower models (solid lines) and the range of values allowed when the continuous $\nu/\bar{\nu}$ nuisance parameter is allowed to float.

month-averaged data releases.

The neutrino flux is predicted month-by-month using the monthly-averaged satellite data sets. Examples of the predicted fluxes are shown in Figure 3.3.13, top, compared with the same prediction assuming the US Standard Atmosphere [338]. The total flux is given by the sum of monthly fluxes weighted to the detector live-time over the IC86 1 year dataset, which is shown in Figure 3.3.13, bottom.

The systematic uncertainty on the satellite measurements can be propagated through the calculation into shape uncertainty on the predicted neutrino flux via random sampling. This uncertainty is largest near the horizon due to both the larger slant-depth of the air-showers and the small geographical region being sampled, resulting in larger variations from local weather effects. The uncertainty band for two energy points are shown as a function of zenith angle in Figure 3.3.14. A continuous nuisance parameter is implemented which distorts the zenith spectrum to cover this band. The prior on this parameter is set model-by-model based on the observed size of the propagated uncertainty.

Flux normalization uncertainty

The goal of this analysis is to search for MSW-resonant depletion of atmospheric $\bar{\nu}_\mu$ associated with sterile neutrino oscillations. This has both rate- and shape-changing effects on the atmospheric neutrino flux. The blind analysis proposal is to use only shape information, and allow the flux normalization, which has large uncertainties from all the above effects, to float as a free parameter with a uniform, positive prior.

As will be discussed in Section 4.4, in some parts of sterile neutrino hypothesis space, in particular those with large mixing and high Δm^2 , the expected signal is a large flux normalization change but very little shape change. These hypotheses are effectively null-like in a shape-only analysis, even though a large oscillation effect

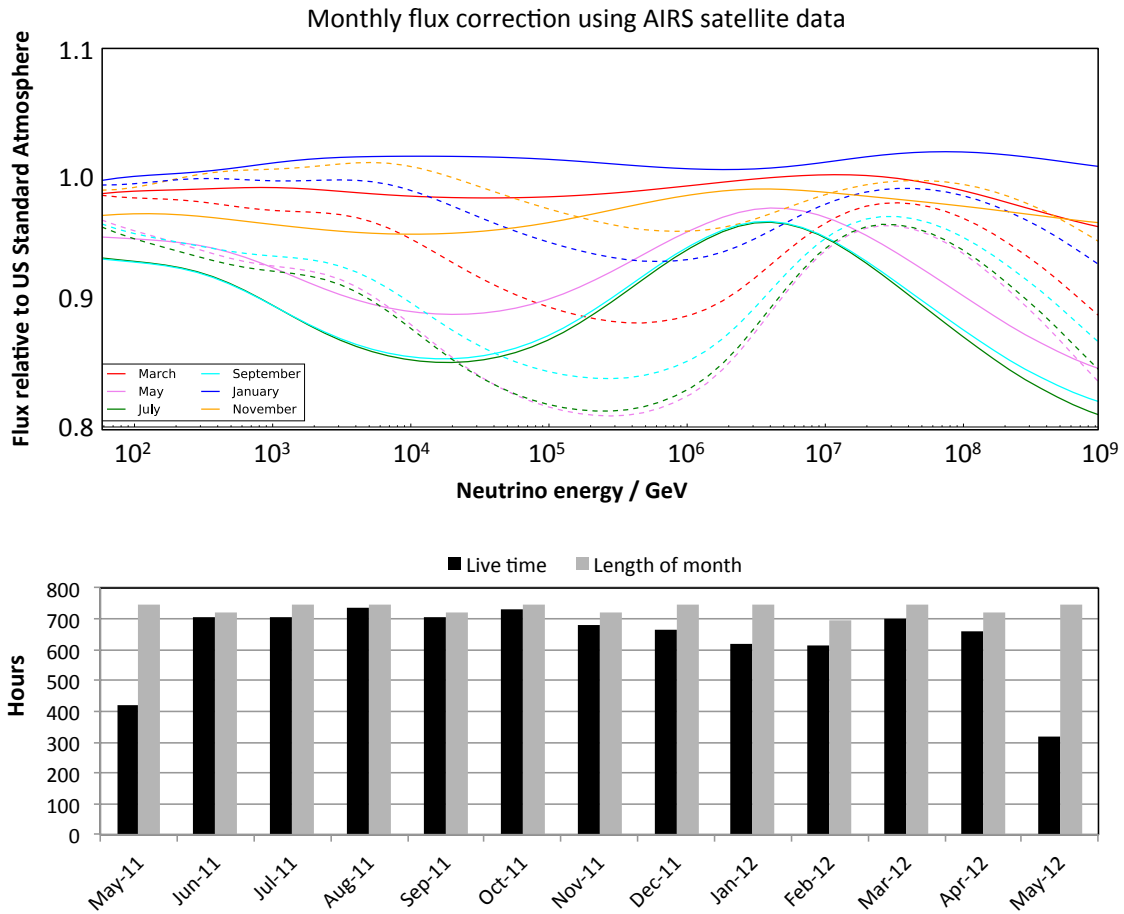


Figure 3.3.13: Top: correction to flux from AIRS measurements of atmospheric density per month. Bottom: Monthly livetime of the detector over the search period.

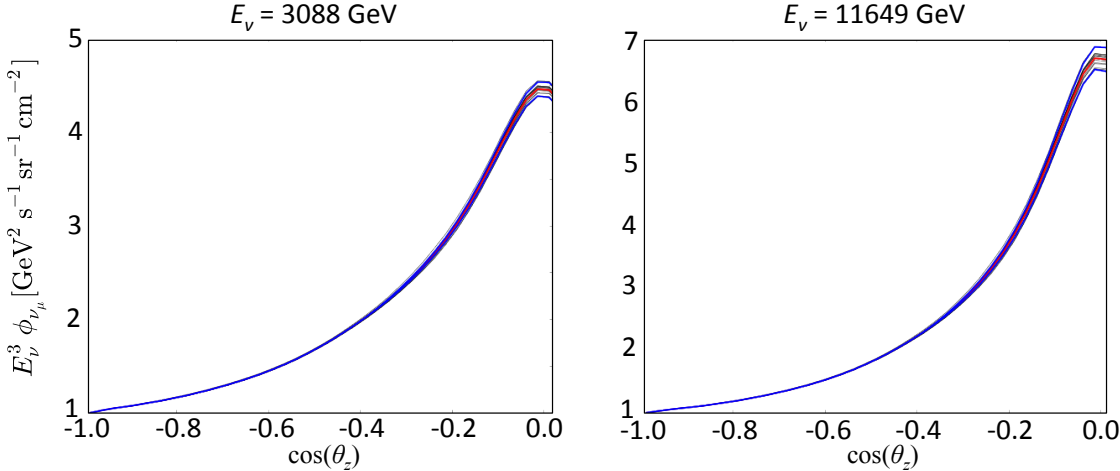


Figure 3.3.14: Effect of atmospheric density uncertainty. Black lines show variations of the flux within AIRS density measurement uncertainty. The blue curves show the $\pm 1\sigma$ band of variations allowed by the atmospheric density nuisance parameter. For illustration, the flux is shown as a function of zenith angle at two fixed energies.

is present. Power to reject these hypotheses can be gained by implementing a finite prior on normalization, changing from shape-only approach to a rate+shape one. The effects of this change were explored post-unblinding. The appropriate normalization prior to use was evaluated using information from three sources:

1. The quoted flux normalization uncertainty from [330], shown in Figure 3.3.15, left. The uncertainty is 30-40% over the energy range of interest for muon neutrinos.
2. The quoted normalization uncertainty in the HKKM calculation [310], shown in Figure 3.3.15, right. The uncertainty at the top end of the HKKM energy range is 25% and is increasing with energy. Our central model matches HKKM to a Gaisser parameterization at 700 GeV, so a direct uncertainty estimate in our energy range for the central model is not available, but 25% is considered as a lower limit.
3. The range of flux normalizations covered by the discrete hadronic and primary models used in this analysis, shown in Figure 3.3.11. Their spread is around $\pm 40\%$, above and below the HKKM model.

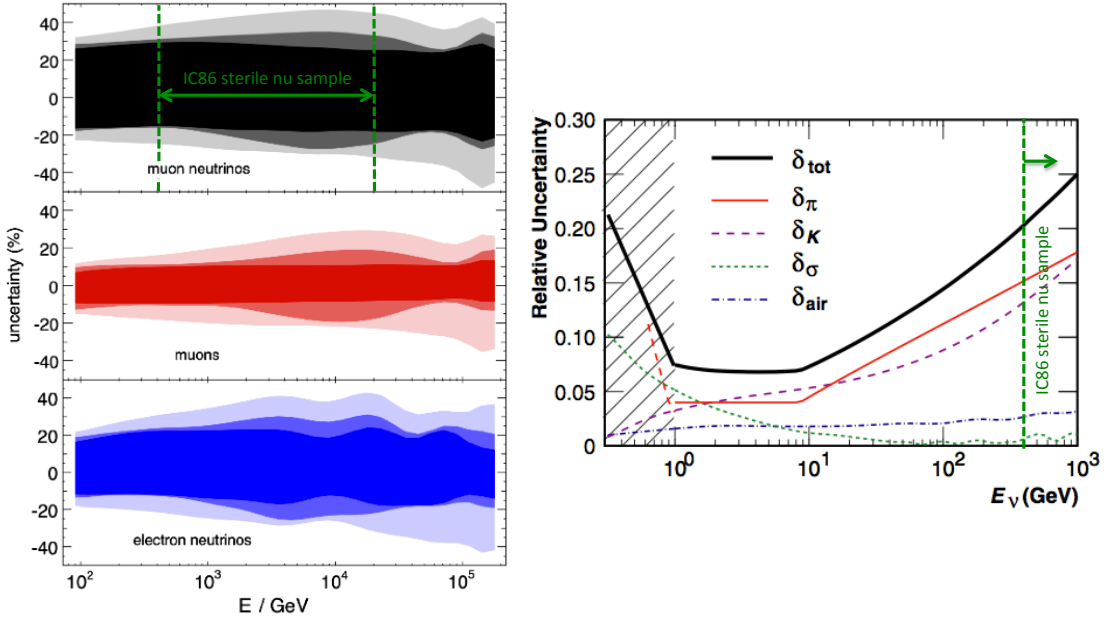


Figure 3.3.15: Flux normalization uncertainties. Left: from [330]. Inner solid bands show normalization uncertainty from variations in hadronic models only. Medium and lighter bands show uncertainty due to variations in both interaction and primary compositions, for two different sets of primary models. Refer to [330] for more information. Right: from [310]. Total normalization uncertainty δ_{tot} is shown in black. Also shown are contributions from the pion production cross section δ_π , kaon production cross section δ_K , hadronic interaction cross sections δ_σ , and atmospheric density δ_{air} .

Based on the above considerations, in the cases where normalization information is included, a 40% normalization prior is used.

Chapter 4

Results of the IC86 Sterile Neutrino Analysis

4.1 Fit procedure and sensitivity

To search for sterile neutrino oscillations in the atmospheric neutrino flux shape we will compare weighted NuFSGen Monte Carlo samples to data, and compute a binned Poisson likelihood for each sterile neutrino hypothesis in energy/zenith space. The binning used is that of Figure 3.2.8. The hypotheses tested are the no-oscillations point, and an array of possible sterile neutrino hypotheses on a uniform grid in $\log(\Delta m^2)$, $\log(\sin^2 2\theta)$ space. Our initial choice of grid has spacing 0.05 in both variables and runs from $10^{-2} < \Delta m^2/eV^2 < 10^1$ and $0.01 < \sin^2 2\theta < 1$. Larger or coarser hypothesis grids are used for some cross checks and frequentist studies.

At each point in the sterile neutrino parameter space, the maximum likelihood allowed within variations of the nuisance parameters will be calculated. The formula for the bin-wise Poisson log-likelihood (LLH) is:

$$LLH = \max_{\vec{\theta}, d} \left(\sum_{i=1}^{N_{bins}} \left[x_i \log \lambda_i(\vec{\theta}, d) - \lambda_i(\vec{\theta}, d) \right] - \sum_{\eta} \frac{(\theta_{\eta} - \Theta_{\eta})^2}{\sigma_{\eta}^2} \right). \quad (4.1)$$

The first term in Eq.4.1 measures the likelihood of statistical fluctuations in the bin

Continuous parameter	Central value	Gaussian prior width
normalization	1	no prior ¹
DOM Efficiency	0.99	no prior
cosmic ray spectral shift	0	0.05
π/K ratio	1	0.1
$\nu/\bar{\nu}$ ratio	1	0.025
atmospheric density shift	0	tuned per-model

Table 4.1: Continuous nuisance parameters used in the fit

contents x_i compared to their expectation values $\lambda_i(\vec{\theta}, d)$ for a given set of continuous nuisance parameters $\vec{\theta}$ and discrete variant d . The second term penalizes the likelihood based on Gaussian priors for the nuisance parameters with central values Θ_η and widths σ_η .

Comparison of LLH at points in the hypothesis space allows us to define confidence intervals in the sterile neutrino parameters ($\log(\Delta m^2)$, $\log(\sin^2 2\theta)$), given a data sample. The test statistic used is the log-likelihood difference ΔLLH between the best-fit hypothesis and the test hypothesis, which allows the construction of a unified confidence interval, avoiding flip-flopping between signal and exclusion results.

One way to calculate a confidence interval given the ΔLLH profile of the hypothesis space is to use Wilks theorem [339], which states that in a likelihood space with two degrees of freedom (DOF), the probability distribution of $2\Delta LLH$ will be a χ^2 distribution with two DOF. The correctness of Wilks confidence intervals depends on assumptions about the Gaussianity of the likelihood space. If these assumptions are strongly violated, the Wilks confidence intervals can have improper coverage. Another method for calculating confidence intervals, which always provides proper coverage, is the frequentist Feldman Cousins method [340]. Our approach will be to derive contours using Wilks' theorem, and check their validity using the Feldman Cousins test. This check will be described in Section 4.6.

Likelihood maximization over nuisance parameters at each hypothesis point has two stages. First, the likelihood is maximized over continuous nuisance parameters

¹The effects of including a normalization prior will be discussed in Section 4.4

Discrete variant	Variant numbers
Central model	0
<i>SPICEMie, PREM, HERAPDF</i>	
Ice absorption +10%	1
Ice scattering +10%	2
SPICELea	3
No hole ice effect	4
Flux variants	5-10
Cross section variants	11-15
Earth model variants	16-24

Table 4.2: Discrete simulation sets compared for maximum likelihood

using an iterative fit procedure. At each step in the fit, each event in the Monte Carlo sample is reweighted according to the local nuisance parameter hypothesis. The likelihoods at this point and a neighborhood of points are evaluated, the maximum is found by gradient descent. The continuous nuisance parameters included in this analysis and their priors are listed in Table 4.1. This fit is performed once for every discrete systematic variant. The discrete systematic variants used in this analysis are listed in Table 4.2. The likelihoods from each discrete variant are compared and the largest is found for each hypothesis point.

The per-bin expectation values, $\lambda_i(\vec{\theta}, d)$, depend not only on the nuisance parameters but also on the oscillation hypothesis. The oscillation weights are assigned by NuSQuIDs based on a pre-calculated solution to the evolution master equation. This pre-calculation was performed on the OSG once for each flux, Earth variant and oscillation hypothesis. This provides the at-detector flux weights for propagated neutrinos and antineutrinos for each point in hypothesis space.

The exclusion region expected if no sterile neutrinos exist was evaluated by running simulated pseudo-experiments 1000 times and evaluating the resulting Wilks contours. Unlike in the case of vacuum-like oscillations, the relationship between $\sin^2 2\theta$ and the disappearance amplitude is non-linear one. This leads to relatively large fluctuations trial-to-trial in the excluded range of mixing angles, giving a wide band of possible exclusion limits. Figure 3.4.1, left shows the range of exclusion contours at 90%

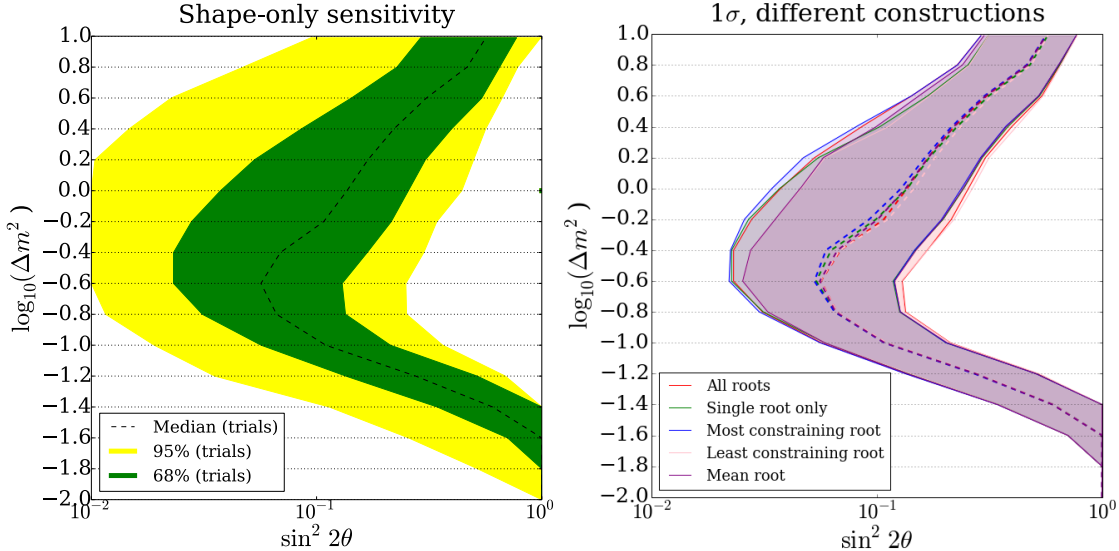


Figure 3.4.1: Left: Shape-only analysis sensitivity. The yellow and green bands contain 68% and 95% of the 90% CL contours from simulated pseudo-experiments, respectively. The dashed line shows the median contour. Right: Median and 1σ bands constructed using different contour-counting protocols.

confidence level (CL). In this figure, the yellow and green bands contain 68% and 95% of the 90% CL contours from simulated pseudo-experiments, respectively. The position of the contour at each of the marked Δm^2 values was calculated in each trial, and the median and counting intervals were calculated from this ensemble at each point.

For psuedo-experiments which produce either closed contours or contours with complicated shapes, there may be multiple points where the contour crosses a given Δm^2 . The protocol for counting these roots can therefore impact the shape of the sensitivity plot. The 1σ band and median sensitivity was evaluated using various root-counting protocols. These are: 1) count every root, so each trial may feature in the distribution multiple times; 2) count only the trials where the contour only crosses the Δm^2 point of interest once, and disregard the ambiguous cases; 3) count only the most constraining root per trial; 4) count only the least constraining root per trials; 4) take the mean Δm^2 over all the observed roots per trial. A comparison of these approaches is shown in Figure 3.4.1, right, and illustrates that the choice of protocol has only a small effect on the sensitivity.

4.2 Pre-unblinding tests of data sample

As an intermediate step towards unblinding, the IC86 1-year data sample was fit to the null hypothesis and projected onto 1D energy and zenith plots using the central Monte Carlo sample, shown in Figure 3.4.2. The Poissonian p-values in energy and zenith are 32.7% and 30.8% respectively, and the best-fit nuisance parameters are tabulated in Table 4.3. Improvements in the behaviour of the nuisance parameter compared with the values obtained using the same sample in [307] were observed. In particular, the measured DOM efficiency is within 0.1% of the independently measured value from stopping muons [308], [316], affected substantially by the removal of the DOM oversizing approximation and other simulation bug fixes.

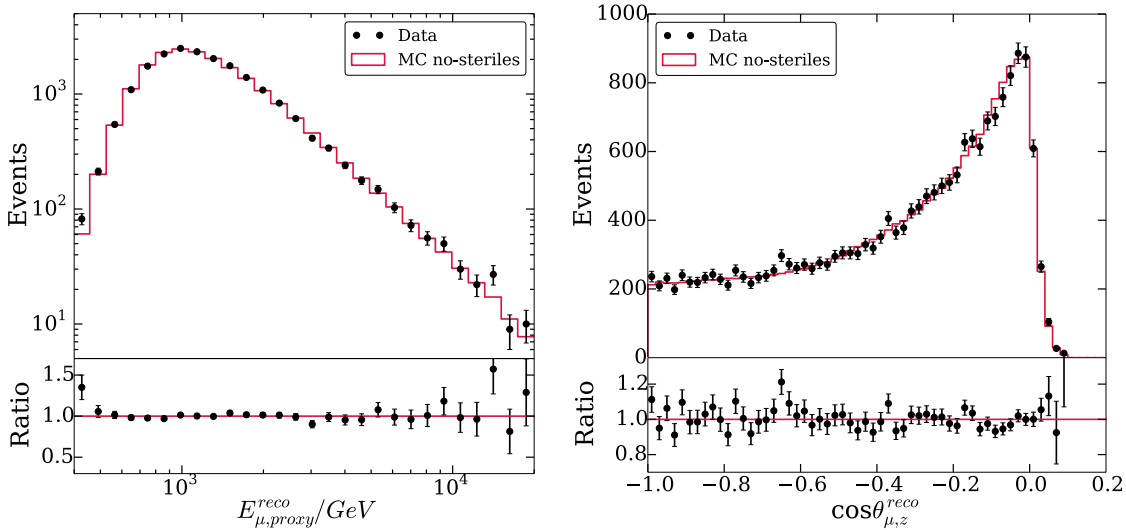


Figure 3.4.2: Best fit no-steriles hypothesis fit to data and projected into energy and zenith distributions.

Parameter	Expectation	Our prior	From [307]	This work
normalization	1	no prior	0.93	1.045
DOM Efficiency	0.99	no prior	1.08	0.990
cosmic ray spectral shift	0	0 ± 0.05	-0.023	0.051
π/K ratio	1	1 ± 0.1	0.15	1.064
$\nu/\bar{\nu}$ ratio	1	1 ± 0.05	not used	1.00
atmospheric density shift	0	0 ± 0.035	not used	-0.043

Table 4.3: Best fit values for the no-steriles hypothesis

4.3 Blind results of shape-only analysis

The IC86 1 year dataset was fully unblinded in May 2015. Bug-fixes were made post-unblinding which in aggregate made negligible changes to the initial result. The event counts per bin and pulls from the no-steriles hypothesis after the nuisance parameter fit are shown in Figure 3.4.3. No evidence for sterile neutrinos was observed. The 90% and 99% Wilks confidence intervals are shown in Figure 3.4.4. The best fit is at $\Delta m^2 = 10\text{eV}^2$ and $\sin^2 2\theta = 0.56$, with a likelihood difference from the no-steriles point of $\Delta LLH = 1.91$ corresponding to a p-value of 14.9%.

The properties of the best fit point were compared to expectations for the no-steriles hypothesis using simulated trials. The positions of the best fit points, and the ΔLLH values between true and best fit hypotheses were evaluated in 1000 no-steriles pseudo-experiments. Figure 3.4.5 shows the positions and depths of the likelihood minima in these trials.

The distribution of minima has two notable features. First, the best-fit points tend to fall in the region where the sterile hypotheses introduce small but nonzero shape effects. This is an expected behavior: very near the null hypothesis, the likelihood space is flat and the significant likelihood fluctuations predicted by Wilks theorem are not accessible. Regions with large shape effects due to the presence of sterile

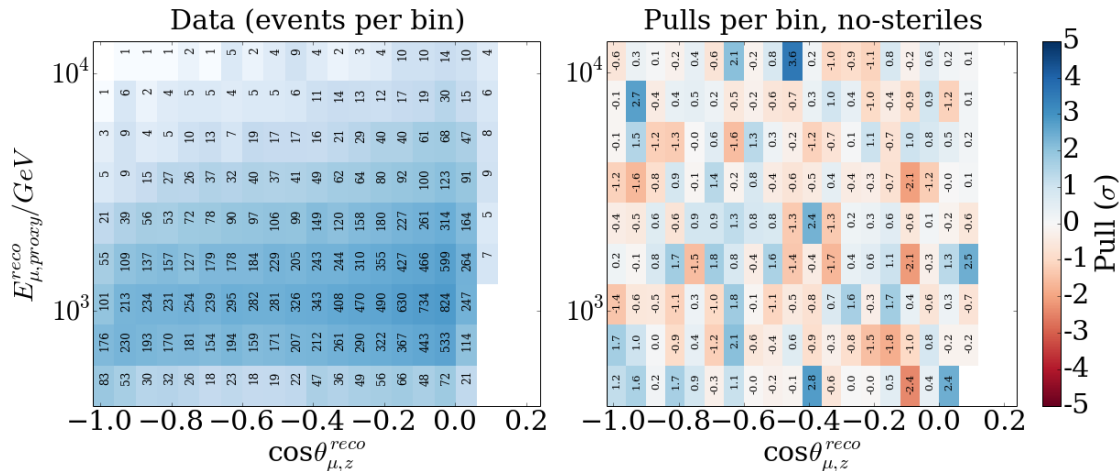


Figure 3.4.3: Left : Events per bin in the unblinded data sample. Right : Pulls per bin between data and the best-fit no-steriles hypothesis.

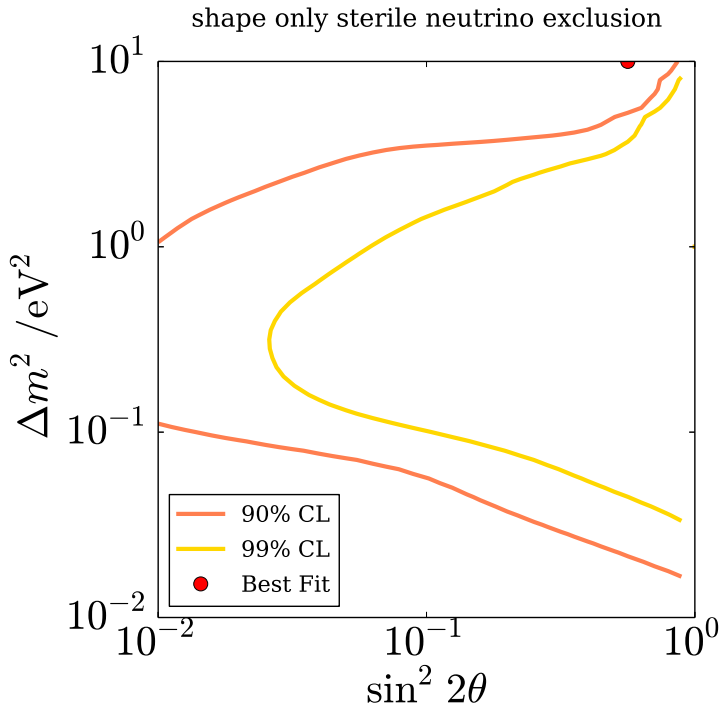


Figure 3.4.4: 90% and 99% CL Wilks confidence intervals from the shape-only analysis.

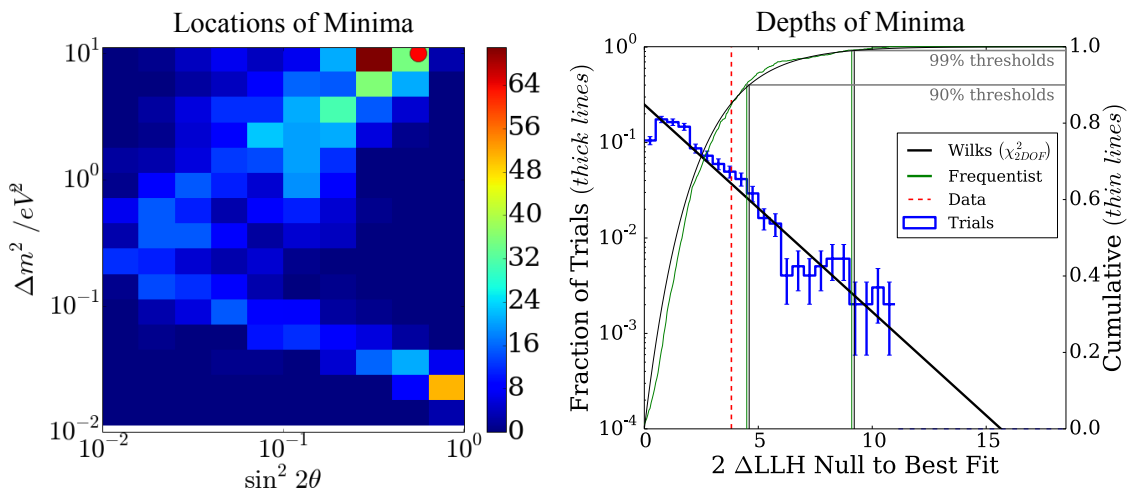


Figure 3.4.5: Positions and depths of minima in no-sterile trials of the shape-only analysis

neutrinos, on the other hand, are reliably rejected. This leaves an area of “null-like” parameter space with small but non-negligible shape effects where the minima tend to fall. Another feature of interest is the preference of the best-fit to appear in the null-like hypotheses which are at high mixing over those which are at lower mixing. This is believed to be a consequence of the coupling between the $\sin^2 2\theta$ and Δm^2 degrees of freedom. When the mixing is small, changing Δm^2 has a small effect on spectral shape. When $\sin^2 2\theta$ is large, on the other hand, small changes to Δm^2 explore a larger range of shape hypotheses, making the high mixing null-like region more likely to be favored over the null.

The depths of the minima, shown in Figure 3.4.5, right, have a distribution which is close to the expected χ^2_{2DOF} distribution predicted by Wilks’ theorem. A small deviation is observed at small ΔLLH , but the frequentist 90% and 99% thresholds are negligibly modified. This implies that despite the nontrivial distribution of minima over the parameter space, conclusions derived from Wilks’ theorem about the no-steriles point are valid.

4.4 Inclusion of rate information

The high and low Δm^2 clusters of null-like solutions in Figure 3.4.5, left, have interesting conceptual differences which are hidden in a shape-only analysis. The low Δm^2 solutions are null-like because 1) the MSW resonance condition is not met at energies where there are high statistics and 2) vacuum-like oscillation occurs on distance scales longer than the size of the Earth. They introduce almost no oscillation effect, and hence almost no shape change. For the high Δm^2 null-like solutions, on the other hand, there is an oscillation, but one which has a rapid energy dependence and is smeared out by the energy resolution of the detector. This introduces a normalization shift in the detected neutrino flux, but minimal shape effect. In a shape-only analysis, these two situations are indistinguishable. In an analysis using rate as well as shape information, they have different behaviors and can be distinguished.

To illustrate this effect, Figure 3.4.6 shows how the best-fit normalization corre-

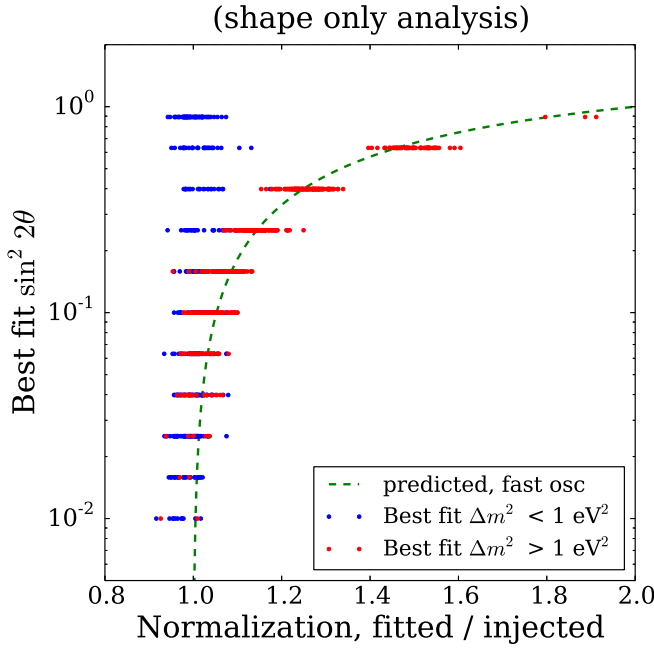


Figure 3.4.6: Correlation between fitted normalization and mixing for no-sterile injected trials in the shape-only analysis

lates with best-fit $\sin^2 2\theta$ in shape-only pseudo-experiments, injecting the no-steriles hypothesis. In the small Δm^2 part of parameter space, the nominal normalization is usually recovered by the fit, even when a high-mixing null-like solution is preferred. In the large Δm^2 part of parameter space, large-mixing solutions induce large normalization changes. The effect is consistent with the theoretical expectation of the normalization shift expected due to fast oscillations, also shown in Figure 3.4.6.

Since normalization is a free parameter in the shape-only analysis, large differences from the nominal value are allowed. Penalizing these differences using a normalization prior converts the analysis from a shape-only analysis to a rate+shape one, and the effects of such a change were investigated after unblinding the sample. Because the best-fit solution is a high Δm^2 null-like point which will be significantly penalized, a reduction in exclusion power of the unified contours compared to the shape-only analysis is expected.

As discussed in Section 3.5, the uncertainty on the normalization prediction in this energy range is around 40%. The analysis result using a 40% normalization prior

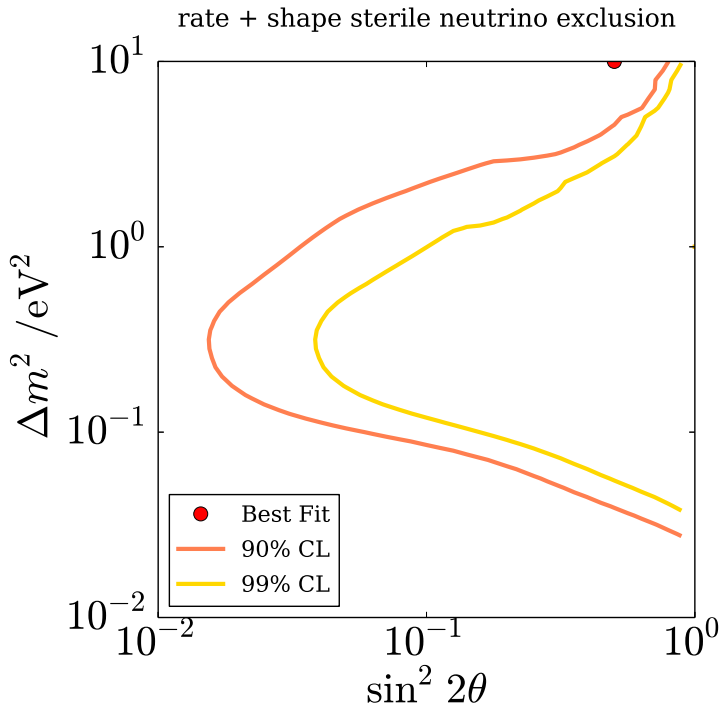


Figure 3.4.7: 90% and 99% CL Wilks confidence intervals from the rate+shape analysis.

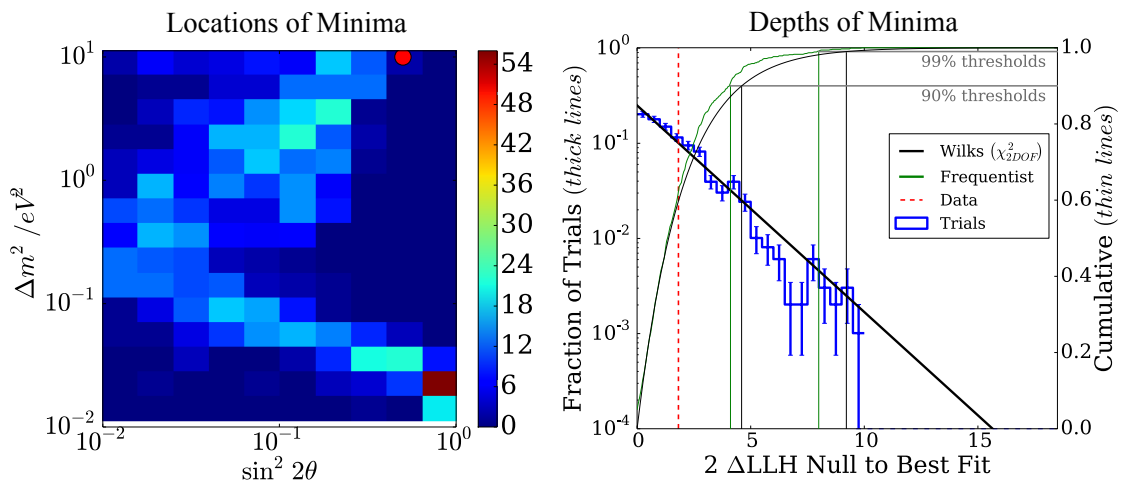


Figure 3.4.8: Positions and depths of minima in no-sterile trials of the rate+shape analysis

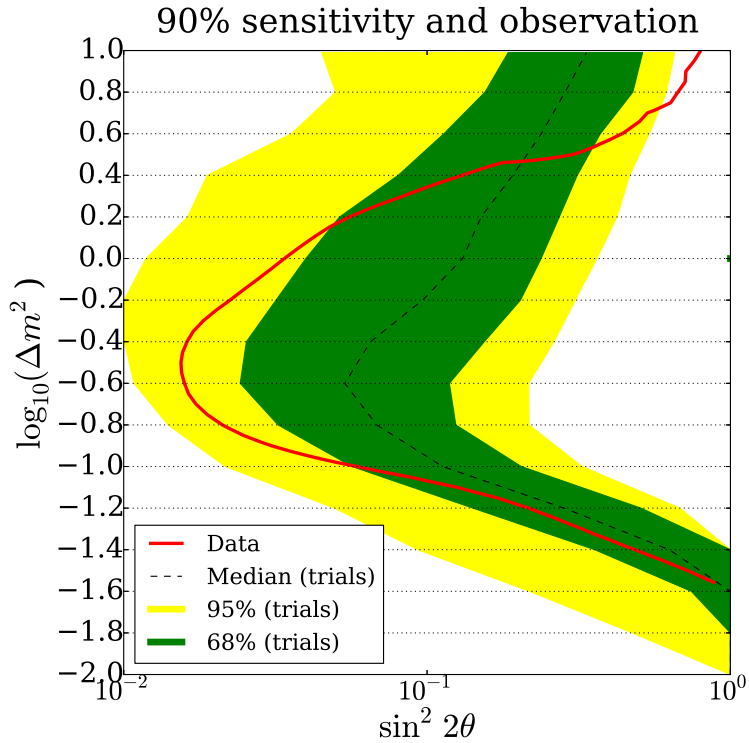


Figure 3.4.9: Comparison of data with expected sensitivity in the rate+shape analysis

is shown in Figure 3.4.7. Again, no evidence for sterile neutrinos is observed. The best fit is at $\Delta m^2 = 10 \text{ eV}^2$ and $\sin^2 2\theta = 0.50$, close to the value in the shape-only fit. The likelihood difference from the no-steriles point is reduced to $\Delta LLH = 0.75$ corresponding to a p-value of 47.2% for the no-sterile hypothesis.

Comparison to the expected sensitivity, computed using 1000 trials of the no-sterile-neutrinos hypothesis is shown in Figure 3.4.9. The contour from data is shown overlaid, and represents an over-fluctuation at some Δm^2 values and an under-fluctuation at others.

The best-fit point is at the edge of the hypothesis space which was investigated. A natural question to ask is whether the true best-fit has been located, or whether a deeper minimum is present at higher Δm^2 . The expected behavior of the likelihood space is to approach flatness outside the sensitive region of the analysis, and the search space should ideally be large enough to extend into this region. The presence of

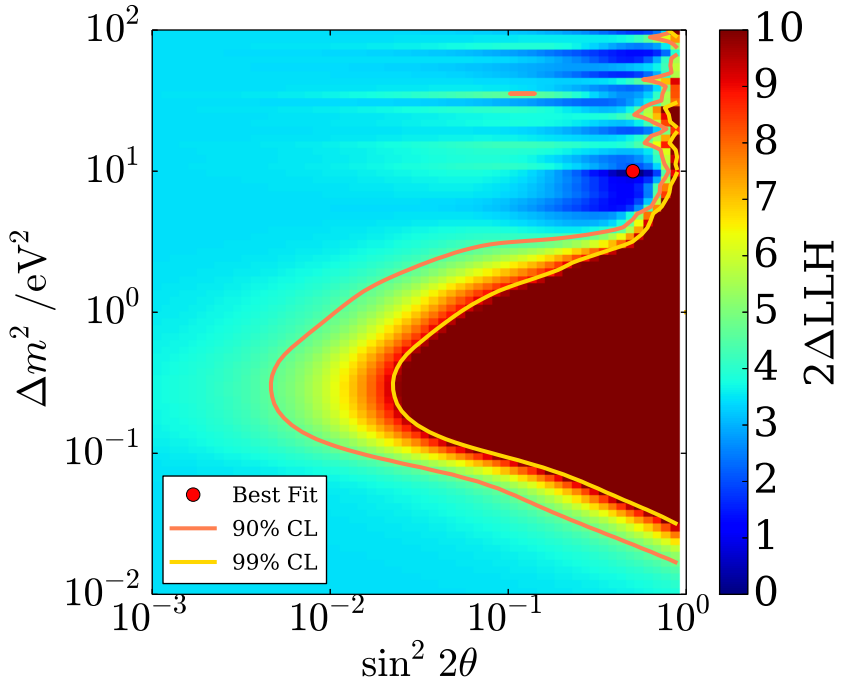


Figure 3.4.10: Rate+shape contour for discrete set 1, which contains the absolute best-fit to data, in a larger hypothesis space. The best-fit is at $\Delta m^2 = 10 \text{ eV}^2$ and enlarging the space does not change the Wilks contours.

minima at the boundary suggests that our grid may not meet this ideal requirement². The LLH map was calculated to larger masses and smaller mixings for the discrete set which contains the absolute best-fit, and is shown in Figure 3.4.10. The true minimum actually is at $\Delta m^2 = 10$, and not at a higher mass point. The ripples at high Δm^2 suggest that the oscillation is not completely smeared relative to the analysis binning in this region. Such ripples are also often seen in the likelihood spaces of vacuum-like oscillation experiments at high Δm^2 [48]. The detailed effects of their impact on this analysis is under further investigation.

²The presence of boundaries in continuous hypothesis spaces is one of the motivating factors for the Feldman Cousins method, discussed in [340] If the likelihood space does not extend into the flat region, the Wilks-based contours may have incorrect coverage, but the Feldman Cousins method will still produce valid confidence intervals of correct coverage.

4.5 Tests of systematic uncertainties

Checks were made to quantify the behaviour of discrete and continuous nuisance parameters for both the shape-only and rate+shape analyses. In the interests of space, here we report only the rate+shape plots, although qualitatively similar behaviour is seen in both cases.

Continuous nuisance parameters

Figures 3.4.11 and 3.4.12 show the fitted values of each continuous parameter at each point in parameter space. In each case, the pull is shown both for the one discrete variant (left) and after maximizing over all variants (right). The single variant chosen for illustration is the Polygonato-QGSJET set, which has the maximal likelihood over the majority of the 90% CL contour. When maximization over discrete variants is performed, discontinuities appear in some of the distributions where a different variant becomes favored, with a different nuisance parameter value. Within a single variant, however, the continuous nuisance parameters vary smoothly over the space in a way which is consistent with expectations. Three are particularly notable:

- *Normalization.* The favored discrete model for shape is Polygonato-GQSJET, which is one of the lower normalization models (see Figure 3.3.11), so over most of the space the normalization takes a value of around 1.4, pulling this model up towards the central model rate prediction. As discussed in the previous section, in the high Δm^2 and large mixing region, normalization compensates for the flux depletion due to fast oscillations, and the normalization is pulled against its prior to larger values.
- *DOM Efficiency.* The DOM efficiency acts to shift the position of the energy peak. Sterile neutrinos with low mass introduce a resonance on the low side of the peak, whereas sterile neutrinos with high mass introduce a resonance on the high side. Thus the DOM efficiency pulls to lower values to compensate for hypotheses with light sterile neutrions, and higher values for heavy ones.

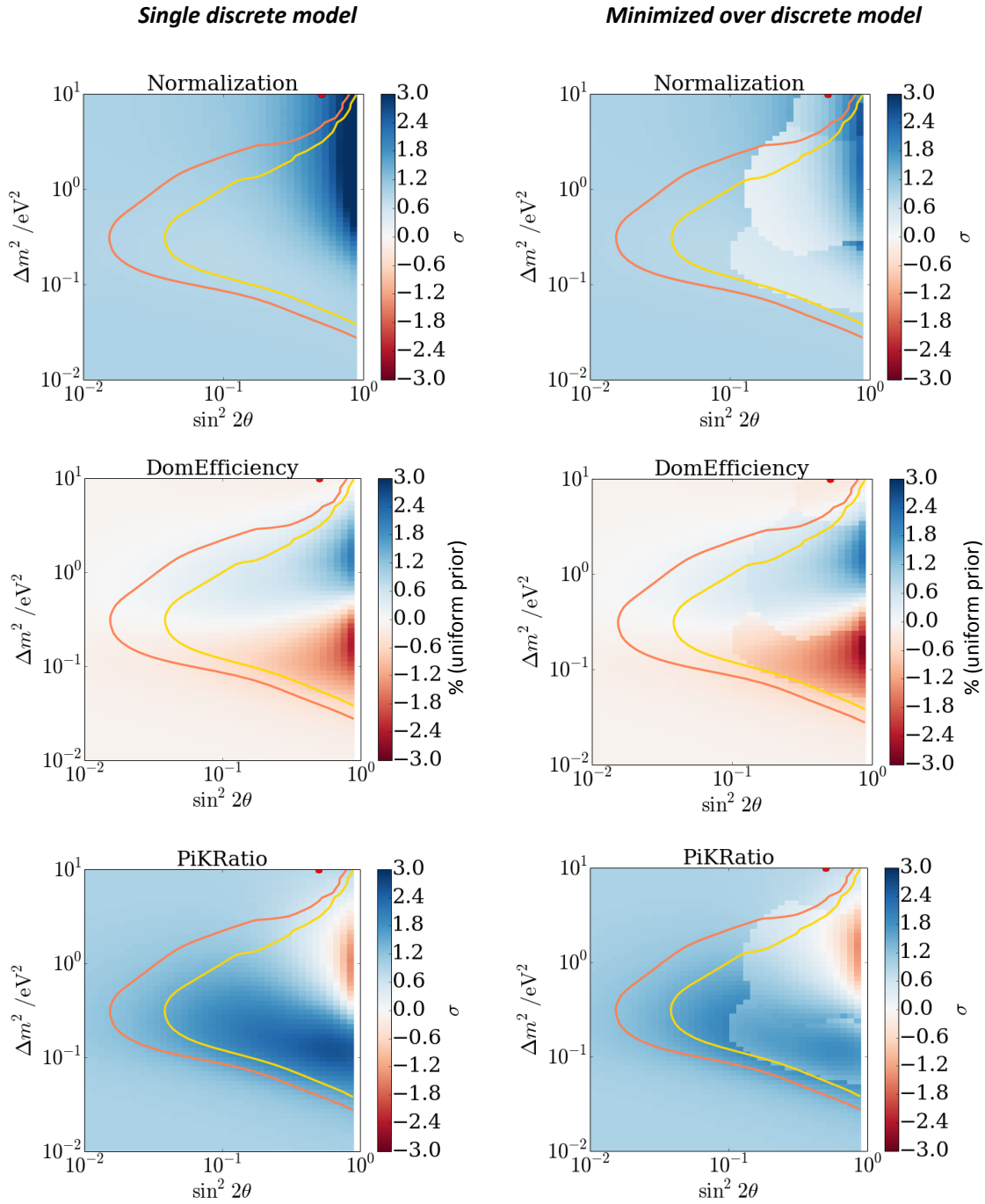


Figure 3.4.11: Pulls of nuisance parameters in rate+shape analysis

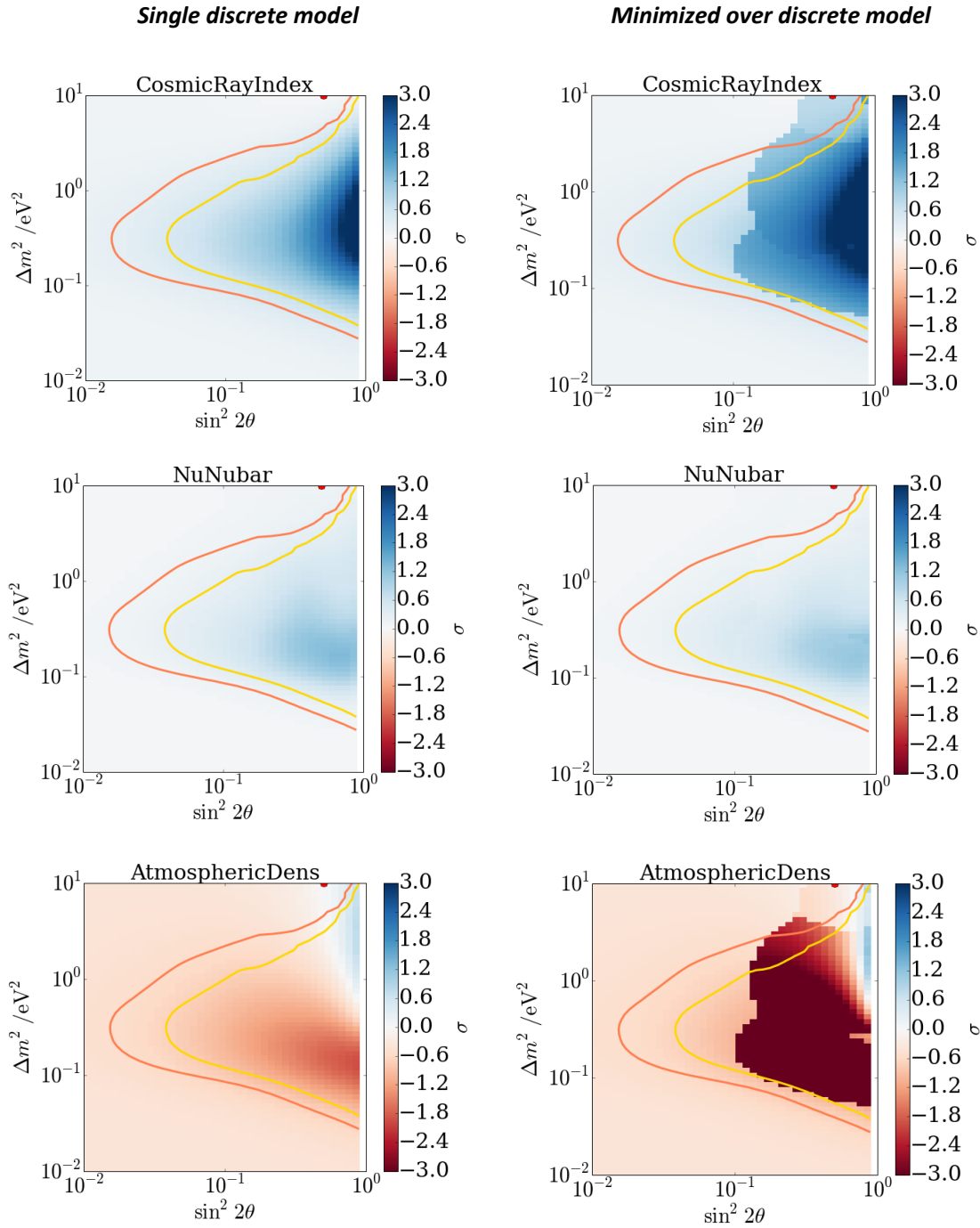


Figure 3.4.12: Pulls of nuisance parameters in rate+shape analysis

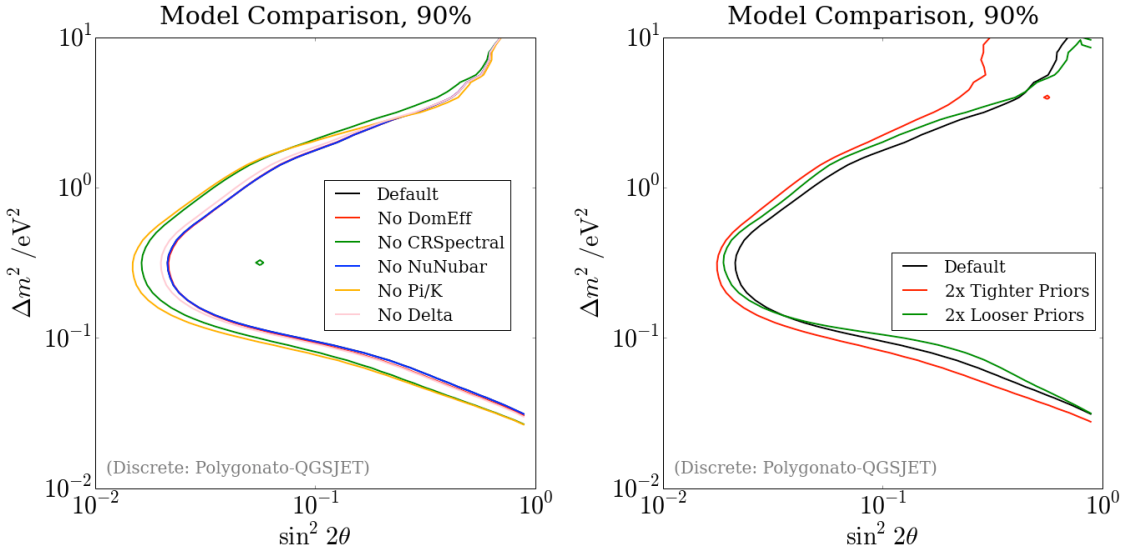


Figure 3.4.13: Continuous parameter checks. Left: n-1 plots, with each parameter held fixed. Right: effect of tightening or loosening all priors. These plots are made using a fixed discrete variant.

- *Pion/Kaon Ratio.* An increase in the pion-induced flux provides an enhancement of the energy spectrum at the lowest energies, whereas an increase in kaon flux enhances the spectrum at higher energies. Similarly to the DOM efficiency behavior, sterile neutrino hypotheses which introduce resonance below the peak of the atmospheric spectrum can be compensated for by increasing the pion fraction, whereas those which introduce resonance above the peak can be compensated for by increasing the kaon fraction.

The remaining three continuous nuisance parameters also exhibit reasonable behavior, developing significant pulls in the large-signal region but falling within their 1σ priors over most of the hypothesis space.

The scale of effect that each nuisance parameter has in the analysis can be evaluated in several ways. One method is to re-perform the fit but hold one parameter fixed at its default value. This produces an “n-1” contour, which can be compared to the fully maximized result. Although they do not show the effects of correlations between nuisance parameters, these plots show how the inclusion of each systematic uncertainty affects the result, given the observed data. n-1 plots for each parameter

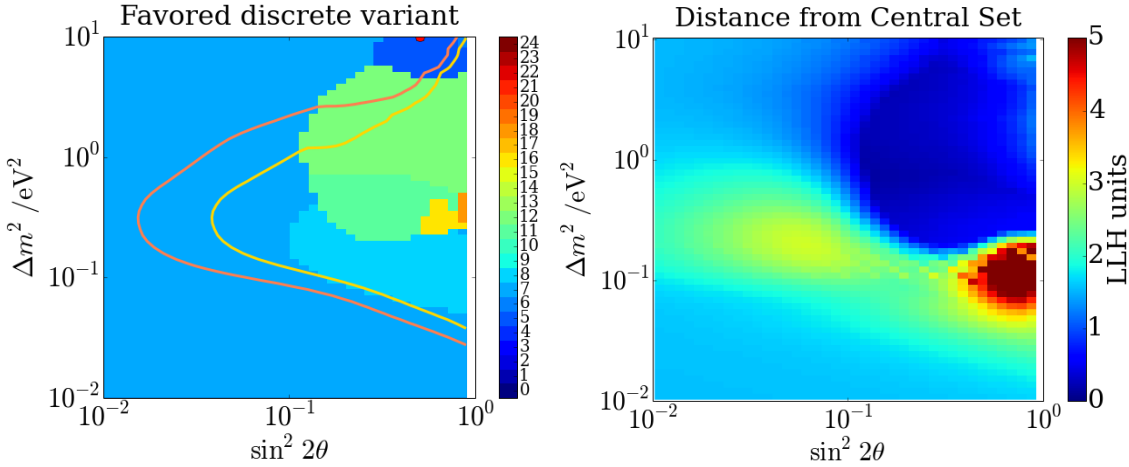


Figure 3.4.14: Left: favored discrete variant at each point in the hypothesis space. Right: distance of the favorite model from the central model.

are shown in Figure 3.4.13, left. These are also made using a the single discrete variant Polygonato-GQSJET.

It is informative to know how dependent the analysis result is upon the priors which have been chosen for the nuisance parameters. If the result is heavily dependent on the prior, its size must be determined very carefully. If the analysis is insensitive to the prior width, a rough estimate of the allowed range can be used. Figure 3.4.13, right shows the results of the fit performed with all priors made $2\times$ tighter and $2\times$ looser. Only a small effect is observed everywhere except at the very highest Δm^2 values, where tightening the priors increases the excluded range. This is primarily a consequence of tighter constrains on the normalization allowing more large-mixing hypotheses to be rejected. Loosening the priors does not have a strong effect on the result, suggesting that our choice of priors is reasonably safe, and the result is not artificially strong due to the values chosen.

Discrete variants

The discrete variant which has the maximal likelihood in at each hypothesis point is shown in Figure 3.4.14, left. Figure 3.4.14, right shows the likelihood distance between the favored variant and the central model, which illustrates the degree to which the likelihood profile is affected by minimizing over variants rather than using

only the central model.

Some of the variants, in particular those relating to ice effects, are strongly disfavored relative to the central model and thus do not have an observable effect on the final contours. These are deliberately extreme model distortions, so this behaviour is unsurprising. The reason for studying these variants is to ensure that ice mismodelling cannot introduce either a signal or an artificially strong exclusion. This can be tested by comparing the contours obtained when each variant is assumed, without discrete maximization. These are shown alongside the central model, the fully maximized contour, and the contour maximized over only subclasses of variants, in Figure 3.4.15. We observe that, although not preferred by data, the exclusion contours derived from each variant are similar to or weaker than the final contour in nearly all cases.

4.6 Frequentist cross-checks using the Feldman Cousins method

The confidence intervals drawn to this point have been based on Wilks' theorem. This is a statement about the probability distribution of the test statistic ΔLLH , defined as the log of the likelihood ratio between the best-fit point and the true parameter point. Wilks' theorem states that in a likelihood space with two degrees of freedom, such as the $(\log(\Delta m^2), \log(\sin^2 2\theta))$ space probed in this analysis, the probability distribution of $2\Delta LLH$ will be a χ^2 distribution with two degrees of freedom.

In cases where Wilks theorem applies, valid contours with proper coverage can be drawn using a simple prescription. A contour of confidence level C passes through all points in the likelihood space where $\Delta LLH = \Delta LLH_C$, where:

$$\int_0^{2\Delta LLH_C} dx \chi_{2DOF}^2(x) = C. \quad (4.2)$$

For the 90% CL contour, this condition is satisfied at $2\Delta LLH_C = 4.6$. For the 99% contour, it is satisfied at $2\Delta LLH_C = 9.21$. These “Wilks thresholds” are tabulated in

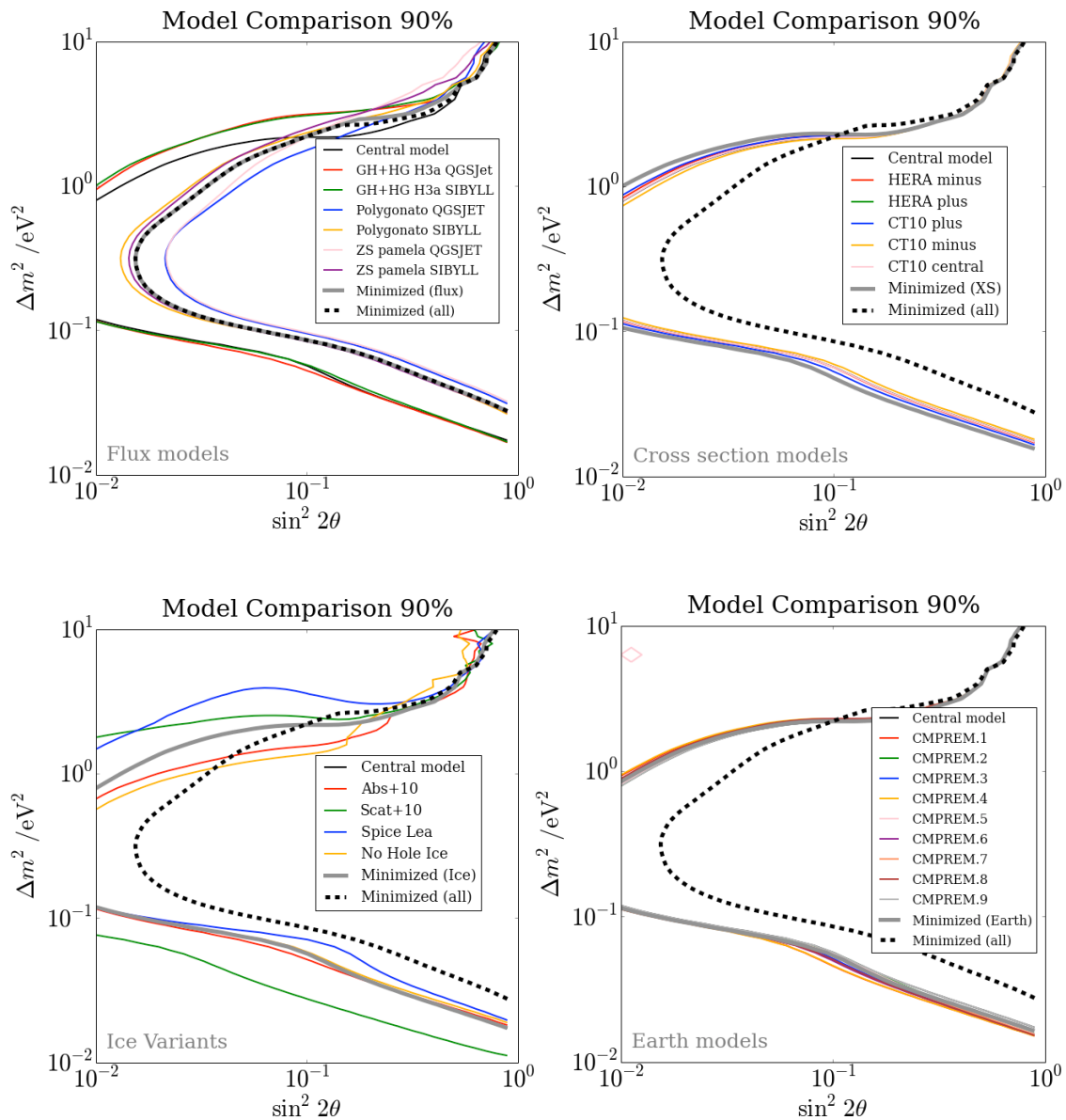


Figure 3.4.15: Contours forcing the choice of each discrete set.

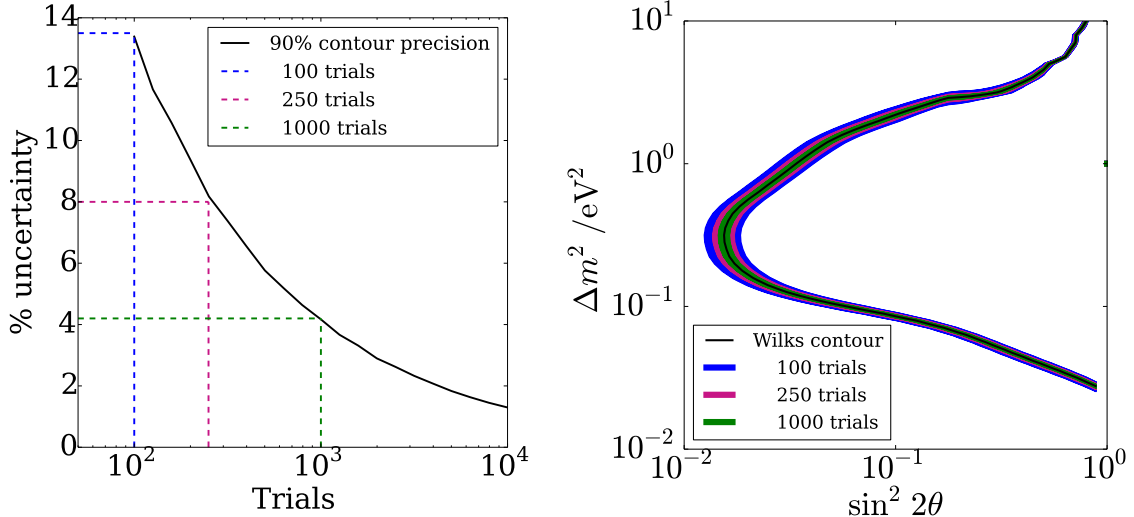


Figure 3.4.16: Precision achievable using the FC method to establish the 90% confidence threshold

the literature [37] and have been used to draw the contours shown on our likelihood spaces so far.

There are several situations in which Wilks' theorem is not a good approximation to the test statistic distribution. These include cases where the parameter space contains a physical boundary, or where the degrees of freedom become degenerate in parts of the space, changing the effective number of degrees of freedom. In these cases, Wilks confidence intervals can have incorrect coverage. A method which always produces contours with the correct coverage is the Feldman Cousins (FC) method. The FC method uses a frequentist approach to determine how the ΔLLH test statistic is distributed. Random realizations of the experiment are simulated many times at each parameter point and the probability density function $P(\Delta LLH)$ is established. The contour of confidence level C passes through all points in the hypothesis space which have ΔLLH satisfying the following condition:

$$\int_0^{\Delta LLH} dx P(x) = C, \quad (4.3)$$

which is similar to Eq.4.3, but with ΔLLH_C no longer being the Wilks threshold, but an FC threshold that can be different at each point in hypothesis space.

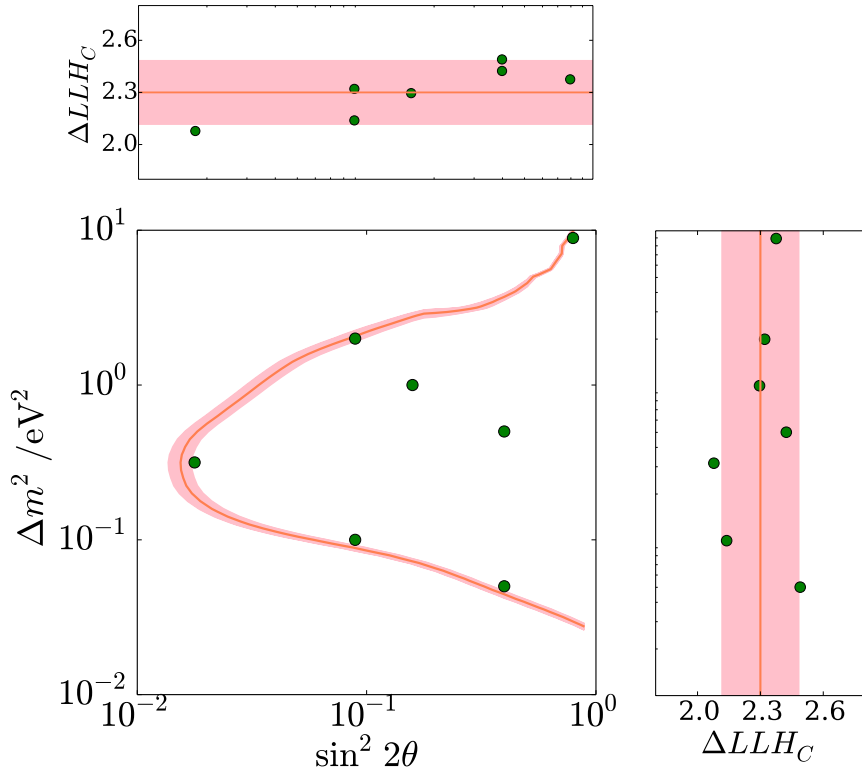


Figure 3.4.17: 90% FC test points

To test the validity of the Wilks contours, we compared the Wilks threshold to the FC threshold at several points in the hypothesis space. If these thresholds are equivalent at all points on the Wilks contour, it satisfies Eq. 4.3 and has proper coverage. If the Wilks threshold is not equal to the FC threshold but the required correction is small, the residual can be parameterized and used to make a small threshold correction. If the violation of Wilks theorem is large, only a full FC scan of the entire parameter space will produce a valid contour.

The number of FC trials required per point depends on the precision required on ΔLLH_C . If the test-statistic distribution is a small perturbation to χ^2_{2DOF} , this can be quantified by drawing random samples from a χ^2 distribution and evaluating the precision with which the Wilks threshold can be recovered from the ensemble. Figure 3.4.16, left shows this precision for the 90% CL contour. As a first-pass, ensembles of 250 trials are used to check the thresholds at several points on the 90%

CL contour to a precision of $\sigma_{\Delta LLH}/\Delta LLH = 8\%$. The range of hypothesis space this corresponds to is narrow and can be seen in Figure 3.4.16, right. Also shown are the precisions achievable with smaller (100 trial) and larger (1000 trial) ensembles.

Figure 3.4.18 shows the likelihood PDFs generated from the ensemble and compared to the Wilks prediction of χ^2_{2DOF} for six of the tested points. The precision on the 90% threshold is shown as a pink band, and the Wilks and Feldman Cousins thresholds are marked. In all cases they are equivalent within the precision of the test. Figure 3.4.17 shows where these test points lie in the hypothesis space and how the threshold correction varies with Δm^2 and $\sin^2 2\theta$. Again, the pink band shows the precision of the 250-trial ensemble test. Based on these studies the Wilks contour is accurate to within the uncertainty shown in Figure 3.4.18, and no modification based on the FC method appears to be necessary.

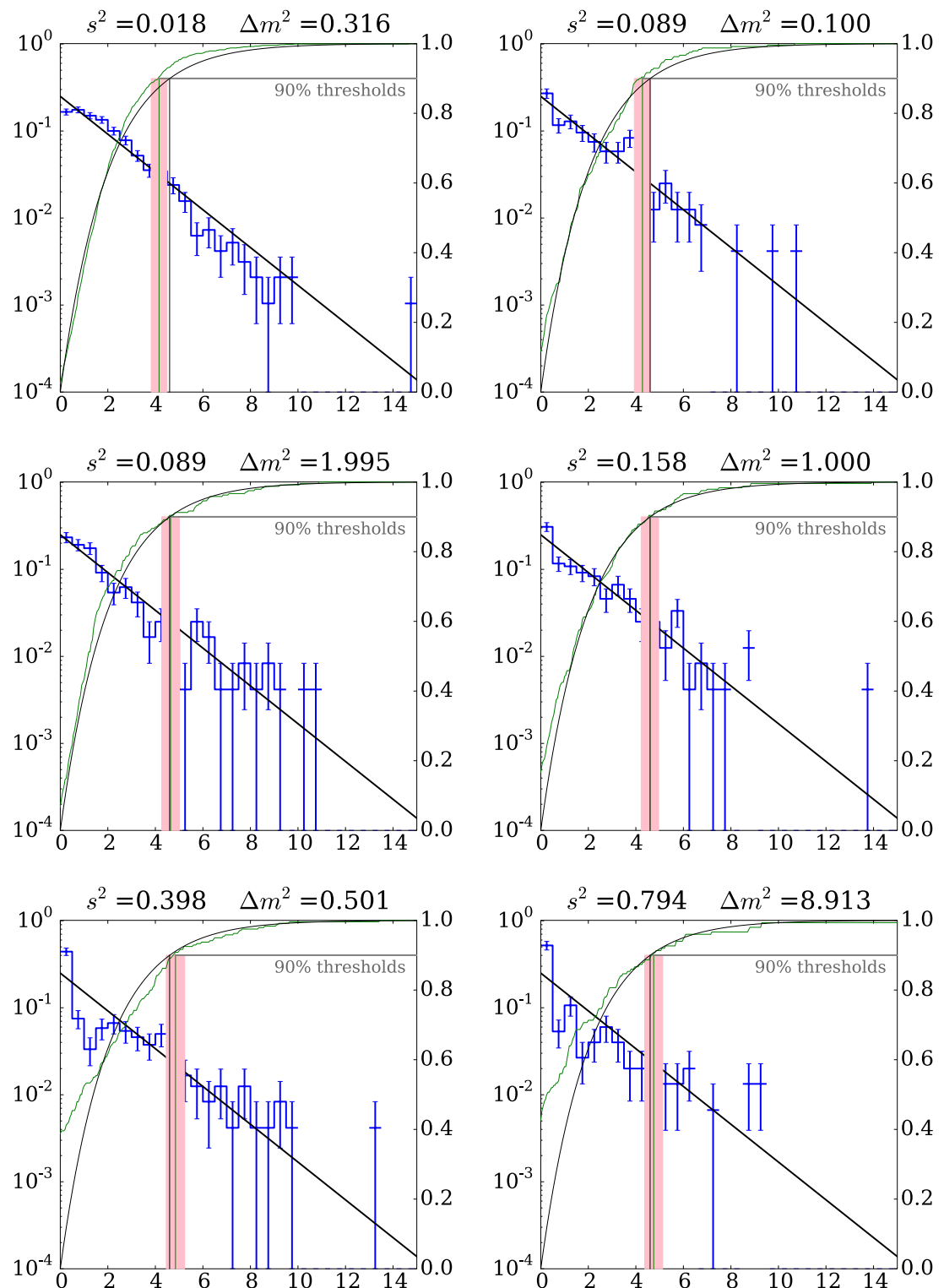


Figure 3.4.18: Several FC points

Chapter 5

Conclusion to Part III

This work represents the first search for sterile neutrino oscillations in the multi-TeV energy range, and provides world’s first experimental constraints on MSW-resonant sterile neutrino oscillations. This section reviews the results and describes them in the context of world data.

Discussion of shape-only and rate+shape results

Two results have been derived using the IC86 1-year data sample. These are expressed as 90% confidence intervals, drawn using Wilks theorem and checked using the FC method, and 99% confidence intervals whose FC checks are ongoing at present time.

The first result, derived from a blindly-designed shape-only analysis, is shown in Figure 3.4.4. After unblinding the shape-only analysis, it was noted that the best-fit is at a hypothesis point which is null-like in the shape-only analysis, but may not be null-like for a rate+shape analysis due to its high fitted normalization. Hence including rate information in the analysis would weaken the exclusion. This was quantified by adding a normalization prior derived from uncertainties quoted in the literature [310], [330] and our own studies (Section 3.5), with care taken to avoid introducing post-unblinding bias. This led to the rate+shape result of Figure 3.4.7.

The reduced strength of the rate+shape analysis relative to shape-only is a property of a known subset of possible realizations of the data. From the distribution of

best-fits for the no-sterile hypothesis (Figure 3.4.5), we find that if no sterile neutrinos exist, the best-fit point falls in the low-mass ($\Delta m^2 \leq 1\text{eV}^2$) null-like region in 484 of 1000 trials and in the high mass ($\Delta m^2 > 1\text{eV}^2$) null-like region in 516 of 1000 trials. As was shown in Figure 3.4.6, the best-fit points with high Δm^2 typically have high fitted normalizations due to the fast-oscillation effect. Therefore, in cases where the high- Δm^2 region is favored, the best-fit is penalized by a normalization prior, weakening the unified exclusion limit in the rate+shape analysis relative to shape-only. Conversely, in cases where the low- Δm^2 region is favored, the best-fit is not penalized, but the exclusion at high- Δm^2 region is improved by the prior. For this other half-space of realizations, the rate+shape analysis is stronger than shape-only.

Comparison of the median sensitivities of the two analyses, from Figures 3.4.1 and 3.4.9, shows a consequence of this trade-off is that neither is significantly more powerful on aggregate, except at high Δm^2 where the rate+shape analysis has more sensitivity. Particular realizations of the data, however, do produce different contours in each analysis. In the data realization we observe, the exclusion limit in the (blind) shape-only analysis is stronger than in the (non-blind) rate+shape one.

Because our results are expressed as classical confidence intervals, there is no conceptual problem with valid but different contours being derived from different analyses. The 90% confidence interval is defined such that, for any true hypothesis, the interval contains the true point in 90% of statistical realizations. By definition, the contour covers different regions trial-to-trial, and is expected to fluctuate differently in different analyses. One mechanism driving these differences was described above.

As the result of this search we present the confidence intervals derived from both versions of the analyses. Both are valid, but with several notable distinctions:

1. The shape-only result is blind, whereas the rate+shape result is not.
2. The rate+shape analysis result produces a weaker exclusion, so is a more conservative interpretation of the data.
3. The rate+shape analysis uses a larger subset of the available information to constrain sterile neutrino hypotheses.

Implications of our result for sterile neutrinos

We have made a measurement of the atmospheric neutrino flux shape and used it to constrain MSW-resonant sterile neutrino oscillations in a 3+1 model with $\theta_{24} \neq 0$ and $\theta_{14} = \theta_{34} = \delta_{24} = 0$, using shape-only and rate+shape analyses. Comparisons to previous disappearance and appearance results can be made, given suitable assumptions about the other mixing angles.

Vacuum-like muon disappearance experiments measure $U_{\mu 4}^2 = \cos\theta_{14}\sin\theta_{24}e^{-i\delta_{24}}$. In our test model, $\delta_{24} = \theta_{14} = 0$ and so $U_{\mu 4}^2 = \sin\theta_{24}$. In this case, comparison with vacuum disappearance measurements can be made trivially. Figure 3.5.1, left shows our result compared with the published limits from SuperKamiokande [62], MINOS [63], CDHS [66], [341], and MiniBooNE/SciBooNE [342]. Our exclusion is significantly stronger than existing limits in both shape-only and rate+shape analyses in the mass range where the MSW resonance is expected to be large.

Vacuum appearance experiments measure $U_{\mu e}^2 = U_{\mu 4}^2 U_{e 4}^2$. In order to compare our measurements of θ_{24} to the results of these experiments, a value for $U_{e 4}$ must be assumed. Following [40], we consider the allowed region when $U_{e 4}$ is set to its best fit value from world data, from [65], $U_{e 4}^2 = 0.023$. The LSND and MiniBooNE allowed region under this assumption is shown in Figure 3.5.1 , right, and is ruled out at 99% confidence level. Comparison to global fits for appearance experiments from [66] using the same protocol also shows a rejection of the allowed region at 99% confidence level.

Under the mixing assumptions made, our measurement has strong implications for the MiniBooNE / LSND anomalies. The MSW resonant sterile neutrino oscillation which would be associated with 3+1 models with $\theta_{24} \neq 0$ has not been observed. An exploration of the wider five-parameter mixing space is required in order to conclusively determine whether there are regions of the vacuum 3+1 model which remain credible to explain the MiniBooNE / LSND anomalies. This will involve comparison to world data in the context of global fits such as [64]–[66].

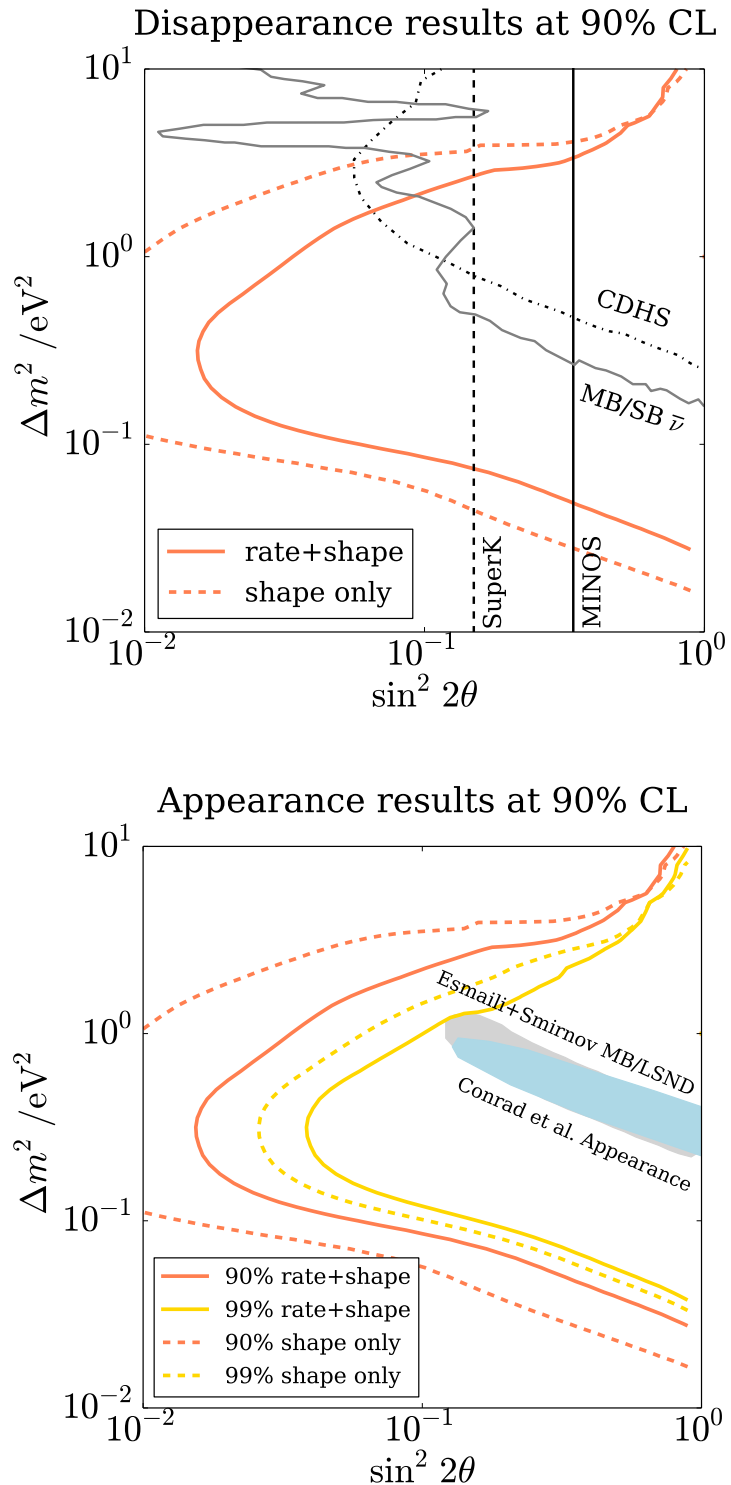


Figure 3.5.1: Comparison to world data. Top: comparison to published 90% CL disappearance limits from SuperK[62], MINOS [63], CDHS [66], [341], Mini-BooNE/SciBooNE [342]. Bottom: comparison to appearance regions from Conrad *et al.* [66], and Esmaili and Smirnov [40], fixing U_{e4} to its best fit from [65].

Prospects for future work

Final checks of this result are ongoing. In particular, the following items are in progress:

- Higher precision Feldman-Cousins tests of the 90% and 99% contours;
- Investigation of the behavior of the likelihood space at very high Δm^2 where the oscillation effect transitions from rate+shape to rate-only;
- Update of the NNPDF cross section spline for inclusion in the analysis.

These tests are expected to be completed by the end of 2015. Following the analysis of the IC86 2011 sample, four years of additional IceCube data are available and can be added. Since the analysis remains statistics limited, significantly improved sensitivity is expected from this additional data.

Other beyond-standard-model processes can also be constrained using this analysis sample and the systematic uncertainty treatments described in this thesis. These include Lorentz invariance violation [343], anomalous decoherence [344] neutrino decay [345] and non-standard interactions [346]. Testing these possibilities using the methods we have developed provides many exciting prospects for future analysis. Thus, this work not only produces strong constraints on sterile neutrinos, but also lays foundations for future BSM physics searches using the atmospheric neutrino flux at IceCube.

Bibliography

- [1] B. Jones, “Dynamical pion collapse and the coherence of conventional neutrino beams,” *Phys.Rev.*, vol. D91, no. 5, p. 053 002, 2015. DOI: 10.1103/PhysRevD.91.053002. arXiv: 1412.2264 [hep-ph].
- [2] T. Briese, L. Bugel, J. Conrad, M. Fournier, C. Ignarra, *et al.*, “Testing of Cryogenic Photomultiplier Tubes for the MicroBooNE Experiment,” *JINST*, vol. 8, T07005, 2013. DOI: 10.1088/1748-0221/8/07/T07005. arXiv: 1304.0821 [physics.ins-det].
- [3] J. Conrad, B. Jones, Z. Moss, T. Strauss, and M. Toups, “The Photomultiplier Tube Calibration System of the MicroBooNE Experiment,” *JINST*, vol. 10, no. 06, T06001, 2015. DOI: 10.1088/1748-0221/10/06/T06001. arXiv: 1502.04159 [physics.ins-det].
- [4] B. Jones, “Results from the Bo Liquid Argon Scintillation Test Stand at Fermilab,” *JINST*, vol. 8, p. C09003, 2013. DOI: 10.1088/1748-0221/8/09/C09003.
- [5] B. Jones, C. Chiu, J. Conrad, C. Ignarra, T. Katori, *et al.*, “A Measurement of the Absorption of Liquid Argon Scintillation Light by Dissolved Nitrogen at the Part-Per-Million Level,” *JINST*, vol. 8, P07011, 2013. DOI: 10.1088/1748-0221/8/07/P07011, 10.1088/1748-0221/8/09/E09001. arXiv: 1306.4605 [physics.ins-det].
- [6] B. Jones, T. Alexander, H. Back, G. Collin, J. Conrad, *et al.*, “The Effects of Dissolved Methane upon Liquid Argon Scintillation Light,” *JINST*, vol. 8, P12015, 2013. DOI: 10.1088/1748-0221/8/12/P12015. arXiv: 1308.3658 [physics.ins-det].
- [7] B. Baptista, L. Bugel, C. Chiu, J. Conrad, C. Ignarra, *et al.*, “Benchmarking TPB-coated Light Guides for Liquid Argon TPC Light Detection Systems,” 2012. arXiv: 1210.3793 [physics.ins-det].
- [8] L. Bugel, J. Conrad, C. Ignarra, B. Jones, T. Katori, *et al.*, “Demonstration of a Lightguide Detector for Liquid Argon TPCs,” *Nucl.Instrum.Meth.*, vol. A640, pp. 69–75, 2011. DOI: 10.1016/j.nima.2011.03.003. arXiv: 1101.3013 [physics.ins-det].
- [9] B. Jones, “A simulation of the optical attenuation of TPB coated light-guide detectors,” *JINST*, vol. 8, p. C10015, 2013. DOI: 10.1088/1748-0221/8/10/C10015. arXiv: 1307.6906.

- [10] Z. Moss, L. Bugel, G. Collin, J. Conrad, B. Jones, *et al.*, “Improved TPB-coated Light Guides for Liquid Argon TPC Light Detection Systems,” 2014. arXiv: 1410.6256 [physics.ins-det].
- [11] C. Chiu, C. Ignarra, L. Bugel, H. Chen, J. Conrad, *et al.*, “Environmental Effects on TPB Wavelength-Shifting Coatings,” *JINST*, vol. 7, P07007, 2012. DOI: 10.1088/1748-0221/7/07/P07007. arXiv: 1204.5762 [physics.ins-det].
- [12] B. Jones, J. VanGemert, J. Conrad, and A. Pla-Dalmau, “Photodegradation Mechanisms of Tetraphenyl Butadiene Coatings for Liquid Argon Detectors,” *JINST*, vol. 8, P01013, 2013. DOI: 10.1088/1748-0221/8/01/P01013. arXiv: 1211.7150 [physics.ins-det].
- [13] L. Bagby, S. Gollapinni, C. James, B. Jones, H. Jostlein, *et al.*, “Breakdown voltage of metal-oxide resistors in liquid argon,” 2014. arXiv: 1408.4013 [physics.ins-det].
- [14] J. Asaadi, J. Conrad, S. Gollapinni, B. Jones, H. Jostlein, *et al.*, “Testing of High Voltage Surge Protection Devices for Use in Liquid Argon TPC Detectors,” 2014. DOI: 10.1088/1748-0221/9/09/P09002. arXiv: 1406.5216 [physics.ins-det].
- [15] M. Antonello *et al.*, “A Proposal for a Three Detector Short-Baseline Neutrino Oscillation Program in the Fermilab Booster Neutrino Beam,” 2015. arXiv: 1503.01520 [physics.ins-det].
- [16] W. Pauli, “Letter to gauverein wien meeting in tubingen.,” from the CERN Pauli Archives.
- [17] J. Chadwick, “Possible Existence of a Neutron,” *Nature*, vol. 129, p. 312, 1932. DOI: 10.1038/129312a0.
- [18] E. Fermi, “Tentativo di una Teoria Dei Raggi β ,” *Il Nuovo Cimento*, vol. 11, no. 1, pp. 1–19, 1934.
- [19] H. Bethe and R. Peierls, “The ‘Neutrino’,” *Nature*, vol. 133, pp. 532–532, 1934.
- [20] B. Pontecorvo, “Inverse β^- process,” Report PD-205, Chalk River Laboratory, 1946.
- [21] R. Davis Jr., “Attempt to detect the antineutrinos from a nuclear reactor by the Cl37(anti-nu,e-) A37 reaction,” *Phys. Rev.*, vol. 97, pp. 766–769, 1955. DOI: 10.1103/PhysRev.97.766.
- [22] F. Reines and C. L. Cowan, “Detection of the free neutrino,” *Phys. Rev.*, vol. 92, pp. 830–831, 1953. DOI: 10.1103/PhysRev.92.830.
- [23] C. L. Cowan, F. Reines, F. B. Harrison, H. W. Kruse, and A. D. McGuire, “Detection of the free neutrino: A Confirmation,” *Science*, vol. 124, pp. 103–104, 1956. DOI: 10.1126/science.124.3212.103.
- [24] R. Davis, “Solar neutrinos. II: Experimental,” *Phys. Rev. Lett.*, vol. 12, pp. 303–305, 1964. DOI: 10.1103/PhysRevLett.12.303.

- [25] J. N. Bahcall, “Solar neutrinos. I: Theoretical,” *Phys. Rev. Lett.*, vol. 12, pp. 300–302, 1964. DOI: 10.1103/PhysRevLett.12.300.
- [26] J. N. Bahcall and R. Davis Jr., “An Account of the Development of the Solar Neutrino Problem,” 1981.
- [27] Y. Fukuda *et al.*, “Evidence for oscillation of atmospheric neutrinos,” *Phys. Rev. Lett.*, vol. 81, pp. 1562–1567, 1998. DOI: 10.1103/PhysRevLett.81.1562. arXiv: hep-ex/9807003 [hep-ex].
- [28] J. N. Abdurashitov *et al.*, “Solar neutrino flux measurements by the Soviet-American Gallium Experiment (SAGE) for half the 22 year solar cycle,” *J. Exp. Theor. Phys.*, vol. 95, pp. 181–193, 2002, [Zh. Eksp. Teor. Fiz.122,211(2002)]. DOI: 10.1134/1.1506424. arXiv: astro-ph/0204245 [astro-ph].
- [29] W. Hampel *et al.*, “GALLEX solar neutrino observations: Results for GALLEX IV,” *Phys. Lett.*, vol. B447, pp. 127–133, 1999. DOI: 10.1016/S0370-2693(98)01579-2.
- [30] B. Pontecorvo, “Mesonium and anti-mesonium,” *Sov. Phys. JETP*, vol. 6, p. 429, 1957, [Zh. Eksp. Teor. Fiz.33,549(1957)].
- [31] ——, “Inverse beta processes and nonconservation of lepton charge,” *Sov. Phys. JETP*, vol. 7, pp. 172–173, 1958, [Zh. Eksp. Teor. Fiz.34,247(1957)].
- [32] L. Wolfenstein, “Neutrino Oscillations in Matter,” *Phys. Rev.*, vol. D17, pp. 2369–2374, 1978. DOI: 10.1103/PhysRevD.17.2369.
- [33] ——, “Neutrino Oscillations and Stellar Collapse,” *Phys. Rev.*, vol. D20, pp. 2634–2635, 1979. DOI: 10.1103/PhysRevD.20.2634.
- [34] S. P. Mikheev and A. Yu. Smirnov, “Resonance Amplification of Oscillations in Matter and Spectroscopy of Solar Neutrinos,” *Sov. J. Nucl. Phys.*, vol. 42, pp. 913–917, 1985, [Yad. Fiz.42,1441(1985)].
- [35] ——, “Neutrino Oscillations in a Variable Density Medium and Neutrino Bursts Due to the Gravitational Collapse of Stars,” *Sov. Phys. JETP*, vol. 64, pp. 4–7, 1986, [Zh. Eksp. Teor. Fiz.91,7(1986)]. arXiv: 0706.0454 [hep-ph].
- [36] User MissMJ, “The standard model,” https://en.wikipedia.org/wiki/Standard_Model.
- [37] K. Olive *et al.*, “Review of Particle Physics,” *Chin.Phys.*, vol. C38, p. 090 001, 2014. DOI: 10.1088/1674-1137/38/9/090001.
- [38] B. Kayser, *The Physics of Massive Neutrinos*. World Scientific, 1989.
- [39] C. W. Kim and A. Pevsner, *Neutrinos in Physics and Astrophysics*. Harwood Academic Publishers, 1993.
- [40] A. Esmaili and A. Y. Smirnov, “Restricting the LSND and MiniBooNE sterile neutrinos with the IceCube atmospheric neutrino data,” *JHEP*, vol. 1312, p. 014, 2013. DOI: 10.1007/JHEP12(2013)014. arXiv: 1307.6824 [hep-ph].

- [41] S. Razzaque and A. Yu. Smirnov, “Searches for sterile neutrinos with IceCube DeepCore,” *Phys. Rev.*, vol. D85, p. 093010, 2012. DOI: 10.1103/PhysRevD.85.093010. arXiv: 1203.5406 [hep-ph].
- [42] ——, “Searching for sterile neutrinos in ice,” *JHEP*, vol. 07, p. 084, 2011. DOI: 10.1007/JHEP07(2011)084. arXiv: 1104.1390 [hep-ph].
- [43] M. C. Gonzalez-Garcia, F. Halzen, and M. Maltoni, “Physics reach of high-energy and high-statistics icecube atmospheric neutrino data,” *Phys. Rev.*, vol. D71, p. 093010, 2005. DOI: 10.1103/PhysRevD.71.093010. arXiv: hep-ph/0502223 [hep-ph].
- [44] C. A. A. Delgado, J. Salvado, and C. N. Weaver, “A Simple Quantum Integro-Differential Solver (SQuIDS),” 2014. arXiv: 1412.3832 [hep-ph].
- [45] C. Arguelles, J. Salvado, and C. Weaver, “The nusquids package,” Paper in preparation. Source code available at <https://github.com/arguelles/nuSQuIDS>.
- [46] K. N. Abazajian *et al.*, “Light Sterile Neutrinos: A White Paper,” 2012. arXiv: 1204.5379 [hep-ph].
- [47] C. Athanassopoulos *et al.*, “The Liquid scintillator neutrino detector and LAMPF neutrino source,” *Nucl. Instrum. Meth.*, vol. A388, pp. 149–172, 1997. DOI: 10.1016/S0168-9002(96)01155-2. arXiv: nucl-ex/9605002 [nucl-ex].
- [48] A. Aguilar-Arevalo *et al.*, “Evidence for neutrino oscillations from the observation of anti-neutrino(electron) appearance in a anti-neutrino(muon) beam,” *Phys. Rev.*, vol. D64, p. 112007, 2001. DOI: 10.1103/PhysRevD.64.112007. arXiv: hep-ex/0104049 [hep-ex].
- [49] A. Aguilar-Arevalo *et al.*, “Improved Search for $\bar{\nu}_\mu \rightarrow \bar{\nu}_e$ Oscillations in the MiniBooNE Experiment,” *Phys. Rev. Lett.*, vol. 110, p. 161801, 2013. DOI: 10.1103/PhysRevLett.110.161801. arXiv: 1207.4809 [hep-ex].
- [50] E. Church *et al.*, “A Letter of intent for an experiment to measure muon-neutrino to electron-neutrino oscillations and muon-neutrino disappearance at the Fermilab booster Boone,” 1997. arXiv: nucl-ex/9706011 [nucl-ex].
- [51] A. Aguilar-Arevalo *et al.*, “Event Excess in the MiniBooNE Search for $\bar{\nu}_\mu \rightarrow \bar{\nu}_e$ Oscillations,” *Phys. Rev. Lett.*, vol. 105, p. 181801, 2010. DOI: 10.1103/PhysRevLett.105.181801. arXiv: 1007.1150 [hep-ex].
- [52] J. N. Abdurashitov *et al.*, “Measurement of the solar neutrino capture rate with gallium metal,” *Phys. Rev.*, vol. C60, p. 055801, 1999. DOI: 10.1103/PhysRevC.60.055801. arXiv: astro-ph/9907113 [astro-ph].
- [53] ——, “Measurement of the solar neutrino capture rate with gallium metal. III: Results for the 2002–2007 data-taking period,” *Phys. Rev.*, vol. C80, p. 015807, 2009. DOI: 10.1103/PhysRevC.80.015807. arXiv: 0901.2200 [nucl-ex].
- [54] M. Cribier *et al.*, “Production of a 62-PBq Cr-51 low-energy neutrino source for GALLEX,” *Nucl. Instrum. Meth.*, vol. A378, pp. 233–250, 1996. DOI: 10.1016/0168-9002(96)00464-0.

- [55] J. N. Abdurashitov *et al.*, “Measurement of the response of the Russian-American gallium experiment to neutrinos from a Cr-51 source,” *Phys. Rev.*, vol. C59, pp. 2246–2263, 1999. DOI: 10.1103/PhysRevC.59.2246. arXiv: hep-ph/9803418 [hep-ph].
- [56] J. N. Bahcall, P. I. Krastev, and E. Lisi, “Limits on electron-neutrino oscillations from the GALLEX Cr-51 source experiment,” *Phys. Lett.*, vol. B348, pp. 121–123, 1995. DOI: 10.1016/0370-2693(95)00111-W. arXiv: hep-ph/9411414 [hep-ph].
- [57] T. A. Mueller *et al.*, “Improved Predictions of Reactor Antineutrino Spectra,” *Phys. Rev.*, vol. C83, p. 054615, 2011. DOI: 10.1103/PhysRevC.83.054615. arXiv: 1101.2663 [hep-ex].
- [58] G. Mention, M. Fechner, T. Lasserre, T. A. Mueller, D. Lhuillier, M. Cribier, and A. Letourneau, “The Reactor Antineutrino Anomaly,” *Phys. Rev.*, vol. D83, p. 073006, 2011. DOI: 10.1103/PhysRevD.83.073006. arXiv: 1101.2755 [hep-ex].
- [59] A. C. Hayes, J. L. Friar, G. T. Garvey, G. Jungman, and G. Jonkmans, “Systematic Uncertainties in the Analysis of the Reactor Neutrino Anomaly,” *Phys. Rev. Lett.*, vol. 112, p. 202501, 2014. DOI: 10.1103/PhysRevLett.112.202501. arXiv: 1309.4146 [nucl-th].
- [60] H. Gemmeke *et al.*, “The High resolution neutrino calorimeter KARMEN,” *Nucl. Instrum. Meth.*, vol. A289, pp. 490–495, 1990. DOI: 10.1016/0168-9002(90)91521-C.
- [61] B. Armbruster *et al.*, “Upper limits for neutrino oscillations muon-anti-neutrino → electron-anti-neutrino from muon decay at rest,” *Phys. Rev.*, vol. D65, p. 112001, 2002. DOI: 10.1103/PhysRevD.65.112001. arXiv: hep-ex/0203021 [hep-ex].
- [62] K. Abe *et al.*, “Limits on sterile neutrino mixing using atmospheric neutrinos in Super-Kamiokande,” *Phys. Rev.*, vol. D91, p. 052019, 2015. DOI: 10.1103/PhysRevD.91.052019. arXiv: 1410.2008 [hep-ex].
- [63] P. Adamson *et al.*, “Active to sterile neutrino mixing limits from neutral-current interactions in MINOS,” *Phys. Rev. Lett.*, vol. 107, p. 011802, 2011. DOI: 10.1103/PhysRevLett.107.011802. arXiv: 1104.3922 [hep-ex].
- [64] C. Giunti and M. Laveder, “3+1 and 3+2 Sterile Neutrino Fits,” *Phys. Rev.*, vol. D84, p. 073008, 2011. DOI: 10.1103/PhysRevD.84.073008. arXiv: 1107.1452 [hep-ph].
- [65] J. Kopp, P. A. N. Machado, M. Maltoni, and T. Schwetz, “Sterile Neutrino Oscillations: The Global Picture,” *JHEP*, vol. 1305, p. 050, 2013. DOI: 10.1007/JHEP05(2013)050. arXiv: 1303.3011 [hep-ph].

- [66] J. M. Conrad, C. M. Ignarra, G. Karagiorgi, M. H. Shaevitz, and J. Spitz, “Sterile Neutrino Fits to Short Baseline Neutrino Oscillation Measurements,” *Adv. High Energy Phys.*, vol. 2013, p. 163897, 2013. DOI: 10.1155/2013/163897. arXiv: 1207.4765 [hep-ex].
- [67] B. Kayser and J. Kopp, “Testing the wave packet approach to neutrino oscillations in future experiments,” 2010. arXiv: 1005.4081 [hep-ph].
- [68] M. Beuthe, “Oscillations of neutrinos and mesons in quantum field theory,” *Phys.Rept.*, vol. 375, pp. 105–218, 2003. DOI: 10.1016/S0370-1573(02)00538-0. arXiv: hep-ph/0109119 [hep-ph].
- [69] M. Beuthe, “Towards a unique formula for neutrino oscillations in vacuum,” *Phys.Rev.*, vol. D66, p. 013003, 2002. DOI: 10.1103/PhysRevD.66.013003. arXiv: hep-ph/0202068 [hep-ph].
- [70] E. K. Akhmedov and A. Y. Smirnov, “Paradoxes of neutrino oscillations,” *Phys.Atom.Nucl.*, vol. 72, pp. 1363–1381, 2009. DOI: 10.1134/S1063778809080122. arXiv: 0905.1903 [hep-ph].
- [71] E. Akhmedov and J. Kopp, “Neutrino oscillations in quantum mechanics and quantum field theory,” *JHEP*, vol. 1004, no. 108, pp. 377–391, 2010.
- [72] E. Akhmedov, D. Hernandez, and A. Smirnov, “Neutrino production coherence and oscillation experiments,” *JHEP*, vol. 1204, p. 052, 2012. DOI: 10.1007/JHEP04(2012)052. arXiv: 1201.4128 [hep-ph].
- [73] D. Hernandez and A. Y. Smirnov, “Active to sterile neutrino oscillations: Coherence and MINOS results,” *Phys.Lett.*, vol. B706, pp. 360–366, 2012. DOI: 10.1016/j.physletb.2011.11.031. arXiv: 1105.5946 [hep-ph].
- [74] D. Boyanovsky, “Short baseline neutrino oscillations: when entanglement suppresses coherence,” *Phys.Rev.*, vol. D84, p. 065001, 2011. DOI: 10.1103/PhysRevD.84.065001. arXiv: 1106.6248 [hep-ph].
- [75] M. A. Schlosshauer, *Decoherence and the Quantum-to-Classical Transition*. Springer, 2008.
- [76] L. Hackermüller, K. Hornberger, B. Brezger, A. Zeilinger, and M. Arndt, “Decoherence in a talbot-lau interferometer: the influence of molecular scattering,” English, *Applied Physics B*, vol. 77, no. 8, pp. 781–787, 2003, ISSN: 0946-2171. DOI: 10.1007/s00340-003-1312-6. [Online]. Available: <http://dx.doi.org/10.1007/s00340-003-1312-6>.
- [77] K. Hornberger, J. E. Sipe, and M. Arndt, “Theory of decoherence in a matter wave talbot-lau interferometer,” *Phys. Rev. A*, vol. 70, p. 053608, 5 2004. DOI: 10.1103/PhysRevA.70.053608. [Online]. Available: <http://link.aps.org/doi/10.1103/PhysRevA.70.053608>.
- [78] B. Brezger, L. Hackermüller, S. Uttenthaler, J. Petschinka, M. Arndt, and A. Zeilinger, “Matter-wave interferometer for large molecules,” *Phys. Rev. Lett.*, vol. 88, p. 100404, 10 2002. DOI: 10.1103/PhysRevLett.88.100404. [Online]. Available: <http://link.aps.org/doi/10.1103/PhysRevLett.88.100404>.

- [79] M. A. Nielsen and I. L Chuang, *Quantum Comptuation and Quantum Information*. Cambridge University Press, 2011.
- [80] M. Tegmark, “Apparent wave function collapse caused by scattering,” *Found.Phys.*, 1993. arXiv: gr-qc/9310032 [gr-qc].
- [81] G. C. Ghirardi, A. Rimini, and T. Weber, “Unified dynamics for microscopic and macroscopic systems,” *Phys. Rev. D*, vol. 34, pp. 470–491, 2 1986. DOI: 10.1103/PhysRevD.34.470. [Online]. Available: <http://link.aps.org/doi/10.1103/PhysRevD.34.470>.
- [82] B. Kayser, “B-Meson and Neutrino Oscillation: A Unified Treatment,” 2011. arXiv: 1110.3047 [hep-ph].
- [83] J. Wu, J. A. Hutasoit, D. Boyanovsky, and R. Holman, “Neutrino Oscillations, Entanglement and Coherence: A Quantum Field theory Study in Real Time,” *Int.J.Mod.Phys.*, vol. A26, pp. 5261–5297, 2011. DOI: 10.1142/S0217751X11054954. arXiv: 1002.2649 [hep-ph].
- [84] ——, “Dynamics of disentanglement, density matrix and coherence in neutrino oscillations,” *Phys.Rev.*, vol. D82, p. 013006, 2010. DOI: 10.1103/PhysRevD.82.013006. arXiv: 1005.3260 [hep-ph].
- [85] A. G. Cohen, S. L. Glashow, and Z. Ligeti, “Disentangling Neutrino Oscillations,” *Phys.Lett.*, vol. B678, pp. 191–196, 2009. DOI: 10.1016/j.physletb.2009.06.020. arXiv: 0810.4602 [hep-ph].
- [86] B. Kayser, J. Kopp, R. H. Roberston, and P. Vogel, “On a theory of neutrino oscillations with entanglement,” *Phys.Rev.*, vol. D82, p. 093003, 2010. DOI: 10.1103/PhysRevD.82.093003. arXiv: 1006.2372 [hep-ph].
- [87] L. Alavarez, “The use of liquid noble gases in particle detectors with 1) high spatial resolution over a large area, and 2) high energy resolution as total absorption counters,” *Lawrence Radiat. Lab. phys. note*, no. 672, 1968.
- [88] W. Willis and V. Radeka, “Liquid Argon Ionization Chambers as Total Absorption Detectors,” *Nucl.Instrum.Meth.*, vol. 120, pp. 221–236, 1974. DOI: 10.1016/0029-554X(74)90039-1.
- [89] S. Abachi *et al.*, “Beam tests of the D0 uranium liquid argon end calorimeters,” *Nucl.Instrum.Meth.*, vol. A324, pp. 53–76, 1993. DOI: 10.1016/0168-9002(93)90965-K.
- [90] “ATLAS liquid argon calorimeter: Technical design report,” 1996.
- [91] D. R. Nygren, “The Time Projection Chamber: A New 4 pi Detector for Charged Particles,” *eConf*, vol. C740805, p. 58, 1974.
- [92] C. Rubbia, “The Liquid Argon Time Projection Chamber: A New Concept for Neutrino Detectors,” 1977.
- [93] S. Amerio *et al.*, “Design, construction and tests of the ICARUS T600 detector,” *Nucl.Instrum.Meth.*, vol. A527, pp. 329–410, 2004. DOI: 10.1016/j.nima.2004.02.044.

- [94] V. Radeka, “Low Noise Techniques in Detectors,” *Ann.Rev.Nucl.Part.Sci.*, vol. 38, pp. 217–277, 1988. DOI: [10.1146/annurev.ns.38.120188.001245](https://doi.org/10.1146/annurev.ns.38.120188.001245).
- [95] O. Bunemann, T. Cranshaw, and J. Harvey, “Design of grid ionization chambers,” *Canadian Journal of Research*, vol. 27a, p. 191, 1949.
- [96] A. Bettini, A. Braggiotti, F. Casagrande, P. Casoli, P. Cennini, *et al.*, “A Study of the factors affecting the electron lifetime in ultrapure liquid argon,” *Nucl.Instrum.Meth.*, vol. A305, pp. 177–186, 1991. DOI: [10.1016/0168-9002\(91\)90532-U](https://doi.org/10.1016/0168-9002(91)90532-U).
- [97] R. Andrews, W. Jaskierny, H. Jostlein, C. Kendziora, S. Pordes, *et al.*, “A system to test the effects of materials on the electron drift lifetime in liquid argon and observations on the effect of water,” *Nucl.Instrum.Meth.*, vol. A608, pp. 251–258, 2009. DOI: [10.1016/j.nima.2009.07.024](https://doi.org/10.1016/j.nima.2009.07.024).
- [98] A. Curioni, B. Fleming, W. Jaskierny, C. Kendziora, J. Krider, *et al.*, “A Regenerable Filter for Liquid Argon Purification,” *Nucl.Instrum.Meth.*, vol. A605, pp. 306–311, 2009. DOI: [10.1016/j.nima.2009.04.020](https://doi.org/10.1016/j.nima.2009.04.020). arXiv: 0903.2066 [physics.ins-det].
- [99] B. Baibussinov, M. B. Ceolin, E. Calligarich, S. Centro, K. Cieslik, *et al.*, “Free electron lifetime achievements in Liquid Argon Imaging TPC,” *JINST*, vol. 5, P03005, 2010. DOI: [10.1088/1748-0221/5/03/P03005](https://doi.org/10.1088/1748-0221/5/03/P03005). arXiv: 0910.5087 [physics.ins-det].
- [100] S. Derenzo, A. Kirschbaum, P. Eberhard, R. Ross, and F. Solmitz, “Test of a Liquid Argon Chamber with 20-Micrometer RMS Resolution,” *Nucl.Instrum.Meth.*, vol. 122, p. 319, 1974. DOI: [10.1016/0029-554X\(74\)90495-9](https://doi.org/10.1016/0029-554X(74)90495-9).
- [101] R. Acciarri *et al.*, “A study of electron recombination using highly ionizing particles in the ArgoNeuT Liquid Argon TPC,” *JINST*, vol. 8, P08005, 2013. DOI: [10.1088/1748-0221/8/08/P08005](https://doi.org/10.1088/1748-0221/8/08/P08005). arXiv: 1306.1712 [physics.ins-det].
- [102] S. Amoruso *et al.*, “Study of electron recombination in liquid argon with the ICARUS TPC,” *Nucl.Instrum.Meth.*, vol. A523, pp. 275–286, 2004. DOI: [10.1016/j.nima.2003.11.423](https://doi.org/10.1016/j.nima.2003.11.423).
- [103] S. Kubota, M. Hishida, M. Suzuki, and J. zhi Ruan, “Dynamical behvaior of free electrons in the recombination process in liquid argon, krypton, and xenon,” *Phys. Rev. B*, vol. 20, no. 8, p. 3486, 1979.
- [104] B. Lenardo, K. Kazkaz, M. Szydagis, and M. Tripathi, “A Global Analysis of Light and Charge Yields in Liquid Xenon,” 2014. arXiv: 1412.4417 [astro-ph.IM].
- [105] P. Amaudruz, D. Bryman, L. Kurchaninov, P. Lu, C. Marshall, *et al.*, “Simultaneous reconstruction of scintillation light and ionization charge produced by 511-keV photons in liquid xenon: Potential application to PET,” *Nucl.Instrum.Meth.*, vol. A607, pp. 668–676, 2009. DOI: [10.1016/j.nima.2009.06.036](https://doi.org/10.1016/j.nima.2009.06.036). arXiv: 0906.4075 [physics.ins-det].

- [106] T. Doke, H. Crawford, A. Hitachi, J. Kikuchi, P. Lindstrom, *et al.*, “Let Dependence of Scintillation Yields in Liquid Argon,” *Nucl.Instrum.Meth.*, vol. A269, pp. 291–296, 1988. DOI: 10.1016/0168-9002(88)90892-3.
- [107] F. Arneodo *et al.*, “First observation of 140-cm drift ionizing tracks in the ICARUS liquid-argon TPC,” *Nucl.Instrum.Meth.*, vol. A449, pp. 36–41, 2000. DOI: 10.1016/S0168-9002(99)01296-6.
- [108] O. Palamara, “The atmospheric and solar neutrino experiment with the ICARUS T600 detector,” *Nucl.Phys.Proc.Suppl.*, vol. 110, pp. 329–332, 2002.
- [109] M. Antonello *et al.*, “Search for anomalies in the ν_e appearance from a ν_μ beam,” *Eur.Phys.J.*, vol. C73, no. 10, p. 2599, 2013. DOI: 10.1140/epjc/s10052-013-2599-z. arXiv: 1307.4699.
- [110] R. Acciarri *et al.*, “First Measurement of Neutrino and Antineutrino Coherent Charged Pion Production on Argon,” 2014. arXiv: 1408.0598 [hep-ex].
- [111] ——, “Detection of back-to-back proton pairs in charged-current neutrino interactions with the ArgoNeuT detector in the NuMI low energy beam line,” *Phys.Rev.*, vol. D90, no. 1, p. 012008, 2014. DOI: 10.1103/PhysRevD.90.012008. arXiv: 1405.4261 [nucl-ex].
- [112] ——, “Measurements of Inclusive Muon Neutrino and Antineutrino Charged Current Differential Cross Sections on Argon in the NuMI Antineutrino Beam,” *Phys.Rev.*, vol. D89, p. 112003, 2014. DOI: 10.1103/PhysRevD.89.112003. arXiv: 1404.4809 [hep-ex].
- [113] C. Anderson *et al.*, “First Measurements of Inclusive Muon Neutrino Charged Current Differential Cross Sections on Argon,” *Phys.Rev.Lett.*, vol. 108, p. 161802, 2012. DOI: 10.1103/PhysRevLett.108.161802. arXiv: 1111.0103 [hep-ex].
- [114] The MicroBooNE Collaboration, “Technical design report,” <http://www-microboone.fnal.gov/publications/TDRCD3.pdf>.
- [115] H. Chen, C. Thorn, D. Lissauer, V. Radeka, B. Yu, *et al.*, “A letter of Intent for a neutrino oscillation experiment on the Booster Neutrino Beamline: LAr1,” 2012.
- [116] C. Adams *et al.*, “LAr1-ND: Testing Neutrino Anomalies with Multiple LArTPC Detectors at Fermilab,” 2013. arXiv: 1309.7987 [physics.ins-det].
- [117] M. Antonello, B. Baibussinov, V. Bellini, H. Bilokon, F. Boffelli, *et al.*, “ICARUS at FNAL,” 2013. arXiv: 1312.7252 [physics.ins-det].
- [118] T. Akiri *et al.*, “The 2010 Interim Report of the Long-Baseline Neutrino Experiment Collaboration Physics Working Groups,” 2011. arXiv: 1110.6249 [hep-ex].
- [119] C. Adams *et al.*, “The Long-Baseline Neutrino Experiment: Exploring Fundamental Symmetries of the Universe,” 2013. arXiv: 1307.7335 [hep-ex].
- [120] A. Aguilar-Arevalo *et al.*, “The Neutrino Flux prediction at MiniBooNE,” *Phys.Rev.*, vol. D79, p. 072002, 2009. DOI: 10.1103/PhysRevD.79.072002. arXiv: 0806.1449 [hep-ex].

- [121] ——, “Unexplained Excess of Electron-Like Events From a 1-GeV Neutrino Beam,” *Phys.Rev.Lett.*, vol. 102, p. 101802, 2009. DOI: 10.1103/PhysRevLett.102.101802. arXiv: 0812.2243 [hep-ex].
- [122] R. Acciarri *et al.*, “First demonstration of $d\epsilon/dx$ based electron-gamma separation using neutrino beam events,” *In preparation*.
- [123] R. J. Hill, “On the single photon background to ν_e appearance at MiniBooNE,” *Phys.Rev.*, vol. D84, p. 017501, 2011. DOI: 10.1103/PhysRevD.84.017501. arXiv: 1002.4215 [hep-ph].
- [124] X. Zhang and B. D. Serot, “Can neutrino-induced photon production explain the low energy excess in MiniBooNE?” *Phys.Lett.*, vol. B719, pp. 409–414, 2013. DOI: 10.1016/j.physletb.2013.01.057. arXiv: 1210.3610 [nucl-th].
- [125] M. Martini, M. Ericson, and G. Chanfray, “Neutrino quasielastic interaction and nuclear dynamics,” *Phys.Rev.*, vol. C84, p. 055502, 2011. DOI: 10.1103/PhysRevC.84.055502. arXiv: 1110.0221 [nucl-th].
- [126] M. Martini, M. Ericson, G. Chanfray, and J. Marteau, “Neutrino and antineutrino quasielastic interactions with nuclei,” *Phys.Rev.*, vol. C81, p. 045502, 2010. DOI: 10.1103/PhysRevC.81.045502. arXiv: 1002.4538 [hep-ph].
- [127] O. Lalakulich, K. Gallmeister, and U. Mosel, “Many-Body Interactions of Neutrinos with Nuclei - Observables,” *Phys.Rev.*, vol. C86, no. 1, p. 014614, 2012. DOI: 10.1103/PhysRevC.86.014614, 10.1103/PhysRevC.90.029902. arXiv: 1203.2935 [nucl-th].
- [128] M. Martini, “Two Particle-Two Hole Excitations in Charged Current Quasielastic Neutrino-Nucleus Interactions,” *J.Phys.Conf.Ser.*, vol. 408, p. 012041, 2013. DOI: 10.1088/1742-6596/408/1/012041. arXiv: 1110.5895 [hep-ph].
- [129] R. Gran, J. Nieves, F. Sanchez, and M. Vicente Vacas, “Neutrino-nucleus quasielastic and 2p2h interactions up to 10 GeV,” *Phys.Rev.*, vol. D88, no. 11, p. 113007, 2013. DOI: 10.1103/PhysRevD.88.113007. arXiv: 1307.8105 [hep-ph].
- [130] M. Ivanov, G. Megias, R. Gonzalez-Jimenez, O. Moreno, M. Barbaro, *et al.*, “Charged-current inclusive neutrino cross sections in the SuperScaling model including quasielastic, pion production and meson-exchange contributions,” 2015. arXiv: 1506.00801 [nucl-th].
- [131] G. Megias, T. Donnelly, O. Moreno, C. Williamson, J. Caballero, *et al.*, “Meson-exchange currents and quasielastic predictions for charged-current neutrino- ^{12}C scattering in the superscaling approach,” *Phys.Rev.*, vol. D91, no. 7, p. 073004, 2015. DOI: 10.1103/PhysRevD.91.073004. arXiv: 1412.1822 [nucl-th].
- [132] J. T. Sobczyk, “Multinucleon ejection model for Meson Exchange Current neutrino interactions,” *Phys.Rev.*, vol. C86, p. 015504, 2012. DOI: 10.1103/PhysRevC.86.015504. arXiv: 1201.3673 [hep-ph].

- [133] L. Alvarez-Ruso, Y. Hayato, and J. Nieves, “Progress and open questions in the physics of neutrino cross sections at intermediate energies,” *New J.Phys.*, vol. 16, p. 075015, 2014. DOI: 10.1088/1367-2630/16/7/075015. arXiv: 1403.2673 [hep-ph].
- [134] M. Martini, M. Ericson, and G. Chanfray, “Energy reconstruction effects in neutrino oscillation experiments and implications for the analysis,” *Phys.Rev.*, vol. D87, no. 1, p. 013009, 2013. DOI: 10.1103/PhysRevD.87.013009. arXiv: 1211.1523 [hep-ph].
- [135] ——, “Neutrino energy reconstruction problems and neutrino oscillations,” *Phys.Rev.*, vol. D85, p. 093012, 2012. DOI: 10.1103/PhysRevD.85.093012. arXiv: 1202.4745 [hep-ph].
- [136] J. Nieves, F. Sanchez, I. Ruiz Simo, and M. Vicente Vacas, “Neutrino Energy Reconstruction and the Shape of the CCQE-like Total Cross Section,” *Phys.Rev.*, vol. D85, p. 113008, 2012. DOI: 10.1103/PhysRevD.85.113008. arXiv: 1204.5404 [hep-ph].
- [137] C. A. Aidala, S. D. Bass, D. Hasch, and G. K. Mallot, “The Spin Structure of the Nucleon,” *Rev.Mod.Phys.*, vol. 85, pp. 655–691, 2013. DOI: 10.1103/RevModPhys.85.655. arXiv: 1209.2803 [hep-ph].
- [138] W. Alberico, S. M. Bilenky, and C. Maierov, “Strangeness in the nucleon: Neutrino - nucleon and polarized electron - nucleon scattering,” *Phys.Rept.*, vol. 358, pp. 227–308, 2002. DOI: 10.1016/S0370-1573(01)00058-8. arXiv: hep-ph/0102269 [hep-ph].
- [139] T. Miceli, V. Papavassiliou, S. Pate, and K. Woodruff, “Improving Dark Matter Searches by Measuring the Nucleon Axial Form Factor: Perspectives from MicroBooNE,” *Phys.Procedia*, vol. 61, pp. 495–501, 2015. DOI: 10.1016/j.phpro.2014.12.113. arXiv: 1406.5204 [hep-ex].
- [140] J. R. Ellis, K. A. Olive, and C. Savage, “Hadronic Uncertainties in the Elastic Scattering of Supersymmetric Dark Matter,” *Phys.Rev.*, vol. D77, p. 065026, 2008. DOI: 10.1103/PhysRevD.77.065026. arXiv: 0801.3656 [hep-ph].
- [141] R. J. Hill and M. P. Solon, “Standard Model anatomy of WIMP dark matter direct detection II: QCD analysis and hadronic matrix elements,” *Phys.Rev.*, vol. D91, p. 043505, 2015. DOI: 10.1103/PhysRevD.91.043505. arXiv: 1409.8290 [hep-ph].
- [142] A. Rodriguez *et al.*, “Measurement of single charged pion production in the charged-current interactions of neutrinos in a 1.3-GeV wide band beam,” *Phys.Rev.*, vol. D78, p. 032003, 2008. DOI: 10.1103/PhysRevD.78.032003. arXiv: 0805.0186 [hep-ex].
- [143] K. Hiraide *et al.*, “Search for Charged Current Coherent Pion Production on Carbon in a Few-GeV Neutrino Beam,” *Phys.Rev.*, vol. D78, p. 112004, 2008. DOI: 10.1103/PhysRevD.78.112004. arXiv: 0811.0369 [hep-ex].

- [144] A. Aguilar-Arevalo *et al.*, “First Observation of Coherent π^0 Production in Neutrino Nucleus Interactions with $E_\nu < 2$ GeV,” *Phys.Lett.*, vol. B664, pp. 41–46, 2008. DOI: 10.1016/j.physletb.2008.05.006. arXiv: 0803.3423 [hep-ex].
- [145] K. Hirata, T. Kajita, M. Koshiba, M. Nakahata, Y. Oyama, *et al.*, “Observation in the Kamiokande-II Detector of the Neutrino Burst from Supernova SN 1987a,” *Phys.Rev.*, vol. D38, pp. 448–458, 1988. DOI: 10.1103/PhysRevD.38.448.
- [146] R. Bionta, G. Blewitt, C. Bratton, D. Casper, A. Ciocio, *et al.*, “Observation of a Neutrino Burst in Coincidence with Supernova SN 1987a in the Large Magellanic Cloud,” *Phys.Rev.Lett.*, vol. 58, p. 1494, 1987. DOI: 10.1103/PhysRevLett.58.1494.
- [147] P. Antonioli, R. T. Fienberg, F. Fleurot, Y. Fukuda, W. Fulgione, *et al.*, “SNEWS: The Supernova Early Warning System,” *New J.Phys.*, vol. 6, p. 114, 2004. DOI: 10.1088/1367-2630/6/1/114. arXiv: astro-ph/0406214 [astro-ph].
- [148] A. S. Dighe and A. Y. Smirnov, “Identifying the neutrino mass spectrum from the neutrino burst from a supernova,” *Phys.Rev.*, vol. D62, p. 033007, 2000. DOI: 10.1103/PhysRevD.62.033007. arXiv: hep-ph/9907423 [hep-ph].
- [149] C. Lunardini and A. Y. Smirnov, “Supernova neutrinos: Earth matter effects and neutrino mass spectrum,” *Nucl.Phys.*, vol. B616, pp. 307–348, 2001. DOI: 10.1016/S0550-3213(01)00468-0. arXiv: hep-ph/0106149 [hep-ph].
- [150] H. Duan, G. M. Fuller, J. Carlson, and Y.-Z. Qian, “Neutrino Mass Hierarchy and Stepwise Spectral Swapping of Supernova Neutrino Flavors,” *Phys.Rev.Lett.*, vol. 99, p. 241802, 2007. DOI: 10.1103/PhysRevLett.99.241802. arXiv: 0707.0290 [astro-ph].
- [151] M. Leurer and J. Liu, “Supernova Implications for the Magnetic Transition Moment of Majorana Neutrinos,” *Phys.Lett.*, vol. B219, p. 304, 1989. DOI: 10.1016/0370-2693(89)90395-X.
- [152] J.-S. Lu, J. Cao, Y.-F. Li, and S. Zhou, “Constraining Absolute Neutrino Masses via Detection of Galactic Supernova Neutrinos at JUNO,” *JCAP*, vol. 1505, no. 05, p. 044, 2015. DOI: 10.1088/1475-7516/2015/05/044. arXiv: 1412.7418 [hep-ph].
- [153] X. Shi and G. Sigl, “A Type II supernovae constraint on electron-neutrino - sterile-neutrino mixing,” *Phys.Lett.*, vol. B323, pp. 360–366, 1994. DOI: 10.1016/0370-2693(94)91232-7. arXiv: hep-ph/9312247 [hep-ph].
- [154] H. Nunokawa, J. Peltoniemi, A. Rossi, and J. Valle, “Supernova bounds on resonant active sterile neutrino conversions,” *Phys.Rev.*, vol. D56, pp. 1704–1713, 1997. DOI: 10.1103/PhysRevD.56.1704. arXiv: hep-ph/9702372 [hep-ph].

- [155] J. Hidaka and G. M. Fuller, “Dark matter sterile neutrinos in stellar collapse: Alteration of energy/lepton number transport and a mechanism for supernova explosion enhancement,” *Phys. Rev.*, vol. D74, p. 125 015, 2006. DOI: 10.1103/PhysRevD.74.125015. arXiv: astro-ph/0609425 [astro-ph].
- [156] P. Keranen, J. Maalampi, M. Myyrylainen, and J. Riittinen, “Sterile neutrino signals from supernovae,” *Phys. Rev.*, vol. D76, p. 125 026, 2007. DOI: 10.1103/PhysRevD.76.125026. arXiv: 0708.3337 [hep-ph].
- [157] I. Tamborra, G. G. Raffelt, L. Hudepohl, and H.-T. Janka, “Impact of eV-mass sterile neutrinos on neutrino-driven supernova outflows,” *JCAP*, vol. 1201, p. 013, 2012. DOI: 10.1088/1475-7516/2012/01/013. arXiv: 1110.2104 [astro-ph.SR].
- [158] M. L. Warren, M. Meixner, G. Mathews, J. Hidaka, and T. Kajino, “Sterile neutrino oscillations in core-collapse supernovae,” *Phys. Rev.*, vol. D90, no. 10, p. 103 007, 2014. DOI: 10.1103/PhysRevD.90.103007. arXiv: 1405.6101 [astro-ph.HE].
- [159] R. Thornton, “Accelerator-Produced Dark Matter Search using MiniBooNE,” 2014. arXiv: 1411.4311 [hep-ex].
- [160] B. A. Dobrescu and C. Frugieule, “GeV-scale dark matter: production at the Main Injector,” *JHEP*, vol. 02, p. 019, 2015. DOI: 10.1007/JHEP02(2015)019. arXiv: 1410.1566 [hep-ph].
- [161] B. Batell, M. Pospelov, and A. Ritz, “Exploring Portals to a Hidden Sector Through Fixed Targets,” *Phys. Rev.*, vol. D80, p. 095 024, 2009. DOI: 10.1103/PhysRevD.80.095024. arXiv: 0906.5614 [hep-ph].
- [162] P. deNiverville, D. McKeen, and A. Ritz, “Signatures of sub-GeV dark matter beams at neutrino experiments,” *Phys. Rev.*, vol. D86, p. 035 022, 2012. DOI: 10.1103/PhysRevD.86.035022. arXiv: 1205.3499 [hep-ph].
- [163] P. deNiverville, M. Pospelov, and A. Ritz, “Observing a light dark matter beam with neutrino experiments,” *Phys. Rev.*, vol. D84, p. 075 020, 2011. DOI: 10.1103/PhysRevD.84.075020. arXiv: 1107.4580 [hep-ph].
- [164] B. Batell, P. deNiverville, D. McKeen, M. Pospelov, and A. Ritz, “Leptophobic Dark Matter at Neutrino Factories,” *Phys. Rev.*, vol. D90, no. 11, p. 115 014, 2014. DOI: 10.1103/PhysRevD.90.115014. arXiv: 1405.7049 [hep-ph].
- [165] Hamamatsu Corporation, “Photon counting,” http://psec.uchicago.edu/links/pmt_handbook_complete.pdf.
- [166] Hamamatsu, “Large area photomultiplier tubes,” http://www.hamamatsu.com/resources/pdf/etd/LARGE_AREA_PMT TPMH1286E05.pdf.
- [167] E. Calvo, M. Cerrada, C. Fernandez-Bedoya, I. Gil-Botella, C. Palomares, *et al.*, “Characterization of large area photomultipliers under low magnetic fields: Design and performances of the magnetic shielding for the Double Chooz neutrino experiment,” *Nucl. Instrum. Meth.*, vol. A621, pp. 222–230, 2010. DOI: 10.1016/j.nima.2010.06.009. arXiv: 0905.3246 [physics.ins-det].

- [168] H. Meyer, “Performance of a photomultiplier at liquid-helium temperature,” *Nuclear Instruments and Methods in Physics Research Section A: Accelerators, Spectrometers, Detectors and Associated Equipment*, vol. 621, no. 1–3, pp. 437–442, 2010, ISSN: 0168-9002. DOI: <http://dx.doi.org/10.1016/j.nima.2010.05.048>. [Online]. Available: <http://www.sciencedirect.com/science/article/pii/S0168900210011496>.
- [169] T. Caldwell, S. Seibert, and S. Jaditz, “Characterization of the R5912-02 MOD photomultiplier tube at cryogenic temperatures,” *JINST*, vol. 8, p. C09004, 2013. DOI: <10.1088/1748-0221/8/09/C09004>.
- [170] K. Saito, H. Tawara, T. Sanami, E. Shibamura, and S. Sasaki, “Absolute number of scintillation photons emitted by alpha-particles in rare gases,” *IEEE Trans.Nucl.Sci.*, vol. 49, pp. 1674–1680, 2002. DOI: <10.1109/TNS.2002.801700>.
- [171] V. Gehman, S. Seibert, K. Rielage, A. Hime, Y. Sun, *et al.*, “Fluorescence Efficiency and Visible Re-emission Spectrum of Tetraphenyl Butadiene Films at Extreme Ultraviolet Wavelengths,” *Nucl.Instrum.Meth.*, vol. A654, pp. 116–121, 2011. DOI: <10.1016/j.nima.2011.06.088>. arXiv: <1104.3259> [astro-ph.IM].
- [172] Sinclair Hermetic Packages, “Optical transmission curves for glasses,” <http://www.sinclairmfg.com/datasheets/optical3.html>.
- [173] Hamamatsu Corporation, “Photocathode technology,” <http://www.hamamatsu.com/us/en/technology/innovation/photocathode/index.html>.
- [174] Rogers Corporation, “Ro4000 laminates,” <http://www.rogerscorp.com/acs/producttypes/9/R04000-Laminates.aspx>.
- [175] S. Mufson and B. Baptista, “Light guide production for LBNE and the effects of UV exposure on VUV waveshifter efficiency,” *JINST*, vol. 8, p. C09012, 2013. DOI: <10.1088/1748-0221/8/12/E12002>, <10.1088/1748-0221/8/09/C09012>.
- [176] E. Garutti, “Silicon Photomultipliers for High Energy Physics Detectors,” *JINST*, vol. 6, p. C10003, 2011. DOI: <10.1088/1748-0221/6/10/C10003>. arXiv: <1108.3166> [physics.ins-det].
- [177] Molex Technologies, “Polymicro technologies silica / silica optical fiber fv,” http://www.literature.molex.com/SQLImages/kelmscott/Molex/PDF_Images/987650-8936.pdf.
- [178] G. Karagiorgi *et al.*, “Description of the microboone trigger system,” *MicroBooNE technote, docdb 2466*, 2013.
- [179] J. Conrad and M. Shaevitz, “The ideas behind the proposed physics triggers and pmt readout (in plain english),” *MicroBooNE technote, docdb 2470*, 2013.
- [180] G. Karagiorgi *et al.*, “Description of the pmt readout test stand at pab,” *MicroBooNE technote, docdb 2819*.
- [181] L. Camilleri *et al.*, “Default setup for bo vst,” *MicroBooNE technote, docdb 2148*.

- [182] B. Jones, T. Katori, and J. Conrad, “What did we learn from the pmt-bo first fill?” *MicroBooNE technote, docdb 2043*.
- [183] E. Morikawa *et al.*, “Argon, krypton, and xenon excimer luminescence: from the dilute gas to the condensed phase,” *J. Chem. Phys.*, vol. 91, p. 1469, 1989.
- [184] W. Schmidt, *Liquid State Electronics of Insulating Liquids*. CRC Press, 1997.
- [185] E. Aprile, K. Giboni, P. Majewski, K. Ni, and M. Yamashita, “Observation of Anti-correlation between Scintillation and Ionization for MeV Gamma-Rays in Liquid Xenon,” *Phys.Rev.*, vol. B76, p. 014115, 2007. DOI: 10.1103/PhysRevB.76.014115. arXiv: 0704.1118 [astro-ph].
- [186] M. G. Boulay and A. Hime, “Direct WIMP detection using scintillation time discrimination in liquid argon,” 2004. arXiv: astro-ph/0411358 [astro-ph].
- [187] W. Lippincott, K. Coakley, D. Gastler, A. Hime, E. Kearns, *et al.*, “Scintillation time dependence and pulse shape discrimination in liquid argon,” *Phys.Rev.*, vol. C78, p. 035801, 2008. DOI: 10.1103/PhysRevC.81.039901, 10.1103/PhysRevC.78.035801. arXiv: 0801.1531 [nucl-ex].
- [188] A. Neumeier, M. Hofmann, L. Oberauer, W. Potzel, S. Schonert, *et al.*, “Attenuation of vacuum ultraviolet light in liquid argon,” *Eur.Phys.J.*, vol. C72, p. 2190, 2012. DOI: 10.1140/epjc/s10052-012-2190-z.
- [189] A. Wright, “Optical attenuation in liquid argon,” <http://darkside-docdb.fnal.gov/cgi-bin/RetrieveFile?docid=41>.
- [190] G. Seidel, R. Lanou, and W. Yao, “Rayleigh scattering in rare gas liquids,” *Nucl.Instrum.Meth.*, vol. A489, pp. 189–194, 2002. DOI: 10.1016/S0168-9002(02)00890-2. arXiv: hep-ex/0111054 [hep-ex].
- [191] N. Ishida, M. Chen, T. Doke, K. Hasuike, A. Hitachi, M. Gaudreau, M. Kase, Y. Kawada, J. Kikuchi, T. Komiyama, K. Kuwahara, K. Masuda, H. Okada, Y. Qu, M. Suzuki, and T. Takahashi, “Attenuation length measurements of scintillation light in liquid rare gases and their mixtures using an improved reflection suppresser,” *Nuclear Instruments and Methods in Physics Research Section A: Accelerators, Spectrometers, Detectors and Associated Equipment*, vol. 384, no. 2–3, pp. 380 –386, 1997, ISSN: 0168-9002. DOI: [http://dx.doi.org/10.1016/S0168-9002\(96\)00740-1](http://dx.doi.org/10.1016/S0168-9002(96)00740-1). [Online]. Available: <http://www.sciencedirect.com/science/article/pii/S0168900296007401>.
- [192] R. K. Teague and C. J. Pings, “Refractive index and the lorentz–lorenz function for gaseous and liquid argon, including a study of the coexistence curve near the critical state,” *The Journal of Chemical Physics*, vol. 48, no. 11, pp. 4973–4984, 1968. DOI: <http://dx.doi.org/10.1063/1.1668164>. [Online]. Available: <http://scitation.aip.org/content/aip/journal/jcp/48/11/10.1063/1.1668164>.

- [193] A. Bideau-Mehu, Y. Guern, R. Abjean, and A. Johannin-Gilles, “Measurement of refractive indices of neon, argon, krypton and xenon in the 253.7–140.4 nm wavelength range. dispersion relations and estimated oscillator strengths of the resonance lines,” *Journal of Quantitative Spectroscopy and Radiative Transfer*, vol. 25, no. 5, pp. 395 –402, 1981, ISSN: 0022-4073. DOI: [http://dx.doi.org/10.1016/0022-4073\(81\)90057-1](http://dx.doi.org/10.1016/0022-4073(81)90057-1). [Online]. Available: <http://www.sciencedirect.com/science/article/pii/0022407381900571>.
- [194] A. C. Sinnock and B. L. Smith, “Refractive indices of the condensed inert gases,” *Phys. Rev.*, vol. 181, pp. 1297–1307, 3 1969. DOI: 10.1103/PhysRev.181.1297. [Online]. Available: <http://link.aps.org/doi/10.1103/PhysRev.181.1297>.
- [195] B. Adams, A. Elagin, H. Frisch, R. Obaid, E. Oberla, *et al.*, “Measurements of the gain, time resolution, and spatial resolution of a 20x20cm² MCP-based picosecond photo-detector,” *Nucl.Instrum.Meth.*, vol. A732, pp. 392–396, 2013. DOI: 10.1016/j.nima.2013.07.091.
- [196] B. Rebel, M. Adamowski, W. Jaskierny, H. Jostlein, C. Kendziora, *et al.*, “Results from the Fermilab materials test stand and status of the liquid argon purity demonstrator,” *J.Phys.Conf.Ser.*, vol. 308, p. 012023, 2011. DOI: 10.1088/1742-6596/308/1/012023.
- [197] LDektek corporation, “Ld8000 trace nitrogen in argon analyzer,” <http://www.ldetek.com/our-products/ld8000/>.
- [198] Servomex, “Servomex process oxygen analyzer,” <https://www.servomex.com/servomex/web/web.nsf/en/delta-f-df-310e>.
- [199] T. Optics, “Halo+ h20 trace moisture analyzer for ultra high purity gases,” www.tigeroptics.com/pdf/HALO+H2O-Specs.pdf.
- [200] Stanford Research Systems, “Universal gas analyzer uga200,” <http://www.thinksrs.com/downloads/PDFs/Manuals/UGAm.pdf>.
- [201] United Nuclear, “Unitec nuclear disc sources,” <https://www.unitednuclear.com/>.
- [202] M. Berger, J. Coursey, M. Zucker, and J. Chang, “Stopping-power and range tables for electrons, protons, and helium ions,” <http://www.nist.gov/pml/data/star/>.
- [203] Douglas Electrical Components, “Ductorseal epoxy potted feedthrough,” <http://www.douglaselectrical.com/ductorseal>.
- [204] D. Whittington and S. Mufson, “Scintillation Light from Cosmic-Ray Muons in Liquid Argon,” *Phys.Rev.D*, 2014. arXiv: 1408.1763 [physics.ins-det].
- [205] M. Adamowski, B. Carls, E. Dvorak, A. Hahn, W. Jaskierny, *et al.*, “The Liquid Argon Purity Demonstrator,” *JINST*, vol. 9, P07005, 2014. DOI: 10.1088/1748-0221/9/07/P07005. arXiv: 1403.7236 [physics.ins-det].

- [206] K. Mavrokoridis, R. Calland, J. Coleman, P. Lightfoot, N. McCauley, *et al.*, “Argon Purification Studies and a Novel Liquid Argon Re-circulation System,” *JINST*, vol. 6, P08003, 2011. DOI: 10.1088/1748-0221/6/08/P08003. arXiv: 1106.5226 [physics.ins-det].
- [207] R. Acciarri *et al.*, “Oxygen contamination in liquid Argon: Combined effects on ionization electron charge and scintillation light,” *JINST*, vol. 5, P05003, 2010. DOI: 10.1088/1748-0221/5/05/P05003. arXiv: 0804.1222 [nucl-ex].
- [208] ——, “Effects of Nitrogen contamination in liquid Argon,” *JINST*, vol. 5, P06003, 2010. DOI: 10.1088/1748-0221/5/06/P06003. arXiv: 0804.1217 [nucl-ex].
- [209] C. S. Chiu, “Liquid Argon scintillation light quenching due to Nitrogen impurities : measurements performed for the MicroBooNE vertical slice test,”
- [210] H Keller-Rudek and G. K. Moortgat, “Mpi-mainz-uv-vis spectral atlas of gaseous molecules,” www.atmosphere.mpg.de/spectral-atlas-mainz.
- [211] R. Brunetti *et al.*, “Warp liquid argon detector for dark matter survey,” *New Astron. Rev.*, vol. 49, pp. 265–269, 2005. DOI: 10.1016/j.newar.2005.01.017. arXiv: astro-ph/0405342 [astro-ph].
- [212] J. Calvo *et al.*, “Status of ArDM-1t: First observations from operation with a full ton-scale liquid argon target,” 2015. arXiv: 1505.02443 [physics.ins-det].
- [213] P. Gorel, “Search for Dark Matter with Liquid Argon and Pulse Shape Discrimination: Results from DEAP-1 and Status of DEAP-3600,” pp. 487–490, 2014. arXiv: 1406.0462 [astro-ph.IM].
- [214] K. Rielage *et al.*, “Update on the MiniCLEAN Dark Matter Experiment,” *Phys. Procedia*, vol. 61, pp. 144–152, 2015. DOI: 10.1016/j.phpro.2014.12.024. arXiv: 1403.4842 [physics.ins-det].
- [215] C. Aalseth, P. Agnes, A. Alton, K. Arisaka, D. Asner, *et al.*, “The DarkSide Multiton Detector for the Direct Dark Matter Search,” *Adv. High Energy Phys.*, vol. 2015, p. 541362, 2015. DOI: 10.1155/2015/541362.
- [216] K. Scholberg, T. Wongjirad, E. Hungerford, A. Empl, D. Markoff, P. Mueller, Y. Efremenko, D. McKinsey, and J. Nikkel, “The CLEAR Experiment,” in *Particles and fields. Proceedings, Meeting of the Division of the American Physical Society, DPF 2009, Detroit, USA, July 26-31, 2009*, 2009. arXiv: 0910.1989 [hep-ex]. [Online]. Available: <https://inspirehep.net/record/833644/files/arXiv:0910.1989.pdf>.
- [217] D. Akerib *et al.*, “First results from the LUX dark matter experiment at the Sanford Underground Research Facility,” *Phys. Rev. Lett.*, vol. 112, p. 091303, 2014. DOI: 10.1103/PhysRevLett.112.091303. arXiv: 1310.8214 [astro-ph.CO].
- [218] P. Agnes *et al.*, “First Results from the DarkSide-50 Dark Matter Experiment at Laboratori Nazionali del Gran Sasso,” *Phys. Lett.*, vol. B743, pp. 456–466, 2015. DOI: 10.1016/j.physletb.2015.03.012. arXiv: 1410.0653 [astro-ph.CO].

- [219] E. Aprile *et al.*, “Dark Matter Results from 225 Live Days of XENON100 Data,” *Phys.Rev.Lett.*, vol. 109, p. 181301, 2012. DOI: 10.1103/PhysRevLett.109.181301. arXiv: 1207.5988 [astro-ph.CO].
- [220] P. Benetti *et al.*, “Measurement of the specific activity of ar-39 in natural argon,” *Nucl.Instrum.Meth.*, vol. A574, pp. 83–88, 2007. DOI: 10.1016/j.nima.2007.01.106. arXiv: astro-ph/0603131 [astro-ph].
- [221] D. Acosta-Kane, R. Acciarri, O. Amaize, M. Antonello, B. Baibussinov, *et al.*, “Discovery of underground argon with low level of radioactive ^{39}Ar and possible applications to WIMP dark matter detectors,” *Nucl.Instrum.Meth.*, vol. A587, pp. 46–51, 2008. DOI: 10.1088/1742-6596/120/4/042015, 10.1016/j.nima.2007.12.032. arXiv: 0712.0381 [astro-ph].
- [222] J. Xu, F. Calaprice, C. Galbiati, A. Goretti, G. Guray, T. Hohman, D. Holtz, A. Ianni, M. Laubenstein, B. Loer, C. Love, C. Martoff, D. Montanari, S. Mukhopadhyay, A. Nelson, S. Rountree, R. Vogelaar, and A. Wright, “A study of the trace ^{39}Ar content in argon from deep underground sources,” *Astroparticle Physics*, vol. 66, no. 0, pp. 53–60, 2015, ISSN: 0927-6505. DOI: <http://dx.doi.org/10.1016/j.astropartphys.2015.01.002>. [Online]. Available: <http://www.sciencedirect.com/science/article/pii/S0927650515000043>.
- [223] H. Back *et al.*, “First Commissioning of a Cryogenic Distillation Column for Low Radioactivity Underground Argon,” 2012. arXiv: 1204.6061 [astro-ph.IM].
- [224] H. O. Back, F. Calaprice, C. Condon, E. de Haas, R. Ford, *et al.*, “First Large Scale Production of Low Radioactivity Argon From Underground Sources,” 2012. arXiv: 1204.6024 [astro-ph.IM].
- [225] E. Aprile, K. Giboni, and C. Rubbia, “Drifting Electrons Over Large Distances in Liquid Argon-Methane Mixtures,” *Nucl.Instrum.Meth.*, vol. A253, pp. 273–277, 1987. DOI: 10.1016/0168-9002(87)90714-5.
- [226] F. Varanini, “Preliminary experimental results from the {icarus} test facility at infn-lnl,” *Nuclear Physics B - Proceedings Supplements*, vol. 197, no. 1, pp. 313 –316, 2009, 11th Topical Seminar on Innovative Particle and Radiation Detectors (IPRD08), ISSN: 0920-5632. DOI: <http://dx.doi.org/10.1016/j.nuclphysbps.2009.10.093>. [Online]. Available: <http://www.sciencedirect.com/science/article/pii/S0920563209008147>.
- [227] T. J. Sumner, G. K. Rochester, P. D. Smith, J. P. Cooch, and R. K. Sood, “Scintillating drift chambers—the nature of the emission process in ar/ch₄,” *Nuclear Science, IEEE Transactions on*, vol. 29, no. 5, pp. 1410–1414, 1982, ISSN: 0018-9499. DOI: 10.1109/TNS.1982.4336365.
- [228] O. Siegmund, P. Sanford, I. Mason, J. Culhane, S. Kellock, *et al.*, “A parallel plate imaging proportional counter with high background rejection capability,” *IEEE Trans.Nucl.Sci.*, vol. 28, pp. 478–482, 1981.
- [229] A. Dobi, “Measurement of the Electron Recoil Band of the LUX Dark Matter Detector With a Tritium Calibration Source,” DOI: 10.13016/M24P5P.

- [230] D. Anderson and D. Lamb, “Saturation Effects in Liquid Argon Doped with Methane,” *Nucl.Instrum.Meth.*, vol. A265, p. 440, 1988. DOI: 10.1016/S0168-9002(98)90010-9.
- [231] W. Burton and B. Powell, “Fluorescence of tetraphenyl-butadiene in the vacuum ultraviolet.,” *Appl Opt.*, vol. 12, no. 1, pp. 87–9, 1973.
- [232] Sigma Aldrich, “Material safety data sheet, product 185213,” <http://www.sigmaaldrich.com/>.
- [233] A. Zani, “The WArP Experiment: A Double-Phase Argon Detector for Dark Matter Searches,” *Adv.High Energy Phys.*, vol. 2014, p. 205107, 2014. DOI: 10.1155/2014/205107.
- [234] P. Cennini, J. Revol, C. Rubbia, F. Sergiampietri, A. Bueno, *et al.*, “Detection of scintillation light in coincidence with ionizing tracks in a liquid argon time projection chamber,” *Nucl.Instrum.Meth.*, vol. A432, pp. 240–248, 1999. DOI: 10.1016/S0168-9002(99)00519-7.
- [235] M. Bossa, “DarkSide-50, a background free experiment for dark matter searches,” *JINST*, vol. 9, p. C01034, 2014. DOI: 10.1088/1748-0221/9/01/C01034.
- [236] M. Boulay, “DEAP-3600 Dark Matter Search at SNOLAB,” *J.Phys.Conf.Ser.*, vol. 375, p. 012027, 2012. DOI: 10.1088/1742-6596/375/1/012027. arXiv: 1203.0604 [astro-ph.IM].
- [237] B. Baptista and S. Mufson, “Comparison of TPB and bis-MSB as VUV waveshifters in prototype LBNE photon detector paddles,” *JINST*, vol. 8, p. C12003, 2013. DOI: 10.1088/1748-0221/8/12/C12003.
- [238] V. Gehman, T. Ito, W. Griffith, and S. Seibert, “Characterization of protonated and deuterated Tetra-Phenyl Butadiene Film in a Polystyrene Matrix,” *JINST*, vol. 8, P04024, 2013. DOI: 10.1088/1748-0221/8/04/P04024. arXiv: 1302.3210 [physics.ins-det].
- [239] R. Francini, R. Montereali, E. Nichelatti, M. Vincenti, N. Canci, *et al.*, “VUV-Vis optical characterization of Tetraphenyl-butadiene films on glass and specular reflector substrates from room to liquid Argon temperature,” *JINST*, vol. 8, P09006, 2013. DOI: doi:10.1088/1748-0221/8/09/P09006.
- [240] C. Ignarra, “Sterile Neutrino Searches in MiniBooNE and MicroBooNE,” PhD Thesis - I would like a URL for this.
- [241] Hamamatsu, “Photomultipler tube r7723, r7724, r7725,” <http://www.hamamatsu.com/resources/pdf/etd/R7723 TPMH1315E01.pdf>.
- [242] J. B. Birks and K. N. Kuchela, “Energy transfer in fluorescent plastic solutions,” *Disc. Faraday. Soc.*, vol. 27, pp. 57–63, 1959.
- [243] J. B. Birks and K. N. Kuchela, “Energy transfer in organic systems ii: solute-solute transfer in liquid solutions,” *Proc. Phys.Soc*, vol. 77, p. 1083, 1961.

- [244] S. Hanagodimath, B. Siddlingeshwar, J. Thipperudrappa, S. Kumar, and B. Hadimani, “Fluorescence-quenching studies and temperature dependence of fluorescence quantum yield, decay time and intersystem crossing activation energy of tpb,” *J. Lumin.*, vol. 129, no. 4, pp. 335–339, 2008.
- [245] L. Liu, “Time resolved fluorescence studies of dye-polymers as excited by laser and beta radiation,” <http://repositories.tdl.org/ttu-ir/bitstream/handle/2346/13744/31295012500558.pdf?sequence=1>.
- [246] With assistance from Antonie Jurkiewicz of the University of Chicago NMR Facility.
- [247] R. Kronig and A. I. V. de Vooren, “On the electrical breakdown in liquefied gases,” *Physica*, vol. 9, p. 139, 1942.
- [248] D. Swan and T. Lewis, “Influence of electrode surface conditions on the electrical strength of liquified gases,” *J.Electrochem.Soc.*, vol. 107, no. 180, 1960.
- [249] F. Bay, C. Cantini, S. Murphy, F. Resnati, A. Rubbia, *et al.*, “Evidence of electric breakdown induced by bubbles in liquid argon,” 2014. arXiv: 1401.2777 [physics.ins-det].
- [250] A. Blatter, A. Ereditato, C.-C. Hsu, S. Janos, I. Kreslo, *et al.*, “Experimental study of electric breakdowns in liquid argon at centimeter scale,” *JINST*, vol. 9, P04006, 2014. DOI: 10.1088/1748-0221/9/04/P04006. arXiv: 1401.6693 [physics.ins-det].
- [251] R. Acciarri *et al.*, “Liquid Argon Dielectric Breakdown Studies with the MicroBooNE Purification System,” *JINST*, 2014. arXiv: 1408.0264 [physics.ins-det].
- [252] R. Rameika, “The microboone tpc field cage resistor problem,” *MicroBooNE technote, docdb 3307-v7*.
- [253] F. Cavanna, M. Kordosky, J. Raaf, and B. Rebel, “LArIAT: Liquid Argon In A Testbeam,” 2014. arXiv: 1406.5560 [physics.ins-det].
- [254] E. D. Church, “LArSoft: A Software Package for Liquid Argon Time Projection Drift Chambers,” 2013. arXiv: 1311.6774 [physics.ins-det].
- [255] C. Andreopoulos *et al.*, “The GENIE Neutrino Monte Carlo Generator,” *Nucl. Instrum. Meth.*, vol. A614, pp. 87–104, 2010. DOI: 10.1016/j.nima.2009.12.009. arXiv: 0905.2517 [hep-ph].
- [256] R. Chytracek, J. McCormick, W. Pokorski, and G. Santin, “Geometry description markup language for physics simulation and analysis applications,” *IEEE Trans.Nucl.Sci.*, vol. 53, no. 5-2, pp. 2892–2896, 2006.
- [257] S. Agostinelli *et al.*, “Geant4—a simulation toolkit,” *Nuclear Instruments and Methods in Physics Research Section A: Accelerators, Spectrometers, Detectors and Associated Equipment*, vol. 506, no. 3, pp. 250 –303, 2003, ISSN: 0168-9002. DOI: [http://dx.doi.org/10.1016/S0168-9002\(03\)01368-8](http://dx.doi.org/10.1016/S0168-9002(03)01368-8). [Online]. Available: <http://www.sciencedirect.com/science/article/pii/S0168900203013688>.

- [258] B. J. P. Jones, “Optical simulations in larsoft - technical manual,” *MicroBooNE technote, docdb 2313* https://cdcvns.fnal.gov/redmine/projects/larsoftsvn/wiki/Optical_Simulations.
- [259] P. Adamson *et al.*, “LArIAT: Liquid Argon TPC in a Test Beam,” 2013.
- [260] A. Hitachi, T. Takahashi, N. Funayama, K. Masuda, J. Kikuchi, *et al.*, “Effect of ionization density on the time dependence of luminescence from liquid argon and xenon,” *Phys. Rev.*, vol. B27, pp. 5279–5285, 1983. DOI: 10.1103/PhysRevB.27.5279.
- [261] T. Doke, A. Hitachi, J. Kikuchi, K. Masuda, H. Okada, and E. Shibamura, “Absolute scintillation yields in liquid argon and xenon for various particles,” *Japanese Journal of Applied Physics*, vol. 41, no. Part 1, No. 3A, pp. 1538–1545, 2002. DOI: 10.1143/JJAP.41.1538. [Online]. Available: <http://jjap.jsap.jp/link?JJAP/41/1538/>.
- [262] M. Antonello, F. Arneodo, A. Bueno, F. Cavanna, D. GarcÁsa-Gamez, S. Navas-Concha, O. Palamara, G. P. Mortari, and E. Segreto, “Analysis of liquid argon scintillation light signals with the icarus t600 detector,” *unpublished*.
- [263] L. Kalousis, “Cosmic muon flux measurements at the liquid argon test facility,” *MicroBooNE technote, docdb 3130*.
- [264] B. J. P. Jones, “Seed finding and bezier tracking in larsoft - technical manual,” *MicroBooNE technote, docdb 3023* https://cdcvns.fnal.gov/redmine/projects/larsoftsvn/wiki/Seed_Finding_and_Bezier_Tracking.
- [265] T. Yang, “Reconstruction report,” *MicroBooNE docdb 3633*.
- [266] C. V. Achar *et al.*, “Detection of muons produced by cosmic ray neutrinos deep underground,” *Phys. Lett.*, vol. 18, pp. 196–199, 1965. DOI: 10.1016/0031-9163(65)90712-2.
- [267] F. Reines, M. F. Crouch, T. L. Jenkins, W. R. Kropp, H. S. Gurr, G. R. Smith, J. P. F. Sellschop, and B. Meyer, “Evidence for high-energy cosmic ray neutrino interactions,” *Phys. Rev. Lett.*, vol. 15, pp. 429–433, 1965. DOI: 10.1103/PhysRevLett.15.429.
- [268] J. Breault, D. Kielczewska, M. Goldhaber, S. T. Dye, C. B. Bratton, J. G. Learned, R. Svoboda, T. J. Haines, and K. Ganezer, “The Irvine-Michigan-Brookhaven Experiment,”
- [269] M. Nakahata *et al.*, “Atmospheric Neutrino Background and Pion Nuclear Effect for Kamioka Nucleon Decay Experiment,” *J. Phys. Soc. Jap.*, vol. 55, p. 3786, 1986. DOI: 10.1143/JPSJ.55.3786.
- [270] K. S. Hirata *et al.*, “Experimental Study of the Atmospheric Neutrino Flux,” *Phys. Lett.*, vol. B205, p. 416, 1988. DOI: 10.1016/0370-2693(88)91690-5.
- [271] Y. Fukuda *et al.*, “Study of the atmospheric neutrino flux in the multi-GeV energy range,” *Phys. Lett.*, vol. B436, pp. 33–41, 1998. DOI: 10.1016/S0370-2693(98)00876-4. arXiv: hep-ex/9805006 [hep-ex].

- [272] T. Kajita, “Atmospheric neutrino results from Super-Kamiokande and Kamiokande: Evidence for neutrino(mu) oscillations,” *Nucl. Phys. Proc. Suppl.*, vol. 77, pp. 123–132, 1999. arXiv: hep-ex/9810001 [hep-ex].
- [273] M. Ambrosio *et al.*, “Measurement of the atmospheric neutrino induced upgoing muon flux using MACRO,” *Phys. Lett.*, vol. B434, pp. 451–457, 1998. DOI: 10.1016/S0370-2693(98)00885-5. arXiv: hep-ex/9807005 [hep-ex].
- [274] W. W. M. Allison *et al.*, “The Atmospheric neutrino flavor ratio from a 3.9 fiducial kiloton year exposure of Soudan-2,” *Phys. Lett.*, vol. B449, pp. 137–144, 1999. DOI: 10.1016/S0370-2693(99)00056-8. arXiv: hep-ex/9901024 [hep-ex].
- [275] M. Aartsen *et al.*, “Determining neutrino oscillation parameters from atmospheric muon neutrino disappearance with three years of IceCube DeepCore data,” 2014. arXiv: 1410.7227 [hep-ex].
- [276] A. Himmel, “Recent results from Super-Kamiokande,” *AIP Conf. Proc.*, vol. 1604, pp. 345–352, 2014. arXiv: 1310.6677 [hep-ex].
- [277] P. Adamson *et al.*, “Measurement of Neutrino and Antineutrino Oscillations Using Beam and Atmospheric Data in MINOS,” *Phys. Rev. Lett.*, vol. 110, no. 25, p. 251801, 2013. DOI: 10.1103/PhysRevLett.110.251801. arXiv: 1304.6335 [hep-ex].
- [278] K. Abe *et al.*, “Precise Measurement of the Neutrino Mixing Parameter θ_{23} from Muon Neutrino Disappearance in an Off-Axis Beam,” *Phys. Rev. Lett.*, vol. 112, no. 18, p. 181801, 2014. DOI: 10.1103/PhysRevLett.112.181801. arXiv: 1403.1532 [hep-ex].
- [279] ——, “Evidence for the Appearance of Atmospheric Tau Neutrinos in Super-Kamiokande,” *Phys. Rev. Lett.*, vol. 110, no. 18, p. 181802, 2013. DOI: 10.1103/PhysRevLett.110.181802. arXiv: 1206.0328 [hep-ex].
- [280] J. Hosaka *et al.*, “Three flavor neutrino oscillation analysis of atmospheric neutrinos in Super-Kamiokande,” *Phys. Rev.*, vol. D74, p. 032002, 2006. DOI: 10.1103/PhysRevD.74.032002. arXiv: hep-ex/0604011 [hep-ex].
- [281] J. Ahrens *et al.*, “Icecube - the next generation neutrino telescope at the south pole,” *Nucl. Phys. Proc. Suppl.*, vol. 118, pp. 388–395, 2003, [,388(2002)]. DOI: 10.1016/S0920-5632(03)01337-9. arXiv: astro-ph/0209556 [astro-ph].
- [282] M. G. Aartsen *et al.*, “Observation of High-Energy Astrophysical Neutrinos in Three Years of IceCube Data,” *Phys. Rev. Lett.*, vol. 113, p. 101101, 2014. DOI: 10.1103/PhysRevLett.113.101101. arXiv: 1405.5303 [astro-ph.HE].
- [283] ——, “Evidence for High-Energy Extraterrestrial Neutrinos at the IceCube Detector,” *Science*, vol. 342, p. 1242856, 2013. DOI: 10.1126/science.1242856. arXiv: 1311.5238 [astro-ph.HE].
- [284] M. Aartsen *et al.*, “First observation of PeV-energy neutrinos with IceCube,” *Phys. Rev. Lett.*, vol. 111, p. 021103, 2013. DOI: 10.1103/PhysRevLett.111.021103. arXiv: 1304.5356 [astro-ph.HE].

- [285] F. Halzen and S. R. Klein, “IceCube: An Instrument for Neutrino Astronomy,” *Rev. Sci. Instrum.*, vol. 81, p. 081101, 2010. DOI: 10.1063/1.3480478. arXiv: 1007.1247 [astro-ph.HE].
- [286] K. Hanson and O. Tarasova, “Design and production of the IceCube digital optical module,” *Nucl. Instrum. Meth.*, vol. A567, pp. 214–217, 2006. DOI: 10.1016/j.nima.2006.05.091.
- [287] R. Abbasi *et al.*, “Calibration and Characterization of the IceCube Photomultiplier Tube,” *Nucl. Instrum. Meth.*, vol. A618, pp. 139–152, 2010. DOI: 10.1016/j.nima.2010.03.102. arXiv: 1002.2442 [astro-ph.IM].
- [288] R. Stokstad, “Design and performance of the IceCube electronics,” in *Proceedings, eleventh Workshop on Electronics for LHC and Future Experiments, Heidelberg, Germany, 12-16 September 2005*, 2005, p. 4. [Online]. Available: <http://lhc-workshop-2005.web.cern.ch/lhc%2Dworkshop%2D2005/PlenarySessions/4-Stokstad.pdf>.
- [289] M. Aartsen *et al.*, “Measurement of South Pole ice transparency with the IceCube LED calibration system,” *Nucl. Instrum. Meth.*, vol. A711, pp. 73–89, 2013. DOI: 10.1016/j.nima.2013.01.054. arXiv: 1301.5361 [astro-ph.IM].
- [290] C. Wiebusch, “Physics Capabilities of the IceCube DeepCore Detector,” 2009. arXiv: 0907.2263 [astro-ph.IM].
- [291] F. Halzen, “The AMANDA neutrino telescope,” *New Astron. Rev.*, vol. 42, pp. 289–299, 1998. DOI: 10.1016/S1387-6473(98)00015-3.
- [292] T. Gaisser and F. Halzen, “IceCube,” *Ann. Rev. Nucl. Part. Sci.*, vol. 64, pp. 101–123, 2014. DOI: 10.1146/annurev-nucl-102313-025321.
- [293] P. Askebjer, S. W. Barwick, L. Bergstrom, A. Bouchta, S. Carius, *et al.*, “Optical properties of deep ice at the South Pole: Absorption,” *Appl. Opt.*, vol. 36, pp. 4168–4180, 1997. DOI: 10.1364/AO.36.004168. arXiv: physics/9701025 [physics].
- [294] P. Askebjer *et al.*, “Optical properties of the South Pole ice at depths between 0.8-km and 1-km,” *Science*, vol. 267, pp. 1147–1150, 1995. DOI: 10.1126/science.267.5201.1147. arXiv: astro-ph/9412028 [astro-ph].
- [295] P. B. Price and L. Bergström, “Optical properties of deep ice at the south pole: scattering,” *Appl. Opt.*, vol. 36, no. 18, pp. 4181–4194, 1997. DOI: 10.1364/AO.36.004181. [Online]. Available: <http://ao.osa.org/abstract.cfm?URI=ao-36-18-4181>.
- [296] H. Craig, H. Shoji, and C. C. Langway Jr, “Nonequilibrium air clathrate hydrates in antarctic ice: a paleopiezometer for polar ice caps,” *Proc. Natl. Acad. Sci. USA*, vol. 90, no. 23, pp. 11416–11418, 1993.
- [297] M. Ackermann *et al.*, “Optical properties of deep glacial ice at the south pole,” *Journal of Geophysical Research: Atmospheres*, vol. 111, no. D13, n/a–n/a, 2006, ISSN: 2156-2202. DOI: 10.1029/2005JD006687. [Online]. Available: <http://dx.doi.org/10.1029/2005JD006687>.

- [298] R. Bay, “Icecube dust map,” <http://icecube.berkeley.edu/~bay/dustmap/>.
- [299] N. E. Bramall, R. C. Bay, K. Woschnagg, R. A. Rohde, and P. B. Price, “A deep high-resolution optical log of dust, ash, and stratigraphy in south pole glacial ice,” *Geophysical Research Letters*, vol. 32, no. 21, n/a–n/a, 2005, ISSN: 1944-8007. DOI: 10.1029/2005GL024236. [Online]. Available: <http://dx.doi.org/10.1029/2005GL024236>.
- [300] P. B. Price, K. Woschnagg, and D. Chirkin, “Age vs depth of glacial ice at south pole,” *Geophysical Research Letters*, vol. 27, no. 14, pp. 2129–2132, 2000, ISSN: 1944-8007. DOI: 10.1029/2000GL011351. [Online]. Available: <http://dx.doi.org/10.1029/2000GL011351>.
- [301] L. G. Henyey and J. L. Greenstein, “Diffuse radiation in the Galaxy,” *Astrophys. J.*, vol. 93, pp. 70–83, 1941. DOI: 10.1086/144246.
- [302] P. Liu, “A new phase function approximating to mie scattering for radiative transport equations,” *Phys. Med. Biol.*, vol. 39, p. 1025, 1994.
- [303] M. Aartsen *et al.*, “The IceCube Neutrino Observatory Part VI: Ice Properties, Reconstruction and Future Developments,” 2013. arXiv: 1309.7010 [astro-ph.HE].
- [304] P. O. Hulth, “Icecube camera summary,” Presentation at IceCube collaboration meeting 2013.
- [305] D. E. Groom, N. V. Mokhov, and S. I. Striganov, “Muon stopping power and range tables 10-MeV to 100-TeV,” *Atom. Data Nucl. Data Tabl.*, vol. 78, pp. 183–356, 2001. DOI: 10.1006/adnd.2001.0861.
- [306] C. Weaver, “Evidence for astrophysical muon neutrinos from the northern sky,” Ph. D. thesis, University of Wisconsin, Madison, 2015; ISBN 978-1-321-68769-9.
- [307] M. G. Aartsen *et al.*, “Evidence for Astrophysical Muon Neutrinos from the Northern Sky with IceCube,” 2015. arXiv: 1507.04005 [astro-ph.HE].
- [308] ——, “Energy Reconstruction Methods in the IceCube Neutrino Telescope,” *JINST*, vol. 9, P03009, 2014. DOI: 10.1088/1748-0221/9/03/P03009. arXiv: 1311.4767 [physics.ins-det].
- [309] T. Sanuki, M. Honda, T. Kajita, K. Kasahara, and S. Midorikawa, “Study of cosmic ray interaction model based on atmospheric muons for the neutrino flux calculation,” *Phys. Rev.*, vol. D75, p. 043 005, 2007. DOI: 10.1103/PhysRevD.75.043005. arXiv: astro-ph/0611201 [astro-ph].
- [310] M. Honda, T. Kajita, K. Kasahara, S. Midorikawa, and T. Sanuki, “Calculation of atmospheric neutrino flux using the interaction model calibrated with atmospheric muon data,” *Phys. Rev.*, vol. D75, p. 043 006, 2007. DOI: 10.1103/PhysRevD.75.043006. arXiv: astro-ph/0611418 [astro-ph].
- [311] T. K. Gaisser, *Cosmic Rays and Particle Physics*. Cambridge University Press, 1990.

- [312] M. G. Aartsen *et al.*, “Search for a diffuse flux of astrophysical muon neutrinos with the IceCube 59-string configuration,” *Phys. Rev.*, vol. D89, no. 6, p. 062007, 2014. DOI: 10.1103/PhysRevD.89.062007. arXiv: 1311.7048 [astro-ph.HE].
- [313] A. Fedynitch, R. Engel, T. K. Gaisser, F. Riehn, and T. Stanev, “Calculation of conventional and prompt lepton fluxes at very high energy,” 2015. arXiv: 1503.00544 [hep-ph].
- [314] J. Lundberg, P. Miocinovic, T. Burgess, J. Adams, S. Hundertmark, *et al.*, “Light tracking for glaciers and oceans: Scattering and absorption in heterogeneous media with Photonics,” *Nucl.Instrum.Meth.*, vol. A581, pp. 619–631, 2007. DOI: 10.1016/j.nima.2007.07.143. arXiv: astro-ph/0702108 [ASTRO-PH].
- [315] M. Larson, “Simulation and identification of non-poissonian noise triggers in the icecube neutrino detector,” IceCube internal report icecube/201312002-v2.
- [316] J. Feintzeig, “Searches for point-like sources of astrophysical neutrinos with the icecube neutrino observatory,” University of Wisconsin, Madison, 2014; ISBN 978-1-321-40689-4.
- [317] N. Whitehorn, J. van Santen, and S. Lafebre, “Penalized Splines for Smooth Representation of High-dimensional Monte Carlo Datasets,” *Comput.Phys.Commun.*, vol. 184, pp. 2214–2220, 2013. DOI: 10.1016/j.cpc.2013.04.008. arXiv: 1301.2184 [physics.data-an].
- [318] F. D. Aaron *et al.*, “Combined Measurement and QCD Analysis of the Inclusive e+ p Scattering Cross Sections at HERA,” *JHEP*, vol. 01, p. 109, 2010. DOI: 10.1007/JHEP01(2010)109. arXiv: 0911.0884 [hep-ex].
- [319] J. Gao, M. Guzzi, J. Huston, H.-L. Lai, Z. Li, *et al.*, “CT10 next-to-next-to-leading order global analysis of QCD,” *Phys.Rev.*, vol. D89, no. 3, p. 033009, 2014. DOI: 10.1103/PhysRevD.89.033009. arXiv: 1302.6246 [hep-ph].
- [320] E. R. Nocera, R. D. Ball, S. Forte, G. Ridolfi, and J. Rojo, “A first unbiased global determination of polarized PDFs and their uncertainties,” *Nucl. Phys.*, vol. B887, pp. 276–308, 2014. DOI: 10.1016/j.nuclphysb.2014.08.008. arXiv: 1406.5539 [hep-ph].
- [321] C. A. Arguelles, F. Halzen, L. Will, M. Kroll, and M. H. Reno, “The High-Energy Behavior of Photon, Neutrino and Proton Cross Sections,” 2015. arXiv: 1504.06639 [hep-ph].
- [322] A. M. Dziewonski and D. L. Anderson, “Preliminary reference earth model,” *Phys. Earth Planet. Interiors*, vol. 25, pp. 297–356, 1981. DOI: 10.1016/0031-9201(81)90046-7.
- [323] Wikipedia, “The structure of the earth,” https://en.wikipedia.org/wiki/Structure_of_the_Earth.
- [324] G. Masters and D. Gubbins, “On the resolution of density within the earth,” *Phys. Earth Planet. Interiors*, vol. 140, no. 1, pp. 159–167, 2003.

- [325] G. D. Barr, T. K. Gaisser, S. Robbins, and T. Stanev, “Uncertainties in Atmospheric Neutrino Fluxes,” *Phys. Rev.*, vol. D74, p. 094009, 2006. DOI: 10.1103/PhysRevD.74.094009. arXiv: astro-ph/0611266 [astro-ph].
- [326] M. Honda, M. S. Athar, T. Kajita, K. Kasahara, and S. Midorikawa, “Atmospheric neutrino flux calculation using the NRLMSISE-00 atmospheric model,” *Phys. Rev.*, vol. D92, no. 2, p. 023004, 2015. DOI: 10.1103/PhysRevD.92.023004. arXiv: 1502.03916 [astro-ph.HE].
- [327] M. Honda, T. Kajita, K. Kasahara, and S. Midorikawa, “Improvement of low energy atmospheric neutrino flux calculation using the JAM nuclear interaction model,” *Phys. Rev.*, vol. D83, p. 123001, 2011. DOI: 10.1103/PhysRevD.83.123001. arXiv: 1102.2688 [astro-ph.HE].
- [328] T. S. Sinegovskaya, A. D. Morozova, and S. I. Sinegovsky, “High-energy neutrino fluxes and flavor ratio in the Earth’s atmosphere,” *Phys. Rev.*, vol. D91, no. 6, p. 063011, 2015. DOI: 10.1103/PhysRevD.91.063011. arXiv: 1407.3591 [astro-ph.HE].
- [329] M. Sajjad Athar, M. Honda, T. Kajita, K. Kasahara, and S. Midorikawa, “Atmospheric neutrino flux at INO, South Pole and Pyhasalmi,” *Phys. Lett.*, vol. B718, pp. 1375–1380, 2013. DOI: 10.1016/j.physletb.2012.12.016. arXiv: 1210.5154 [hep-ph].
- [330] A. Fedynitch, J. Becker Tjus, and P. Desiati, “Influence of hadronic interaction models and the cosmic ray spectrum on the high energy atmospheric muon and neutrino flux,” *Phys. Rev.*, vol. D86, p. 114024, 2012. DOI: 10.1103/PhysRevD.86.114024. arXiv: 1206.6710 [astro-ph.HE].
- [331] T. K. Gaisser, T. Stanev, and S. Tilav, “Cosmic Ray Energy Spectrum from Measurements of Air Showers,” *Front.Phys.China*, vol. 8, pp. 748–758, 2013. DOI: 10.1007/s11467-013-0319-7. arXiv: 1303.3565 [astro-ph.HE].
- [332] V. I. Zatsepin and N. V. Sokolskaya, “Three component model of cosmic ray spectra from 100-gev up to 100-pev,” *Astron. Astrophys.*, vol. 458, pp. 1–5, 2006. DOI: 10.1051/0004-6361:20065108. arXiv: astro-ph/0601475 [astro-ph].
- [333] J. R. Hoerandel, “On the knee in the energy spectrum of cosmic rays,” *Astropart. Phys.*, vol. 19, pp. 193–220, 2003. DOI: 10.1016/S0927-6505(02)00198-6. arXiv: astro-ph/0210453 [astro-ph].
- [334] G. Collin, “An estimation of systematics for up-going atmospheric muon neutrino flux at the south pole.,” <http://hdl.handle.net/1721.1/98078>, Aug. 2015.
- [335] S. Ostapchenko, “Monte Carlo treatment of hadronic interactions in enhanced Pomeron scheme: I. QGSJET-II model,” *Phys. Rev.*, vol. D83, p. 014018, 2011. DOI: 10.1103/PhysRevD.83.014018. arXiv: 1010.1869 [hep-ph].

- [336] R. S. Fletcher, T. K. Gaisser, P. Lipari, and T. Stanev, “SIBYLL: An Event generator for simulation of high-energy cosmic ray cascades,” *Phys. Rev.*, vol. D50, pp. 5710–5731, 1994. DOI: 10.1103/PhysRevD.50.5710.
- [337] AIRS / AMSU / HSB, “Version 6 level 3 product user guide, version 1.2, jet propulsion laboratory,” <http://airs.jpl.nasa.gov/>.
- [338] U. S. C. on Extension to the Standard Atmosphere, *U.S. standard atmosphere, 1976*. National Oceanic and Amospheric [sic] Administration : for sale by the Supt. of Docs., U.S. Govt. Print. Off., 1976. [Online]. Available: <https://books.google.com/books?id=x488AAAAIAAJ>.
- [339] S. S. Wilks, “The large-sample distribution of the likelihood ratio for testing composite hypotheses,” *Ann. Math. Statist.*, vol. 9, no. 1, pp. 60–62, Mar. 1938. DOI: 10.1214/aoms/1177732360. [Online]. Available: <http://dx.doi.org/10.1214/aoms/1177732360>.
- [340] G. J. Feldman and R. D. Cousins, “Unified approach to the classical statistical analysis of small signals,” *Phys. Rev. D*, vol. 57, pp. 3873–3889, 7 1998. DOI: 10.1103/PhysRevD.57.3873. [Online]. Available: <http://link.aps.org/doi/10.1103/PhysRevD.57.3873>.
- [341] F. Dydak *et al.*, “A Search for Muon-neutrino Oscillations in the Delta m**2 Range 0.3-eV**2 to 90-eV**2,” *Phys. Lett.*, vol. B134, p. 281, 1984. DOI: 10.1016/0370-2693(84)90688-9.
- [342] G. Cheng *et al.*, “Dual baseline search for muon antineutrino disappearance at $0.1\text{eV}^2 < \Delta m^2 < 100\text{eV}^2$,” *Phys. Rev.*, vol. D86, p. 052009, 2012. DOI: 10.1103/PhysRevD.86.052009. arXiv: 1208.0322.
- [343] J. S. Diaz, “Neutrinos as probes of Lorentz invariance,” *Adv. High Energy Phys.*, vol. 2014, p. 962410, 2014. DOI: 10.1155/2014/962410. arXiv: 1406.6838 [hep-ph].
- [344] D. Morgan, E. Winstanley, J. Brunner, and L. F. Thompson, “Probing quantum decoherence in atmospheric neutrino oscillations with a neutrino telescope,” *Astropart. Phys.*, vol. 25, pp. 311–327, 2006. DOI: 10.1016/j.astropartphys.2006.03.001. arXiv: astro-ph/0412618 [astro-ph].
- [345] V. D. Barger, J. G. Learned, P. Lipari, M. Lusignoli, S. Pakvasa, and T. J. Weiler, “Neutrino decay and atmospheric neutrinos,” *Phys. Lett.*, vol. B462, pp. 109–114, 1999. DOI: 10.1016/S0370-2693(99)00887-4. arXiv: hep-ph/9907421 [hep-ph].
- [346] N. Fornengo, M. Maltoni, R. Tomas, and J. W. F. Valle, “Probing neutrino nonstandard interactions with atmospheric neutrino data,” *Phys. Rev.*, vol. D65, p. 013010, 2002. DOI: 10.1103/PhysRevD.65.013010. arXiv: hep-ph/0108043 [hep-ph].